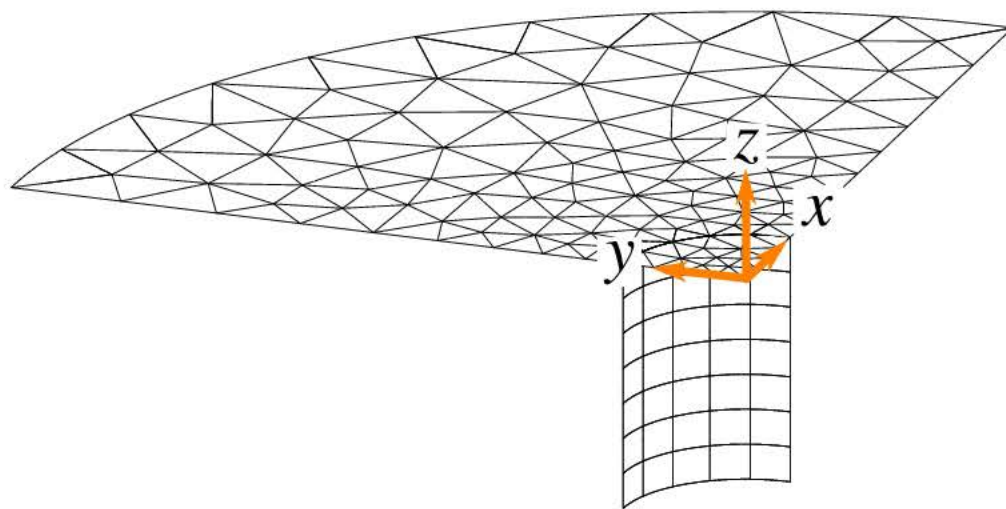# Coupled model of finite elements and boundary elements for the dynamic analysis of buried shell structures

Jacob David Rodríguez Bordón

UNIVERSIDAD DE LAS PALMAS DE GRAN CANARIA
Instituto Universitario de Sistemas Inteligentes
y Aplicaciones Numéricas en Ingeniería

EDUARDO M. RODRÍGUEZ BARRERA, CON DNI 437352427X, PROFESOR TITULAR DE UNIVERSIDAD Y SECRETARIO DEL INSTITUTO UNIVERSITARIO DE SISTEMAS INTELIGENTES Y APLICACIONES NUMÉRICAS EN INGENIERÍA (SIANI) DE LA UNIVERSIDAD DE LAS PALMAS DE GRAN CANARIA,

CERTIFICA

Que el Consejo de Doctores del Instituto Universitario de Sistemas Inteligentes y Aplicaciones Numéricas en Ingeniería (SIANI), en su sesión de fecha 8 de junio de 2017, tomó el acuerdo de dar el consentimiento para la tramitación de la Tesis Doctoral titulada *Modelo acoplado de Elementos Finitos - Elementos de Contorno para el análisis dinámico de estructuras laminares enterradas*, presentada por el doctorando D. Jacob David Rodríguez Bordón, dirigida por el Dr. D. Juan José Aznárez González, a la vista de la idoneidad y calidad de su contenido, interés y relevancia del tema.

Para que así conste, y a los efectos oportunos se expide el correspondiente certificado a 8 de junio de 2017.

Coupled model of finite elements and boundary elements for the dynamic analysis of buried shell structures

Jacob David Rodríguez Bordón

Programa de doctorado

Sistemas Inteligentes y
Aplicaciones Numéricas en Ingeniería

Director:
Juan José Aznárez González

Las Palmas de Gran Canaria, June 2017

To my parents and to María
for their daily understanding,
infinite patience and support.

I hear and I forget.
I see and I remember.
I do and I understand.
Confucius

Acknowledgements

I am highly grateful to my supervisor Prof. Juan José Aznárez for his constant encouragement, advices, patience, support and for being sometimes a shoulder to cry on during these unforgettable years. It would have been impossible to arrive at this point without his many "disquisiciones", which, in the end, are the core of this work. I am also highly grateful to Prof. Orlando Maeso for his invaluable advices, caring and support. Thank you for giving me the opportunity to be part of such an excellent research team.

I wish to thank Prof. Luis A. Padrón for his encouragement, useful advices, support, and many conversations about almost everything. I would like to thank all the wonderful people I have had the pleasure to work with at our Continuum Mechanics and Structures Division, beginning from Prof. Francisco Chirino, Prof. José María Emperador, Prof. Fidel García, and continuing with Ariel Santana, Rayco Toledo, Cristina Medina, José María Zarzalejos, Guillermo Álamo, Francisco González, Lorenzo Baños, María Castro and Román Quevedo.

I would also like to thank all the people involved in the SIANI University Institute for providing a very pleasant environment for work (and live). Especially Rafael Montenegro, José María Escobar, Gustavo Montero, David Greiner, Eduardo Barrera, Juan Ignacio González, Marina Brovka, José Iván González, Jabel Ramírez and Albert Oliver.

I would like to deeply thank Prof. Geert Lombaert for allowing me to work alongside him and his research team at KU Leuven, and for his guidance and patience. I would also like to thank Prof. Mattias Schevenels and Cedric Van hoorickx for their support and advice during the stay. My initiation on gradient-based optimisation arose from this research stay. I would like to thank the Department, especially to my friends Manthos Papadopoulos and Dimitrios Anastasopoulos for such good moments.

I would like to thank Prof. Subhamoy Bhattacharya for receiving and giving me the opportunity to be at his Department. I wish to thank Abhijith K. V., Daniele Cardente and Ioar Rivas for being a great support during my stay in Guildford.

My sincere thanks to my friend Santiago Padrón.

There is no way of expressing my gratitude to my parents, not only because they turned the light on, but they taught me a long time ago to keep it lighting against all odds.

What can I say to María? Thank you for walking beside me. I love you.

Las Palmas de Gran Canaria, June 2017.
Jacob David Rodríguez Bordón

Contents

List of Figures

List of Tables

1.1 Introduction

The role of mathematics, physics and engineering was, has been and will be crucial in the progress of the humanity. It is fascinating to see that mathematics is able to describe the physical world, and that this description facilitates the construction and operation of many extraordinary devices, machines and infrastructures. The success has been such that we are now aware of our potential to change the environment on a global scale, and that such changes may be irreversible and can potentially put in danger the humanity. Therefore, we have been forced probably for the first time to set some limits and to adapt our progress. In this sense, governments through the United Nations Framework Convention on Climate Change have been taking actions towards the stabilisation of greenhouse gas concentrations. The responsibility of the scientific community is hence to conduct research in this direction.

Computers have allowed mathematics, physics and engineering to further materialise their power, particularly through numerical methods that allow to solve the governing equations of many problems. One of the major exponents in this regard is the Finite Element Method (FEM), which has a very rich history [1] where, through the years, the collaboration of scientists of many fields have produced a numerical tool that has been used to design most of the objects that we use everyday. Another important numerical tool is the Boundary Element Method (BEM), which share many ideas with the FEM, but it has its own rich history [2–4] and its own range of applications where it excels. In the field of computational mechanics, both numerical methods have been largely used alone [5–7] but also in combination. The main advantage of the FEM is perhaps its versatility, as it can handle many problems including continuum or structural members (beams/arches, plates/shells), geometrical and material nonlinearities and anisotropy. When unbounded regions are present, however, it requires the truncation of the domain discretisation, and, in the case of wave propagation phenomena, it additionally needs some devices that help to impose the Sommerfeld radiation condition [8]. On the other hand, this is in fact the main advantage of the BEM, which, furthermore, only requires the discretisation of the boundary. Also, the BEM is capable of dealing with cracks in a very accurate and efficient manner. Therefore, they can complement each other in many applications. Already in 1977, Zienkiewicz et al. [9] recognised that the intrinsic merits of the BEM should be used together with the FEM in exterior and crack problems in order to combine the best of both worlds.

The Continuum Mechanics and Structures Division has been working on the numerical solution of wave propagation phenomena in continua for more than 20 years. The Boundary Element Method has been used to tackle many different problems of Mechanical and Civil Engineering. It was introduced in the group by Professor José Domínguez, and this has allowed having two- and three-dimensional BEM codes where multi-region problems involving regions of different nature can be handled. Related to the present thesis, it must be mentioned some previous works within the group:

- Chirino and Domínguez [10] presented a procedure for the evaluation of dynamic stress intensity factors using the sub-regioning approach with traction singular quarter-point boundary elements.

- Emperador and Domínguez [11] used an axisymmetric boundary element formulation to obtain dynamic stiffness functions of rigid foundations.

- In line with a previous work of Sáez et al. [12] for static problems, Chirino and Abascal [13] conducted static and dynamic analyses of two-dimensional cracks using the hypersingular formulation, more commonly known as the Dual Boundary Element Method (DBEM).

- Maeso, Aznárez and Domínguez [14,15] analysed the seismic behaviour of arch dams by using three-dimensional multi-region BEM models, which are inspired in a previous two-dimensional approach for the analysis of gravity dams developed by Medina and Domínguez [16].

- Maeso, Aznárez and García [17] investigated the dynamic impedances of piles and groups of piles in saturated soils.

- Padrón, Aznárez, Maeso, Medina and Santana [18–22] studied the dynamic behaviour of piled structures by using a coupled model of finite elements (pile) and boundary elements (soil). More recently, Álamo, Padrón, Aznárez, Maeso, Martínez-Castro and Gallego [23] enriched this model by using a multilayered half-space fundamental solution.

- Toledo, Aznárez, Maeso and Greiner [24,25] performed the optimisation of two-dimensional thick and thin rigid noise barriers by using Genetic Algorithms and the DBEM.

The present thesis is closely related to the work of Padrón et al. [20] in the sense that it gives a further step in the idea of modelling soil-structure problems by using a coupled boundary element and structural finite element model, but where the structure is a shell instead of a beam (pile). Figure 1.1 shows a comparison between both soil-structure ideas, on the left hand side a fully detailed geometry of a pile and a wall, while on the right hand side each simplified approach. Such models are also called mixed-dimensional models since elements of different dimensions are coupled, typically structural elements with continuum elements.

The key idea for the present soil-shell simplified model is using the DBEM to obtain the displacement and traction fields of the soil on both faces of the shell considered as a null-thickness inclusion, and coupling these to shell finite elements at the mid-surface level. This model has been called DBEM–FEM model.

(a) Soil-pile (Padrón et al. [20])

(b) Soil-shell (present research)
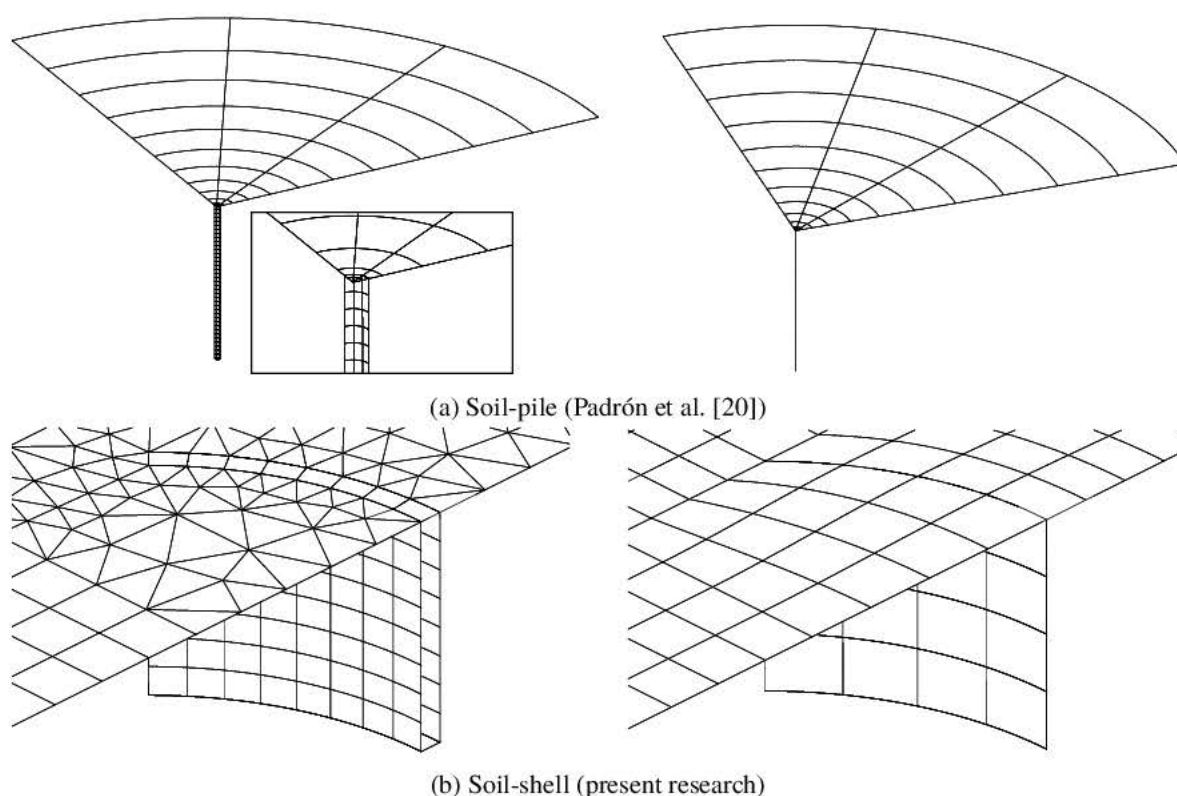
Figure 1.1: Types of soil-structure mixed-dimensional models

1.2 Aims and objectives

The aim of the present research is to formulate and implement a coupled model of finite elements and boundary elements for the dynamic analysis of soil-structure interaction problems involving structures where shell hypotheses are valid.

In order to do so, two parallel developments are required: a) formulations for the Dual Boundary Element Method, and b) shell finite element suitable for the purposes of the model. The resulting code should be able to perform the analysis of problems of seismic wave propagation phenomena of buried shell structures, dynamic response of walls and retaining structures, and dynamic characterisation (impedances and kinematic interaction) of foundations based on shell structures. The simplified methodology would ease the pre-processing stage since a fully detailed geometry of the shell structure is not required. Also, this would lead to a reduction of the number of degrees of freedom and computational resources.

On the path towards the achievement of the main objectives, there are a number of partial objectives to be considered:

1. Study of the theoretical and practical framework, which includes linear elastodynamics and poroelastodynamics, conventional boundary elements and finite elements in dynamics, and the codes already developed by the Research Team. This provides a solid foundation for the steps ahead.

2. Formulate and implement the coupled model for two-dimensional problems. The aim at this stage is to assess the possibilities of the model in a more simple setting.

3. Select the appropriate shell finite element for the purposes of the model, and formulate and implement it.

4. Formulate and implement the Dual Boundary Element Method for three-dimensional wave propagation through ideal fluids and elastic solids.

5. Formulate and implement the three-dimensional coupled model.

6. Extension of the DBEM and the coupled model for Biot's poroelastic medium.

7. Application of the developed model to the study of dynamic interaction problems involving shell structures. These include the analysis of vibration isolation problems, as well as the dynamic response of bucket foundations, which are being used as foundations of offshore wind turbines.

8. Diffusion of research results to the scientific community in the form of publications in referred journals and international conferences.

1.3 Framework. Research Project BIA2014-57640-R

The present Ph. D. Thesis is currently part of the Research Project BIA2014-57640-R supported by the Subdirección General de Proyectos de Investigación of the Ministerio de Economía y Competitividad (MINECO) of Spain and the European Regional Development Fund (ERDF) or, in Spanish, Fondo Europeo de Desarrollo Regional (FEDER). The project is entitled "Advances in the development of numerical models for the dynamic characterisation of wind turbines".

The support structures of wind turbines must be designed so that natural frequencies of the whole system are kept far enough from frequencies where the most important dynamic excitations are generated [26]. These excitations arise from rotor, rotor blades passing in front of the tower, wind and, in offshore locations, sea waves. One of the system components that involve higher level uncertainties and simplifications is the soil-foundation part, mainly in the case of deep foundations. As the number of offshore and land-based wind farms increases, the probability of being forced to install wind turbines on poorer soils gets higher. Standard shallow foundations might be unsuitable in such soils, and hence deep foundations such as piles and buckets (also called suction caissons) [27] should be considered. This is particularly true for offshore wind turbines. Figure 1.2 shows some of the types of foundation systems (foundation and submerged structure) that are considered for the installation of offshore wind turbines for shallow (below 30 meters) and moderately (between 30 and 60 meters) deep waters.

These facts explain the need for the development of computational models able to estimate, more accurately and efficiently than it is done today, the dynamic properties of the
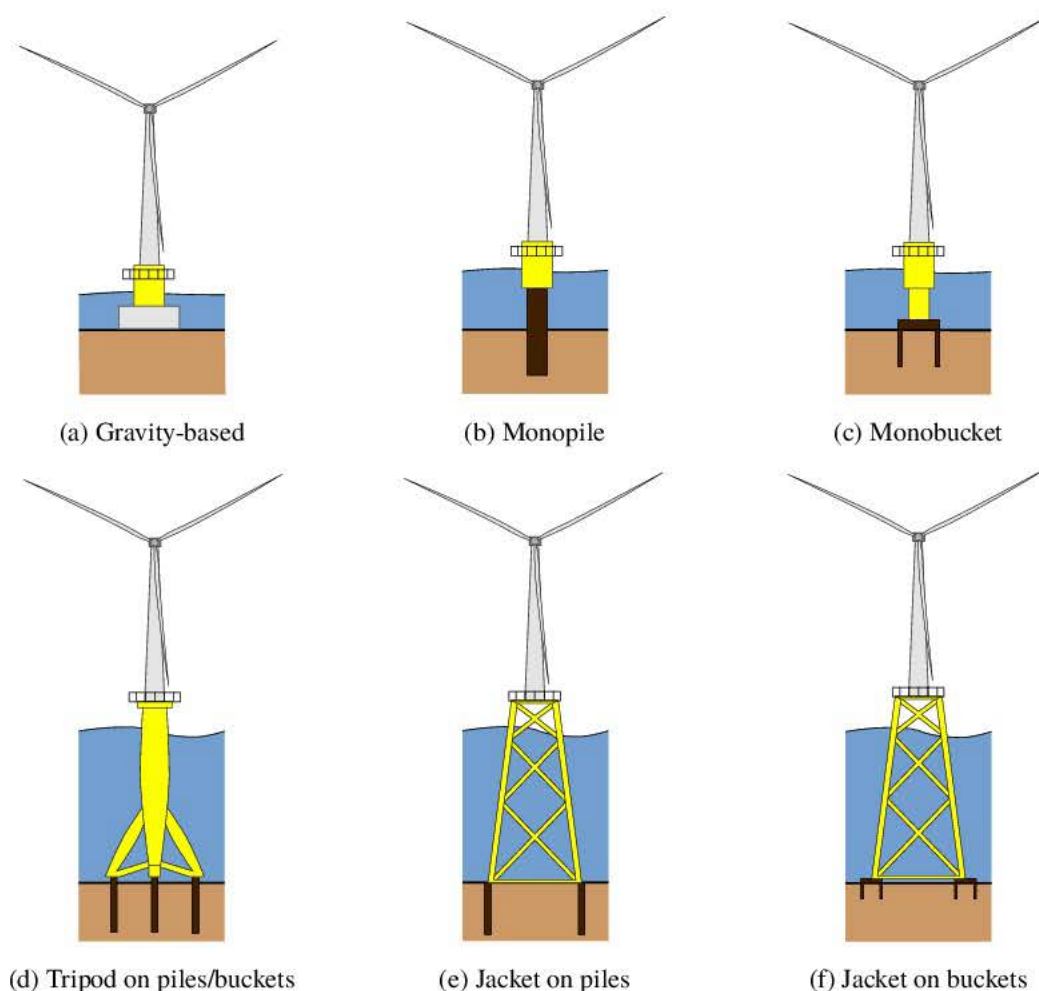
Figure 1.2: Types of foundation systems for offshore wind turbines

(a) Gravity-based   (b) Monopile   (c) Monobucket

(d) Tripod on piles/buckets   (e) Jacket on piles   (f) Jacket on buckets

above-mentioned foundations types, which will contribute to the design of safer and more op-
timised wind turbine structures with longer service lifetimes (due to lower fatigue loading),
helping to reduce the cost per unit of energy.

In order to make a contribution in this direction, the aim of the Research Project is the
development of two computational models that will allow more accurate dynamic analysis of
the two types of foundations mentioned above:

1. A model for the dynamic analysis of pile foundations in layered soils, through the de-
   velopment and implementation of a collocation methodology based on the integral for-
   mulation of the problem for the soil and making use of an advanced three-dimensional
   fundamental solution for the layered half-space.

2. A model for the dynamic analysis of buried thin flexible structures such as bucket

foundations, through the development and implementation of a dual formulation of the Boundary Element Method coupled to shell Finite Elements.

Achieving the first goal will allow the analysis of pile foundations in stratified soils without the need for meshing any soil boundaries or domains, in such a way that only the piles themselves will be discretised, using beam finite elements. This will allow to tackle problems with complex stratigraphies that are computationally unapproachable using the formulations and codes developed so far by the research team. The second goal implies the formulation and implementation of boundary element codes that make use of a dual boundary element formulation, combining the standard singular boundary integral equation for viscoelastic and poroelastic media, with its hypersingular form. This allows the numerical treatment of problems involving thin inclusions with a reduced computational cost and improved accuracy.

Both models will be used to contribute to the scientific knowledge related to the dynamic characterisation of wind turbine foundations, both land based and offshore in shallow and moderately deep waters.

1.4 Published works derived from the Ph. D. Thesis

A portion of the work done during the past four years have resulted in a number of publications and communications. These are detailed in the present section.

1.4.1 Contributions in JCR journals

- J. D. R. Bordón, J. J. Aznárez, and O. Maeso. A 2D BEM-FEM approach for time harmonic fluid-structure interaction analysis of thin elastic bodies. *Engineering Analysis with Boundary Elements*, 43:19–29, 2014

- J. D. R. Bordón, J. J. Aznárez, and O. Maeso. Two-dimensional numerical approach for the vibration isolation analysis of thin walled wave barriers in poroelastic soils. *Computers and Geotechnics*, 71:168–179, 2016

- J. D. R. Bordón, J. J. Aznárez, and O. Maeso. Dynamic model of open shell structures buried in poroelastic soils. *Computational Mechanics*, (accepted), available online on April 2017

- G. M. Álamo, J. D. R. Bordón, J. J. Aznárez, and O. Maeso. Relevance of soil-pile tangential tractions for the estimation of kinematic seismic forces: a Winkler approach. *Bulletin of Earthquake Engineering*, (under review), submitted on January 2017

1.4.2 Conference contributions

- J. D .R. Bordón, J. J. Aznárez, and O. Maeso. A 2D BEM-FEM model of thin structures for time harmonic fluid-soil-structure interaction analysis including poroelastic media. In V. Mallardo and M. H. Aliabadi, editors, *Advances in Boundary Element and Meshless Techniques XV*, pages 375–382, Florence, Italy, 15–17 July 2014

- J. D. R. Bordón, J. J. Aznárez, and O. Maeso. Three-dimensional BE–FE model of bucket foundations in poroelastic soils. In M. Papadrakakis, V. Papadopoulos, G. Stefanou, and V. Plevris, editors, *VII European Congress on Computational Methods in Applied Sciences and Engineering*, Crete Island, Greece, 5–10 June 2016. ECCOMAS

- G. M. Álamo, J. D. R. Bordón, F. García, J. J. Aznárez, L. A. Padrón, F. Chirino, and O. Maeso. Revisión de modelos numéricos para el estudio del comportamiento dinámico de cimentaciones profundas para el diseño y proyecto de aerogeneradores. In *Proceedings of 20th International Congress on Project Management and Engineering*, Cartagena, Spain, 13–15 July 2016

1.5 Structure of the dissertation

The dissertation is structured in seven chapters, where the first one is the present chapter and the last one gives the conclusions and future research. Given the relatively heterogeneous content of the dissertation, it has been chosen to give a literature review in each chapter rather than in this introductory chapter. The early chapters present the theoretical developments, then a chapter presenting some advances on the numerical treatment of boundary element integrals, and the last chapters contain the studied problems. The dissertation is complemented by several appendices, where the last one is a summary in Spanish. A more detailed description is given in the following.

The main contribution is presented in Chapter 2, where the coupled model of boundary elements and finite elements for dynamic analysis of buried shell structures is described and developed in detail. It begins reviewing the governing equations of isotropic and homogeneous ideal fluids, elastic solids and Biot's poroelastic media, which constitute the considered types of surrounding medium for the shell structures. Then, the core aspects of the Boundary Element Method for continuum mechanics relevant to the present work are developed. In this sense, the Singular, Hypersingular and Dual Boundary Integral Equations for two- and three-dimensional Biot's poroelastic medium are presented. Since the corresponding equations for ideal fluids and elastic solids can be considered as limiting cases of Biot's poroelasticity, these are not described in the text although they are used in some of the problems studied. The shell finite element formulation used for modelling the shell structure is described next. Once both ingredients have been described, the coupled model of boundary elements and finite elements (DBEM–FEM model) is presented. Finally, the boundary element formulation is validated and a convergence study of the singular and hypersingular formulations is performed. The validation of the DBEM–FEM model is performed through several problems in Chapters 5 and 6.

Chapter 3 collects the first steps to further develop the same idea for gradient-based shape optimisation. It gives an introduction to the subject of gradient-based shape optimisation, and the role of shape sensitivity analysis. Then, the Boundary Element Method for shape sensitivity analysis of scalar and elastic media in a two-dimensional multi-region setting is described. The aim of this chapter is to describe this formulation, which is later used in Chapter 5.

Chapter 4 studies the problem of numerical integration in the context of the Boundary Element Method, and describes the strategies used in the present work. Some advances on the integration of weakly singular and nearly singular integrals are presented.

Chapter 5 collects the study of several problems related to wave barriers. In the first place, a problem of flexible noise barriers is addressed, which makes use of the DBEM–FEM model in its simpler fashion. Several multi-edge noise barriers made of different materials are studied. Also, a parametric fluid-structure interaction study is performed in order to assess the relevance of using a fully coupled model in situations where simplifying hypotheses may be used. The second problem is the study of two-dimensional wave barriers in poroelastic soils. The effects of different poroelastic properties on the amplitude reduction ratio are studied for several wave barrier topologies: open trench, simple barrier and open trench-wall. The third problem is a three-dimensional curved wave barrier in a poroelastic soil, whose aim is studying the applicability of the DBEM–FEM model regarding near- and far-field variables, and also its performance when compared to multi-region BEM models. Finally, the methodology developed in Chapter 3 is used for optimising single and double wall barriers in elastic soils.

In Chapter 6, the three-dimensional DBEM–FEM model is used to study the impedances of bucket foundations. It begins with a general overview of bucket foundations and its applicability to offshore wind turbines. Then, a comparison against already published results regarding impedances of bucket foundations in elastic soils is made. Lastly, the impedances of bucket foundations buried in several poroelastic soils are studied, and the relevance of the hydraulic conductivity in this problem is analysed.

Finally, a summary with the most relevant conclusions derived from the present work is given in Chapter 7. Also, a number of recommendations for future research in the short- and medium-term are pointed out.

Following the main text, there are several appendices supporting the content of the main text with auxiliary material. In particular, the last appendix contains a summary of the dissertation in Spanish.

The document concludes with a section with the bibliographic references arranged by order of appearance in the main text.

2.1 Introduction

The Finite Element Method (FEM) and the Boundary Element Method (BEM) are well known numerical methods that can handle a wide variety of problems [5, 7]. Nevertheless, there are problems where neither of those methods is capable of solving these problems in an efficient manner. The main advantages of the FEM are its versatility in handling a huge collection of problems that may include structural members (beams, arches, plates, shells), nonlinearities, anisotropy and many other aspects, and its ability to manage large-scale problems. However, when unbounded domains are present in a wave propagation problem, it requires a truncation of the volume mesh and the presence of some absorbing device that allow to impose the Sommerfeld radiation condition [8]. Although this has been acceptably solved by Perfectly Matched Layers [35], the BEM is more appealing as it requires only the discretisation of surfaces and it intrinsically satisfies the radiation condition. The BEM has other disadvantages such as a more involved mathematical formulation and implementation, and more memory and time computational complexity than the FEM. The latter disadvantage can be overcome by using different techniques such as the Fast Multipole Method [36], the Panel Clustering Method [37], or methods based on hierarchical matrices [38].

In the present research, both numerical methods are combined in order to efficiently solve two- and three-dimensional linear Fluid-Structure and Soil-Structure Interaction problems, where the fluid is ideal, the soil can be an isotropic and homogeneous elastic solid or a Biot poroelastic medium [39], and the structure is an elastic shell structure immersed or buried in such types of surrounding media.

A buried open shell structure is characterised by being in contact with the same surrounding region on both faces of the shell. On the other hand, a buried closed shell structure, such as a tunnel or a box-like structure, is in contact with different regions on each side of the shell. In both cases, a conventional multi-region BEM approach can be used to deal with the soil and the structure, e.g. [6, 14, 17], but undoubtedly the structure would be more easily handled if treated by the FEM. In the case of closed shell structures, conventional multi-region BEM coupled with shell finite elements can be used [40]. In the case of open shell structures, it can still be used by artificially transforming them into closed ones. However, fictitious (non-physical) interfaces must be created, see e.g. [41], unnecessarily increasing the number of degrees of freedom. In order to obtain a direct and efficient model, we propose a BEM–FEM model where the key idea is using the Dual BEM (DBEM) [42–44], which is more commonly used in crack analysis, to treat the interaction between the shell and its surrounding media. Thus, the proposed model is denoted as DBEM–FEM model.

The rest of the chapter is organised as follows. In Section 2.2, the basic equations of the types of media considered in this work are described. In Section 2.3, the main aspects of the Boundary Element Method are described, and in particular, the Singular, Hypersingular and Dual Boundary Integral Equations for two- and three-dimensional Biot's poroelasticity are derived. The modelling of the shell structure is described in Section 2.4, and the DBEM–FEM model is described in Section 2.5.

2.2 Basic equations

In this section, the basic equations for the time harmonic analysis of mechanical wave propagation phenomena in different types of continua are described. Since the derivation of these equations can be found in many references, a concise presentation is given. It serves as a starting point regarding notation and general assumptions omitted in the rest of the text in order to avoid repetition.

2.2.1 Generalities

Let $\Omega \subseteq \mathbb{R}^{N_d}$ ($N_d = 2, 3$) be the domain (finite, semi-infinite or infinite) of interest where a mechanical wave propagation phenomenon is taking place. The symbol Γ denotes the boundary of the domain, i.e. $\Gamma = \partial\Omega$, and its orientation is defined by the outward unit normal vector $\mathbf{n}$. In a more general setting, the domain Ω is composed by N_R regions $\Omega = \cup_{r=1}^{N_R}\Omega_r | \Omega_j \cap \Omega_k = \varnothing, j \neq k$. Also, a set of N_B boundaries/interfaces is defined $B = \{\Gamma_b | b = 1, \ldots, N_B | \Gamma_j \cap \Gamma_k = \varnothing, j \neq k\}$. Thus, the boundary of each region Ω_r can be defined from a subset $B_r \subseteq B$ as $\partial\Omega_r = \cup_{b \in B_r}(\pm\Gamma_b) | \Gamma_j \cap \Gamma_k = \varnothing, j \neq k$, where $\pm\Gamma_b$ denotes the required positive or negative orientation of Γ_b in order to have an outward unit normal vector with respect to Ω_r.

Figure 2.1 shows the types of boundaries and interfaces that are considered here. Figures 2.1a and 2.1b depict an ordinary boundary and interface, respectively. In the former case, a Neumann, Dirichlet or Robin boundary condition must be imposed. In the latter case, a contact condition between both regions must be established, typically a welded interface or a smooth interface. Figures 2.1c depicts a crack where, given the small distance between both faces, edges can be collapsed (crack tip or front) and the geometrical location of both faces can be considered coincident when modelling it (crack bottom and top surfaces). Depending on the real physical situation, each face can be treated as an ordinary boundary where some boundary condition is established. On the other hand, there may be situations where both faces are treated as an interface where some contact conditions are defined. The DBEM–FEM model proposed in this work exploits this peculiarity in order to give mass and stiffness to the crack by coupling these faces to a shell finite element.

The mechanical behaviour of each region Ω_r is modelled according to the materials from which they are made of, and the excitation levels, among others factors. In the present work, only linear models of fluids, elastic solids and porous media are considered, whose basic equations are described in the following sections.

2.2.2 Ideal fluid

The propagation of small-amplitude mechanical waves through a homogeneous compressible fluid with negligible viscosity and isotropic linear elastic behaviour (ideal fluid) is governed by the Helmholtz partial differential equation. The governing equations can be derived from physical principles, which is common in the field of Acoustics, see e.g. [45,46], but also from elastodynamics, see e.g. [47]. In the time domain, the governing equation can be written in terms of the dynamic pressure $p = p(\mathbf{x}, t)$, which is defined positive in compression ($\sigma_{ij} =$

$$\partial\Omega_r = \ldots \cup \Gamma_b \cup \ldots$$

(a) Ordinary boundary

$$\partial\Omega_s = \ldots \cup (-\Gamma_b) \cup \ldots$$
$$\partial\Omega_r = \ldots \cup \Gamma_b \cup \ldots$$

(b) Ordinary interface

$$w \ll l \qquad \longrightarrow \qquad w = 0$$
$$\partial\Omega_r = \ldots \cup \Gamma_b^+ \cup \Gamma_b^- \cup \Gamma_b^e \cup \ldots \qquad \partial\Omega_r = \ldots \cup \Gamma_b \cup \ldots$$

(c) Crack-like boundary/interface idealisation
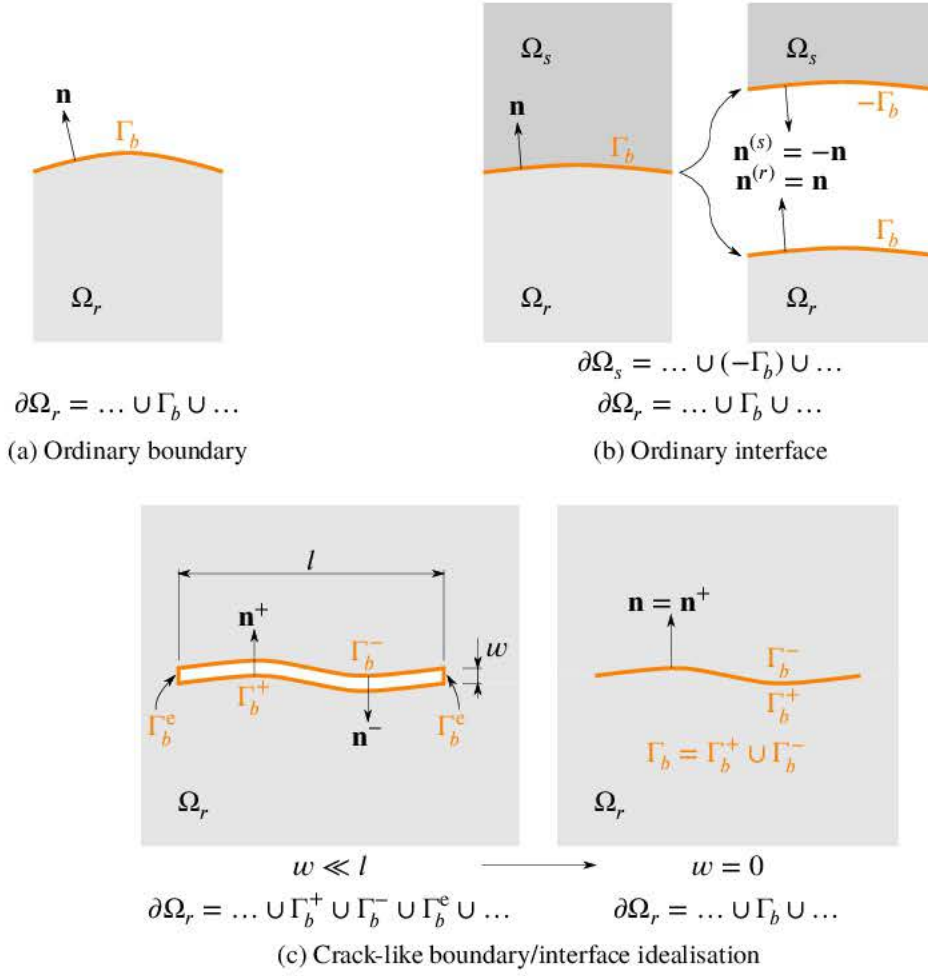
Figure 2.1: Types of boundaries/interfaces

$-p\delta_{ij}$), as primary variable:

$$\nabla^2 p - \nabla \cdot \mathbf{X}' = \frac{1}{c^2}\ddot{p} \tag{2.1}$$

where $\mathbf{X}' = \mathbf{X}'(\mathbf{x}, t)$ is the body load vector, $c = \sqrt{K_f/\rho}$ is the wave propagation velocity, K_f is the fluid bulk modulus and ρ is the fluid density. Assuming a time variation $\exp(i\omega t)$, where ω is the circular frequency, then $p = p(\mathbf{x}, t) = p(\mathbf{x}, \omega) \cdot \exp(i\omega t)$, and the time harmonic governing equation becomes:

$$\nabla^2 p + k^2 p = \nabla \cdot \mathbf{X}' \tag{2.2}$$

where $k = \omega/c$ is the wavenumber. In the following, $\exp(i\omega t)$ is omitted onwards when writing equations in the frequency domain for the sake of brevity. Likewise, variables should be understood as position and frequency dependent. The stress-strain relationship is:

$$p = -K_f \nabla \cdot \mathbf{U} \tag{2.3}$$

where $\mathbf{U} = \mathbf{U}(\mathbf{x}, \omega)$ is the fluid displacement. The secondary variable can be chosen as the pressure flux $q = q(\mathbf{x}, \omega)$:

$$q = \nabla p \cdot \mathbf{n} = \frac{\partial p}{\partial n} \tag{2.4}$$

or as the normal displacement $U_n = U_n(\mathbf{x}, \omega)$:

$$U_n = \frac{1}{\rho \omega^2} \frac{\partial p}{\partial n} \tag{2.5}$$

The solution of a boundary value problem containing an ideal fluid region requires appropriate boundary and interface conditions resulting in a well-posed problem. These are given in terms of prescribed pressures p (Dirichlet boundary conditions), pressure fluxes q or normal displacements U_n (Neumann boundary conditions), or relationships between pressure and pressure flux $q = q(p)$ or normal displacements $U_n = U_n(p)$ (Robin boundary conditions). Also, if the region is in contact with another region, an interface contact condition must be defined. In the case two ideal fluid regions are in perfect contact, say Ω_s and Ω_r are in contact through an interface Γ_b, the interface conditions at Γ_b are:

$$\text{Compatibility: } \mathbf{U}^{(r)} \cdot \mathbf{n}^{(r)} = \mathbf{U}^{(s)} \cdot \mathbf{n}^{(s)} \Rightarrow U_n^{(r)} = -U_n^{(s)} \tag{2.6a}$$

$$\text{Equilibrium: } - p^{(r)} \mathbf{n}^{(r)} - p^{(s)} \mathbf{n}^{(s)} = \mathbf{0} \Rightarrow p^{(r)} - p^{(s)} = 0 \tag{2.6b}$$

The first condition establishes equal normal displacements of both regions throughout the interface, and the second condition establishes the equilibrium of tractions.

2.2.3 Elastic solid

The propagation of small-amplitude mechanical waves through an isotropic, homogeneous and linear elastic solid is governed by Navier's system of partial differential equations, which can be written in the time domain as [47]:

$$\mu \nabla^2 \mathbf{u} + (\lambda + \mu) \nabla (\nabla \cdot \mathbf{u}) + \mathbf{X} = \rho \ddot{\mathbf{u}} \tag{2.7}$$

where $\mathbf{u} = \mathbf{u}(\mathbf{x}, t)$ is the displacement vector (primary variable), $\mathbf{X} = \mathbf{X}(\mathbf{x}, t)$ is the body load vector, λ and μ are respectively Lamé's first parameter and Lamé's second parameter (or shear modulus), and ρ is the density. The stress-strain relationship (Hooke's law) is:

$$\sigma_{ij} = \delta_{ij} \lambda \epsilon_{kk} + 2\mu \epsilon_{ij} \tag{2.8}$$

where σ_{ij} is the stress tensor and $\epsilon_{ij} = (u_{i,j} + u_{j,i})/2$ is the strain tensor. The traction vector $t_i = \sigma_{ij} n_j$ is the secondary variable. Assuming a time variation $\exp(i\omega t)$, the time harmonic governing equation becomes:

$$\mu \nabla^2 \mathbf{u} + (\lambda + \mu) \nabla (\nabla \cdot \mathbf{u}) + \mathbf{X} = -\rho \omega^2 \mathbf{u} \tag{2.9}$$

This equation can be decoupled via Helmholtz decomposition (displacement potentials) [47], or taking divergence and curl of the equation and expressing them respectively in terms of

dilation $\epsilon = \nabla \cdot \mathbf{u}$ and rotation $\boldsymbol{\omega} = \nabla \times \mathbf{u}$, see e.g. [48]. Decoupling process gives rise to one scalar and one vector wave equation, which, in the absence of body loads, can be respectively written as:

$$\nabla^2 \epsilon + k_{\mathrm{P}}^2 \epsilon = 0 \tag{2.10a}$$

$$\nabla^2 \boldsymbol{\omega} + k_{\mathrm{S}}^2 \boldsymbol{\omega} = 0 \tag{2.10b}$$

where $k_{\mathrm{P}} = \omega/c_{\mathrm{P}}$ is the wavenumber of the scalar wave equation governing the propagation of irrotational/dilatational P (primary) waves which have phase velocity $c_{\mathrm{P}} = \sqrt{(\lambda + 2\mu)/\rho}$, and $k_{\mathrm{S}} = \omega/c_{\mathrm{S}}$ is the wavenumber of the vector wave equation governing the propagation of divergence-free/equivolumial S (secondary) waves which have phase velocity $c_{\mathrm{S}} = \sqrt{\mu/\rho}$. These are the two types of body waves present in this type of medium.

The solution of a boundary value problem containing an elastic solid region requires appropriate boundary and interface conditions that produce a well-posed problem [48, 49]. Boundary conditions are given in terms of prescribed displacements $\mathbf{u}$ (Dirichlet boundary conditions), tractions $\mathbf{t}$ (Neumann boundary conditions), or even an impedance kind of relationship between tractions and displacements $\mathbf{t} = \mathbf{t}(\mathbf{u})$ (Robin boundary conditions). If the region is in contact with another region, an interface contact condition must be defined. In the case two elastic regions are in contact, say Ω_r and Ω_s are in contact through an interface Γ_b, the bonded or welded interface conditions at Γ_b are simply:

$$\text{Compatibility: } \mathbf{u}^{(r)} = \mathbf{u}^{(s)} \tag{2.11a}$$

$$\text{Equilibrium: } \mathbf{t}^{(r)} + \mathbf{t}^{(s)} = \mathbf{0} \tag{2.11b}$$

In the case an elastic region Ω_r and an ideal fluid region Ω_s are in contact through an interface Γ_b, interface conditions at Γ_b are:

$$\text{Compatibility: } \mathbf{u}^{(r)} \cdot \mathbf{n}^{(s)} = \mathbf{U}^{(s)} \tag{2.12a}$$

$$\text{Equilibrium: } \mathbf{t}^{(r)} - p^{(s)} \mathbf{n}^{(s)} = \mathbf{0} \tag{2.12b}$$

2.2.4 Biot's poroelastic medium

The theory of poroelasticity presented by Biot [39] is able to model the propagation of small-amplitude mechanical waves in a two-phase medium consisting of an elastic solid frame saturated by a compressible viscous fluid. The governing equations in the time domain for the isotropic case can be written as:

$$\mu \nabla^2 \mathbf{u} + \nabla \left[N \left(\nabla \cdot \mathbf{u} \right) + Q \left(\nabla \cdot \mathbf{U} \right) \right] + \mathbf{X} = \rho_{11} \ddot{\mathbf{u}} + \rho_{12} \ddot{\mathbf{U}} + b \left(\dot{\mathbf{u}} - \dot{\mathbf{U}} \right) \tag{2.13a}$$

$$\nabla \left[Q \left(\nabla \cdot \mathbf{u} \right) + R \left(\nabla \cdot \mathbf{U} \right) \right] + \mathbf{X}' = \rho_{12} \ddot{\mathbf{u}} + \rho_{22} \ddot{\mathbf{U}} - b \left(\dot{\mathbf{u}} - \dot{\mathbf{U}} \right) \tag{2.13b}$$

and the stress-strain relationships as:

$$\tau_{ij} = \delta_{ij} \left[(N - \mu) \left(\nabla \cdot \mathbf{u} \right) + Q \left(\nabla \cdot \mathbf{U} \right) \right] + \mu \left(u_{i,j} + u_{j,i} \right) \tag{2.14a}$$

$$\tau = Q \left(\nabla \cdot \mathbf{u} \right) + R \left(\nabla \cdot \mathbf{U} \right) \tag{2.14b}$$

where $N = \lambda + \mu + Q^2/R$, $i,j = 1, \ldots, N_d$, u_i and τ_{ij} are respectively the displacements and stresses of the solid phase, U_i and τ the displacements and equivalent stress of the fluid phase, and $\mathbf{X}$ and $\mathbf{X}'$ the body loads of solid and fluid phases. The material properties λ and μ are the Lamé's parameters of the solid phase, Q and R are the Biot's coupling parameters, b is the dissipation constant, and $\rho_{11} = (1 - \phi)\rho_s + \rho_a$, $\rho_{12} = -\rho_a$, $\rho_{22} = \phi\rho_f + \rho_a$, being ϕ the porosity, ρ_s the solid phase density, ρ_f the fluid phase density, and ρ_a the additional apparent density. The dissipation constant b is related to the hydraulic conductivity k by the relationship $b = \rho_f g \phi^2/k$, where g is the gravitational acceleration [50]. The fluid equivalent stress is related to the dynamic pressure by $\tau = -\phi p$. Assuming a time variation $\exp(i\omega t)$, Equations (2.13a-2.13b) become:

$$\mu \nabla^2 \mathbf{u} + \nabla \left[N \left(\nabla \cdot \mathbf{u} \right) + Q \left(\nabla \cdot \mathbf{U} \right) \right] + \mathbf{X} = -\omega^2 \left(\hat{\rho}_{11} \mathbf{u} + \hat{\rho}_{12} \mathbf{U} \right) \tag{2.15a}$$

$$\nabla \left[Q \left(\nabla \cdot \mathbf{u} \right) + R \left(\nabla \cdot \mathbf{U} \right) \right] + \mathbf{X}' = -\omega^2 \left(\hat{\rho}_{12} \mathbf{u} + \hat{\rho}_{22} \mathbf{U} \right) \tag{2.15b}$$

where $\hat{\rho}_{11} = \rho_{11} - ib/\omega$, $\hat{\rho}_{22} = \rho_{22} - ib/\omega$ and $\hat{\rho}_{12} = \rho_{12} + ib/\omega$. By considering the Helmholtz decomposition:

$$\mathbf{u} = \nabla \varphi_1 + \nabla \times \boldsymbol{\psi}_1 \tag{2.16}$$

$$\mathbf{U} = \nabla \varphi_2 + \nabla \times \boldsymbol{\psi}_2 \tag{2.17}$$

and considering null body loads, two decoupled sets of two equations are obtained from Equations (2.15a-2.15b):

$$\varphi_1, \varphi_2 \begin{cases} (N + \mu) \nabla^2 \varphi_1 + Q \nabla^2 \varphi_2 = -\omega^2 \left(\hat{\rho}_{11} \varphi_1 + \hat{\rho}_{12} \varphi_2 \right) \\ Q \nabla^2 \varphi_1 + R \nabla^2 \varphi_2 = -\omega^2 \left(\hat{\rho}_{12} \varphi_1 + \hat{\rho}_{22} \varphi_2 \right) \end{cases} \tag{2.18}$$

$$\boldsymbol{\psi}_1, \boldsymbol{\psi}_2 \begin{cases} \mu \nabla^2 \boldsymbol{\psi}_1 = -\omega^2 \left(\hat{\rho}_{11} \boldsymbol{\psi}_1 + \hat{\rho}_{12} \boldsymbol{\psi}_2 \right) \\ 0 = -\omega^2 \left(\hat{\rho}_{12} \boldsymbol{\psi}_1 + \hat{\rho}_{22} \boldsymbol{\psi}_2 \right) \end{cases} \tag{2.19}$$

The first set is related with a irrotational/dilatational P (primary) displacement field due to scalar potentials φ_1 (solid phase) and φ_2 (fluid phase), and the second set with a divergence-free/equivolumial S (secondary) displacement field due to vector potentials $\boldsymbol{\psi}_1$ (solid phase) and $\boldsymbol{\psi}_2$ (fluid phase). If a plane wave propagating along $+x_1$ is considered $\varphi_i = P_i \exp(-ik_P x_1)$, then P modes are obtained from:

$$P_1, P_2 \begin{cases} \left[\omega^2 \hat{\rho}_{11} - k_P^2 (N + \mu) \right] P_1 + \left[\omega^2 \hat{\rho}_{12} - k_P^2 Q \right] P_2 = 0 \\ \left[\omega^2 \hat{\rho}_{12} - k_P^2 Q \right] P_1 + \left[\omega^2 \hat{\rho}_{22} - k_P^2 R \right] P_2 = 0 \end{cases} \tag{2.20}$$

where wavenumber k_P is obtained from the characteristic equation:

$$k_P = \pm \sqrt{\frac{a_1 \pm \sqrt{a_1^2 - 4a_0}}{2}}, \quad a_0 = \omega^4 \frac{\hat{\rho}_{11} \hat{\rho}_{22} - \hat{\rho}_{12}^2}{R(\lambda + 2\mu)} \tag{2.21}$$

$$a_1 = \omega^2 \left(\frac{\hat{\rho}_{22}}{R} + \frac{\hat{\rho}_{11} + \hat{\rho}_{22} Q^2/R^2 - \hat{\rho}_{12} 2Q/R}{\lambda + 2\mu} \right)$$

where two of the solutions are relevant incoming waves ($\mathrm{Re}(k_\mathrm{P}) > 0$). Hence, two P modes exist: the wavenumber associated with the fastest wave speed is k_P1, while the wavenumber associated with the slowest wave speed is k_P2. If a plane wave propagating along $+x_1$ is considered $\boldsymbol{\psi}_i = \mathbf{S}_i \exp(-ik_\mathrm{S}x_1)$, then the S mode is obtained from:

$$\mathbf{S}_1, \mathbf{S}_2 \begin{cases} \left[\omega^2 \hat{\rho}_{11} - k_\mathrm{S}^2 \mu\right] \mathbf{S}_1 + \omega^2 \hat{\rho}_{12} \mathbf{S}_2 = \mathbf{0} \\ \omega^2 \hat{\rho}_{12} \mathbf{S}_1 + \omega^2 \hat{\rho}_{22} \mathbf{S}_2 = \mathbf{0} \end{cases} \tag{2.22}$$

and the wavenumber k_S is obtained from the characteristic equation:

$$k_\mathrm{S} = \pm\omega \sqrt{\frac{\hat{\rho}_{11} - \hat{\rho}_{12}^2/\hat{\rho}_{22}}{\mu}} \tag{2.23}$$

where only one solution is a relevant incoming wave ($\mathrm{Re}(k_S) > 0$). Biot theory of poroelasticity was experimentally confirmed by Plona [51, 52], who detected P2 waves for the first time.

The solution of a boundary value problem containing a Biot poroelastic region requires the appropriate boundary and interface conditions that lead to a well-posed problem. The conditions for solution uniqueness were derived by Biot [53] and Deresiewicz and Skalak [54], which lead to a set of possible boundary and interface conditions. Despite there has been some debate [55, 56] regarding the validity of interface conditions formulated by Deresiewicz and Skalak [54], these remain valid and hence widely used. Boundary and interface conditions vary from open-pore (permeable) to closed-pore (impervious or impermeable), and also the intermediate case of partially open pores.

2.3 Boundary Element Method for continua

The Boundary Element Method is nowadays used in many areas of the industry where its advantages are exploited. The effort of numerous researchers and developers has allowed the BEM to be a well established methodology [2–4]. In particular, the BEM is widely used in Noise Propagation and Soil-Structure Interaction problems [6, 7], where the presence of unbounded domains is very naturally treated.

The main ingredients of the BEM are the Boundary Integral Equations (BIE), which, after a proper discretisation, are used to build a solvable linear system of equations where often only boundary values are unknown. BIEs can be obtained from several starting points, typically from a weighted residual formulation of governing equations or directly from reciprocity relationships [6, 7, 57]. Then, the solution of the governing equation for a point load (collocation point), i.e. the fundamental solution or Green's function, allows removing domain integrals. Some domain integrals remain when body loads are involved, but they can later be transformed into boundary integrals by using the Dual Reciprocity Method [58]. Since detailed derivations of Singular BIEs for the types of media considered in this work can be found elsewhere, e.g. [6, 7, 59], the starting point in the present text is directly the Singular BIE for interior collocation points. In particular, we discuss the regularisation of the Singular BIE and the derivation and regularisation of the Hypersingular BIE when the collocation

point is a boundary point, for two- and three-dimensional Biot's poroelastic medium. We use the approach of Sáez, Gallego and Domínguez [12, 60] in 2D and Ariza, Gallego and Domínguez [61, 62] in 3D, who solved the regularisation for potential and elastic problems. Our final goal is obtaining the Dual BIEs [42] for Biot poroelasticity, which are used for treating crack-like boundaries and eventually in the proposed DBEM-FEM model.

2.3.1 Boundary Integral Equations

Let $\mathbf{x}^i \in \Omega$ be an interior collocation point, then a Boundary Integral Equation relates the value of a variable $\mathbf{f}$ (dynamic pressure, displacement, strain tensor or other meaningful one) at the collocation point $\mathbf{x}^i$, i.e. $\mathbf{f}^i = \mathbf{f}(\mathbf{x}^i)$, as a function of the values of primary and secondary variables along boundaries $\Gamma = \partial\Omega$, and, if present, body loads throughout the region Ω:

$$\mathbf{f}^i = \int_\Gamma (\dots)\, d\Gamma + \int_\Omega (\dots)\, d\Omega \tag{2.24}$$

In this case, the evaluation of the BIE usually presents no major mathematical difficulties since all boundary integrals are non-singular and Riemann integrable despite their integrands actually contain singular functions (the fundamental solution and derivatives). When proper body loads are present, i.e. volume loads in 3D problems or surface loads in 2D problems, domain integrals are singular but Riemann integrable (at least in the range of BIEs treated in this work). When the collocation point is an exterior point ($\mathbf{x}^i \notin \Omega$), the Boundary Integral Equation simply relates the values of primary and secondary variables along boundaries Γ, and, if present, body loads throughout the region Ω:

$$\mathbf{0} = \int_\Gamma (\dots)\, d\Gamma + \int_\Omega (\dots)\, d\Omega \tag{2.25}$$

When the collocation point is near the boundary (distance$(\mathbf{x}^i, \Gamma) \ll 1$), numerical difficulties related to the accurate evaluation of boundary integrals appear because singularities are near the integration domain. This is further discussed in Chapter 4. When the collocation point is a boundary point ($\mathbf{x}^i \in \Gamma$), boundary integrals contain singularities which may lead to non-Riemann-integrable integrals. Solving this difficulty is usually the crucial step in any BEM formulation. This process is commonly called regularisation, and there are many techniques to address it. Tanaka, Sladek and Sladek [63] offer a comprehensive review (up to 1994) about regularisation techniques.

The term "Boundary Integral Equation (BIE)" is often accompanied by some adjectives or prefixes that try to emphasise some aspects of it and to be self-explanatory. However, the terminology may sometimes be confusing and not consistent, hence some discussion is given here. Probably, the most widespread adjectives are related to the most severe kind of singularity the BIE can have: weakly singular (or regularised) BIE, strongly singular (or Singular) BIE (SBIE), and Hypersingular BIE (HBIE). Other widespread prefixes refer to the variable associated to the BIE: Displacement BIE (DBIE) or u-BIE, flux or Traction BIE (TBIE) or q-BIE , tangential flux or traction BIE or q_t-BIE, and others. There is a somewhat widespread convention in the BEM community, although it is not always consistent. The

SBIE corresponds to the BIE related to the primary variable (potential, displacement), and, since it is the most used one, it is also often called Conventional BIE (CBIE). The HBIE corresponds to the BIE related to the secondary variable (normal flux, normal traction). Note that this convention holds despite the actual BIE is not singular or hypersingular when the collocation point is an interior point. In this sense, it seems more appropriate to use the variable of the BIE as a prefix. Nevertheless, the convention (SBIE, HBIE) is assumed in the present work.

By differentiating the SBIE with respect to the coordinates of the collocation point, it is possible to build other BIEs that allow obtaining other variables of interest at the collocation point. A very important one is the BIE obtained after applying the constitutive law, which allows obtaining the secondary variable, i.e. the HBIE. Another useful one is the HBIE for calculating the tangential flux or traction [64–66].

Both the SBIE and the HBIE can be used together in order to overcome some difficulties that may appear if only the SBIE or the HBIE is used. When using the SBIE or the HBIE to solve some exterior problems, the uniqueness of the solution is not guaranteed, and it turns out that this happens at the resonant frequencies of a complementary interior problem. A solution of this issue was offered by Burton and Miller [67], which proposed to add appropriately the SBIE and the HBIE to build a new kind of BIE which guarantees uniqueness. Another difficult situation arises when dealing with a region that have a nearly or totally degenerate geometry which encloses very small or no area or volume. This is the situation of crack-like geometries, where exclusively using the SBIE or the HBIE lead to linear system of equations with very bad conditioning, or even singular in the case of a completely degenerate geometry, i.e. an idealised crack-like boundary. This is due to the relative closeness or even identical locations of collocation points along the degenerate geometry. For idealised crack-like, it was Hong and Chen [42] who apparently first proposed the simultaneous use of the SBIE and the HBIE for solving this degeneracy, leading to a new pair of BIEs called Dual BIEs (DBIEs). This is achieved because both are linearly independent, and hence, despite the primary and secondary variables of both crack faces are geometrically coincident, the same number of unknowns and linearly independent equations is obtained.

2.3.2 SBIE, HBIE and DBIEs for Biot's poroelastic media

In the context of Biot poroelasticity, several BIEs have been proposed [68–73], which, among other aspects, differ from each other in the selection of the variables. The pore pressure p is often used instead of the fluid equivalent stress (or fluid partial stress) τ, being both related by $\tau = -\phi p$. Likewise, the specific fluid flux $\mathbf{q} = -\phi(\dot{\mathbf{u}} - \dot{\mathbf{U}})$ or the specific normal fluid flux $q_n = \mathbf{q} \cdot \mathbf{n}$ is often used instead of the fluid displacements $\mathbf{U}$ or the normal displacement $U_n = \mathbf{U} \cdot \mathbf{n}$. The choice is a matter of preference or convenience.

The Singular BIE (SBIE) proposed by Domínguez [70] is especially advantageous here as it uses a reduced set of four variables (fluid normal displacement U_n, fluid equivalent stress τ, solid displacements $\mathbf{u}$ and solid tractions $\mathbf{t}$) that leads to simple coupling equations, as it will be seen later in Equations (2.134-2.135). Domínguez [74] presented the corresponding BEM for two-dimensional problems, while Maeso et al. [14, 17] extended it for three-dimensional problems. Another advantage is that, as done in [17], the fundamental solution can be written

in a way that resembles the fundamental solutions of acoustics and elastodynamics, which eases later developments by identifying similar terms. In fact, this strategy is particularly useful in this work for presenting fully regularised two- and three-dimensional Hypersingular BIE (HBIE) and Dual BIEs (DBIEs) for Biot poroelasticity valid for curved elements.

The regularisation process of these is an application of the developments done in the works of Sáez, Gallego and Domínguez [12] for the two-dimensional problem and Domínguez, Ariza and Gallego [61] for the three-dimensional problem, which deal with potential and elastic problems. The two-dimensional procedure explicitly reduces all strongly singular and hypersingular line integrals to regular integrals and analytical terms by using a careful interpretation of some geometrical terms. The three-dimensional procedure explicitly reduces all strongly singular and hypersingular surface integrals to weakly singular surface integrals and line integrals by making use of some specific vector identities and the Stokes' theorem. Unlike the approach of Guiggiani et al. [75,76], it is all performed in the physical space rather than in the reference space. For three-dimensional Biot poroelasticity, we must mention the work of Messner and Schanz, who had already presented a regularised HBIE for collocation BEM [72] and Galerkin BEM [73] following a similar philosophy.

2.3.2.1 Two-dimensional problem

Singular Boundary Integral Equation   Let Ω be a given region, and $\Gamma = \partial\Omega$ its boundary with outward unit normal $\mathbf{n}$. Using the weighted residual formulation proposed by Domínguez [74], the SBIE for a collocation point $\mathbf{x}^i \notin \Gamma$ can be written as:

$$\delta_\Omega^i \begin{bmatrix} J & 0 \\ 0 & \delta_{lk} \end{bmatrix} \begin{Bmatrix} \tau^i \\ u_k^i \end{Bmatrix} + \int_\Gamma \begin{bmatrix} -(U_{n00}^* + J X_j^{'*} n_j) t_{0k}^* & \tau_{0k}^* \\ -U_{nl0}^* & t_{lk}^* \end{bmatrix} \begin{Bmatrix} \tau \\ u_k \end{Bmatrix} \mathrm{d}\Gamma = \int_\Gamma \begin{bmatrix} -\tau_{00}^* & u_{0k}^* \\ -\tau_{l0}^* & u_{lk}^* \end{bmatrix} \begin{Bmatrix} U_n \\ t_k \end{Bmatrix} \mathrm{d}\Gamma \quad (2.26)$$

where body loads have not been considered, and indices $l, k = 1, 2$ with Einstein's summation implied after performing matrix operations. The scalar δ_Ω^i takes the value 1 if the collocation point is an interior point ($\mathbf{x}^i \in \Omega \Rightarrow \delta_\Omega^i = 1$), whereas it is zero if the collocation point is an exterior point ($\mathbf{x}^i \notin \Omega \cup \Gamma \Rightarrow \delta_\Omega^i = 0$). The parameter $J = 1/(\hat{\rho}_{22}\omega^2)$ depends on medium properties and frequency. The primary variables (field variables) are fluid equivalent stress $\tau = \tau(\mathbf{x}, \omega)$ and solid displacements $u_k = u_k(\mathbf{x}, \omega)$, and the secondary variables (field variables derivatives) are the fluid normal displacement $U_n = U_n(\mathbf{x}, \omega) = U_k n_k$ and solid traction $t_l = t_l(\mathbf{x}, \omega) = \tau_{lk} n_k$. In particular, the primary variables at the collocation point are denoted with the superscript i ($\tau^i = \tau(\mathbf{x}^i, \omega)$, $u_k^i = u_k(\mathbf{x}^i, \omega)$). Unlike in Domínguez [74], variables are arranged according to their mathematical role rather than by their physical meaning. The SBIE can be written in a more concise form as:

$$\delta_\Omega^i \mathbf{I}_S^i \mathbf{u}^i + \int_\Gamma \mathbf{T}^* \mathbf{u} \, \mathrm{d}\Gamma = \int_\Gamma \mathbf{U}^* \mathbf{t} \, \mathrm{d}\Gamma \mid \mathbf{x}^i \notin \Gamma, \ \delta_\Omega^i = \begin{cases} 0 & \mathbf{x}^i \notin \Omega \cup \Gamma \\ 1 & \mathbf{x}^i \in \Omega \end{cases} \quad (2.27)$$

where here the vector $\mathbf{u}$ contains all the primary variables, while $\mathbf{t}$ contains all the secondary variables. The fundamental solution matrix $\mathbf{U}^*$ was obtained by Domínguez [74] using the Kupradze procedure [49] for the full-space (infinite domain) problem, and it is written in a very compact form. However, in order to ease the developments done here, we follow the

approach of Maeso et al. [17] of writing the fundamental solution separately in a way that resembles fundamental solutions of acoustics and elastodynamics:

$$\tau_{00}^* = \frac{1}{2\pi}\eta \tag{2.28}$$

$$\eta = \frac{1}{k_1^2 - k_2^2}\left[\alpha_1 K_0\left(ik_1r\right) - \alpha_2 K_0\left(ik_2r\right)\right] \tag{2.29}$$

$$\alpha_j = k_j^2 - \frac{\mu}{\lambda + 2\mu}k_3^2 \tag{2.30}$$

$$u_{0k}^* = -\frac{1}{2\pi}\Theta r_{,k} \tag{2.31}$$

$$\Theta = \left(\frac{Q}{R} - Z\right)\frac{1}{\lambda + 2\mu}\frac{1}{k_1^2 - k_2^2}\left[ik_1 K_1\left(ik_1r\right) - ik_2 K_1\left(ik_2r\right)\right] \tag{2.32}$$

$$\tau_{l0}^* = \frac{1}{2\pi J}\Theta r_{,l} \tag{2.33}$$

$$u_{lk}^* = \frac{1}{2\pi\mu}\left(\psi\delta_{lk} - \chi r_{,l}r_{,k}\right) \tag{2.34}$$

$$\psi = K_0\left(ik_3r\right) + \frac{K_1\left(ik_3r\right)}{ik_3r} - \frac{1}{k_1^2 - k_2^2}\left[\frac{\beta_1}{ik_1r}K_1\left(ik_1r\right) - \frac{\beta_2}{ik_2r}K_1\left(ik_2r\right)\right] \tag{2.35}$$

$$\chi = K_2\left(ik_3r\right) - \frac{1}{k_1^2 - k_2^2}\left[\beta_1 K_2\left(ik_1r\right) - \beta_2 K_2\left(ik_2r\right)\right] \tag{2.36}$$

$$\beta_j = \frac{\mu}{\lambda + 2\mu}k_j^2 - \frac{k_1^2 k_2^2}{k_3^2} \tag{2.37}$$

where $r = |\mathbf{x} - \mathbf{x}^{i}|$ is the distance between collocation and observation points, $k_1 = k_{P1}$, $k_2 = k_{P2}$, $k_3 = k_S$, $J = 1/(\hat{\rho}_{22}\omega^2)$, $Z = \hat{\rho}_{12}/\hat{\rho}_{22}$, and $K_n(z)$ is the modified Bessel function of the second kind, order n and argument z. By doing so, the fundamental solution matrix $\mathbf{U}^*$ and derivatives are composed by four submatrices: 00, $0k$, $l0$ and lk; where the first index is associated with the load and the second index with the observation, being 0 associated with the fluid phase and l, k with the solid phase:

$$\square^* = \begin{bmatrix} \square_{00}^* & \square_{0k}^* \\ \square_{l0}^* & \square_{lk}^* \end{bmatrix} \tag{2.38}$$

The diagonal submatrices $\square_{00}^*$ and $\square_{lk}^*$ are essentially similar and have the same kind of singularities as those of acoustics and elastodynamics problems, respectively. Therefore, their treatment is fundamentally the same. On the other hand, the off-diagonal submatrices $\square_{0k}^*$ and $\square_{l0}^*$ associated with the coupling between phases are different, and they have one lower order of singularity than the diagonal submatrices, as it will be seen later in this section. Using
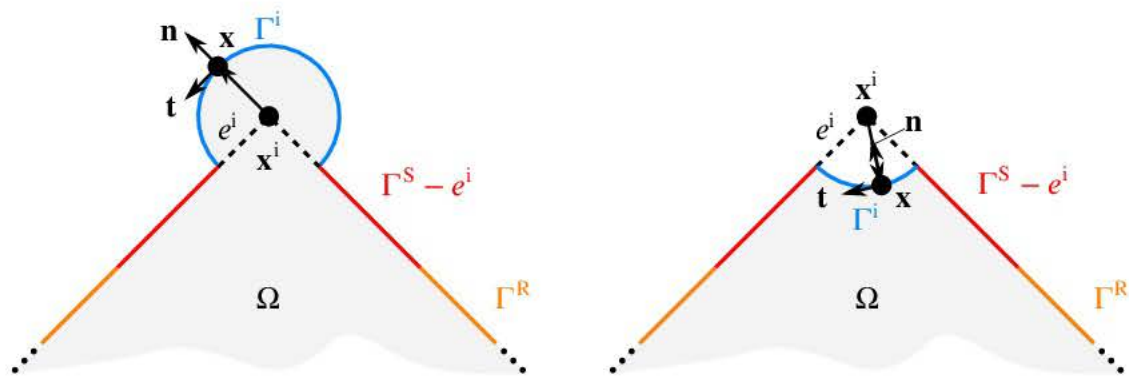
(a) Circular bump / limit from the interior ($\delta_\Omega^i = 1$): ($\mathbf{x}^i \in \Omega$) → ($\mathbf{x}^i \in \Gamma$)

(b) Circular hole / limit from the exterior ($\delta_\Omega^i = 0$): ($\mathbf{x}^i \notin \Omega \cup \Gamma$) → ($\mathbf{x}^i \in \Gamma$)

Figure 2.2: Integration domain considered when $\mathbf{x}^i \in \Gamma$

Eqs. (2.14a), (2.14b) and (2.15b), the fundamental solution matrix $\mathbf{T}^*$ is obtained from:

$$U_{n00}^* + J X_j'^* n_j = -J \tau_{00,j}^* n_j - Z u_{0j}^* n_j \tag{2.39}$$

$$t_{0k}^* = \left[\lambda u_{0m,m}^* \delta_{kj} + \mu \left(u_{0k,j}^* + u_{0j,k}^* \right) \right] n_j + \frac{Q}{R} \tau_{00}^* n_k \tag{2.40}$$

$$U_{nl0}^* = -J \tau_{l0,j}^* n_j - Z u_{lj}^* n_j \tag{2.41}$$

$$t_{lk}^* = \left[\lambda u_{lm,m}^* \delta_{kj} + \mu \left(u_{lk,j}^* + u_{lj,k}^* \right) \right] n_j + \frac{Q}{R} \tau_{l0}^* n_k \tag{2.42}$$

where final results after performing the operations can be seen in Appendix A. So far, the SBIE (2.27) for interior or exterior collocation points has been described. It is commonly used at a post-processing stage, where it is used to calculate the values of the primary variables at the collocation point (τ^i, u_k^i) once the solution throughout the boundary is known.

At this point, we are able to pose the SBIE for a boundary collocation point $\mathbf{x}^i \in \Gamma$. If in Equation (2.27) the collocation point is taken to the boundary ($\mathbf{x}^i \to \Gamma$), integrals become singular. In order to handle this, it must be further developed by considering an augmented integration domain Γ around the collocation point, which is taken as the following limit:

$$\Gamma = \Gamma^R + \lim_{\epsilon \to 0^+} \left[(\Gamma^S - e^i) + \Gamma^i \right] \tag{2.43}$$

where Γ^S is a portion of the Γ that contains the singularity, Γ^R is the complementary part of Γ^S, e^i is portion of Γ^S centred at the collocation point with radius ϵ, and Γ^i is an arc with radius ϵ centred at the collocation point. The arc can be oriented to the outside (circular bump) or to the inside (circular hole) with respect to Ω. In the former, the collocation point is an interior point ($\delta_\Omega^i = 1$), while, in the latter, it is an exterior point ($\delta_\Omega^i = 0$). This can be visualised in Figure 2.2, where a general angular point is considered ($\Gamma(\mathbf{x}^i) \in \mathscr{C}^0$). Integrals over Γ^R do not contain any singularity and hence they do not require further treatment. On the other hand, integrals over the integration domain under the limit, i.e. $(\Gamma^S - e^i) + \Gamma^i$, requires that functions f multiplying the singular term $1/r$ must be Hölder continuous $f \in \mathscr{C}^{0,\alpha}$ [77].

Therefore, a zero-order Taylor expansion of primary variables at the collocation point (τ, u_k) is required:

$$\tau = \tau^{\mathrm{i}} + \mathcal{O}(r) \tag{2.44a}$$

$$u_k = u_k^{\mathrm{i}} + \mathcal{O}(r) \tag{2.44b}$$

Such requirement is not only physically mandatory, but also needed for the regularisation of the SBIE, in particular for some integrals of $\mathbf{T}^*$. For the integration over $(\Gamma^{\mathrm{S}} - e^{\mathrm{i}}) + \Gamma^{\mathrm{i}}$, the limiting forms of $\mathbf{U}^*$ and $\mathbf{T}^*$ as $r \to 0$ should be carefully handled. Considering a circular bump, the only non-null integrals over the arc Γ^{i} are:

$$\lim_{\epsilon \to 0^+} \int_{\Gamma^{\mathrm{i}}} (U_{n00}^* + J X_j'^* n_j) \tau \, \mathrm{d}\Gamma = J \frac{\Delta\theta}{2\pi} \tau^{\mathrm{i}} \tag{2.45}$$

$$\lim_{\epsilon \to 0^+} \int_{\Gamma^{\mathrm{i}}} t_{lk}^* u_k \, \mathrm{d}\Gamma = - \begin{bmatrix} \dfrac{\Delta\theta}{2\pi} + \dfrac{\sin(2\theta_2) - \sin(2\theta_1)}{8\pi(1-\nu)} & -\dfrac{\cos(2\theta_2) - \cos(2\theta_1)}{8\pi(1-\nu)} \\ -\dfrac{\cos(2\theta_2) - \cos(2\theta_1)}{8\pi(1-\nu)} & \dfrac{\Delta\theta}{2\pi} - \dfrac{\sin(2\theta_2) - \sin(2\theta_1)}{8\pi(1-\nu)} \end{bmatrix} \begin{Bmatrix} u_1^{\mathrm{i}} \\ u_2^{\mathrm{i}} \end{Bmatrix} \tag{2.46}$$

where θ_1 and θ_2 are respectively the initial and final angles of the arc such that $0 < \Delta\theta < 2\pi$ with $\Delta\theta = \theta_2 - \theta_1$, and $\nu = \lambda/(2(\lambda + \mu))$ is the drained (solid skeleton) Poisson's ratio. If a circular hole were considered, these integrals only differ in minor details. In both cases, once these integrals (with the appropriate sign) are substituted in Equation (2.27) for $\delta_\Omega^{\mathrm{i}} = 1$ (circular bump) or $\delta_\Omega^{\mathrm{i}} = 0$ (circular hole), the same result is obtained:

$$\begin{bmatrix} J c_{00}^{\mathrm{i}} & 0 \\ 0 & c_{lk}^{\mathrm{i}} \end{bmatrix} \mathbf{u}^{\mathrm{i}} + \int_{\Gamma^{\mathrm{R}}} \mathbf{T}^* \mathbf{u} \, \mathrm{d}\Gamma + \lim_{\epsilon \to 0^+} \int_{\Gamma^{\mathrm{S}} - e^{\mathrm{i}}} \mathbf{T}^* \mathbf{u} \, \mathrm{d}\Gamma = \int_{\Gamma^{\mathrm{R}}} \mathbf{U}^* \mathbf{t} \, \mathrm{d}\Gamma + \lim_{\epsilon \to 0^+} \int_{\Gamma^{\mathrm{S}} - e^{\mathrm{i}}} \mathbf{U}^* \mathbf{t} \, \mathrm{d}\Gamma \tag{2.47}$$

where $c_{00}^{\mathrm{i}} = 1 - \Delta\theta/(2\pi)$ is the classical free-term of potential problems, and c_{lk}^{i} is the free-term of elastic problems resulting from subtracting the matrix in Equation (2.46) from δ_{lk}, which was first obtained by Ricardella [78]. In the particular case of a smooth boundary at the collocation point $(\Gamma(\mathbf{x}^{\mathrm{i}}) \in \mathscr{C}^1)$, these simplify to $c_{00}^{\mathrm{i}} = 1/2$ and $c_{lk}^{\mathrm{i}} = \delta_{lk}/2$.

Considering now the integrals over $\Gamma^{\mathrm{S}} - e^{\mathrm{i}}$, it can be seen that all of them are at most weakly singular, except some integrals related to t_{lk}^* that are strongly singular. These are the only ones requiring analytical treatment, which can be done by first segregating the problematic part $t_{lk}^{*(\mathrm{S})}$ from the rest:

$$t_{lk}^* = t_{lk}^{*(\mathrm{W})} + \frac{\tilde{\mu}}{2\pi} \frac{r_{,l} n_k - r_{,k} n_l}{r} = t_{lk}^{*(\mathrm{W})} + t_{lk}^{*(\mathrm{S})} \tag{2.48}$$

where $\tilde{\mu} = \mu/(\lambda + 2\mu)$. Taking into account that the unit tangent vector $\mathbf{t}$ and the unit normal vector satisfy $\mathbf{n} = (n_1, n_2) = (t_2, -t_1)$, it is possible to write [12]:

$$r_{,l} n_k - r_{,k} n_l = -\epsilon_{lk} \frac{\partial r}{\partial \Gamma} \tag{2.49}$$

$$\frac{\partial r}{\partial \Gamma} = \frac{\mathbf{r}}{r} \cdot \mathbf{t} < 0, \quad \left(\frac{\partial r}{\partial \Gamma}\right)^{i} = -1 \qquad \frac{\partial r}{\partial \Gamma} = \frac{\mathbf{r}}{r} \cdot \mathbf{t} > 0, \quad \left(\frac{\partial r}{\partial \Gamma}\right)^{i} = 1$$

$$\frac{\partial r}{\partial n} = \frac{\mathbf{r}}{r} \cdot \mathbf{n} \to 0 \text{ as } r \to 0$$

$$\frac{\partial r}{\partial n^{i}} = -\frac{\mathbf{r}}{r} \cdot \mathbf{n}^{i} \to 0 \text{ as } r \to 0$$

$$\mathbf{n} \cdot \mathbf{n}^{i} \to 1 \text{ as } r \to 0$$
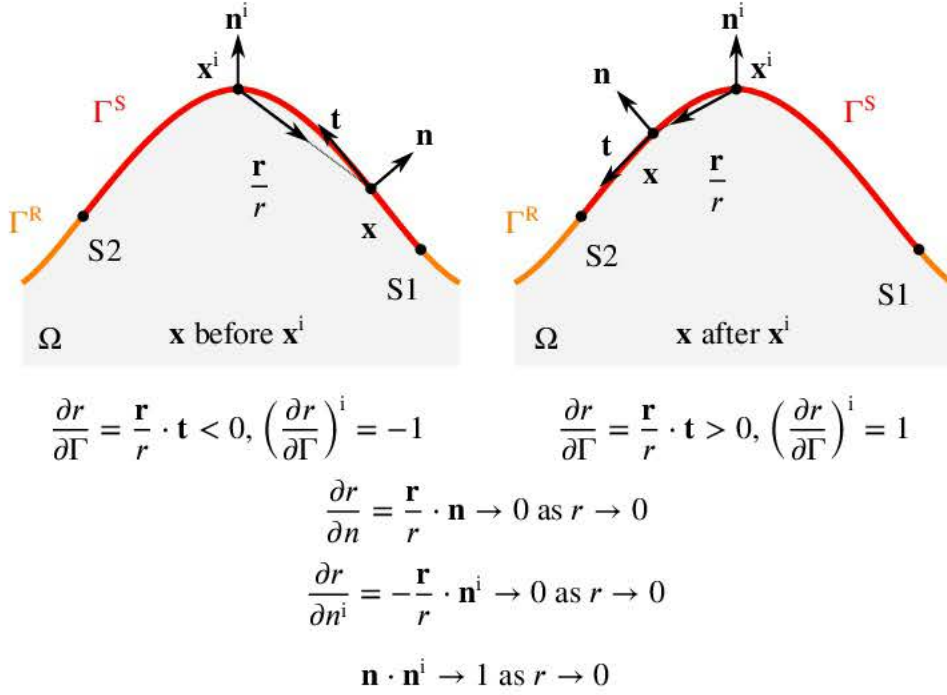
Figure 2.3: Behaviour of some relevant geometrical terms near the collocation point

where ϵ_{lk} is the two-dimensional Levi-Civita symbol ($\epsilon_{11} = \epsilon_{22} = 0$, $\epsilon_{12} = -\epsilon_{21} = 1$). By using the Taylor expansion of solid displacements, Equation (2.44b), the corresponding strongly singular integral is turned into a regular integral and an analytical term:

$$H_{l}^{(S)} = \lim_{\epsilon \to 0^{+}} \int_{\Gamma^{S} - e^{i}} t_{lk}^{*(S)} u_{k} \, d\Gamma = \frac{\tilde{\mu}}{2\pi} \left[\lim_{\epsilon \to 0^{+}} \int_{\Gamma^{S} - e^{i}} \frac{r_{,l} n_{k} - r_{,k} n_{l}}{r} \left(u_{k} - u_{k}^{i} \right) \, d\Gamma - \right.$$
$$\left. \epsilon_{lk} \left(\ln r^{S2} - \ln r^{S1} \right) u_{k}^{i} \right] \quad (2.50)$$

where r^{S1} and r^{S2} are the distances from the collocation point to respectively initial and final extremes of Γ^{S}, see Figure 2.3. By substituting this result into Equation (2.47), the regularised SBIE for a boundary collocation point can be written as:

$$\mathbf{C}^{i} \mathbf{u}^{i} + \int_{\Gamma^{R}} \mathbf{T}^{*} \mathbf{u} \, d\Gamma + \lim_{\epsilon \to 0^{+}} \int_{\Gamma^{S} - e^{i}} \mathbf{T}^{*(W)} \mathbf{u} \, d\Gamma + \left\{ \begin{matrix} 0 \\ H_{l}^{(S)} \end{matrix} \right\} = \int_{\Gamma^{R}} \mathbf{U}^{*} \mathbf{t} \, d\Gamma + \lim_{\epsilon \to 0^{+}} \int_{\Gamma^{S} - e^{i}} \mathbf{U}^{*} \mathbf{t} \, d\Gamma \quad (2.51)$$

where $\mathbf{C}^{i}$ is the free-term matrix from Equation (2.47). Usually, the SBIE is written more concisely by hiding the details and using the Cauchy Principal Value integral notation ($\fint$):

$$\mathbf{C}^{i} \mathbf{u}^{i} + \fint_{\Gamma} \mathbf{T}^{*} \mathbf{u} \, d\Gamma = \int_{\Gamma} \mathbf{U}^{*} \mathbf{t} \, d\Gamma \quad (2.52)$$

Hypersingular Boundary Integral Equation The HBIE is obtained by building the secondary variables at the collocation point from Equations (2.13b) and (2.14), which requires the SBIE (2.26) and its derivatives with respect to the collocation point ($\square_{,k} = \partial\square/\partial x_k^i$):

$$U_n^i = U_j^i n_j^i = -J\tau_{,j}^i n_j^i - Z u_j^i n_j^i \tag{2.53}$$

$$t_l^i = \tau_{lj}^i n_j^i = \left[\lambda u_{m,m}^i \delta_{lj} + \mu\left(u_{l,j}^i + u_{j,l}^i\right)\right] n_j^i + \frac{Q}{R}\tau^i n_l^i \tag{2.54}$$

where $\mathbf{n}^i$ is the unit normal at the collocation point. After performing all the operations, the HBIE for an interior or exterior collocation point can be written as:

$$\delta_\Omega^i \begin{bmatrix} 1 & 0 \\ 0 & \delta_{lk} \end{bmatrix} \left\{ \begin{matrix} U_n^i \\ t_k^i \end{matrix} \right\} + \int_\Gamma \begin{bmatrix} -s_{00}^* & s_{0k}^* \\ -s_{l0}^* & s_{lk}^* \end{bmatrix} \left\{ \begin{matrix} \tau \\ u_k \end{matrix} \right\} \, d\Gamma = \int_\Gamma \begin{bmatrix} -d_{00}^* & d_{0k}^* \\ -d_{l0}^* & d_{lk}^* \end{bmatrix} \left\{ \begin{matrix} U_n \\ t_k \end{matrix} \right\} \, d\Gamma \tag{2.55}$$

or more concisely:

$$\delta_\Omega^i \mathbf{I}_H^i \mathbf{t}^i + \int_\Gamma \mathbf{S}^* \mathbf{u} \, d\Gamma = \int_\Gamma \mathbf{D}^* \mathbf{t} \, d\Gamma \mid \mathbf{x}^i \notin \Gamma, \ \delta_\Omega^i = \begin{cases} 0 & \mathbf{x}^i \notin \Omega \cup \Gamma \\ 1 & \mathbf{x}^i \in \Omega \end{cases} \tag{2.56}$$

Analogously to the SBIE, here the secondary variables at the collocation point are denoted with the superscript i ($U_n^i = U_n(\mathbf{x}^i, \omega), t_k^i = t_k(\mathbf{x}^i, \omega)$), and $\mathbf{t}^i = \mathbf{t}(\mathbf{x}^i, \omega)$ gathers both secondary variables. The matrices $\mathbf{D}^*$ and $\mathbf{S}^*$ can be found in Appendix A. It is used for calculating the values of the secondary variables at the collocation point (U_n^i, t_k^i) at a post-processing stage.

The process of taking the collocation point to the boundary ($\mathbf{x}^i \to \Gamma$) is essentially similar to the process followed for the SBIE. Differences lie in the severity of singularities, which lead to up to hypersingular integrals, and in the requirements that these impose. Hypersingular integrals require that first derivatives of functions f multiplying the singular term $1/r^2$ must be Hölder continuous, i.e. $f \in \mathscr{C}^{1,\alpha}$ [77]. Under such circumstances, primary variables at the collocation point admit a first-order Taylor expansion:

$$\tau = \tau^i + \tau_{,j}^i r_j + \mathcal{O}\left(r^2\right) \tag{2.57}$$

$$u_k = u_k^i + u_{k,j}^i r_j + \mathcal{O}\left(r^2\right) \tag{2.58}$$

where here $\tau_{,j}^i$ and $u_{k,j}^i$ should be understood as tangential gradients on $\Gamma(\mathbf{x}^i)$. An alternative way or writing this expansion is:

$$\tau = \tau^i + \left(\frac{\partial\tau}{\partial r}\right)^i r + \mathcal{O}\left(r^2\right) \tag{2.59}$$

$$u_k = u_k^i + \left(\frac{\partial u_k}{\partial r}\right)^i r + \mathcal{O}\left(r^2\right) \tag{2.60}$$

where $(\partial\square/\partial r)_i = (\partial\square/\partial\Gamma)_i/(\partial r/\partial\Gamma)_i$, see Figure 2.3. The case of a geometrically smooth boundary point is considered here, i.e. Γ^i a semicircular arc, although non-smooth points

could be considered at a considerably greater analytical cost, see Mantič [79] for the potential case. Considering a circular bump, the non-null integrals over the arc Γ^i are:

$$\lim_{\epsilon \to 0^+} \int_{\Gamma^i} d_{00}^* U_n \, d\Gamma = -\frac{1}{4} U_n^i \tag{2.61}$$

$$\lim_{\epsilon \to 0^+} \int_{\Gamma^i} d_{lk}^* t_k \, d\Gamma = \left[\frac{2\lambda^2 + \mu(3\lambda - \mu)}{4(\lambda + 2\mu)} u_{m,m}^i \delta_{kj} + \frac{\lambda + 3\mu}{4(\lambda + 2\mu)} \mu \left(u_{k,j}^i + u_{j,k}^i \right) + \right.$$
$$\left. \frac{\lambda + \mu}{2(\lambda + 2\mu)} \frac{Q}{R} \tau^i \delta_{kj} \right] n_j^i \delta_{lk} \tag{2.62}$$

$$\lim_{\epsilon \to 0^+} \int_{\Gamma^i} s_{00}^* \tau \, d\Gamma = -\frac{J}{\pi} \tau^i \left(\lim_{\epsilon \to 0^+} \frac{1}{\epsilon} \right) - \frac{J}{4} \tau_{,j}^i n_j^i \tag{2.63}$$

$$\lim_{\epsilon \to 0^+} \int_{\Gamma^i} s_{0k}^* u_k \, d\Gamma = \frac{Z}{4} u_k n_k^i \tag{2.64}$$

$$\lim_{\epsilon \to 0^+} \int_{\Gamma^i} s_{l0}^* \tau \, d\Gamma = \frac{1}{2} \frac{Q}{R} \frac{\mu}{\lambda + 2\mu} \tau^i n_l^i \tag{2.65}$$

$$\lim_{\epsilon \to 0^+} \int_{\Gamma^i} s_{lk}^* u_k \, d\Gamma = - \left[\frac{\mu(\lambda + \mu)}{4(\lambda + 2\mu)} u_{m,m}^i \delta_{kj} + \frac{\lambda + \mu}{4(\lambda + 2\mu)} \mu \left(u_{k,j}^i + u_{j,k}^i \right) \right] n_j^i \delta_{lk} -$$
$$\frac{1}{\pi} \frac{2\mu(\lambda + \mu)}{\lambda + 2\mu} \delta_{lk} u_k^i \left(\lim_{\epsilon \to 0^+} \frac{1}{\epsilon} \right) \tag{2.66}$$

where Taylor expansions (2.58-2.57) has been used, as well as the limiting forms of $\mathbf{D}^*$ and $\mathbf{S}^*$ as $r \to 0$. Substituting these results back into Equation (2.56), the HBIE apparently turns to be unbounded:

$$\frac{1}{2} \mathbf{I}_H^i \mathbf{t}^i + \int_{\Gamma^R} \mathbf{S}^* \mathbf{u} \, d\Gamma + \lim_{\epsilon \to 0^+} \int_{\Gamma^{S-e^i}} \mathbf{S}^* \mathbf{u} \, d\Gamma + \mathbf{M}^{\Gamma^i} \mathbf{u}^i \left(\lim_{\epsilon \to 0^+} \frac{1}{\epsilon} \right) =$$
$$\int_{\Gamma^R} \mathbf{D}^* \mathbf{t} \, d\Gamma + \lim_{\epsilon \to 0^+} \int_{\Gamma^{S-e^i}} \mathbf{D}^* \mathbf{t} \, d\Gamma \tag{2.67}$$

where:

$$\mathbf{M}^{\Gamma^i} = \frac{1}{\pi} \begin{bmatrix} J & 0 \\ 0 & -\frac{2\mu(\lambda + \mu)}{\lambda + 2\mu} \delta_{lk} \end{bmatrix} \tag{2.68}$$

The integration over $\Gamma^S - e^i$ is more involved that in the case of the SBIE. The integrals related to d_{00}^*, d_{0k}^* and d_{l0}^* are at most weakly singular, and thus no further analytical treatment is required for them. On the other hand, some of the integrals related to d_{lk}^* are strongly singular, but fortunately their treatment is very similar to those of t_{lk}^* of the SBIE, see Equation (2.50). In this case, the problematic part $d_{lk}^{*(S)}$ segregated from the rest is:

$$d_{lk}^* = d_{lk}^{*(W)} + \frac{\tilde{\mu}}{2\pi} \frac{r_{,l} n_k^i - r_{,k} n_l^i}{r} = d_{lk}^{*(W)} + d_{lk}^{*(S)} \tag{2.69}$$

where the only difference with respect to $t_{lk}^{*(S)}$ is that unit normal components are those at the collocation point rather than at the observation point. By adding and subtracting unit normal components at the observation point from those at the collocation point, it is possible to write:

$$L_l^{(S)} = \lim_{\epsilon \to 0^+} \int_{\Gamma^S - e^i} d_{lk}^{*(S)} t_k \, d\Gamma = \frac{\tilde{\mu}}{2\pi} \left[\lim_{\epsilon \to 0^+} \int_{\Gamma^S - e^i} \frac{r_{,l}(n_k^i - n_k) - r_{,k}(n_l - n_l^i)}{r} t_k \, d\Gamma + \right.$$
$$\left. \lim_{\epsilon \to 0^+} \int_{\Gamma^S - e^i} \frac{r_{,l} n_k - r_{,k} n_l}{r} \left(t_k - t_k^i \right) \, d\Gamma - \epsilon_{lk} \left(\ln r^{S2} - \ln r^{S1} \right) t_k^i \right] \tag{2.70}$$

where now all integrals are regular. The integrals related to s_{0k}^* and s_{l0}^* contain terms that lead to strongly singular integrals. It is possible to segregate the problematic terms $s_{0k}^{*(S)}$ and $s_{l0}^{*(S)}$ from the rest as:

$$s_{0k}^* = s_{0k}^{*(W)} + \frac{\tilde{\mu}}{2\pi} \frac{Q}{R} \frac{r_{,k}(\mathbf{n} \cdot \mathbf{n}^i)}{r} = s_{0k}^{*(W)} + s_{0k}^{*(S)} \tag{2.71}$$

$$s_{l0}^* = s_{l0}^{*(W)} - \frac{\tilde{\mu}}{2\pi} \frac{Q}{R} \frac{r_{,l}(\mathbf{n} \cdot \mathbf{n}^i)}{r} = s_{l0}^{*(W)} + s_{l0}^{*(S)} \tag{2.72}$$

The key for regularising the corresponding integrals is using an expansion of $r_{,k}$ and $\mathbf{n} \cdot \mathbf{n}^i$ as $r \to 0$ from each side of the singularity [12]. By examining Figure 2.3, it is possible to establish that:

$$r_{,k} = \left(\frac{\partial r}{\partial \Gamma} \right)^i t_k^i + \mathcal{O}(r) \tag{2.73}$$

$$\mathbf{n} \cdot \mathbf{n}^i = 1 + \mathcal{O}(r^2) \tag{2.74}$$

where t_k^i is the unit tangent vector at the collocation point, and $(\partial r/\partial \Gamma)^i = \lim_{r \to 0} \partial r/\partial \Gamma = \pm 1$ which sign depends on the side of the observation point. By using these expansions, and taking only the zero-order part of expansions shown in Equations (2.57–2.58), it is possible

to obtain the following regularised integrals:

$$M_0^{(S)} = \lim_{\epsilon \to 0^+} \int_{\Gamma^{S-e^i}} s_{0k}^{*(S)} u_k \, d\Gamma = \frac{\tilde{\mu}}{2\pi} \frac{Q}{R} \left[\lim_{\epsilon \to 0^+} \int_{\Gamma^{S-e^i}} \frac{r_{,k} (\mathbf{n} \cdot \mathbf{n}^i)}{r} \left(u_k - u_k^i \right) \, d\Gamma + \right.$$

$$\left(\lim_{\epsilon \to 0^+} \int_{\Gamma^{S-e^i}} \frac{1}{r} \left(r_{,k} (\mathbf{n} \cdot \mathbf{n}^i) - \left(\frac{\partial r}{\partial \Gamma} \right)^i t_k^i \right) \, d\Gamma + \right.$$

$$\left. \left. \lim_{\epsilon \to 0^+} \int_{\Gamma^{S-e^i}} \frac{1}{r} \left(\left(\frac{\partial r}{\partial \Gamma} \right)^i - \frac{\partial r}{\partial \Gamma} \right) t_k^i \, d\Gamma + t_k^i \left(\ln r^{S2} - \ln r^{S1} \right) \right) u_k^i \right] \quad (2.75)$$

$$M_l^{(S)} = \lim_{\epsilon \to 0^+} \int_{\Gamma^{S-e^i}} s_{l0}^{*(S)} \tau \, d\Gamma = -\frac{\tilde{\mu}}{2\pi} \frac{Q}{R} \left[\lim_{\epsilon \to 0^+} \int_{\Gamma^{S-e^i}} \frac{r_{,l} (\mathbf{n} \cdot \mathbf{n}^i)}{r} \left(\tau - \tau^i \right) \, d\Gamma + \right.$$

$$\left(\lim_{\epsilon \to 0^+} \int_{\Gamma^{S-e^i}} \frac{1}{r} \left(r_{,l} (\mathbf{n} \cdot \mathbf{n}^i) - \left(\frac{\partial r}{\partial \Gamma} \right)^i t_l^i \right) \, d\Gamma + \right.$$

$$\left. \left. \lim_{\epsilon \to 0^+} \int_{\Gamma^{S-e^i}} \frac{1}{r} \left(\left(\frac{\partial r}{\partial \Gamma} \right)^i - \frac{\partial r}{\partial \Gamma} \right) t_l^i \, d\Gamma + t_l^i \left(\ln r^{S2} - \ln r^{S1} \right) \right) \tau^i \right] \quad (2.76)$$

which consist only of regular integrals and analytical terms. The regularisation of integrals related to s_{00}^* and s_{lk}^* is more involved because they lead to hypersingular integrals. In this process, the key is the term $|\partial r / \partial \Gamma|$ and its geometrical interpretation from Figure 2.3. The following Taylor expansion can be considered [12]:

$$\left| \frac{\partial r}{\partial \Gamma} \right| = \cos \alpha = 1 + \mathcal{O} \left(\alpha^2 \right) = 1 + \mathcal{O} \left(r^2 \right) \quad (2.77)$$

where $\alpha \propto r$ as $r \to 0$. In the first place, the problematic part in s_{00}^* is segregated as $s_{00}^{*(H)}$:

$$s_{00}^* = s_{00}^{*(W)} + \frac{J}{2\pi} \frac{\mathbf{n} \cdot \mathbf{n}^i}{r^2} = s_{00}^{*(W)} + s_{00}^{*(H)} \quad (2.78)$$

Recalling expansions shown in Equations (2.74) and (2.77), and the expansion of τ shown in Equation (2.59), it is possible to obtain:

$$M_0^{(H)} = \lim_{\epsilon \to 0^+} \int_{\Gamma^{S-e^i}} s_{00}^{*(H)} \tau \, d\Gamma = \frac{J}{2\pi} \left[\lim_{\epsilon \to 0^+} \int_{\Gamma^{S-e^i}} \frac{1}{r^2} \left((\mathbf{n} \cdot \mathbf{n}^i) - \left| \frac{\partial r}{\partial \Gamma} \right| \right) \tau \, d\Gamma + \right.$$

$$\lim_{\epsilon \to 0^+} \int_{\Gamma^{S-e^i}} \frac{1}{r^2} \left| \frac{\partial r}{\partial \Gamma} \right| \left(\tau - \tau^i - \left(\frac{\partial \tau}{\partial r} \right)^i r \right) \, d\Gamma - \left(\frac{1}{r^{S1}} + \frac{1}{r^{S2}} \right) \tau^i + \right.$$

$$\left. \left(\ln r^{S2} - \ln r^{S1} \right) \left(\frac{\partial \tau}{\partial \Gamma} \right)^i \right] + \frac{J}{\pi} \tau^i \left(\lim_{\epsilon \to 0^+} \frac{1}{\epsilon} \right) = M_0^{(Hb)} + \frac{J}{\pi} \tau^i \left(\lim_{\epsilon \to 0^+} \frac{1}{\epsilon} \right) \quad (2.79)$$

In the case of s_{lk}^*, the problematic part $s_{lk}^{*(H)}$ is obtained after some manipulation of its static part, as done in [12] for the elastostatic case, and it turns out to be similar to that of s_{00}^*:

$$s_{lk}^* = s_{lk}^{*(W)} + \frac{2\mu(\lambda + \mu)}{\lambda + 2\mu}\delta_{lk}\frac{\mathbf{n} \cdot \mathbf{n}^i}{r^2} = s_{lk}^{*(W)} + s_{lk}^{*(H)} \tag{2.80}$$

Therefore, following a similar procedure as before, but taking into account that the integral contains u_k rather than τ, it is possible to obtain:

$$M_l^{(H)} = \lim_{\epsilon \to 0^+} \int_{\Gamma^{S-e^i}} s_{lk}^{*(H)} u_k \, d\Gamma = \frac{2\mu(\lambda + \mu)}{\lambda + 2\mu}\delta_{lk} \left[\lim_{\epsilon \to 0^+} \int_{\Gamma^{S-e^i}} \frac{1}{r^2}\left((\mathbf{n} \cdot \mathbf{n}^i) - \left|\frac{\partial r}{\partial \Gamma}\right|\right) u_k \, d\Gamma + \right.$$

$$\lim_{\epsilon \to 0^+} \int_{\Gamma^{S-e^i}} \frac{1}{r^2}\left|\frac{\partial r}{\partial \Gamma}\right| \left(u_k - u_k^i - \left(\frac{\partial u_k}{\partial r}\right)^i r\right) d\Gamma - \left(\frac{1}{r^{S1}} + \frac{1}{r^{S2}}\right) u_k^i +$$

$$\left. \left(\ln r^{S2} - \ln r^{S1}\right)\left(\frac{\partial u_k}{\partial \Gamma}\right)^i \right] + \frac{2\mu(\lambda + \mu)}{\lambda + 2\mu}\delta_{lk} u_k^i \left(\lim_{\epsilon \to 0^+} \frac{1}{\epsilon}\right) =$$

$$M_l^{(Hb)} + \frac{2\mu(\lambda + \mu)}{\lambda + 2\mu}\delta_{lk} u_k^i \left(\lim_{\epsilon \to 0^+} \frac{1}{\epsilon}\right) \tag{2.81}$$

Substituting results from Equations (2.70), (2.75), (2.76), (2.79) and (2.81), leads to a fully regularised HBIE:

$$\frac{1}{2}\mathbf{I}_H^i \mathbf{t}^i + \int_{\Gamma^R} \mathbf{S}^* \mathbf{u} \, d\Gamma + \lim_{\epsilon \to 0^+} \int_{\Gamma^{S-e^i}} \mathbf{S}^{*(W)} \mathbf{u} \, d\Gamma + \left\{ \begin{array}{c} -M_0^{(Hb)} + M_0^{(S)} \\ -M_l^{(S)} + M_l^{(Hb)} \end{array} \right\} =$$

$$\int_{\Gamma^R} \mathbf{D}^* \mathbf{t} \, d\Gamma + \lim_{\epsilon \to 0^+} \int_{\Gamma^{S-e^i}} \mathbf{D}^{*(W)} \mathbf{t} \, d\Gamma + \left\{ \begin{array}{c} 0 \\ L_l^{(S)} \end{array} \right\} \tag{2.82}$$

because unbounded terms from Equations (2.79) and (2.81) cancel out with the term from Equation (2.68). Usually, the HBIE is written more concisely by hiding the details and using the Cauchy Principal Value integral notation ($\fint$) and the Hadamard Finite Part integral notation ($=\!\!\!\!\!\!\int$):

$$\frac{1}{2}\mathbf{I}_H^i \mathbf{t}^i + =\!\!\!\!\!\!\int_\Gamma \mathbf{S}^* \mathbf{u} \, d\Gamma = \fint_\Gamma \mathbf{D}^* \mathbf{t} \, d\Gamma \tag{2.83}$$

Despite the CPV and HFP concepts are the underlying abstractions behind the regularisation of the SBIE and the HBIE, the process proposed in [12,61] does not rely on them since it deals explicitly with the singularities and directly gives the finite parts by analytically cancelling out all unbounded terms, as it has been shown in this case. Nevertheless, this notation is convenient for the sake of clarity.
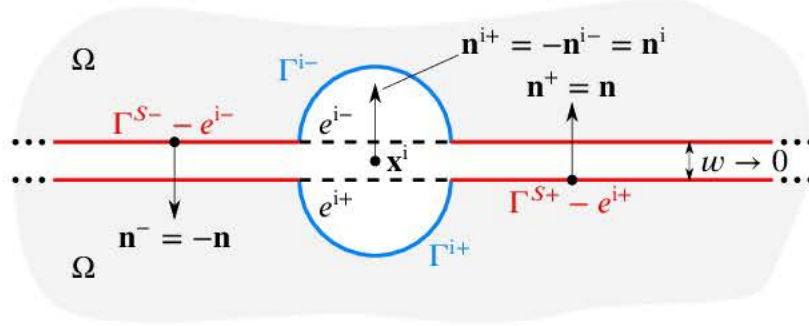
Figure 2.4: Integration domain when $\mathbf{x}^i \in \Gamma$ and Γ is a crack-like boundary (exploded view)

Dual Boundary Integral Equations   The SBIE and HBIE previously derived are valid for interior and exterior collocation points, and collocation points located at ordinary boundaries. In order to incorporate crack-like boundaries in a problem, their own distinctive features must be conveniently addressed. The corresponding BIEs are called Dual BIEs [42], and their application to the BEM is usually called the Dual BEM [43, 44].

A crack-like boundary is composed by two sub-boundaries, denoted as positive + and negative − faces. Hence, the integration domain associated with a crack-like boundary can be divided into these two faces, which are geometrically coincident but have opposite orientations, see Figure 2.1c. One of the faces is taken as the reference for the crack-like boundary considered as a whole, in our case it is the positive face. This means that any integral over one of the faces only differs in sign with respect to the same integral over the opposite face depending on the sign changes of the kernels ($\mathbf{U}^*$, $\mathbf{T}^*$, $\mathbf{D}^*$ and $\mathbf{S}^*$) with respect to $\mathbf{n}$ and $\mathbf{n}^i$. Therefore, the previous developments have already solved the mathematical difficulties when taking the SBIE and HBIE to a crack-like boundary. In this case, the only thing left to do is to define the augmented integration domain around the collocation point. The considered augmented integration domain is depicted in Figure 2.4, and can be expressed as:

$$\Gamma = \Gamma^R + \lim_{\epsilon \to 0^+} \left[\left(\Gamma^{S+} - e^{i+} \right) + \Gamma^{i+} + \left(\Gamma^{S-} - e^{i-} \right) + \Gamma^{i-} \right] \tag{2.84}$$

The limit is taken from the exterior (from inside the crack void), and the arches surrounding the collocation points are semicircular holes on each face. The resulting Dual BIEs are:

$$\frac{1}{2}\mathbf{I}_S^i \left(\mathbf{u}^{i+} + \mathbf{u}^{i-} \right) + \fint_\Gamma \mathbf{T}^* \mathbf{u}\, d\Gamma = \int_\Gamma \mathbf{U}^* \mathbf{t}\, d\Gamma \tag{2.85}$$

$$\frac{1}{2}\mathbf{I}_H^i \left(\mathbf{t}^{i+} - \mathbf{t}^{i-} \right) + \fintdbl_\Gamma \mathbf{S}^* \mathbf{u}\, d\Gamma = \fint_\Gamma \mathbf{D}^* \mathbf{t}\, d\Gamma \tag{2.86}$$

where it has been assumed that $\Gamma(\mathbf{x}^i) \in \mathscr{C}^1$ for both equations. In these equations, $(\mathbf{u}^{i+}, \mathbf{t}^{i+})$ are the primary and secondary variables of the positive face at the collocation point, and conversely for $(\mathbf{u}^{i-}, \mathbf{t}^{i-})$. Therefore, at a given collocation point we have four variables, from which tractions are typically null in elastic crack analysis. It is hence clear that neither the Dual SBIE (2.85) nor the Dual HBIE (2.86) is able to give independently enough conditions. Therefore, both BIEs must be simultaneously used in order to have the same number of equations as unknowns [42].

2.3.2.2 Three-dimensional problem

The development of Singular, Hypersingular and Dual BIEs for the three-dimensional problem follows the same path, although it is more involved. Thus, some steps in the process are reduced or skipped.

Singular Boundary Integral Equation   Using the weighted residual formulation proposed by Domínguez [17, 70], the SBIE at a collocation point $\mathbf{x}^i \notin \Gamma$ can be written as:

$$\delta_\Omega^i \mathbf{I}_S^i \mathbf{u}^i + \int_\Gamma \mathbf{T}^* \mathbf{u} \, d\Gamma = \int_\Gamma \mathbf{U}^* \mathbf{t} \, d\Gamma \mid \mathbf{x}^i \notin \Gamma, \ \delta_\Omega^i = \begin{cases} 0 & \mathbf{x}^i \notin \Omega \cup \Gamma \\ 1 & \mathbf{x}^i \in \Omega \end{cases} \tag{2.87}$$

All terms are similar to the two-dimensional case, with the obvious difference that fundamental solution matrices $\mathbf{U}^*$ and $\mathbf{T}^*$ are different and $l, k = 1, 2, 3$. The fundamental solution matrices $\mathbf{U}^*$ and $\mathbf{T}^*$ are fully described in Appendix A. When the collocation point is a boundary point ($\mathbf{x}^i \in \Gamma$), the integrals contain a singularity, and thus the integration domain is taken as the following limit:

$$\Gamma = \Gamma^R + \lim_{\epsilon \to 0^+} \left[\left(\Gamma^S - e^i \right) + \Gamma^i \right] \tag{2.88}$$

where Γ^S is a portion of the Γ that contains the singularity, Γ^R is the complementary part of Γ^S, e^i is a circular surface of Γ^S with radius ϵ centred at the collocation point, and Γ^i is a spherical surface with radius ϵ centred at the collocation point. The spherical surface can be oriented to the outside (spherical bump) or to the inside (spherical hole) with respect to Ω. In the former, the collocation point is an interior point, while, in the latter, it is an exterior point, see Figure 2.5. After carrying out the integration over the spherical surface Γ^i, both alternatives lead to the same SBIE:

$$\begin{bmatrix} Jc_{00}^i & 0 \\ 0 & c_{lk}^i \end{bmatrix} \mathbf{u}^i + \int_{\Gamma^R} \mathbf{T}^* \mathbf{u} \, d\Gamma + \lim_{\epsilon \to 0^+} \int_{\Gamma^S - e^i} \mathbf{T}^* \mathbf{u} \, d\Gamma = \int_{\Gamma^R} \mathbf{U}^* \mathbf{t} \, d\Gamma + \lim_{\epsilon \to 0^+} \int_{\Gamma^S - e^i} \mathbf{U}^* \mathbf{t} \, d\Gamma \tag{2.89}$$

For a collocation point located at a general non-smooth boundary point, the free-terms c_{00}^i and c_{lk}^i can be obtained from the closed analytical formulas provided by Mantič [80], being c_{00}^i the potential free-term, and c_{lk}^i the elastostatic free-term with drained properties. The integrals over Γ^R are regular. The integrals over $\Gamma^S - e^i$ are at most weakly singular, except an integral associated with t_{lk}^* that is strongly singular. The fundamental solution t_{lk}^* can be decomposed in such a way that the term that leads to the strongly singular integral is isolated from the rest:

$$t_{lk}^* = t_{lk}^{*(W)} + \frac{\tilde{\mu}}{4\pi} \frac{r_{,l} n_k - r_{,k} n_l}{r^2} = t_{lk}^{*(W)} + t_{lk}^{*(S)} \tag{2.90}$$

where $\tilde{\mu} = \mu / (\lambda + 2\mu)$. Thus, by using Equation (C.1) and the Stokes' theorem, the strongly singular surface integral is turned into a weakly singular surface integral and a nearly singular line integral over $\Lambda^S = \partial \Gamma^S$:

$$H_l^{(S)} = \frac{\tilde{\mu}}{4\pi} \left[\lim_{\epsilon \to 0^+} \int_{\Gamma^S - e^i} \frac{r_{,l} n_k - r_{,k} n_l}{r^2} \left(u_k - u_k^i \right) \, d\Gamma + \left(\epsilon_{lkj} \int_{\Lambda^S} \frac{\mathbf{e}_j \cdot \mathbf{t}}{r} \, d\Lambda \right) u_k^i \right] \tag{2.91}$$
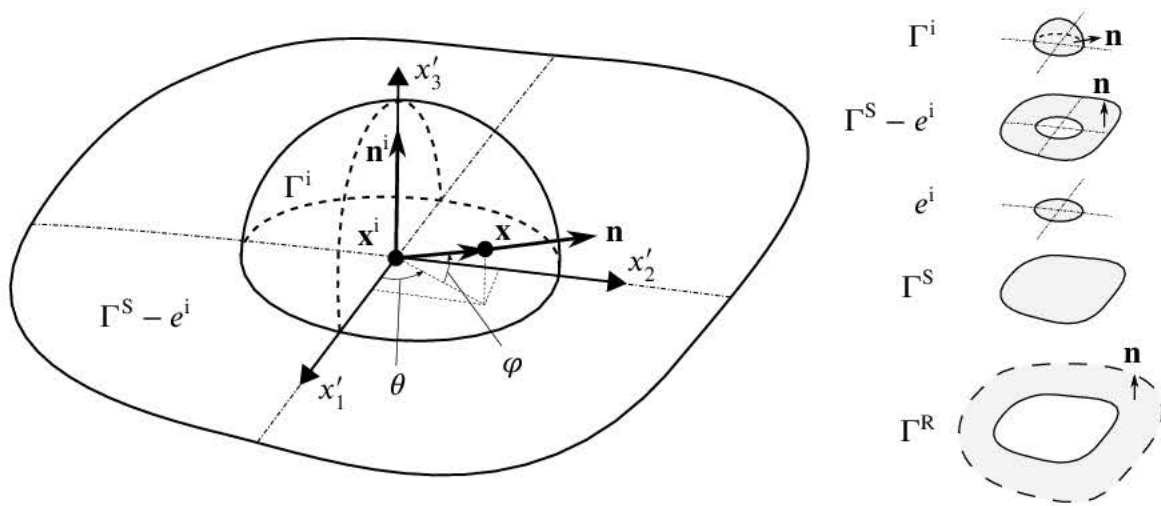
(a) Spherical bump / limit from the interior ($\delta_\Omega^i = 1$): $(\mathbf{x}^i \in \Omega) \to (\mathbf{x}^i \in \Gamma)$
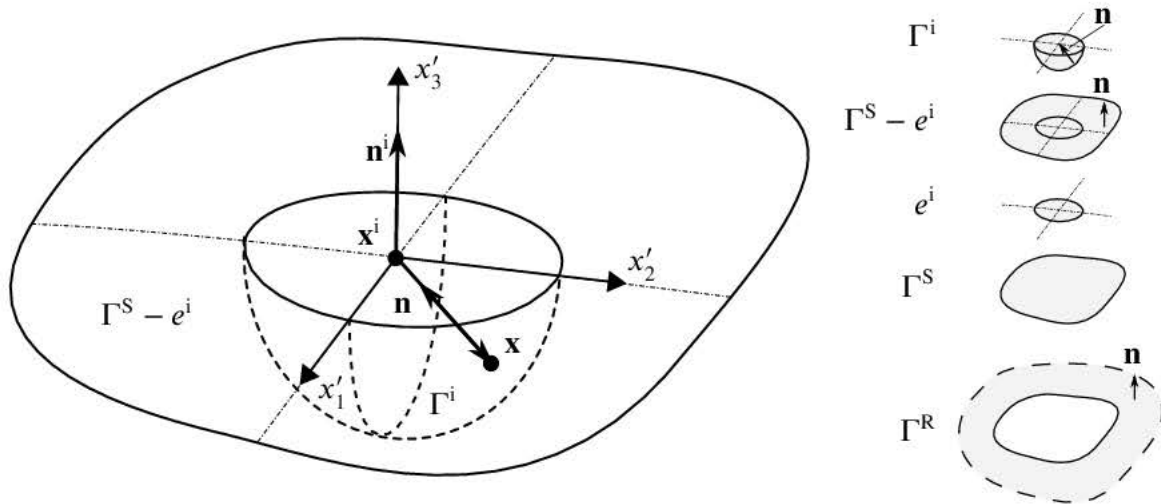
(b) Spherical hole / limit from the exterior ($\delta_\Omega^i = 0$): $(\mathbf{x}^i \notin \Omega \cup \Gamma) \to (\mathbf{x}^i \in \Gamma)$

Figure 2.5: Integration domain considered when $\mathbf{x}^i \in \Gamma$

where ϵ_{lkj} is the Levi-Civita symbol, $\mathbf{e}_j$ is the unit vector along x_j axis, and $\mathbf{t}$ is the unit tangent vector at the observation point. Finally, the regularised SBIE for a boundary collocation point can be written as:

$$\mathbf{C}^i\mathbf{u}^i + \int_{\Gamma^R} \mathbf{T}^*\mathbf{u}\, d\Gamma + \lim_{\epsilon\to 0^+} \int_{\Gamma^{S}-e^i} \mathbf{T}^{*(W)}\mathbf{u}\, d\Gamma + \left\{ \begin{matrix} 0 \\ H_l^{(S)} \end{matrix} \right\} = \int_{\Gamma^R} \mathbf{U}^*\mathbf{t}\, d\Gamma + \lim_{\epsilon\to 0^+} \int_{\Gamma^{S}-e^i} \mathbf{U}^*\mathbf{t}\, d\Gamma \tag{2.92}$$

Hypersingular Boundary Integral Equation The HBIE is built by establishing the secondary variables at the collocation point:

$$U_n^i = U_j^i n_j^i = -J\,\tau_{,j}^i n_j^i - Z u_j^i n_j^i \tag{2.93}$$

$$t_l^i = \tau_{lj}^i n_j^i = \left[\lambda u_{m,m}^i \delta_{lj} + \mu \left(u_{l,j}^i + u_{j,l}^i \right) \right] n_j^i + \frac{Q}{R}\tau^i n_l^i \tag{2.94}$$

where $Z = \hat{\rho}_{12}/\hat{\rho}_{22}$, $\mathbf{n}^i$ is the unit normal vector at the collocation point, and the comma derivative notation denotes $\partial/\partial x_k^i$. Hence, Equations (2.93-2.94) require a combination of the SBIE and its derivatives with respect to the coordinates of the collocation point. This fact imposes that the primary variables at the collocation point must have continuous first derivatives, i.e. $\tau(\mathbf{x}^i), u_k(\mathbf{x}^i) \in \mathscr{C}^1$. After carrying out all the required operations, the HBIE at a collocation point $\mathbf{x}^i \notin \Gamma$ can be written as:

$$\delta_\Omega^i \mathbf{I}_H^i \mathbf{t}^i + \int_\Gamma \mathbf{S}^*\mathbf{u}\, d\Gamma = \int_\Gamma \mathbf{D}^*\mathbf{t}\, d\Gamma \mid \mathbf{x}^i \notin \Gamma, \ \delta_\Omega^i = \begin{cases} 0 & \mathbf{x}^i \notin \Omega \cup \Gamma \\ 1 & \mathbf{x}^i \in \Omega \end{cases} \tag{2.95}$$

where the fundamental solution matrices $\mathbf{D}^*$ and $\mathbf{S}^*$ are fully written in Appendix A.

When the collocation point is a boundary point, it is again necessary to take the integration domain presented in Equation (2.88). The case of a geometrically smooth boundary point is considered here, i.e. e^i is a circle and Γ^i a hemisphere. Non-smooth points could be considered, as shown in Mantič [79] for the potential case, but this is considerably more difficult. Given that $\tau(\mathbf{x}^i), u_k(\mathbf{x}^i) \in \mathscr{C}^1$, the primary variables admit the expansion:

$$\tau = \tau^i + \tau_{,j}^i r_j + \mathcal{O}\left(r^2\right) \tag{2.96}$$

$$u_k = u_k^i + u_{k,j}^i r_j + \mathcal{O}\left(r^2\right) \tag{2.97}$$

where $\tau_{,j}^i$ and $u_{k,j}^i$ must be understood as tangential gradients on $\Gamma(\mathbf{x}^i)$. By using these expansions and considering a spherical bump (Figure 2.5a), the integration over Γ^i lead to the following integrals:

$$\lim_{\epsilon\to 0^+} \int_{\Gamma^i} d_{00}^* U_n\, d\Gamma = -\frac{1}{6} U_n^i \tag{2.98}$$

$$\lim_{\epsilon \to 0^+} \int_{\Gamma^i} d_{lk}^* t_k \, d\Gamma = \left[\frac{15\lambda^2 + 2\mu(8\lambda - 2\mu)}{30(\lambda + 2\mu)} u_{m,m}^i \delta_{kj} + \frac{6\lambda + 16\mu}{30(\lambda + 2\mu)} \mu \left(u_{k,j}^i + u_{j,k}^i \right) \right.$$

$$\left. + \frac{3\lambda + 2\mu}{6(\lambda + 2\mu)} \frac{Q}{R} \tau^i \delta_{kj} \right] n_j^i \delta_{lk} \quad (2.99)$$

$$\lim_{\epsilon \to 0^+} \int_{\Gamma^i} s_{00}^* \tau \, d\Gamma = -\frac{1}{2} J \tau^i \left(\lim_{\epsilon \to 0^+} \frac{1}{\epsilon} \right) - \frac{1}{3} J \tau_{,j} n_j^i \quad (2.100)$$

$$\lim_{\epsilon \to 0^+} \int_{\Gamma^i} s_{0k}^* u_k \, d\Gamma = \frac{1}{3} Z u_k^i n_k^i \quad (2.101)$$

$$\lim_{\epsilon \to 0^+} \int_{\Gamma^i} s_{l0}^* \tau \, d\Gamma = \frac{4\mu}{6(\lambda + 2\mu)} \frac{Q}{R} \tau^i \delta_{kj} n_j^i \delta_{lk} \quad (2.102)$$

$$\lim_{\epsilon \to 0^+} \int_{\Gamma^i} s_{lk}^* u_k \, d\Gamma = - \left[\frac{2\mu(7\lambda + 2\mu)}{30(\lambda + 2\mu)} u_{m,m}^i \delta_{kj} + \frac{9\lambda + 14\mu}{30(\lambda + 2\mu)} \mu \left(u_{k,j}^i + u_{j,k}^i \right) \right] n_j^i \delta_{lk}$$

$$- \frac{\mu}{4} \left[\frac{3\lambda + 4\mu}{\lambda + 2\mu} \delta_{lk} + \frac{\lambda}{\lambda + 2\mu} n_l^i n_k^i \right] u_k^i \left(\lim_{\epsilon \to 0^+} \frac{1}{\epsilon} \right) \quad (2.103)$$

where only non-null integrals are shown. Once these integrals over Γ^i are obtained, they can be substituted back into Equation (2.95), leading to an apparently unbounded HBIE:

$$\frac{1}{2} I_H^i t^i + \int_{\Gamma^R} S^* u \, d\Gamma + \lim_{\epsilon \to 0^+} \int_{\Gamma^{S-e^i}} S^* u \, d\Gamma + M^{\Gamma^i} u^i \left(\lim_{\epsilon \to 0^+} \frac{1}{\epsilon} \right) =$$

$$\int_{\Gamma^R} D^* t \, d\Gamma + \lim_{\epsilon \to 0^+} \int_{\Gamma^{S-e^i}} D^* t \, d\Gamma \quad (2.104)$$

where:

$$M^{\Gamma^i} = \begin{bmatrix} \dfrac{J}{2} & 0 \\ 0 & -\dfrac{\tilde{\mu}}{4} \left[(3\lambda + 4\mu)\delta_{lk} + \lambda n_l^i n_k^i \right] \end{bmatrix} \quad (2.105)$$

The integral over $\Gamma^S - e^i$ in the right hand side of Equation (2.104) is essentially similar to that of the left hand side of Equation (2.89). The term of d_{lk}^* leading to the strongly singular integral can be treated in a similar way:

$$d_{lk}^* = d_{lk}^{*(W)} + \frac{\tilde{\mu}}{4\pi} \frac{r_{,l} n_k^i - r_{,k} n_l^i}{r^2} = d_{lk}^{*(W)} + d_{lk}^{*(S)} \quad (2.106)$$

where the regularised integral associated with $d_{lk}^{*(\mathrm{S})}$ is:

$$
L_l^{(\mathrm{S})} = \frac{\tilde{\mu}}{4\pi} \left[\lim_{\epsilon \to 0^+} \int\limits_{\Gamma^{\mathrm{S}} - e^{\mathrm{i}}} \frac{r_{,l}(n_k^{\mathrm{i}} - n_k) - r_{,k}(n_l^{\mathrm{i}} - n_l)}{r^2} t_k \, \mathrm{d}\Gamma + \right.
$$

$$
\left. \lim_{\epsilon \to 0^+} \int\limits_{\Gamma^{\mathrm{S}} - e^{\mathrm{i}}} \frac{r_{,l} n_k - r_{,k} n_l}{r^2} \left(t_k - t_k^{\mathrm{i}} \right) \, \mathrm{d}\Gamma + \left(\epsilon_{lkj} \int\limits_{\Lambda^{\mathrm{S}}} \frac{\mathbf{e}_j \cdot \mathbf{t}}{r} \, \mathrm{d}\Lambda \right) t_k^{\mathrm{i}} \right] \quad (2.107)
$$

The integral over $\Gamma^{\mathrm{S}} - e^{\mathrm{i}}$ associated with $\mathbf{S}^*$ in Equation (2.104) is much more complicated. The integrals associated with s_{00}^* and s_{lk}^* are hypersingular, while the integrals associated with s_{0k}^* and s_{l0}^* are strongly singular. For the latter integrals, s_{0k}^* and s_{l0}^* can be split up into a term leading to weakly singular integrals at most, and a term leading to strongly singular integrals:

$$
s_{0k}^* = s_{0k}^{*(\mathrm{W})} + \frac{\tilde{\mu}}{4\pi} \frac{Q}{R} \frac{r_{,k} \left(\mathbf{n} \cdot \mathbf{n}^{\mathrm{i}} \right)}{r^2} = s_{0k}^{*(\mathrm{W})} + s_{0k}^{*(\mathrm{S})} \quad (2.108)
$$

$$
s_{l0}^* = s_{l0}^{*(\mathrm{W})} - \frac{\tilde{\mu}}{4\pi} \frac{Q}{R} \frac{r_{,l} \left(\mathbf{n} \cdot \mathbf{n}^{\mathrm{i}} \right)}{r^2} = s_{l0}^{*(\mathrm{W})} + s_{l0}^{*(\mathrm{S})} \quad (2.109)
$$

The integrals associated with $s_{0k}^{*(\mathrm{S})}$ and $s_{l0}^{*(\mathrm{S})}$ are both similar in nature, and can be regularised by using Equation (C.3) and the Stokes' theorem:

$$
M_0^{(\mathrm{S})} = \frac{\tilde{\mu}}{4\pi} \frac{Q}{R} \left[\lim_{\epsilon \to 0^+} \int\limits_{\Gamma^{\mathrm{S}} - e^{\mathrm{i}}} \frac{r_{,k} \left(\mathbf{n} \cdot \mathbf{n}^{\mathrm{i}} \right)}{r^2} \left(u_k - u_k^{\mathrm{i}} \right) \, \mathrm{d}\Gamma + \right.
$$

$$
\left. \left(- \lim_{\epsilon \to 0^+} \int\limits_{\Gamma^{\mathrm{S}} - e^{\mathrm{i}}} \frac{n_k}{r^2} \frac{\partial r}{\partial n^{\mathrm{i}}} \, \mathrm{d}\Gamma + \int\limits_{\Lambda^{\mathrm{S}}} \frac{\left(\mathbf{e}_k \times \mathbf{n}^{\mathrm{i}} \right) \cdot \mathbf{t}}{r} \, \mathrm{d}\Lambda \right) u_k^{\mathrm{i}} \right] \quad (2.110)
$$

$$
M_l^{(\mathrm{S})} = -\frac{\tilde{\mu}}{4\pi} \frac{Q}{R} \left[\lim_{\epsilon \to 0^+} \int\limits_{\Gamma^{\mathrm{S}} - e^{\mathrm{i}}} \frac{r_{,l} \left(\mathbf{n} \cdot \mathbf{n}^{\mathrm{i}} \right)}{r^2} \left(\tau - \tau^{\mathrm{i}} \right) \, \mathrm{d}\Gamma + \right.
$$

$$
\left. \left(- \lim_{\epsilon \to 0^+} \int\limits_{\Gamma^{\mathrm{S}} - e^{\mathrm{i}}} \frac{n_l}{r^2} \frac{\partial r}{\partial n^{\mathrm{i}}} \, \mathrm{d}\Gamma + \int\limits_{\Lambda^{\mathrm{S}}} \frac{\left(\mathbf{e}_l \times \mathbf{n}^{\mathrm{i}} \right) \cdot \mathbf{t}}{r} \, \mathrm{d}\Lambda \right) \tau^{\mathrm{i}} \right] \quad (2.111)
$$

The hypersingular integrals associated with s_{00}^* and s_{lk}^* can be treated in a similar way. The fundamental solution s_{00}^* can be split up in order to isolate the term leading to the hypersingular integral:

$$
s_{00}^* = s_{00}^{*(\mathrm{W})} + \frac{J}{4\pi} \frac{\mathbf{n} \cdot \mathbf{n}^{\mathrm{i}}}{r^3} = s_{00}^{*(\mathrm{W})} + s_{00}^{*(\mathrm{H})} \quad (2.112)
$$

The hypersingular integral associated with $s_{00}^{*(H)}$ can be regularised by using Equations (2.96), (C.2) and (C.3), and the Stokes' theorem:

$$
M_0^{(H)} = \frac{J}{2}\tau^i \left(\lim_{\epsilon \to 0^+} \frac{1}{\epsilon} \right) + \frac{J}{4\pi} \left[\lim_{\epsilon \to 0^+} \int_{\Gamma^{S-e^i}} \frac{\mathbf{n} \cdot \mathbf{n}^i}{r^3} \left(\tau - \tau^i - \tau^i_{,j} r_j \right) \, d\Gamma + \right.
$$

$$
\left(-\lim_{\epsilon \to 0^+} \int_{\Gamma^{S-e^i}} \frac{3}{r^3} \frac{\partial r}{\partial n} \frac{\partial r}{\partial n^i} \, d\Gamma + \int_{\Lambda^S} \frac{(\mathbf{r} \times \mathbf{n}^i) \cdot \mathbf{t}}{r^3} \, d\Lambda \right) \tau^i +
$$

$$
\left. \left(-\lim_{\epsilon \to 0^+} \int_{\Gamma^{S-e^i}} \frac{n_j}{r^2} \frac{\partial r}{\partial n^i} \, d\Gamma + \int_{\Lambda^S} \frac{(\mathbf{e}_j \times \mathbf{n}^i) \cdot \mathbf{t}}{r} \, d\Lambda \right) \tau^i_{,j} \right] = M_0^{(Hb)} + \frac{J}{2}\tau^i \left(\lim_{\epsilon \to 0^+} \frac{1}{\epsilon} \right) \quad (2.113)
$$

In order to treat the integral associated with s_{lk}^*, it is split up into three parts: a part leading to weakly singular integrals at most, a part leading to a hypersingular integral basically similar to Equation (2.113), and a part leading to a much more involved hypersingular integral:

$$
s_{lk}^* = s_{lk}^{*(W)} + \frac{\mu}{4\pi} 2\tilde{\mu}\delta_{lk} \frac{\mathbf{n} \cdot \mathbf{n}^i}{r^3} + \frac{\mu}{4\pi} \left[3\tilde{\lambda} \left(\frac{r_{,l} n_k^i}{r^3} \frac{\partial r}{\partial n} - \frac{r_{,k} n_l}{r^3} \frac{\partial r}{\partial n^i} + \frac{r_{,l} r_{,k} (\mathbf{n} \cdot \mathbf{n}^i)}{r^3} \right) + \right.
$$

$$
\left. 6\tilde{\mu} \left(\frac{r_{,k} n_l^i}{r^3} \frac{\partial r}{\partial n} - \frac{r_{,l} n_k}{r^3} \frac{\partial r}{\partial n^i} \right) + 2\tilde{\mu} \frac{n_l n_k^i}{r^3} + 2(\tilde{\lambda} - \tilde{\mu}) \frac{n_k n_l^i}{r^3} \right] = s_{lk}^{*(W)} + s_{lk}^{*(H1)} + s_{lk}^{*(H2)}
$$

$$(2.114)$$

where $\tilde{\lambda} = \lambda/(\lambda + 2\mu)$. The regularisation of the hypersingular integral associated with $s_{lk}^{*(H1)}$ gives:

$$
M_l^{(H1)} = \mu\tilde{\mu}\delta_{lk} u_k^i \left(\lim_{\epsilon \to 0^+} \frac{1}{\epsilon} \right) + \frac{\mu}{4\pi} 2\tilde{\mu}\delta_{lk} \left[\lim_{\epsilon \to 0^+} \int_{\Gamma^{S-e^i}} \frac{\mathbf{n} \cdot \mathbf{n}^i}{r^3} \left(u_k - u_k^i - u_{k,j}^i r_j \right) \, d\Gamma + \right.
$$

$$
\left(-\lim_{\epsilon \to 0^+} \int_{\Gamma^{S-e^i}} \frac{3}{r^3} \frac{\partial r}{\partial n} \frac{\partial r}{\partial n^i} \, d\Gamma + \int_{\Lambda^S} \frac{(\mathbf{r} \times \mathbf{n}^i) \cdot \mathbf{t}}{r^3} \, d\Lambda \right) u_k^i +
$$

$$
\left. \left(-\lim_{\epsilon \to 0^+} \int_{\Gamma^{S-e^i}} \frac{n_j}{r^2} \frac{\partial r}{\partial n^i} \, d\Gamma + \int_{\Lambda^S} \frac{(\mathbf{e}_j \times \mathbf{n}^i) \cdot \mathbf{t}}{r} \, d\Lambda \right) u_{k,j}^i \right] = M_l^{(H1b)} + \mu\tilde{\mu}\delta_{lk} u_k^i \left(\lim_{\epsilon \to 0^+} \frac{1}{\epsilon} \right)
$$

$$(2.115)$$

The regularisation process of the hypersingular integral associated with $s_{lk}^{*(H2)}$ starts by using

the expansion of u_k given in Equation (2.97):

$$M_l^{(H2)} = \lim_{\epsilon \to 0^+} \int_{\Gamma^S - e^i} s_{lk}^{*(H2)} \left(u_k - u_k^i - u_{k,j}^i r_j \right) \, d\Gamma + \left(\lim_{\epsilon \to 0^+} \int_{\Gamma^S - e^i} s_{lk}^{*(H2)} d\Gamma \right) u_k^i +$$

$$\left(\lim_{\epsilon \to 0^+} \int_{\Gamma^S - e^i} r_j s_{lk}^{*(H2)} d\Gamma \right) u_{k,j}^i = M_l^{(H21)} + M_l^{(H22)} + M_l^{(H23)} \quad (2.116)$$

where the integral $M_l^{(H21)}$ is weakly singular, $M_l^{(H22)}$ is hypersingular, and $M_l^{(H23)}$ is strongly singular. The hypersingular integral $M_l^{(H22)}$ is regularised by using Equations (C.4) and (C.5), and the Stokes' theorem, which gives:

$$M_l^{(H22)} = \frac{\mu}{4\pi} \left\{ \lim_{\epsilon \to 0^+} \int_{\Gamma^S - e^i} \left[3\tilde{\lambda} \frac{r_{,k}}{r^3} \left(n_l^i \frac{\partial r}{\partial n} - n_l \frac{\partial r}{\partial n^i} \right) + 6\tilde{\mu} \frac{r_{,l}}{r^3} \left(n_k^i \frac{\partial r}{\partial n} - n_k \frac{\partial r}{\partial n^i} \right) - 15\tilde{\lambda} \frac{r_{,l} r_{,k}}{r^3} \frac{\partial r}{\partial n} \frac{\partial r}{\partial n^i} \right] d\Gamma + \right.$$

$$3\tilde{\lambda} \int_{\Lambda^S} \frac{r_{,l} r_{,k} (\mathbf{r} \times \mathbf{n}^i) \cdot \mathbf{t}}{r^3} \, d\Lambda + 2\tilde{\mu} n_k^i \int_{\Lambda^S} \frac{(\mathbf{r} \times \mathbf{e}_l) \cdot \mathbf{t}}{r^3} \, d\Lambda + 2 \left(\tilde{\lambda} - \tilde{\mu} \right) n_l^i \int_{\Lambda^S} \frac{(\mathbf{r} \times \mathbf{e}_k) \cdot \mathbf{t}}{r^3} \, d\Lambda \left. \right\} u_k^i +$$

$$\frac{\tilde{\mu}\lambda}{4} \left(3\delta_{lk} + n_l^i n_k^i \right) u_k^i \left(\lim_{\epsilon \to 0^+} \frac{1}{\epsilon} \right) = M_l^{(H22b)} + \frac{\tilde{\mu}\lambda}{4} \left(3\delta_{lk} + n_l^i n_k^i \right) u_k^i \left(\lim_{\epsilon \to 0^+} \frac{1}{\epsilon} \right) \quad (2.117)$$

The strongly singular integral $M_l^{(H23)}$ is regularised by using Equation (C.6), then adding and subtracting respectively $n_l^i \left(\mathbf{n} \cdot \mathbf{n}^i \right)$ and $n_k^i \left(\mathbf{n} \cdot \mathbf{n}^i \right)$ from some of the n_l and n_k terms, and eventually using Equation (C.3) and the Stokes' theorem:

$$M_l^{(H23)} = \frac{\mu}{4\pi} \left\{ \lim_{\epsilon \to 0^+} \int_{\Gamma^S - e^i} \frac{1}{r^2} \left[3\tilde{\lambda} r_{,j} \left(r_{,l} n_k^i \frac{\partial r}{\partial n} - r_{,k} n_l \frac{\partial r}{\partial n^i} \right) + 6\tilde{\mu} r_{,j} \left(r_{,k} n_l^i \frac{\partial r}{\partial n} - r_{,l} n_k \frac{\partial r}{\partial n^i} \right) - \right. \right.$$

$$\tilde{\lambda} r_{,j} r_{,l} n_k \frac{\partial r}{\partial n^i} + \tilde{\lambda} \left(r_{,j} n_l^i - r_{,l} n_j^i \right) \left(n_k - n_k^i \left(\mathbf{n} \cdot \mathbf{n}^i \right) \right) + 2\tilde{\mu} r_{,j} \left(n_l n_k^i - n_k n_l^i \right) -$$

$$\tilde{\lambda} \left(\left(\delta_{lk} + n_l^i n_k^i \right) n_j + \left(\delta_{jk} - n_j^i n_k^i \right) n_l \right) \frac{\partial r}{\partial n^i} \right] d\Gamma + \tilde{\lambda} \left[\left(\delta_{lk} + n_l^i n_k^i \right) \int_{\Lambda^S} \frac{(\mathbf{e}_j \times \mathbf{n}^i) \cdot \mathbf{t}}{r} \, d\Lambda + \right.$$

$$\left(\delta_{jk} - n_j^i n_k^i \right) \int_{\Lambda^S} \frac{(\mathbf{e}_l \times \mathbf{n}^i) \cdot \mathbf{t}}{r} d\Lambda + \int_{\Lambda^S} \frac{r_{,l} r_{,j} (\mathbf{e}_k \times \mathbf{n}^i) \cdot \mathbf{t}}{r} d\Lambda \left. \left. \right] \right\} u_{k,j}^i \quad (2.118)$$

After developing the integrals over $\Gamma^S - e^i$ of Equation (2.104) throughout Equations (2.106-2.118), these can be substituted back into Equation (2.104) to obtain a fully regularised HBIE:

$$\frac{1}{2} \mathbf{I}_H^i \mathbf{t}^i + \int_{\Gamma^R} \mathbf{S}^* \mathbf{u} \, d\Gamma + \lim_{\epsilon \to 0^+} \int_{\Gamma^S - e^i} \mathbf{S}^{*(W)} \mathbf{u} \, d\Gamma + \left\{ \begin{array}{c} -M_0^{(Hb)} + M_0^{(S)} \\ -M_l^{(S)} + M_l^{(H1b)} + M_l^{(H22b)} + M_l^{(H23)} \end{array} \right\} =$$

$$\int_{\Gamma^R} \mathbf{D}^* \mathbf{t} \, d\Gamma + \lim_{\epsilon \to 0^+} \int_{\Gamma^S - e^i} \mathbf{D}^{*(W)} \mathbf{t} \, d\Gamma + \left\{ \begin{array}{c} 0 \\ L_l^{(S)} \end{array} \right\} \quad (2.119)$$

due to the cancellation of all unbounded terms appearing in Equations (2.113), (2.115) and (2.117) with the unbounded term appearing in Equation (2.104).

Dual Boundary Integral Equations The discussion given about DBIEs for the two-dimensional problem is similar to that of the three-dimensional problem, except for the logical changes regarding dimension. Abstract Dual BIEs shown by Equations (2.85) and (2.86) also hold for three-dimensional problems.

2.3.3 Discretisation, collocation techniques and integration

In this section, the relevant aspects of the implementation of the BEM used in this work are briefly described. The discretisation is performed using classical continuous isoparametric Lagrange elements. Two classes of boundary elements are considered: ordinary (or conventional) and crack-like. Crack boundary elements consider the crack as a whole, and thus they incorporate both faces. As previously commented, all calculations are performed over the reference face (positive face) and then the resulting integrals only differ in sign for the negative face.

In order to build up a solvable linear system of equations, an appropriate collocation of SBIEs and/or HBIEs is done throughout ordinary boundary elements, whereas the collocation of DBIEs is done throughout crack-like boundary elements. The HBIEs impose one important restriction on the choice of elements for the discretisation: the collocation point must be in a point where the primary variables are differentiable, i.e. $\mathbf{u}(\mathbf{x}^i) \in \mathscr{C}^1$. A typical solution used in crack analysis is to make use of discontinuous elements [43, 44], where nodes are located inside the elements and hence nodal collocation meets automatically this requirement. However, the usage of continuous boundary elements is more appropriate in this work for two reasons: they can be directly and efficiently coupled to most classical shell finite elements, and the continuity requirement can be avoided by using the Multiple Collocation Approach (MCA) proposed by Gallego et al. [60–62].

Consider a node κ shared by N continuous boundary elements. For a given boundary element e, the node κ has the local index k. MCA consists in building a BIE associated with κ by adding several BIEs, one BIE per each element e containing the node with a collocation point $\mathbf{x}^i$ located towards inside the element at a local coordinate ξ_k^i. The local coordinate ξ_k^i of the interior collocation point can be controlled by the dimensionless displacement parameter $\delta \in (0, 1)$, which allows calculating $\mathbf{x}^i$ as:

$$\mathbf{x}^i = \mathbf{x}^i(\xi_k^i) \text{ for } \begin{cases} \text{line elements: } \xi_k^i = (1 - \delta)\,\xi_k \\ \text{quadrilateral elements: } \xi_k^i = (1 - \delta)\,\xi_k \\ \text{triangular elements: } \xi_k^i = (1 - \delta)\,\xi_k + \delta/3 \end{cases} \tag{2.120}$$

where ξ_k is the local coordinate of the node k of the element. Therefore, the BIE for the node κ is obtained from:

$$\text{BIE}_\kappa = \sum_{e=1}^{e=N} \text{BIE}_k^e \left(\mathbf{x}^i(\xi_k^i) \right) \tag{2.121}$$

For crack-like boundary elements, where MCA is applied on every node, appropriate values of δ are those that produce collocation points located near Gaussian points ($\delta = 0.423$ for linear elements and $\delta = 0.225$ for quadratic elements). This is often used in the literature related to discontinuous and semi-discontinuous elements [7, 81, 82], and also leads to satisfactory results in this case [62]. Section 2.3.4 contains a study of the convergence using the SBIE with nodal and MCA collocation, and the HBIE with MCA collocation, for different values of δ, which again demonstrates this.

Figure 2.6 shows a mesh portion with collocation points required for nodal collocation and MCA approach for continuous elements, and also and the case of nodal collocation for discontinuous elements. Different colours are used for denoting when an the integration over an element is singular, quasi-singular or non-severe quasi-singular. It shows that nodal collocation requires the evaluation or more singular integrals, and there is no severe quasi-singular integrals unless thin geometries are present. The MCA approach not only requires the same number of singular integrals, but also present several quasi-singular integrals. In the case of discontinuous elements, only one singular integral is present in each case, but also quasi-singular integrals are present. The severity of the quasi-singular integrals depends on δ. These difficulties in the numerical integration are addressed in Chapter 4.

MCA can also be used to solve the indeterminacy present when using multiple nodes, being only used at those nodes. Although multiple nodes are not needed in many cases, see e.g. [83], and also other approaches like the use of semi-discontinuous can be used, the application of the MCA approach to solve this issue is particularly simple and effective. Subia et al. [84] compared semi-discontinuous and an approach similar to the MCA in potential problems, and concluded that both are reliable, but the former leads to better conditioning. They also concluded that the collocation point shifting δ has little influence over solutions when δ is between 0.1 to 0.6, and hence appropriate values of δ in this case are not that clear. If δ is relatively big, e.g. $\delta = 0.3$, then the indeterminacy problem is clearly solved, but the continuity of the primary variable across the multiple nodes is compromised. On the other hand, if δ is relatively small, e.g. $\delta = 0.001$, the primary variable is nearly continuous, but the condition number of the resulting linear system of equations could become too big, and also numerical integration issues could appear due to highly quasi-singular integrals. For those reasons, an intermediate value of $\delta = 0.05$ is considered in this work.

After the regularisation process shown in Section 2.3.2, numerically evaluated integrals can be regular or weakly singular. The way these are treated in this work can be found in Chapter 4.

2.3.4 Validation and convergence study

In this section, the three-dimensional regularised SBIE and HBIE for Biot's poroelasticity are validated. For this purpose, the problem of a spherical cavity of radius R_s in a poroelastic full-space and under harmonic radial excitation is considered. This problem has analytical solution, and its curved geometry allows to test all the terms involved in the Boundary Integral Equations.

The analytical solution is obtained by applying the Helmholtz decomposition to the radial displacements after expressing Equations (2.15a) and (2.15b) in spherical coordinates.

(a) NC for vertex node   (b) NC for edge node   (c) NC and MCA for face node

(d) MCA for vertex node   (e) MCA for edge node

(f) NC for a corner node   (g) NC for a lateral node   (h) NC for a central node
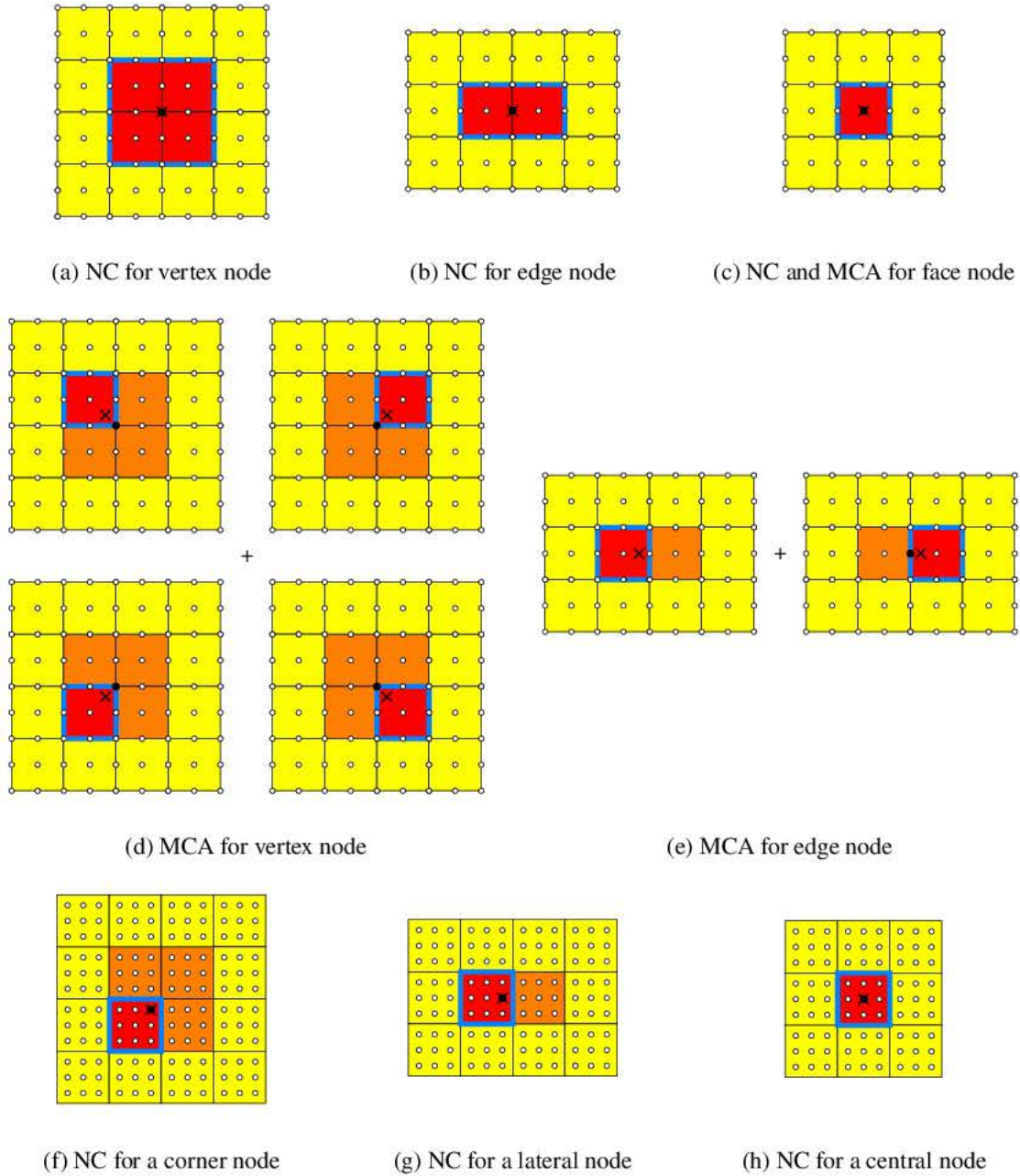
Figure 2.6: Nodal Collocation (NC) versus Multiple Collocation Approach (MCA) for continuous Lagrange elements (a-e). NC for discontinuous Lagrange elements (f-h). Red (singular integrals), orange (quasi-singular integrals) and yellow (non-severe quasi-singular integrals).

Taking into account that only outgoing P1 and P2 waves exist in this problem, solid and fluid displacements in the radial direction can be written as:

$$u_r(r) = -\sum_{j=1}^{j=2} D_j \left(ik_{\mathrm{P}j} + \frac{1}{r} \right) \frac{e^{-ik_{\mathrm{P}j}r}}{r} \varphi_{\mathrm{f}j} \tag{2.122}$$

$$U_r(r) = -\sum_{j=1}^{j=2} \left(ik_{\mathrm{P}j} + \frac{1}{r} \right) \frac{e^{-ik_{\mathrm{P}j}r}}{r} \varphi_{\mathrm{f}j} \tag{2.123}$$

where $D_j = \varphi_{\mathrm{s}j}/\varphi_{\mathrm{f}j} = -(\omega^2 \hat{\rho}_{22} - Rk_{\mathrm{P}j}^2)/(\omega^2 \hat{\rho}_{12} - Qk_{\mathrm{P}j}^2)$, and $\varphi_{\mathrm{s}j}$ and $\varphi_{\mathrm{f}j}$ are amplitudes of solid and fluid displacement potentials. Solid stress in the radial direction and fluid equivalent stress can be expressed as:

$$\tau_r(r) = \sum_{j=1}^{j=2} \left[\frac{4\mu D_j}{r} \left(ik_{\mathrm{P}j} + \frac{1}{r} \right) - \left(D_j \lambda_u + Q \right) k_{\mathrm{P}j}^2 \right] \frac{e^{-ik_{\mathrm{P}j}r}}{r} \varphi_{\mathrm{f}j} \tag{2.124}$$

$$\tau(r) = -\sum_{j=1}^{j=2} \left(QD_j + R \right) k_{\mathrm{P}j}^2 \frac{e^{-ik_{\mathrm{P}j}r}}{r} \varphi_{\mathrm{f}j} \tag{2.125}$$

where $\lambda_u = N + \mu$. The amplitudes $\varphi_{\mathrm{f}j}$ are obtained from the linear system of equations formed by the boundary conditions at $r = R_s$. The results presented in this work correspond to the following two sets of boundary conditions: $\tau_r(R_s) = P$ and $\tau(R_s) = 0$ (permeable cavity), and $\sigma_r(R_s) = \tau_r(R_s) + \tau(R_s) = P$ and $U_r(R_s) = u_r(R_s)$ (impermeable cavity).

The problem is solved for a spherical cavity of radius $R_s = 1$ m, and the following properties of the poroelastic medium (Berea Sandstone [74]): $\rho_{\mathrm{f}} = 1000$ kg/m^3, $\rho_{\mathrm{s}} = 2800$ kg/m^3, $\rho_{\mathrm{a}} = 150$ kg/m^3, $\lambda = 4$ GPa, $\mu = 6$ GPa, $\phi = 0.19$, $R = 0.444$ GPa, $Q = 1.399$ GPa and $b = 0.19 \cdot 10^9$ N · s/m^4. In order to present the results in a dimensionless fashion, dimensionless frequency $a_0 = \omega R_s/c_{\mathrm{P}}^u$ is used, where $c_{\mathrm{P}}^u = \sqrt{\lambda_u/(\phi \rho_{\mathrm{f}} + (1 - \phi)\rho_{\mathrm{s}})}$ is the undrained P wave propagation speed. Likewise, the quasi-static solid radial displacement $u_r^0 = \lim_{\omega \to 0} u_r$ is used to normalise the displacements.

BEM numerical solutions are obtained by collocating the BIE (SBIE or HBIE) using the MCA with $\delta = 0.225$. Only one-octant of the spherical cavity is discretised, and symmetry conditions with respect to the xy, yz and zx planes are enforced by the classical mirroring approach. Five isoparametric meshes of quadratic triangular elements are considered, including a crude mesh of only 1 element. This is a demanding set of meshes from the point of view of testing the BEM formulation for general curved elements. Since the solution is one-dimensional in the radial direction, i.e. radial displacements and stresses are constant over the cavity's surface, numerical errors are mainly due to the geometric discretisation error. The average geometric discretisation error E_{G} for a spherical surface can be defined as:

$$E_{\mathrm{G}} = \frac{\int_{A_{\mathrm{mesh}}} \left| \mathbf{x}_{\mathrm{mesh}} - \mathbf{x}_{\mathrm{surface}} \right| /R_s \, \mathrm{d}A}{\pi R_s^2/2} \tag{2.126}$$

where $\mathbf{x}_{\mathrm{surface}}$ is the nearest point of the spherical surface to a point of the mesh $\mathbf{x}_{\mathrm{mesh}}$.
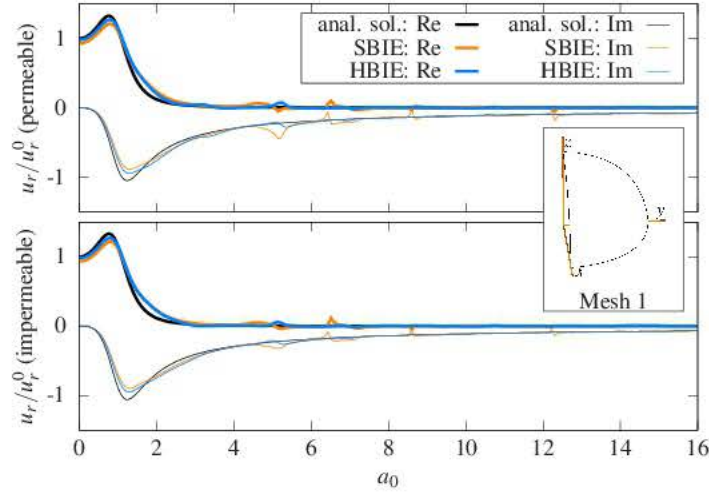
Figure 2.7: Comparison between analytical and BEM numerical solutions

Figure 2.7 shows analytical and BEM numerical solutions using the crude mesh of only one triangular element, for the frequency range $a_0 = (0, 16]$ and both sets of boundary conditions. Figures 2.8 and 2.9 show BEM numerical errors and orders of convergence. BEM numerical results are shown as average absolute errors:

$$E = \frac{\int_{A_{\text{mesh}}} |u_r^{(\text{numerical})} - u_r| / |u_r^0| \, dA}{\pi R_s^2 / 2} \tag{2.127}$$

The experimental order of convergence eoc between results obtained from two different meshes i and j is defined as:

$$eoc = \frac{\log E^{(i)} - \log E^{(j)}}{\log h^{(i)} - \log h^{(j)}} \tag{2.128}$$

where h denotes element size, and mesh j is finer than i. Table 2.1 shows a summary of mesh data and results, where frequency-averaged errors and experimental orders of convergence are denoted respectively as $\widetilde{E}$ and $\widetilde{eoc}$. These averaged values are computed from the frequency range $(0, \pi/h]$, i.e. the range where there are at least two elements per wavelength.

Results show that the SBIE and the HBIE behave hand in hand regarding the error levels for all meshes and frequencies. Convergence of the BEM using both the SBIE and the HBIE is demonstrated since E reduces in the same way as E_G does for each mesh, and within the whole frequency range. The expected order of convergence for quadratic elements is 3. However, the observed eoc within the relevant frequency range varies around 4, being very similar to the order of convergence of the geometric discretisation eoc_G.

When observing the obtained experimental orders of convergence, it is possible to distinguish three zones within the frequency range. For frequencies where there are less than two elements per wavelength, eoc is highly oscillatory. For frequencies where there are between two and approximately four elements per wavelength, eoc is higher than expected. And finally, for frequencies where there are more than approximately four elements per wavelength, eoc smoothly varies around eoc_G.
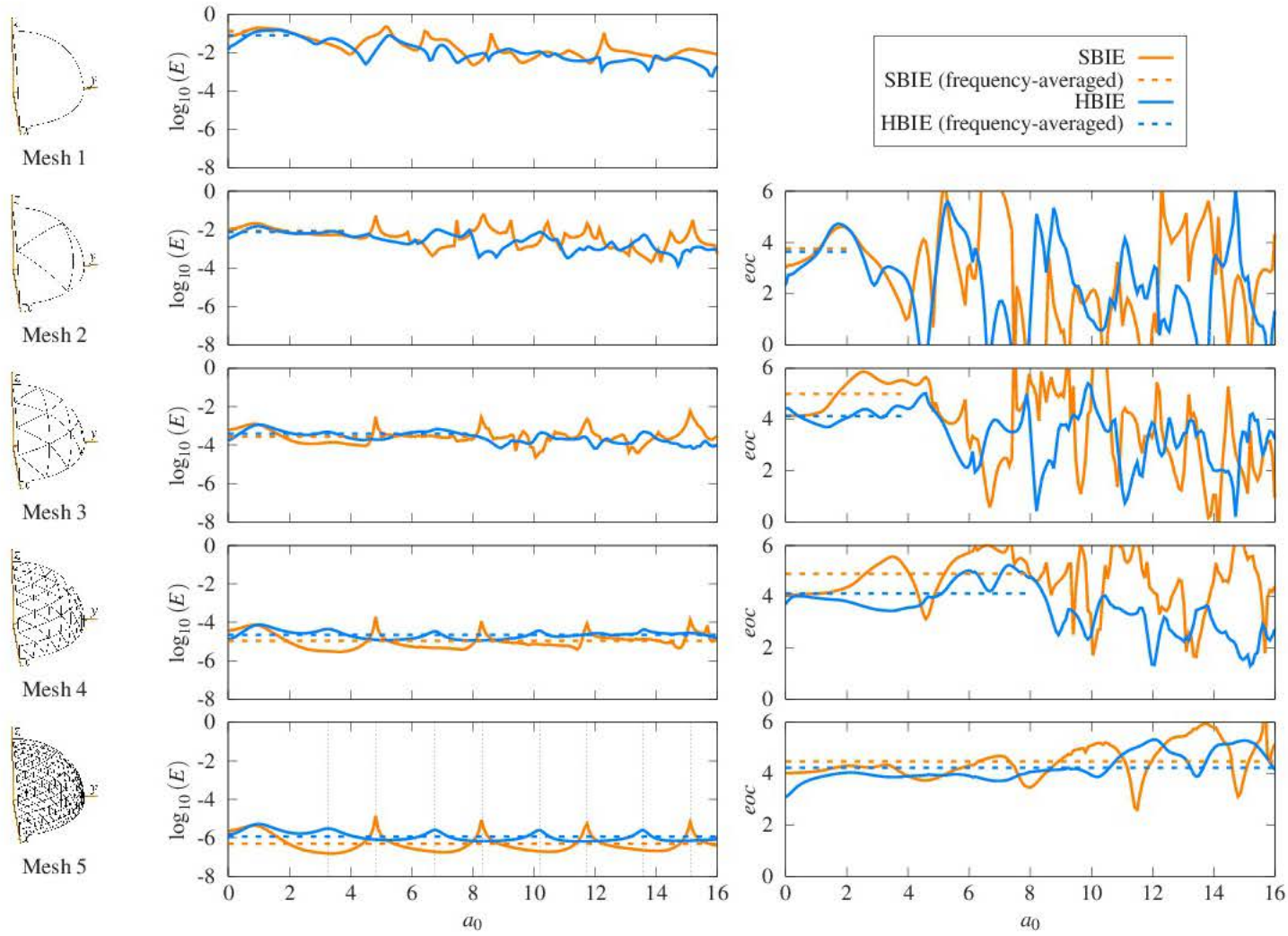
Figure 2.8: Validation. Spherical cavity with $\tau_r(R_s) = P$ and $\tau(R_s) = 0$ (permeable).
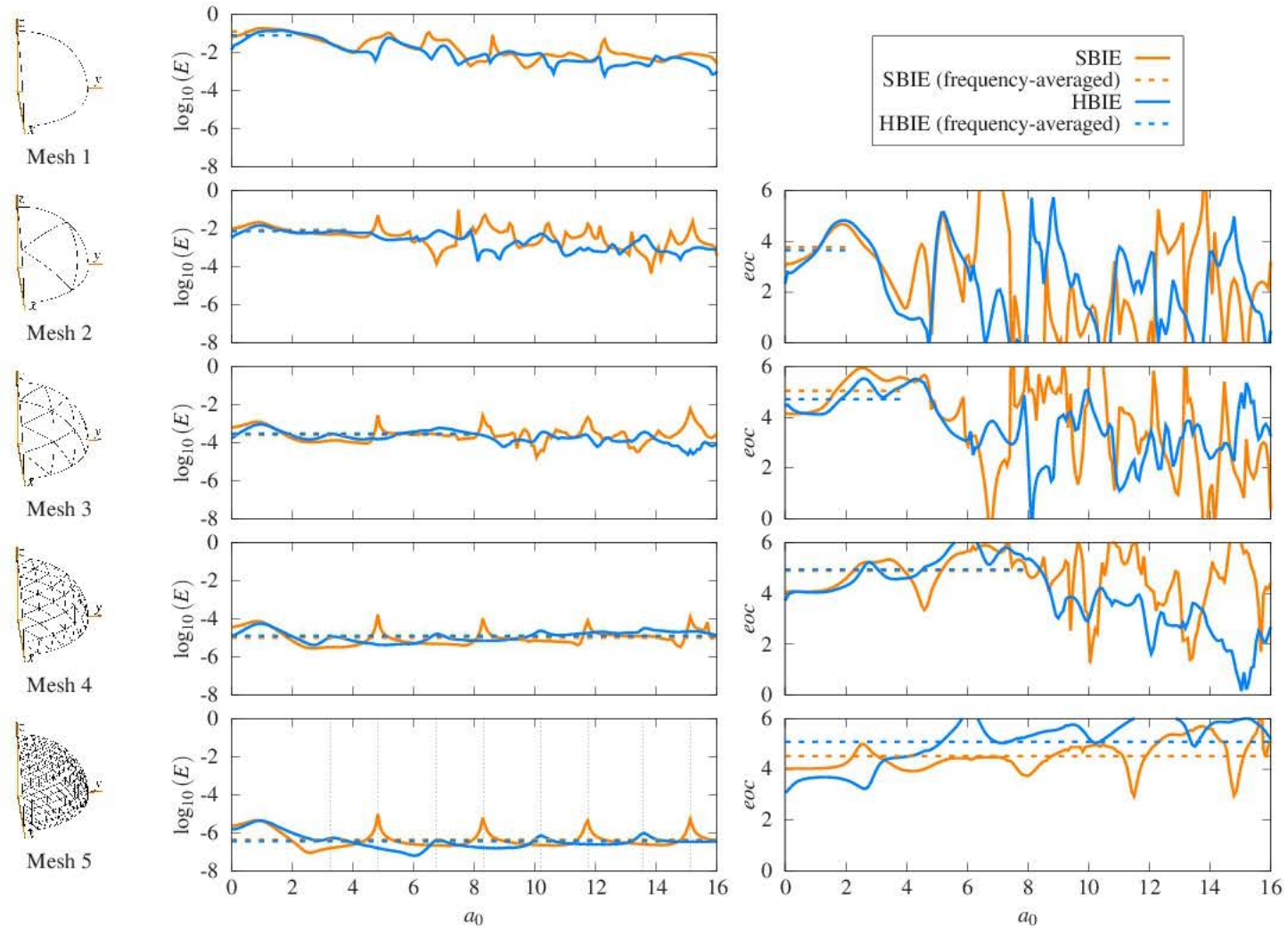
Figure 2.9: Validation. Spherical cavity with $\sigma_r(R_s) = \tau_r(R_s) + \tau(R_s) = P$ and $U_r(R_s) = u_r(R_s)$ (impermeable).

Mesh	1	2	3	4	5
N_{elements}	1	4	16	64	256
h [m]	1.41	0.77	0.39	0.20	0.10
E_{G}	2.3E-2	2.2E-3	1.6E-4	1.0E-5	1.2E-6
$\widetilde{E}$ (p, SBIE)	1.3E-1	8.7E-3	2.7E-4	1.1E-5	4.8E-7
$\widetilde{E}$ (p, HBIE)	7.9E-2	7.6E-3	4.0E-4	2.2E-5	1.2E-6
$\widetilde{E}$ (i, SBIE)	1.3E-1	8.5E-3	2.6E-4	1.0E-5	4.4E-7
$\widetilde{E}$ (i, HBIE)	8.1E-2	7.4E-3	3.0E-4	1.2E-5	3.7E-7
eoc_{G}	N/A	3.73	4.06	4.01	4.03
$\widetilde{eoc}$ (p, SBIE)	N/A	3.76	5.00	4.89	4.48
$\widetilde{eoc}$ (p, HBIE)	N/A	3.63	4.14	4.12	4.23
$\widetilde{eoc}$ (i, SBIE)	N/A	3.76	5.04	4.88	4.53
$\widetilde{eoc}$ (i, HBIE)	N/A	3.66	4.71	4.94	5.09

Table 2.1: Convergence of the BEM numerical solution for permeable (p) and impermeable (i) boundary conditions.
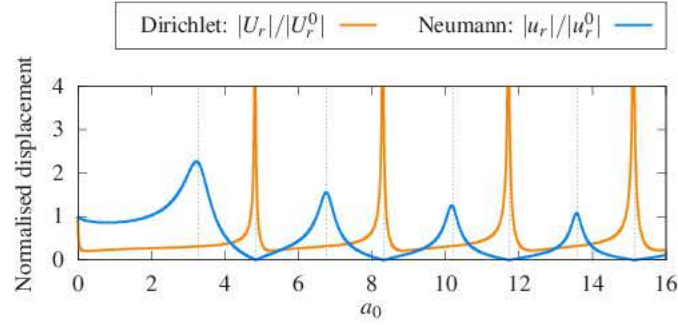
Figure 2.10: Analytical solution of a sphere with Dirichlet B.C. ($\tau_r(R_s) = 0$, $u_r(R_s) = U$) and Neumann B.C. ($U_r(R_s) = U$, $\tau_r(R_s) = 0$)

Regarding the BEM numerical errors, several peaks are observed at different frequencies for the SBIE and HBIE. They are related to the ill-conditioning of the exterior problem (spherical cavity) near the natural frequencies of an interior problem (sphere), see e.g. [67]. These natural frequencies correspond to the sphere with Dirichlet boundary conditions ($\tau_r(R_s)$ and $u_r(R_s)$ prescribed) for the spherical cavity solved using the SBIE, and to the sphere with Neumann boundary conditions ($U_r(R_s)$ and $\tau_r(R_s)$ prescribed) for the spherical cavity solved using the HBIE. Figure 2.10 shows the analytical solution of the Dirichlet and Neumann interior problems, and the observed natural frequencies are indicated by vertical dashed lines. For comparison purposes, they are also indicated in the bottom error graphs in Figures 2.8 and 2.9.

Figures 2.11 to 2.17 show results for the impermeable spherical cavity for different values of δ, from $\delta = 0.01$ to $\delta = 0.30$. In all graphs, it has also been included the case of using the SBIE with nodal collocation. As expected, the SBIE with MCA collocation tends to the SBIE with nodal collocation as $\delta \to 0$. The peaks associated with the interior problem are in the case of the SBIE with nodal collocation more pronounced. The order of convergence is slightly better in the case of MCA collocation as frequency increases, but overall there is

little difference for the range of δ studied. On the other hand, the convergence of the HBIE do depend on the collocation point shifting. It is observed that the order of convergence is one degree lower that in the case of the SBIE as $\delta \to 0$. From $\delta = 0.01$ to $\delta = 0.225$ the order of convergence improves until it reaches approximately that of the SBIE. From $\delta > 0.225$ onwards, it again starts to worsen. Therefore, optimal performance is achieved at $\delta = 0.225$.

We recognise that we are not in the position of fully explaining the obtained results regarding the convergence of the HBIE. The only references we have so far found regarding convergence of the HBIE are the works of Costabel and Stephan [85] and Amini and Kirkup [86], where the Helmholtz Equation is considered. The former paper is very difficult to understand for us, while the latter is more approachable. The results of Amini and Kirkup showed no difference between the convergence of the SBIE and the HBIE for a two-dimensional circle (interior problem) or cavity (exterior problem). The correspondence between their study and our numerical study is limited since it is not only performed for another type of problem, but is also uses constant elements, thus. The fact that we are able to achieve very small errors with the HBIE, and that the order of convergence for very small δ keeps almost parallel and one order lower than that of the SBIE, seems to indicate that either some subtle mistake is present in the formulation or implementation, or that this behaviour is intrinsic of this problem. Therefore, this issue requires further investigation in the future.
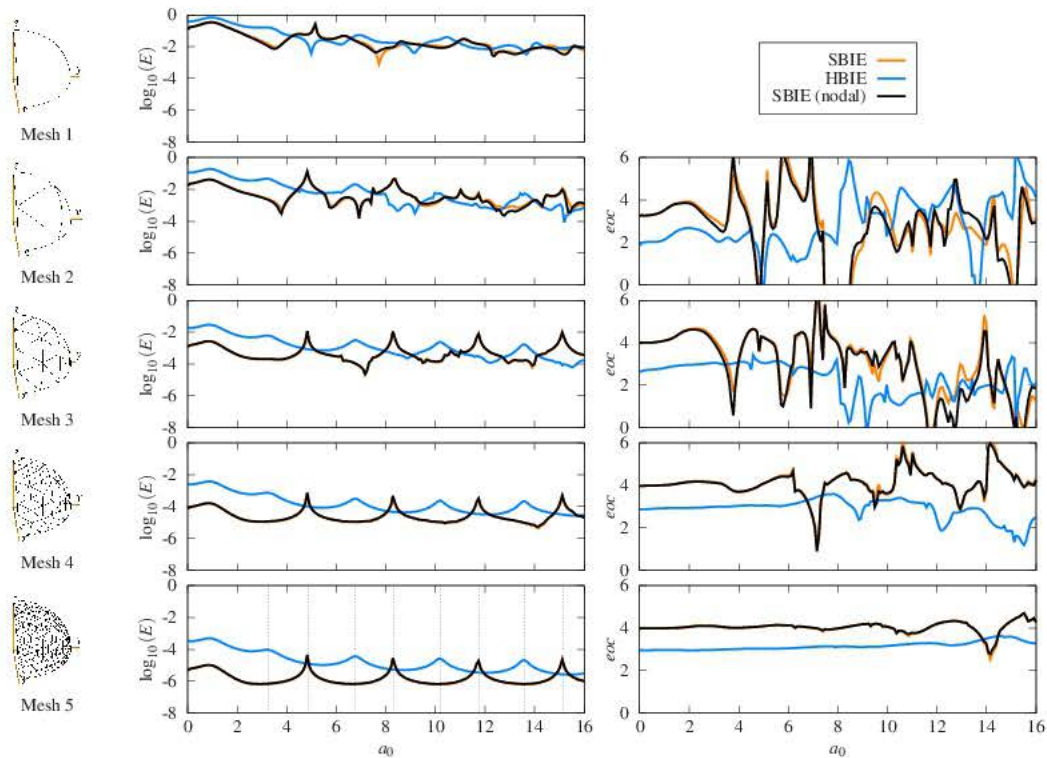
Figure 2.11: Spherical cavity with (impermeable B.C.). Case $\delta = 0.01$.
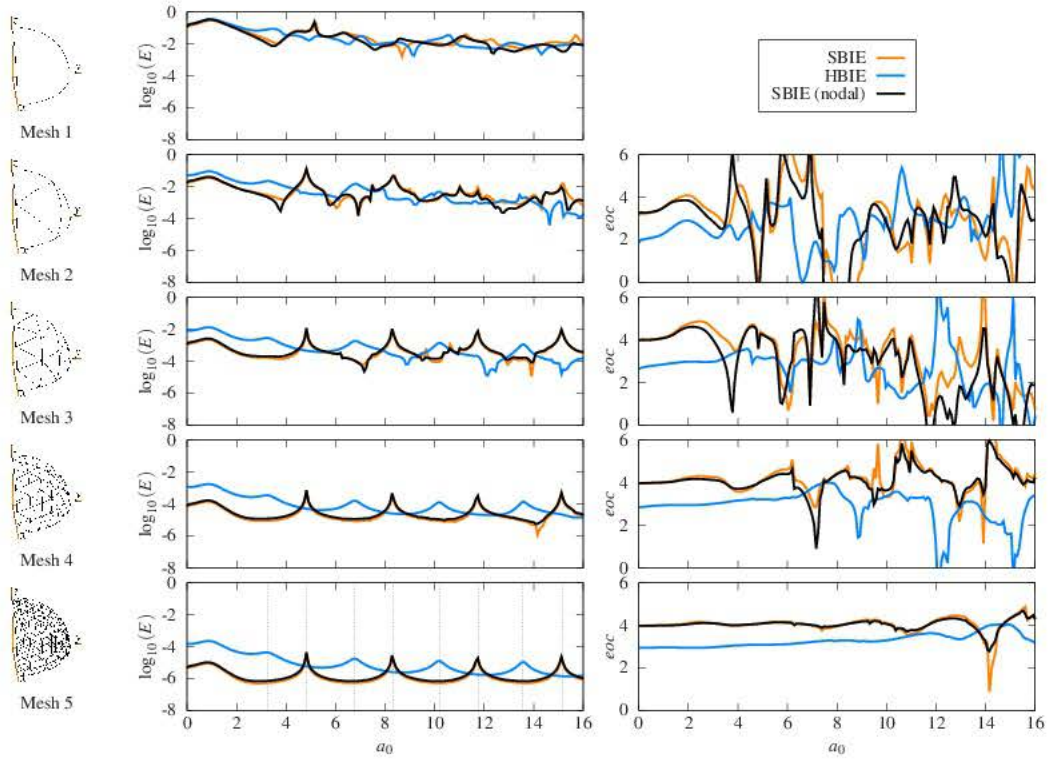
Figure 2.12: Spherical cavity with (impermeable B.C.). Case $\delta = 0.05$.
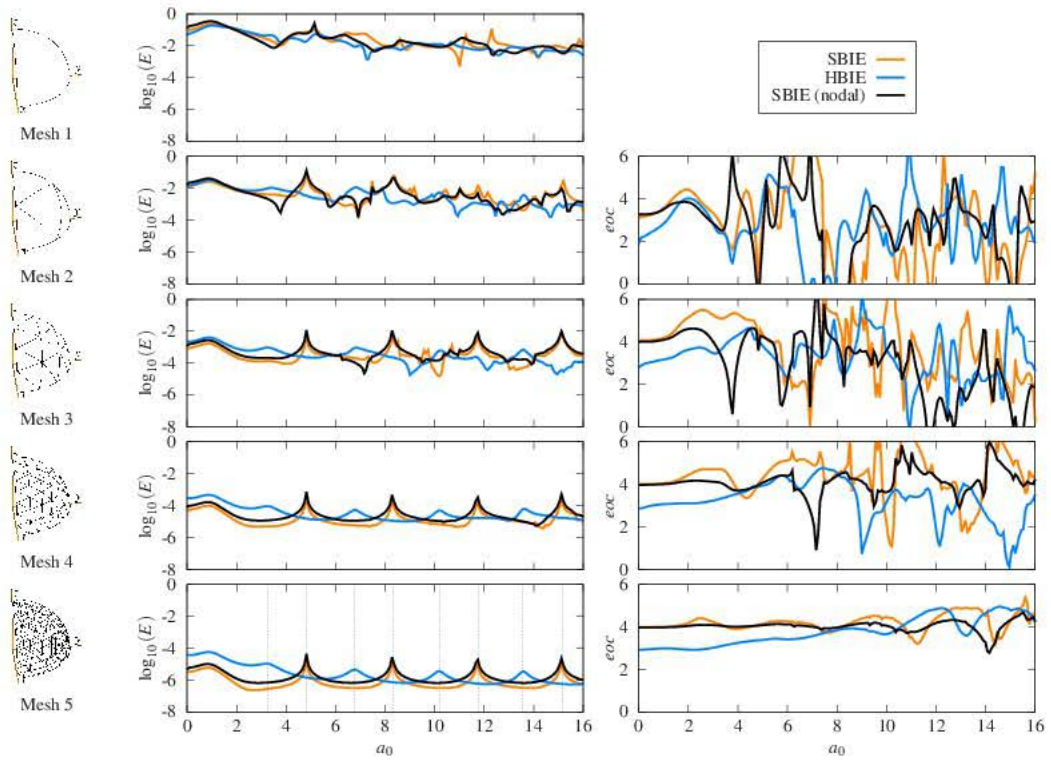
Figure 2.13: Spherical cavity with (impermeable B.C.). Case $\delta = 0.15$.
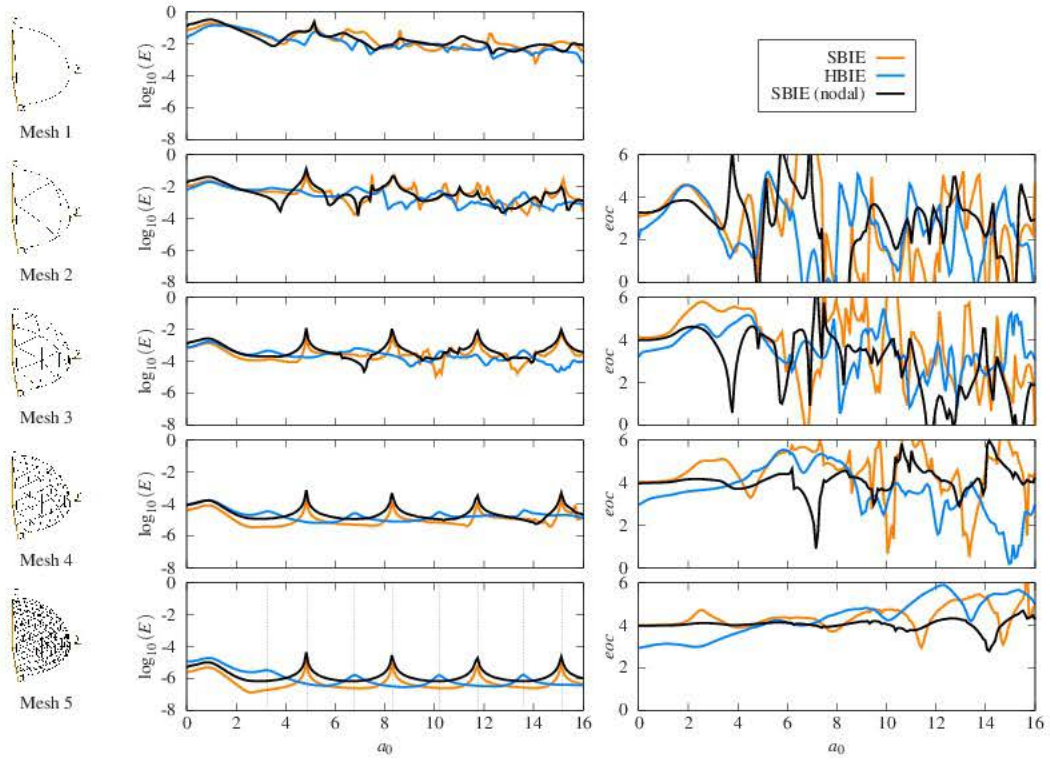
Figure 2.14: Spherical cavity with (impermeable B.C.). Case $\delta = 0.20$.
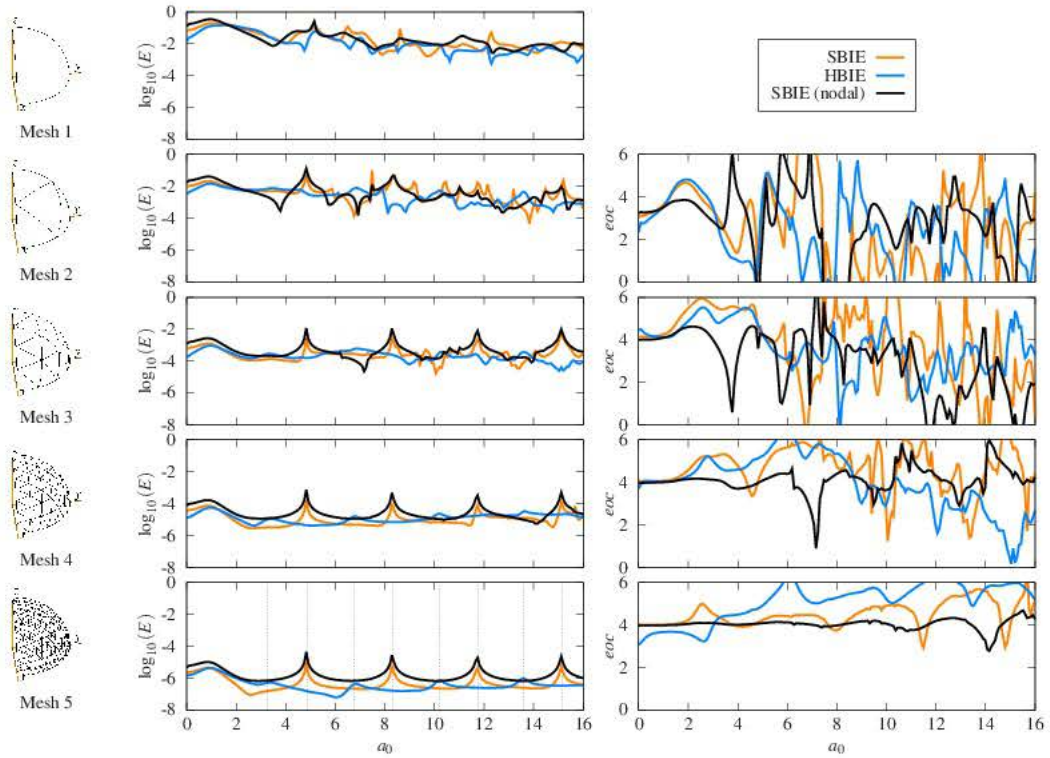
Figure 2.15: Spherical cavity with (impermeable B.C.). Case $\delta = 0.225$.
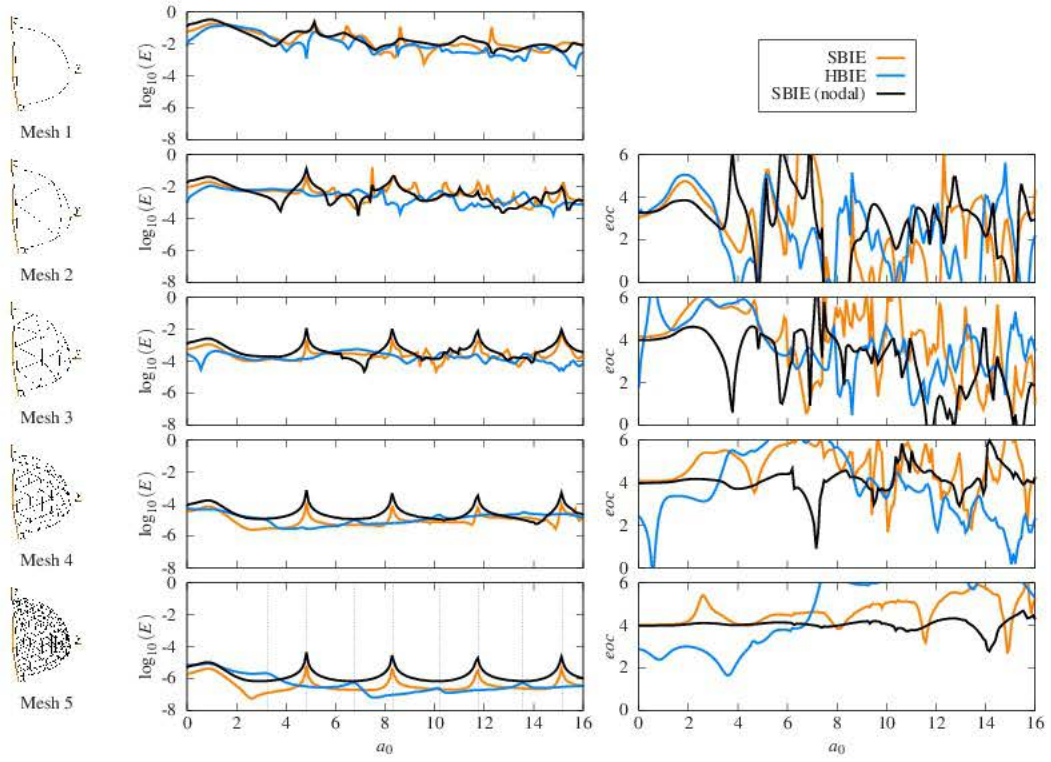
Figure 2.16: Spherical cavity with (impermeable B.C.). Case $\delta = 0.25$.
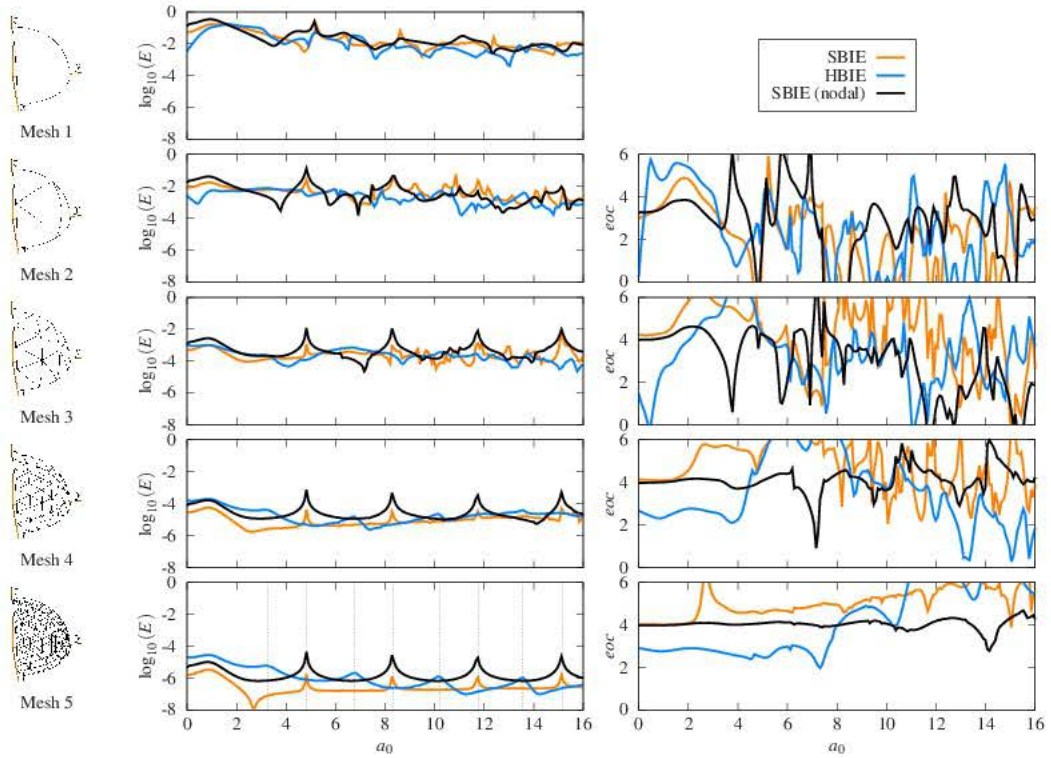
Figure 2.17: Spherical cavity with (impermeable B.C.). Case $\delta = 0.30$.

2.4 Finite Element Method for shell structures

The shell structure is modelled using shell finite elements based on the degenerated solid approach [87] for three-dimensional problems, and curved beam finite elements also based on the degeneration from the solid [88] for two dimensional problems. In the latter case, the two-dimensional shell conditions are achieved by considering a beam cross-section of unit depth and a modified Young's modulus $E/(1 - v^2)$. In the two-dimensional problems addressed in Chapter 5, a simpler straight Euler-Bernoulli beam of three nodes [18] is used.

The structural elements degenerated from the solid are versatile and relatively easy to handle. Their major drawback is the presence of shear and membrane locking, which are due to the inability of the displacement interpolation to represent thin shell (vanishing out-of-plane shear stresses in bending) and curved shell (vanishing in-plane stresses in inextensional bending) situations, respectively. Locking can be improved by using selective or reduced integration [88–90]. This lead to a versatile curved beam (arch) finite element. However, the resulting shell elements contain spurious zero-energy (hourglass) modes and hence are not reliable [91]. There are several approaches to obtain shell elements free from locking and spurious modes [92]. In this work, the family of Mixed Interpolation of Tensorial Components (MITC) shell elements [88, 93–96] developed by Bathe and co-workers is chosen because of its robustness and predictive capability. The approach consists in using covariant strains rather than local or global Cartesian strains, and different interpolation schemes for each strain component. The MITC9 shell element [94] is used in the present work.

The equilibrium equation of a shell finite element e can be written as:

$$\tilde{\mathbf{K}}^{(e)}\mathbf{a}^{(e)} - \mathbf{Q}^{(e)}\mathbf{t}^{(e)} = \mathbf{q}^{(e)} \tag{2.129}$$

where $\tilde{\mathbf{K}}^{(e)} = \mathbf{K}^{(e)} - \omega^2\mathbf{M}^{(e)}$ is the stiffness matrix for time harmonic analysis, $\mathbf{Q}^{(e)}$ is the distributed mid-surface load matrix and $\mathbf{q}^{(e)}$ is the vector of equilibrating nodal forces and moments. The vector of element Degrees Of Freedom (DOF) $\mathbf{a}^{(e)}$ is composed of vectors of nodal DOF:

$$\mathbf{a}^{(e)} = \begin{pmatrix} \mathbf{a}_1^{(e)} & \dots & \mathbf{a}_p^{(e)} & \dots & \mathbf{a}_N^{(e)} \end{pmatrix}^T \tag{2.130}$$

where N is the number of nodes of the shell finite element. Each node p has three DOF associated with the displacement of the mid-surface, and two local or three global rotations of the cross-section:

$$5\,\text{DOF node:} \quad \mathbf{a}_p^{(e)} = \begin{pmatrix} u_{1p}^{(e)} & u_{2p}^{(e)} & u_{3p}^{(e)} & \alpha_p^{(e)} & \beta_p^{(e)} \end{pmatrix}^T \tag{2.131}$$

$$6\,\text{DOF node:} \quad \mathbf{a}_p^{(e)} = \begin{pmatrix} u_{1p}^{(e)} & u_{2p}^{(e)} & u_{3p}^{(e)} & \theta_{1p}^{(e)} & \theta_{2p}^{(e)} & \theta_{3p}^{(e)} \end{pmatrix}^T \tag{2.132}$$

For efficiency reasons, nodes with 5 DOF are used by default. Nodes with 6 DOF are used only when strictly required, e.g. folded shells, or when they facilitate the application of boundary conditions, e.g. symmetry conditions. The vector of nodal values of the distributed mid-surface load $\mathbf{t}^{(e)}$ can be written as:

$$\mathbf{t}^{(e)} = \begin{pmatrix} \mathbf{t}_1^{(e)} & \dots & \mathbf{t}_p^{(e)} & \dots & \mathbf{t}_N^{(e)} \end{pmatrix}^T, \mathbf{t}_p^{(e)} = \begin{pmatrix} t_{1p}^{(e)} & t_{2p}^{(e)} & t_{3p}^{(e)} \end{pmatrix}^T \tag{2.133}$$

where $\mathbf{t}_p^{(e)}$ is expressed in global coordinates.

2.5 DBEM–FEM model

Let Ω_{shell} denotes the region occupied by the shell and $\Omega_{\text{surr. medium}}$ be the surrounding medium, which can totally or partially cover the shell. The main hypothesis of the proposed model over the reality is to assume that the interaction is established between the mid-surface of the shell structure and the surrounding medium – shell interface idealised as a crack-like boundary. Figure 2.18 illustrates this hypothesis by using a straight wall in a half-space. From the point of view of the surrounding medium, the shell structure is hence geometrically seen as a null thickness inclusion. From the point of view of the shell, the surrounding medium interacts only on its mid-surface. Therefore, it leads to two approximations:

- Wave diffraction is produced over the mid-surface of the shell structure rather than over its real boundaries, i.e. top-surface, bottom-surface, and edges are ignored. This approximation gets worse as thickness increases, being more pronounced near the shell edges, and also depends on the frequency, as it will be seen later.

- Stiffness and inertia are overestimated by the model if real elastic modulus and densities are used for the shell and the surrounding medium. This can be observed on the right part of Figure 2.18, where the shell region overlaps the surrounding medium added when assuming a crack-like boundary. An analogous phenomenon occurs in other soil-structure models, particularly in pile-soil interaction [18, 97]. Some authors propose using corrected properties for the structure ($\tilde{\rho}_{\text{structure}} = \rho_{\text{structure}} - \rho_{\text{soil}}$, $\tilde{E}_{\text{structure}} = E_{\text{structure}} - E_{\text{soil}}$) in order to compensate for them.

There are several methods of coupling boundary and finite elements in our context, see e.g. the classical work of Zienkiewicz et al. [9] or the textbook of Brebbia et al. [98]. From these, the most simple is the engineering direct approach where, from a conforming interface,

(a) Complete interaction   (b) Assumed interaction
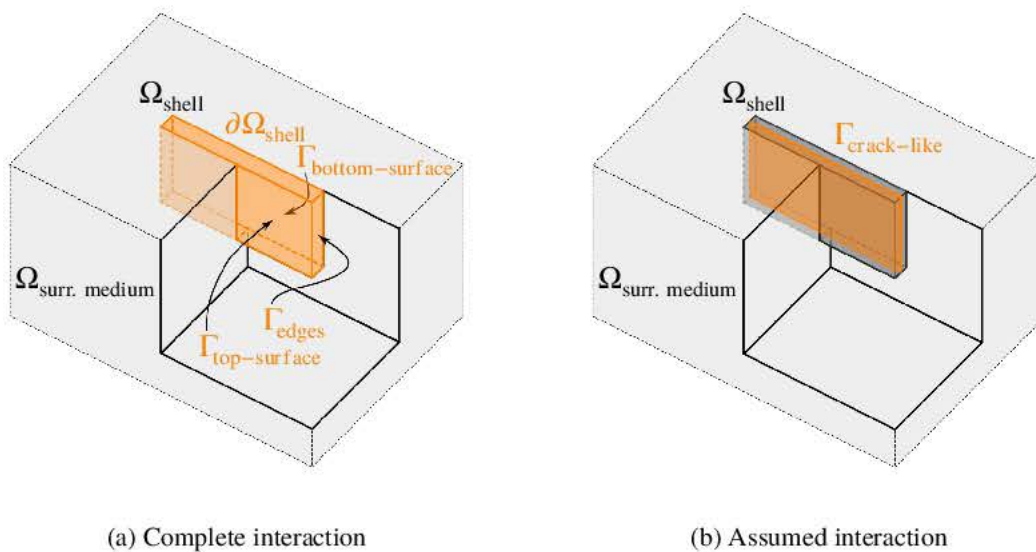
Figure 2.18: Main hypothesis of the proposed DBEM–FEM model

it is possible to establish compatibility of displacements and equilibrium of tractions. One of the ways of performing such coupling is the method called "nodal force matching" [99], where BEM tractions are considered as distributed loads of the FEM. This method is simple and effective, and this is the method considered here. A more rigorous and more precise coupling is that proposed by Belytschko et al. [100–102], where a global variational formulation including both the boundary element and the finite element region is stated. However, despite its potential benefits, we have chosen the direct approach as a cost effective solution.

Therefore, a direct BE–FE coupling after discretisation is considered, where both crack boundary element mesh and shell finite element mesh must be conforming, see Figure 2.19. There are hence three nodes at a given nodal position: a BE node related to the positive face of the soil, a BE node related to the negative face of the soil, and a FE node related to the shell. Let n_k^+, U_n^+, u_k^+, τ^+ and t_k^+ be respectively the unit normal, fluid normal displacement, solid displacement, fluid equivalent stress and solid traction of the BE node related to the positive face of the soil. Similarly, negative superscripts indicate variables on the negative face. The displacement of the shell mid-surface is denoted as u_k^s, and the distributed mid-surface load as t_k^s. Although other contact conditions may be considered, in the following it is assumed that the shell mid-surface and the soil crack-like boundary are in perfectly welded and impermeable contact. Therefore, compatibility and equilibrium coupling conditions can be written as:

Compatibility: $u_k^+ = u_k^s,\ u_k^- = u_k^s,\ U_n^+ = u_j^s n_j^+,\ U_n^- = u_j^s n_j^-$ \hfill (2.134)

Equilibrium: $\tau^+ n_k^+ + t_k^+ + \tau^- n_k^- + t_k^- + t_k^s = 0$ \hfill (2.135)

where $j = 1, \ldots, N_d$. Coupling equations (2.134) and (2.135) can easily be simplified for an elastic solid as surrounding medium:

Compatibility: $u_k^+ = u_k^s,\ u_k^- = u_k^s$ \hfill (2.136)

Equilibrium: $t_k^+ + t_k^- + t_k^s = 0$ \hfill (2.137)

And for an ideal fluid:

Compatibility: $U_n^+ = u_j^s n_j^+,\ U_n^- = u_j^s n_j^-$ \hfill (2.138)

Equilibrium: $-p^+ n_k^+ - p^- n_k^- + t_k^s = 0$ \hfill (2.139)

These coupling conditions are coherent with the location of all variables involved along the interfaces, except shell rotations, which are not present as degrees of freedom along the soil boundary. It means that there is not a complete displacement coupling because displacement continuity is only guaranteed at nodes. Also, tangential loads acting along the top- and bottom-surfaces of the shell that produce distributed bending moments are completely ignored. Both deficiencies, however, have little significance in most applications. Given that shell structures are almost always stiffer than soils, and the discretisation must be conforming, the size of shell elements are likely to be smaller than required by the elements-per-wavelength criterion, and thus the first deficiency is automatically alleviated. Because of the way most buried shell structures are loaded, the second deficiency is unlikely to be appreciable except for thick shells.

The proposed DBEM–FEM model has several advantages over other purely continuum or mixed continuum - structural models, which can be grouped into two categories:

$$U_n^+, u_k^+, \tau^+, t_k^+ \qquad u_k^s, \rho_r^s, t_k^s \qquad U_n^-, u_k^-, \tau^-, t_k^-$$

$$\mathbf{n}^+ \qquad\qquad \mathbf{n}^-$$

crack BE (+ face)   crack BE (− face)

shell FE (mid surface)
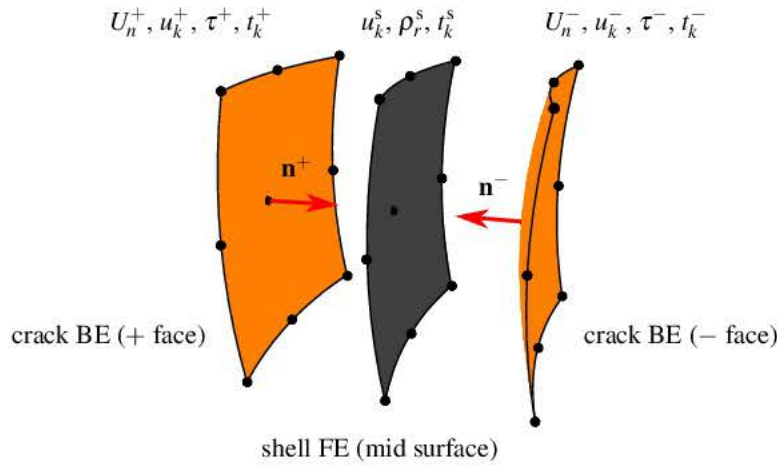
Figure 2.19: Exploded view of the BE–FE coupling

Methodological advantages It combines the well known ability of the BEM to deal with wave propagation phenomena in soils with the natural way shell structures are treated by the FEM. Since the shape and thickness of shell finite elements are considered independently, there is no need to define a fully detailed volume geometry. Consequently, the same surface mesh of shell finite elements can be used for studying shell structures of different thicknesses. Likewise, since the soil-shell interface is located at the shell mid-surface due to the use of the DBEM, a surface mesh of crack boundary elements conforming to the shell finite element mesh is all that is needed to model the soil in contact with the structure. Therefore, these simple surface meshes are able to represent the buried open shell structure, being furthermore thickness-independent.

Computational advantages Although it is difficult to quantify the computational advantage of this model because it depends on its implementation and the particular problem at hand, some comparative facts can be given:

- When compared to a multi-region BEM model (see e.g. [14, 17]) using the same element sizes, the number of degrees of freedom per shell node is reduced from 14 to 13 (-7%).

- A reduction in the number of degrees of freedom is automatically achieved since the edges of the shell structure are not discretised, and its thickness does not influence the mesh generation.

- The proposed model avoids common issues related to the BEM when dealing with thin geometries, i.e. quasi-singular integration and bad conditioning issues. Both issues are often alleviated by performing the integrals with a higher number of integration points and/or decreasing the element sizes, consequently increasing computational costs.

- When compared to a conventional multi-region BEM-FEM model applied to open shell structures (see e.g. [41]), there is no need to create fictitious interfaces that produce superfluous degrees of freedom.

- The main disadvantage of this model is the need of a regularised HBIE for the surrounding medium, which has to be obtained, and is computationally costlier than the SBIE. For homogeneous media, this is commonly affordable, but for inhomogeneous (layered, anisotropic, etcetera) media this could be a formidable task.

Regarding the quantification of the computational advantage, a first look is given in Section 5.4, where the proposed DBEM–FEM model and a multi-region BEM model [14, 17] are compared. It is observed that a relevant computation time reduction is achieved mainly due to the decrease of the number of degrees of freedom. The DBEM–FEM model is validated for two- and three-dimensional problems involving ideal fluids, elastic solids and poroelastic media in Chapters 5 and 6.

3.1 Introduction

In this chapter, the initial steps towards the development of a multi-region model are described. The Singular Boundary Integral Equations for shape sensitivity analysis on Laplace, Helmholtz, elastostatic and elastodynamic two-dimensional problems have been formulated and implemented in a multi-region code. The formulations were developed by Gallego and Rus [103–107], although here they are again derived in a slightly different manner. The aim is to describe the work done in this field, which is used to solve the shape optimisation of wave barriers in Chapter 5.

The rest of the chapter is organised as follows. An introduction to the subject is given through Sections 3.2, 3.3 and 3.4. A brief literature review about the BEM for shape sensitivity is given in Section 3.5. From Section 3.6 to 3.10, the BEM formulation for shape sensitivity is described for different problems. In Section 3.11, coupling conditions for shape sensitivity are described. The chapter concludes with Section 3.12, where the formulation and implementation is validated against simple problems with analytical solution.

3.2 Optimisation

Nowadays, design optimisation is a crucial field in engineering. When facing a design problem, the very first step is to come out with a solution or a concept that simply works, i.e. the design does what is required. In our competitive environment this is not enough, and the design must fulfil several constraints and perform well under different conditions. Furthermore, the main objectives are usually accompanied by other secondary objectives, which can even be in conflict. In order to achieve such a task, it is necessary to define appropriately these objectives and constraints, then select a suitable optimisation algorithm, which, eventually, requires a numerical simulation of the problem.

The mathematical formulation of an optimisation problem can be written as [108]:

$$\min_{a \in \mathbb{R}^n} f_i(a), i \in \mathscr{F} \text{ subject to } \begin{cases} g_i(a) \leq 0, \ i \in \mathscr{I} \\ h_i(a) = 0, \ i \in \mathscr{E} \end{cases} \tag{3.1}$$

where f_i, g_i and h_i are scalar valued functions of the variables a, and $\mathscr{F}$, $\mathscr{I}$ and $\mathscr{E}$ are sets of indices. The variable a is the vector of design variables. The functions f_i are the objective functions, g_i the inequality constraints, and h_i the equality constraints. Optimisation is a very active field of research because of its complexity and usefulness. There are a plethora of optimisation algorithms, each of one designed to target a range of problems. They can be mainly divided into deterministic and heuristic approaches. The deterministic approach take analytical properties of the problem to generate points that converge to optimal solutions. The heuristic approach is more flexible than the deterministic one, but the quality of the obtained solution cannot be guaranteed and the number of evaluations of the objective function is usually greater. A good reference on deterministic algorithms is [108], and on heuristic algorithms [109, 110].

The structural optimisation problem can be explained using the paradigm of three interacting models [111]: the design model, the analysis model and the optimisation model. Here,

we give a slightly broader definition of this paradigm in order to include other aspects than geometry.

The design model is a subset of all possible designs. Thus, it is a decisive step that needs some knowledge about the problem at hand. The description of a design model comprises information about its geometry, materials and conditions. The most important piece of information is the geometrical one. All others are somehow supported on it. The geometric description consists of information related to the topology, i.e. number of sub-domains and their connectivity, and information related to the shape of each sub-domain. The material information offers data about the type of material and its properties at each point of the domain. Each sub-domain is usually made of the same type of material with homogeneous properties, but in general the properties could vary over it. The description about conditions consists of support, interface and load information. All this information must be expressed in a mathematical form as a set of equations, inequalities and variables (continuous or discrete). Eventually, some of the variables become constants, parameters or design variables, being these latter those that actually change during the optimisation process.

The analysis model allows evaluation of objective and constraint functions, and their gradient or even Hessian if needed by the optimisation model. This model must be equivalent to the design model, but ready to be used by an analysis procedure. The analysis procedure can be a closed-form analytical solution, but more often is a semi-analytical or numerical procedure.

The optimisation model selects the best design according to the objective and constraint functions from the possibilities offered by the design model. For a multi-objective optimisation, it gives a range of designs which defines the Pareto front. The model requires the definition of the design variables and their domains, the objective and constraint functions, and the optimisation algorithm. The optimisation model acts as the job manager in the optimisation process, i.e. it decides at each step what designs have to be analysed and then takes further decisions using the analysis results.

3.3 Sensitivity analysis

Most of the analyses consist in obtaining the response of a given design, these are the usual zero-order static, time harmonic, transient, modal, etc. analyses. In order to study the influence of some design parameters, it is possible to run several zero-order analyses with different values of these design parameters, i.e. a parametric study. It is appropriate when the engineer would like to have a global idea of the performance of the design for a range of variation of a small number of parameters. For other purposes like optimisation, identification or reliability studies, zero-order analyses are usually not enough. Sensitivity analyses consist in obtaining first- and second-order static, time harmonic, transient, modal, etc. analyses of a design with respect to the variation of continuous design parameters [112].

Let $\mathbf{a}$ be a vector of continuous design parameters, and $f = f(\mathbf{a})$ a field variable (displacement, velocity, stress, etc.) or combination of field variables (performance, constraints, etc.). If f is smooth enough ($f \in \mathscr{C}^2$), it is possible to build a Taylor's approximation of f

near a given set of values of the design parameters $\mathbf{a}^0$:

$$f\left(\mathbf{a}\right) = f^0 + f_{,j}^0 \left(a_j - a_j^0\right) + f_{,jk}^0 \left(a_j - a_j^0\right)\left(a_k - a_k^0\right) + \mathcal{O}\left[(\Delta a)^3\right] \tag{3.2}$$

where f^0 is obtained from a zero-order analysis, $f_{,j}^0$ from a first-order sensitivity analysis (gradient), and $f_{,jk}^0$ from a second-order sensitivity analysis (Hessian), all at $\mathbf{a} = \mathbf{a}^0$. Note that indicial notation, comma notation for derivatives with respect to the design parameters, and Einstein summation convention are used in Equation (3.2). Most of the literature about sensitivity analysis is focused on first-order analysis. Second-order analysis, although useful for checking optimality conditions, is seldom performed because of its computational cost and its comparatively narrow range of applications [112]. Therefore, in the following, the term "sensitivity" is used as a synonym of "first-order sensitivity".

There are four major methodologies for obtaining sensitivities [113]: overall or global finite differences, continuum derivatives, discrete derivatives and computational or automatic differentiation. The last three methodologies can be formulated as direct and adjoint methods. In the direct approach, the derivatives of the entire structural response are obtained, and then the performance functions can be obtained by using the chain rule of differentiation. In the adjoint approach, an adjoint problem is formulated for each performance function, and hence not all derivatives of the structural response are obtained. Roughly speaking, the direct approach focuses on structural response, while the adjoint approach focuses on structural performance. The former is appropriate for a small number of design variables and a big number of performance functions, and the latter is appropriate for the opposite. In both approaches, the obtained matrix of the linear system of equations (stiffness or influence matrix) is exactly equal to that of the zero-order analysis, and thus its factorisation could be used for the sensitivity analysis. The effort is employed in building the vector of the linear system of equations (load vector). Van Keulen et al. [113] give a very complete review of methods of structural sensitivity analysis. Next, a brief overview is given.

The Global Finite Differences (GFD) methodology is based on estimating the performance sensitivity $f_{,j}^0$ by using a finite difference formula which requires only zero-order analyses:

$$f_{,j}^0 \simeq \mathrm{FD}\left[f^0, \Delta a_j^0\right] \tag{3.3}$$

where the FD operator can represent a forward, central, 4-point central, etc. finite difference formula with a perturbation Δa_j^0 on the j-th design variable. It is the easiest method to implement. However, it is computationally inefficient and unreliable as an appropriate value of the perturbation is needed. Furthermore, not always is possible to find a finite difference formula and a value of the perturbation that lead to a sensitivity with the required precision. Therefore, GFD should be the last resort for computing sensitivities.

In the Continuum Derivatives (CD) approach, the sensitivities are obtained by differentiating the continuum governing equations (partial differential or integro-differential equations). It leads to a set of continuum sensitivity equations which are then usually solved numerically. For shape sensitivities, because the domain itself becomes a design variable, a material differentiation approach or a control volume approach must be used [114].

In the Discrete Derivatives (DD) approach, the sensitivities are obtained by differentiating the discretised set of equations. Thus, in the DD approach the differentiation and discretisation processes are reversed with respect to the CD approach. For some cases, if the same numerical method and discretisation is used, it has been proven that both approaches lead to the same solution [111]. The element-wise matrices obtained after differentiation involves derivatives of the stiffness and load matrices. Although these derivatives can be evaluated analytically, they are particularly involved and lengthy for shape sensitivities. Therefore, they are usually approximated by finite differences, which not only is much more easy to implement, but also is cheaper computationally. In this case, the approach is called semi-analytical.

Automatic Differentiation (AD) approach consists in the differentiation of the computer code itself. Although finite element codes are composed of many more or less complex subroutines and functions, they are basically a collection of elementary functions. AD approach defines the partial derivatives of these elementary functions, and then the derivatives of complicated subroutines and functions are computed using propagation and the chain rule of differentiation. Although it may appear to be simple and straightforward, it is not. It requires enough skills to apply the tools to the source code, and a judicious choice of where to apply it in order to get an efficient code. Furthermore, it could require the modification of the original code before applying the tools.

3.4 Parametrisation

Parametrisation (or parameterisation) is the process by which some entity is described in terms of parameters. In our context, this is done over the description of the design model. The parametrisation of a design is not unique nor trivial, it has a huge impact on the result of an optimisation process. In fact, it materialises the design model by setting a set of parameters and mathematical expressions that defines the geometry, material and conditions of a design model. The parameters that are used in an optimisation process are the design variables.

In structural design, there are mainly five kinds of parameters [112]: material parameters (Young's modulus, fiber orientation, etc.), size parameters (thickness, cross-section, etc.), shape parameters (length, radius, etc.), configuration parameters (orientation and location of structural elements), and topological parameters (number and connectivity of structural elements). Note that some of them are closely related, and, for example, the last four could be grouped as geometrical parameters. These parameters can be also classified as discrete (boolean or integer) or continuous (real) parameters.

The literature about geometric parametrisation is vast and specialised, particularly in shape parametrisation, which is probably the most involved. Before going further, it is necessary to define some concepts related to shape parametrisation and sensitivity analysis. For first-order analyses, each shape parameter is studied independently from others, i.e. the sensitivities are obtained without considering other shape parameters. Although several parameters could be linked through some constraints in order to obtain a feasible design, this is something managed by the optimisation algorithm and does not influence the first-order sensitivity analysis. For this reason, it is possible to build a Taylor's expansion of the geometrical

design with respect to the parameter a around a given state $a = a^0$:

$$\tilde{\mathbf{x}} = \mathbf{x} + \mathbf{v}\left(a - a^0\right) + \mathcal{O}\left[\left(a - a^0\right)^2\right] \tag{3.4}$$

where $\mathbf{x}$ is a point of the domain $\Omega(a^0)$, $\mathbf{v} = \mathbf{v}(\mathbf{x}, a^0) = (\partial \mathbf{x}/\partial a)_{a^0}$ is the design velocity field, and $\tilde{\mathbf{x}} = \tilde{\mathbf{x}}(\mathbf{x}, a)$ is the new location of the point $\mathbf{x}$ for a parameter value a. This is a linear mapping of points of the domain $\Omega(a^0)$ to $\tilde{\Omega}$, that approximates the domain for a small variation of a, see Fig. 3.1. It must obviously be continuous, i.e. $\mathbf{v} \in \mathcal{C}^0$, otherwise the mapping breaks the domain.
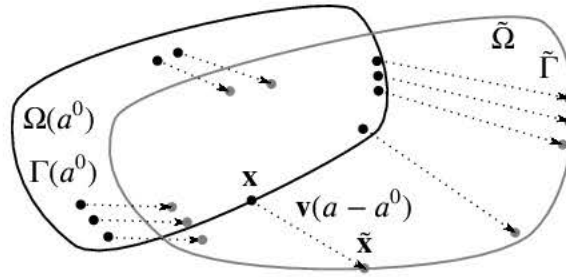
Figure 3.1: Taylor's expansion of the shape parametrisation

For first-order shape sensitivity analysis, the design velocity field $\mathbf{v}$ of each design variable has to be defined for all points of the domain. There are a large number of strategies to build and update this mapping during optimisation processes [111, 112, 115–117]. Although it is difficult to classify all these strategies, there are three main philosophies:

Based on geometry. In order to build the geometry, it is necessary to use a CAD (Computer Aided Design) tool which can use a Boundary REPresentation (BREP), Function REPresentation (FREP), Constructive Solid Geometry (CSG) or other representation. Since the representation is based on a set of equations and parameters, these parameters are available as design variables. Once the mesh is obtained from the CAD model by a mesher, the design velocity field of each design variable can be inherited to the nodes of the mesh by differentiation of the representation with respect to the design variable at the position of the nodes.

Based on mesh. Instead of working with the representation given by the CAD model, it is possible to use the representation provided by the mesh. The nodal coordinates are used as design variables, which lead to a big set of design variables. It is also called parameter-free or FE-based parametrisation.

Based on a free-form deformation. An auxiliary design mesh consisting of isoparametric elements, B-splines or NURBS is defined in order to deform the CAD model or the mesh. The points of the CAD model or the nodes of the mesh are connected to the design mesh by position, i.e. there is a one-to-one correspondence (a mapping) between the design model and the CAD model or mesh. The design mesh acts as a canvas where the CAD model or the mesh is stuck, and any deformation applied to the canvas

is accordingly done over them. The design variables can be the nodal coordinates or control points of the design mesh.

None of the strategies are of general applicability. The strategies based on geometry are useful for clearly defined shape optimisations, for example when the design variables are radii, lengths or positions of straight or arc-like lines. If the CAD model allows patches of variable order, then it would be possible to obtain more complicated shapes. A major drawback is that CAD tools do not usually come with all the necessary features to apply these strategies easily. The strategies based on mesh movement offer more freedom to the shape optimisation. However, this freedom comes with some additional costs. Regularisation and remeshing processes are needed after each optimisation step in order to obtain a feasible design and a valid mesh. Furthermore, because of the number of design variables and the post-processing stages after each iteration, they can be relatively expensive computationally. The strategies based on a free-form deformation have characteristics of the latter two. They offer a selective in-between flexibility with respect to shape variations, from very simple and constrained shapes to very complex shapes. Moreover, they have much less problems associated with the distortion of the mesh, and thus regularisation and remeshing are hardly needed.

3.5 BEM applied to sensitivity analysis

The application of the BEM to sensitivity analysis is an active research field that started in the early 1980s. Barone et al. [118] applied a special form of the BEM to the optimal arrangement of holes in a two-dimensional domain. Meric used the BEM with the Adjoint Variable Method (AVM) in order to study heat transfer and mechanical behaviour of solids [119–121]. Mota Soares et al. [122] applied the BEM to optimal shape design for minimum compliance. Kane et al. [123] used implicit differentiation of the discretised equations for plane elasticity. Barone et al. [124, 125] used the material derivative over the Boundary Integral Equations (BIE), including the Hypersingular (stress) BIE (HBIE), for three-dimensional elasticity. Aithal and Saigal [126, 127] applied the AVM and the material derivative to obtain the shape sensitivities for thermal and elasticity problems.

Besides being useful by itself or for shape optimisation, shape sensitivity analysis using the BEM fits particularly well with inverse problems. Mellings and Aliabadi [128, 129] used the BEM and the Dual BEM for identification of cavities and cracks on potential and elastic problems. Also, Nishimura and Kobayashi [130] developed a BEM formulation for identification of cracks with complex shapes. Bonnet [131–134] covered almost all aspects of shape sensitivity analysis using the BEM and a rigorous mathematical treatment. In particular, Bonnet [135] proved that material differentiation formulas for regular integrals still hold true for strongly singular and hypersingular integrals, which demonstrated that material differentiation can be applied to non-regularised as well as regularised BIEs. Gallego, Rus and Suarez [103–107] used the BEM for cavities and crack identification on potential and elastic problems using a free-form approach for the flaw parametrisation, and a sensitivity BIE derived from the Taylor's expansion of the shape perturbation. In the present work, the latter

approach is used to obtain the sensitivity or variation BIE (δBIE) which is the fundamental ingredient to build the BEM for sensitivity analysis. It is esentially similar to applying the material differentiation formulas to the BIE.

3.6 Generalities

The superscript i over a symbol $\square$ representing a position vector, unit normal, field variable, etc., i.e. $\square^i$, is used to indicate if the object is associated with the collocation point, rather than with the observation point. It is not an index, thus no summation is implied for it.

Let Ω be a region in $\mathbb{R}^2$ with boundary $\Gamma = \partial\Omega$ whose orientation is defined by the outward unit normal vector $\mathbf{n} = (n_1, n_2)$. Following the usual convention, the orientation of Γ can be equally defined by the unit tangent vector $\mathbf{t} = (t_1, t_2) = (-n_2, n_1)$. Consider a boundary element $\Phi \subset \Gamma$ with N_n^Φ nodes, then any point $\mathbf{x}$ of the boundary element is described by:

$$x_j = \phi_p x_{jp}^\Phi \tag{3.5}$$

where $j = 1, 2$ is the coordinate index, $p = 1, \dots, N_n^\Phi$ is the node index of the boundary element, x_{jp}^Φ is the j-th component of the position vector of the p-th node, $\phi_p = \phi_p(\xi)$ is the shape function of the p-th node, and ξ is the local curvilinear coordinate. The transformation between the local curvilinear coordinate and the global cartesian coordinates is governed by the Jacobian vector $\mathbf{J}$:

$$J_j = \frac{\partial x_j}{\partial \xi} = \frac{\mathrm{d}\phi_p}{\mathrm{d}\xi} x_{jp}^\Phi \tag{3.6}$$

$$\mathrm{d}\Gamma = \sqrt{J_j J_j}\, \mathrm{d}\xi = |\mathbf{J}|\, \mathrm{d}\xi \tag{3.7}$$

where summation convention is implied for j. Thus, the unit tangent can be calculated as $\mathbf{t} = \mathbf{J}/|\mathbf{J}|$ and the unit normal $\mathbf{n} = (t_2, -t_1)$.

For first-order shape sensitivity analysis, the region $\Omega = \Omega(a^0)$ is perturbed with respect to a given design velocity field $\mathbf{v} = \mathbf{v}(\mathbf{x}, a^0)$ that is produced by a design variable a when $a = a^0$, see Figure 3.2. The following linear mapping builds the perturbed domain $\tilde{\Omega}$ from the reference domain $\Omega = \Omega(a^0)$ for a small variation of a around a^0:

$$\tilde{\mathbf{x}} = \mathbf{x} + \mathbf{v}\left(a - a^0\right) \tag{3.8}$$

The design velocity field acts basically as a displacement field, thus a constant design velocity field throughout the domain does not produce any shape variation. It can be easily seen that a material vector $\mathbf{w}$, i.e. a vector whose origin and orientation are sticked to a point, follows this linear mapping [136]:

$$\tilde{w}_i = w_i + v_{i,j} w_j \left(a - a^0\right) \tag{3.9}$$

where the comma notation for derivatives with respect to x is implied. The following notation is going to be used for the vector sensitivity (or vector material derivative):

$$\delta w_i = v_{i,j} w_j \tag{3.10}$$
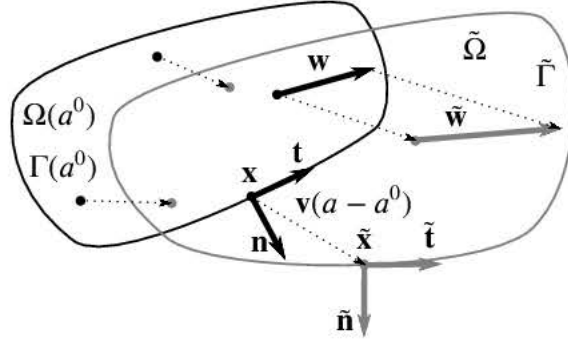
Figure 3.2: Taylor's expansion of the shape parametrisation

Thus, the linear mapping of the vector length is:

$$\tilde{w} = \tilde{w}_i \tilde{w}_i = w_i w_i + w_i v_{i,j} w_j \left(a - a^0\right) = w + \delta w \left(a - a^0\right) \tag{3.11}$$

where only linear terms are retained, and summation convention is implied for i and j. With this in mind, the linear mapping of an infinitesimal part of the boundary $d\Gamma$ is easily obtained by using the length variation of the unit tangent considered as a material vector:

$$d\tilde{\Gamma} = d\Gamma + t_i v_{i,j} t_j \, d\Gamma \left(a - a^0\right) = d\Gamma + \delta J \, d\Gamma \left(a - a^0\right) = \left(1 + \delta J \left(a - a^0\right)\right) \, d\Gamma \tag{3.12}$$

The unit tangent and normal vectors are not material vectors. The unit tangent is only material with respect to orientation, and the unit normal is completely dependant on the tangent plane. Hence, the linear mapping of the unit tangent is similar to that of a material vector but substracting the length increase:

$$\tilde{t}_i = t_i + \left(v_{i,j} t_j - t_k v_{k,j} t_j t_i\right)\left(a - a^0\right) = t_i + \left(v_{i,j} t_j - \delta J t_i\right)\left(a - a^0\right) = t_i + \delta t_i \left(a - a^0\right) \tag{3.13}$$

The variation of the unit tangent $\delta \mathbf{t}$ can only be perpendicular to the unit tangent $\mathbf{t}$. Hence, it can further be simplified to:

$$\delta t_i = v_{i,j} t_j - \delta J t_i \;\Rightarrow\; \delta t_i n_i = n_i v_{i,j} t_j \;\Rightarrow\; \delta t_k n_k n_i = \delta t_i = n_i n_k v_{k,j} t_j \tag{3.14}$$

The linear mapping of the unit normal is obtained by rotation of that of the unit tangent:

$$\epsilon_{ij} \tilde{t}_j = \epsilon_{ij} t_j + \epsilon_{ij} \delta t_j \left(a - a^0\right) = \tilde{n}_i = n_i + \delta n_i \left(a - a^0\right) \tag{3.15}$$

where ϵ_{ij} is the two-dimensional Levi-Civita symbol, and then $\delta n_i = -t_i n_k v_{k,j} t_j$.

The design velocity field $\mathbf{v} = \mathbf{v}(\mathbf{x}, a^0)$ throughout the domain is defined by using a design mesh (auxiliary mesh) connected to the physical mesh by position, i.e. the so-called free-form deformation approach (see Section 3.4). The geometry and the design velocity field of a design element $\Psi \subset \Omega$ with N_n^{Ψ} nodes are interpolated similarly (isoparametric):

$$x_j = \psi_q x_{jq}^{\Psi} \tag{3.16}$$

$$v_j = \psi_q v_{jq}^{\Psi} \tag{3.17}$$

where $q = 1, \ldots, N_{\mathrm{n}}^{\Psi}$ is the node index of the design element, and x_{jq}^{Ψ} and v_{jq}^{Ψ} are the j-th components of the position vector and design velocity field of the q-th node, respectively. The element can be a one-dimensional or a two-dimensional element, i.e. shape functions can be $\psi_q = \psi_q(\eta)$ or $\psi_q = \psi_q(\eta_1, \eta_2)$, respectively. In general, they can be written as $\psi_q = \psi_q(\boldsymbol{\eta})$. As it will be seen later, shape functions $\psi_q(\boldsymbol{\eta})$ only appear in the calculation of the integrals. Thus, for an integration point i with position vector $\mathbf{x}^{(i)}$ located within a design element Ψ, the calculation of the local curvilinear coordinate $\boldsymbol{\eta}^{(i)}$ is required:

$$\boldsymbol{\eta}^{(i)} \text{ such that } x_j^{(i)} = \psi_q\left(\boldsymbol{\eta}^{(i)}\right) x_{jq}^{\Psi} \tag{3.18}$$

which can be done by a simple iterative minimisation algorithm (convergent if $\mathbf{x}^{(i)} \in \Psi$). The connectivity between the physical mesh and the design mesh is built in the initialisation stage of the solver, allowing a good initial guess for the minimisation algorithm.

Strictly speaking, the design velocity field must be at least continuous throughout the domain, i.e. $\mathscr{C}^0$, otherwise it breaks the domain. Hence, the design mesh should fill the whole domain, should be conforming, and only elements with the same dimension as the ambient space should be used. However, for shape sensitivity calculation using finite elements, the design velocities are required only at the nodes of the finite elements. Thus, neither the design mesh must fill the domain (by default a null design velocity field can be assigned to physical nodes not connected to the design mesh) nor the elements must have the same dimension as the ambient space. This fact justifies using the boundary layer technique as a way to reduce the computational cost (elements with null design velocity fields have null matrices derivatives with respect to the design variables) at the expense of a moderate but acceptable error increase in unstructured meshes . As it will be shown later in this chapter, for shape sensitivity calculation using boundary elements, the design velocity field at the collocation point must be at least differentiable, i.e. $\mathscr{C}^1$. The same strategy as with finite elements can be followed, although, in that case, a computationally expensive non-nodal collocation is required. In order to use nodal collocation, an element with the same dimension as the ambient space must be present at the collocation point. More details about these issues will be given later in this chapter.

As shown above, the calculation of the gradient of the design velocity field is needed. For a point located at a design element Ψ, it means that the derivatives of shape functions with respect to the global coordinates are required:

$$v_{i,j} = \psi_{q,j} v_{iq}^{\Psi} \tag{3.19}$$

If the design element is a one-dimensional element, then the shape functions are $\psi_q = \psi_q(\xi)$, and their derivatives with respect to the global coordinates are:

$$\psi_{q,j} = \frac{\partial \psi_q}{\partial x_j} = \frac{J_j}{|\mathbf{J}|^2} \frac{\partial \psi_q}{\partial \xi} \tag{3.20}$$

where the Jacobian vector is:

$$J_j = \frac{\partial x_j}{\partial \xi} = \frac{\partial \psi_q}{\partial \xi} x_{jq}^{\Psi} \tag{3.21}$$

If the design element is a two-dimensional element, then the shape functions are $\psi_q = \psi_q(\xi_1, \xi_2)$, and their derivatives with respect to the global coordinates are:

$$\psi_{q,j} = \frac{\partial \psi_q}{\partial x_j} = G_{jk} \frac{\partial \psi_q}{\partial \xi_k} \tag{3.22}$$

where $\mathbf{G} = \mathbf{J}^{-1}$ and the elements of the Jacobian matrix $\mathbf{J}$ are:

$$J_{jk} = \frac{\partial x_k}{\partial \xi_j} = \frac{\partial \psi_q}{\partial \xi_j} x_{kq}^{\Psi} \tag{3.23}$$

The linear mapping corresponding to a field variable u is:

$$\tilde{u} = u + \delta u \left(a - a^0\right) = u + \left(\frac{\partial u}{\partial a} + \frac{\partial u}{\partial x_j} v_j\right)_{a=a^0} \left(a - a^0\right) \tag{3.24}$$

where the sensitivity δu can be evaluated using the expression shown above only when u is explicit. When used in the FEM or BEM sensitivity analysis, δu is a degree of freedom. Field variables and their sensitivities are interpolated using the same shape functions as the geometry, hence an isoparametric boundary element representation is considered. For a vector variable $\mathbf{u}$:

$$u_j = \phi_p u_{jp}^{\Phi} \tag{3.25}$$
$$\delta u_j = \phi_p \delta u_{jp}^{\Phi} \tag{3.26}$$

where $p = 1, \dots, N_n^{\Phi}$ is the node index of the boundary element, and u_{jp}^{Φ} and δu_{jp}^{Φ} are the j-th components of the vector variable and its sensitivity of the p-th node, respectively.

3.7 Laplace problem

A problem governed by the Laplace equation is considered. The potential (primary variable) is denoted by p, while the flux is the potential derivative in the $\mathbf{n}$ direction (secondary variable) and is denoted by $q = \nabla p \cdot \mathbf{n}$.

3.7.1 δSBIE for non-boundary collocation points

The Singular BIE (SBIE) for an interior or exterior collocation point with respect to the reference domain Ω can be written as [6, 105]:

$$\delta_{\Omega}^{i} p^{i} + \int_{\Gamma} q^* p \, d\Gamma = \int_{\Gamma} p^* q \, d\Gamma, \quad \delta_{\Omega}^{i} = \begin{cases} 1, \ \mathbf{x}^{i} \in \Omega \\ 0, \ \mathbf{x}^{i} \notin \Omega \cup \Gamma \end{cases} \tag{3.27}$$

where:

$$p^* = -\frac{1}{2\pi} \ln r \tag{3.28}$$

$$p^*_{,j} = -\frac{1}{2\pi} \frac{1}{r} r_{,j} \tag{3.29}$$

$$q^* = p^*_{,j} n_j = -\frac{1}{2\pi} \frac{1}{r} \frac{\partial r}{\partial n} \tag{3.30}$$

$$r = \left| \mathbf{x} - \mathbf{x}^i \right| \tag{3.31}$$

and $\mathbf{x}$ and $\mathbf{x}^i$ are the observation and collocation points, respectively. Likewise, for the perturbed domain $\tilde{\Omega}$:

$$\delta^i_{\tilde{\Omega}} \tilde{p}^i + \int_{\tilde{\Gamma}} \tilde{q}^* \tilde{p} \, d\tilde{\Gamma} = \int_{\tilde{\Gamma}} \tilde{p}^* \tilde{q} \, d\tilde{\Gamma}, \quad \delta^i_{\tilde{\Omega}} = \begin{cases} 1, \, \mathbf{x}^i \in \tilde{\Omega} \\ 0, \, \mathbf{x}^i \notin \tilde{\Omega} \cup \tilde{\Gamma} \end{cases} \tag{3.32}$$

As seen in the previous section, the relationships of geometrical objects and variables between the reference domain Ω and the perturbed domain $\tilde{\Omega}$ are given by linear mappings:

$$\tilde{p}^i = p^i + \delta p^i \left(a - a^0 \right) \tag{3.33}$$

$$\tilde{p} = p + \delta p \left(a - a^0 \right) \tag{3.34}$$

$$\tilde{p}_{,j} = p_{,j} + \delta p_{,j} \left(a - a^0 \right) \tag{3.35}$$

$$\tilde{n}_j = n_j + \delta n_j \left(a - a^0 \right) \tag{3.36}$$

$$\tilde{q} = \tilde{p}_{,j} \tilde{n}_j = q + \left(p_{,j} \delta n + \delta p_{,j} n_j \right) \left(a - a^0 \right) = q + \delta q \left(a - a^0 \right) \tag{3.37}$$

$$d\tilde{\Gamma} = \left[1 + \delta J \left(a - a^0 \right) \right] d\Gamma \tag{3.38}$$

where $(a - a^0)^2$ terms have been disregarded. Since the shape parametrisation does not change the topology of the domain, i.e. an interior (or exterior) point remains interior (or exterior), then $\delta^i_{\tilde{\Omega}} = \delta^i_{\Omega}$. The fundamental solution p^* depends on the observation and collocation points $p^* = p^*(\mathbf{x}, \mathbf{x}^i)$, hence its linear mapping must be built from the Taylor's expansion with respect to both points:

$$\tilde{p}^* = p^* + \frac{\partial p^*}{\partial x_j} v_j \left(a - a^0 \right) + \frac{\partial p^*}{\partial x^i_j} v^i_j \left(a - a^0 \right) = p^* + p^*_{,j} \left(v_j - v^i_j \right) \left(a - a^0 \right) \tag{3.39}$$

where $\square_{,j} = \partial \square / \partial x_j = -\partial \square / \partial x^i_j$ holds for any fundamental solution and its derivatives since $\mathbf{x}$ and $\mathbf{x}^i$ only appear inside of terms depending on the distance vector $\mathbf{r} = \mathbf{x} - \mathbf{x}^i$. Furthermore, from the linear mapping of observation and collocation points, it is possible to write:

$$\begin{aligned} \tilde{\mathbf{x}} &= \mathbf{x} + \mathbf{v} \left(a - a^0 \right) \\ \tilde{\mathbf{x}}^i &= \mathbf{x}^i + \mathbf{v}^i \left(a - a^0 \right) \\ \tilde{\mathbf{x}} - \tilde{\mathbf{x}}^i &= \mathbf{x} - \mathbf{x}^i + \left(\mathbf{v} - \mathbf{v}^i \right) \left(a - a^0 \right) \\ \tilde{\mathbf{r}} &= \mathbf{r} + \delta \mathbf{r} \left(a - a^0 \right) \end{aligned} \tag{3.40}$$

where it is obvious that $\delta \mathbf{r} \to \mathbf{0}$ as $\mathbf{x} \to \mathbf{x}^{\mathrm{i}}$, i.e. $\delta \mathbf{r} = \mathcal{O}(r)$. This important fact is used later to study the integration of the SBIE for collocation points located at the boundary. Therefore, $\tilde{p}^*$ can be written as:

$$\tilde{p}^* = p^* + p^*_{,j}\delta r_j \left(a - a^0\right) = p^* + \delta p^* \left(a - a^0\right) \tag{3.41}$$

The linear mapping of $\tilde{q}^*$ is built by using the linear mapping of its components:

$$\begin{aligned}
\tilde{q}^* &= \tilde{p}^*_{,j}\tilde{n}_j = \left[p^*_{,j} + p^*_{,jm}\delta r_m \left(a - a^0\right)\right]\left[n_j + \delta n_j \left(a - a^0\right)\right] \\
&= q^* + \left(p^*_{,j}\delta n_j + p^*_{,jm}\delta r_m n_j\right)\left(a - a^0\right) = q^* + \delta q^* \left(a - a^0\right)
\end{aligned} \tag{3.42}$$

where only linear terms are kept. Note that $p^*_{,jm}$ is obtained differentiating Equation (3.29):

$$p^*_{,jm} = -\frac{1}{2\pi}\frac{1}{r^2}\left(\delta_{jm} - 2r_{,j}r_{,m}\right) \tag{3.43}$$

where δ_{ij} is the Kronecker delta. Last, substituting all these linear mappings into Equation (3.32), keeping only linear terms $(a - a^0)$, substracting Equation (3.27) from it, and dropping out $(a - a^0)$ terms, give the sensitivity SBIE (or δSBIE):

$$\delta^{\mathrm{i}}_{\Omega}\delta p^{\mathrm{i}} + \int_{\Gamma} q^*\delta p \, \mathrm{d}\Gamma + \int_{\Gamma} \left(\delta q^* + q^*\delta J\right)p \, \mathrm{d}\Gamma = \int_{\Gamma} p^*\delta q \, \mathrm{d}\Gamma + \int_{\Gamma} \left(\delta p^* + p^*\delta J\right)q \, \mathrm{d}\Gamma \tag{3.44}$$

The first and third integrals are analogous to the integrals of the SBIE, except that instead of p and q, their sensitivities δp and δq appear. The second and fourth integrals are new integrals that depend on p and q, hence only once the zero-order solution is known they can be evaluated. Since the integration domain Γ does not contain the collocation point, all integrals are regular but nearly singular if the collocation point is close to Γ.

3.7.2 δSBIE for boundary collocation points

The δSBIE presented in Equation (3.44) is valid only for interior or exterior collocation points. In order to obtain the δSBIE for boundary collocation points ($\mathbf{x}^{\mathrm{i}} \in \Gamma$), it is possible to perform the integration of Equation (3.44) but along a modified path avoiding the collocation point:

$$\Gamma = \lim_{\epsilon \to 0^+}\left[\left(\Gamma - e^{\mathrm{i}}\right) + \Gamma^{\mathrm{i}}\right] \tag{3.45}$$

where ϵ is the radius of a circular arc Γ^{i} that substitutes a neighbourhood e^{i} of the collocation point on Γ. As seen in Figure 3.3, this limiting process can be done from the interior ($\delta^{\mathrm{i}}_{\Omega} = 1$) or from the exterior ($\delta^{\mathrm{i}}_{\Omega} = 0$), both leading to the same final result. In the following, the former is used:
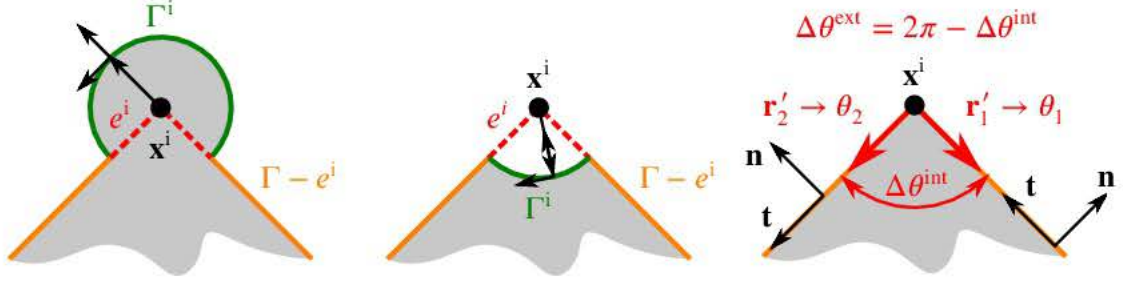
Figure 3.3: Integration path near boundary collocation points. Left: from the interior. Center: from the exterior. Right: criteria for angles θ_1 and θ_2

$$\delta p^{\mathrm{i}} + \lim_{\epsilon \to 0^+} \int_{\Gamma - e^{\mathrm{i}}} q^* \delta p \, \mathrm{d}\Gamma + \lim_{\epsilon \to 0^+} \int_{\Gamma^{\mathrm{i}}} q^* \delta p \, \mathrm{d}\Gamma + \lim_{\epsilon \to 0^+} \int_{\Gamma - e^{\mathrm{i}}} (\delta q^* + q^* \delta J) \, p \, \mathrm{d}\Gamma$$

$$+ \lim_{\epsilon \to 0^+} \int_{\Gamma^{\mathrm{i}}} (\delta q^* + q^* \delta J) \, p \, \mathrm{d}\Gamma = \lim_{\epsilon \to 0^+} \int_{\Gamma - e^{\mathrm{i}}} p^* \delta q \, \mathrm{d}\Gamma + \lim_{\epsilon \to 0^+} \int_{\Gamma^{\mathrm{i}}} p^* \delta q \, \mathrm{d}\Gamma$$

$$+ \lim_{\epsilon \to 0^+} \int_{\Gamma - e^{\mathrm{i}}} (\delta p^* + p^* \delta J) \, q \, \mathrm{d}\Gamma + \lim_{\epsilon \to 0^+} \int_{\Gamma^{\mathrm{i}}} (\delta p^* + p^* \delta J) \, q \, \mathrm{d}\Gamma \quad (3.46)$$

Integration over Γ^{i}   In order to evaluate the integrals along Γ^{i}, a polar system of coordinates (ϵ, θ) centered at the collocation point and oriented counterclockwise is considered. The polar angle θ is in the domain $\theta_1 \leq \theta \leq \theta_2$, where θ_1 and θ_2 are shown in Figure 3.3. The main geometrical terms along Γ^{i} are:

$$\mathbf{x}^{\mathrm{i}} = \mathbf{0} \tag{3.47}$$

$$\mathbf{x} = (\epsilon \cos \theta, \epsilon \sin \theta) \tag{3.48}$$

$$\mathbf{r} = \mathbf{x}, \; r = \epsilon \tag{3.49}$$

$$r_{,j} = r_j / r \tag{3.50}$$

$$n_j = r_{,j}, \; \mathbf{n} = (\cos \theta, \sin \theta) \tag{3.51}$$

$$t_i = \epsilon_{ij} n_j, \; \mathbf{t} = (-\sin \theta, \cos \theta) \tag{3.52}$$

$$\partial r / \partial n = r_{,j} n_j = 1 \tag{3.53}$$

$$r_{,j} t_j = 0 \tag{3.54}$$

$$\mathrm{d}\Gamma = \epsilon \, \mathrm{d}\theta \tag{3.55}$$

where ϵ_{ij} is the two-dimensional Levi-Civita symbol. The evaluation of the first integral over Γ^{i} of Equation (3.46) gives:

$$\lim_{\epsilon \to 0^+} \int_{\Gamma^{\mathrm{i}}} q^* \delta p \, \mathrm{d}\Gamma = -\frac{1}{2\pi} \lim_{\epsilon \to 0^+} \int_{\theta_1}^{\theta_2} \frac{1}{\epsilon} 1 \left(\delta p^{\mathrm{i}} + \mathcal{O}\left(\epsilon\right) \right) \epsilon \, \mathrm{d}\theta = -\frac{\theta_2 - \theta_1}{2\pi} \delta p^{\mathrm{i}} = -\frac{\Delta \theta^{\mathrm{ext}}}{2\pi} \delta p^{\mathrm{i}} \quad (3.56)$$

where a simple zero-order expansion $\delta p = \delta p^i + \mathcal{O}(\epsilon)$ is required. The second integral over Γ^i is:

$$\lim_{\epsilon \to 0^+} \int_{\Gamma^i} (\delta q^* + q^* \delta J) p \, d\Gamma = \lim_{\epsilon \to 0^+} \int_{\Gamma^i} \left(p^*_{,j} \delta n_j + p^*_{,jm} \delta r_m n_j + q^* \delta J \right) p \, d\Gamma$$

$$= -\frac{1}{2\pi} \lim_{\epsilon \to 0^+} \int_{\theta_1}^{\theta_2} \left[\frac{1}{\epsilon} n_j \delta n_j + \frac{1}{\epsilon^2} \left(\delta_{jm} - 2 n_j n_m \right) \delta r_m n_j + \frac{1}{\epsilon} 1 \delta J \right] \left(p^i + \mathcal{O}(\epsilon) \right) \epsilon \, d\theta$$

(3.57)

where a zero-order expansion $p = p^i + \mathcal{O}(\epsilon)$ is used. In order to evaluate the integral, expansions of several terms of the kernel around the collocation point are needed. For the sensitivity of the unit normal δn_j, a zero-order expansion is required:

$$\delta n_j = -t_j n_m v^i_{m,k} t_k + \mathcal{O}(\epsilon)$$

(3.58)

Likewise, for the sensitivity of the boundary length δJ

$$\delta J = t_m v^i_{m,j} t_j + \mathcal{O}(\epsilon)$$

(3.59)

For the design velocity field, however, a first-order expansion is required:

$$v_m = v^i_m + v^i_{m,j}(x_j - x^i_j) + \mathcal{O}(r^2) = v^i_m + v^i_{m,j} r_{,j} \epsilon + \mathcal{O}(\epsilon^2)$$

(3.60)

and hence:

$$\delta r_m = v_m - v^i_m = v^i_{m,j} r_{,j} \epsilon + \mathcal{O}(\epsilon^2)$$

(3.61)

Therefore, since the gradient of the design velocity field at the collocation point $v^i_{m,j}$ is required, the design velocity field must be differentiable, i.e. $\mathbf{v}(\mathbf{x}^i) \in \mathscr{C}^1$. Substituting these expansions into Equation (3.57) leads to:

$$\lim_{\epsilon \to 0^+} \int_{\Gamma^i} (\delta q^* + q^* \delta J) p \, d\Gamma = \frac{1}{2\pi} \left(\int_{\theta_1}^{\theta_2} n_m n_j \, d\theta - \int_{\theta_1}^{\theta_2} t_m t_j \, d\theta \right) v^i_{m,j} p^i = b^i_{mj} v^i_{m,j} p^i$$

(3.62)

where b^i_{mj} is:

$$\left(b^i_{mj} \right) = \frac{1}{4\pi} \begin{pmatrix} \sin 2\theta_2 - \sin 2\theta_1 & -\left(\cos 2\theta_2 - \cos 2\theta_1 \right) \\ -\left(\cos 2\theta_2 - \cos 2\theta_1 \right) & -\left(\sin 2\theta_2 - \sin 2\theta_1 \right) \end{pmatrix}$$

(3.63)

which is null if the collocation point is located at a smooth point of the boundary, i.e $\Gamma(\mathbf{x}^i) \in \mathscr{C}^1 \Rightarrow b^i_{mj} = 0$. The third integral over Γ^i is null:

$$\lim_{\epsilon \to 0^+} \int_{\Gamma^i} p^* \delta q \, d\Gamma = -\frac{1}{2\pi} \delta q \left(\lim_{\epsilon \to 0^+} \epsilon \ln \epsilon \right) \left(\int_{\theta_1}^{\theta_2} d\theta \right) = 0$$

(3.64)

where δq must be bounded. The fourth integral over Γ^{i} is also null:

$$\lim_{\epsilon \to 0^+} \int_{\Gamma^{\mathrm{i}}} (\delta p^* + p^* \delta J)\, q \; \mathrm{d}\Gamma = -\frac{1}{2\pi} \lim_{\epsilon \to 0^+} \int_{\theta_1}^{\theta_2} \left(\frac{1}{\epsilon} n_m v^{\mathrm{i}}_{m,j} \epsilon n_j + (\ln \epsilon)\, \delta J \right) q\epsilon \; \mathrm{d}\theta = 0 \quad (3.65)$$

where q must be bounded. Substituting all these results into Equation (3.46) gives:

$$c^{\mathrm{i}} \delta p^{\mathrm{i}} + b^{\mathrm{i}}_{mj} v^{\mathrm{i}}_{m,j} p^{\mathrm{i}} + \lim_{\epsilon \to 0^+} \int_{\Gamma - e^{\mathrm{i}}} q^* \delta p \; \mathrm{d}\Gamma + \lim_{\epsilon \to 0^+} \int_{\Gamma - e^{\mathrm{i}}} (\delta q^* + q^* \delta J)\, p \; \mathrm{d}\Gamma$$

$$= \lim_{\epsilon \to 0^+} \int_{\Gamma - e^{\mathrm{i}}} p^* \delta q \; \mathrm{d}\Gamma + \lim_{\epsilon \to 0^+} \int_{\Gamma - e^{\mathrm{i}}} (\delta p^* + p^* \delta J)\, q \; \mathrm{d}\Gamma \quad (3.66)$$

where $c^{\mathrm{i}} = \Delta\theta^{\mathrm{int}}/2\pi$ is the free-term similar to that of the SBIE, and b^{i}_{mj} is a new free-term appearing in the δSBIE. The integrals over $\Gamma - e^{\mathrm{i}}$ are at most strongly singular, and their evaluation requires additional work.

Integration over $\Gamma - e^{\mathrm{i}}$ The evaluation of the integrals in Equation (3.66) can be performed in different ways, from a pure analytical approach (doable for straight elements) to a pure numerical approach using special quadrature formulae (Kutt's quadrature). In this work, an analytical regularisation leading to at most weakly singular integrals is applied before any numerical integration is done. By doing so, only regular and weakly singular integrals are numerically managed, which are easily tractable and controllable.

The integrands are composed mainly of geometrical terms and field variables, thus their behaviour near the collocation point must be studied. The behaviour of the relevant geometrical terms is illustrated in Figure 3.4. The field variables are at least bounded, and hence $p, q, \delta p, \delta q$ are $\mathcal{O}(r^0)$. The first integral of Equation (3.66) is regular:

$$H = \lim_{\epsilon \to 0^+} \int_{\Gamma - e^{\mathrm{i}}} q^* \delta p \; \mathrm{d}\Gamma \text{ is regular } \because q^* = -\frac{1}{2\pi} \underbrace{\frac{1}{r}}_{\mathcal{O}(r^{-1})} \underbrace{\frac{\partial r}{\partial n}}_{\mathcal{O}(r^1)} = \mathcal{O}\left(r^0\right) \quad (3.67)$$

The third integral is weakly singular:

$$G = \lim_{\epsilon \to 0^+} \int_{\Gamma - e^{\mathrm{i}}} p^* \delta q \; \mathrm{d}\Gamma \text{ is weakly singular } \because p^* = -\frac{1}{2\pi} \ln r = \mathcal{O}\left(\ln r\right) \quad (3.68)$$

The fourth integral can be split into two parts:

$$\delta G = \lim_{\epsilon \to 0^+} \int_{\Gamma - e^{\mathrm{i}}} (\delta p^* + p^* \delta J)\, q \; \mathrm{d}\Gamma = \delta G^{\mathrm{R}} + \delta G^{\mathrm{J}} \quad (3.69)$$
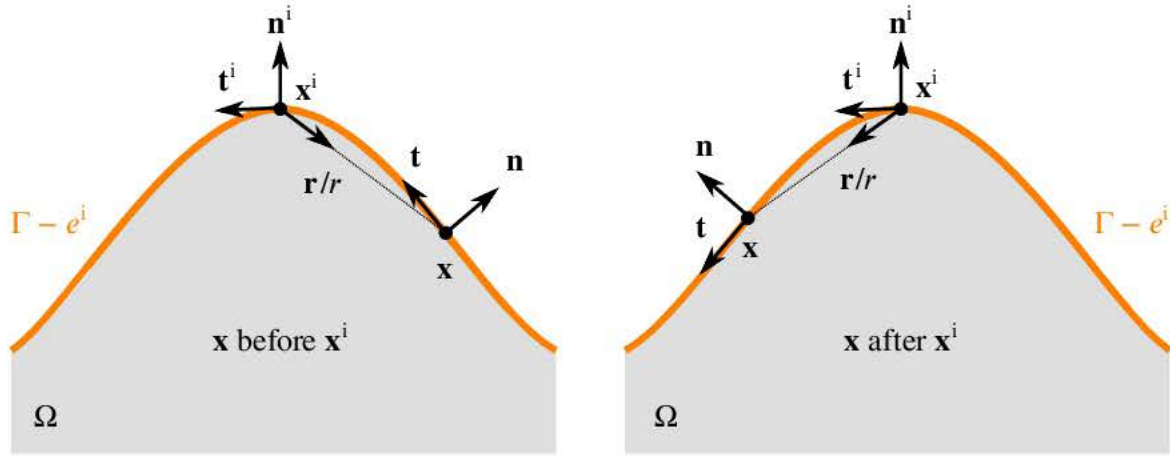
$$\frac{\partial r}{\partial \Gamma} = \frac{\mathbf{r}}{r} \cdot \mathbf{t} < 0, \quad \left(\frac{\partial r}{\partial \Gamma}\right)^{\mathrm{i}} = -1 \qquad\qquad \frac{\partial r}{\partial \Gamma} = \frac{\mathbf{r}}{r} \cdot \mathbf{t} > 0, \quad \left(\frac{\partial r}{\partial \Gamma}\right)^{\mathrm{i}} = 1$$

$$\frac{\partial r}{\partial n} = \frac{\mathbf{r}}{r} \cdot \mathbf{n} \to 0 \text{ when } r \to 0 \Rightarrow \frac{\partial r}{\partial n} = \mathcal{O}(r)$$

Figure 3.4: Limiting behaviour of geometrical vectors around the collocation point

where:

$$\delta G^{\mathrm{R}} = \lim_{\epsilon \to 0^+} \int_{\Gamma - e^{\mathrm{i}}} \delta p^* q \, \mathrm{d}\Gamma \text{ is regular } \because \delta p^* = \underbrace{p^*_{,j}}_{\mathcal{O}(r^{-1})} \underbrace{\delta r_j}_{\mathcal{O}(r^1)} = \mathcal{O}\left(r^0\right) \qquad (3.70)$$

$$\delta G^{\mathrm{J}} = \lim_{\epsilon \to 0^+} \int_{\Gamma - e^{\mathrm{i}}} p^* \delta J q \, \mathrm{d}\Gamma \text{ is weakly singular } \because \underbrace{p^*}_{\mathcal{O}(\ln r)} \underbrace{\delta J}_{\mathcal{O}(r^0)} = \mathcal{O}(\ln r) \qquad (3.71)$$

The second integral can be split into three parts:

$$\delta H = \lim_{\epsilon \to 0^+} \int_{\Gamma - e^{\mathrm{i}}} \left(p^*_{,j}\delta n_j + p^*_{,jm}\delta r_m n_j + q^* \delta J\right) p \, \mathrm{d}\Gamma = \delta H^{\mathrm{N}} + \delta H^{\mathrm{R}} + \delta H^{\mathrm{J}} \qquad (3.72)$$

where:

$$\delta H^{\mathrm{N}} = \lim_{\epsilon \to 0^+} \int_{\Gamma - e^{\mathrm{i}}} p^*_{,j}\delta n_j p \, \mathrm{d}\Gamma \text{ is strongly singular } \because \underbrace{p^*_{,j}}_{\mathcal{O}(r^{-1})} \underbrace{\delta n_j}_{\mathcal{O}(r^0)} = \mathcal{O}\left(r^{-1}\right) \qquad (3.73)$$

$$\delta H^{\mathrm{R}} = \lim_{\epsilon \to 0^+} \int_{\Gamma - e^{\mathrm{i}}} p^*_{,jm}\delta r_m n_j p \, \mathrm{d}\Gamma \text{ is strongly sing. } \because \underbrace{p^*_{,jm}}_{\mathcal{O}(r^{-2})} \underbrace{\delta r_m}_{\mathcal{O}(r^1)} \underbrace{n_j}_{\mathcal{O}(r^0)} = \mathcal{O}\left(r^{-1}\right) \qquad (3.74)$$

$$\delta H^{\mathrm{J}} = \lim_{\epsilon \to 0^+} \int_{\Gamma - e^{\mathrm{i}}} q^* \delta J p \, \mathrm{d}\Gamma \text{ is regular } \because \underbrace{q^*}_{\mathcal{O}(r^0)} \underbrace{\delta J}_{\mathcal{O}(r^0)} = \mathcal{O}\left(r^0\right) \qquad (3.75)$$

Therefore, δH^{N} and δH^{R} require further treatment. δH^{N} can be regularised by substracting and adding the limit when $r \to 0$ of a part of the integrand:

$$\delta H^{\mathrm{N}} = \frac{1}{2\pi} \lim_{\epsilon \to 0^+} \int_{\Gamma - e^{\mathrm{i}}} \frac{1}{r} r_{,j} t_j n_m v_{m,k} t_k p \, \mathrm{d}\Gamma = \frac{1}{2\pi} \lim_{\epsilon \to 0^+} \int_{\Gamma - e^{\mathrm{i}}} \frac{1}{r} \frac{\partial r}{\partial \Gamma} n_m v_{m,k} t_k p \, \mathrm{d}\Gamma$$

$$= \frac{1}{2\pi} \left[\lim_{\epsilon \to 0^+} \int_{\Gamma - e^{\mathrm{i}}} \frac{1}{r} \frac{\partial r}{\partial \Gamma} \left(n_m v_{m,k} t_k p - n_m^{\mathrm{i}} v_{m,k}^{\mathrm{i}} t_k^{\mathrm{i}} p^{\mathrm{i}} \right) \mathrm{d}\Gamma + n_m^{\mathrm{i}} v_{m,k}^{\mathrm{i}} t_k^{\mathrm{i}} p^{\mathrm{i}} \lim_{\epsilon \to 0^+} \int_{\Gamma - e^{\mathrm{i}}} \frac{1}{r} \, \mathrm{d}r \right] \quad (3.76)$$

leading to one regular integral and another integral $\int 1/r \, \mathrm{d}r$ that can be solved analytically. For δH^{R}, first, it is necessary to expand the integrand:

$$\delta H^{\mathrm{R}} = -\frac{1}{2\pi} \lim_{\epsilon \to 0^+} \int_{\Gamma - e^{\mathrm{i}}} \frac{1}{r^2} \left(\delta_{jm} - 2 r_{,j} r_{,m} \right) \left(v_m - v_m^{\mathrm{i}} \right) n_j p \, \mathrm{d}\Gamma$$

$$= \frac{1}{2\pi} \left[\lim_{\epsilon \to 0^+} \int_{\Gamma - e^{\mathrm{i}}} \frac{2}{r^2} \frac{\partial r}{\partial n} \left(v_m - v_m^{\mathrm{i}} \right) r_{,m} p \, \mathrm{d}\Gamma - \lim_{\epsilon \to 0^+} \int_{\Gamma - e^{\mathrm{i}}} \frac{1}{r^2} \left(v_m - v_m^{\mathrm{i}} \right) n_m p \, \mathrm{d}\Gamma \right] \quad (3.77)$$

which gives one regular integral and another strongly singular integral. Then, taking into account that:

$$v_m = v_m^{\mathrm{i}} + v_{m,j}^{\mathrm{i}} r_j + \mathcal{O}\left(r^2 \right) \;\Rightarrow\; v_m - v_m^{\mathrm{i}} - v_{m,j}^{\mathrm{i}} r_j = \mathcal{O}\left(r^2 \right) \quad (3.78)$$

and adding and substracting $v_{m,j}^{\mathrm{i}} r_j$:

$$\delta H^{\mathrm{R}} = \frac{1}{2\pi} \left[\lim_{\epsilon \to 0^+} \int_{\Gamma - e^{\mathrm{i}}} \frac{2}{r^2} \frac{\partial r}{\partial n} \left(v_m - v_m^{\mathrm{i}} \right) r_{,m} p \, \mathrm{d}\Gamma - \lim_{\epsilon \to 0^+} \int_{\Gamma - e^{\mathrm{i}}} \frac{1}{r^2} \left(v_m - v_m^{\mathrm{i}} - v_{m,j}^{\mathrm{i}} r_j \right) n_m p \, \mathrm{d}\Gamma \right.$$

$$\left. - \lim_{\epsilon \to 0^+} \int_{\Gamma - e^{\mathrm{i}}} \frac{1}{r} v_{m,j}^{\mathrm{i}} r_{,j} n_m p \, \mathrm{d}\Gamma \right] \quad (3.79)$$

a new regular integral and a new strongly singular integral appear. By checking out Figure 3.4, it is easy to see that:

$$r_{,j} = \left(\frac{\partial r}{\partial \Gamma} \right)^{\mathrm{i}} t_j^{\mathrm{i}} + \mathcal{O}\left(r \right) \quad (3.80)$$

which can be used to add and substract a part of the integrand of the strongly singular integral:

$$\delta H^{\mathrm{R}} = \frac{1}{2\pi} \left[\lim_{\epsilon \to 0^+} \int_{\Gamma - e^{\mathrm{i}}} \frac{2}{r^2} \frac{\partial r}{\partial n} \left(v_m - v_m^{\mathrm{i}} \right) r_{,m} p \, \mathrm{d}\Gamma - \lim_{\epsilon \to 0^+} \int_{\Gamma - e^{\mathrm{i}}} \frac{1}{r^2} \left(v_m - v_m^{\mathrm{i}} - v_{m,j}^{\mathrm{i}} r_j \right) n_m p \, \mathrm{d}\Gamma \right.$$

$$\left. - \lim_{\epsilon \to 0^+} \int_{\Gamma - e^{\mathrm{i}}} \frac{1}{r} \left(v_{m,j}^{\mathrm{i}} r_{,j} n_m p - v_{m,j}^{\mathrm{i}} \left(\frac{\partial r}{\partial \Gamma} \right)^{\mathrm{i}} t_j^{\mathrm{i}} n_m^{\mathrm{i}} p^{\mathrm{i}} \right) \mathrm{d}\Gamma - n_m^{\mathrm{i}} v_{m,j}^{\mathrm{i}} t_j^{\mathrm{i}} p^{\mathrm{i}} \lim_{\epsilon \to 0^+} \int_{\Gamma - e^{\mathrm{i}}} \frac{1}{r} \left(\frac{\partial r}{\partial \Gamma} \right)^{\mathrm{i}} \mathrm{d}\Gamma \right]$$

$$(3.81)$$

leading to a new regular integral and another strongly singular integral. Finally, by adding and substracting the limit of $\partial r / \partial \Gamma$ when $r \to 0$ leads to:

$$
\delta H^{\mathrm{R}} = \frac{1}{2\pi} \left[\lim_{\epsilon \to 0^+} \int\limits_{\Gamma - e^{\mathrm{i}}} \frac{2}{r^2} \frac{\partial r}{\partial n} \left(v_m - v_m^{\mathrm{i}} \right) r_{,m} p \, \mathrm{d}\Gamma - \lim_{\epsilon \to 0^+} \int\limits_{\Gamma - e^{\mathrm{i}}} \frac{1}{r^2} \left(v_m - v_m^{\mathrm{i}} - v_{m,j}^{\mathrm{i}} r_j \right) n_m p \, \mathrm{d}\Gamma \right.
$$

$$
- \lim_{\epsilon \to 0^+} \int\limits_{\Gamma - e^{\mathrm{i}}} \frac{1}{r} \left(v_{m,j}^{\mathrm{i}} r_{,j} n_m p - v_{m,j}^{\mathrm{i}} \left(\frac{\partial r}{\partial \Gamma} \right)^{\mathrm{i}} t_j^{\mathrm{i}} n_m^{\mathrm{i}} p^{\mathrm{i}} \right) \, \mathrm{d}\Gamma - n_m^{\mathrm{i}} v_{m,j}^{\mathrm{i}} t_j^{\mathrm{i}} p^{\mathrm{i}} \lim_{\epsilon \to 0^+} \int\limits_{\Gamma - e^{\mathrm{i}}} \frac{1}{r} \left(\left(\frac{\partial r}{\partial \Gamma} \right)^{\mathrm{i}} - \frac{\partial r}{\partial \Gamma} \right) \, \mathrm{d}\Gamma
$$

$$
\left. - n_m^{\mathrm{i}} v_{m,j}^{\mathrm{i}} t_j^{\mathrm{i}} p^{\mathrm{i}} \lim_{\epsilon \to 0^+} \int\limits_{\Gamma - e^{\mathrm{i}}} \frac{1}{r} \, \mathrm{d}r \right] \quad (3.82)
$$

which is a set of regular integrals and an integral $\int 1/r \, \mathrm{d}r$ analytically solvable. It must be noticed that terms involving the integral $\int 1/r \, \mathrm{d}r$ cancel out when δH is evaluated using Equation (3.72).

3.7.3 Discretisation, collocation techniques, integration and solution

The boundary Γ is discretised using a set of N_{be} boundary elements: $\Gamma = \cup_{i=1}^{i=N_{\mathrm{be}}} \Phi_i$ where $\Phi_i \cap \Phi_j = \varnothing$ when $i \neq j$. As explained above, the discretisation is performed using isoparametric elements. For a given boundary element Φ with N_{n}^{Φ} nodes:

$$
\begin{aligned}
&\text{Geometry:} \quad x_j = \phi_p x_{jp}^{\Phi} \\
&\text{Variables:} \quad p = \phi_p p_p^{\Phi}, \; q = \phi_p q_p^{\Phi}, \; \delta p = \phi_p \delta p_p^{\Phi}, \; \delta q = \phi_p \delta q_p^{\Phi}
\end{aligned} \quad (3.83)
$$

where $p = 1, \ldots, N_{\mathrm{n}}^{\Phi}$ is the node index of the boundary element. The design domain is discretised using a set of N_{de} design elements: $\Upsilon = \cup_{i=1}^{i=N_{\mathrm{de}}} \Psi_i$ where $\Psi_i \cap \Psi_j = \varnothing$ when $i \neq j$. For a given design element Ψ with N_{n}^{Ψ} nodes:

$$
\begin{aligned}
&\text{Geometry:} \quad x_j = \psi_q x_{jq}^{\Psi} \\
&\text{Design velocity field:} \quad v_j = \psi_q v_{jq}^{\Psi}
\end{aligned} \quad (3.84)
$$

where $q = 1, \ldots, N_{\mathrm{n}}^{\Psi}$ is the node index of the design element. In the following, the indices p and q are exclusively related to node indices of boundary and design elements, respectively, and any other index is related to a coordinate index.

It was shown in the previous section that the collocation point $\mathbf{x}^i$ must be in a point where $\mathbf{v}(\mathbf{x}^i) \in \mathscr{C}^1$. Figure 3.5 shows a design mesh consisting of two two-dimensional design elements (Ψ_1 and Ψ_2) with a common edge, and two one-dimensional design elements (Ψ_3 and Ψ_4) with a common node. Design elements Ψ_2 (two-dimensional) and Ψ_3 (one-dimensional) share a common node. By defining the values of the design velocity field at each node, a $\mathscr{C}^{\infty}$ design velocity field is built throughout the design mesh except at some locations where it is guaranteed only to be $\mathscr{C}^0$. These locations are the edges and nodes shared by two or more
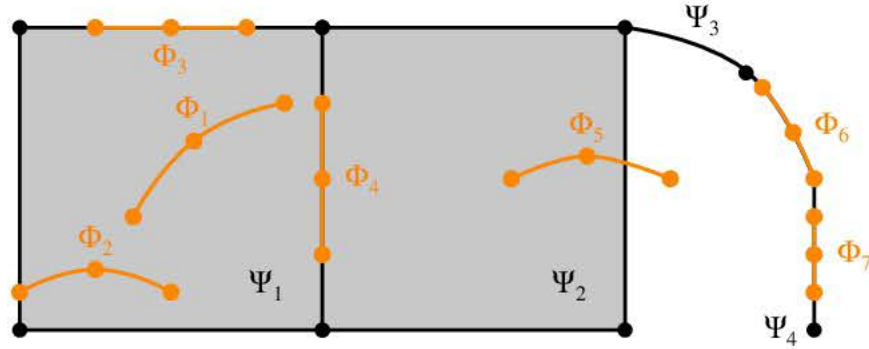
Figure 3.5: Possible positions of a boundary element throughout a design mesh

design elements. The existence of these locations conditions the collocation procedure of the BIEs in the sensitivity analysis (and the required zero-order analysis). There are two ways of dealing with it:

Fully isoparametric approach The design velocity field is interpolated also with the shape functions of the boundary element Φ:

$$
\begin{aligned}
\text{Geometry:} \quad & x_j = \phi_p x_{jp}^{\Phi} \\
\text{Variables:} \quad & p = \phi_p p_p^{\Phi}, \, q = \phi_p q_p^{\Phi}, \, \delta p = \phi_p \delta p_p^{\Phi}, \, \delta q = \phi_p \delta q_p^{\Phi} \quad (3.85) \\
\text{Design velocity field:} \quad & v_j = \phi_q v_{jq}^{\Phi}
\end{aligned}
$$

where $p, q = 1, \ldots, N_n^{\Phi}$ is the node index of the boundary element. The design velocity field at nodes v_{jq}^{Φ} are calculated from the design mesh. This interpolation guarantees differentiability along the boundary element except at the end nodes. Hence, a Multiple Collocation Approach (MCA) is used [60], where the collocation is performed only inside the boundary element. This fully isoparametric approach using the MCA is simple and applicable to all possible positions of the boundary elements shown in Figure 3.5. It is even possible to consider the boundary element Φ_5 if a null design velocity field is assigned to the node located outside the design mesh. Despite its versatility, it comes with a big disadvantage: its computational cost.

Mixed approach Nodal collocation is used for boundary elements whose nodes are located at points where $\mathbf{v}(\mathbf{x}^i) \in \mathscr{C}^1$. For boundary elements where at least one node violates this condition, the full isoparametric approach is used. This approach is versatile and, at the same time, as computationally cheap as possible. The only disadvantage is the implementation effort needed to automatically distinguise between both situations. In Figure 3.5, nodal collocation is used on boundary elements Φ_1, Φ_2, Φ_3 and Φ_7, while the full isoparametric approach is used on boundary elements Φ_4, Φ_5 and Φ_6.

Once discretisation and collocation procedures have been described, it is possible to present the discretised form of Boundary Integral Equations (3.44) and (3.66). For any col-

location point $\mathbf{x}^i$, both can be written in a generic way as:

$$c^i \delta p^i + b^i_{mj} v^i_{m,j} p^i + \sum_{e=1}^{N_{be}} \left(H_p \delta p_p \right)^{\Phi_e} + \sum_{e=1}^{N_{be}} \left(\delta H_p p_p \right)^{\Phi_e} = \sum_{e=1}^{N_{be}} \left(G_p \delta q_p \right)^{\Phi_e} + \sum_{e=1}^{N_{be}} \left(\delta G_p q_p \right)^{\Phi_e}$$

(3.86)

where:

- If $\mathbf{x}^i \in \Gamma$, then:

$$\Phi^i = \left\{ \Phi_e, e = 1, \ldots, N_{be} : \mathbf{x}^i \in \Phi_e \right\}$$
$$\Psi^i = \left\{ \Psi_d, d = 1, \ldots, N_{de} : \mathbf{x}^i \in \Psi_d \right\}$$
$$p^i = \left(\phi^i_p p_p \right)^{\Phi^i}$$
$$\delta p^i = \left(\phi^i_p \delta p_p \right)^{\Phi^i}$$
$$v^i_{m,j} = \left(\psi^i_{q,j} v_{mq} \right)^{\Psi^i}$$

and c^i and b^i_{mj} are calculated as shown previously according to the local geometry of the boundary at the collocation point.

- If $\mathbf{x}^i \notin \Gamma$, then $c^i = \delta^i_\Omega$ and $b^i_{mj} = 0$.

For a boundary element Φ associated with a design element Ψ, two different situations must be considered:

Exterior integration, $\mathbf{x}^i \notin \Phi$. All integrals are strictly regular, and standard Gauss-Legendre quadrature is able to approximate them numerically. However, the case of collocation points near the element lead to quasi-singular integrals. More details are given in Chapter 4. The contributions of a boundary element Φ similar to those of the SBIE are:

$$H_p = \int_\Phi q^* \phi_p \, d\Gamma$$

(3.87)

$$G_p = \int_\Phi p^* \phi_p \, d\Gamma$$

(3.88)

The contributions of the new integrals arising in the δSBIE consider separately the design velocity field along the boundary element (through the design element Ψ) and the design velocity field at the collocation point:

$$\delta H_p = \delta H^{T1}_{mqp} v^\Psi_{mq} - \delta H^{T2}_{mp} v^i_m = \left(\delta H^{N1}_{mqp} + \delta H^{R1}_{mqp} + \delta H^{J1}_{mqp} \right) v^\Psi_{mq} - \delta H^{R2}_{mp} v^i_m$$

(3.89)

$$\delta G_p = \delta G^{T1}_{mqp} v^\Psi_{mq} - \delta G^{T2}_{mp} v^i_m = \left(\delta G^{R1}_{mqp} + \delta G^{J1}_{mqp} \right) v^\Psi_{mq} - \delta G^{R2}_{mp} v^i_m$$

(3.90)

where:

$$\delta H_{mqp}^{N1} = -\int_{\Phi} p_{,j}^* t_j n_m \psi_{q,k} t_k \phi_p \, d\Gamma \qquad (3.91)$$

$$\delta H_{mqp}^{R1} = \int_{\Phi} p_{,jm}^* n_j \psi_q \phi_p \, d\Gamma \qquad (3.92)$$

$$\delta H_{mp}^{R2} = \int_{\Phi} p_{,jm}^* n_j \phi_p \, d\Gamma \qquad (3.93)$$

$$\delta H_{mqp}^{J1} = \int_{\Phi} q^* t_m \psi_{q,k} t_k \phi_p \, d\Gamma \qquad (3.94)$$

$$\delta G_{mqp}^{R1} = \int_{\Phi} p_{,m}^* \psi_q \phi_p \, d\Gamma \qquad (3.95)$$

$$\delta G_{mp}^{R2} = \int_{\Phi} p_{,m}^* \phi_p \, d\Gamma \qquad (3.96)$$

$$\delta G_{mqp}^{J1} = \int_{\Phi} p^* t_m \psi_{q,k} t_k \phi_p \, d\Gamma \qquad (3.97)$$

Interior integration, $\mathbf{x}^i \in \Phi$.   The integrals contain a singularity, which can be integrable in the Riemann sense (regular or weakly singular) or in the more general Finite Part sense. The regularisation performed in the previous section leads to a set of integrals integrable in the Riemann sense, making explicit the Finite Part of the original integral. In any case, the integrand is unbounded at the collocation point, and hence no integration point can lie at it. Only regular and weakly singular integrals have to be integrated, which is done according to Chapter 4. The contributions of Φ similar to those of the SBIE are:

$$H_p = \lim_{\epsilon \to 0^+} \int_{\Phi - e^i} q^* \phi_p \, d\Gamma \qquad (3.98)$$

$$G_p = \lim_{\epsilon \to 0^+} \int_{\Phi - e^i} p^* \phi_p \, d\Gamma \qquad (3.99)$$

Since $\mathbf{x}^i \in \Phi$, the contributions of the new integrals arising in the δSBIE consider only the design velocity field along the boundary element (through the design element Ψ):

$$\delta H_p = \delta H_{mqp}^{T1} v_{mq}^{\Psi} = \left(\delta H_{mqp}^{N1} + \delta H_{mqp}^{R1} + \delta H_{mqp}^{J1} \right) v_{mq}^{\Psi} \qquad (3.100)$$

$$\delta G_p = \delta G_{mqp}^{T1} v_{mq}^{\Psi} = \left(\delta G_{mqp}^{R1} + \delta G_{mqp}^{J1} \right) v_{mq}^{\Psi} \qquad (3.101)$$

where:

$$\delta H_{mqp}^{N1} = \frac{1}{2\pi} \lim_{\epsilon \to 0^+} \int_{\Phi - e^i} \frac{1}{r} \frac{\partial r}{\partial \Gamma} \left(n_m \psi_{q,k} t_k \phi_p - n_m^i \psi_{q,k}^i t_k^i \phi_p^i \right) \, \mathrm{d}\Gamma \tag{3.102}$$

$$\delta H_{mqp}^{R1} = \frac{1}{2\pi} \left\{ \int_{\Phi - e^i} \frac{2r_{,m}}{r^2} \frac{\partial r}{\partial n} \left(\psi_q - \psi_q^i \right) \phi_p \, \mathrm{d}\Gamma - \int_{\Phi - e^i} \frac{n_m}{r^2} \left(\psi_q - \psi_q^i - \psi_{q,j}^i r_j \right) \phi_p \, \mathrm{d}\Gamma - \right.$$
$$\left. \int_{\Phi - e^i} \frac{1}{r} \left[n_m \phi_p \psi_{q,j}^i r_{,j} - \left(\frac{\partial r}{\partial \Gamma} \right)^i n_m^i \phi_p^i \psi_{q,j}^i t_j^i \right] \, \mathrm{d}\Gamma - n_m^i \phi_p^i \psi_{q,j}^i t_j^i \int_{\Phi - e^i} \frac{1}{r} \left(\left(\frac{\partial r}{\partial \Gamma} \right)^i - \frac{\partial r}{\partial \Gamma} \right) \, \mathrm{d}\Gamma \right\} \tag{3.103}$$

$$\delta H_{mqp}^{J1} = \lim_{\epsilon \to 0^+} \int_{\Phi - e^i} q^* t_m \psi_{q,k} t_k \phi_p \, \mathrm{d}\Gamma \tag{3.104}$$

$$\delta G_{mqp}^{R1} = \lim_{\epsilon \to 0^+} \int_{\Phi - e^i} p_{,m}^* \left(\psi_q - \psi_q^i \right) \phi_p \, \mathrm{d}\Gamma \tag{3.105}$$

$$\delta G_{mqp}^{J1} = \lim_{\epsilon \to 0^+} \int_{\Phi - e^i} p^* t_m \psi_{q,k} t_k \phi_p \, \mathrm{d}\Gamma \tag{3.106}$$

where the limit notation $\lim_{\epsilon \to 0^+}$ before some integrals has been omitted for brevity. Note that terms involving the integral $\int 1/r \, \mathrm{d}\Gamma$ has been removed from δH_{mqp}^{N1} and δH_{mqp}^{R1} since they cancel out when evaluating δH_{mqp}^{T1}.

The solution of the sensitivity problem requires the solution of the zero-order solution. As it is well known, the discretised form of the SBIE is:

$$c^i p^i + \sum_{e=1}^{N_{be}} \left(H_p p_p \right)^{\Phi_e} = \sum_{e=1}^{N_{be}} \left(G_p q_p \right)^{\Phi_e} \tag{3.107}$$

which is somewhat a simplified version of the δSBIE (3.86). Performing a suitable collocation of the SBIE throughout the discretisation leads to the influence matrices $\mathbf{H}$ and $\mathbf{G}$, which are built by assembling free-terms and H_p integrals into $\mathbf{H}$, and G_p integrals into $\mathbf{G}$. The discretised system is transformed into a system of linear equations once the boundary conditions are applied:

$$\mathbf{Hp} = \mathbf{Gq} \quad \xrightarrow[\quad\quad\quad\quad\quad]{\text{boundary conditions}} \quad \mathbf{Ax} = \mathbf{B\bar{x}} = \mathbf{b} \tag{3.108}$$

where $\mathbf{A}$ is composed of components of $\mathbf{H}$ and $\mathbf{G}$ related to the unknown components of $\mathbf{p}$ and $\mathbf{q}$ (gathered into $\mathbf{x}$), and $\mathbf{B}$ is composed of components of $\mathbf{H}$ and $\mathbf{G}$ related to the known

components of $\mathbf{p}$ and $\mathbf{q}$ (gathered into $\bar{\mathbf{x}}$). Following a similar procedure but using the δSBIE (3.86), the first-order discretised system is:

$$\mathbf{H}\delta\mathbf{p} + \delta\mathbf{H}\mathbf{p} = \mathbf{G}\delta\mathbf{q} + \delta\mathbf{G}\mathbf{q} \quad \xrightarrow{\text{boundary conditions}} \quad \mathbf{A}\delta\mathbf{x} = \mathbf{B}\delta\bar{\mathbf{x}} + \delta\mathbf{G}\mathbf{q} - \delta\mathbf{H}\mathbf{p} = \mathbf{b}^{\delta} \quad (3.109)$$

where $\mathbf{A}$ and $\mathbf{B}$ is similar to that of the zero-order system (if the same discretisation and collocation is used), and the components of $\delta\bar{\mathbf{x}}$ are related to the sensitivities of the boundary conditions.

3.8 Helmholtz problem

The previous section deals with the Laplace problem, which, despite being the simplest case, it is very useful to explain, discuss and understand in detail all the steps to obtain a BEM formulation for sensitivity analysis. Furthermore, the crucial part already solved for the Laplace problem is applicable with small modifications to other problems. A simple change of flux variable $f = -kq$, where f is the physical flux and k is the conductivity, make possible to use the already developed formulation for heat transfer or electrostatics problems. By expanding the fundamental solution, it is also possible to obtain the BEM formulation for the Helmholtz problem, which with simple change of flux variables allows the study of wave propagation within ideal fluids or the anti-plane wave motion in two-dimensional elastodynamics. In the present section, the BEM formulation (SBIE and δSBIE) for sensitivity analysis for the Helmholtz problem is developed.

Concerning the BIEs, the only formal difference between the Laplace problem and the Helmholtz problem is the fundamental solution [6], which represents a dynamic event with a propagation speed c in the frequency domain ω. Being $k = \omega/c$ the wavenumber, the fundamental solution p^* and its derivatives are:

$$p^* = \frac{1}{2\pi}\mathrm{K}_0\,(ikr) = \frac{1}{2\pi}P \quad (3.110)$$

$$p^*_{,j} = \frac{1}{2\pi}\frac{\partial P}{\partial r}r_{,j} = \frac{1}{2\pi}Qr_{,j} \quad (3.111)$$

$$p^*_{,jm} = \frac{1}{2\pi}\left[\frac{1}{r}\frac{\partial P}{\partial r}\delta_{jm} + \left(\frac{\partial^2 P}{\partial r^2} - \frac{1}{r}\frac{\partial P}{\partial r}\right)r_{,j}r_{,m}\right] = \frac{1}{2\pi}\left(R_1\delta_{jm} + R_2 r_{,j}r_{,m}\right) \quad (3.112)$$

$$q^* = p^*_{,j}n_j = \frac{1}{2\pi}\frac{\partial P}{\partial r}\frac{\partial r}{\partial n} = \frac{1}{2\pi}Q\frac{\partial r}{\partial n} \quad (3.113)$$

where i is the imaginary unit, and $\mathrm{K}_n\,(z)$ is the modified Bessel function of the second kind of order n and argument z. Terms Q, R_1 and R_2 depend exclusively on r and k:

$$Q = -ik\mathrm{K}_1\,(ikr) \quad (3.114)$$

$$R_1 = \frac{1}{r}Q \quad (3.115)$$

$$R_2 = (ik)^2\mathrm{K}_2\,(ikr) \quad (3.116)$$

Bessel functions $K_n(z)$ can be decomposed as shown in Appendix B. By using this decomposition, P, Q, R_1 and R_2 can be written is such a way that a part depending only on r is segregated from another parts depending on r and k:

$$P = -\ln r - \ln \frac{ik}{2} - \gamma + K_0^R(ikr) = -\ln r + \mathcal{O}(r^0) \tag{3.117}$$

$$Q = -\frac{1}{r} + \frac{k^2}{2} r \ln r + \frac{k^2}{2}\left(\ln\frac{ik}{2} + \gamma - \frac{1}{2}\right) r - ikK_1^R(ikr) = -\frac{1}{r} + \mathcal{O}(r\ln r) \tag{3.118}$$

$$R_1 = -\frac{1}{r^2} + \frac{k^2}{2}\ln r + \frac{k^2}{2}\left(\ln\frac{ik}{2} + \gamma - \frac{1}{2}\right) - \frac{ik}{r}K_1^R(ikr) = -\frac{1}{r^2} + \mathcal{O}(\ln r) \tag{3.119}$$

$$R_2 = \frac{2}{r^2} + \frac{k^2}{2} - \frac{k^4}{8}r^2\ln r - \frac{k^4}{8}\left(\ln\frac{ik}{2} + \gamma - \frac{3}{4}\right) r^2 - k^2 K_2^R(ikr) = \frac{2}{r^2} + \mathcal{O}(r^0) \tag{3.120}$$

Therefore, the fundamental solution and its derivatives can be written as:

$$p^* = \left(p^*\right)^{\text{static}} + \left(p^*\right)^{\text{dynamic}} \tag{3.121}$$

$$p^*_{,j} = \left(p^*_{,j}\right)^{\text{static}} + \left(p^*_{,j}\right)^{\text{dynamic}} \tag{3.122}$$

$$p^*_{,jm} = \left(p^*_{,jm}\right)^{\text{static}} + \left(p^*_{,jm}\right)^{\text{dynamic}} \tag{3.123}$$

$$q^* = \left(q^*\right)^{\text{static}} + \left(q^*\right)^{\text{dynamic}} \tag{3.124}$$

where the static parts correspond to the Laplace problem. Dynamic parts lead to at most weakly singular integrals, hence neither produce additional free-terms nor require further treatment.

3.8.1 Ideal fluid

Consider an ideal fluid with density ρ and bulk modulus K. The wave propagation speed is then $c = \sqrt{K/\rho}$. Within the small perturbation hypothesis, the wave propagation in this medium follows the Helmholtz equation with the dynamic pressure p as the primary variable [6]. The flux variable (secondary variable) is the fluid normal displacement u_n:

$$u_n = \frac{1}{\rho\omega^2}\frac{\partial p}{\partial n} = \frac{1}{\rho\omega^2} q \tag{3.125}$$

Thus, simply by making the change of variable $q = \rho\omega^2 u_n$, the formulation can be used to study this problem.

3.8.2 Anti-plane elastodynamics

Consider an elastic solid with density ρ and shear modulus μ. The shear wave propagation speed is then $c_2 = \sqrt{\mu/\rho}$. The two-dimensional analysis of the anti-plane motion is governed by the Helmholtz equation with the anti-plane displacement $u_3 = p$ as the primary variable, and $c_2 = c$ as the wave propagation speed [6]. The flux variable is now the anti-plane traction:

$$t_3 = \sigma_{3\alpha} n_\alpha = \mu u_{3,\alpha} n_\alpha = \mu q \tag{3.126}$$

where $\alpha = 1, 2$, and summation convention is implied. Hence, by making the change of variable $q = t_3/\mu$, the formulation can be used to study this problem.

3.9 Elastostatics

Consider the static analysis of an elastic solid with Poisson's ratio v and shear modulus (or Lamé's second parameter) μ. Lamé's first parameter is then $\lambda = 2\mu v/(1 - 2v)$. The primary variable of the governing differential equations for the in-plane problem are the displacements u_k, and the secondary variables are the tractions $t_k = \sigma_{kj} n_j$, where the stress tensor is $\sigma_{kj} = \lambda u_{m,m} \delta_{kj} + \mu(u_{k,j} + u_{j,k})$, and $k, j, m = 1, 2$. In the present work, the plane strain problem is considered, although the plane stress problem can be obtained easily from it [137].

3.9.1 δSBIE for non-boundary collocation points

The Singular BIE (SBIE) for an interior or exterior collocation point with respect to the reference domain Ω can be written as [137]:

$$\delta_\Omega^i u_l^i + \int_\Gamma t_{lk}^* u_k \, \mathrm{d}\Gamma = \int_\Gamma u_{lk}^* t_k \, \mathrm{d}\Gamma, \quad \delta_\Omega^i = \begin{cases} 1, \ \mathbf{x}^i \in \Omega \\ 0, \ \mathbf{x}^i \notin \Omega \cup \Gamma \end{cases} \tag{3.127}$$

where the body loads have been discarded, $l = 1, 2$ is the live index related to the load direction, $k = 1, 2$ is the dummy index related to the observation direction, and:

$$u_{lk}^* = \frac{1}{8\pi\mu(1 - v)} \left[-\delta_{lk}(3 - 4v)\ln r + r_{,l} r_{,k} \right] \tag{3.128}$$

$$u_{lk,j}^* = \frac{1}{8\pi\mu(1 - v)} \frac{1}{r} \left[-\delta_{lk}(3 - 4v)r_{,j} + \delta_{jl}r_{,k} + \delta_{kj}r_{,l} - 2r_{,l}r_{,k}r_{,j} \right] \tag{3.129}$$

$$\sigma_{lkm}^* = \lambda u_{lj,j}^* \delta_{km} + \mu \left(u_{lk,m}^* + u_{lm,k}^* \right) \tag{3.130}$$

$$\sigma_{lkm}^* = -\frac{1}{4\pi(1 - v)} \frac{1}{r} \left[2r_{,l}r_{,k}r_{,m} + (1 - 2v) \left(\delta_{lk}r_{,m} + \delta_{lm}r_{,k} - \delta_{km}r_{,l} \right) \right] \tag{3.131}$$

$$t_{lk}^* = \sigma_{lkm}^* n_m \tag{3.132}$$

$$t_{lk}^* = -\frac{1}{4\pi(1 - v)} \frac{1}{r} \left\{ \frac{\partial r}{\partial n} \left[\delta_{lk}(1 - 2v) + 2r_{,l}r_{,k} \right] + (1 - 2v) \left(n_l r_{,k} - n_k r_{,l} \right) \right\} \tag{3.133}$$

Likewise, for the perturbed domain $\tilde{\Omega}$:

$$\delta_{\tilde{\Omega}}^i \tilde{u}_l^i + \int_\Gamma \tilde{t}_{lk}^* \tilde{u}_k \, \mathrm{d}\tilde{\Gamma} = \int_\Gamma \tilde{u}_{lk}^* \tilde{t}_k \, \mathrm{d}\tilde{\Gamma}, \quad \delta_{\tilde{\Omega}}^i = \begin{cases} 1, \ \mathbf{x}^i \in \tilde{\Omega} \\ 0, \ \mathbf{x}^i \notin \tilde{\Omega} \cup \tilde{\Gamma} \end{cases} \tag{3.134}$$

As seen in previous sections, the relationships of geometrical objects and variables between the reference domain Ω and the perturbed domain $\tilde{\Omega}$ are given by linear mappings:

$$\tilde{u}_k^i = u_k^i + \delta u_k^i \left(a - a^0\right) \tag{3.135}$$

$$\tilde{u}_k = u_k + \delta u_k \left(a - a^0\right) \tag{3.136}$$

$$\tilde{u}_{k,j} = u_{k,j} + \delta u_{k,j} \left(a - a^0\right) \tag{3.137}$$

$$\tilde{n}_j = n_j + \delta n_j \left(a - a^0\right) \tag{3.138}$$

$$\tilde{\sigma}_{kj} = \lambda \tilde{u}_{m,m} \delta_{kj} + \mu(\tilde{u}_{k,j} + \tilde{u}_{j,k}) = \sigma_{kj} + \delta\tilde{\sigma}_{kj} \left(a - a^0\right) \tag{3.139}$$

$$\tilde{t}_k = \tilde{\sigma}_{kj} \tilde{n}_j = \sigma_{kj} n_j + \left(\sigma_{kj}\delta n_j + \delta\sigma_{kj} n_j\right) \left(a - a^0\right) = t_k + \delta t_k \left(a - a^0\right) \tag{3.140}$$

$$d\tilde{\Gamma} = \left[1 + \delta J \left(a - a^0\right)\right] \, d\Gamma \tag{3.141}$$

where only linear terms $(a - a^0)$ are kept. The fundamental solution u_{lk}^* depends on the observation and collocation points $u_{lk}^* = u_{lk}^*(\mathbf{x}, \mathbf{x}^i)$, hence its linear mapping must be built from the Taylor's expansion with respect to both points. As seen with the Laplace problem, this means that the linear mapping can be written as:

$$\tilde{u}_{lk}^* = u_{lk}^* + u_{lk,j}^* \delta r_j \left(a - a^0\right) = u_{lk}^* + \delta u_{lk}^* \left(a - a^0\right) \tag{3.142}$$

The linear mapping of $\tilde{t}_{lk}^*$ is built by using the linear mapping of its components:

$$\begin{aligned}
\tilde{t}_{lk}^* = \tilde{\sigma}_{lkm}^* \tilde{n}_m &= \left[\sigma_{lkm}^* + \sigma_{lkm,j}^* \delta r_j \left(a - a^0\right)\right] \left[n_m + \delta n_m \left(a - a^0\right)\right] \\
&= \sigma_{lkm}^* n_m + \left(\sigma_{lkm}^* \delta n_m + \sigma_{lkm,j}^* \delta r_j n_m\right) \left(a - a^0\right) \\
&= t_{lk}^* + \delta t_{lk}^* \left(a - a^0\right)
\end{aligned} \tag{3.143}$$

and keeping only linear terms $(a - a^0)$. Note that $\sigma_{lkm,j}^*$ is obtained by differentiation of Equation (3.131):

$$\begin{aligned}
\sigma_{lkm,j}^* = -\frac{1}{4\pi(1 - \nu)}\frac{1}{r^2}\Big[&-8r_{,l}r_{,k}r_{,m}r_{,j} - 2(1 - 2\nu)\left(\delta_{lk}r_{,m}r_{,j} + \delta_{lm}r_{,k}r_{,j} - \delta_{km}r_{,l}r_{,j}\right) \\
&+ 2\left(\delta_{lj}r_{,k}r_{,m} + \delta_{kj}r_{,l}r_{,m} + \delta_{mj}r_{,l}r_{,k}\right) + (1 - 2\nu)\left(\delta_{lk}\delta_{mj} + \delta_{lm}\delta_{kj} - \delta_{km}\delta_{lj}\right)\Big]
\end{aligned} \tag{3.144}$$

Finally, substituting all these linear mappings into Equation (3.134), keeping only linear terms $(a - a^0)$, substracting Equation (3.127) from it, and dropping out $(a - a^0)$ terms, give the sensitivity SBIE (or δSBIE):

$$\delta_\Omega^i \delta u_l^i + \int_\Gamma t_{lk}^* \delta u_k \, d\Gamma + \int_\Gamma \left(\delta t_{lk}^* + t_{lk}^* \delta J\right) u_k \, d\Gamma = \int_\Gamma u_{lk}^* \delta t_k \, d\Gamma + \int_\Gamma \left(\delta u_{lk}^* + u_{lk}^* \delta J\right) t_k \, d\Gamma \tag{3.145}$$

The first and third integrals are similar to the integrals of the SBIE, except that now the sensitivities δu_k and δt_k appear. The second and fourth integrals are new integrals that depend on u_k and t_k, thus they can be evaluated only once the zero-order solution is known.

3.9.2 δSBIE for boundary collocation points

The process to obtain the δSBIE for boundary collocation points is analogous to the process performed for the Laplace problem, so many aspects are skipped and assumed similar here. The limiting process is also done from an interior collocation point ($\delta_\Omega^i = 1$). The integration path of the integrals of Equation (3.145) is modified according to Equation (3.45), then:

$$\int_\Gamma (\ldots) \, d\Gamma = \lim_{\epsilon \to 0^+} \int_{\Gamma^i} (\ldots) \, d\Gamma + \lim_{\epsilon \to 0^+} \int_{\Gamma - e^i} (\ldots) \, d\Gamma \qquad (3.146)$$

Integration over Γ^i   In order to perform the integration over the arc Γ^i, a polar system of coordinates centered at the collocation point is used, see Section 3.7.2. Assuming that the displacement sensitivity is continuous, i.e. $\delta u_k = \delta u_k^i + \mathcal{O}(\epsilon)$, the evaluation of the first integral of Equation (3.145) leads to:

$$\delta u_l^i + \lim_{\epsilon \to 0^+} \int_{\Gamma^i} t_{lk}^* \delta u_k \, d\Gamma = \left[\delta_{lk} - \frac{1}{4\pi(1-v)} \left((1-2v)\delta_{lk}\Delta\theta^{\text{ext}} + 2\int_{\theta_1}^{\theta_2} n_l n_k \, d\theta \right) \right] \delta u_k^i \qquad (3.147)$$
$$= c_{lk}^i \delta u_k^i$$

where c_{lk}^i is the well-known elastic free-term:

$$\left(c_{lk}^i \right) = \frac{\Delta\theta^{\text{ext}}}{2\pi} \left(\delta_{lk} \right) - \frac{1}{8\pi(1-v)} \begin{pmatrix} \sin 2\theta_2 - \sin 2\theta_1 & -\left(\cos 2\theta_2 - \cos 2\theta_1\right) \\ -\left(\cos 2\theta_2 - \cos 2\theta_1\right) & -\left(\sin 2\theta_2 - \sin 2\theta_1\right) \end{pmatrix} \qquad (3.148)$$

Given that the displacement is continuous: $u_k = u_k^i + \mathcal{O}(\epsilon)$; and the design velocity field is differentiable: $v_m = v_m^i + v_{m,j}^i r_{,j}\epsilon + \mathcal{O}(\epsilon^2)$; the second integral of Equation (3.145) can be written as:

$$\lim_{\epsilon \to 0^+} \int_{\Gamma^i} \left(\delta t_{lk}^* + t_{lk}^* \delta J \right) u_k \, d\Gamma = \lim_{\epsilon \to 0^+} \int_{\Gamma^i} \left(\sigma_{lkm}^* \delta n_m + \sigma_{lkm,j}^* \delta r_j n_m + t_{lk}^* \delta J \right) u_k \, d\Gamma = b_{lkjm}^i v_{j,m}^i u_k^i \qquad (3.149)$$

where b^{i}_{lkjm} is:

$$
\begin{aligned}
b^{\mathrm{i}}_{lkjm} = -\frac{1}{4\pi(1-\nu)} \Bigg[&-6 \int_{\theta_1}^{\theta_2} n_l n_k n_j n_m \, \mathrm{d}\theta - (1-2\nu)\,\delta_{lk} \int_{\theta_1}^{\theta_2} n_j n_m \, \mathrm{d}\theta \\
&+ (1+2\nu)\,\delta_{lj} \int_{\theta_1}^{\theta_2} n_k n_m \, \mathrm{d}\theta + (3-2\nu)\,\delta_{kj} \int_{\theta_1}^{\theta_2} n_l n_m \, \mathrm{d}\theta - (1-2\nu) \int_{\theta_1}^{\theta_2} t_l n_k n_j t_m \, \mathrm{d}\theta \\
&+ (1-2\nu) \int_{\theta_1}^{\theta_2} n_l t_k n_j t_m \, \mathrm{d}\theta + 2 \int_{\theta_1}^{\theta_2} n_l n_k t_j t_m \, \mathrm{d}\theta + (1-2\nu)\,\delta_{lk} \int_{\theta_1}^{\theta_2} t_j t_m \, \mathrm{d}\theta \Bigg]
\end{aligned}
\tag{3.150}
$$

and its evaluation can be found in Appendix D. The new free-term b^{i}_{lkjm} is null if the collocation point is located at a smooth boundary point. Assuming that traction t_k and traction sensitivity δt_k are bounded, the third and fourth integrals of Equation (3.145) are null:

$$
\lim_{\epsilon \to 0^+} \int_{\Gamma^{\mathrm{i}}} u^*_{lk} \delta t_k \, \mathrm{d}\Gamma = 0
\tag{3.151}
$$

$$
\lim_{\epsilon \to 0^+} \int_{\Gamma^{\mathrm{i}}} \left(\delta u^*_{lk} + u^*_{lk} \delta J \right) t_k \, \mathrm{d}\Gamma = 0
\tag{3.152}
$$

Therefore, after performing the integration over Γ^{i}, the δSBIE for boundary collocation points can be written as:

$$
\begin{aligned}
c^{\mathrm{i}}_{lk} \delta u^{\mathrm{i}}_k + b^{\mathrm{i}}_{lkjm} v^{\mathrm{i}}_{j,m} u^{\mathrm{i}}_k + \lim_{\epsilon \to 0^+} \int_{\Gamma - e^{\mathrm{i}}} t^*_{lk} \delta u_k \, \mathrm{d}\Gamma + \lim_{\epsilon \to 0^+} \int_{\Gamma - e^{\mathrm{i}}} \left(\delta t^*_{lk} + t^*_{lk} \delta J \right) u_k \, \mathrm{d}\Gamma \\
= \lim_{\epsilon \to 0^+} \int_{\Gamma - e^{\mathrm{i}}} u^*_{lk} \delta t_k \, \mathrm{d}\Gamma + \lim_{\epsilon \to 0^+} \int_{\Gamma - e^{\mathrm{i}}} \left(\delta u^*_{lk} + u^*_{lk} \delta J \right) t_k \, \mathrm{d}\Gamma
\end{aligned}
\tag{3.153}
$$

Integration over $\Gamma - e^{\mathrm{i}}$ The first integral of Equation (3.153) is clearly strongly singular:

$$
H_l = \lim_{\epsilon \to 0^+} \int_{\Gamma - e^{\mathrm{i}}} t^*_{lk} \delta u_k \, \mathrm{d}\Gamma \text{ is strongly singular } \because t^*_{lk} = \mathcal{O}\left(r^{-1}\right)
\tag{3.154}
$$

The term leading to the strongly singular part can be segregated:

$$
\begin{aligned}
H_l = -\frac{1}{4\pi(1-\nu)} \Bigg\{ &\lim_{\epsilon \to 0^+} \int_{\Gamma - e^{\mathrm{i}}} \frac{1}{r} \frac{\partial r}{\partial n} \left[\delta_{lk}(1-2\nu) + 2 r_{,l} r_{,k} \right] \delta u_k \, \mathrm{d}\Gamma \\
&+ (1-2\nu) \lim_{\epsilon \to 0^+} \int_{\Gamma - e^{\mathrm{i}}} \frac{1}{r} \left(n_l r_{,k} - n_k r_{,l} \right) \delta u_k \, \mathrm{d}\Gamma \Bigg\}
\end{aligned}
\tag{3.155}
$$

Because the displacement sensitivity is continuous, one can add and substract δu_k^i from δu_k in order to further segregate the strongly singular term:

$$H_l = -\frac{1}{4\pi (1-v)} \left\{ \lim_{\epsilon \to 0^+} \int_{\Gamma - e^i} \frac{1}{r} \frac{\partial r}{\partial n} \left[\delta_{lk} (1 - 2v) + 2r_{,l} r_{,k} \right] \delta u_k \, d\Gamma \right.$$

$$\left. + (1-2v) \left[\lim_{\epsilon \to 0^+} \int_{\Gamma - e^i} \frac{1}{r} \left(n_l r_{,k} - n_k r_{,l} \right) \left(\delta u_k - \delta u_k^i \right) \, d\Gamma + \delta u_k^i \lim_{\epsilon \to 0^+} \int_{\Gamma - e^i} \frac{1}{r} \left(n_l r_{,k} - n_k r_{,l} \right) \, d\Gamma \right] \right\}$$

$$(3.156)$$

It is easy to see that:

$$\frac{\partial r}{\partial \Gamma} = r_{,1} t_{,1} + r_{,2} t_{,2} = -r_{,1} n_2 + r_{,2} n_1 = n_1 r_{,2} - n_2 r_{,1} \Rightarrow n_l r_{,k} - n_k r_{,l} = \epsilon_{lk} \frac{\partial r}{\partial \Gamma} \quad (3.157)$$

Hence, the regularised integral can be written as:

$$H_l = -\frac{1}{4\pi (1-v)} \left\{ \lim_{\epsilon \to 0^+} \int_{\Gamma - e^i} \frac{1}{r} \frac{\partial r}{\partial n} \left[\delta_{lk} (1 - 2v) + 2r_{,l} r_{,k} \right] \delta u_k \, d\Gamma \right.$$

$$\left. + (1-2v) \left[\lim_{\epsilon \to 0^+} \int_{\Gamma - e^i} \frac{1}{r} \left(n_l r_{,k} - n_k r_{,l} \right) \left(\delta u_k - \delta u_k^i \right) \, d\Gamma + \epsilon_{lk} \delta u_k^i \lim_{\epsilon \to 0^+} \int_{\Gamma - e^i} \frac{1}{r} \, dr \right] \right\}$$

$$(3.158)$$

where $\int 1/r \, dr$ is analytically solvable. The second integral of Equation (3.153) can be split into three integrals:

$$\delta H_l = \lim_{\epsilon \to 0^+} \int_{\Gamma - e^i} \left(\delta t_{lk}^* + t_{lk}^* \delta J \right) u_k \, d\Gamma = \lim_{\epsilon \to 0^+} \int_{\Gamma^i} \left(\sigma_{lkm}^* \delta n_m + \sigma_{lkm,j}^* \delta r_j n_m + t_{lk}^* \delta J \right) u_k \, d\Gamma$$

$$= \delta H_l^N + \delta H_l^R + \delta H_l^J$$

$$(3.159)$$

δH_l^N is a strongly singular integral:

$$\delta H_l^N = \lim_{\epsilon \to 0^+} \int_{\Gamma - e^i} \sigma_{lkm}^* \delta n_m u_k \, d\Gamma \text{ is strongly singular } \because \sigma_{lkm}^* = \mathcal{O} \left(r^{-1} \right) \quad (3.160)$$

If its integrand is expanded, two integrals are obtained:

$$\delta H_l^N = -\lim_{\epsilon \to 0^+} \int_{\Gamma - e^i} \sigma_{lkm}^* t_m n_r v_{r,s} t_s u_k \, d\Gamma$$

$$= \frac{1}{4\pi (1-v)} \lim_{\epsilon \to 0^+} \int_{\Gamma - e^i} \frac{1}{r} \left[2r_{,l} r_{,k} \frac{\partial r}{\partial \Gamma} + (1 - 2v) \left(\delta_{lk} \frac{\partial r}{\partial \Gamma} + t_l r_{,k} - t_k r_{,l} \right) \right] n_r v_{r,s} t_s u_k \, d\Gamma$$

$$= \frac{1}{4\pi (1-v)} \left\{ (1 - 2v) \lim_{\epsilon \to 0^+} \int_{\Gamma - e^i} \frac{1}{r} \left(t_l r_{,k} - t_k r_{,l} \right) n_r v_{r,s} t_s u_k \, d\Gamma \right.$$

$$\left. + \lim_{\epsilon \to 0^+} \int_{\Gamma - e^i} \frac{1}{r} \frac{\partial r}{\partial \Gamma} \left[2r_{,l} r_{,k} + (1 - 2v) \delta_{lk} \right] n_r v_{r,s} t_s u_k \, d\Gamma \right\} \quad (3.161)$$

where the first integral is regular because $t_l r_{,k} - t_k r_{,l} = \mathcal{O}(r)$. In the second integral, it is possible to add and substract $n_r^i v_{r,s}^i t_s^i$ from $n_r v_{r,s} t_s u_k$:

$$\delta H_l^N = \frac{1}{4\pi (1-v)} \left\{ (1 - 2v) \lim_{\epsilon \to 0^+} \int_{\Gamma - e^i} \frac{1}{r} \left(t_l r_{,k} - t_k r_{,l} \right) n_r v_{r,s} t_s u_k \, d\Gamma \right.$$

$$+ \lim_{\epsilon \to 0^+} \int_{\Gamma - e^i} \frac{1}{r} \frac{\partial r}{\partial \Gamma} \left[2r_{,l} r_{,k} + (1 - 2v) \delta_{lk} \right] \left(n_r v_{r,s} t_s u_k - n_r^i v_{r,s}^i t_s^i u_k^i \right) \, d\Gamma$$

$$\left. + n_r^i v_{r,s}^i t_s^i u_k^i \lim_{\epsilon \to 0^+} \int_{\Gamma - e^i} \frac{1}{r} \frac{\partial r}{\partial \Gamma} \left[2r_{,l} r_{,k} + (1 - 2v) \delta_{lk} \right] \, d\Gamma \right\} \quad (3.162)$$

where new regular and strongly singular integrals are obtained. In the new strongly singular integral, one of its terms lead to an integral $\int 1/r \, dr$:

$$\delta H_l^N = \frac{1}{4\pi (1-v)} \left\{ (1 - 2v) \lim_{\epsilon \to 0^+} \int_{\Gamma - e^i} \frac{1}{r} \left(t_l r_{,k} - t_k r_{,l} \right) n_r v_{r,s} t_s u_k \, d\Gamma \right.$$

$$+ \lim_{\epsilon \to 0^+} \int_{\Gamma - e^i} \frac{1}{r} \frac{\partial r}{\partial \Gamma} \left[2r_{,l} r_{,k} + (1 - 2v) \delta_{lk} \right] \left(n_r v_{r,s} t_s u_k - n_r^i v_{r,s}^i t_s^i u_k^i \right) \, d\Gamma$$

$$\left. + n_r^i v_{r,s}^i t_s^i u_k^i \left[(1 - 2v) \delta_{lk} \lim_{\epsilon \to 0^+} \int_{\Gamma - e^i} \frac{1}{r} \, dr + 2 \lim_{\epsilon \to 0^+} \int_{\Gamma - e^i} \frac{1}{r} \frac{\partial r}{\partial \Gamma} r_{,l} r_{,k} \, d\Gamma \right] \right\} \quad (3.163)$$

and the other term can be expanded as:

$$r_{,l} r_{,k} = \left(\frac{\partial r}{\partial \Gamma} \right)^i t_l^i \left(\frac{\partial r}{\partial \Gamma} \right)^i t_k^i + \mathcal{O}(r) = t_l^i t_k^i + \mathcal{O}(r) \quad (3.164)$$

which leads to:

$$
\begin{aligned}
\delta H_l^{\mathrm{N}} = \frac{1}{4\pi(1-\nu)} &\left\{ (1-2\nu) \lim_{\epsilon\to 0^+} \int_{\Gamma-e^{\mathrm{i}}} \frac{1}{r} \left(t_l r_{,k} - t_k r_{,l} \right) n_r \upsilon_{r,s} t_s u_k \, \mathrm{d}\Gamma \right. \\
&+ \lim_{\epsilon\to 0^+} \int_{\Gamma-e^{\mathrm{i}}} \frac{1}{r} \frac{\partial r}{\partial\Gamma} \left[2r_{,l} r_{,k} + (1-2\nu)\delta_{lk} \right] \left(n_r \upsilon_{r,s} t_s u_k - n_r^{\mathrm{i}} \upsilon_{r,s}^{\mathrm{i}} t_s^{\mathrm{i}} u_k^{\mathrm{i}} \right) \, \mathrm{d}\Gamma \\
&+ n_r^{\mathrm{i}} \upsilon_{r,s}^{\mathrm{i}} t_s^{\mathrm{i}} u_k^{\mathrm{i}} \left[2\lim_{\epsilon\to 0^+} \int_{\Gamma-e^{\mathrm{i}}} \frac{1}{r} \frac{\partial r}{\partial\Gamma} \left(r_{,l} r_{,k} - t_l^{\mathrm{i}} t_k^{\mathrm{i}} \right) \, \mathrm{d}\Gamma + \left[(1-2\nu)\delta_{lk} + 2t_l^{\mathrm{i}} t_k^{\mathrm{i}} \right] \lim_{\epsilon\to 0^+} \int_{\Gamma-e^{\mathrm{i}}} \frac{1}{r} \, \mathrm{d}r \right] \right\}
\end{aligned}
$$
(3.165)

Hence, δH_l^{N} can be written as a set of regular integrals and one integral $\int 1/r \, \mathrm{d}r$. The integral δH_l^{R} is also strongly singular:

$$
\delta H_l^{\mathrm{R}} = \lim_{\epsilon\to 0^+} \int_{\Gamma-e^{\mathrm{i}}} \sigma_{lkm,j}^* \delta r_j n_m u_k \, \mathrm{d}\Gamma \text{ is strongly singular} \because \underbrace{\sigma_{lkm,j}^*}_{\mathcal{O}(r^{-2})} \underbrace{\delta r_j}_{\mathcal{O}(r)} = \mathcal{O}\left(r^{-1}\right) \quad (3.166)
$$

If the following part of the integrand is expanded:

$$
\begin{aligned}
\sigma_{lkm,j}^* n_m = -\frac{1}{4\pi(1-\nu)} &\left\{ \frac{1}{r^2} \frac{\partial r}{\partial n} \left[-8r_{,l} r_{,k} r_{,j} - 2(1-2\nu)\delta_{lk} r_{,j} + 2\left(\delta_{lj} r_{,k} + \delta_{kj} r_{,l}\right) \right] \right. \\
&\left. + \frac{1}{r^2} \left[-2(1-2\nu) r_{,j} \left(n_l r_{,k} - n_k r_{,l} \right) + 2n_j r_{,l} r_{,k} + (1-2\nu)\left(\delta_{lk} n_j + \delta_{kj} n_l - \delta_{lj} n_k \right) \right] \right\} \\
&= \underbrace{\tilde{\sigma}_{lkj}^{\mathrm{a}}}_{\mathcal{O}(r^{-1})} + \underbrace{\tilde{\sigma}_{lkj}^{\mathrm{b}}}_{\mathcal{O}(r^{-2})} \quad (3.167)
\end{aligned}
$$

It is easy to see that $\tilde{\sigma}_{lkj}^{\mathrm{a}}$ leads to a regular integral while $\tilde{\sigma}_{lkj}^{\mathrm{b}}$ leads to a strongly singular integral:

$$
\delta H_l^{\mathrm{R}} = \lim_{\epsilon\to 0^+} \int_{\Gamma-e^{\mathrm{i}}} \tilde{\sigma}_{lkj}^{\mathrm{a}} \left(\upsilon_j - \upsilon_j^{\mathrm{i}} \right) u_k \, \mathrm{d}\Gamma + \lim_{\epsilon\to 0^+} \int_{\Gamma-e^{\mathrm{i}}} \tilde{\sigma}_{lkj}^{\mathrm{b}} \left(\upsilon_j - \upsilon_j^{\mathrm{i}} \right) u_k \, \mathrm{d}\Gamma \quad (3.168)
$$

Given that the design velocity field is differentiable, i.e. $\upsilon_j - \upsilon_j^{\mathrm{i}} - \upsilon_{j,s}^{\mathrm{i}} r_s = \mathcal{O}\left(r^2\right)$, one can add and substract $\upsilon_{j,s}^{\mathrm{i}} r_s$ from δr_j leading to new regular and strongly singular integrals:

$$
\begin{aligned}
\delta H_l^{\mathrm{R}} = \lim_{\epsilon\to 0^+} \int_{\Gamma-e^{\mathrm{i}}} \tilde{\sigma}_{lkj}^{\mathrm{a}} \left(\upsilon_j - \upsilon_j^{\mathrm{i}} \right) u_k \, \mathrm{d}\Gamma &+ \lim_{\epsilon\to 0^+} \int_{\Gamma-e^{\mathrm{i}}} \tilde{\sigma}_{lkj}^{\mathrm{b}} \left(\upsilon_j - \upsilon_j^{\mathrm{i}} - \upsilon_{j,s}^{\mathrm{i}} r_s \right) u_k \, \mathrm{d}\Gamma \\
&+ \lim_{\epsilon\to 0^+} \int_{\Gamma-e^{\mathrm{i}}} r\tilde{\sigma}_{lkj}^{\mathrm{b}} \upsilon_{j,s}^{\mathrm{i}} r_{,s} u_k \, \mathrm{d}\Gamma \quad (3.169)
\end{aligned}
$$

This new strongly singular integral can be further reduced by adding and substracting $\lim_{r \to 0} \left(r_{,s} u_k \right) = \left(\partial r / \partial \Gamma \right)^i t_s^i u_k^i$ to $r_{,s} u_k$:

$$
\delta H_l^{\mathrm{R}} = \lim_{\epsilon \to 0^+} \int_{\Gamma - e^i} \tilde{\sigma}_{lkj}^{\mathrm{a}} \left(v_j - v_j^i \right) u_k \, \mathrm{d}\Gamma + \lim_{\epsilon \to 0^+} \int_{\Gamma - e^i} \tilde{\sigma}_{lkj}^{\mathrm{b}} \left(v_j - v_j^i - v_{j,s}^i r_s \right) u_k \, \mathrm{d}\Gamma
$$
$$
+ \lim_{\epsilon \to 0^+} \int_{\Gamma - e^i} r \tilde{\sigma}_{lkj}^{\mathrm{b}} \left(v_{j,s}^i r_{,s} u_k - v_{j,s}^i \left(\frac{\partial r}{\partial \Gamma} \right)^i t_s^i u_k^i \right) \, \mathrm{d}\Gamma + v_{j,s}^i t_s^i u_k^i \lim_{\epsilon \to 0^+} \int_{\Gamma - e^i} r \tilde{\sigma}_{lkj}^{\mathrm{b}} \left(\frac{\partial r}{\partial \Gamma} \right)^i \, \mathrm{d}\Gamma
$$

$$
\tag{3.170}
$$

The latter integral can be expanded and written as:

$$
A = \lim_{\epsilon \to 0^+} \int_{\Gamma - e^i} r \tilde{\sigma}_{lkj}^{\mathrm{b}} \left(\frac{\partial r}{\partial \Gamma} \right)^i \, \mathrm{d}\Gamma = -\frac{1}{4\pi (1 - v)} \lim_{\epsilon \to 0^+} \int_{\Gamma - e^i} \frac{1}{r} \left(\frac{\partial r}{\partial \Gamma} \right)^i \left[-2 (1 - 2v) r_{,j} \left(n_l r_{,k} - n_k r_{,l} \right) \right.
$$
$$
\left. + 2 n_j r_{,l} r_{,k} + (1 - 2v) \left(\delta_{lk} n_j + \delta_{kj} n_l - \delta_{lj} n_k \right) \right] \, \mathrm{d}\Gamma \quad (3.171)
$$

By adding and substracting the following, already used, expansions: $r_{,j} = \left(\partial r / \partial \Gamma \right)^i t_j^i + \mathcal{O} (r)$, $r_{,l} r_{,k} = t_l^i t_k^i + \mathcal{O} (r)$ and $n_{,j} = n_j^i + \mathcal{O} (r)$; it can be written as:

$$
A = -\frac{1}{4\pi (1 - v)} \left\{ \lim_{\epsilon \to 0^+} \int_{\Gamma - e^i} \frac{1}{r} \left(\frac{\partial r}{\partial \Gamma} \right)^i \left[-2 (1 - 2v) \left(r_{,j} - \left(\frac{\partial r}{\partial \Gamma} \right)^i t_j^i \right) \left(n_l r_{,k} - n_k r_{,l} \right) \right. \right.
$$
$$
\left. + 2 \left(n_j r_{,l} r_{,k} - n_j^i t_l^i t_k^i \right) + (1 - 2v) \left(\delta_{lk} \left(n_j - n_j^i \right) + \delta_{kj} \left(n_l - n_l^i \right) - \delta_{lj} \left(n_k - n_k^i \right) \right) \right] \, \mathrm{d}\Gamma
$$
$$
- 2 (1 - 2v) t_j^i \lim_{\epsilon \to 0^+} \int_{\Gamma - e^i} \frac{1}{r} \left(n_l r_{,k} - n_k r_{,l} \right) \, \mathrm{d}\Gamma
$$
$$
+ \left[2 n_j^i t_l^i t_k^i + (1 - 2v) \left(\delta_{lk} n_j^i + \delta_{kj} n_l^i - \delta_{lj} n_k^i \right) \right] \lim_{\epsilon \to 0^+} \int_{\Gamma - e^i} \frac{1}{r} \left(\frac{\partial r}{\partial \Gamma} \right)^i \, \mathrm{d}\Gamma \right\} \quad (3.172)
$$

where the second integral is similar to the strongly singular integral appearing in the regularisation process of H_l. Also, it is easy to see by inspection that $\delta_{kj} n_l^i - \delta_{lj} n_k^i = \epsilon_{lk} t_j^i$. The third

integral can be regularised by adding and substracting $\partial r/\partial \Gamma$ to $(\partial r/\partial \Gamma)^{\mathrm{i}}$:

$$
\begin{aligned}
A = -\frac{1}{4\pi(1-v)} \Bigg\{ & \lim_{\epsilon\to 0^+} \int_{\Gamma - e^{\mathrm{i}}} \frac{1}{r}\left(\frac{\partial r}{\partial \Gamma}\right)^{\mathrm{i}} \Bigg[-2(1-2v)\left(r_{,j} - \left(\frac{\partial r}{\partial \Gamma}\right)^{\mathrm{i}} t_j^{\mathrm{i}}\right)(n_l r_{,k} - n_k r_{,l}) \\
& + 2\left(n_j r_{,l} r_{,k} - n_j^{\mathrm{i}} t_l^{\mathrm{i}} t_k^{\mathrm{i}}\right) + (1-2v)\left(\delta_{lk}(n_j - n_j^{\mathrm{i}}) + \delta_{kj}(n_l - n_l^{\mathrm{i}}) - \delta_{lj}(n_k - n_k^{\mathrm{i}})\right) \Bigg]\, \mathrm{d}\Gamma \\
& + \left[2n_j^{\mathrm{i}} t_l^{\mathrm{i}} t_k^{\mathrm{i}} + (1-2v)\left(\delta_{lk}n_j^{\mathrm{i}} + \epsilon_{lk} t_j^{\mathrm{i}}\right)\right] \lim_{\epsilon\to 0^+} \int_{\Gamma - e^{\mathrm{i}}} \frac{1}{r}\left(\left(\frac{\partial r}{\partial \Gamma}\right)^{\mathrm{i}} - \frac{\partial r}{\partial \Gamma}\right)\, \mathrm{d}\Gamma \\
& + \left[n_j^{\mathrm{i}}\left(2t_l^{\mathrm{i}} t_k^{\mathrm{i}} + (1-2v)\delta_{lk}\right) - (1-2v)\epsilon_{lk} t_j^{\mathrm{i}}\right] \lim_{\epsilon\to 0^+} \int_{\Gamma - e^{\mathrm{i}}} \frac{1}{r}\, \mathrm{d}r \Bigg\} \quad (3.173)
\end{aligned}
$$

Therefore, δH_l^{R} can be written as a set of regular integrals and an integral $\int 1/r\ \mathrm{d}r$. The integral δH_l^{J} can be easily regularised. If, in the first place, the expansion of $\delta J = t_{lk}^* t_j v_{j,s} t_s = t_j^{\mathrm{i}} v_{j,s}^{\mathrm{i}} t_s^{\mathrm{i}} + \mathcal{O}(r)$ is considered:

$$
\begin{aligned}
\delta H_l^{\mathrm{J}} &= \lim_{\epsilon\to 0^+} \int_{\Gamma - e^{\mathrm{i}}} t_{lk}^* \delta J u_k\, \mathrm{d}\Gamma = \lim_{\epsilon\to 0^+} \int_{\Gamma - e^{\mathrm{i}}} t_{lk}^* t_j v_{j,s} t_s u_k\, \mathrm{d}\Gamma \\
&= \lim_{\epsilon\to 0^+} \int_{\Gamma - e^{\mathrm{i}}} t_{lk}^* \left(t_j v_{j,s} t_s - t_j^{\mathrm{i}} v_{j,s}^{\mathrm{i}} t_s^{\mathrm{i}}\right) u_k\, \mathrm{d}\Gamma + t_j^{\mathrm{i}} v_{j,s}^{\mathrm{i}} t_s^{\mathrm{i}} \lim_{\epsilon\to 0^+} \int_{\Gamma - e^{\mathrm{i}}} t_{lk}^* u_k\, \mathrm{d}\Gamma \quad (3.174)
\end{aligned}
$$

then the resulting strongly singular integral is similar to H_l. Hence, the regularised form of δH_l^{J} can be written as:

$$
\begin{aligned}
\delta H_l^{\mathrm{J}} = &\lim_{\epsilon\to 0^+} \int_{\Gamma - e^{\mathrm{i}}} t_{lk}^* \left(t_j v_{j,s} t_s - t_j^{\mathrm{i}} v_{j,s}^{\mathrm{i}} t_s^{\mathrm{i}}\right) u_k\, \mathrm{d}\Gamma \\
& - \frac{1}{4\pi(1-v)} t_j^{\mathrm{i}} v_{j,s}^{\mathrm{i}} t_s^{\mathrm{i}} \Bigg\{ \lim_{\epsilon\to 0^+} \int_{\Gamma - e^{\mathrm{i}}} \frac{1}{r}\frac{\partial r}{\partial n}\left[\delta_{lk}(1-2v) + 2r_{,l}r_{,k}\right] u_k\, \mathrm{d}\Gamma \\
& + (1-2v)\left[\lim_{\epsilon\to 0^+} \int_{\Gamma - e^{\mathrm{i}}} \frac{1}{r}\left(n_l r_{,k} - n_k r_{,l}\right)\left(u_k - u_k^{\mathrm{i}}\right)\, \mathrm{d}\Gamma + \epsilon_{lk} u_k^{\mathrm{i}} \lim_{\epsilon\to 0^+} \int_{\Gamma - e^{\mathrm{i}}} \frac{1}{r}\, \mathrm{d}r\right] \Bigg\} \quad (3.175)
\end{aligned}
$$

Eventually, we are in the position to evaluate $\delta H_l = \delta H_l^{\mathrm{N}} + \delta H_l^{\mathrm{R}} + \delta H_l^{\mathrm{J}}$ by simply adding the three contributions. It is easy to see that all terms related to the integral $\int 1/r\ \mathrm{d}r$ cancel out when adding all the contributions.

The third integral of Equation (3.153) is weakly singular:

$$
G_l = \lim_{\epsilon\to 0^+} \int_{\Gamma - e^{\mathrm{i}}} u_{lk}^* \delta t_k\, \mathrm{d}\Gamma \text{ is weakly singular } \because u_{lk}^* = \mathcal{O}(\ln r) \quad (3.176)
$$

The fourth integral of Equation (3.153) can be split into two integrals:

$$\delta G_l = \lim_{\epsilon \to 0^+} \int_{\Gamma - e^i} \left(\delta u^*_{lk} + u^*_{lk} \delta J \right) t_k \, d\Gamma = \delta G^R_l + \delta G^J_l \tag{3.177}$$

where:

$$\delta G^R_l = \lim_{\epsilon \to 0^+} \int_{\Gamma - e^i} u^*_{lk,j} \delta r_j t_k \, d\Gamma \text{ is regular } \because \underbrace{u^*_{lk,j}}_{\mathcal{O}(r^{-1})} \underbrace{\delta r_j}_{\mathcal{O}(r)} = \mathcal{O}\left(r^0 \right) \tag{3.178}$$

$$\delta G^J_l = \lim_{\epsilon \to 0^+} \int_{\Gamma - e^i} u^*_{lk} \delta J t_k \, d\Gamma \text{ is weakly singular } \because \underbrace{u^*_{lk}}_{\mathcal{O}(\ln r)} \underbrace{\delta J}_{\mathcal{O}(r^0)} = \mathcal{O}\left(\ln r \right) \tag{3.179}$$

3.9.3 Discretisation and solution

The discussion done in Section 3.7.3 about discretisation, collocation, numerical integration and solution of the Laplace BEM sensitivity problem holds for the elastostatic case. The difference is in the length of the formulation, which is also more involved as it has been shown in the previous section.

The discretised form of Boundary Integral Equations (3.145) and (3.153) for any collocation point $\mathbf{x}^i$ can be written in a generic way as:

$$c^i_{lk} \delta u^i_k + b^i_{lkjm} v^i_{j,m} u^i_k + \sum_{e=1}^{N_{be}} \left(H_{lkp} \delta u_{kp} \right)^{\Phi_e} + \sum_{e=1}^{N_{be}} \left(\delta H_{lkp} u_{kp} \right)^{\Phi_e} = \sum_{e=1}^{N_{be}} \left(G_{lkp} \delta t_{kp} \right)^{\Phi_e} + \sum_{e=1}^{N_{be}} \left(\delta G_{lkp} t_{kp} \right)^{\Phi_e}$$

$$\tag{3.180}$$

where:

- If $\mathbf{x}^i \in \Gamma$, then:

$$\Phi^i = \left\{ \Phi_e, e = 1, \dots, N_{be} : \mathbf{x}^i \in \Phi_e \right\}$$
$$\Psi^i = \left\{ \Psi_d, d = 1, \dots, N_{de} : \mathbf{x}^i \in \Psi_d \right\}$$
$$u^i_k = \left(\phi^i_p u_{kp} \right)^{\Phi^i}$$
$$\delta u^i_k = \left(\phi^i_p \delta u_{kp} \right)^{\Phi^i}$$
$$v^i_{j,m} = \left(\psi^i_{q,m} v_{jq} \right)^{\Psi^i}$$

and c^i_{lk} and b^i_{lkjm} are calculated as shown previously according to the local geometry of the boundary at the collocation point.

- If $\mathbf{x}^i \notin \Gamma$, then $c^i_{lk} = \delta_{lk} \delta^i_\Omega$ and $b^i_{lkjm} = 0$.

For a boundary element Φ associated with a design element Ψ, two different situations must be considered:

Exterior integration, $\mathbf{x}^{\mathrm{i}} \notin \Phi$. When $\mathbf{x}^{\mathrm{i}} \notin \Phi$, the contributions of a boundary element Φ similar to those of the SBIE are:

$$H_{lkp} = \int_{\Phi} t_{lk}^{*} \phi_p \, \mathrm{d}\Gamma \tag{3.181}$$

$$G_{lkp} = \int_{\Phi} u_{lk}^{*} \phi_p \, \mathrm{d}\Gamma \tag{3.182}$$

The contributions of the new integrals arising in the δSBIE consider separately the design velocity field along the boundary element (through the design element Ψ) and the design velocity field at the collocation point:

$$\delta H_{lkp} = \delta H_{lkmqp}^{T1} v_{mq}^{\Psi} - \delta H_{lkmp}^{T2} v_{m}^{\mathrm{i}} = \left(\delta H_{lkmqp}^{N1} + \delta H_{lkmqp}^{R1} + \delta H_{lkmqp}^{J1} \right) v_{mq}^{\Psi} - \delta H_{lkmp}^{R2} v_{m}^{\mathrm{i}} \tag{3.183}$$

$$\delta G_{lkp} = \delta G_{lkmqp}^{T1} v_{mq}^{\Psi} - \delta G_{lkmp}^{T2} v_{m}^{\mathrm{i}} = \left(\delta G_{lkmqp}^{R1} + \delta G_{lkmqp}^{J1} \right) v_{mq}^{\Psi} - \delta G_{lkmp}^{R2} v_{m}^{\mathrm{i}} \tag{3.184}$$

where:

$$\delta H_{lkmqp}^{N1} = -\int_{\Phi} \sigma_{lkj}^{*} t_j n_m \psi_{q,s} t_s \phi_p \, \mathrm{d}\Gamma \tag{3.185}$$

$$\delta H_{lkmqp}^{R1} = \int_{\Phi} \sigma_{lkj,m}^{*} n_j \psi_q \phi_p \, \mathrm{d}\Gamma \tag{3.186}$$

$$\delta H_{lkmp}^{R2} = \int_{\Phi} \sigma_{lkj,m}^{*} n_j \phi_p \, \mathrm{d}\Gamma \tag{3.187}$$

$$\delta H_{lkmqp}^{J1} = \int_{\Phi} t_{lk}^{*} t_m \psi_{q,s} t_s \phi_p \, \mathrm{d}\Gamma \tag{3.188}$$

$$\delta G_{lkmqp}^{R1} = \int_{\Phi} u_{lk,m}^{*} \psi_q \phi_p \, \mathrm{d}\Gamma \tag{3.189}$$

$$\delta G_{lkmp}^{R2} = \int_{\Phi} u_{lk,m}^{*} \phi_p \, \mathrm{d}\Gamma \tag{3.190}$$

$$\delta G_{lkmqp}^{J1} = \int_{\Phi} u_{lk}^{*} t_m \psi_{q,s} t_s \phi_p \, \mathrm{d}\Gamma \tag{3.191}$$

Interior integration, $\mathbf{x}^i \in \Phi$. When $\mathbf{x}^i \in \Phi$, the contributions of Φ similar to those of the SBIE are:

$$
H_{lkp} = -\frac{1}{4\pi(1-\nu)} \left\{ \lim_{\epsilon \to 0^+} \int_{\Phi-e^i} \frac{1}{r}\frac{\partial r}{\partial n} \left[\delta_{lk}(1-2\nu) + 2r_{,l}r_{,k} \right] \phi_p \, d\Gamma \right.
$$

$$
\left. + (1-2\nu) \left[\lim_{\epsilon \to 0^+} \int_{\Phi-e^i} \frac{1}{r} \left(n_l r_{,k} - n_k r_{,l} \right) \left(\phi_p - \phi_p^i \right) \, d\Gamma + \epsilon_{lk}\phi_p^i \lim_{\epsilon \to 0^+} \int_{\Phi-e^i} \frac{1}{r} \, dr \right] \right\} \quad (3.192)
$$

$$
G_{lkp} = \lim_{\epsilon \to 0^+} \int_{\Phi-e^i} u_{lk}^* \phi_p \, d\Gamma \quad (3.193)
$$

Since $\mathbf{x}^i \in \Phi$, the contributions of the new integrals arising in the δSBIE consider only the design velocity field along the boundary element (through the design element Ψ):

$$
\delta H_{lkp} = \delta H_{lkmqp}^{T1} v_{mq}^{\Psi} = \left(\delta H_{lkmqp}^{N1} + \delta H_{lkmqp}^{R1} + \delta H_{lkmqp}^{J1} \right) v_{mq}^{\Psi} \quad (3.194)
$$

$$
\delta G_{lkp} = \delta G_{lkmqp}^{T1} v_{mq}^{\Psi} = \left(\delta G_{lkmqp}^{R1} + \delta G_{lkmqp}^{J1} \right) v_{mq}^{\Psi} \quad (3.195)
$$

where:

$$
\delta H_{lkmqp}^{N1} = \frac{1}{4\pi(1-\nu)} \left\{ (1-2\nu) \int_{\Phi-e^i} \frac{1}{r} \left(t_l r_{,k} - t_k r_{,l} \right) n_m \psi_{q,s} t_s \phi_p \, d\Gamma \right.
$$

$$
+ \int_{\Phi-e^i} \frac{1}{r}\frac{\partial r}{\partial \Gamma} \left[2r_{,l}r_{,k} + (1-2\nu)\delta_{lk} \right] \left(n_m \psi_{q,s} t_s \phi_p - n_m^i \psi_{q,s}^i t^i \phi_p^i \right) \, d\Gamma
$$

$$
\left. + 2n_m^i \psi_{q,s}^i t_s^i \phi_p^i \int_{\Phi-e^i} \frac{1}{r}\frac{\partial r}{\partial \Gamma} \left(r_{,l}r_{,k} - t_l^i t_k^i \right) \, d\Gamma \right\} \quad (3.196)
$$

$$
\delta H_{lkmqp}^{R1} = \int_{\Gamma - e^i} \tilde{\sigma}_{lkm}^{a} \left(\psi_q - \psi_q^i\right) \phi_p \, d\Gamma + \int_{\Gamma - e^i} \tilde{\sigma}_{lkm}^{b} \left(\psi_q - \psi_q^i - \psi_{q,s}^i r_s\right) \phi_p \, d\Gamma
$$

$$
+ \int_{\Gamma - e^i} r \tilde{\sigma}_{lkm}^{b} \left(\psi_{q,s}^i r_s \phi_p - \psi_{q,s}^i \left(\frac{\partial r}{\partial \Gamma}\right)^i t_s^i \phi_p^i\right) \, d\Gamma
$$

$$
- \frac{1}{4\pi(1-v)} \psi_{q,s}^i t_s^i \phi_p^i \left\{ \int_{\Gamma - e^i} \frac{1}{r} \left(\frac{\partial r}{\partial \Gamma}\right)^i \left[-2(1-2v)\left(r_{,m} - \left(\frac{\partial r}{\partial \Gamma}\right)^i t_m^i\right)(n_l r_{,k} - n_k r_{,l}) \right.\right.
$$

$$
\left. + 2\left(n_m r_{,l} r_{,k} - n_m^i t_l^i t_k^i\right) + (1-2v)\left(\delta_{lk}(n_m - n_m^i) + \delta_{km}(n_l - n_l^i) - \delta_{lm}(n_k - n_k^i)\right)\right] d\Gamma
$$

$$
\left. + \left[2 n_m^i t_l^i t_k^i + (1-2v)\left(\delta_{lk} n_m^i + \epsilon_{lk} t_m^i\right)\right] \int_{\Gamma - e^i} \frac{1}{r} \left(\left(\frac{\partial r}{\partial \Gamma}\right)^i - \frac{\partial r}{\partial \Gamma}\right) d\Gamma \right\} \quad (3.197)
$$

$$
\delta H_{lkmqp}^{J1} = \int_{\Phi - e^i} t_{lk}^{*} \left(t_m \psi_{q,s} t_s - t_m^i \psi_{q,s}^i t_s^i\right) \phi_p \, d\Gamma
$$

$$
- \frac{1}{4\pi(1-v)} t_m^i \psi_{q,s}^i t_s^i \left\{ \int_{\Phi - e^i} \frac{1}{r} \frac{\partial r}{\partial n} \left[\delta_{lk}(1-2v) + 2 r_{,l} r_{,k}\right] \phi_p \, d\Gamma \right.
$$

$$
\left. + (1-2v) \int_{\Phi - e^i} \frac{1}{r} \left(n_l r_{,k} - n_k r_{,l}\right)\left(\phi_p - \phi_p^i\right) d\Gamma \right\} \quad (3.198)
$$

$$
\delta G_{lkmqp}^{R1} = \lim_{\epsilon \to 0^+} \int_{\Phi - e^i} u_{lk,m}^{*} \left(\psi_q - \psi_q^i\right) \phi_p \, d\Gamma \quad (3.199)
$$

$$
\delta G_{lkmqp}^{J1} = \lim_{\epsilon \to 0^+} \int_{\Phi - e^i} u_{lk}^{*} t_m \psi_{q,s} t_s \phi_p \, d\Gamma \quad (3.200)
$$

where the limit notation $\lim_{\epsilon \to 0^+}$ before some integrals has been omitted for brevity. Note that terms involving the integral $\int 1/r \, d\Gamma$ has been removed from δH_{lkmqp}^{N1}, δH_{lkmqp}^{R1} and δH_{lkmqp}^{J1} since they cancel out when evaluating δH_{lkmqp}^{T1}.

The solution of the sensitivity problem requires the solution of the zero-order solution. As it is well known, the discretised form of the SBIE is:

$$
c_{lk}^i u_k^i + \sum_{e=1}^{N_{be}} \left(H_{lkp} u_{kp}\right)^{\Phi_e} = \sum_{e=1}^{N_{be}} \left(G_{lkp} t_{kp}\right)^{\Phi_e} \quad (3.201)
$$

Performing a suitable collocation of the SBIE throughout the discretisation leads to the influence matrices **H** and **G**, which are built by assembling free-terms and H_{lkp} integrals into

$\mathbf{H}$, and G_{lkp} integrals into $\mathbf{G}$. The discretised system is transformed into a system of linear equations once the boundary conditions are applied:

$$\mathbf{Hu} = \mathbf{Gt} \quad \xrightarrow{\text{boundary conditions}} \quad \mathbf{Ax} = \mathbf{B\bar{x}} = \mathbf{b} \tag{3.202}$$

where $\mathbf{A}$ is composed of components of $\mathbf{H}$ and $\mathbf{G}$ related to the unknown components of $\mathbf{u}$ and $\mathbf{t}$ (gathered into $\mathbf{x}$), and $\mathbf{B}$ is composed of components of $\mathbf{H}$ and $\mathbf{G}$ related to the known components of $\mathbf{u}$ and $\mathbf{t}$ (gathered into $\mathbf{\bar{x}}$). Following a similar procedure but using the δSBIE (3.180), the first-order discretised system is:

$$\mathbf{H}\delta\mathbf{u} + \delta\mathbf{Hu} = \mathbf{G}\delta\mathbf{t} + \delta\mathbf{Gt} \quad \xrightarrow{\text{boundary conditions}} \quad \mathbf{A}\delta\mathbf{x} = \mathbf{B}\delta\mathbf{\bar{x}} + \delta\mathbf{Gt} - \delta\mathbf{Hu} = \mathbf{b}^{\delta} \tag{3.203}$$

where $\mathbf{A}$ and $\mathbf{B}$ is similar to that of the zero-order system, and the components of $\delta\mathbf{\bar{x}}$ are related to the sensitivities of the boundary conditions.

3.10 Elastodynamics

In the present section, the time harmonic counterpart of the elastostatic problem is studied. The formulation is completely analogous to the elastostatic problem, except that the fundamental solution is more involved. However, it can be split into a part similar to the elastostatic one, and another part that leads to at most weakly singular integrals. This splitting process was also applied to the Helmholtz problem in Section 3.8.

Consider the time harmonic analysis of an elastic solid with density ρ, Poisson's ratio ν and shear modulus μ. Lamé's first parameter is then $\lambda = 2\mu\nu/(1 - 2\nu)$. As it is well known [6], two body modes exist: the longitudinal mode (primary wave or P-wave) with a propagation speed $c_1 = \sqrt{(\lambda + 2\mu)/\rho}$, and the transversal mode (secondary wave or S-wave) with a propagation speed $c_2 = \sqrt{\mu/\rho}$. The P and S wavenumbers are denoted as $k_1 = \omega/c_1$ and $k_2 = \omega/c_2$, respectively, where ω is the circular frequency.

The fundamental solution and its derivatives can be written as [6]:

$$
\begin{aligned}
u_{lk}^* &= \frac{1}{2\pi\mu}\left[U_1\delta_{lk} - U_2 r_{,l} r_{,k}\right] \\
U_1 &= \mathrm{K}_0\left(ik_2 r\right) + \frac{1}{ik_2 r}\left[\mathrm{K}_1\left(ik_2 r\right) - \frac{k_1}{k_2}\mathrm{K}_1\left(ik_1 r\right)\right] \\
U_2 &= \mathrm{K}_2\left(ik_2 r\right) - \frac{k_1^2}{k_2^2}\mathrm{K}_2\left(ik_1 r\right)
\end{aligned}
\tag{3.204}
$$

$$
\begin{aligned}
u_{lk,m}^* &= \frac{1}{2\pi\mu}\left[V_1\delta_{lk}r_{,m} + V_2 r_{,l} r_{,j} r_{,m} + V_3\left(\delta_{lm}r_{,k} + \delta_{km}r_{,l}\right)\right] \\
V_1 &= \frac{\partial U_1}{\partial r} \\
V_2 &= \frac{2}{r}U_2 - \frac{\partial U_2}{\partial r} \\
V_3 &= -\frac{1}{r}U_2
\end{aligned}
\tag{3.205}
$$

$$\sigma_{lkm}^* = \frac{1}{2\pi}\left[T_1 r_{,l} r_{,k} r_{,m} + T_2\left(\delta_{lk} r_{,m} + \delta_{lm} r_{,k}\right) + T_3 \delta_{km} r_{,l}\right]$$

$$T_1 = 2\left(\frac{2}{r}U_2 - \frac{\partial U_2}{\partial r}\right)$$

$$T_2 = \frac{\partial U_1}{\partial r} - \frac{1}{r}U_2$$

$$T_3 = \frac{\lambda}{\mu}\left(\frac{\partial U_1}{\partial r} - \frac{\partial U_2}{\partial r} - \frac{1}{r}U_2\right) - \frac{2}{r}U_2$$

(3.206)

$$t_{lk}^* = \sigma_{lkm}^* n_m = \frac{1}{2\pi}\left[T_1 r_{,l} r_{,k}\frac{\partial r}{\partial n} + T_2\left(\delta_{lk}\frac{\partial r}{\partial n} + \delta_{lm} r_{,k}\right) + T_3 n_k r_{,l}\right]$$

(3.207)

$$\sigma_{lkm,j}^* = \frac{1}{2\pi}\left[R_1\left(\delta_{lj} r_{,m} r_{,k} + \delta_{kj} r_{,l} r_{,m} + \delta_{mj} r_{,l} r_{,k}\right) + R_2 r_{,j}\left(\delta_{lk} r_{,m} + \delta_{lm} r_{,k}\right)\right.$$

$$\left. + R_3 r_{,l} r_{,k} r_{,m} r_{,j} + R_4 \delta_{km} \delta_{lj} + R_5 \delta_{km} r_{,l} r_{,j} + R_6\left(\delta_{lk}\delta_{mj} + \delta_{lm}\delta_{kj}\right)\right]$$

$$R_1 = \frac{1}{r}T_1$$

$$R_2 = \frac{\partial^2 U_1}{\partial r^2} - \frac{1}{r}\left(\frac{\partial U_1}{\partial r} + \frac{\partial U_2}{\partial r} - \frac{2}{r}U_2\right)$$

$$R_3 = 2\left[-\frac{\partial^2 U_2}{\partial r^2} + \frac{1}{r}\left(5\frac{\partial U_2}{\partial r} - \frac{8}{r}U_2\right)\right]$$

(3.208)

$$R_4 = \frac{1}{r}T_3$$

$$R_5 = \frac{\lambda}{\mu}\left(\frac{\partial^2 U_1}{\partial r^2} - \frac{\partial^2 U_2}{\partial r^2} - \frac{1}{r}\frac{\partial U_1}{\partial r} + \frac{2}{r^2}U_2\right) - \frac{2}{r}\frac{\partial U_2}{\partial r} + \frac{4}{r^2}U_2$$

$$R_6 = \frac{1}{r}T_2$$

where terms U_i, V_i, T_i and R_i depend on distance r, frequency ω and material properties. By using the decomposition of Bessel functions presented in Equation (B.1), the non-frequency dependant part (static) of each term can be segregated. Their full decomposition can be found in Appendix D. Terms U_i, V_i, T_i and R_i can be written as:

$$U_1 = -\frac{3-4v}{4(1-v)}\ln r + \mathcal{O}\left(r^0\right)$$

$$U_2 = -\frac{1}{4(1-v)} + \mathcal{O}\left(r^2 \ln r\right)$$

(3.209)

$$V_1 = -\frac{3-4v}{4(1-v)}\frac{1}{r} + \mathcal{O}\left(r\ln r\right)$$

$$V_2 = -\frac{1}{2(1-v)}\frac{1}{r} + \mathcal{O}\left(r\right)$$

(3.210)

$$T_1 = -\frac{1}{1-v}\frac{1}{r} + \mathcal{O}(r)$$

$$T_2 = -\frac{1-2v}{2(1-v)}\frac{1}{r} + \mathcal{O}(r\ln r) \tag{3.211}$$

$$T_3 = \frac{1-2v}{2(1-v)}\frac{1}{r} + \mathcal{O}(r\ln r)$$

$$R_2 = \frac{1-2v}{1-v}\frac{1}{r^2} + \mathcal{O}\left(r^0\right)$$

$$R_3 = \frac{4}{1-v}\frac{1}{r^2} + \mathcal{O}\left(r^0\right) \tag{3.212}$$

$$R_5 = -\frac{1-2v}{1-v}\frac{1}{r^2} + \mathcal{O}\left(r^0\right)$$

where terms V_3, R_1, R_4 and R_6 have been omitted for brevity, see Equations (3.205) and (3.208). Also, in order to be able to verify that the static parts lead to the elastostatic fundamental solution, the following relationships have been used:

$$\frac{c_2^2}{c_1^2} = \frac{1-2v}{2(1-v)} \tag{3.213}$$

$$\frac{\lambda}{\mu} = \frac{c_1^2}{c_2^2} - 2 \tag{3.214}$$

By substituting these decompositions into Equations (3.204-3.208), it is very easy to see that the static parts lead to the elastostatic fundamental solution and its derivatives, and that the "dynamic residues" lead to at most weakly singular integrals:

$$u_{lk}^* = \left(u_{lk}^*\right)^{\text{static}} + \left(u_{lk}^*\right)^{\text{dynamic}} \tag{3.215}$$

$$u_{lk,m}^* = \left(u_{lk,m}^*\right)^{\text{static}} + \left(u_{lk,m}^*\right)^{\text{dynamic}} \tag{3.216}$$

$$t_{lk}^* = \left(t_{lk}^*\right)^{\text{static}} + \left(t_{lk}^*\right)^{\text{dynamic}} \tag{3.217}$$

$$\sigma_{lkm}^* = \left(\sigma_{lkm}^*\right)^{\text{static}} + \left(\sigma_{lkm}^*\right)^{\text{dynamic}} \tag{3.218}$$

$$\sigma_{lkm,j}^* = \left(\sigma_{lkm,j}^*\right)^{\text{static}} + \left(\sigma_{lkm,j}^*\right)^{\text{dynamic}} \tag{3.219}$$

3.11   Discretisation and collocation in multi-region problems

The boundary of a region $\partial\Omega_i$ is split into several boundaries Γ_k in order to assign a different boundary or interface condition to each one of them. Also, it is split at sharp corners in order to have a better representation of tractions there. Since it has been established that each boundary has its own nodes, double nodes appear at points where different boundaries meet. If standard nodal collocation is applied at these nodes, then a singular system of linear equations could be obtained. There are several ways to overcome this difficulty, for example using discontinuous elements, special corner elements, alternative BIEs, or additional equations. In

the present work, non-nodal collocation is used at these nodes, where the collocation points are located inside the elements but near the nodes. This approach not only solves the degeneracy problem with an acceptable error, but is also quite simple. The meshes obtained from standard pre-processors do not require modifications. Furthermore, it can be fully automated without much difficulty.

Coupling is directly performed by establishing compatibility and equilibrium along both faces of the interface at the level of discretised equations. Consider two BEM regions Ω_i and Ω_j ($i \neq j$) connected through an interface boundary Γ_k with orientation defined by its unit normal $\mathbf{n}$, see Figure 3.6. Relative to region Ω_i, Γ_k has positive orientation, hence $\mathbf{n}^{(i)} = \mathbf{n}$. However, relative to region Ω_j, Γ_k has negative orientation, and thus $\mathbf{n}^{(j)} = -\mathbf{n}$. Following this notation, coupling conditions between BEM regions are described next.

BEM (Ω_i: elastic solid) – BEM (Ω_j: elastic solid)   The compatibility and equilibrium at the interface in a nodal fashion can be written as:

$$\begin{aligned} \mathbf{u}^{(i)} &= \mathbf{u}^{(j)} \\ \mathbf{t}^{(i)} + \mathbf{t}^{(j)} &= \mathbf{0} \end{aligned} \tag{3.220}$$

$$\begin{aligned} \delta\mathbf{u}^{(i)} &= \delta\mathbf{u}^{(j)} \\ \delta\mathbf{t}^{(i)} + \delta\mathbf{t}^{(j)} &= \mathbf{0} \end{aligned} \tag{3.221}$$

where it must be noticed that displacements and tractions and their sensitivities have the same coupling equations. In the following, we denote $\mathbf{u}_i$ and $\mathbf{t}_i$ as vectors of displacements and tractions in all boundaries of Ω_i except Γ_k, and $\mathbf{u}_k^{(i)}$ and $\mathbf{t}_k^{(i)}$ as vectors of displacements and tractions of Γ_k with respect to Ω_i. Also, we denote $\mathbf{u}_j$ and $\mathbf{t}_j$ as vectors of displacements and tractions in all boundaries of Ω_j except Γ_k, and $\mathbf{u}_k^{(j)}$ and $\mathbf{t}_k^{(j)}$ as vectors of displacements and tractions of Γ_k with respect to Ω_j. The equations obtained after collocating the SBIE for both regions are:

$$\begin{pmatrix} \mathbf{H}_{ii} & \mathbf{H}_{ik} \\ \mathbf{H}_{ki} & \mathbf{H}_{kk}^{(i)} \end{pmatrix} \begin{Bmatrix} \mathbf{u}_i \\ \mathbf{u}_k^{(i)} \end{Bmatrix} - \begin{pmatrix} \mathbf{G}_{ii} & \mathbf{G}_{ik} \\ \mathbf{G}_{ki} & \mathbf{G}_{kk}^{(i)} \end{pmatrix} \begin{Bmatrix} \mathbf{t}_i \\ \mathbf{t}_k^{(i)} \end{Bmatrix} = \begin{Bmatrix} \mathbf{0}_i \\ \mathbf{0}_k \end{Bmatrix} \tag{3.222}$$
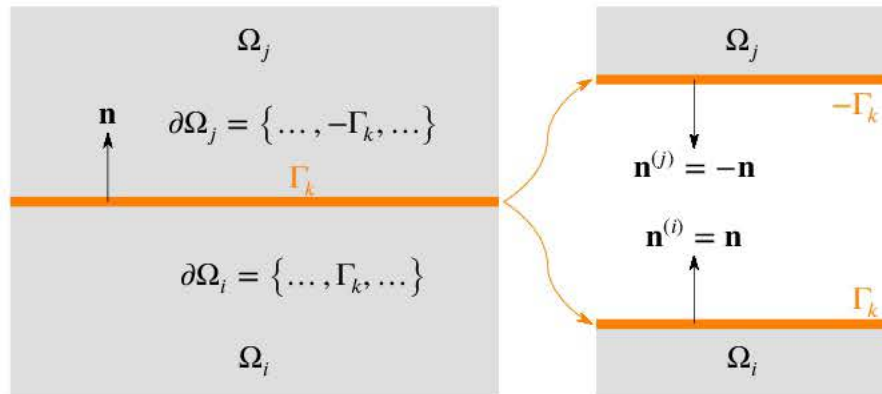

Figure 3.6: Boundary Γ_k acting as an interface between BEM regions Ω_i and Ω_j

$$
\begin{pmatrix} \mathbf{H}_{jj} & \mathbf{H}_{jk} \\ \mathbf{H}_{kj} & \mathbf{H}_{kk}^{(j)} \end{pmatrix} \begin{Bmatrix} \mathbf{u}_j \\ \mathbf{u}_k^{(j)} \end{Bmatrix} - \begin{pmatrix} \mathbf{G}_{jj} & \mathbf{G}_{jk} \\ \mathbf{G}_{kj} & \mathbf{G}_{kk}^{(j)} \end{pmatrix} \begin{Bmatrix} \mathbf{t}_j \\ \mathbf{t}_k^{(j)} \end{Bmatrix} = \begin{Bmatrix} \mathbf{0}_j \\ \mathbf{0}_k \end{Bmatrix} \tag{3.223}
$$

which reduce to:

$$
\begin{pmatrix} \mathbf{H}_{ii} & \mathbf{H}_{ik} & \mathbf{G}_{ik} & \mathbf{0}_{ij} \\ \mathbf{H}_{ki} & \mathbf{H}_{kk}^{(i)} & \mathbf{G}_{kk}^{(i)} & \mathbf{0}_{kj} \\ \mathbf{0}_{ki} & \mathbf{H}_{kk}^{(j)} & -\mathbf{G}_{kk}^{(j)} & \mathbf{H}_{kj} \\ \mathbf{0}_{ji} & \mathbf{H}_{jk} & \mathbf{G}_{jk} & \mathbf{H}_{jj} \end{pmatrix} \begin{Bmatrix} \mathbf{u}_i \\ \mathbf{u}_k^{(i)} \\ \mathbf{t}_k^{(j)} \\ \mathbf{u}_j \end{Bmatrix} - \begin{pmatrix} \mathbf{G}_{ii} & \mathbf{0}_{ij} \\ \mathbf{G}_{ki} & \mathbf{0}_{kj} \\ \mathbf{0}_{ki} & \mathbf{G}_{kj} \\ \mathbf{0}_{ji} & \mathbf{G}_{jj} \end{pmatrix} \begin{Bmatrix} \mathbf{t}_i \\ \mathbf{t}_j \end{Bmatrix} = \begin{Bmatrix} \mathbf{0}_i \\ \mathbf{0}_k \\ \mathbf{0}_k \\ \mathbf{0}_j \end{Bmatrix} \tag{3.224}
$$

once coupling conditions are applied maintaining $\mathbf{u}_k^{(i)}$ and $\mathbf{t}_k^{(i)}$ as active degrees of freedom along the interface. The final system of linear equations is obtained after applying the boundary conditions:

$$
\begin{pmatrix} \mathbf{A}_{ii} & \mathbf{H}_{ik} & \mathbf{G}_{ik} & \mathbf{0}_{ij} \\ \mathbf{A}_{ki} & \mathbf{H}_{kk}^{(i)} & \mathbf{G}_{kk}^{(i)} & \mathbf{0}_{kj} \\ \mathbf{0}_{ki} & \mathbf{H}_{kk}^{(j)} & -\mathbf{G}_{kk}^{(j)} & \mathbf{A}_{kj} \\ \mathbf{0}_{ji} & \mathbf{H}_{jk} & \mathbf{G}_{jk} & \mathbf{A}_{jj} \end{pmatrix} \begin{Bmatrix} \mathbf{x}_i \\ \mathbf{u}_k^{(i)} \\ \mathbf{t}_k^{(j)} \\ \mathbf{x}_j \end{Bmatrix} = \begin{pmatrix} \mathbf{B}_{ii} & \mathbf{0}_{ij} \\ \mathbf{B}_{ki} & \mathbf{0}_{kj} \\ \mathbf{0}_{ki} & \mathbf{B}_{kj} \\ \mathbf{0}_{ji} & \mathbf{B}_{jj} \end{pmatrix} \begin{Bmatrix} \tilde{\mathbf{x}}_i \\ \tilde{\mathbf{x}}_j \end{Bmatrix} = \begin{Bmatrix} \mathbf{b}_i \\ \mathbf{b}_k^{(i)} \\ \mathbf{b}_k^{(j)} \\ \mathbf{b}_j \end{Bmatrix} \tag{3.225}
$$

where $\mathbf{x}_i$ and $\mathbf{x}_j$ gather unknown displacements and tractions, and $\tilde{\mathbf{x}}_i$ and $\tilde{\mathbf{x}}_j$ gather known displacements and tractions. Matrices $\mathbf{A}$ and $\mathbf{B}$ combine terms of $\mathbf{H}$ and $\mathbf{G}$ matrices according the known and unknown displacements and tractions. Once this system of equations is solved, all displacements and tractions are known.

Therefore, in order to solve the sensitivity problem, we proceed following a similar process but collocating the δSBIE instead of the SBIE:

$$
\begin{pmatrix} \mathbf{A}_{ii} & \mathbf{H}_{ik} & \mathbf{G}_{ik} & \mathbf{0}_{ij} \\ \mathbf{A}_{ki} & \mathbf{H}_{kk}^{(i)} & \mathbf{G}_{kk}^{(i)} & \mathbf{0}_{kj} \\ \mathbf{0}_{ki} & \mathbf{H}_{kk}^{(j)} & -\mathbf{G}_{kk}^{(j)} & \mathbf{A}_{kj} \\ \mathbf{0}_{ji} & \mathbf{H}_{jk} & \mathbf{G}_{jk} & \mathbf{A}_{jj} \end{pmatrix} \begin{Bmatrix} \delta\mathbf{x}_i \\ \delta\mathbf{u}_k^{(i)} \\ \delta\mathbf{t}_k^{(j)} \\ \delta\mathbf{x}_j \end{Bmatrix} = \begin{pmatrix} \mathbf{B}_{ii} & \mathbf{0}_{ij} \\ \mathbf{B}_{ki} & \mathbf{0}_{kj} \\ \mathbf{0}_{ki} & \mathbf{B}_{kj} \\ \mathbf{0}_{ji} & \mathbf{B}_{jj} \end{pmatrix} \begin{Bmatrix} \delta\tilde{\mathbf{x}}_i \\ \delta\tilde{\mathbf{x}}_j \end{Bmatrix}
$$
$$
- \begin{pmatrix} \delta\mathbf{H}_{ii} & \delta\mathbf{H}_{ik} & \mathbf{0}_{ik} & \mathbf{0}_{ij} \\ \delta\mathbf{H}_{ki} & \delta\mathbf{H}_{kk}^{(i)} & \mathbf{0}_{kk} & \mathbf{0}_{kj} \\ \mathbf{0}_{ki} & \mathbf{0}_{kk} & \delta\mathbf{H}_{kk}^{(j)} & \delta\mathbf{H}_{kj} \\ \mathbf{0}_{ji} & \mathbf{0}_{jk} & \delta\mathbf{H}_{jk} & \delta\mathbf{H}_{jj} \end{pmatrix} \begin{Bmatrix} \mathbf{u}_i \\ \mathbf{u}_k^{(i)} \\ \mathbf{u}_k^{(j)} \\ \mathbf{u}_j \end{Bmatrix} + \begin{pmatrix} \delta\mathbf{G}_{ii} & \delta\mathbf{G}_{ik} & \mathbf{0}_{ik} & \mathbf{0}_{ij} \\ \delta\mathbf{G}_{ki} & \delta\mathbf{G}_{kk}^{(i)} & \mathbf{0}_{kk} & \mathbf{0}_{kj} \\ \mathbf{0}_{ki} & \mathbf{0}_{kk} & \delta\mathbf{G}_{kk}^{(j)} & \delta\mathbf{G}_{kj} \\ \mathbf{0}_{ji} & \mathbf{0}_{jk} & \delta\mathbf{G}_{jk} & \delta\mathbf{G}_{jj} \end{pmatrix} \begin{Bmatrix} \mathbf{t}_i \\ \mathbf{t}_k^{(i)} \\ \mathbf{t}_k^{(j)} \\ \mathbf{t}_j \end{Bmatrix}
$$
$$
\tag{3.226}
$$

where the left hand side matrix is exactly the same as before.

BEM (Ω_i: ideal fluid) – BEM (Ω_j: ideal fluid)   The nodal compatibility and equilibrium at the interface can be written as:

$$
\begin{aligned}
u_n^{(i)} \mathbf{n}^{(i)} = u_n^{(j)} \mathbf{n}^{(j)} &\quad \Rightarrow \quad u_n^{(i)} = -u_n^{(j)} \\
-p^{(i)} \mathbf{n}^{(i)} - p^{(j)} \mathbf{n}^{(j)} = \mathbf{0} &\quad \Rightarrow \quad p^{(i)} = p^{(j)}
\end{aligned} \tag{3.227}
$$

$$\delta u_n^{(i)} = -\delta u_n^{(j)}$$
$$\delta p^{(i)} = \delta p^{(j)}$$

(3.228)

where, as in the previous case, normal displacements and pressures and their sensitivities have the same coupling equations. The procedure to obtain the final system of equations is analogous to the process followed in the previous case.

BEM (Ω_i: ideal fluid) – BEM (Ω_j: elastic solid)   In this case, the nodal compatibility and equilibrium is:

$$u_n^{(i)} \mathbf{n}^{(i)} = \mathbf{u}^{(j)} \quad \Rightarrow \quad u_n^{(i)} = -\mathbf{u}^{(j)} \cdot \mathbf{n}^{(j)}$$
$$-p^{(i)} \mathbf{n}^{(i)} + \mathbf{t}^{(j)} = \mathbf{0} \quad \Rightarrow \quad \mathbf{t}^{(j)} = p^{(i)} \mathbf{n}^{(i)}$$

(3.229)

$$\delta u_n^{(i)} = -\delta \mathbf{u}^{(j)} \cdot \mathbf{n}^{(j)} - \mathbf{u}^{(j)} \cdot \delta \mathbf{n}^{(j)}$$
$$\delta \mathbf{t}^{(j)} = \delta p^{(i)} \mathbf{n}^{(i)} + p^{(i)} \delta \mathbf{n}^{(i)}$$

(3.230)

where, unlike the previous cases, the sensitivities do not follow exactly the same coupling equations due to an additional term that takes into account the variation of the unit normal. This, however, does not lead to difficulties. The only difference with respect to the previous cases is a new term in the right hand side of the system of equations.

3.12 Validation examples

In this section, some examples with analytical solution are used to validate the formulation and its implementation. Only dynamic problems are considered since their static counterparts can be checked by simply making $\omega \to 0$. In the same line as in the previous chapter, the example is a square domain with boundary conditions such that a one-dimensional wave phenomenon occurs. However, in order to validate the formulation for curved geometries, the domain is divided into two regions with the same material properties but with curved interfaces.

3.12.1 Ideal fluid problem

3.12.1.1 Analytical solution

Consider a rectangular domain Ω with the geometry and boundary conditions shown in Figure 3.7. The domain Ω contain an ideal fluid with density ρ, and bulk modulus K. The solution of the related Helmholtz equation consists of two pressure waves travelling in opposite directions along x_1:

$$p\left(x_1\right) = A \mathrm{e}^{-ikx_1} + B \mathrm{e}^{ikx_1}$$

(3.231)

where A and B are the amplitudes of the waves, $k = \omega/c$ is the wavenumber, ω is the circular frequency, and $c = \sqrt{K/\rho}$ is the wave propagation speed. Once boundary conditions are
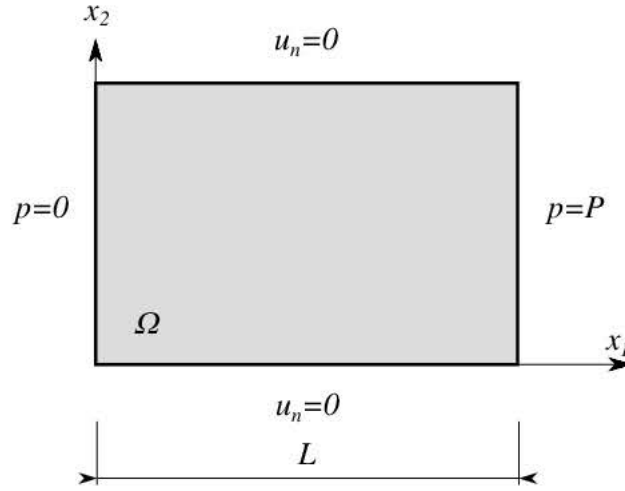
Design velocity field: $v_1(x)=x/L$, $v_2(x)=0$

Figure 3.7: Problem layout (ideal fluid problem)

considered, the pressure p and fluid displacement in the x_1 direction ($u_1 = 1/(\rho\omega^2)p_{,1}$) can be written as:

$$p\left(x_1\right) = \frac{P}{\sin kL} \sin kx_1 \tag{3.232}$$

$$u_1\left(x_1\right) = \frac{Pk}{\rho\omega^2 \sin kL} \cos kx_1 \tag{3.233}$$

If L is taken as the shape design variable with a design velocity field $\mathbf{v} = (x/L, 0)$, then the sensitivities are:

$$\delta p\left(x_1\right) = \frac{Pk}{\sin kL} \left(-\frac{\cos kL}{\sin kL} \sin kx_1 + \frac{x_1}{L} \cos kx_1\right) \tag{3.234}$$

$$\delta u_1\left(x_1\right) = -\frac{Pk^2}{\rho\omega^2 \sin kL} \left(\frac{\cos kL}{\sin kL} \cos kx_1 + \frac{x_1}{L} \sin kx_1\right) \tag{3.235}$$

3.12.1.2 BEM solution

The problem is solved numerically by using the BEM sensitivity analysis with the δSBIE developed in this chapter. The domain is a square with side length L, and is meshed using different element sizes ($L/4$, $L/10$) and different element order (linear, quadratic). By doing so, h and p convergence can be tested. Also, a fictitious circular inclusion filled with the same material is considered in order to demonstrate that the formulation works well also for curved elements. All meshes used here are shown in Figure 3.8. Dimensionless frequency $a_0 = \omega L/c$ is used, which is in the range $(0, 6]$.

The design velocity field is defined by a design mesh containing one 4-node quadrilateral element covering the domain Ω, and appropriate values of $\mathbf{v}$ are assigned to the four nodes in order to define $\mathbf{v} = \partial\mathbf{x}/\partial L = (x_1/L, 0)$.
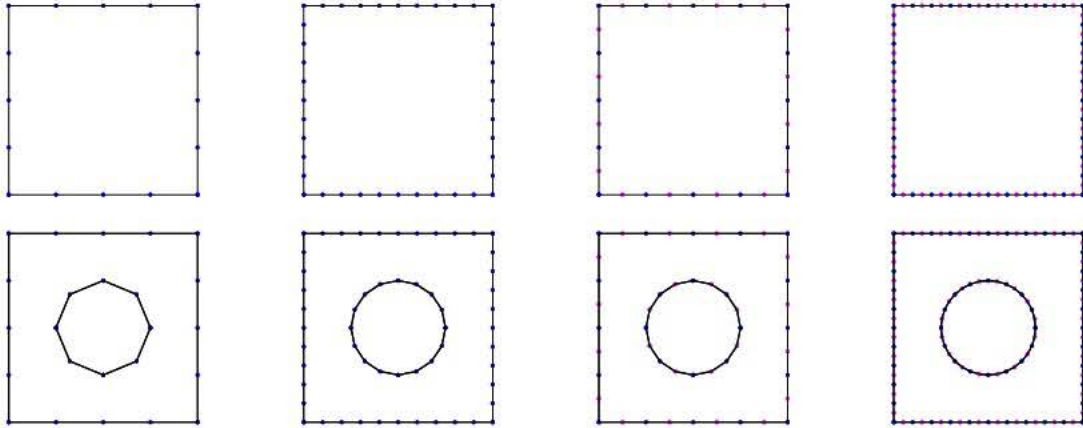
Figure 3.8: Linear and quadratic meshes with $L/4$ and $L/10$ element sizes, and with and without a fictitious circular inclusion.

Figure 3.9 shows the normalised displacement u_1 and sensitivity δu_1 at $x_1 = L$, and their relative errors with respect to the analytical solution. These results are obtained for the upper meshes in Figure 3.8. Figure 3.10 shows the same results but using the meshes with the fictitious circular inclusion, i.e. the lower meshes in Figure 3.8. In all cases, error levels are so small that the differences between numerical and analytical solutions can only be seen in the relative error graphs. These graphs clearly demonstrate the h and p convergence of the developed BEM sensitivity analysis for plane and curved boundary elements. The error levels at low frequencies are higher when using the meshes with the fictitious circular inclusion. However, the same phenomenon is seen in both the displacement and the displacement sentitivity, and hence it seems to be related to the discretisation itself.

3.12.2 Elastodynamic problem

3.12.2.1 Analytical solution

Consider an elastic two-dimensional rectangular domain Ω with the geometry and boundary conditions that Figure 3.11 shows. The domain Ω has a density ρ, shear modulus μ and Poisson's ratio ν. Despite being a two-dimensional domain, boundary conditions lead to a one-dimensional behaviour. The solution of the time harmonic elastodynamic governing equations consists of two waves travelling in opposite directions along x_1:

$$u_1\left(x_1\right) = A\mathrm{e}^{-ikx_1} + B\mathrm{e}^{ikx_1} \tag{3.236}$$

where A and B are the amplitudes of the waves, $k = \omega/c_P$ is the wavenumber, ω is the circular frequency, and $c_P = \sqrt{(\lambda + 2\mu)/\rho}$ is the P-wave propagation speed. Once boundary
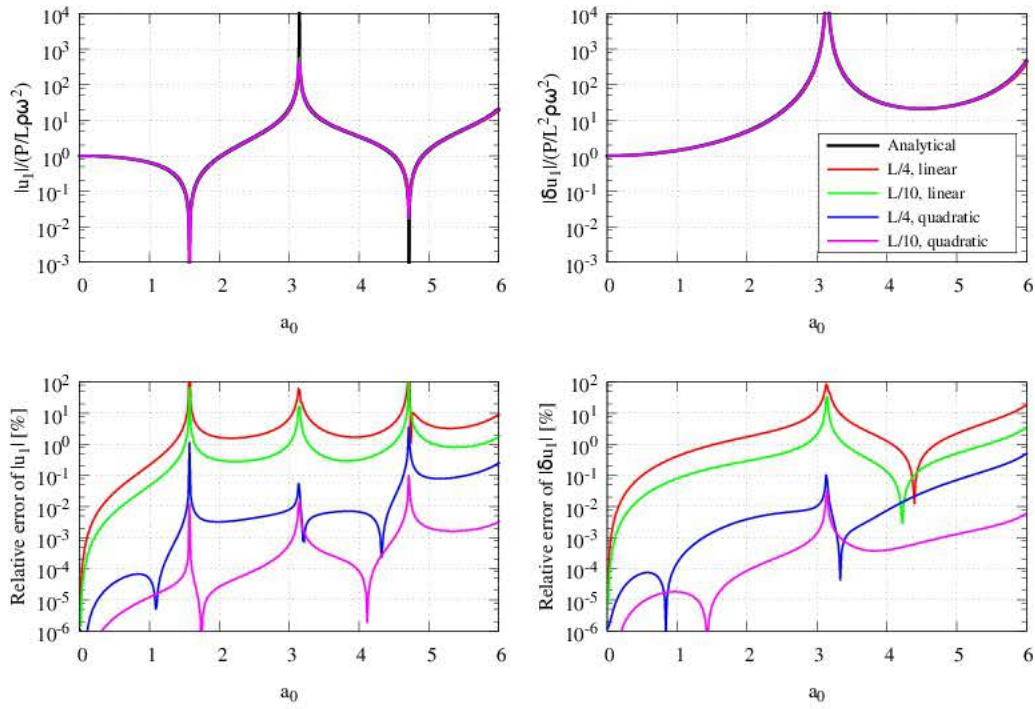
Figure 3.9: Convergence of $u_1(L)$ and $\delta u_1(L)$ for the ideal fluid problem
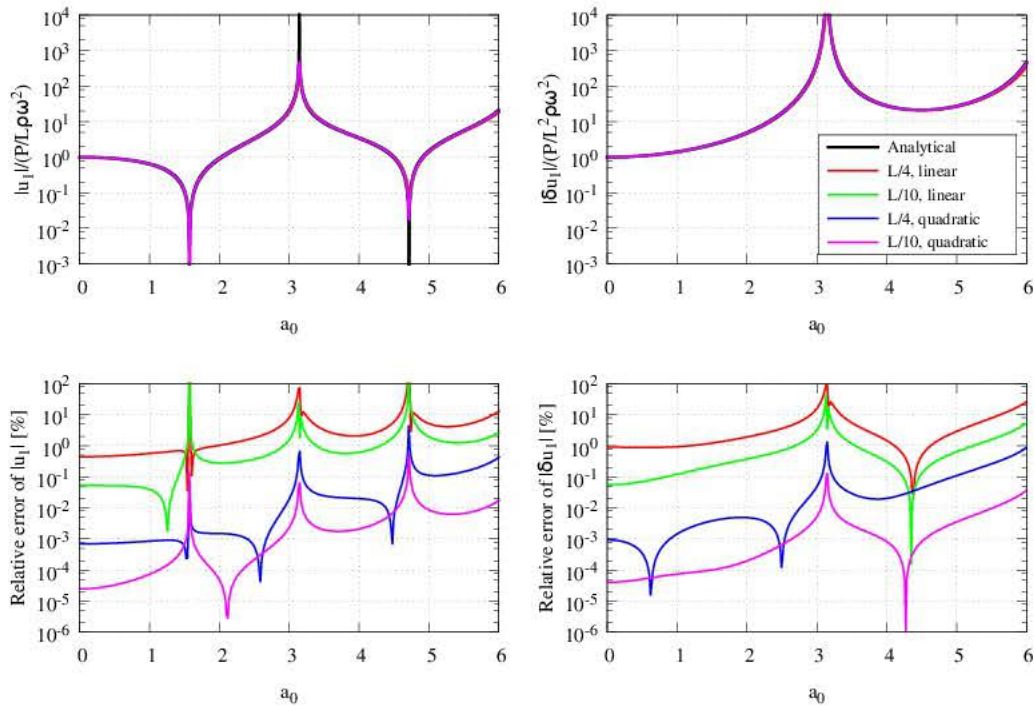
Figure 3.10: Convergence of $u_1(L)$ and $\delta u_1(L)$ for the ideal fluid problem (meshes with a fictitious circular inclusion)
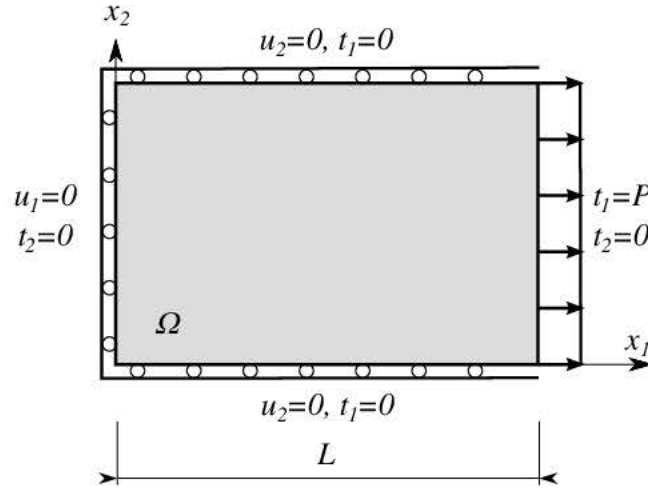
Design velocity field: $v_1(x)=x/L$, $v_2(x)=0$

Figure 3.11: Problem layout

conditions are considered, the displacement u_1 and stress σ_{11} can be written as:

$$u_1\left(x_1\right) = \frac{P}{\rho c_P^2 \cos kL}\frac{\sin kx_1}{k} \tag{3.237}$$

$$\sigma_{11}\left(x_1\right) = \frac{P}{\cos kL}\cos kx_1 \tag{3.238}$$

If L is taken as the shape design variable with a design velocity field $\mathbf{v} = (x/L, 0)$, then the sensitivities are:

$$\delta u_1\left(x_1\right) = \frac{P}{\rho c_P^2}\left(\frac{\sin kL}{\cos^2 kL}\sin kx_1 + \frac{1}{\cos kL}\frac{x_1}{L}\cos kx_1\right) \tag{3.239}$$

$$\delta \sigma_{11}\left(x_1\right) = Pk\left(\frac{\sin kL}{\cos^2 kL}\cos kx_1 - \frac{1}{\cos kL}\frac{x_1}{L}\sin kx_1\right) \tag{3.240}$$

where $\delta = \mathrm{d}/\mathrm{d}L = \partial/\partial L + (\partial/\partial x_j)v_j$ is the simplified notation for the field variable sensitivity (or material derivative).

3.12.2.2 Numerical solution

The numerical solution is obtained using the same configuration and the same set of meshes as in the previous section. Poisson's ratio is assumed to be $v = 1/4$. In this case, the dimensionless frequency is $a_0 = \omega L/c_1$, where c_1 is the P-wave propagation speed.

Figure 3.12 shows the normalised displacement u_1 and sensitivity δu_1 at $x_1 = L$, and their relative errors with respect to the analytical solution. Figure 3.13 shows the same results but using the meshes with the fictitious circular inclusion. As in the previous section, h and p convergence can be seen in these graphs for straight and curved boundary elements.
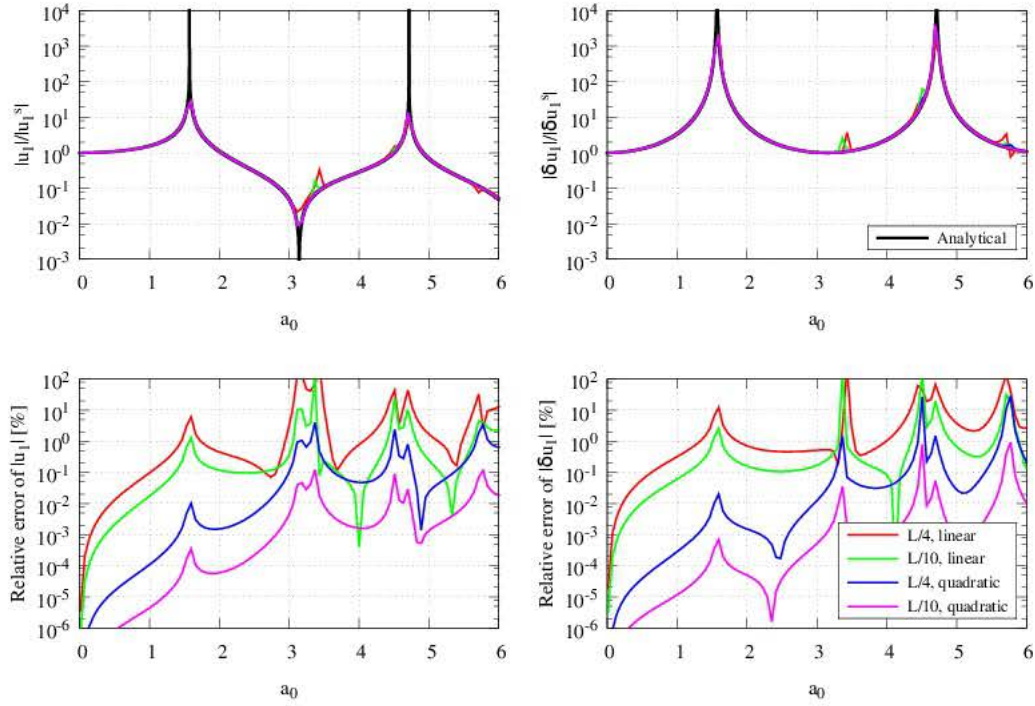
Figure 3.12: Convergence of $u_1(L)$ and $\delta u_1(L)$ for the elastodynamic problem
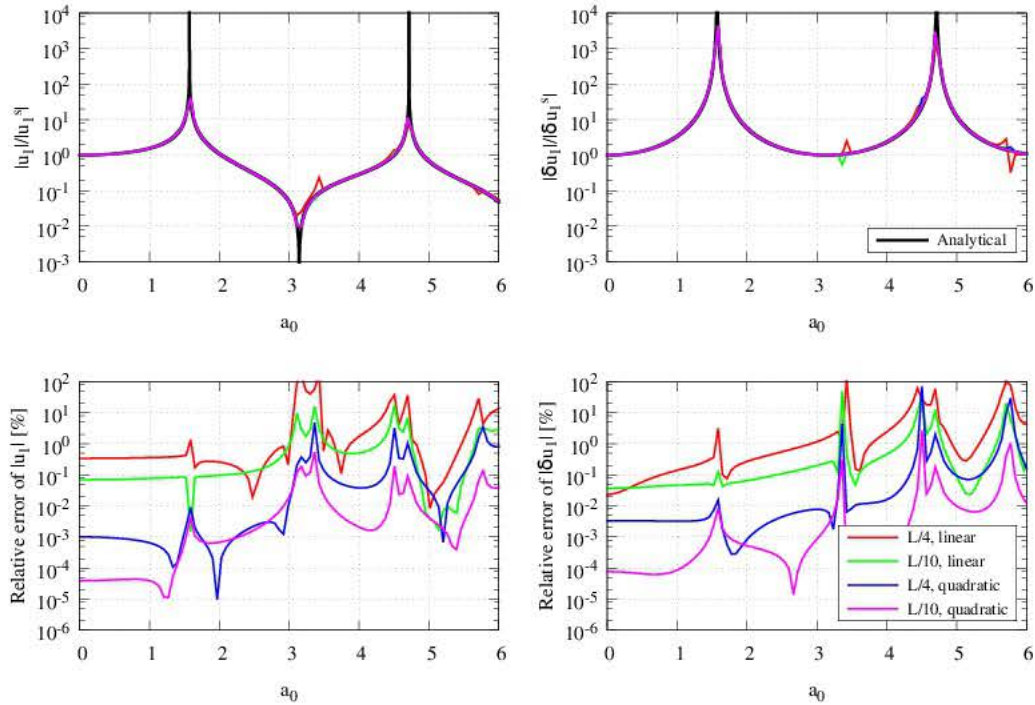
Figure 3.13: Convergence of $u_1(L)$ and $\delta u_1(L)$ for the elastodynamic problem (meshes with a fictitious circular inclusion)

4.1 Introduction

In previous chapters, two- and three-dimensional non-standard BEM formulations such as the Dual BEM and the Geometric Sensitivity BEM have been studied. These lead to the numerical evaluation of a greater number, more difficult and costlier integrals when compared to the conventional BEM. Therefore, there is a strong need to explore safe, systematic and economical numerical treatments of these integrals.

In this chapter, the main aspects related to the numerical evaluation of BEM integrals are reviewed, and some practical improvements are proposed. Since any attempt to provide a literature review in this field is inevitably incomplete because it is quite vast, a broad classification including the most relevant techniques is considered. Our effort is directed towards using simple algorithms where little or no tuning regarding the required number of integration points is needed. We propose some simple estimators of the required number of integration points as a function of the required error, and other measurable magnitudes of the element and collocation point. In particular, a strategy to obtain formulas for the numerical evaluation of weakly singular integrals by using polar coordinates with angular $\ln \tan f\,(\theta)$ transformation [138] and conformal mapping [139] is proposed.

The rest of the chapter is organised as follows. BEM integrals are described in Section 4.2, while the main issues related to their evaluation are presented in Section 4.3. In Section 4.4, the evaluation of the integral of the Jacobian is studied, while in Section 4.5 different methods for evaluating weakly singular integrals are analysed.

4.2 Description of BEM integrals

The basic structure of integrals arising in the Boundary Element Method is:

$$I = \int_X Y \, \mathrm{d}X = \int_\Xi F^* \Phi J \, \mathrm{d}\Xi \tag{4.1}$$

where F^* corresponds to a fundamental solution term, Φ to a shape function/s term, J to the Jacobian of the element transformation between reference Ξ (local) and real X (global) spaces, and $\mathrm{d}\Xi$ to a differential length ($\mathrm{d}\Xi \equiv \mathrm{d}\xi$), area ($\mathrm{d}\Xi \equiv \mathrm{d}\xi_1 \mathrm{d}\xi_2$) or volume ($\mathrm{d}\Xi \equiv \mathrm{d}\xi_1 \mathrm{d}\xi_2 \mathrm{d}\xi_3$) in the reference space. Figure 4.1 depicts some boundary and body load elements that may be present in two-dimensional and three-dimensional BEM problems. The most important objects influencing the integrand are also shown: position vector $\mathbf{x}$ and unit normal vector $\mathbf{n}$ at the observation point (integration point), position vector $\mathbf{x}^i$ and unit normal vector $\mathbf{n}^i$ at the collocation point (singularity) $\mathbf{x}^i$, and the distance vector $\mathbf{r} = \mathbf{x} - \mathbf{x}^i$.

Fundamental solution (F^*)

The fundamental solution F^* is the most challenging part of the integrand. Time harmonic fundamental solutions can generally be expressed as the following linear combination of N_{F^*}

line element   surface element   line element   surface element   volume element

(a) Two-dimensional problems   (b) Three-dimensional problems
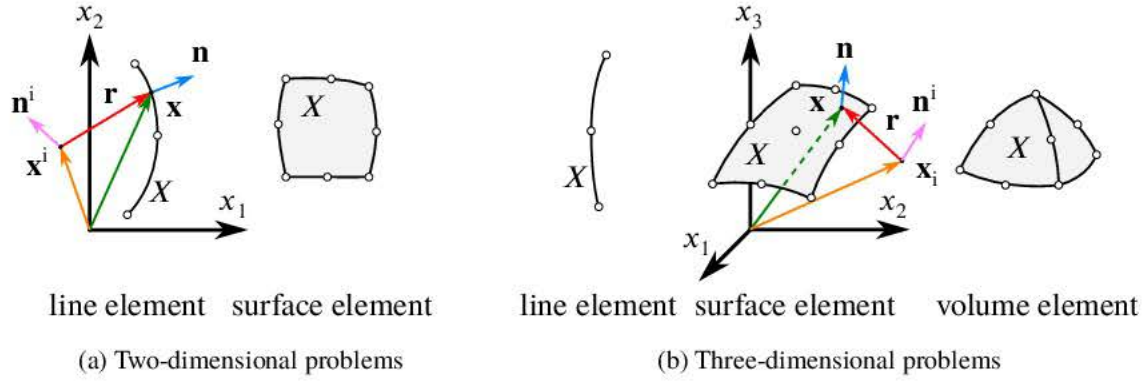
Figure 4.1: Layout of the integration problem in the Boundary Element Method

terms:

$$F^* = F^{(\text{cte})}(\omega, \text{properties}) \cdot \sum_{a=1}^{N_{F^*}} \left[F_a^{(\text{rad})}(r, \omega, \text{properties}) \cdot F_a^{(\text{geo})}\left(\mathbf{x}, \mathbf{n}, \mathbf{x}^i, \mathbf{n}^i\right) \right] \qquad (4.2)$$

where, for given frequency ω and material properties, $F_a^{(\text{cte})}$ are constants, $F_a^{(\text{rad})}$ are radial functions with respect to the distance r between observation $\mathbf{x}$ and collocation point $\mathbf{x}^i$ ($r = |\mathbf{x} - \mathbf{x}^i|$), and $F_a^{(\text{geo})}$ are functions of geometric nature depending on position and unit normal vectors at the observation and collocation points. Each radial function $F_a^{(\text{rad})}$ can be further decomposed as:

$$F_a^{(\text{rad})} = \sum_{b=1}^{N_{F_a}} F_{ab}^{(\text{cte})}(\omega, \text{properties}) \cdot F_{ab}^{(\text{rad})}(r, \omega, \text{properties}) \qquad (4.3)$$

where again, for given frequency ω and material properties, $F_{ab}^{(\text{cte})}$ are constants, and $F_{ab}^{(\text{rad})}$ are radial functions. Radial functions $F_{ab}^{(\text{rad})}$ can be classified as:

Singular. The radial function is one of the following types:

$$\frac{1}{r^p}, \; p = 1, 2, \ldots \qquad (4.4a)$$

$$\ln r \qquad (4.4b)$$

where $\lim_{r \to 0} F_{ab}^{(\text{rad})}$ is unbounded.

Regular. The radial function is one of the following types:

$$1 \tag{4.5a}$$

$$r^p \ln r, \ p = 1, 2 \ldots \tag{4.5b}$$

$$r^p, \ p = 1, 2 \ldots \tag{4.5c}$$

$$\frac{K_n^R (ikr)}{r^n} = \mathcal{O}\left(\omega^{n+2} r^2 \ln(\omega r)\right), \ n = 0, 1, 2 \tag{4.5d}$$

$$\frac{E_{n+1}^R (-ikr)}{r^n} = \mathcal{O}\left(\omega^{n+1} r\right), \ n = 0, 1, 2, \ldots \tag{4.5e}$$

where $\lim_{r \to 0} F_{ab}^{(rad)}$ is bounded. Note that k is a wavenumber, $K_n^R(z)$ is the rest after decomposing a modified Bessel function of the second kind of order n, and $E_n^R(z)$ is the rest of order n after decomposing the exponential function. These decompositions are described in Appendix B. In most cases, Bessel functions are related to 2D fundamental solutions, while exponential functions are related to 3D fundamental solutions.

Each function $F_a^{(geo)}$ contains one or several factors of the following types:

Distance gradient components: $r_{,k}$**.** The gradient of the distance r between observation and collocation points is:

$$\tilde{\mathbf{r}} = \mathbf{grad}(r) = \frac{\mathbf{x} - \mathbf{x}^i}{r} = \frac{\mathbf{r}}{r} = r_{,j} \mathbf{e}_j \tag{4.6}$$

which is an unit vector with direction pointing from the collocation point to the observation point, and will be called unit distance vector. In the 2D case, by applying a polar coordinates (ρ, θ) transformation centred at the collocation point $(x_1 = x_1^i + \rho \cos \theta, x_2 = x_2^i + \rho \sin \theta)$, each component becomes:

$$r_{,1} = \cos \theta \tag{4.7a}$$

$$r_{,2} = \sin \theta \tag{4.7b}$$

In the 3D case, by applying a spherical coordinates (ρ, θ, φ) transformation $(x_1 = x_1^i + \rho \cos \varphi \cos \theta, x_2 = x_2^i + \rho \cos \varphi \sin \theta, x_3 = x_3^i + \rho \sin \varphi)$, each component becomes:

$$r_{,1} = \cos \varphi \cos \theta \tag{4.8a}$$

$$r_{,2} = \cos \varphi \sin \theta \tag{4.8b}$$

$$r_{,3} = \sin \varphi \tag{4.8c}$$

They are thus purely angular functions centred at $\mathbf{x}^i$, bounded within $[-1, 1]$, and continuous everywhere except at $\mathbf{x} = \mathbf{x}^i$, where they have a jump discontinuity. Despite their relative simplicity in polar or spherical coordinates, they have a number of peculiarities in Cartesian coordinates. Algebraically, they are the quotient of a polynomial of order p and the square root of a polynomial of order $2p$, where p is the element order and both polynomials are in terms of reference coordinates.
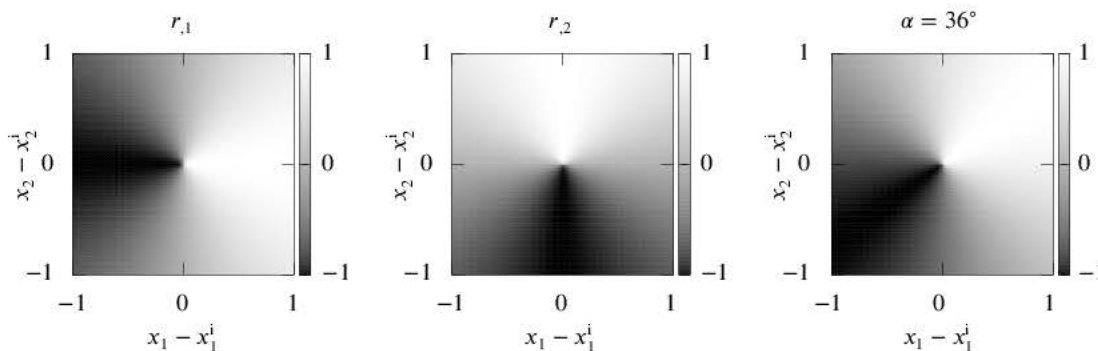
Figure 4.2: Colour maps of functions $r_{,1}$, $r_{,2}$ and $\tilde{\mathbf{r}} \cdot \mathbf{d}$ with $\alpha = 36°$

In order to show how these components behave along an integration domain, instead of showing $r_{,k}$, the more general directional derivative $\partial r / \partial d = \tilde{\mathbf{r}} \cdot \mathbf{d}$ is shown, where $\mathbf{d}$ is a unit direction vector. Figure 4.2 shows colour maps of $r_{,1}$, $r_{,2}$ and $\tilde{\mathbf{r}} \cdot \mathbf{d}$, where the unit direction vector is $\mathbf{d} = (\cos \alpha, \sin \alpha)$ with $\alpha = 36°$. The jump discontinuity can clearly be seen at $\mathbf{x} = \mathbf{x}^i$, and it is present at any line through point $\mathbf{x}^i$ except for a line perpendicular to $\mathbf{d}$, where the function is zero.

Figure 4.3 shows the values of the directional derivative $\tilde{\mathbf{r}} \cdot \mathbf{d}$ along a straight element with end-nodes at $(-1, 0)$ and $(1, 0)$, and collocation points at $(0, 1)$, $(0, 0.1)$ and $(0, 0)$. The unit direction vector is again taken as $\mathbf{d} = (\cos \alpha, \sin \alpha)$, and angles $\alpha = \{0°, 18°, 36°, 54°, 72°, 90°\}$ are considered. Figure 4.4 shows the same results but for a quadratic curved element with mid-node at $(0, 0)$ and end-nodes at $(-1, -0.2)$ and $(1, 0.2)$. Note that ξ is the element local coordinate. When the collocation point is relatively far from the element, the integrand varies smoothly. When the collocation point is relatively near the element, the integrand has a smooth but abrupt step for angles less than approximately 45°, and a peak for angles greater than approximately 45°. When the element contains the collocation point, a discontinuity is present in the integrand. However, the integrand is very smooth at both sides of the discontinuity. In the case $\alpha = 90°$ for a straight element, the discontinuity disappears and the integrand is zero. When the curved element is considered, the discontinuity becomes a kink point (discontinuous derivative) and the integrand is zero at it.

Figure 4.5 shows $r_{,1}$, $r_{,2}$, $1/r^p$ and some combinations of them for a straight element similar to that of Figure 4.3, and different minimum distances $r_{\min}$ between element and collocation points. It is observed that the behaviour of $r_{,2}$ ($\alpha = 90°$) is similar to $1/r$, except for the sign. The behaviour of $r_{,1}$ ($\alpha = 0°$) is very different from $1/r$ because at $\xi = 0$ it goes to zero, and it has a stronger variation around that zone. A similar behaviour is observed between $r_{,2}/r$ and $1/r^2$, except again for the sign. In the case of $r_{,1}/r$, two sharp peaks are present at both sides of $\xi = 0$, where the function is zero.

Components of the unit normal vector at the observation point: n_k. It is bounded inside $[-1, 1]$, and it is continuous on a given element. For Lagrange elements of order p, it is generally the quotient of a polynomial of order $p - 1$ (line and triangular elements)
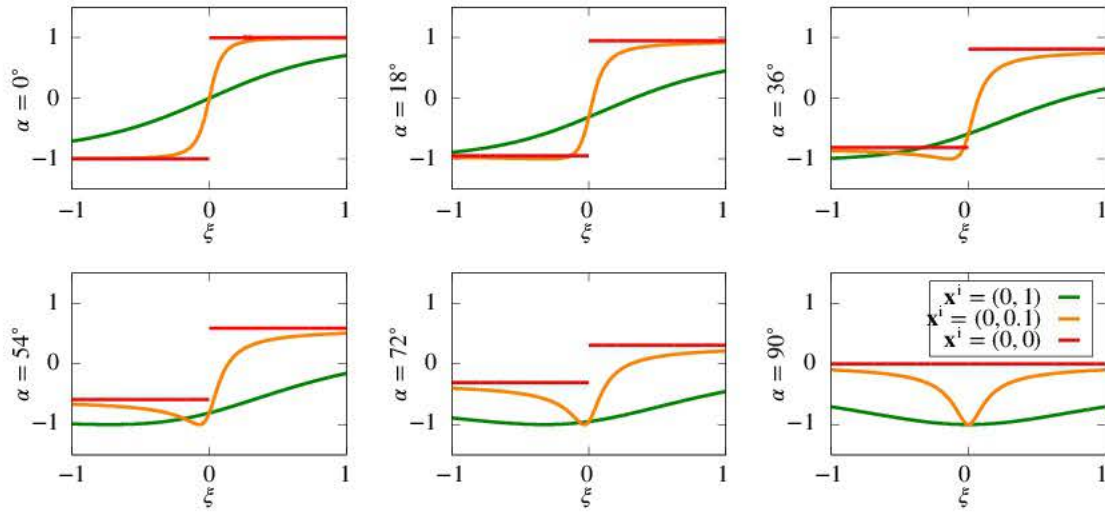
Figure 4.3: Behaviour of $\tilde{\mathbf{r}} \cdot \mathbf{d}$ along a straight element with end-nodes at $(-1, 0)$ and $(1, 0)$.
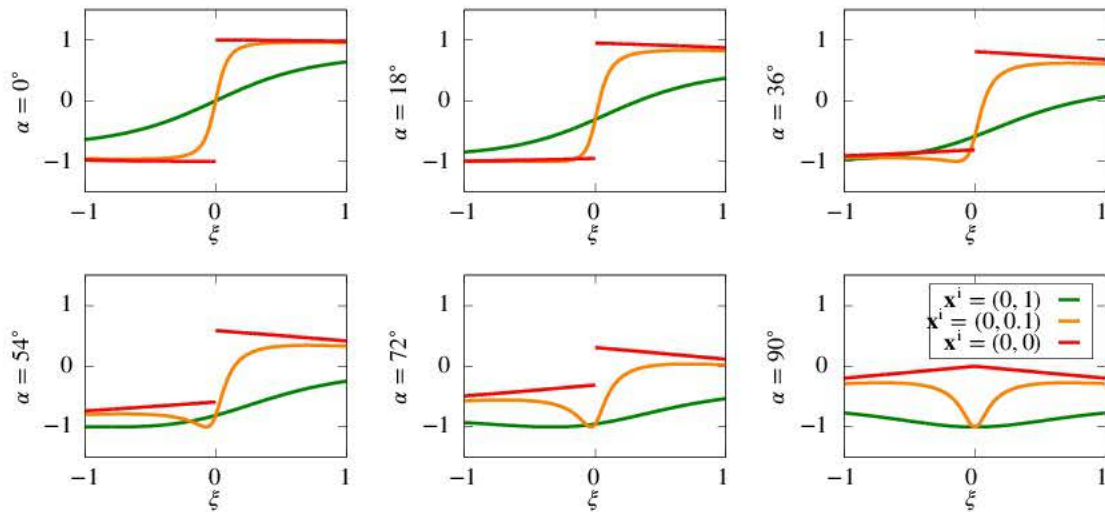
Figure 4.4: Behaviour of $\tilde{\mathbf{r}} \cdot \mathbf{d}$ along a quadratic curved element with mid-node at $(0, 0)$, and end-nodes at $(-1, -0.2)$ and $(1, -0.2)$.
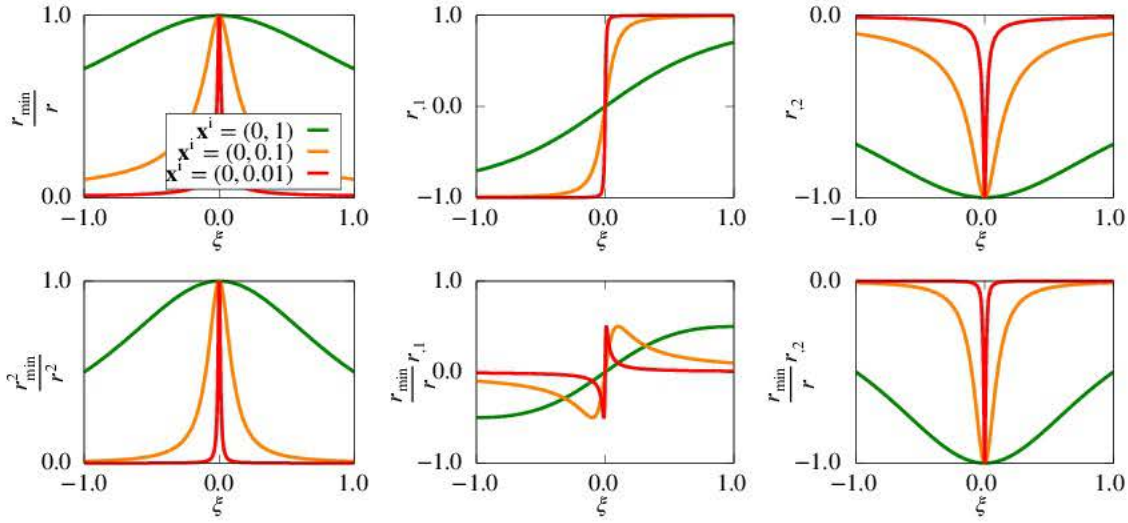
Figure 4.5: Comparison between $r_{,1}$, $r_{,2}$, $1/r^p$ and some combinations of them along a straight element with end-nodes at $(-1,0)$ and $(1,0)$.

or $2p - 1$ (quadrilateral elements) and the square root of a polynomial of order $2(p-1)$ (line and triangular elements) or $2(2p-1)$ (quadrilateral elements). Polynomials are in terms of reference coordinates. Nonetheless, if a line element is straight or a surface element is planar, n_k is simply constant.

Components of the unit normal vector at the collocation point: n_k^i**.** It is merely a constant for a given collocation point.

Distance derivative with respect to n: $\partial r/\partial n$**.** This is a particular case of the first case studied, where the direction **d** is now the unit normal at the observation point **n**:

$$\frac{\partial r}{\partial n} = \tilde{\mathbf{r}} \cdot \mathbf{n} = r_{,j} n_j \tag{4.9}$$

Therefore, it behaves always in a very similar fashion as the case $\alpha = 90°$ shown in Figures 4.3 and 4.4. When the element contains the collocation point, one important property is $\partial r/\partial n = \mathcal{O}(r)$, and thus $\lim_{r \to 0} \partial r/\partial n = 0$.

Distance derivative with respect to n^i: $\partial r/\partial n^i$**.** This is a particular case of the first case studied, where the direction **d** is now the unit normal at the collocation point **n^i**:

$$\frac{\partial r}{\partial n^i} = -\tilde{\mathbf{r}} \cdot \mathbf{n}^i = -r_{,j} n_j^i \tag{4.10}$$

and the negative sign is due to differentiation with respect to the coordinates of the collocation point. It behaves in a similar fashion as the case $\alpha = 90°$ only when the element contains the collocation point, because $\mathbf{n}^i$ is in fact associated with the element. However, for collocation points outside the element, $\mathbf{n}^i$ can have any direction α.

When the element contains the collocation point, one important property to keep in mind is $\partial r/\partial n^i = \mathcal{O}(r)$, and hence $\lim_{r \to 0} \partial r/\partial n^i = 0$.

Scalar product between n and $\mathbf{n}^i$: $\mathbf{n} \cdot \mathbf{n}^i$. Given that $\mathbf{n}$ is continuous within an element, and $\mathbf{n}^i$ is a constant vector, this scalar product is also continuous. When the element contains the collocation point, one important property is $\lim_{r \to 0} \mathbf{n} \cdot \mathbf{n}^i = 1$.

As a summary, for given ω and material properties, F^* can be decomposed as:

$$F^* = F^{(cte)} \cdot \sum_{a=1}^{N_{F^*}} \left\{ \sum_{b=1}^{N_{F_a}} \left[F_{ab}^{(cte)} \cdot F_{ab}^{(rad)}(r) \right] \cdot F_a^{(geo)} \left(\mathbf{x}, \mathbf{n}, \mathbf{x}^i, \mathbf{n}^i \right) \right\} \tag{4.11}$$

where:

$$F_{ab}^{(rad)}(r) = \text{one of} \begin{cases} \text{Singular} \begin{cases} r^{-p}, \, p = 1, 2, \ldots \\ \ln r \end{cases} \\ \text{Regular} \begin{cases} 1 \\ r^p \ln r, \, p = 1, 2 \ldots \\ r^p, \, p = 1, 2 \ldots \\ K_n^R (ikr)/r^n, \, n = 0, 1, 2 \\ E_{n+1}^R (-ikr)/r^n, \, n = 0, 1, 2, \ldots \end{cases} \end{cases} \tag{4.12}$$

$$F_a^{(geo)} \left(\mathbf{x}, \mathbf{n}, \mathbf{x}^i, \mathbf{n}^i \right) = \text{a product of} \left\{ 1, r_{,l}, n_k, n_j^i, \frac{\partial r}{\partial n}, \frac{\partial r}{\partial n^i}, \mathbf{n} \cdot \mathbf{n}^i \right\} \tag{4.13}$$

Each fundamental solution is then a linear combination of products of $F_{ab}^{(rad)}$ and $F_a^{(geo)}$, which are purely geometric. This systematic way of decomposing the fundamental solution is well known [6], and allows to apply a divide and conquer strategy to the evaluation of BEM integrals.

The presence of the collocation point in the integration domain or not leads to the main division of BEM integrals: potentially singular integrals ($\mathbf{x}^i \in X$) and regular integrals ($\mathbf{x}^i \notin X$). In the former case, only singular $F_{ab}^{(rad)}$ may lead to singular integrals, all other combinations lead to regular integrals. In the latter case, although all integrals are regular, their evaluation may be quite difficult when the collocation point is near the element. This is due to the presence of abrupt steps and peaks in the integrand, as illustrated in Figures 4.3, 4.4 and 4.5.

Shape function (Φ)

The shape function Φ commonly comes from a Lagrange basis $\phi (\Xi)$, thus it is often a polynomial function. When dealing with singular integrals, it may be absent, or transformed into one of the following forms appearing after performing the regularisation:

$$\Phi (\Xi) = \phi (\Xi) - \phi (\Xi^i) \tag{4.14}$$

$$\Phi (\Xi) = \phi (\Xi) - \phi (\Xi^i) - \phi_{,k} (\Xi^i) (x_k - x_k^i) \tag{4.15}$$

where Ξ^i is the position of the collocation point in the reference coordinates, and $\phi_{,k} = \partial \phi / \partial x_k$ is the tangential gradient. In the former case, Φ remains as a polynomial since $\phi (\Xi^i)$

is a constant. In the latter case, it also remains as a polynomial since $\phi_{,k}\left(\Xi^i\right)$ and x_k^i are constants and x_k is obtained from a Lagrange interpolation.

In the case of integrals arising in Geometric Sensitivity BEM, Φ consists of the product between a shape function coming from field variable interpolation, and a shape function coming from design velocity interpolation or its gradient. Therefore, high-order polynomials and also rational polynomial functions can also be present.

Jacobian (J)

The Jacobian J represents the relationship between infinitesimal lengths, areas or volumes in the transformation T_g from a reference space Ξ to the real space $\mathbf{x}$ ($T_g : \Xi \to \mathbf{x}$). Elements must be valid, i.e. $\min(J) > 0$, and preferably of good quality, i.e. J approximately constant. The Jacobian of boundary elements comes from the transformation $T_g \colon \mathbb{R}^{n-1} \to \mathbb{R}^n$:

$$n = 2 : \quad d\Gamma = J\,d\xi, \; J = \left|\frac{\partial \mathbf{x}}{\partial \xi}\right| = |\mathbf{T}| \tag{4.16a}$$

$$n = 3 : \quad d\Gamma = J\,d\xi_1 d\xi_2, \; J = \left|\frac{\partial \mathbf{x}}{\partial \xi_1} \times \frac{\partial \mathbf{x}}{\partial \xi_2}\right| = \left|\mathbf{T}_1 \times \mathbf{T}_2\right| = |\mathbf{N}| \tag{4.16b}$$

The Jacobian of a line element embedded in a three-dimensional ambient space ($T_g \colon \mathbb{R} \to \mathbb{R}^3$) follows also Equation (4.16a). The Jacobian of domain elements comes from the transformation $T_g \colon \mathbb{R}^n \to \mathbb{R}^n$:

$$n = 2 : \quad d\Omega = J\,d\xi_1 d\xi_2 \tag{4.17a}$$

$$n = 3 : \quad d\Omega = J\,d\xi_1 d\xi_2 d\xi_3 \tag{4.17b}$$

which is the usual determinant of the Jacobian matrix $J = \det(\mathbf{J})$, where $J_{ij} = \partial x_i / \partial \xi_j$, $i, j = 1, \ldots, n$. For Lagrange boundary elements, J is the square root of a polynomial of order $2(p-1)$ (line elements), $2(2p-2)$ (triangular elements) or $2(2p-1)$ (quadrilateral elements), where p is the order of the geometric interpolation. When a line element is straight (constant direction of the tangent vector) or a surface element is planar (constant direction of the normal vector), it reduces to a polynomial of order $p-1$ (line elements), $2p-2$ (triangular elements) or $2p - 1$ (quadrilateral elements). This polynomial can further reduce its order depending on the location of the higher-order nodes within the line or plane. For Lagrange domain elements, J is a polynomial of order $2p-2$ (triangular elements), $2p-1$ (quadrilateral elements), $3p - 3$ (tetrahedral elements), or $3p - 1$ (hexahedral elements).

4.3 Evaluation of BEM integrals

BEM integrals as those represented by Equation (4.1) can be evaluated analytically only in certain cases, usually for planar and low-order elements, and simple fundamental solutions, see e.g. [140–142]. Integrals associated with free-terms for non-smooth points can also be evaluated analytically for typical fundamental solutions [79, 80]. Nonetheless, most of BEM

integrals are generally evaluated by numerical integration [143]. Before performing the numerical integration, some analytical transformation (change of variables, integration by parts) may be applied in order facilitate the computation. The number of developed techniques for handling BEM integrals is quite large, and brief reviews are given in later sections for the type of integrals managed in this work. In this section, some general aspects regarding numerical integration are described.

When facing the numerical evaluation of an integral, the first question that arises is what method is able to approximate the integral with a given prescribed error and a reasonable computational cost. In this sense, Gaussian quadratures are commonly used due to its efficiency in most cases [143, 144], and the BEM is not an exception [6]. One-dimensional Gaussian quadratures are directly applied to line integrals after possibly performing a linear coordinate transformation to a normalised coordinate, typically in a [0, 1] or [−1, 1] domain. For surface integrals, a Gaussian quadrature product rule can be used for both quadrilateral and triangular elements. For triangular domains, besides the well-known low-order symmetric quadrature rules used in finite elements [145–147], there exists high-order Gaussian quadrature rules [148, 149]. These are more appropriate than product rules since integration points are symmetrically distributed over the triangle, and the number of points is considerably lower. Wandzura [149] obtained rules[1] up to order 30, all with positive weights and interior integration points, unlike older rules of Dunavant [148].

The second question that arises is what quadrature order and/or integration domain subdivision are required. To answer this question one can explore two main possibilities: automatic integrator algorithms with a posteriori local or global error estimators, or adaptive algorithms with a priori error estimators based on a study of the integral. Clearly, the former is expensive since much more integrand evaluations than strictly needed are necessary in order to obtain an integral approximation and an error estimation. It should only be used in general-purpose environments where a wide spectrum of integrals are expected. When the integral class is known beforehand, and it is possible to obtain an error estimator, the latter should be used. This is the case of BEM integrals, where, in addition to that, a large number of them have to be evaluated. A priori error estimators allow a prediction of the required quadrature order, which leads to a reliable and efficient evaluation of the integrals. The more accurate and adaptive the error estimator is, the less quadrature points need to be evaluated. Nonetheless, it does not directly lead to computational savings as it also depends on the ratio between error estimator and quadrature point evaluation costs.

An analytical upper bound of the error of Gauss–Legendre quadratures may be obtained from Stroud and Secrest's book [144]. For one-dimensional integrals, the absolute error E is bounded by:

$$E = \left| \int_{-1}^{1} f(\eta) \, d\eta - \sum_{k=1}^{N} f\left(\eta^{(k)}\right) w^{(k)} \right| \leq eH, \; e \approx \frac{4}{2^{2N}(2N)!}, \; H \geq \left| \frac{d^{2N} f}{d\eta^{2N}} \right| \quad (4.18)$$

---

[1] In the paper [149] only some quadratures are shown. We would like to thank Stephen Wandzura for providing us with several scripts for a symbolic computation program which were used to build all quadrature rules from order 1 to order 30.

where $\eta^{(k)}$ and $w^{(k)}$ are respectively the k-th quadrature point and weight of the quadrature rule with N points. For two-dimensional integrals:

$$E = \left| \int_{-1}^{1} \int_{-1}^{1} f\left(\eta_1, \eta_2\right) \, \mathrm{d}\eta_1 \mathrm{d}\eta_2 - \sum_{k_1=1}^{N_1} \sum_{k_2=1}^{N_2} f\left(\eta_1^{(k_1)}, \eta_2^{(k_2)}\right) w^{(k_1)} w^{(k_2)} \right| \leq 2 \sum_{j=1}^{2} e_j H_j,$$

$$e_j \approx \frac{4}{2^{2N_j} \left(2N_j\right)!}, \quad H_j \geq \left| \frac{\partial^{2N_j} f}{\partial \eta_j^{2N_j}} \right| \quad (4.19)$$

where $\eta^{(k_j)}$, $w^{(k_j)}$, k and N_j correspond to the quadrature rule applied to the j-th dimension. These inequalities are able to show the relationship between error, number of quadrature points and integrand. Despite leading to useful error estimators, these are often very conservative and quite complex since they require high-order derivatives. Furthermore, they usually are obtained as $E = E\,(N, \text{integrand parameters})$ functions rather than as more practical $N = N(E, \text{integrand parameters})$ functions. Within the BEM context, these facts can be observed in many works, see e.g. [150–152]. Therefore, comprehensive numerical experiments with curve fitting can also be used in order to provide these estimators.

From the description of BEM integrals given in Section 4.2, it is concluded that integrands contain linear combinations of products of several rational polynomial and radical functions. That means that a purely analytical approach for the study of numerical integration errors of the whole integral is quite difficult. Fortunately, focusing only in the most problematic terms, particularly those that contain radial functions $F_{ab}^{(\text{rad})}$ of singular nature ($\ln r$, $1/r^p$), is often enough to provide good answers. These terms require to consider two different situations for evaluating the integral: the collocation point is present in the integration domain, and the collocation point is outside the integration domain.

If the element contains the collocation point ($\mathbf{x}^i \in X$), integrals may be singular. In any case, for these integrals it must be guaranteed that no integration point is located at the collocation point. This can be assured by cutting the integration domain at the collocation point when Gaussian quadratures are used. Singular integrals can be classified into weakly singular (integrable in the Riemann sense), strongly singular (integrable in the Cauchy Principal Value), hypersingular (integrable in the Hadamard Finite Part) or supersingular [153]. This classification depends on the singularity order $\mathcal{O}\,(s\,(r))$, where s is a function of the distance r between the collocation point and any element point, and the dimension m of the integration domain. In the context of the BEM, one can find functions $s(r)$ of the type $s = \ln r$ or $s = r^{-n}$. For the case $s = \ln r$, integrals are weakly singular irrespective of the dimension of the integration domain. For the case $s = r^{-n}$, integrals are classified according to Table 4.1. In this work, however, only weakly singular integrals are numerically treated since strongly singular and hypersingular integrals are transformed into regular and weakly singular integrals. As Riemann integrals, weakly singular integrals can be evaluated by any classical numerical integration scheme. Although not strictly needed, additional transformations or specialised quadratures should be used in order to reduce the required number of integration points.

If the element does not contain the collocation point ($\mathbf{x}^i \notin X$), integrals are regular. In principle, plain Gaussian quadratures are able to evaluate these integrals. However, a costly

Condition	Type of integral
$n \leq 0$	regular
$0 < n < m$	weakly singular
$n = m$	strongly singular
$n = m + 1$	hypersingular
$n > m + 1$	supersingular

Table 4.1: Types of integrals of dimension m and $Y \sim \mathcal{O}\left(r^{-n}\right)$ [153–155]

and even prohibitive quadrature order would be needed when the collocation point is near the element, say $0 < \min\left(r\right)/\text{diameter}\left(X\right) \leq 1$, and hence they are generally referred as nearly- or quasi-singular integrals. In order to keep a moderate computational cost, additional treatment is required for this situation. When $\min\left(r\right)/\text{diameter}\left(X\right) > 1$, there still is some quadrature order dependency with respect to r, but no further treatment is needed. Depending on the element order and curvature, shape function and Jacobian may instead determine the quadrature order required for these integrals. The numerical evaluation of quasi-singular integrals by using subdivision with quadrature order selection methods [150, 151] (hp strategy), and cubic polynomial (Telles) or sinh non-linear coordinate transformation methods [156–158] (peak smoothing strategy) have been proposed. Granados and Gallego [159] developed a different technique based on a regularisation in the complex plane. In this work, we use curves like those obtained by Jun et al. [151] but for the Telles' transformation, and then we apply a recursive algorithm based on a uniform refinement at each level when the required order of quadrature is not available.

Radial functions $F_{ab}^{(\text{rad})}$ of regular nature always lead to regular integrals. When considered together with $F_a^{(\text{geo})}$, shape functions and Jacobian, they are of second importance. Their only difficulty is that terms like those of Equations (4.5d) and (4.5e) are oscillatory with wavelengths related to medium properties and frequency. However, given that the maximum size of elements must be chosen according to the element order and wavelengths, i.e. at least six linear or three quadratic elements per wavelength [160], these regular parts can be considered within the element as polynomials of lower order than element order.

4.4 Integral of the Jacobian

In this section, the numerical evaluation of the integral of the Jacobian $J\left(T_g : \varXi \rightarrow \mathbf{x}\right)$ is studied:

$$I_{\text{size}} = \int_X \mathrm{d}X = \int_\varXi J \, \mathrm{d}\varXi \tag{4.20}$$

This elementary integral gives the size (length, area or volume) of an element, and its numerical evaluation does not have any particular difficulty. However, its study is interesting since the Jacobian J is always present in the integrand. The Jacobian may be the leading component of the integrand together with the shape function when the fundamental solution is smooth ($\min\left(r\right)/\text{diameter}\left(X\right) \gg 1$) and the element has some distortion. This can also

be the case in weakly singular and quasi-singular integrals when a transformation or quadrature which completely cancels out the singularity is used. Another cases are those regular integrals arising when the collocation point is in the integration domain.

The aim is obtaining simple formulas for the estimation of the required quadrature order as a function of the desired relative error. Some alternatives to such formula would be obtaining a rigorous error bound [143, 144], or using an iterative numerical integration procedure. Because of their costs, results should be obtained at a pre-processing stage and stored for later usage. The formulas, however, can be inexpensively used inside monolithic integration procedures. We have only been able to obtain a reliable formula for quadratic line elements, which can also be used for higher-order line elements. Nevertheless, the main ideas developed in this case should be useful for obtaining similar formulas for other elements.

The Jacobian is the square root of a polynomial when the element has a lower dimension than the ambient space, which is the case of boundary elements. The Jacobian is a simple polynomial when the dimension of the element and the dimension of the ambient space are equal, and also when, although dimensions are not equal, the element is planar. In the latter case, by the very definition of Gaussian quadratures, the integral can be integrated exactly by a quadrature rule of equal order than the polynomial. In the former case, however, an appropriate quadrature rule achieving the desired error should be chosen. It is intuitive to state that it is related to the deviation of the curved element from the planar configuration.

In order to assess the effect of such deviation, a numerical experiment using a quadratic line element with end-nodes located at $(-l/2, 0)$ and $(l/2, 0)$, and mid-node located at $(0, s_2)$ is considered. A dimensionless measure of the deviation can be defined as $c = s/l$, where l is the distance between end-nodes and $s = s_2$ is the distance between the mid-node and the mid-point between end-nodes. For a set of values of relative error ϵ and deviation c, the required number of integration points (Gauss-Legendre quadrature) for calculating I_{size} has been obtained. Figure 4.6a shows the obtained results together with the following estimation:

$$N(\epsilon, c) = \text{nint} \left[(0.7 - 0.25 \log_{10} \epsilon) - \left(5 + 4 \log_{10} \epsilon \right) c \right] \tag{4.21}$$

which is valid for $c \in [0, 1/2]$ and $\epsilon \in [10^{-15}, 10^{-3}]$. Figure 4.6a shows that a fast change occurs in N between $c = 0$ and $c = 0.1$, especially for the lowest errors. Equation (4.21) provides a conservative estimation in that range and does not converge to the theoretical N at $c = 0$. Therefore, the particular case of a straight element should be handled separately. For a more general configuration with the mid-node located at (s_1, s_2), and defining $s = (s_1^2 + s_2^2)^{1/2}$, Equation (4.21) still provides a very good estimation when $|s_1| \leq l/6$. Figure 4.6b shows a comparison between numerical experiments and Equation (4.21) where the mid-node is located at $(l/6, s_2)$ and $s = ((l/6)^2 + s_2^2)^{1/2}$. The fast change occurs now near $c = 1/6$, and it is more abrupt than before, showing that the curvature produced by mid-nodes located far from the mid-length point is more critical from the integration point of view. For locations of the mid-node nearer to the quarter point, i.e. the well-known point where the element degenerates, the formula considerably underestimates the required N. Thus, we propose the following predictive formula:

(a) Mid-node at $(0, s_2)$ and $c = s_2/l$ (b) Mid-node at $(l/6, s_2)$ and $c = ((l/6)^2 + s_2^2)^{1/2}/l$
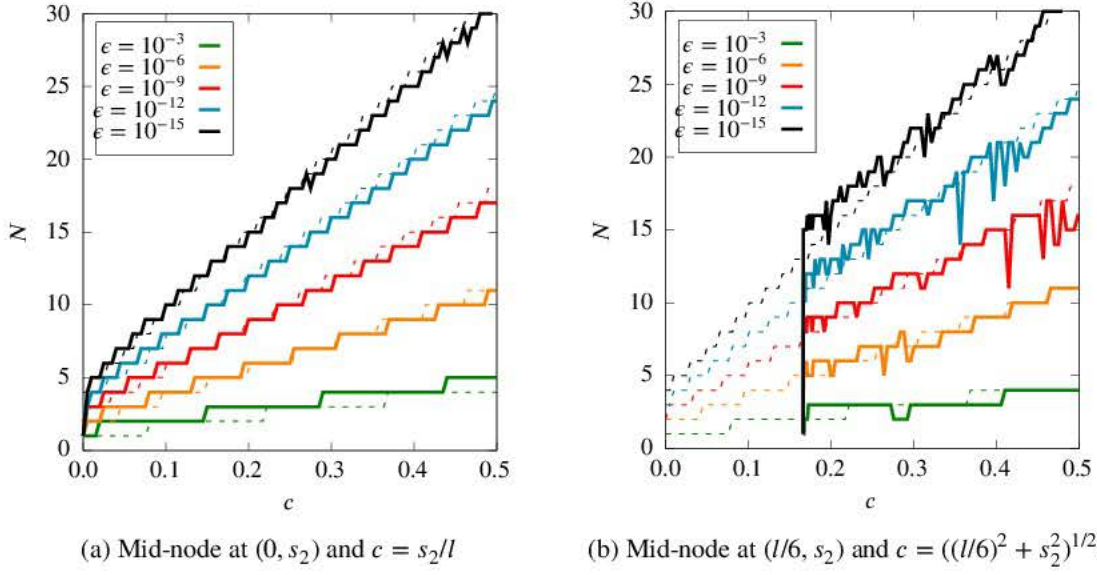
Figure 4.6: Comparison between numerical experiment results (solid lines) and estimation provided by Equation (4.21) (dashed lines)

$$\mathbf{s} = \mathbf{x}^{(3)} - \frac{\mathbf{x}^{(1)} + \mathbf{x}^{(2)}}{2} \qquad \mathbf{l} = \mathbf{x}^{(2)} - \mathbf{x}^{(1)}$$

$$p = \frac{\|\mathbf{l} \times \mathbf{s}\|}{l \, s} \qquad c = \frac{s}{l}$$
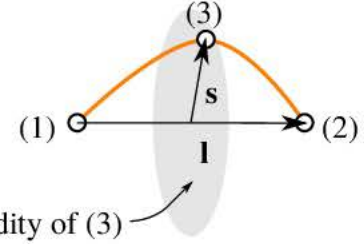
domain of validity of (3)

$$N(\epsilon, p, c) = \begin{cases} 1, & p = 0 \\ \mathrm{int}\left[(0.7 - 0.25 \log_{10} \epsilon) - \left(5 + 4 \log_{10} \epsilon\right) c\right], & p > 0, \ c \le \dfrac{p}{3} + \dfrac{1}{6} \end{cases} \qquad (4.22)$$

where $\mathbf{x}^{(1)}$ and $\mathbf{x}^{(2)}$ are the position vectors of end-nodes, $\mathbf{x}^{(3)}$ the position vector of the mid-node, and it is valid for $\epsilon \in [10^{-15}, 10^{-3}]$.

This formula virtually covers all quadratic line elements that may be encountered in a mesh. It can obviously be used for a subdivision $[\xi^{(1)-S}, \xi^{(2)-S}]$ of an element by using $\mathbf{x}(\xi^{(1)-S})$, $\mathbf{x}(\xi^{(2)-S})$ and $\mathbf{x}((\xi^{(1)-S} + \xi^{(2)-S})/2)$ instead of respectively $\mathbf{x}^{(1)}$, $\mathbf{x}^{(2)}$ and $\mathbf{x}^{(3)}$. By using an appropriate subdivision strategy, the required N for higher-order line elements can also be estimated.

When the curvature radius of an element is approximately constant, s represents the sagitta and l the chord length of an arc. In that situation, the ratio $s/l^2 = c/l$ is approximately constant for any subdivision of the element, and $p \approx 1$. The required N for a subdivision can be estimated in that case as:

$$N(\epsilon, c, \Delta\xi^S) = \mathrm{int}\left[(0.7 - 0.25 \log_{10} \epsilon) - \left(5 + 4 \log_{10} \epsilon\right) \frac{\Delta\xi^S}{2} c\right], \quad c \le \frac{1}{2} \qquad (4.23)$$

where $\Delta\xi^S = \xi^{(2)-S} - \xi^{(1)-S}$, and c are obtained from the parent element, i.e. by using $\mathbf{x}^{(1)}$, $\mathbf{x}^{(2)}$ and $\mathbf{x}^{(3)}$. This assumption avoids obtaining $\mathbf{x}(\xi^{(1)-S})$, $\mathbf{x}(\xi^{(2)-S})$ and $\mathbf{x}((\xi^{(1)-S} + \xi^{(2)-S})/2)$ for each subdivision.

4.5 Weakly singular integrals

Weakly singular integrals are those that despite containing a singularity, the integral can be understood in the Riemann sense, i.e. the integrand is absolutely integrable. As previously stated, any standard numerical integration scheme is able to perform the evaluation as long as the integrand at the collocation point is not evaluated. A coordinate transformation that smooths out the weak singularity is highly recommended in order to reduce the number of integration points. This is done by finding a transformation whose Jacobian is at least null at the weak singularity. An optimal coordinate transformation would be such that the Jacobian completely cancels out the singularity behaviour all over the integration domain. Another option is using specialised quadratures which somehow include the singularity as a weighting function. It is a less flexible but more straightforward approach. Different strategies work better for line integrals (weak singularity $\ln r$), for surface integrals (weak singularities $\ln r$ or $1/r$), and for volume integrals (weak singularities $1/r$ or $1/r^2$).

Coordinate transformations are performed over subdivisions of the original integration domain. Within each subdivision, the weak singularity is located at one of the two extremes of the subdivision (in line integrals) or at a vertex of the subdivision (in surface and volume integrals). By doing so, the integrand is never evaluated at the collocation point. There are mainly three families of coordinate transformations that are used:

One-dimensional non-linear transformations In this family, one can include Telles' cubic polynomial transformation [156, 161], sigmoidal transformation [157] and many others [162]. These transformations are able to produce a null Jacobian at the collocation point, and thus are effective for weakly singular integrals. One of the advantages of these transformations is its versatility, as they can be applied to a wide variety of situations including integrals of any dimension.

Degenerated mapping The idea is using a coordinate mapping with some points at locations where the resulting Jacobian is null at the collocation point. The main idea behind this transformation is similar to that of well-known quarter-point quadratic elements proposed by Barsoum [163], where mid-nodes are moved so that the resulting Jacobian becomes of order $\sqrt{r}$. In the present case, however, the degeneration is produced by locating two or more vertices (corner nodes) at the same position. Duffy [164] probably was the first using such an idea for evaluating weakly singular volume integrals over pyramids or cubes in a purely mathematical context. Li et al. [165] proposed a similar technique for surface and volume integrals arising in the BEM, which is known as triangle/tetrahedron polar coordinates. It consists in mapping a quadrilateral/hexahedron into a degenerated quadrilateral/hexahedron with two/four of the vertices located at the collocation point, in such a way that it resembles a triangle/tetrahedron. The resulting Jacobian is null at the collocation point, and varies linearly/quadratically along

rays from the collocation point, and hence smoothing out the weak singularity in surface/volume integrals. The main advantages of this transformation are its simplicity and effectiveness.

Polar/spherical coordinate transformations This family of transformations uses a polar/-spherical coordinate transformation centred at the collocation point for managing surface/volume weakly singular integrals. The basic polar/spherical transformation produces a null Jacobian at the collocation point, which is besides linear/quadratic with respect to the radial coordinate in the reference space. It is the most natural approach as it incorporates the polar/spherical nature of fundamental solutions. However, the transformation from these coordinates to normalised coordinates, where Gaussian quadratures are applied, introduces new difficulties as the Jacobian has a quasi-singularity when the collocation point is near edges/faces. Fortunately, there exists a transformation proposed by Khayat et al. [138] which completely cancels out it for surface integrals.

Coordinate transformations are probably the most flexible and powerful way of evaluating these integrals. As it will be seen later, in order to produce such integrands more than one are usually required.

There are many specialised quadratures for managing weakly singular integrals. These methods provide algorithms for the calculation of quadrature points and weights and/or directly give tables of quadrature rules for some assumed weighting function. Anderson [166] contributed with tables of quadrature rules for evaluating integrals of the type $-\int_0^1 \ln(x) f(x) \, dx$, which is the most common type of one-dimensional weakly singular integral encountered in BEM. Crow [167] proposed a quadrature scheme for the more general integrals of the type $\int_0^1 [a + b \ln(x)] f(x) \, dx$, where a and b are polynomials. Following the same idea, Smith [168] obtained ad hoc quadratures for logarithmic singularities within isoparametric elements. For two-dimensional weakly singular integrals with $1/r$ kernels, Cristescu and Laubignac [169] offered a direct Gaussian scheme for integrating over triangular and quadrilateral domains. Schwab and Wendland [170] presented a comprehensive paper where they proposed and discussed several methods for the evaluation of weakly singular as well as strongly and hypersingular integrals, including error estimation.

4.5.1 Line integrals

Weakly singular line integrals of logarithmic type are generally encountered in the SBIE as well as in the HBIE for two-dimensional problems. Taking into account Equation (4.11), this type of integrals appear as:

$$I_{ab} = \int_{-1}^{1} F^{(\text{cte})} F_{ab}^{(\text{cte})} \ln(r) F_a^{(\text{geo})} \Phi J \, d\xi \tag{4.24}$$

where a reference space $\xi \in [-1, 1]$ is assumed. Since $F_a^{(\text{geo})}$ and Φ may appear in a number of different forms, it is useful to segregate the evaluation of the weakly singular integral as:

$$I_{ab} = F^{(\text{cte})} F_{ab}^{(\text{cte})} \left[\int_{-1}^{1} \ln(r) \left[F_a^{(\text{geo})} \Phi - \left(F_a^{(\text{geo})} \Phi \right)^{\text{i}} \right] J \, d\xi + \left(F_a^{(\text{geo})} \Phi \right)^{\text{i}} \int_{-1}^{1} \ln(r) J \, d\xi \right]$$

(4.25)

where $\left(F_a^{(\text{geo})} \Phi \right)^{\text{i}} = \lim_{r \to 0} \left(F_a^{(\text{geo})} \Phi \right)$. Now, the first integral is regular, and the weak singularity is concentrated in the second one. In order to evaluate the weakly singular integral, the original integration domain is cut at the collocation point:

$$I_{\ln r} = \int_{-1}^{\xi^{\text{i}}} \ln(r) J \, d\xi + \int_{\xi^{\text{i}}}^{1} \ln(r) J \, d\xi = \sum_{d=1}^{2} \int_{0}^{1} \ln(r) J J_{Sd} \, d\xi' = I_{\ln r - \text{S1}} + I_{\ln r - \text{S2}} \quad (4.26)$$

where $J_{Sd} = d\xi/d\xi'$, and ξ' is the reference coordinate $\xi' \in [0, 1]$ of each subdivision: for $d = 1$ the transformation is $\xi = -1 + (1 + \xi^{\text{i}})\xi'$, and for $d = 2$ the transformation is $\xi = \xi^{\text{i}} + (1 - \xi^{\text{i}})\xi'$. In this form, the weak singularity is always located at an extreme of each integration domain.

The direct integration of these weakly singular integrals using Gauss–Legendre quadratures is very inefficient since the convergence is very slow. The two main ways of appropriately dealing with it are using a non-linear transformation [156–158] which smooth out the singularity, or using specialised Gaussian quadratures [166–168] which include a logarithmic weighting function. Despite all these methods are powerful, they have their own advantages and disadvantages in terms of analytical effort, efficiency and availability. Non-linear transformations do not require to modify the integrand, and since simple Gauss–Legendre quadrature are used, high-order quadrature rules are available. Gauss–Anderson quadrature [166] need an expansion of r in terms of the quadrature reference coordinate in order to isolate and remove the weighting function from the integrand [171]. High-order Gauss–Anderson quadrature rules are available from several sources [6, 144, 172, 173]. Gauss–Crow quadrature [167] does not require isolating the weighting function, but unfortunately only quadrature rules of low-order (up to 7 points quadrature) are available since obtaining them is problematic. The quadrature proposed by Smith [168] gives a further step by establishing single quadrature rules for several positions of the collocation point for quadratic elements. It inherits the difficulty of obtaining high-order quadrature rules, but it is the most efficient as it is able to evaluate a set of integrals with the position of the collocation point at different locations with the same quadrature rule. All these specialised quadratures deal with the logarithmic singularity in an optimal way while non-linear transformations do it in a approximate way.

In order to illustrate the efficiency of some of the methods described above, the required number of integration points N for evaluating $I_{\ln r - \text{S1}}$ with a prescribed relative error $\epsilon = |I_{\ln r - \text{S1}}^{\text{num}} / I_{\ln r - \text{S1}}^{\text{ref}} - 1|$ is calculated. The reference value of each integral $I_{\ln r - \text{S1}}^{\text{ref}}$ is obtained using a Gauss–Anderson quadrature of 32 points. Three different integration domains defined by a quadratic element are considered: a straight element, a curved element along a quarter
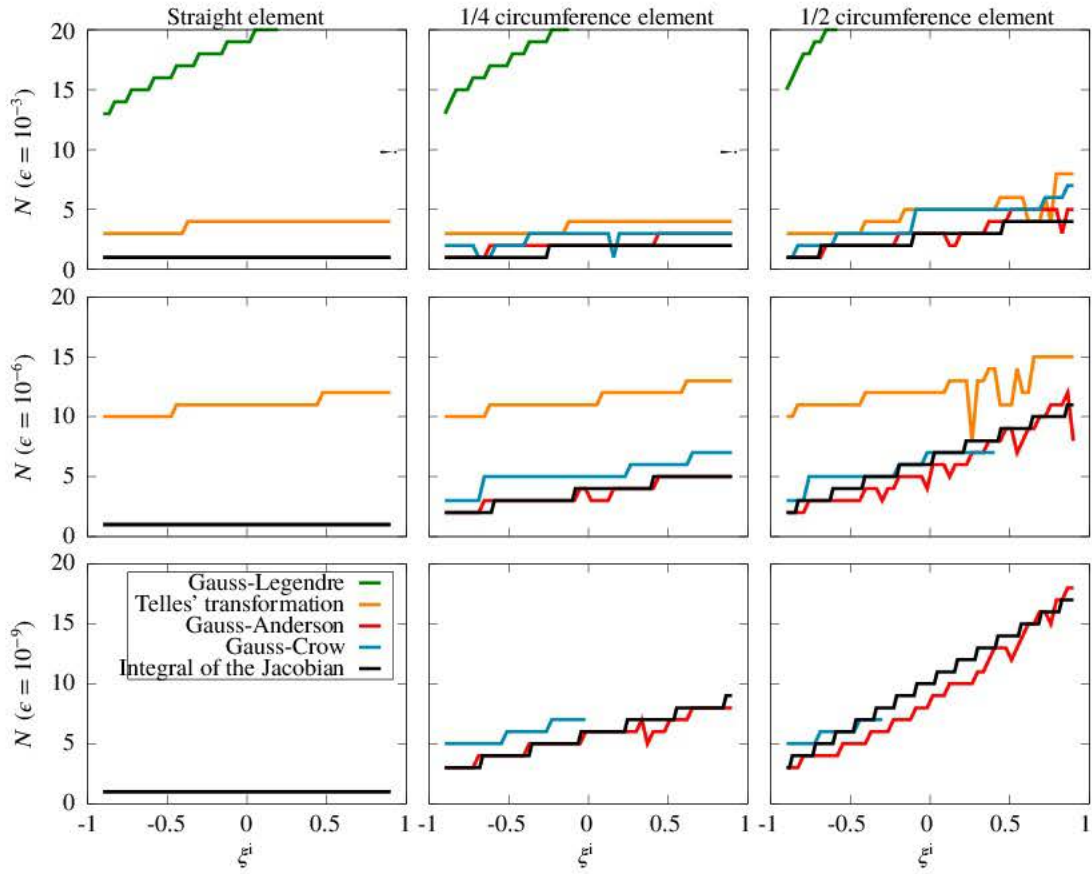
Figure 4.7: Number of integration points N required for integrating $I_{\ln r - S1}$ with a prescribed relative error ϵ

of a circumference, and a curved element along a half of a circumference. The location of the collocation point in the reference space ξ^i varies from -1 to 1. Figure 4.7 depicts the results for several relative errors $\epsilon = \{10^{-3}, 10^{-6}, 10^{-9}\}$. It shows the inefficacy of Gauss-Legendre quadratures for dealing with this type of integral. Telles' transformation is effective in reducing the number of integration points, but only when moderate errors are demanded. The two specialised quadratures Gauss–Anderson and Gauss–Crow are the best methods for obtaining accurate evaluations, being Gauss–Anderson slightly better. However, in the latter case it must be noticed that the number of function evaluations are greater since $I_{\ln r - S1}$ is further split into a weakly singular part evaluated using the Gauss–Anderson quadrature, and a regular part evaluated using a Gauss-Legendre quadrature. Gauss–Crow quadrature does not need this splitting process, but the available quadrature is limited up to a 7 integration points rule. The complete cancellation of the weak singularity provided by the Gauss–Anderson quadrature is confirmed by observing that N is similar to that obtained by Equation (4.23), which is the N required by the integral of the Jacobian. In this work, the Gauss–Anderson quadrature is used due to its robustness, efficiency and the availability of high-order rules.

4.5.2 Surface integrals

Weakly singular surface integrals contain singularities of order $1/r$, and they appear in two-dimensional problems (in body load elements) and three-dimensional problems (in boundary elements and surface loads). Unlike weakly singular line integrals, they appear in a number of different forms. For example, up to five different integrals appear in the three-dimensional potential problem:

$$I_1 = \int_\Xi \frac{1}{r} \phi J \, \mathrm{d}\xi_1 \mathrm{d}\xi_2 \tag{4.27a}$$

$$I_2 = \int_\Xi \frac{1}{r^2} \frac{\partial r}{\partial n} \phi J \, \mathrm{d}\xi_1 \mathrm{d}\xi_2 \tag{4.27b}$$

$$I_3 = \int_\Xi \frac{1}{r^2} \frac{\partial r}{\partial n^i} \phi J \, \mathrm{d}\xi_1 \mathrm{d}\xi_2 \tag{4.27c}$$

$$I_4 = \int_\Xi \frac{1}{r^3} \frac{\partial r}{\partial n} \frac{\partial r}{\partial n^i} \phi J \, \mathrm{d}\xi_1 \mathrm{d}\xi_2 \tag{4.27d}$$

$$I_5 = \int_\Xi \frac{\mathbf{n} \cdot \mathbf{n}^i}{r^3} \left(\phi - \phi^i - \phi^i_{,j} r_j \right) J \, \mathrm{d}\xi_1 \mathrm{d}\xi_2 \tag{4.27e}$$

where integrals I_2, I_3 and I_4 become null for a planar element since $\partial r/\partial n = 0$ and $\partial r/\partial n^i = 0$. In the elastic and poroelastic cases, a much greater number of different weakly singular integrals appear, where numerators contain several factors of the type n_k, n^i_k, $r_{,k}$ $\partial r/\partial n$ and $\partial r/\partial n^i$.

As in the case of weakly singular line integrals, Gauss-Legendre quadratures or other numerical integration schemes for regular integrals may be used to evaluate these integrals, but they are extremely inefficient. One-dimensional non-linear transformations, for example Telles' transformation [156, 161], can be used for each direction, which improves the performance. However, there are much better ways of dealing with them. The two main families of efficient methods are the degenerated mapping [165] (also known as triangle polar coordinates) and the polar coordinates. In their basic form, both methods perform similarly. However, polar coordinates can easily be improved after some transformations, leading to a very robust integration technique.

4.5.2.1 Degenerated mapping

The degenerated mapping for surface integrals is a straightforward technique, but repeated here using a different convention from the original paper [165] for the sake of completeness and later comparison. It requires a preliminary stage where, depending on the location of the collocation point, the element is subdivided into a number of triangular regions in the reference space ξ. Each triangular subdivision is mapped as a degenerated bilinear quadrilateral element where nodes 3 and 4 of the quadrilateral are located at the collocation point, i.e. $\xi^{(3)-Sd} = \xi^{(4)-Sd} = \xi^i$, and nodes 1 and 2 are located at the boundary of the element, see Figure 4.8. The minimal and usual subdivision pattern takes up to three subdivisions for
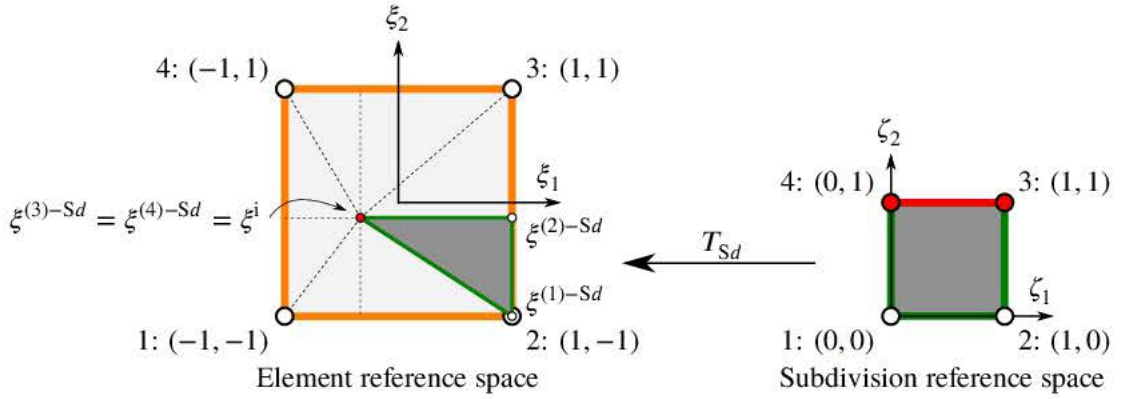
Figure 4.8: Degenerated mapping technique

triangular elements and four subdivisions for quadrilateral elements. From the adaptability point of view, it will be demonstrated later that a better subdivision pattern is obtained when each triangular subdivision is further subdivided into two right-angle triangular regions, see Figures 4.9 and 4.10. The contribution of each subdivision d is obtained by using two transformations:

1. Transformation from the element reference space to the real space $T_g : \xi \to \mathbf{x}$:

$$\mathbf{x} = \sum_{k=1}^{N_n} \phi^{(k)}(\xi) \cdot \mathbf{x}^{(k)} \tag{4.28}$$

where ϕ are the geometric interpolation shape functions, and the Jacobian J is that of Equation (4.17a) for a two-dimensional ambient space or Equation (4.16b) for a three-dimensional ambient space.

2. Transformation from the subdivision reference space to the element reference space $T_{Sd} : \zeta \to \xi$:

$$\xi = \zeta_2 \xi^i + \left(1 - \zeta_2\right) \left[\left(1 - \zeta_1\right) \xi^{(1)-Sd} + \zeta_1 \xi^{(2)-Sd}\right] \tag{4.29}$$

where the Jacobian $J_{Sd} = \left|\partial(\xi_1, \xi_2)/\partial(\zeta_1, \zeta_2)\right|$ is:

$$J_{Sd} = \left(\xi_1^{(1)-Sd} - \xi_1^{(2)-Sd}\right)\left(\xi_2 - \xi_2^i\right) - \left(\xi_2^{(1)-Sd} - \xi_2^{(2)-Sd}\right)\left(\xi_1 - \xi_1^i\right) \tag{4.30}$$

The Jacobian is a plane in the element reference space, and is null at the collocation point. A Gauss–Legendre product rule of $N_1 \times N_2$ points is used in the region $\eta \in [0, 1] \times [0, 1]$.

Therefore, for a weakly singular integrand f, the integral is evaluated as:

$$I = \int_X f \, \mathrm{d}X = \sum_{d=1}^{N_S} \sum_{k_1=1}^{N_1} \sum_{k_2=1}^{N_2} f\left(\zeta_1^{(k_1)}, \zeta_2^{(k_2)}\right) \cdot J \cdot J_{Sd} \cdot w^{(k_1)} \cdot w^{(k_2)} \tag{4.31}$$

Collocation point				Subdivision d					
at element	ξ_1^i	ξ_2^i	N_S	1	2	3	4	5	6
Vertex 1	1	0	2	T3	T4				
Vertex 2	0	1	2	T5	T6				
Vertex 3	1	0	2	T1	T2				
Edge 1-2	$(0,1)$	$1-\xi_1^i$	4	T3	T4	T5	T6		
Edge 2-3	0	$(0,1)$	4	T5	T6	T1	T2		
Edge 3-1	$(0,1)$	0	4	T1	T2	T3	T4		
Interior	$(0,1)$	$(0,1-\xi_1^i)$	6	T1	T2	T3	T4	T5	T6

(a) Subdivisions (triangular regions) to be integrated

	$\xi_1^{(1)-Sd}$	$\xi_2^{(1)-Sd}$	$\xi_1^{(2)-Sd}$	$\xi_2^{(2)-Sd}$
T1	1	0	$\frac{1+\xi_1^i-\xi_2^i}{2}$	$\frac{1-\xi_1^i+\xi_2^i}{2}$
T2	$\frac{1+\xi_1^i-\xi_2^i}{2}$	$\frac{1-\xi_1^i+\xi_2^i}{2}$	0	1
T3	0	1	0	$\frac{\xi_1^i}{2}+\xi_2^i$
T4	0	$\frac{\xi_1^i}{2}+\xi_2^i$	0	0
T5	0	0	$\xi_1^i+\frac{\xi_2^i}{2}$	0
T6	$\xi_1^i+\frac{\xi_2^i}{2}$	0	1	0

(b) Vertices of triangular regions except ξ^i
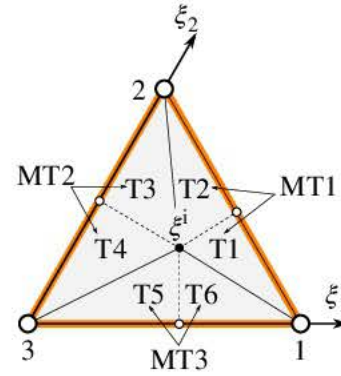
(c) Subdivision pattern of the element

Figure 4.9: Subdivision pattern of triangular elements. The minimal subdivision pattern is obtained as $\mathrm{MT}_j = \mathrm{T}_{2j-1} \cup \mathrm{T}_{2j}$, $j = 1, 2, 3$.

4.5.2.2 Basic polar transformation

The transformation to polar coordinates is the most natural approach since it incorporates the symmetric nature of fundamental solutions. It is more involved than the degenerated mapping technique, but it is considerably more powerful, as it will be seen in the following.

As in the previous methodology, a subdivision pattern of the element into triangular regions is required, see Figures 4.9 and 4.10. It can be formulated in several ways, typically directly in the element reference space ξ, i.e. $(\xi_1, \xi_2) = (\xi_1^i, \xi_2^i) + \rho \cdot (\cos\theta, \sin\theta)$. In that case, it is necessary to handle a piece-wise definition of the (ρ, θ) domain, with different equations between edges of triangular and quadrilateral elements. A more systematic approach can be achieved by rotating and scaling each triangular region such that the opposite side of the collocation point is horizontal and normalised, and the collocation point has positive vertical coordinate. After this simple linear transformation, the remaining transformations for each subdivision are similar, and thus eases later developments. Figure 4.11 shows the complete transformation. The contribution of each subdivision d is obtained after five transformations:

1. Transformation from the element reference space to the real space $T_g : \xi \to \mathbf{x}$, which

Collocation point				Subdivision d							
at element	ξ_1^i	ξ_2^i	N_S	1	2	3	4	5	6	7	8
Vertex 1	-1	-1	2	T4	T5						
Vertex 2	1	-1	2	T6	T7						
Vertex 3	1	1	2	T8	T1						
Vertex 4	-1	1	2	T2	T3						
Edge 1-2	$(-1,1)$	-1	4	T4	T5	T6	T7				
Edge 2-3	1	$(-1,1)$	4	T6	T7	T8	T1				
Edge 3-4	$(-1,1)$	1	4	T8	T1	T2	T3				
Edge 4-1	-1	$(-1,1)$	4	T2	T3	T4	T5				
Interior	$(-1,1)$	$(-1,1)$	8	T1	T2	T3	T4	T5	T6	T7	T8

(a) Subdivisions (triangular regions) to be integrated

	$\xi_1^{(1)-Sd}$	$\xi_2^{(1)-Sd}$	$\xi_1^{(2)-Sd}$	$\xi_2^{(2)-Sd}$
T1	-1	-1	ξ_1^i	-1
T2	ξ_1^i	-1	1	-1
T3	1	-1	1	ξ_2^i
T4	1	ξ_2^i	1	1
T5	1	1	ξ_1^i	1
T6	ξ_1^i	1	-1	1
T7	-1	1	-1	ξ_2^i
T8	-1	ξ_2^i	-1	-1

(b) Vertices of triangular regions except ξ^i

(c) Subdivision pattern of the element

Figure 4.10: Subdivision pattern of quadrilateral elements. The minimal subdivision pattern is obtained as $MT_j = T_{2j-1} \cup T_{2j}$, $j = 1, 2, 3, 4$.

is similar to the previous case.

2. Transformation from subdivision reference space to element reference space $T_{Sd} : \zeta \to \xi$:

$$\xi = \xi^i + \mathbf{S}^{Sd} \zeta \tag{4.32a}$$

$$\mathbf{S}^{Sd} = \begin{pmatrix} \xi_1^{(1)-Sd} - \xi_1^i & \xi_1^{(2)-Sd} - \xi_1^i \\ \xi_2^{(1)-Sd} - \xi_2^i & \xi_2^{(2)-Sd} - \xi_2^i \end{pmatrix} \tag{4.32b}$$

$$J_{Sd} = (\xi_1^{(1)-Sd} - \xi_1^i)(\xi_2^{(2)-Sd} - \xi_2^i) - (\xi_1^{(2)-Sd} - \xi_1^i)(\xi_2^{(1)-Sd} - \xi_2^i) \tag{4.32c}$$

3. Transformation from the subdivision space to subdivision reference space $T_{Cd} : \eta \to \zeta$:

$$\zeta = \mathbf{C}^{Sd} \left(\eta - \eta^i \right) \tag{4.33a}$$

$$\mathbf{C}^{Sd} = \begin{pmatrix} -1 & (\eta_1^{i-Sd} - 1)/\eta_2^{i-Sd} \\ 1 & -\eta_1^{i-Sd}/\eta_2^{i-Sd} \end{pmatrix} \tag{4.33b}$$
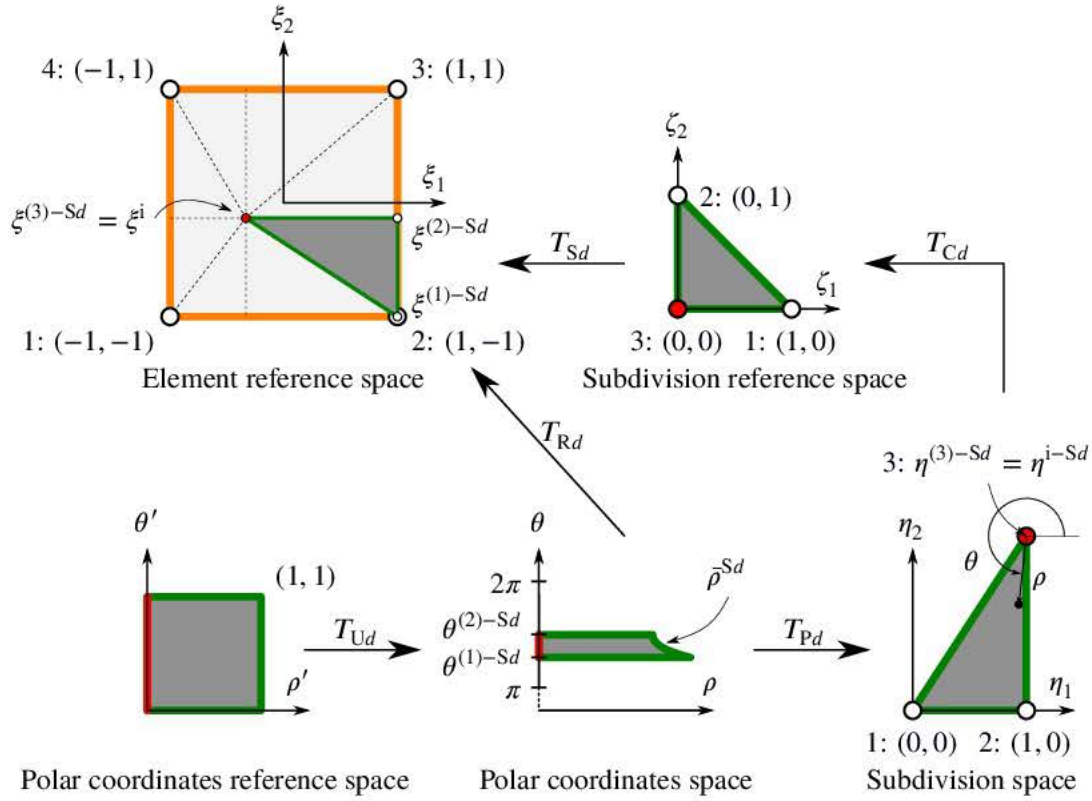
Figure 4.11: Basic polar transformation

where the Jacobian $J_{Cd} = \left| \partial(\zeta_1, \zeta_2)/\partial(\eta, \eta) \right|$ is simply:

$$J_{Cd} = 1/\eta_2^{\mathrm{i}-Sd} \tag{4.34}$$

The location of the collocation point in η space, i.e. $\eta^{\mathrm{i}-Sd}$, is such that the resulting triangle is similar to that in the element reference space. This leads to:

$$\eta_1^{\mathrm{i}-Sd} = \frac{\left(\xi^{\mathrm{i}} - \xi^{(1)-Sd} \right) \cdot \left(\xi^{(2)-Sd} - \xi^{(1)-Sd} \right)}{\left\| \xi^{(2)-Sd} - \xi^{(1)-Sd} \right\|^2} \tag{4.35a}$$

$$\eta_2^{\mathrm{i}-Sd} = \frac{\left(\xi^{(1)-Sd} - \xi^{\mathrm{i}} \right) \times \left(\xi^{(2)-Sd} - \xi^{\mathrm{i}} \right)}{\left\| \xi^{(2)-Sd} - \xi^{(1)-Sd} \right\|^2} \tag{4.35b}$$

4. Transformation from polar coordinates to subdivision coordinates $T_{Pd} : (\rho, \theta) \to \eta$:

$$\eta = \eta^{\mathrm{i}} + \left\{ \begin{array}{c} \rho \cos \theta \\ \rho \sin \theta \end{array} \right\} \tag{4.36}$$

where the Jacobian $J_{Pd} = \left| \partial(\eta_1, \eta_2)/\partial(\rho, \theta) \right|$ is:

$$J_{Pd} = \rho \tag{4.37}$$

The Jacobian is proportional to the radial coordinate ρ in the reference space, and thus cancels out the weak singularity very well. The domain of polar coordinates is $(\rho, \theta) \in \left[0, \bar{\rho}^{Sd}\right] \times \left[\theta^{(1)-Sd}, \theta^{(2)-Sd}\right]$, where:

$$\bar{\rho}^{Sd} = -\frac{\eta_2^{i-Sd}}{\sin\theta} \tag{4.38a}$$

$$\theta^{(1)-Sd} = \pi + \arccos \frac{\eta_1^{i-Sd}}{\sqrt{\left(\eta_1^{i-Sd}\right)^2 + \left(\eta_2^{i-Sd}\right)^2}} \tag{4.38b}$$

$$\theta^{(2)-Sd} = 2\pi - \arccos \frac{1 - \eta_1^{i-Sd}}{\sqrt{\left(1 - \eta_1^{i-Sd}\right)^2 + \left(\eta_2^{i-Sd}\right)^2}} \tag{4.38c}$$

5. Transformation from polar coordinates reference space to polar coordinates space T_{Ud} : $(\rho', \theta') \rightarrow (\rho, \theta)$:

$$\left\{\begin{array}{c} \rho \\ \theta \end{array}\right\} = \left\{\begin{array}{c} 0 \\ \theta^{(1)-Sd} \end{array}\right\} + \left(\begin{array}{cc} \bar{\rho}^{Sd} & 0 \\ 0 & \theta^{(2)-Sd} - \theta^{(1)-Sd} \end{array}\right) \left\{\begin{array}{c} \rho' \\ \theta' \end{array}\right\} \tag{4.39}$$

where the Jacobian $J_{Ud} = |\partial(\rho, \theta)/\partial(\rho', \theta')|$ is:

$$J_{Ud} = \bar{\rho}^{Sd} \left(\theta^{(2)-Sd} - \theta^{(1)-Sd}\right) = -\frac{\eta_2^{i-Sd}}{\sin\theta} \left(\theta^{(2)-Sd} - \theta^{(1)-Sd}\right) \tag{4.40}$$

A Gauss–Legendre product rule of $N_\rho \times N_\theta$ points is used in the region $(\rho', \theta') \in [0, 1] \times [0, 1]$. The normalisation of ρ introduces a peak-like Jacobian with respect to θ due to the term $1/\sin\theta$. It becomes problematic when the triangular region is flat, i.e. when $\eta_2^{i-Sd} \ll 1$ and thus $\theta^{(1)-Sd} \approx \pi$ and/or $\theta^{(2)-Sd} \approx 2\pi$. Quasi-singularities occur at those extremes. If $\theta \rightarrow \theta^{(1)-Sd} \approx \pi$, then $1/\sin\theta \approx 1/(\pi - \theta)$. If $\theta \rightarrow \theta^{(2)-Sd} \approx 2\pi$, then $1/\sin\theta \approx 1/(\theta - 2\pi)$. Therefore, they are strong quasi-singularities with respect to the angular coordinate.

Since transformations T_{Sd} and T_{Cd} are linear, it is possible to directly combine both transformations into T_{Pd}, and build a straightforward transformation T_{Rd} : $(\rho, \theta) \rightarrow \xi$:

$$\xi = \xi^i + \mathbf{R}^{Sd} \left\{\begin{array}{c} \rho\cos\theta \\ \rho\sin\theta \end{array}\right\} \tag{4.41a}$$

$$\mathbf{R}^{Sd} = \left(\begin{array}{cc} \xi_1^{(2)} - \xi_1^{(1)} & -\left(\xi_2^{(2)} - \xi_2^{(1)}\right) \\ \xi_2^{(2)} - \xi_2^{(1)} & \xi_1^{(2)} - \xi_1^{(1)} \end{array}\right) \tag{4.41b}$$

$$J_{Rd} = \rho \left\|\xi^{(2)-Sd} - \xi^{(1)-Sd}\right\| \tag{4.41c}$$

which reduces the complete transformation to three transformations. Therefore, for a weakly singular integrand f, the integral is evaluated as:

$$I = \int_X f \, \mathrm{d}X = \sum_{d=1}^{N_S} \sum_{k_\rho=1}^{N_\rho} \sum_{k_\theta=1}^{N_\theta} f\left(\rho'^{(k_\rho)}, \theta'^{(k_\theta)}\right) \cdot J \cdot J_{\mathrm{R}d} \cdot J_{\mathrm{U}d} \cdot w^{(k_\rho)} \cdot w^{(k_\theta)} \tag{4.42}$$

In this basic form, the polar transformation is not better than the degenerated mapping technique, as it will be seen in Section 4.5.2.5.

4.5.2.3 Polar transformation without the main angular strong quasi-singularity

The Jacobian $J_{\mathrm{U}d}$ from Equation (4.40) induces a quasi-singularity in the basic polar transformation when the collocation point is near an edge. There are many ways to mitigate it. Partheymüler et al. [174] proposed a self-adaptive hp strategy for the angular coordinate. Other authors use some non-linear coordinate transformation, e.g. Hayami [175] used a proposed angular transformation and Rong et al. [139] used a sigmoidal transformation. Khayat et al. [138] proposed a transformation of the type $\ln \tan f(\theta)$ that produces Jacobians of the type $\sin \theta$, $\cos \theta$ or $(\sin \theta + \cos \theta)$. It seems that their work is unknown within the BEM community, except Rong et al. [139] who did not use it because "(...) our numerical experience indicates a better overall performance by using sigmoidal transformation (...)". However, it seems unreasonable to us since there is no better way to deal with that term than cancelling it analytically. Therefore, Khayat's type of transformation is used in this work.

Based on the basic framework shown in Figure 4.11, it is necessary to deal only with one kind of $J_{\mathrm{U}d}$ due to the use of transformations $T_{\mathrm{S}d}$ and $T_{\mathrm{C}d}$. Otherwise, one would have to find several $\ln \tan f(\theta)$ transformations, which are different for each edge of triangular and quadrilateral elements. For the complete cancellation of the quasi-singularity, the last transformation of the basic polar transformation should be replaced by the following two transformations:

5. Transformation from altered polar coordinates to polar coordinates $T_{\mathrm{A}d} : (\rho, \tilde{\theta}) \rightarrow (\rho, \theta)$:

$$\theta = \pi + 2 \arctan \exp \frac{\tilde{\theta}}{\eta_2^{\mathrm{i}-\mathrm{S}d}}, \quad \tilde{\theta} = \eta_2^{\mathrm{i}-\mathrm{S}d} \ln \tan \frac{\theta - \pi}{2} \tag{4.43}$$

where the Jacobian $J_{\mathrm{A}d} = \partial \theta / \partial \tilde{\theta}$ is:

$$J_{\mathrm{A}d} = -\frac{\sin \theta}{\eta_2^{\mathrm{i}-\mathrm{S}d}} \tag{4.44}$$

and the domain $\tilde{\theta} \in \left[\tilde{\theta}^{(1)-\mathrm{S}d}, \tilde{\theta}^{(2)-\mathrm{S}d}\right]$ is:

$$\tilde{\theta}^{(1)-\mathrm{S}d} = \eta_2^{\mathrm{i}-\mathrm{S}d} \ln \tan \frac{\theta^{(1)-\mathrm{S}d} - \pi}{2} \tag{4.45a}$$

$$\tilde{\theta}^{(2)-\mathrm{S}d} = \eta_2^{\mathrm{i}-\mathrm{S}d} \ln \tan \frac{\theta^{(2)-\mathrm{S}d} - \pi}{2} \tag{4.45b}$$

6. Transformation normalised polar coordinates to the altered polar coordinates $T_{\mathrm{UA}d}$: $(\rho', \theta') \rightarrow (\rho, \tilde{\theta})$:

$$
\left\{ \begin{array}{c} \rho \\ \tilde{\theta} \end{array} \right\} = \left\{ \begin{array}{c} 0 \\ \tilde{\theta}^{(1)-Sd} \end{array} \right\} + \left(\begin{array}{cc} \bar{\rho}^{Sd} & 0 \\ 0 & \tilde{\theta}^{(2)-Sd} - \tilde{\theta}^{(1)-Sd} \end{array} \right) \left\{ \begin{array}{c} \rho' \\ \theta' \end{array} \right\}
\tag{4.46}
$$

where the Jacobian $J_{\mathrm{UA}d} = \left| \partial(\rho, \tilde{\theta}) / \partial(\rho', \theta') \right|$ is:

$$
J_{\mathrm{UA}d} = \bar{\rho}^{Sd} \left(\tilde{\theta}^{(2)-Sd} - \tilde{\theta}^{(1)-Sd} \right) = -\frac{\eta_2^{\mathrm{i}-Sd}}{\sin\theta} \left(\tilde{\theta}^{(2)-Sd} - \tilde{\theta}^{(1)-Sd} \right)
\tag{4.47}
$$

A Gauss–Legendre product rule of $N_\rho \times N_\theta$ points is used in the region $(\rho', \theta') \in [0, 1] \times [0, 1]$.

The complete cancellation of the quasi-singularity is obtained from the product of Jacobians present in Equations (4.44) and (4.47). Then, the integral is evaluated as:

$$
I = \int_X f \, dX = \sum_{d=1}^{N_S} \sum_{k_\rho=1}^{N_\rho} \sum_{k_\theta=1}^{N_\theta} f \left(\rho'^{(k_\rho)}, \theta'^{(k_\theta)} \right) \cdot J \cdot J_{\mathrm{R}d} \cdot J_{\mathrm{A}d} \cdot J_{\mathrm{UA}d} \cdot w^{(k_\rho)} \cdot w^{(k_\theta)}
\tag{4.48}
$$

where the product of Jacobians introduced by the polar transformation:

$$
J_{\mathrm{R}d} \cdot J_{\mathrm{A}d} \cdot J_{\mathrm{UA}d} = \rho \left\| \xi^{(2)-Sd} - \xi^{(1)-Sd} \right\| \left(\tilde{\theta}^{(2)-Sd} - \tilde{\theta}^{(1)-Sd} \right)
\tag{4.49}
$$

is now strictly proportional to ρ.

4.5.2.4 Polar transformation with ρ^0 conformality at the collocation point

In the seminal works of Guiggiani et al. [75, 76] about CPV and HFP surface integrals, a Taylor expansion of the distance between observation and collocation points with respect to the radial coordinate is performed. They used this expansion to properly regularise these integrals from the reference space, where a polar transformation is used. They observed that in general any circular neighbourhood around the collocation point in the real space is an ellipse in the reference space when $r \rightarrow 0$. Conversely, any circular neighbourhood around the collocation point in the reference space is in general an ellipse in the real space. Therefore, this expansion allows measuring the goodness of the mapping of polar coordinates from the reference space to the real space. The expansion of the distance components $r_k = x_k - x_k^{\mathrm{i}}$ at the collocation point can be written as:

$$
\begin{aligned}
r_k &= \left(\frac{\partial x_k}{\partial \rho} \right)^{\mathrm{i}} \rho + \frac{1}{2} \left(\frac{\partial^2 x_k}{\partial \rho^2} \right)^{\mathrm{i}} \rho^2 + \frac{1}{6} \left(\frac{\partial^3 x_k}{\partial \rho^3} \right)^{\mathrm{i}} \rho^3 + \frac{1}{24} \left(\frac{\partial^4 x_k}{\partial \rho^4} \right)^{\mathrm{i}} \rho^4 + \mathcal{O}\left(\rho^5\right) \\
&= \rho \left[A_k + B_k \rho + C_k \rho^2 + D_k \rho^3 + \mathcal{O}\left(\rho^4\right) \right]
\end{aligned}
\tag{4.50}
$$

where, following our usual convention, $(\square)^{\mathrm{i}}$ indicates that $\square$ is evaluated at the collocation point. Assuming that polar coordinates are established at the reference space ξ, i.e. $\xi = \xi^{\mathrm{i}} + \rho (\cos\theta, \sin\theta)^T$, the first two terms of the expansion can be expressed as:

$$
A_k = \left(\frac{\partial x_k}{\partial \xi_1} \right)^{\mathrm{i}} \cos\theta + \left(\frac{\partial x_k}{\partial \xi_2} \right)^{\mathrm{i}} \sin\theta
\tag{4.51a}
$$

$$B_k = \left(\frac{\partial^2 x_k}{\partial \xi_1^2}\right)^i \frac{\cos^2 \theta}{2} + \left(\frac{\partial^2 x_k}{\partial \xi_1 \partial \xi_2}\right)^i \sin \theta \cos \theta + \left(\frac{\partial^2 x_k}{\partial \xi_2^2}\right)^i \frac{\sin^2 \theta}{2} \tag{4.51b}$$

which contains trigonometric functions and tangent vectors (and higher-order derivatives) with respect to the reference coordinates at the collocation point. Hence, the distance $r = \sqrt{r_k r_k}$ is:

$$r = \rho \sqrt{A_k A_k + 2 A_k B_k \rho + \left(2 A_k C_k + B_k B_k\right) \rho^2 + \mathcal{O}\left(\rho^3\right)} = \rho M\left(\rho, \theta\right) \tag{4.52}$$

where the function $M\left(\rho, \theta\right)$ is the key ingredient for measuring the quality of the mapping. The first two terms under the square root are:

$$A_k A_k = \left(\frac{\partial x_k}{\partial \xi_1}\right)^i \left(\frac{\partial x_k}{\partial \xi_1}\right)^i \cos^2 \theta + \left(\frac{\partial x_k}{\partial \xi_2}\right)^i \left(\frac{\partial x_k}{\partial \xi_2}\right)^i \sin^2 \theta + \left(\frac{\partial x_k}{\partial \xi_1}\right)^i \left(\frac{\partial x_k}{\partial \xi_2}\right)^i 2 \sin \theta \cos \theta \tag{4.53a}$$

$$A_k B_k = \left(\frac{\partial x_k}{\partial \xi_1}\right)^i \left(\frac{\partial^2 x_k}{\partial \xi_1^2}\right)^i \frac{\cos^3 \theta}{2} + \left(\frac{\partial x_k}{\partial \xi_1}\right)^i \left(\frac{\partial^2 x_k}{\partial \xi_1 \partial \xi_2}\right)^i \sin \theta \cos^2 \theta + \left(\frac{\partial x_k}{\partial \xi_1}\right)^i \left(\frac{\partial^2 x_k}{\partial \xi_2^2}\right)^i \frac{\sin^2 \theta \cos \theta}{2}$$

$$+ \left(\frac{\partial x_k}{\partial \xi_2}\right)^i \left(\frac{\partial^2 x_k}{\partial \xi_1^2}\right)^i \frac{\sin \theta \cos^2 \theta}{2} + \left(\frac{\partial x_k}{\partial \xi_2}\right)^i \left(\frac{\partial^2 x_k}{\partial \xi_1 \partial \xi_2}\right)^i \sin^2 \theta \cos \theta + \left(\frac{\partial x_k}{\partial \xi_2}\right)^i \left(\frac{\partial^2 x_k}{\partial \xi_2^2}\right)^i \frac{\sin^3 \theta}{2} \tag{4.53b}$$

The limit of $M\left(\rho, \theta\right)$ when $\rho \to 0$ is $\sqrt{A_k A_k}$. Therefore, Equation (4.53a) indicates that the shape of the neighbourhood in the limit $\rho \to 0$ is an oblique ellipse, as already shown by Guiggiani and Gigante [75]. Furthermore, when $\rho \to 0$, elements with aspect ratios far from 1 produces $\sqrt{A_k A_k} \approx K \sin \theta$ or $\sqrt{A_k A_k} \approx K \cos \theta$, and hence $1/r \approx 1/(\rho K \sin \theta)$ or $1/r \approx 1/(\rho K \cos \theta)$, where K is a constant. Likewise, for skewed elements $1/r \approx 1/(\rho \sqrt{K \sin \theta \cos \theta})$. Therefore, as it happened with the Jacobian J_{Ud} of Equation (4.40), this is another source of quasi-singularities when the collocation point is close to the edges of the element. If we were able to make $A_k A_k$ constant, a perfect cancellation of the $1/r$ weak singularity would be achieved in the limit $\rho \to 0$.

These facts were already identified by Hayami [175], and partially enforced by using the polar coordinates over triangles obtained from the projection of the element. Despite producing only an approximately constant $A_k A_k$, it is a very effective strategy. Rong et al. [139] proposed a methodology for obtaining a rigorous constant $A_k A_k$ for triangular elements. From Equation (4.53a), it is straightforward to see that if the following conformality conditions are met:

$$\text{Condition I (equal length):} \quad \left(\frac{\partial x_k}{\partial \xi_1}\right)^i \left(\frac{\partial x_k}{\partial \xi_1}\right)^i = \left(\frac{\partial x_k}{\partial \xi_2}\right)^i \left(\frac{\partial x_k}{\partial \xi_2}\right)^i \tag{4.54a}$$

$$\text{Condition II (orthogonality):} \quad \left(\frac{\partial x_k}{\partial \xi_1}\right)^i \left(\frac{\partial x_k}{\partial \xi_2}\right)^i = 0 \tag{4.54b}$$

then:

$$A_k A_k = \left(\frac{\partial x_k}{\partial \xi_1}\right)^i \left(\frac{\partial x_k}{\partial \xi_1}\right)^i = \left(\frac{\partial x_k}{\partial \xi_2}\right)^i \left(\frac{\partial x_k}{\partial \xi_2}\right)^i \tag{4.55}$$

In order to enforce these, they make a linear transformation of the triangle in the reference space ξ to another triangle in a parametric space η. One vertex of the triangle in the parametric space is chosen such that conformality conditions are met. This is a ρ^0 conformality, i.e. conformality is guaranteed only at the collocation point. Depending on the actual element geometry, approximate conformality is also present in certain neighbourhood around the collocation point.

The proposed framework shown in Figure 4.11 lets us to easily generalise their method also to quadrilateral elements. For each subdivision d, we have to calculate $\eta^{\text{i}-Sd}$ that fulfil the conformality conditions:

$$\text{Condition I (equal length):} \quad \mathbf{T}_1^{\eta} \cdot \mathbf{T}_1^{\eta} = \mathbf{T}_2^{\eta} \cdot \mathbf{T}_2^{\eta} \tag{4.56a}$$

$$\text{Condition II (orthogonality):} \quad \mathbf{T}_1^{\eta} \cdot \mathbf{T}_2^{\eta} = 0 \tag{4.56b}$$

where:

$$\mathbf{T}_j^{\eta} = \left(\frac{\partial \mathbf{x}}{\partial \eta_j}\right)^{\text{i}} = \left(\frac{\partial \mathbf{x}}{\partial \xi_l}\right)^{\text{i}} \frac{\partial \xi_l}{\partial \zeta_k} \frac{\partial \zeta_k}{\partial \eta_j} = \mathbf{T}_l^{\xi} S_{lk}^{Sd} C_{kj}^{Sd}, \, j,k,l = 1,2 \tag{4.57}$$

which leads to the following solution:

$$\eta_1^{\text{i}-Sd} = -\frac{a_l b_k \left(\mathbf{T}_l^{\xi} \cdot \mathbf{T}_k^{\xi}\right)}{a_l a_k \left(\mathbf{T}_l^{\xi} \cdot \mathbf{T}_k^{\xi}\right)}, \, \eta_2^{\text{i}-Sd} = \sqrt{\frac{b_l b_k \left(\mathbf{T}_l^{\xi} \cdot \mathbf{T}_k^{\xi}\right)}{a_l a_k \left(\mathbf{T}_l^{\xi} \cdot \mathbf{T}_k^{\xi}\right)} - \left(\eta_1^{\text{i}-Sd}\right)^2} \tag{4.58}$$

where $a_j = \xi_j^{(2)-Sd} - \xi_j^{(1)-Sd}$ and $b_j = \xi_j^{(1)-Sd} - \xi_j^{\text{i}}$. Therefore, the only modification that is necessary is the new conformality position of $\eta^{\text{i}-Sd}$ instead of that indicated by Equation (4.35). In order to use the straightforward transformation $T_{Rd} : (\rho, \theta) \rightarrow \xi$, instead of using Equation (4.41), it is necessary to use the following:

$$\xi = \xi^{\text{i}} + \mathbf{R}^{Sd} \left\{ \begin{array}{c} \rho \cos \theta \\ \rho \sin \theta \end{array} \right\} \tag{4.59a}$$

$$\mathbf{R}^{Sd} = \left(\begin{array}{cc} \xi_1^{(2)-Sd} - \xi_1^{(1)-Sd} & \left[\left(1 - \eta_1^{\text{i}-Sd}\right)\xi_1^{(1)-Sd} + \eta_1^{\text{i}-Sd}\xi_1^{(2)-Sd} - \xi_1^{\text{i}}\right]/\eta_2^{\text{i}-Sd} \\ \xi_2^{(2)-Sd} - \xi_2^{(1)-Sd} & \left[\left(1 - \eta_1^{\text{i}-Sd}\right)\xi_2^{(1)-Sd} + \eta_1^{\text{i}-Sd}\xi_2^{(2)-Sd} - \xi_2^{\text{i}}\right]/\eta_2^{\text{i}-Sd} \end{array} \right) \tag{4.59b}$$

$$J_{Rd} = \rho \frac{(\xi_1^{(1)-Sd} - \xi_1^{\text{i}})(\xi_2^{(2)-Sd} - \xi_2^{\text{i}}) - (\xi_1^{(2)-Sd} - \xi_1^{\text{i}})(\xi_2^{(1)-Sd} - \xi_2^{\text{i}})}{\eta_2^{\text{i}-Sd}} \tag{4.59c}$$

For a weakly singular integrand f, the integral is evaluated as:

$$I = \int_X f \, dX = \sum_{d=1}^{N_S} \sum_{k_\rho=1}^{N_\rho} \sum_{k_\theta=1}^{N_\theta} f\left(\rho'^{(k_\rho)}, \theta'^{(k_\theta)}\right) \cdot J \cdot J_{Rd} \cdot J_{Ad} \cdot J_{UAd} \cdot w^{(k_\rho)} \cdot w^{(k_\theta)} \tag{4.60}$$

The resulting polar transformation is free from any source of quasi-singularities. Due to conformality at the collocation point, angles measured at that point in the η space are equal to those measured in the physical space. Also, r and ρ becomes proportional as $r \to 0$, which guarantees a perfect cancellation of the weak singularity. Incidentally, approximate conformality is also achieved in some neighbourhood around the collocation point, and, for moderately curved elements, in the whole element. Thus, purely angular terms like $r_{,k}$ becomes approximately independent of ρ and resemble trigonometric functions of θ. This makes numerical integration very insensitive to the aspect ratio and the skewness of elements.

4.5.2.5 A comparison between methodologies

The aim of this section is comparing the methodologies for evaluating weakly singular surface integrals presented in previous sections:

DM Degenerated mapping.

PTB Basic polar transformation.

PTQ Polar transformation without the strong angular quasi-singularity.

PTC Polar transformation without the main angular strong quasi-singularity, and without the angular quasi-singularity due to shape aspect ratio and skewness of elements (ρ^0 conformality).

The comparison is made in terms of the number of integration points required along each coordinate for achieving a desired relative error, which is assumed $\epsilon = \mathrm{abs}((I^{\mathrm{num}} - I^{\mathrm{ref}})/I^{\mathrm{ref}}) = 10^{-6}$. Reference solutions are calculated using a $N_\rho \times N_\theta = 32 \times 32$ quadrature rule, while numerical solutions are limited up to rules of $N_\rho \times N_\theta = 30 \times 30$. According to Figures 4.8 and 4.11, the number of integration points N_1 used by the degenerated mapping technique assumes the role of N_θ of polar transformations, and similarly N_2 with respect to N_ρ. Hence, this is assumed in all graphs. Seven nine nodes quadratic quadrilaterals are considered in the numerical experiment, see Table 4.2 and Figure 4.12. These elements allow studying the influence of shape aspect ratio, skewness, curvature in the plane and spatial curvature. Four different integrals A, B, C and D are considered:

$$I_{\mathrm{A}} = \int_{\mathrm{S1}} \frac{1}{r} J \, \mathrm{d}\xi_1 \mathrm{d}\xi_2 \tag{4.61a}$$

$$I_{\mathrm{B}} = \int_{\mathrm{S1}} \frac{1}{r} \phi J \, \mathrm{d}\xi_1 \mathrm{d}\xi_2 \tag{4.61b}$$

$$I_{\mathrm{C}} = \int_{\mathrm{S1}} \frac{1}{r} r_{,1} r_{,2} \phi J \, \mathrm{d}\xi_1 \mathrm{d}\xi_2 \tag{4.61c}$$

$$I_{\mathrm{D}} = \int_{\mathrm{S1}} \frac{1}{r^2} \frac{\partial r}{\partial n} \phi J \, \mathrm{d}\xi_1 \mathrm{d}\xi_2 \tag{4.61d}$$

which are all expressed in terms of the reference coordinates, but later solved using each one of the four methodologies. These integrals are evaluated only over the first subdivision S1,

Id	Description		N1	N2	N3	N4	N5	N6	N7	N8	N9
PR1	Square 1×1	x_1	0.000	1.000	1.000	0.000	0.500	1.000	0.500	0.000	0.500
		x_2	0.000	0.000	1.000	1.000	0.000	0.500	1.000	0.500	0.500
		x_3	0.000	0.000	0.000	0.000	0.000	0.000	0.000	0.000	0.000
PR2	Rectangle 2×1	x_1	0.000	2.000	2.000	0.000	1.000	2.000	1.000	0.000	1.000
		x_2	0.000	0.000	1.000	1.000	0.000	0.500	1.000	0.500	0.500
		x_3	0.000	0.000	0.000	0.000	0.000	0.000	0.000	0.000	0.000
PO1	Oblique 1×1	x_1	0.000	1.000	1.707	0.707	0.500	1.354	1.207	0.354	0.854
		x_2	0.000	0.000	0.707	0.707	0.000	0.354	0.707	0.354	0.354
		x_3	0.000	0.000	0.000	0.000	0.000	0.000	0.000	0.000	0.000
PO2	Oblique 2×1	x_1	0.000	2.000	3.414	1.414	1.000	2.707	2.414	0.707	1.707
		x_2	0.000	0.000	0.707	0.707	0.000	0.354	0.707	0.354	0.354
		x_3	0.000	0.000	0.000	0.000	0.000	0.000	0.000	0.000	0.000
PQR	Straight sides $\approx 1 \times 1$	x_1	0.000	1.000	0.750	0.250	0.500	0.875	0.500	0.125	0.500
		x_2	0.000	0.250	1.000	1.250	0.125	0.625	1.125	0.625	0.625
		x_3	0.000	0.000	0.000	0.000	0.000	0.000	0.000	0.000	0.000
PQC	Curved sides $\approx 1 \times 1$	x_1	0.000	1.000	0.750	0.250	0.500	0.938	0.500	0.068	0.500
		x_2	0.000	0.250	1.000	1.250	0.068	0.625	1.198	0.625	0.625
		x_3	0.000	0.000	0.000	0.000	0.000	0.000	0.000	0.000	0.000
QSS	Spherical	x_1	0.000	0.707	0.577	0.000	0.368	0.686	0.303	0.000	0.367
		x_2	0.000	0.000	0.577	0.707	0.000	0.244	0.674	0.368	0.367
		x_3	1.000	0.707	0.577	0.707	0.930	0.686	0.674	0.930	0.855

Table 4.2: Quadratic quadrilateral elements used in the numerical experiment

and for a set of collocation points located at a regular grid of 100×100 points in the interior of the element $\xi^i \in [-0.999, 0.999] \times [-0.999, 0.999]$. Therefore, this numerical experiment is a comprehensive testing of the capabilities of each methodology.

The first task is to choose the appropriate subdivision pattern which will later offer a reliable and efficient way of selecting the required quadrature rules. The subdivision pattern of triangular and quadrilateral elements was shown in Figures 4.9 and 4.10, respectively. The minimal subdivision pattern make use of the triangles MT_j, with $j = 1, 2, 3$ for triangular elements and $j = 1, 2, 3, 4$ for quadrilateral elements. Each triangle MT_j can be further subdivided into two right-angle triangles T_{2j-1} and T_{2j}. For an arbitrary location of the collocation point within the element, the minimal subdivision pattern produces a small set of triangular regions of very different shapes. The subdivision pattern of right-angle triangles has a bigger set of triangular regions, but all with that feature in common. For locations of the collocation points near the corner of elements, two very unequal right-angle triangles are produced, which indicates that a very different quadrature rule may be needed for the radial coordinate of each right-angle triangle. Hence, the subdivision into right-angle triangles is chosen.

In order to describe the type of graphs where the comparison is made, a full example is shown in Figure 4.13. The integral I_B extended over the subdivision $\text{S1} \equiv \text{T1}$ of the element PQC is considered, and it is evaluated by using the basic polar transformation. Figure 4.13a
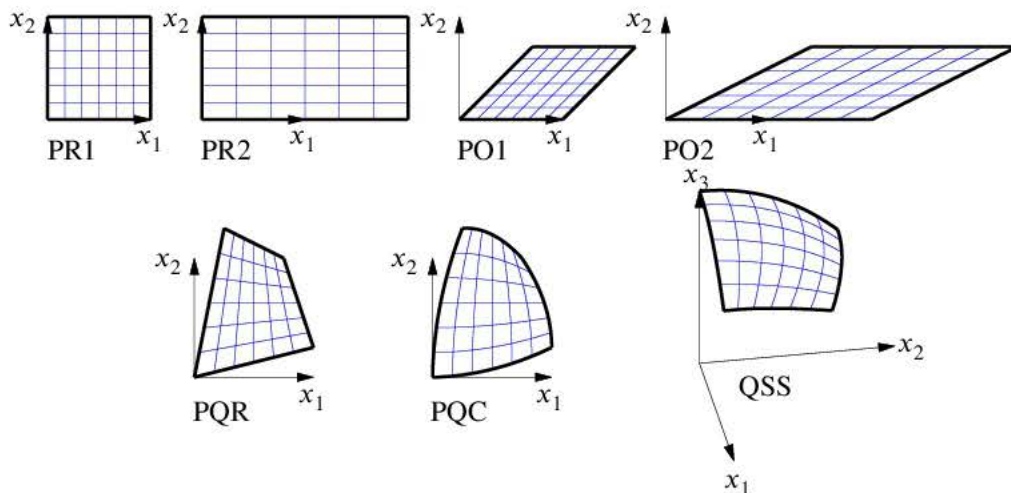
Figure 4.12: Quadratic quadrilateral elements used in the numerical experiment. Blue lines are ξ_1 and ξ_2 isolines.

shows two colour maps of the required N_ρ and N_θ for each location of the collocation point ξ^i. They reveal that the required N_ρ mainly depends on the length of the hypotenuse h of the triangle T1, and the required N_θ mainly depends on the angle $\Delta\theta$ of triangle T1 at the collocation point. Both facts are reasonable since they are the maximum lengths of ρ and θ paths measured in the reference space. Preferably, these lengths should be given in the real space, which produces graphs more independent from shape aspect ratio and skewness of the actual element. However, for the sake of comparison between all methodologies, the former lengths are used in the present section. Figure 4.13b synthesises these maps as $N_\theta = N_\theta(\Delta\theta)$ and $N_\rho = N_\rho(h)$ filled curves between maximum and minimum values of the ordinate. They clearly show the correlation in both cases. Note how $N_\theta = N_\theta(\Delta\theta)$ reflects the presence of the quasi-singularity as $\Delta\theta \to \pi/2$, which is intrinsic to the basic polar transformation due to the Jacobian $J_{\mathrm{U}d}$ (Equation (4.40)).

Figure 4.14 shows the required N_θ when integrating the most simple integral I_{A} for plane elements with constant tangent vectors (PR1, PR2, PO1, PO2), and for all methodologies. The required N_ρ is 1 as the weak singularity is perfectly cancelled along the radial coordinate in all methodologies, and hence the integrand does not depend on ρ. On the other hand, there is dependence of N_θ with respect to $\Delta\theta$ for all methodologies, except for the PTC because it enforces a constant $A_k A_k$ (Equation (4.53a)). In the particular case of the square element, PTQ also has angular independence because $A_k A_k$ is already constant. DM and PTB present the strong quasi-singularity in all cases. PTQ presents the quasi-singularity due to $A_k A_k$, which emerges only when the element has a shape aspect ratio different from 1 or some skewness. The insensitivity of PTC methodology with respect to shape aspect ratio and skewness can be seen in Figure 4.16, where ρ and θ isolines are drawn in the physical space.
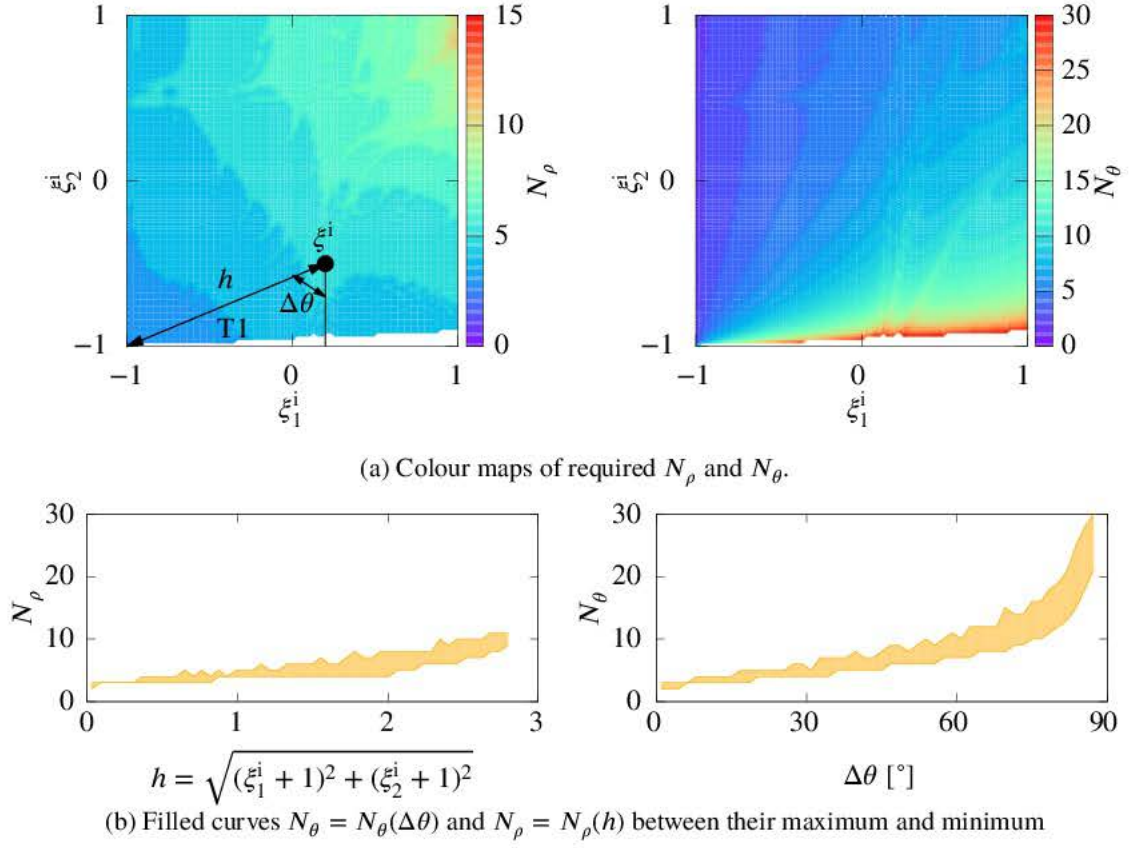
(a) Colour maps of required N_ρ and N_θ.

(b) Filled curves $N_\theta = N_\theta(\Delta\theta)$ and $N_\rho = N_\rho(h)$ between their maximum and minimum

Figure 4.13: Required N_ρ and N_θ for different locations of the collocation point ξ^i. The integral is I_B extended over the subdivision $S1 \equiv T1$ of element PQC, and evaluated by using the basic polar transformation.

Figure 4.15 shows the required N_ρ and N_θ when integrating the integral I_A for elements where the Jacobian is not constant (PQR, PQC and QSS). Figure 4.17 shows the mapping of polar coordinates for planar elements PQR and PQC, where it can be seen that PTC is no longer capable of producing a perfect mapping of polar coordinates to the physical space. Results related to N_ρ show that all methodologies are equally efficient when managing the radial coordinate. $N_\rho = N_\rho(h)$ can be approximated by a linear function, which for all these three elements are quite similar. The Jacobian of the planar elements PQR and PQC is a bivariate polynomial of degree 6 when expressed in terms of reference coordinates ξ_1, ξ_2. Once the polar transformation is applied, it becomes a linear combination of terms $\rho^p \sin^r \theta \cos^s \theta$ where $r + s = p$ and $p \leq 6$. Therefore, if the other terms of the integrand are ignored, the required N_ρ is 4 since $p = 2N_\rho - 1$ for the Gauss-Legendre quadrature. The maximum of $N_\rho = N_\rho(h)$ is approximately 6, which is greater than 4 but not too far from it. The Jacobian of the spherical element QSS is the square root of a bivariate polynomial of degree 12, which in general can not be integrated exactly by a Gauss-Legendre quadrature. However, results show that the required N_ρ for this spherical element is close to that of planar elements.
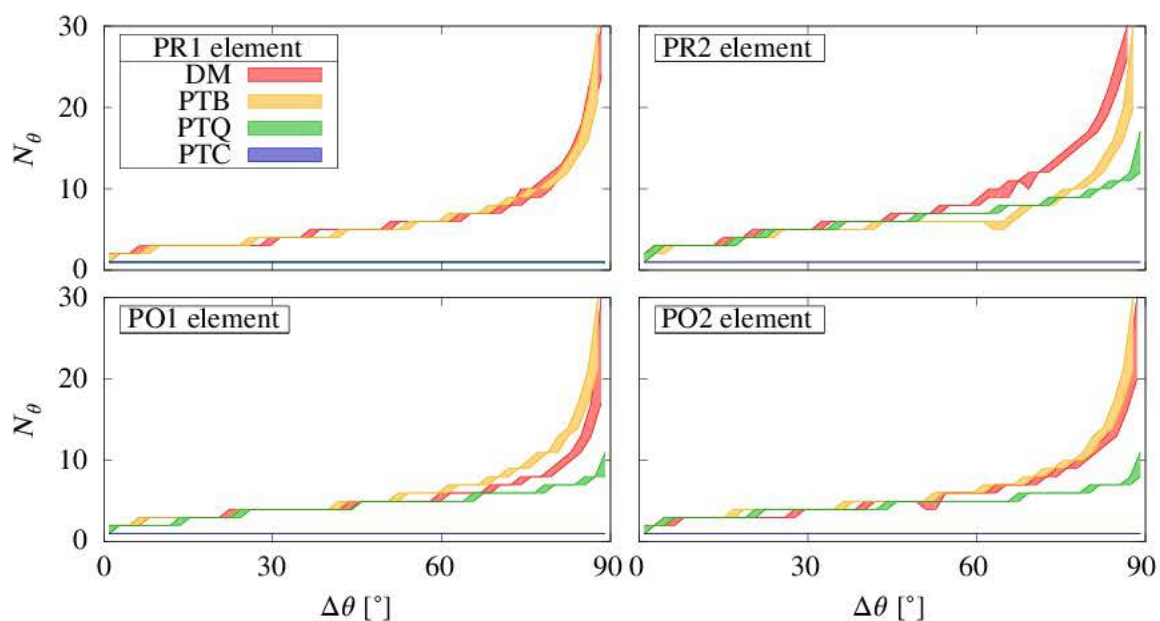
Figure 4.14: Required N_θ when integrating I_A for plane elements with constant tangent vectors (PR1, PR2, PO1, PO2). Required N_ρ is 1 in all cases (constant Jacobian J).
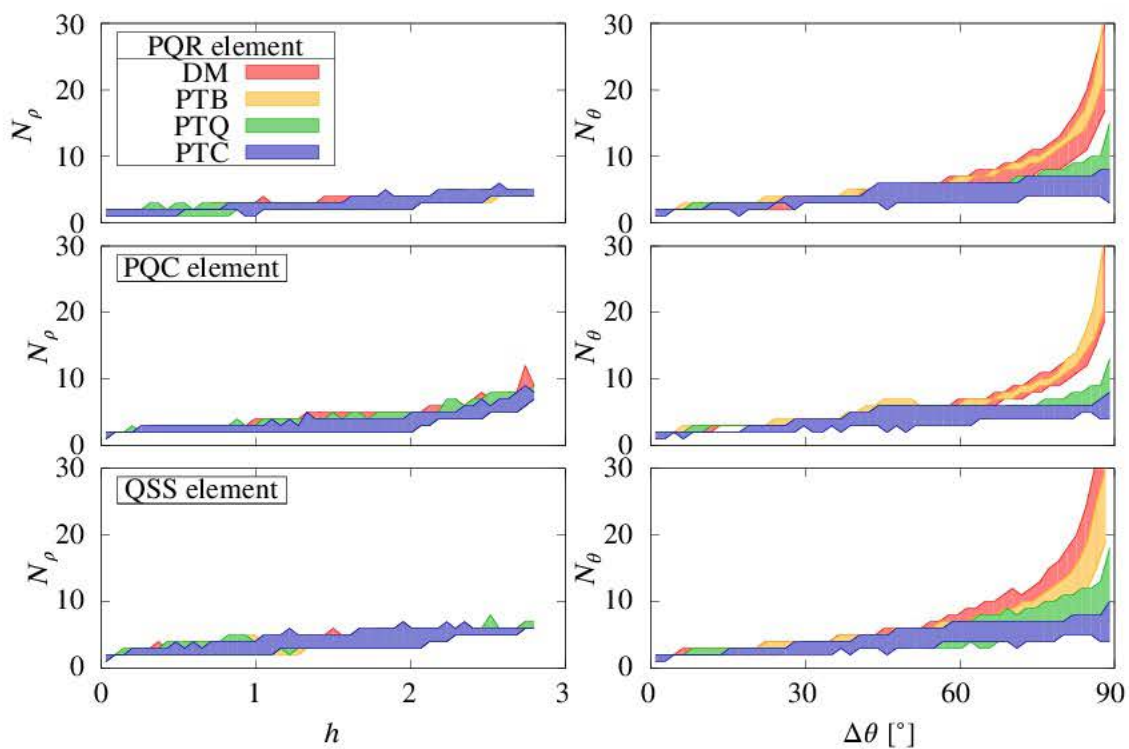

Figure 4.15: Required N_ρ and N_θ when integrating I_A for elements PQR, PQC and QSS

(a) PTB or PTQ   (b) PTC
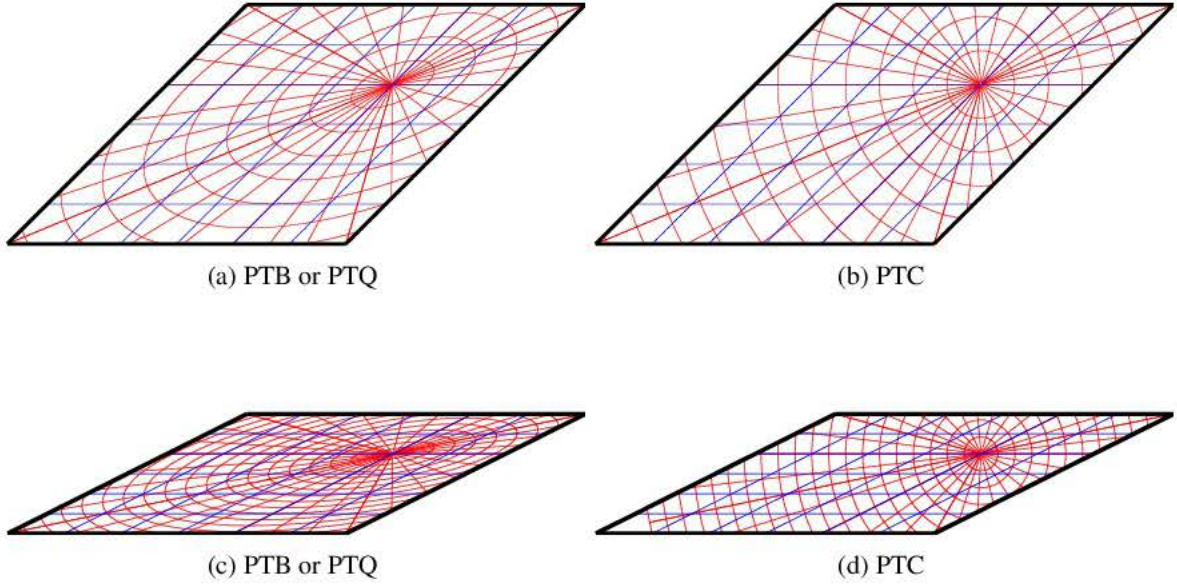
(c) PTB or PTQ   (d) PTC

Figure 4.16: Mapping of polar coordinates ρ and θ to the physical space for elements PO1 (a)-(b) and PO2 (c)-(d) with collocation point $\xi^i = (1/3, 1/3)$. Blue lines are ξ_1 and ξ_2 isolines, and red lines are ρ and θ isolines.

Regarding the angular coordinate, PTC shows some dependence of N_θ with respect to $\Delta\theta$ due to the loss of a perfect mapping of polar coordinates to the physical space. Unlike the other methodologies, PTC shows a stable $N_\theta = N_\theta(\Delta\theta)$ curve even when $\Delta\theta \to 90°$. It is remarkable that all methodologies have virtually the same efficiency for $\Delta\theta < 60°$.

Figures 4.18 and 4.19 show the required N_ρ and N_θ when integrating the integral I_B for all elements and methodologies. The difference between I_B with respect to I_A is the presence of shape functions. In the case of nine node quadrilateral elements, shape functions are bivariate polynomials of degree 4, which after the polar transformation lead to a linear combination of terms $\rho^p \sin^r \theta \cos^s \theta$ where $r + s = p$ and $p \leq 4$. As explained before, the Jacobian for planar elements is a linear combination of terms $\rho^p \sin^r \theta \cos^s \theta$ where $r + s = p$ and $p \leq 6$. Therefore, if only the shape function is considered (elements with constant J), then the required N_ρ is 3. If both shape function and Jacobian are considered, then the required N_ρ is 6. As observed in Figure 4.19, the maximum of $N_\rho = N_\rho(h)$ is approximately 9 in all cases, which is greater than 6 but not too far from it. For elements with constant J, the required N_θ is no longer constant for the PTC methodology due to the presence of trigonometric functions. For elements with non-constant J, the behaviour of $N_\theta = N_\theta(\Delta\theta)$ is similar to the integral I_B, except that slopes are slightly higher due to the presence of trigonometric functions.

Figures 4.20 and 4.21 show the required N_ρ and N_θ when integrating the integral I_C for all elements and methodologies. The difference between I_C with respect to I_B is the presence of distance gradient components $r_{,1} r_{,2}$, which are purely angular terms in the physical space. Results show that in fact $N_\rho = N_\rho(h)$ curves for elements with a non-constant J remain
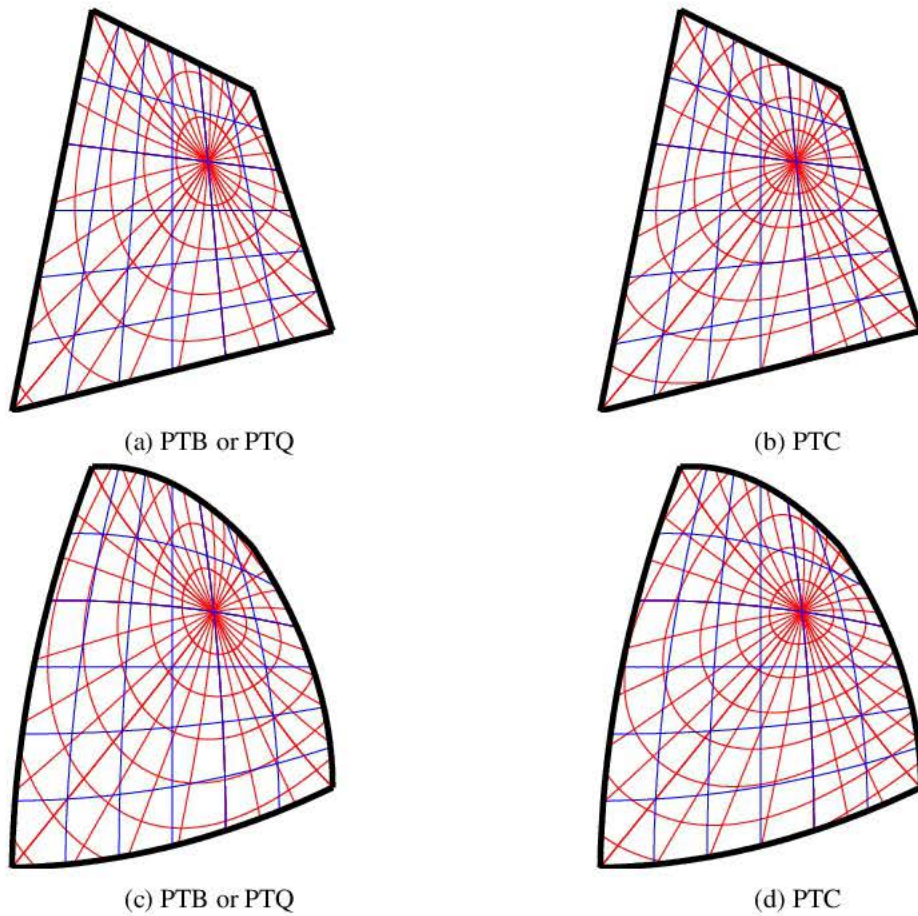
Figure 4.17: Mapping of polar coordinates ρ and θ to the physical space for elements PQR (a)-(b) and PQC (c)-(d) with collocation point $\xi^i = (1/3, 1/3)$. Blue lines are ξ_1 and ξ_2 isolines, and red lines are ρ and θ isolines.

approximately equal. Obviously, N_ρ remains equal to 3 for elements with constant J (not shown in Figure 4.20 for brevity). On the other hand, $N_\theta = N_\theta(\Delta\theta)$ curves have a higher slope. This is due to the additional factors $r_{,1}r_{,2}$, which, considering only the linear terms of expansions shown in Equations (4.52) and (4.50), can be expressed as a linear combination of terms $\sin^r\theta\cos^s\theta$ where $r + s = 2$. This effect can be clearly observed by comparing Figure 4.20 and Figure 4.18 for elements with constant J. In the case of elements with non-constant J, the effect is still present, but is less pronounced.

Figure 4.22 shows the required N_ρ and N_θ when integrating the integral I_D for the spherical element QSS, which is the only with one where $I_D \neq 0$. The difference between I_D with respect to the previous ones is that now the fundamental solution term contains $\partial r/\partial n$. As previously discussed, this term has the peculiarity that $\lim_{r\to 0}\partial r/\partial n = 0$, and vanishes everywhere for planar elements. Taking into account that it can be expressed as $\partial r/\partial n = (\mathbf{r}/r) \cdot \mathbf{n}$, it becomes clear that is a smooth function for moderately curved elements. Results show that N_ρ and N_θ maintain the same behaviour as in previous integrals.

Figure 4.18: Required N_θ when integrating I_B for plane elements with constant tangent vectors (PR1, PR2, PO1, PO2). Required N_ρ is 3 in all cases (constant Jacobian J).

Figure 4.19: Required N_ρ and N_θ when integrating I_B for elements PQR, PQC and QSS
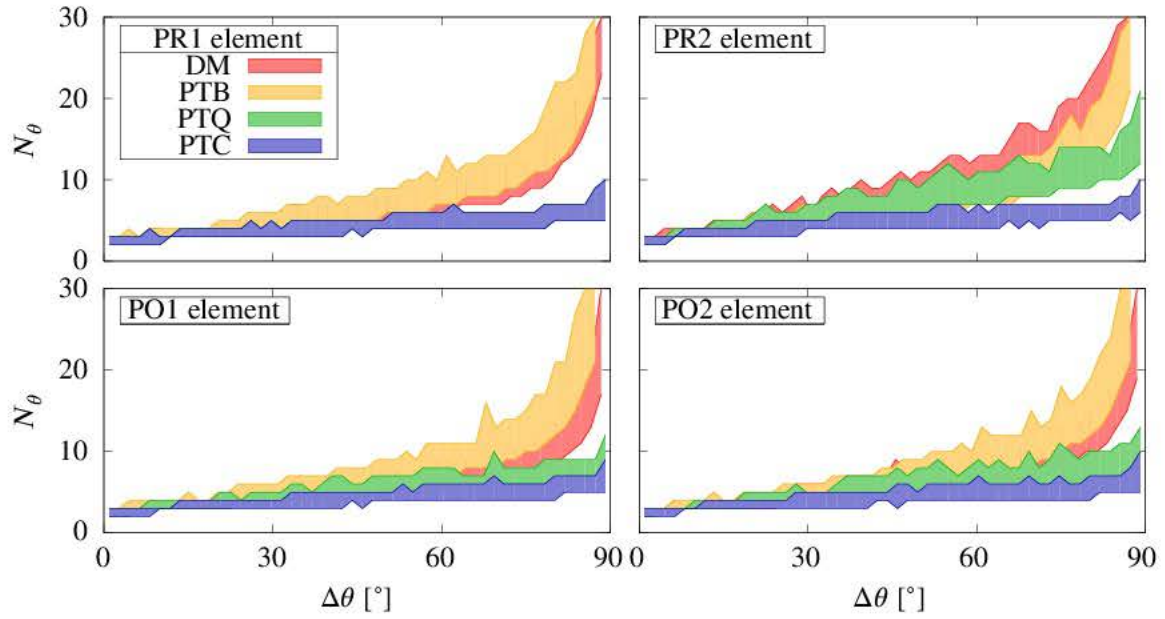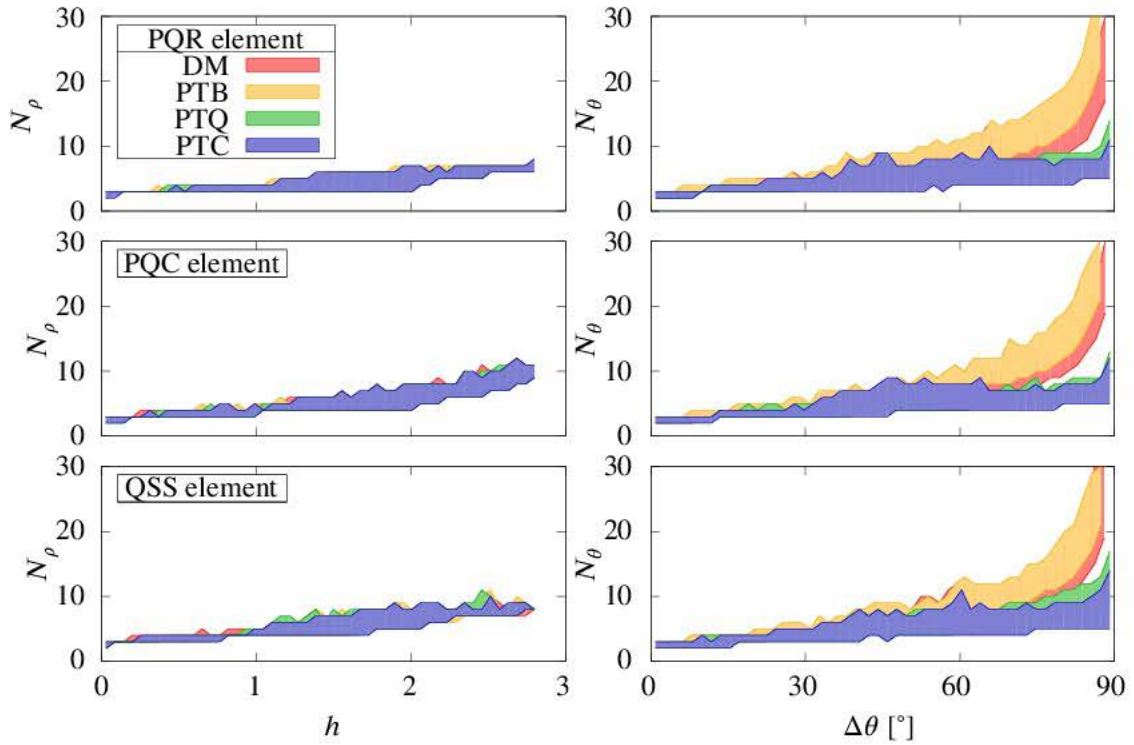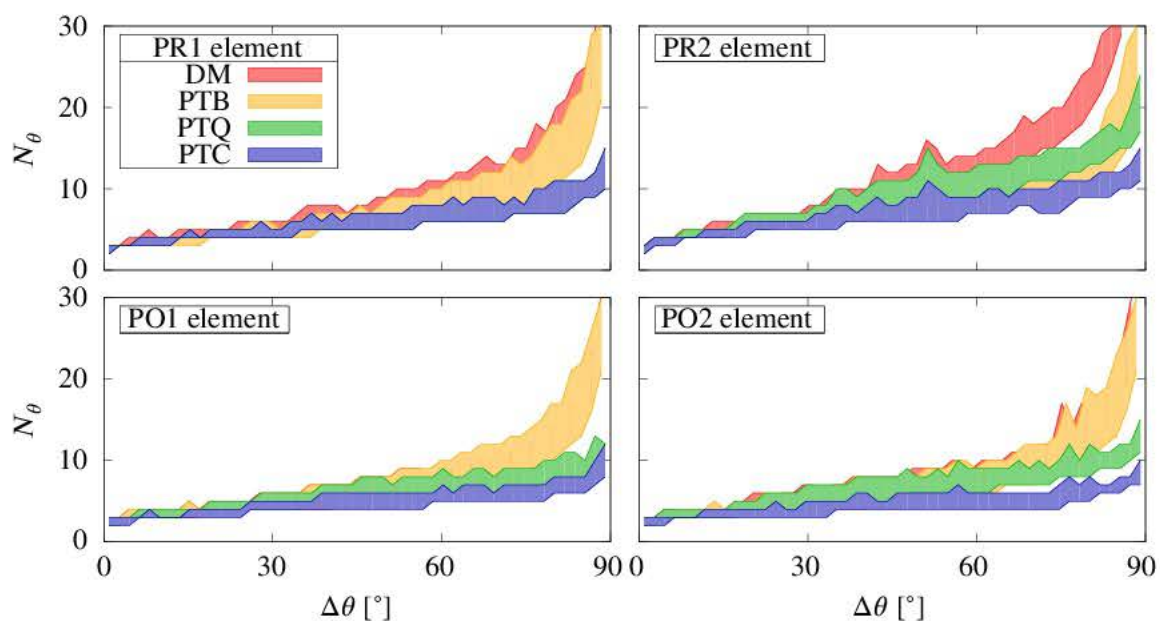
Figure 4.20: Required N_θ when integrating I_C for plane elements with constant tangent vectors (PR1, PR2, PO1, PO2). Required N_ρ is 3 in all cases (constant Jacobian J).
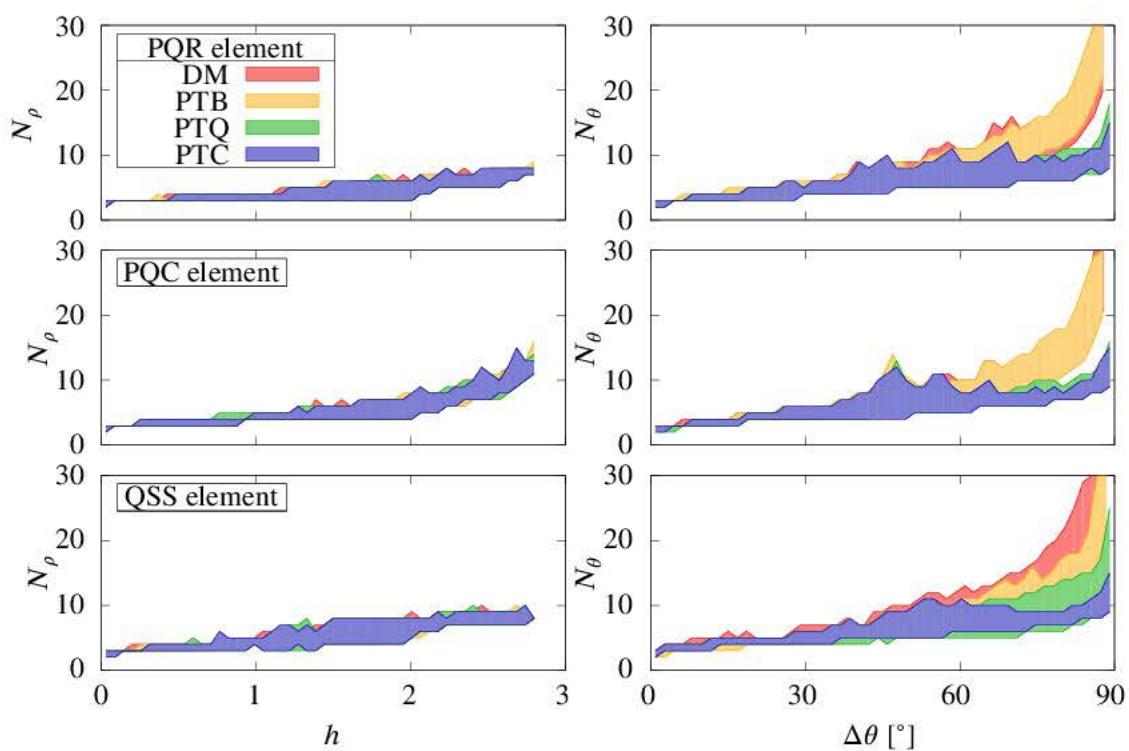

Figure 4.21: Required N_ρ and N_θ when integrating I_C for elements PQR, PQC and QSS
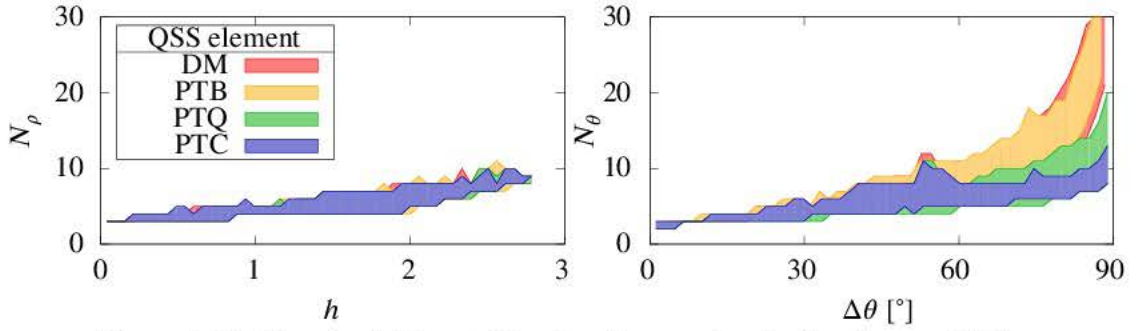
Figure 4.22: Required N_ρ and N_θ when integrating I_D for element QSS

In summary, all methodologies perform with a similar efficiency regarding the radial co-ordinate. The same occurs for the angular coordinate when the angle of the triangular region at the collocation point is approximately $\Delta\theta < 60°$. When $\Delta\theta > 60°$, both the degenerated mapping technique and the basic polar transformation perform equally bad. Polar transformation with the angular strong quasi-singularity removed virtually allow treating triangular regions with $\Delta\theta \to 90°$. If additionally ρ^0 conformality conditions are forced in the polar transformation, the efficiency becomes practically independent from shape aspect ratio and skewness of element.

4.5.2.6 Adaptive non-iterative algorithm

In the previous section, results show that the subdivision pattern of the element into right-angle triangular regions in the reference space ξ leads to certain $N_\rho = N_\rho(h)$ and $N_\theta = N_\theta(\Delta\theta)$ relationships, which, in the case of the polar transformation without any source of quasi-singularities (PTC) are highly independent from the actual element geometry. This is due to a mapping of polar coordinates to the physical space of a very good quality, and also to the analytical removal of the angular strong quasi-singularity arising in the normalisation of the radial coordinate. Therefore, it allows using a simple adaptive non-iterative numerical integration algorithm based on a priori error estimation of simple functions in a reliable manner.

The required N_θ can be related to the problem of the numerical integration of product of trigonometric functions:

$$I_{\text{aux}-\theta} = \int_{\theta_1}^{\theta_2} \sin^r \theta \cos^s \theta \, d\theta \qquad (4.62)$$

where θ is the angular coordinate in the physical space. Since PTC methodology enforces conformality at the collocation point, the angular coordinate θ can be taken as that of the η space, where θ_1 and θ_2 is directly provided by Equations (4.38b), (4.38c) and (4.58). An error estimation can be provided by Equation (4.18):

$$E \le eH = \tilde{E}, \; e \approx \frac{4}{2^{2N}(2N)!}\left(\frac{\Delta\theta}{2}\right)^{2N+1}, \; H \ge \left|\frac{d^{2N}f}{d\theta^{2N}}\right| \qquad (4.63)$$

where $f = \sin^r \theta \cos^s \theta$. Given the nature of f, H can be obtained by finding the maximum absolute value of the $2N$-th derivative of f. A tighter value would be to find the maximum within θ_1 and θ_2, but it seems rather complicated to obtain a closed-form expression of H in that situation. For the cases $f = \sin^p \theta$ (and $f = \cos^p \theta$), the maximum absolute value of the $2N$-th derivative can be obtained by using elementary trigonometric power and addition formulas. Table 4.3 shows the obtained H from $p = 1$ to $p = 8$, their asymptotic values when $N \to \infty$, and the general formulas obtained by generalisation. For all other r, s pairs we have not obtained general formulas of H, but at least for pairs with odd $r + s$, it is easy to verify that $H_{r,s} \leq H_{r+s,0} = H_{0,r+s}$. Therefore, H shown in Table 4.3 provide a conservative estimator for all other r, s pairs when $p = r + s$ is used. Error estimator $\tilde{E}$ can be further simplified by using the asymptotic value of H, and the Stirling's formula for the factorial, leading to a very compact equation:

$$\tilde{E}(N_\theta, p, \theta_1, \theta_2) = \frac{\theta_2 - \theta_1}{2^p} \frac{1}{\sqrt{N_\theta}} \left(\frac{\mathrm{e}}{8N_\theta} \cdot (\theta_2 - \theta_1) \cdot p \right)^{2N_\theta} \tag{4.64}$$

Figure 4.23 shows numerical errors E and error estimations provided by Equation (4.64) for a number of r, s cases. It can be seen that $\tilde{E}$ is conservative, but care must be taken for higher values of p and small values of N_θ since the asymptotic H is assumed in Equation (4.64). In terms of relative error, the following estimator can be used:

$$\tilde{\epsilon}(N_\theta, p, \theta_1, \theta_2) = \frac{\tilde{E}(N_\theta, p, \theta_1, \theta_2)}{\tilde{I}(p, \theta_1, \theta_2)}, \quad \tilde{I}(p, \theta_1, \theta_2) = \mathrm{abs}\left(\int_{\theta_1}^{\theta_2} \sin^p \theta \, \mathrm{d}\theta \right) \tag{4.65}$$

where $\tilde{I}$ is calculated by a simple 2-point Gauss–Legendre quadrature.

Figures 4.24 and 4.25 show a comparison between previous results and required N_θ provided by Equation (4.65). The comparison is made against results when integrating I_A and I_C for PQR, PQC and QSS elements. The angle measured in the reference space is still used in abscissas, see Figure 4.13a, which is now indicated as $\Delta\theta^{(\xi)}$ in order to avoid confusion. According to the discussion given in the Section 4.5.2.5, for the integral I_A it is appropriate to consider $p = 6$, and for I_C it is appropriate to consider $p = 12$. Results show that the estimator provides an acceptable estimation of the required N_θ for different relative errors, and different integrands. However, it underestimates the required N_θ for low values of N_θ and high values of p. This can be explained from the fact that the asymptotic value of H is used in the estimator.
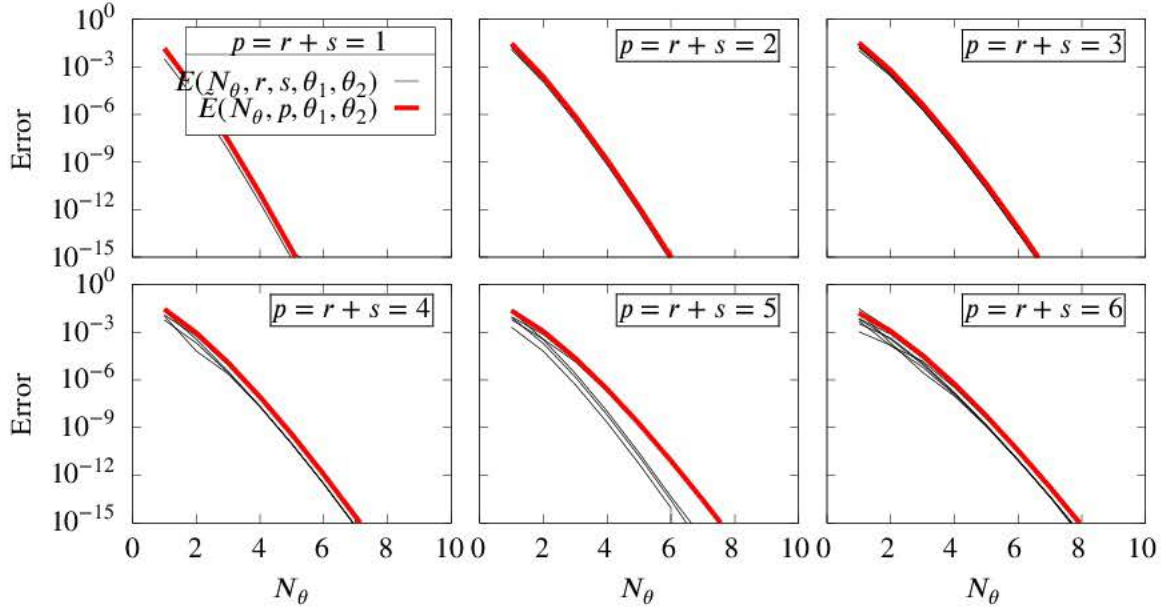
Figure 4.23: Numerical error E and error estimation $\tilde{E}$ for the integral $\int_{\theta_1}^{\theta_2} \sin^r \theta \cos^s \theta \, \mathrm{d}\theta$ for all pairs r, s from $p = r + s = 1$ to $p = 6$ ($\theta_2 - \theta_1 = \pi/5$)

p	H	$\lim_{N \to \infty} H$
1	1	1
2	$\left(2^{2N}\right)/2$	$2^{2N}/2$
3	$\left(3^{2N} + 3\right)/2^2$	$3^{2N}/2^2$
4	$\left(4^{2N} + 4 \cdot 2^{2N}\right)/2^3$	$4^{2N}/2^3$
5	$\left(5^{2N} + 5 \cdot 3^{2N} + 10\right)/2^4$	$5^{2N}/2^4$
6	$\left(6^{2N} + 6 \cdot 4^{2N} + 15 \cdot 2^{2N}\right)/2^5$	$6^{2N}/2^5$
7	$\left(7^{2N} + 7 \cdot 5^{2N} + 21 \cdot 3^{2N} + 35\right)/2^6$	$7^{2N}/2^6$
8	$\left(8^{2N} + 8 \cdot 6^{2N} + 28 \cdot 4^{2N} + 56 \cdot 2^{2N}\right)/2^7$	$8^{2N}/2^7$
...	...	...
p even	$\displaystyle\sum_{k=0}^{k=p/2} \binom{p}{k} (p-2k)^{2N}$	$p^{2N}/2^{p-1}$
p odd	$\displaystyle\sum_{k=0}^{k=(p-1)/2} \binom{p}{k} (p-2k)^{2N}$	

Table 4.3: Values of $H = \max \left| \mathrm{d}^{2N} f / \mathrm{d}\theta^{2N} \right|$ for $f(\theta) = \sin^p \theta$ and $f(\theta) = \cos^p \theta$

Figure 4.24: Comparison between required N_θ obtained from numerical experiment (left) and from error estimator $\tilde\epsilon(N_\theta, 6, \theta_1, \theta_2)$ (right) when integrating I_A
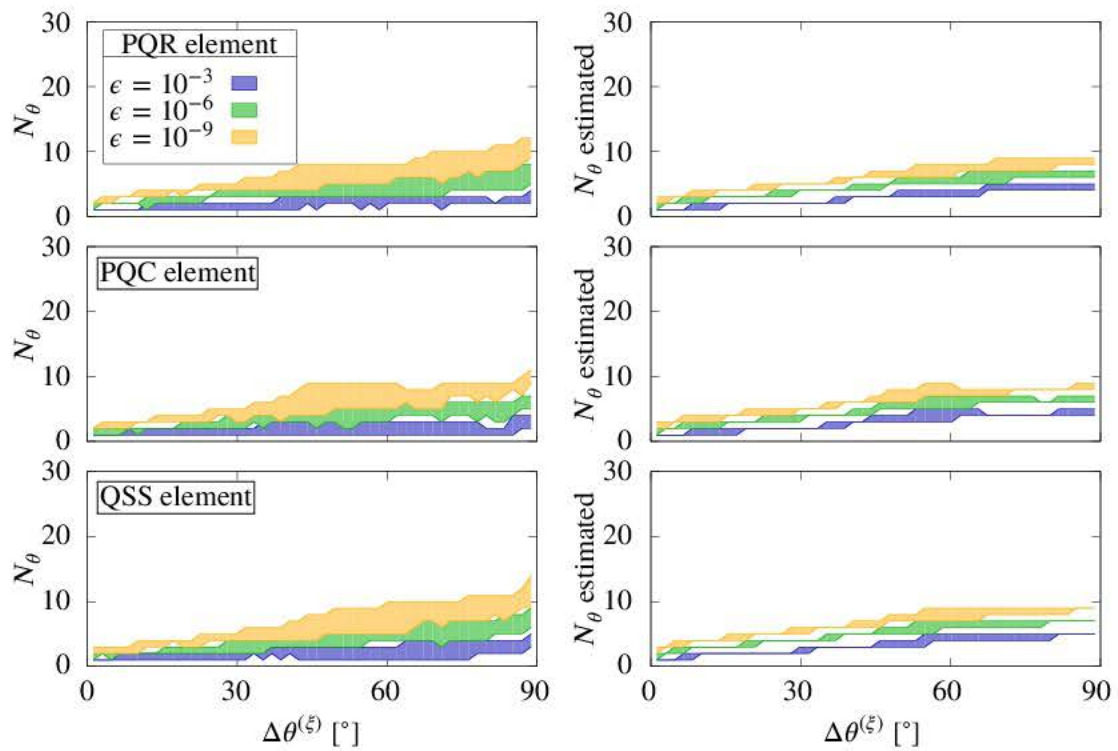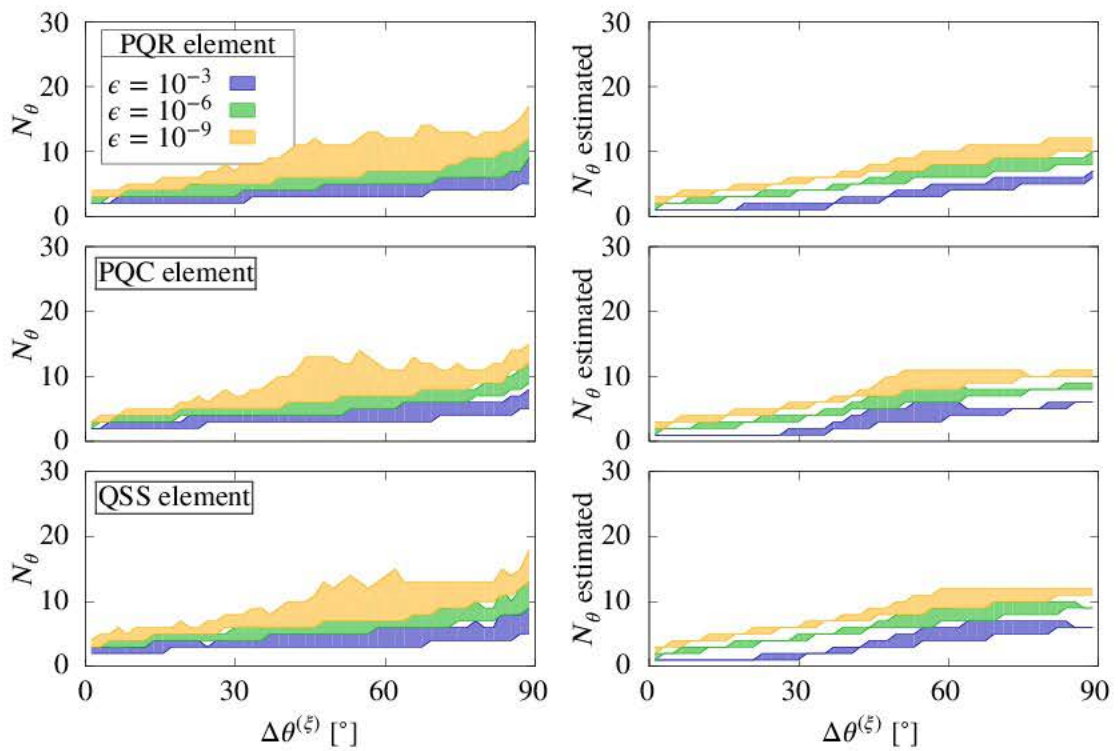
Figure 4.25: Comparison between required N_θ obtained from numerical experiment (left) and from error estimator $\tilde{\varepsilon}(N_\theta, 12, \theta_1, \theta_2)$ (right) when integrating I_C

5.1 Introduction

In this chapter, the methodologies described in previous chapters are used for studying some aspects of wave barriers. A wave barrier is a passive method of reducing the amplitude of mechanical waves at certain areas (receivers) produced by some sources of vibrations. The vibrations produced by overground or underground machinery or vehicles can travel through the air, ground and structures to places where they can annoy people or cause the failure or malfunction of equipment. A wave barrier is an appropriate discontinuity installed at a point of the transmission path which produces such reduction. The design of each wave barrier depends on the source of vibrations, the properties of the transmission path, costs, and the isolation requirements imposed by regulations, customers or manufacturers.

A clear distinction must be made between overground and underground wave barriers. The former case refers to sound waves barriers, most commonly known as sound or noise barriers, and their aim is reducing the dynamic sound pressure up to certain limits such that these are acceptable by human auditory perception in our activities. For defining such limits, regulations take into account, among other things, the average human hearing capabilities: a typical frequency range of $f = [20, 20000]$ Hz, and a typical dynamic pressure between threshold of hearing and pain of $p = [20 \cdot 10^{-6}, 63]$ Pa (frequency dependent) or sound pressure levels $L_p = [0, 130]$ dB (A-weighted) [176]. The latter case refers to elastic waves barriers, in the following simply "wave barriers", and their aim is reducing the acceleration up to certain limits in order to guarantee health and comfort and to avoid perception and motion sickness, particularly in buildings (ISO 2631-1:1997 [177]). The range of frequencies of interest is within $f = [0.1, 80]$ Hz, and acceleration limits are defined such that acceleration perception is avoided. Typical acceleration perception thresholds vary between 0.01 and 0.02 m/s^2, although recommended maximum accelerations are also frequency-weighted and depend on multiple factors.

Another relevant difference between overground and underground wave barriers is their costs and feasibility. Noise barriers are relatively easy to install, and their designs can a priori reach some level of complexity. In this sense, there have been many developments, mostly at the top of the barrier. Hothersall et al. [178, 179] considered T-, Y-, and arrow profile barriers, Crombie et al. [180] studied multiple-edge barriers, and Watts and Morgan [181] used an interference based device at the top of the barrier. Okubo and Fujiwara [182] considered a waterwheel cylinder installed on the top, while Monazzam and Lam [183] used a quadratic residue diffuser. An exhaustive study about noise barriers can be found in Maeso and Aznárez [46]. Toledo et al. performed a comprehensive study of optimised noise barriers of many different topologies [24, 25]. On the other hand, underground wave barriers tend to be simple designs because of installation costs. Their effectiveness mostly depends on the ratio between the Rayleigh wavelength and barrier depth. Simple open trenches provide considerable vibration reduction because their stress-free boundaries act as perfect reflectors of elastic waves [184]. However, a pure open trench can not be excavated to any desired depth for soil stability reasons. Therefore, alternative systems such as open trenches reinforced with retaining sheet piles or concrete walls [185], in-filled trenches with soft or stiff materials [186–188], or the installation of sheet piles [189] or rows of piles [190, 191], have also been considered.

The aim of this chapter is present several contributions in this field, mostly in a two-dimensional setting. In the case of noise barriers, we study to what extent to common assumption of rigidity is valid for this kind of problems in Section 5.2. In the case of wave barriers, we study the effect of considering a poroelastic soil for several topologies in Section 5.3. In Section 5.4, a three-dimensional curved wave barrier buried in a poroelastic soil is studied for the purpose of studying the fidelity of the DBEM–FEM model. In Section 5.5, we study the optimisation of single and double wall barriers buried in elastic soils.

5.2 Two-dimensional flexible noise barriers

In this section, the DBEM–FEM model is used for the analysis of two-dimensional flexible noise barriers. Also, in order to quantify Fluid-Structure Interaction (FSI) in this type of problems, a parametric study of a wall is performed. Therefore, this is the simplest case from those explained in Chapter 2, where the shell is modelled as an equivalent beam ($E_{\text{beam}} = E/(1 - v^2)$) surrounded by an ideal fluid.

As a first step, the DBEM–FEM model has been validated against results published by Jean [192], where a simple noise barrier is studied. The problem description is outlined in Figure 5.1. The fluid Ω_f is air with $\tilde{\rho} = 1.3$ kg/m^3 and $\tilde{c} = 340$ m/s. The thin elastic body Ω_s is a simple noise barrier 3 m high and 0.01 m thick, and it is clamped to the ground. Three different materials are considered for the barrier Ω_f (see Table 5.1). The ground is a perfectly reflecting surface, i.e. fluid displacement and pressure flux are null at the ground, for which the half-plane fundamental solution based on the method of images is used [6]. A point source located at $\mathbf{x}_s = (-2.3, 0.5)$ is used. The point source is easily added to the BEM equations, see e.g. [17].

A comparison between results from Jean [192] and results from the proposed model is shown in Figure 5.2. The results from [192] are shown as a coloured background image from the original paper. The figure shows three graphs, one for each material. The y axis of each plot is the difference between pressures absolute values at a point $\mathbf{x}$ when using a rigid barrier ($U_n = 0$) and when using a flexible barrier. The natural frequencies f_n of each case are plotted as vertical lines, and they are calculated using the cantilever beam equations [193].

The model used in [192] takes into account the real geometry of the barrier, while the proposed model uses a null thickness barrier. The slenderness is $L/w = 333$, so from the barrier behaviour point of view, the Euler-Bernoulli hypotheses are valid. Thus, the proposed model should be able to reproduce the results from [192].

Figure 5.2 shows excellent agreement between Jean's model and the proposed model. Peak frequencies and amplitudes are very well reproduced, although some small discrepancies appear in the wood case at frequencies around 850 Hz.

5.2.1 Complex noise barrier shapes

Jean [192] made a broad study comparing results between flexible and rigid simple noise barriers when varying material, thickness, damping coefficient, receiver and source position, and barrier height. In this section, some more complex barrier shapes are considered.
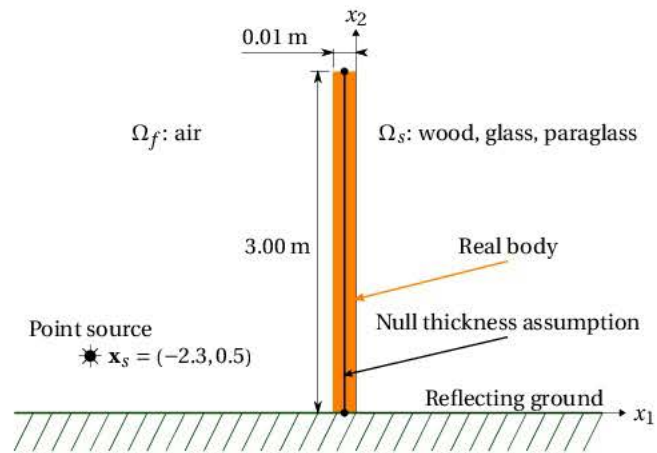
Figure 5.1: Noise barrier problem studied by Jean [192] (thickness not to scale)

Ω_s	$\rho \left[\text{kg/m}^3\right]$	E [GPa]	ν	ξ
Wood	650	12.0	0.01	0.0100
Glass	2400	87.0	0.24	0.0005
Paraglass	1190	3.3	0.40	0.0150

Table 5.1: Materials for the barrier considered by Jean [192]
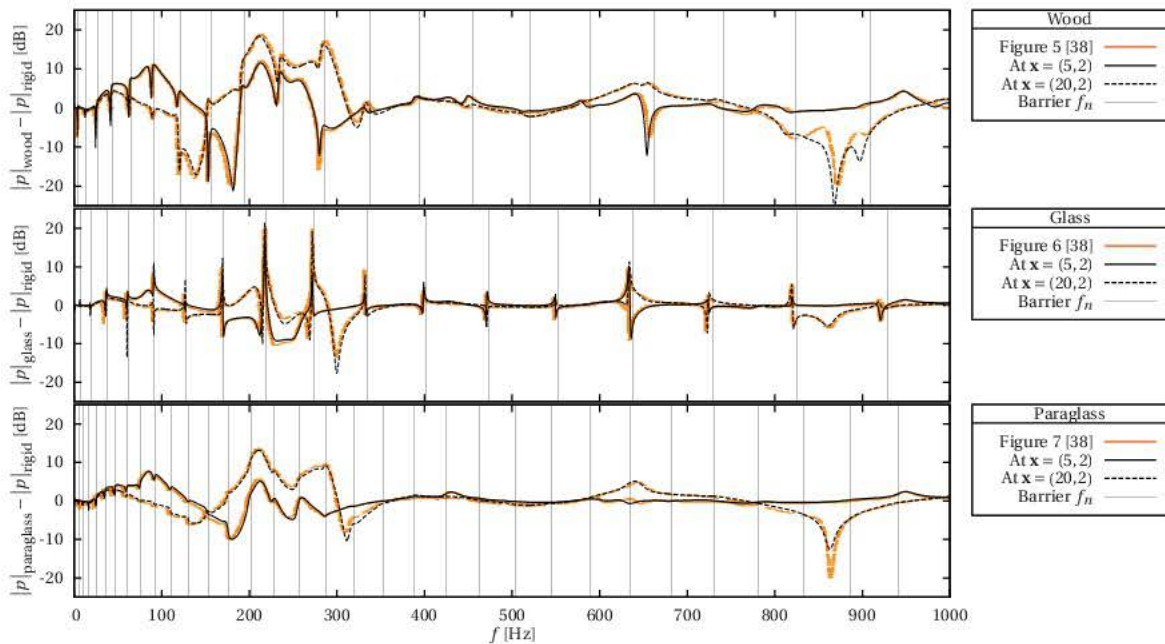
Figure 5.2: Comparison between results from Jean [192] and DBEM–FEM model
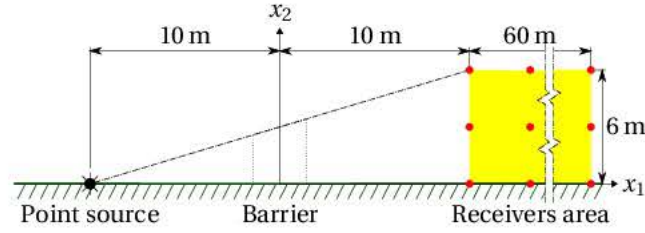
Figure 5.3: Layout for studying complex sound barrier shapes
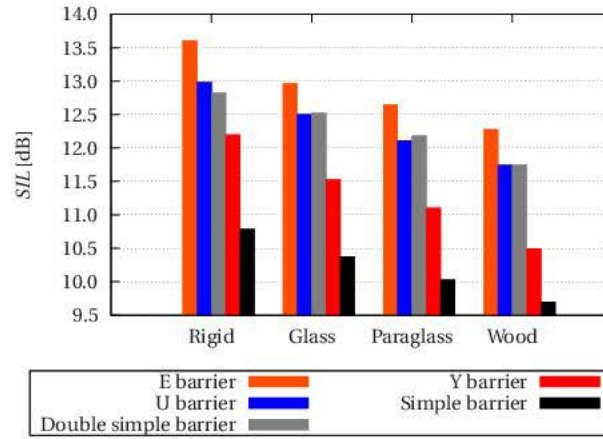
Figure 5.4: SIL for different barrier shapes and materials

The layout of the numerical experiments is depicted in Figure 5.3. Two simple screen barriers (simple barrier and double simple barrier) together with three multi-edge barrier shapes (Y barrier, U barrier and E barrier) are considered. For each shape, all materials from the Table 5.1 are used, the thickness is $w = 0.01$ m for all pieces, and the effective height is 3 m. The point source is located at ground level and 10 m ahead the barrier [17, 178, 194]. A grid of 3×11 receivers covering 6×60 m^2 is considered. A thousand frequencies uniformly distributed in $\log_{10}(f)$ space from $f_{min} = 20$ Hz to $f_{max} = 4000$ Hz are used.

Instead of taking the pressure as the variable of interest, the Insertion Loss IL is used [17]. The IL is the difference between pressures (in dB) when there is no barrier and when the barrier is placed, so it measures the effectiveness of the barrier. We also consider the average Spectral Insertion Loss SIL, which is simply the average IL in the spectrum, leading to a frequency-independent indicator. The IL and the SIL are averaged values over all receivers.

In the literature, it is often assumed that noise barriers are rigid, so it is interesting to find when this hypothesis is valid or not. A first step is using the SIL, Figure 5.4 shows the SIL for all considered barrier shapes and materials, including the rigid case. It is seen that the rigid case is not conservative when using the SIL as an indicator. However, the maximum difference between the rigid case and any case is below 2 dB, being 1 dB for the simple barrier and double simple barrier, and 2 dB for the Y barrier. Thus, when a global indicator such as the SIL is going to be studied, the rigid assumption seems to be valid.

As Jean [192] showed for the simple barrier, when considering the elastic nature of the

barrier there is a widespread pressure increment at low frequencies. Although this behaviour seems reasonable, it is interesting to analyse what happens when barriers more complex than the simple one are used. Figure 5.5 shows the IL spectrum for all studied barrier shapes and materials, including the rigid case.

For low frequencies ($f < 200\,\text{Hz}$) appreciable differences between rigid and flexible barriers are obtained. The simple barrier behaves as Jean described, with increments of pressure below 5 dB, i.e. IL decrements below 5 dB. The other barrier shapes have IL decrements below 10 dB. For very low frequencies ($f < 80\,\text{Hz}$) there is virtually no noise attenuation. The considered complex barrier shapes strongly influence the IL spectrum, especially at low frequencies.

For mid-high frequencies ($f > 500\,\text{Hz}$) the IL spectrum is very similar to a rigid barrier. For simple and double simple barriers, the differences are very small. For Y, U and E barriers, the differences are more noticeable, reaching up to 5 dB at some frequencies. Nevertheless, these differences seem to be irrelevant for noise propagation problems.

The human ear is less sensitive at low frequencies than at high frequencies, so, at first, this behaviour at low frequencies could be neglected. However, high frequencies are attenuated by losses in the air and on the absorbing surfaces, while low frequencies are not. Furthermore, when a building with windows closed is near the noise barrier, low frequency noises may be amplified inside the building. Therefore, depending on the context, the elasticity of a barrier similar to those studied should be considered.

5.2.2 Parametric study of a straight wall

The present problem consists of a straight wall (beam) $(2L, w, \rho, E_m, v, \xi)$ with its centre clamped, surrounded by a fluid $(\tilde{\rho}, \tilde{c})$, where a pressure plane wave is propagating with unity amplitude, perpendicular direction, and angular frequency ω, see Figure 5.6. The problem parameters can be reduced to six dimensionless ones:

- Wave velocity ratio: $\tilde{c}/c$, where $c = \sqrt{E_m/\rho}$ is the beam axial wave velocity.

- Densities ratio: $\tilde{\rho}/\rho$.

- Geometrical slenderness: L/w.

- Dimensionless frequency: $a_0 = (\omega L)/\tilde{c}$.

- Damping coefficient: ξ

- Poisson's ratio: v

Table 5.2 shows the studied values of the dimensionless parameters. The wave velocity ratio and the densities ratio have ranges that include the most extreme fluid-structure combinations. The geometrical slenderness starts from $L/w = 10$ to $L/w = 1000$, which are within the validity interval. The dimensionless frequency range has been chosen so that at least the first natural frequency is clearly captured in all cases.
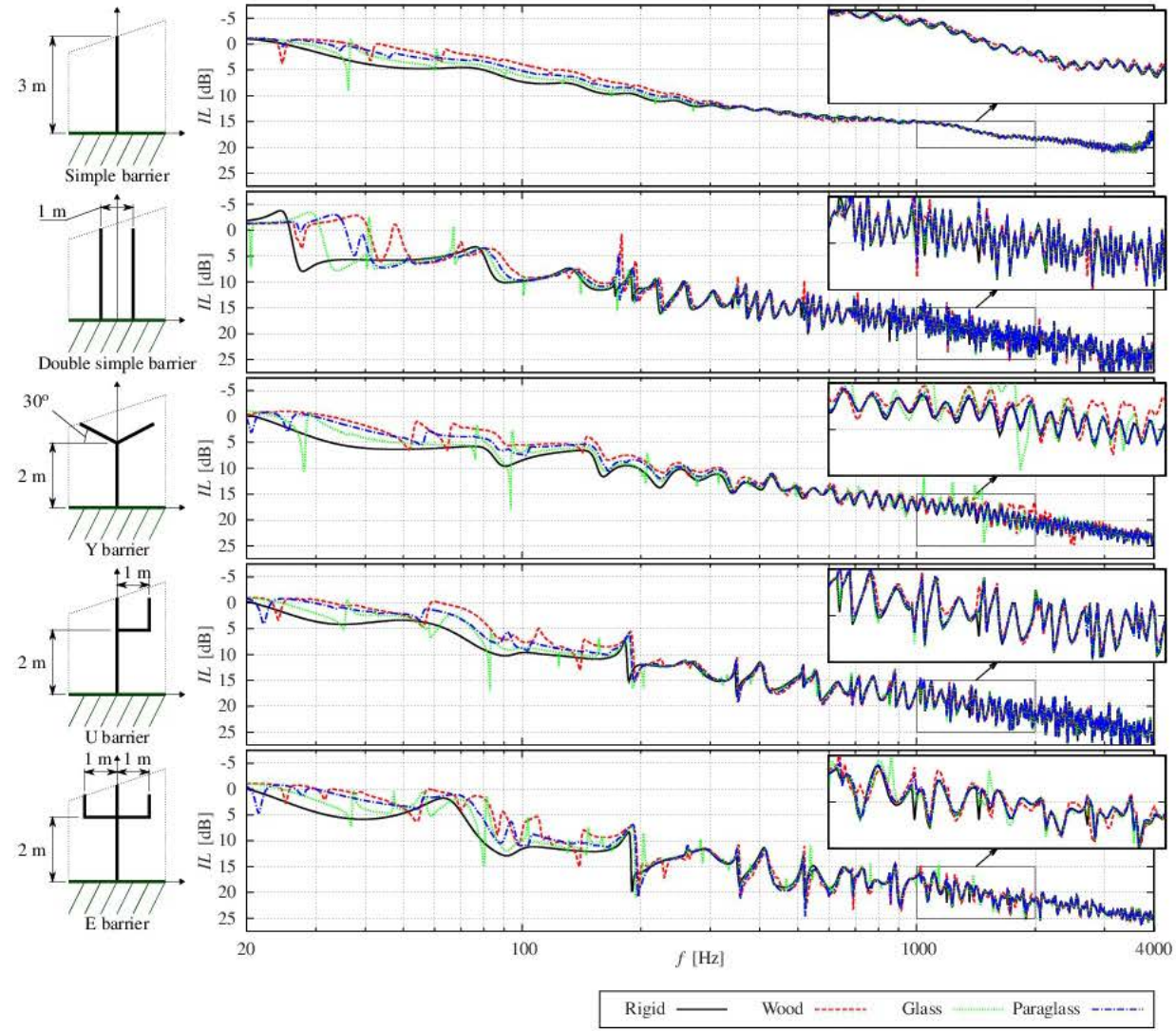
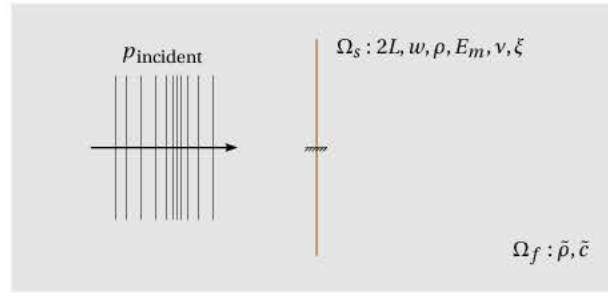Figure 5.5: IL for different barrier shapes and materials

Figure 5.6: Problem layout

Parameter	Studied values
ξ	0.05
ν	0.30
$\tilde{c}/c$	$\{1/50, 1/20, 1/10, 1/5, 1/2, 1/1, 2/1\}$
$\tilde{\rho}/\rho$	$\{1/10^5, 1/10^4, 1/10^3, 1/10^2, 1/10, 1/1, 10/1\}$
L/w	$\{10, 20, 50, 100, 200, 500, 1000\}$
a_0	$[10^{-4}, 10]$

Table 5.2: Studied values of each dimensionless parameter

This parametric study is oriented to know the FSI coupling degree. It seems obvious that a decoupled model could be used for extreme cases, e.g. a thick steel wall in air. In these extreme cases, the pressure field in the air is calculated considering a rigid obstacle, and if needed, the pressure field can be used as the obstacle load. However, there are cases like a thin wall in water, or a thin steel wall in oil, or other similar cases where interaction relevance is not so clear. All dimensionless parameters combinations of Table 5.2 are studied.

Figure 5.7 shows the average relative pressure difference at nodes between a given case and the rigid case. The relative pressure difference is averaged over frequencies. It has been built in order to know if a wall could be considered rigid or not when one is interested in the pressure field. It has been found that the wave velocities ratio has a small influence over it. The densities ratio and the geometrical slenderness strongly influence the average relative pressure differences. The contour lines clearly show that, for a given pressure difference, there is a region where the straight beam can be considered rigid. A rule of thumb can be established: for $L/w < 1000$, if $\tilde{\rho}/\rho < 1/1000$, the straight beam can be considered rigid.

Figure 5.8 shows the $\tilde{\omega}_1/\omega_1$ ratio, where $\tilde{\omega}_1$ is the first natural frequency of the fluid-structure system, and ω_1 is the first natural frequency of the structure in vacuum [193]. It has been built in order to know if the fluid must be taken into account when one is interested in the straight beam behaviour. Analogously to the previous analysis, the wave velocity ratio has a small influence over $\tilde{\omega}_1/\omega_1$. The densities ratio and the geometrical slenderness are the main influences over the variable of interest. The $\tilde{\omega}_1/\omega_1$ ratio is < 1, so the fluids roughly acts as an added mass, as it is well known. The obtained $\tilde{\omega}_1/\omega_1$ contour lines can be used to quantify the fluid influence over the FSI problem.

(a) $\tilde{c}/c = 1/50$

(b) $\tilde{c}/c = 1/20$

(c) $\tilde{c}/c = 1/10$

(d) $\tilde{c}/c = 1/5$

(e) $\tilde{c}/c = 1/2$

(f) $\tilde{c}/c = 1/1$
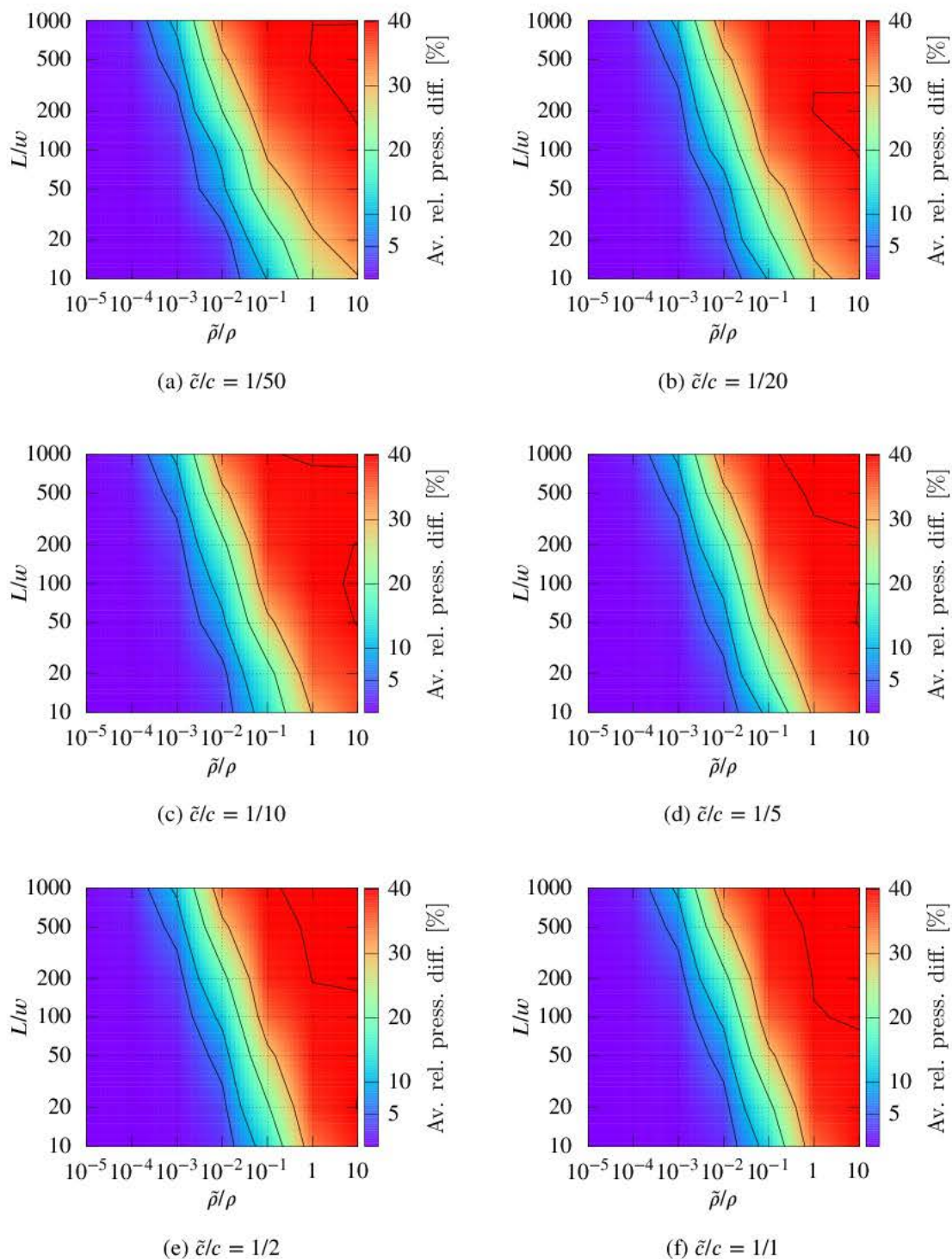
Figure 5.7: Average relative pressure differences between elastic case and rigid case

(a) $\tilde{c}/c = 1/50$

(b) $\tilde{c}/c = 1/20$

(c) $\tilde{c}/c = 1/10$

(d) $\tilde{c}/c = 1/5$

(e) $\tilde{c}/c = 1/2$

(f) $\tilde{c}/c = 1/1$
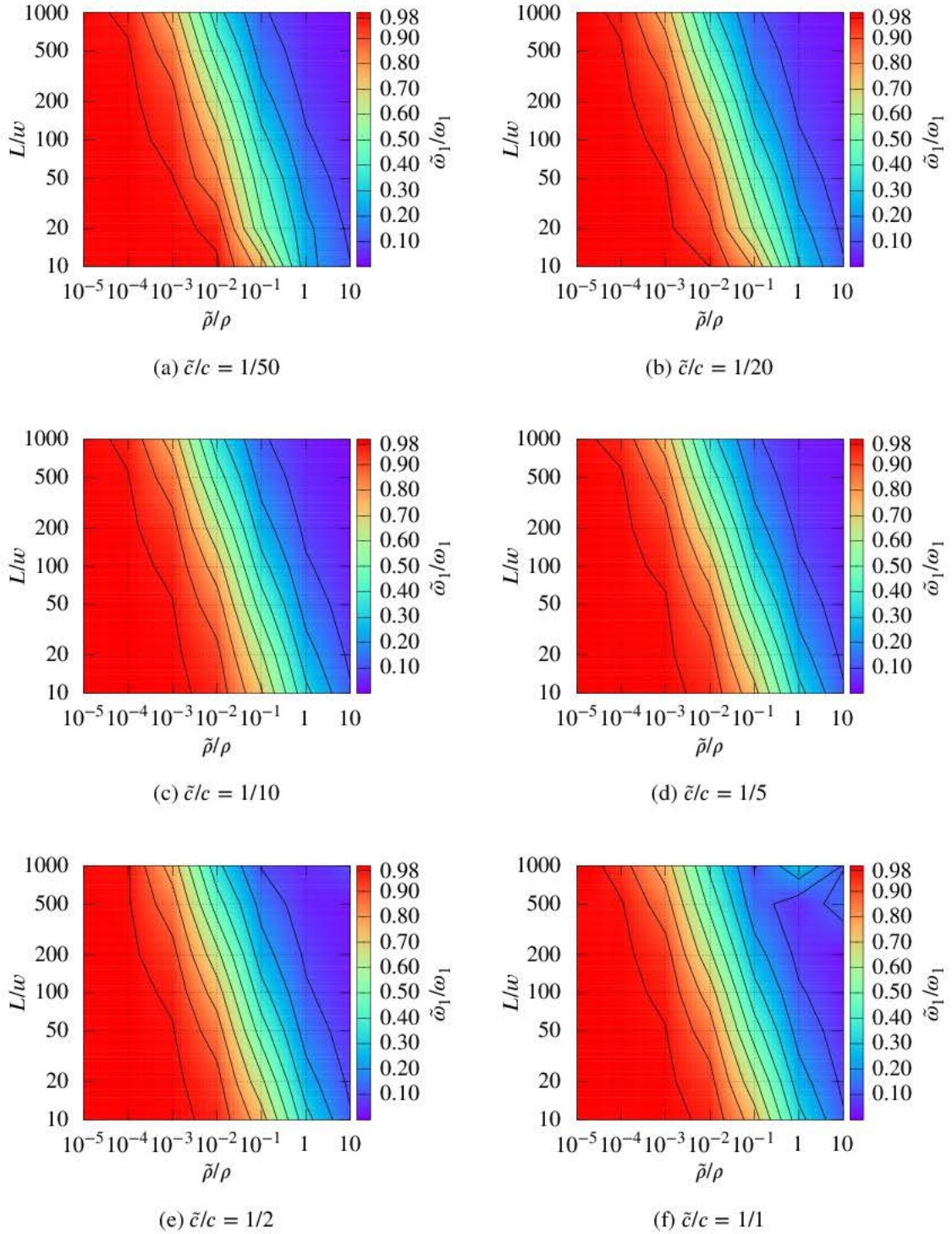
Figure 5.8: First natural frequencies ratio $\tilde{\omega}_1/\omega_1$

5.3 Two-dimensional wave barriers in poroelastic soils

In this section, the vibration isolation effectiveness of two-dimensional totally or partially buried thin walled wave barriers in poroelastic soils is studied. Ground vibrations are considered to be Rayleigh waves propagating on a permeable free-surface, see Appendix E. As in the previous case, the shell is modelled as an equivalent beam ($E_{\text{beam}} = E/(1 - v^2)$), but it is now surrounded by a poroelastic medium. Two different types of coupling of the beam with the surrounding medium appear: with an ordinary boundary (BEM-FEM), and with a crack-like boundary (DBEM-FEM).

Firstly, some results from the classical vibration isolation paper by Beskos et al. [186] are compared to our models as a way of verification of our models. Beskos et al. studied the vibration isolation of open and filled trenches using a two-dimensional conventional elastodynamic BEM model. The problem under consideration is a trench, open or filled with concrete, with a depth to width ratio $d/w = 10$, impinged by waves coming from a footing $5d$ behind the trench, vibrating with a frequency corresponding to a Rayleigh wavelength λ_R equal to the depth d. The elastic soil has a density $\rho = 1785$ kg/m^3, shear modulus $\mu = 132$ MPa, Poisson's ratio $v = 0.25$ and hysteretic damping $\xi = 0.03$. The equivalent poroelastic soil used in our model has a porosity $\phi = 0.001$, fluid density $\rho_f = 0.001$ kg/m^3, solid density $\rho_s = 1785$ kg/m^3, null additional aparent density, solid Lamé's parameters $\mu = \lambda = 132$ MPa, solid phase hysteretic damping $\xi_s = 0.03$, Biot's parameters $R = Q = 0.1$ MPa, and null dissipation coefficient. The concrete for the filled trench barrier has a density $\rho = 2449$ kg/m3, shear modulus $\mu = 4.52628$ GPa, Poisson's ratio $v = 0.25$ and hysteretic damping $\xi = 0.15$.

Fig. 5.9 shows a comparison between their results and our results using the vertical displacement amplitude reduction ratio A_y:

$$A_y(x) = \frac{\left| u_y^{\text{with barrier}}(x, y = 0) \right|}{\left| u_y^{\text{without barrier}}(x, y = 0) \right|} \tag{5.1}$$

For the open trench, we have used an open trench with $d/w = 10$ using a conventional BEM model, but also an open trench with the null width assumption ($d/w \rightarrow \infty$) using the Dual BEM. For the filled trench, we have used a filled trench with $d/w = 10$ using a conventional multidomain BEM model, and also a filled trench using our DBEM-FEM model, i.e. from the soil point of view the trench has null thickness but preserves its structural behaviour. There exist differences between the results of Beskos et al. and our results, although the main tendencies are similar. It is probably due to the fact that they used constant boundary elements and an important truncation of the free-surface mesh, which was also noticed by Ahmad et al. [187]. In both problems, the differences between the results using the real geometry (conventional BEM) and the results using the null width assumption (DBEM) are very small. Therefore, it is justified using the proposed DBEM-FEM model for thin structures ($d/w \leq 10$) in these kinds of problems.

In the following sections, three kinds of wave barrier systems are studied: open trench, simple wall and open trench-wall; see Fig. 5.10. An open trench system is defined by its depth d and width w. Qualitatively, it acts as a perfect reflector where surface waves having a wavelength less than its depth are filtered out. A pure open trench is the perfect solution,
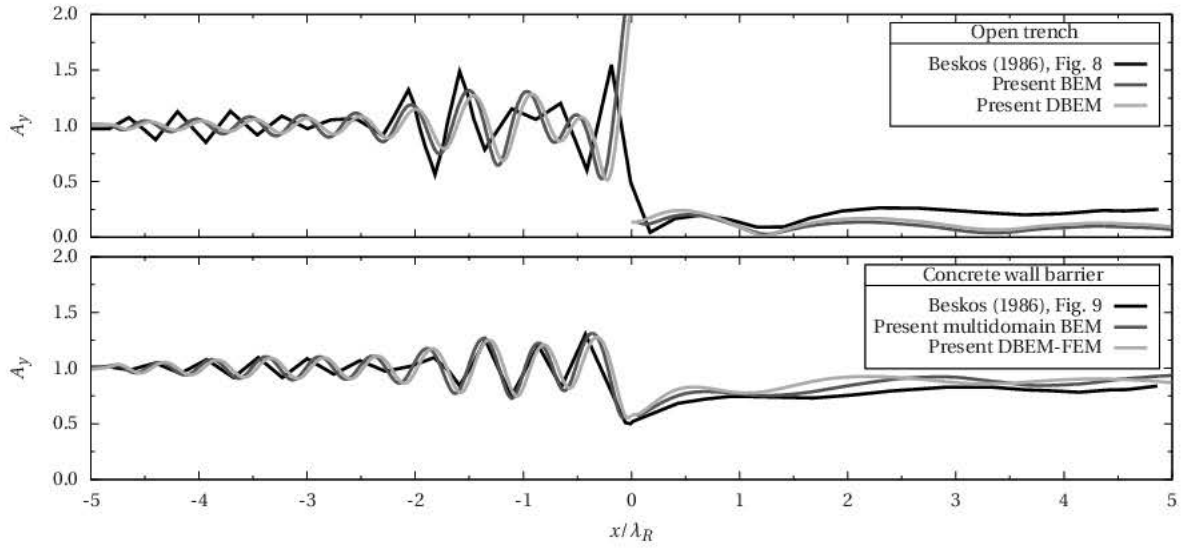
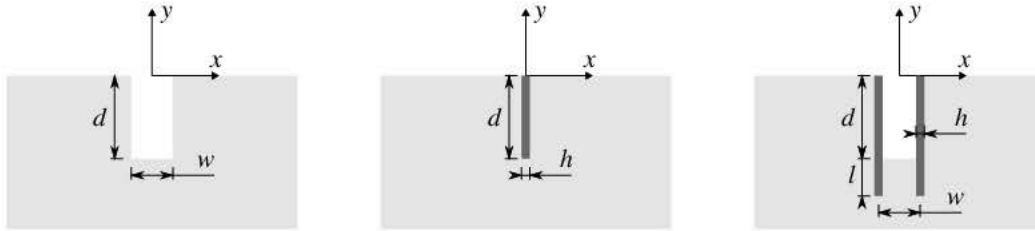Figure 5.9: Comparison with Beskos et al. [186]

Figure 5.10: Wave barrier topologies. Left: open trench. Center: simple wall. Right: open trench-wall.

however, systems using walls are needed in situations where the soil stability is compromised. In this study, we consider a wall characterized by its top view cross-section per unit length, see Fig. 5.11. It is defined by the total width h and the wall thickness t, being $t \leq h$. Hence, the cross-section area is $A = t$ and the inertia is $I = t^3/12 + t(h/2 - t/2)^2$. When $t = h$, it represents exactly a plate with uniform cross-section. When $t < h$, it represents a two-dimensional simplified version of a sheet pile, whose three-dimensional geometry and structural behaviour as a transversely isotropic plate are neglected. This simplification is valid as long as we are interested in far-field variables. A simple wall barrier system is defined by its depth d and wall cross-section. An open trench-wall system is defined by its trench depth d, trench width w, wall cross-section, and wall burial depth l. Hence, these problems are defined by their geometry: d, w, l, h and t; by the properties of their regions: poroelastic soil (ϕ, ρ_f, ρ_s, μ_s, λ_s, ξ_s, Q, R, ρ_a, b) and wall (ρ_b, E_b, ν_b, ξ_b); and by the frequency ω.

For elastic soils, the open trench and the simple wall problems have been extensively studied, whereas the open trench-wall system has been rarely studied [185]. In these cases, each problem is easily nondimensionalized to a small set of parameters of general applicability. Basically, ratios of lengths (d/w, d/h, etc.), Poisson's ratios of the soil ν_s and wall ν_b, ratios
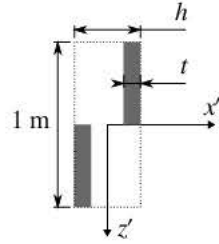
Figure 5.11: Wall cross-section

of densities ρ_s/ρ_b and Young's modulus E_s/E_b between soil and wall, and a dimensionless frequency ω^* defined by using the Rayleigh wave velocity and some length, for example d. However, such a broad study for poroelastic soils is difficult due to the number of properties involved, and the question if a set of values for these properties represents an existing soil or not.

Therefore, in order to obtain realistic results of practical usage, we limit our study to water-saturated sandstones whose properties are based on experimental data. The poroelastic approximation of water-saturated sandstones is taken from [195], although a more general dissipative soil ($b \neq 0$) is considered here. The main hypothesis is the linear relationship between porosity ϕ and solid dry bulk modulus K_s:

$$K_s = K_{cr} + \left(1 - \frac{\phi}{\phi_{cr}}\right)\left(K_g - K_{cr}\right) \tag{5.2}$$

where $K_{cr} = 200\,\text{MPa}$ is the critical bulk modulus for the dry frame, $\phi_{cr} = 0.36$ is the critical porosity and $K_g = 36000\,\text{MPa}$ is the bulk modulus of a solid grain. The critical porosity ϕ_{cr} is the point where the porosity is too large to form a sustainable dry frame. Several porosities and Poisson's ratios are considered: $\phi = \{0.10, 0.20, 0.30\}$ and $v_s = \{0.20, 0.30, 0.40\}$. Thus, Lamé parameters are $\lambda_s = (3v_s)/(1 + v_s)K_s$ and $\mu_s = [3(1 - 2v_s)]/[2(1 + v_s)]K_s$. The density of the solid phase is $\rho_s = 2650\,\text{kg/m}^3$, and the damping ratio is null ($\xi_s = 0$). The fluid phase (water) properties are $K_f = 2000\,\text{MPa}$ and $\rho_f = 1000\,\text{kg/m}^3$. The Biot's coupling parameters Q and R are:

$$Q = \phi\frac{1 - \phi - K_s/K_g}{(1 - \phi - K_s/K_g) + \phi K_g/K_f}K_g, \quad R = \frac{\phi^2}{(1 - \phi - K_s/K_g) + \phi K_g/K_f}K_g \tag{5.3}$$

Berryman's model for the additional aparent density [52] is used assuming spherical grains: $\rho_a = (1 - \phi)\rho_f/2$. The dissipation coefficient is $b = \rho_f g\phi^2/\kappa$, where κ is the hydraulic conductivity. In order to present a dimensionless problem, a dimensionless dissipation coefficient $b^* = bd/\sqrt{\mu_s\rho}$ is defined, where $\rho = \phi\rho_f + (1 - \phi)\rho_s$ is the bulk density. Also, it is necessary to use a dimensionless frequency ω^*. One representing the ratio between the barrier system depth and the Rayleigh wavelength $\omega^* = d/\lambda_{R0} = (\omega d)/(2\pi c_{R0})$ is defined, where c_{R0} is the wave velocity of the Rayleigh waves assuming $b = 0$. Assuming a typical barrier depth $d \sim 5$ m, and taking into account that $\kappa \in [10^{-6}, 10^{-2}]$ m/s (see [195, Fig. 1]), $\phi \in [0.10, 0.30]$ and $v \in [0.20, 0.40]$, an appropriate set of values for the dimensionless dissipation coefficient is

$b^* = \{0, 0.2, 5, 100, 2000\}$. For the dimensionless frequency, a suitable range $\omega^* \in [0.5, 1.5]$ is used. The thin walls are considered made of steel: $\rho_b = 7850\,\text{kg/m}^3$, $E_b = 210\,\text{GPa}$, $\nu_b = 0.30$, $\xi_b = 0.05$.

All the boundaries in contact with air are considered permeable, and given that the bulk modulus of the air is much more lower than any of the porous media, the fluid dynamic stress τ and the solid stresses τ_{ij} can be considered null at those boundaries. Specifically, these boundaries are the free-surface of the half-space and the bottom of the open trench-wall.

The isolation effectiveness of each configuration is measured by using the average vertical displacement amplitude reduction ratio $\bar{A}_y$:

$$\bar{A}_y = \frac{1}{10\lambda_{R0} - a/2} \int_{a/2}^{10\lambda_{R0}} A_y(x)\,dx \tag{5.4}$$

where $a = w$ for the open trench and open trench-wall, and $a = 0$ for the simple barrier. It synthesizes the behaviour of $A_y(x)$ along the shadow zone of the wave barrier up to $10\lambda_{R0}$, as suggested by Ahmad et al. [187].

5.3.1 Open trench

Three geometrical configurations of the open trench are studied: $d/w = \{1, 2, 10\}$; which correspond to a very wide, wide and narrow open trenches, respectively. Although it does not use any of the new features proposed here, it seems mandatory since, to the authors' knowledge, previous results about this problem does not exist in the literature.

Fig. 5.12 shows $\bar{A}_y$ response for the ranges of variation of porosity ϕ, Poisson's ratio ν_s, dimensionless dissipation coefficient b^*, and dimensionless frequency ω^*, for the wide trench ($d/w = 2$). The main behaviour of open trenches in poroelastic soils are similar to those in elastic soils. The dimensionless frequency $\omega^* = d/\lambda_R = 1$ is a key point. Below this frequency, the effectiveness gets worse increasingly, and above it, the effectiveness improves up to a maximum effectiveness, approximately constant for $\omega^* > 1.2$. In most cases, the Poisson's ratio has a small influence on $\bar{A}_y$ when $\omega^* > 0.8$. It becomes more important when the porosity is near ϕ_{cr} and the dimensionless dissipation coefficient is $b^* < 1$. The dimensionless dissipation coefficient b^* has a very small influence on $\bar{A}_y$ for $b^* > 5$. For $b^* < 5$, b^* becomes more influential when the porosity approaches ϕ_{cr}.

Fig. 5.13 shows $\bar{A}_y$ responses for the different d/w ratios, when $\nu_s = 0.30$ and $b^* \leq 5$. In general terms, the smaller d/w ratio the more efficient is the open trench, which is physically obvious. The influence of d/w increases as ω^* decreases, especially when $\omega^* < 0.6$. When $\omega^* > 1.2$, although differences exist, they are less important given the high effectiveness ($\bar{A}_y < 0.05$) of all the studied d/w ratios. The influence of the porosity ϕ and the dissipation coefficient b^* is similar for the different studied d/w ratios.

5.3.2 Simple barrier

The simple barrier is studied for three depth to cross-section width ratios: $d/h = \{10, 20, 100\}$; and each of them for four cross-section width to wall thickness ratios: $h/t = \{1, 6, 10, 20\}$.
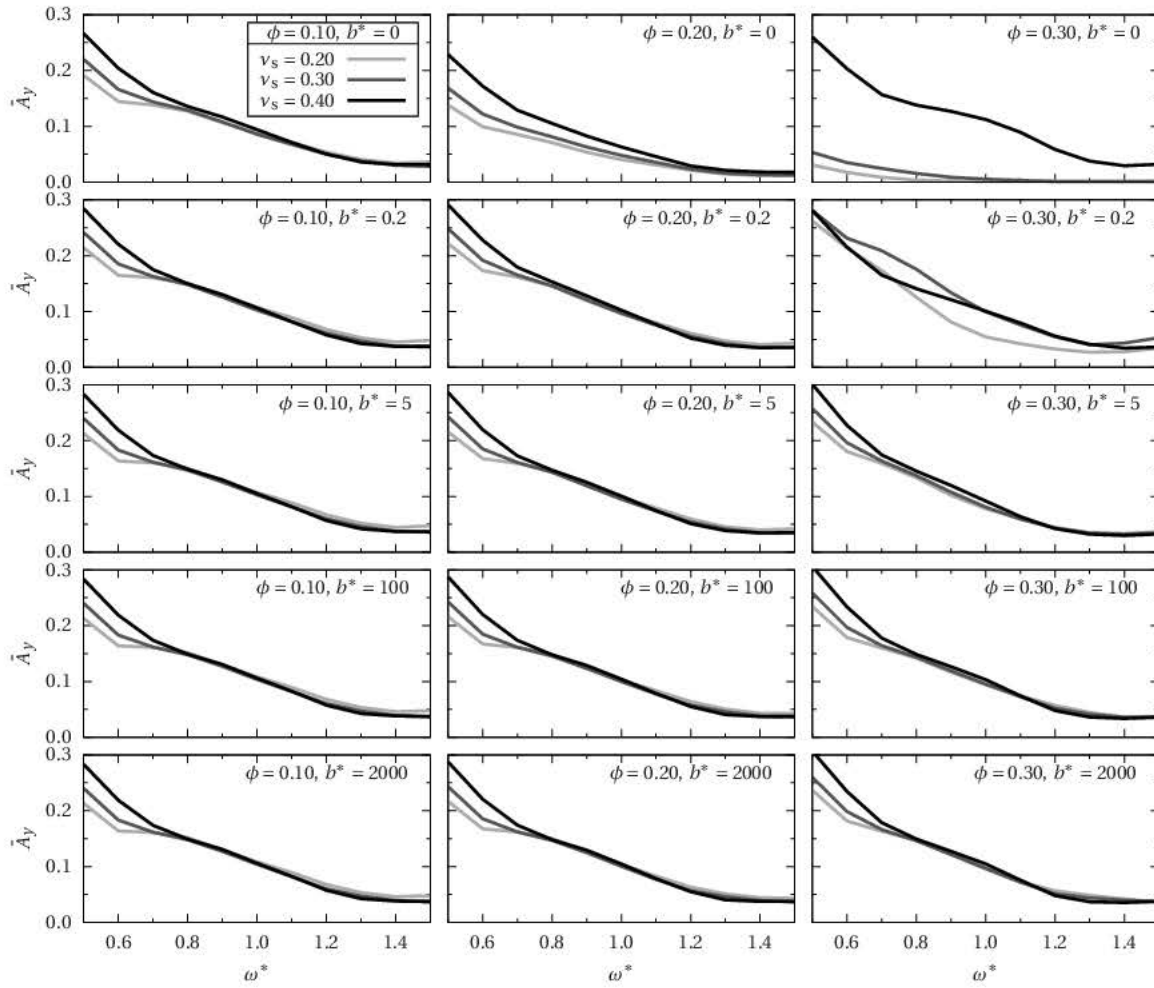
Figure 5.12: $\bar{A}_y$ response for open trench $d/w = 2$

Except for the average effectiveness level, which is much more lower, the influence of soil properties over the $\bar{A}_y$ response for simple barriers are similar to those of open trenches. Therefore, in order to compare the influence of the wall configuration, the soil properties are fixed to: $\phi = 0.20$, $b^* = 0.2$, $\nu_s = 0.30$. These problems are solved using the proposed DBEM-FEM coupling. Hence, the soil sees a null thickness barrier which maintains its effective structural response. Additionally, the real three-dimensional behaviour of cross-sections with $h/t \neq 1$ is approximated by a two-dimensional behaviour, which is a valid assumption as long as we are not concerned about near-field variables.

Fig. 5.14 shows $\bar{A}_y$ response for different d/h and h/t ratios. For the studied range of ω^*, the effectiveness of the simple barrier is much more lower than the effectiveness of any open trench. While the open trench acts as a perfect reflector, the simple barrier partially converts surface waves into body waves. As pointed out by Ahmad et al. [187, Fig. 12], the effectiveness of this type of barriers depends mostly on the wall area $d \cdot t$. In order to show this relationship for the present study, Fig. 5.15 has been built using the $\bar{A}_y$ analysis
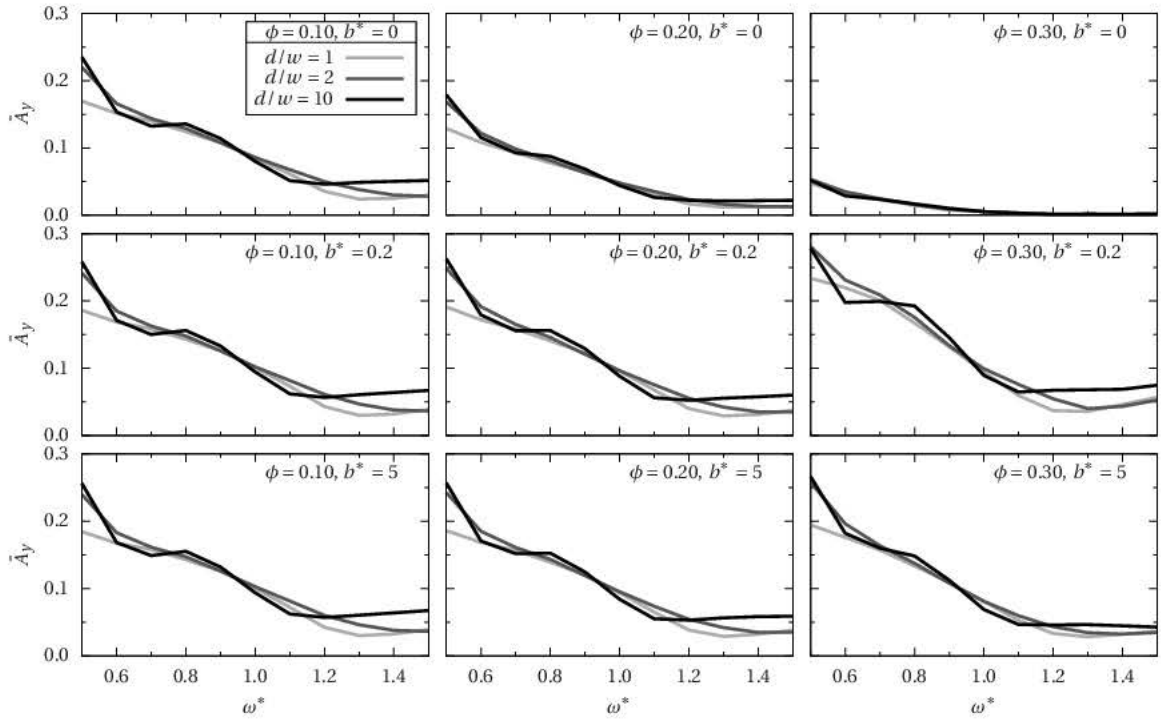
Figure 5.13: $\bar{A}_y$ comparison between open trenches with different d/w ratios ($\nu_s = 0.30$)
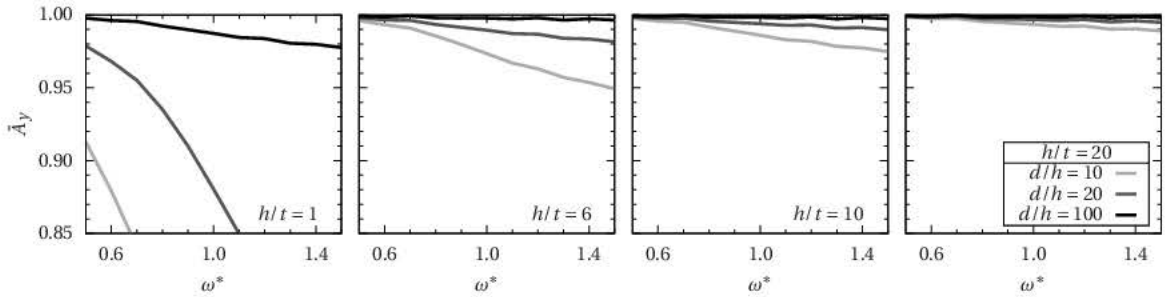
Figure 5.14: $\bar{A}_y$ comparison between simple barriers with different d/h and h/t ratios ($\phi = 0.20$, $b^* = 0.2$, $\nu_s = 0.30$)

points of all cases shown in Fig. 5.14 in ordinates, and a dimensionless area $(d/\lambda_{R0})(t/\lambda_{R0}) = (\omega^*)^2(h/d)(t/h)$ in abscissas. The left graph shows a global picture of the results, and the right graph shows a detailed view of the results for smaller cross-sections. Although the observed slope is different for each specific cross-section, it is shown that, as found by Ahmad et al., a roughly linear relationship exists between the effectiveness and the dimensionless area.

5.3.3 Open trench-wall

The open trench-wall is studied for three depth to width ratios: $d/w = \{1, 2, 10\}$; three wall burial depth to trench depth ratios: $l/d = \{0, 0.25, 0.50\}$; three trench depth to cross-section

Figure 5.15: $\bar{A}_y$ comparison between simple barriers using the dimensionless area in abscissas ($\phi = 0.20$, $b^* = 0.2$, $v_s = 0.30$)

width ratios: $d/h = \{10, 20, 100\}$; and four cross-section width to wall thickness ratios: $h/t = \{1, 6, 10, 20\}$. The influence of the dimensionless dissipation coefficient b^* and the Poisson's ratio v_s is similar to that of the open trenches, i.e. their influence is relatively small, thus $b^* = 0.2$ and $v_s = 0.30$ are assumed. These problems are solved using both the BEM-FEM and DBEM-FEM couplings, being the BEM-FEM coupling applied to the retaining part of walls, and the DBEM-FEM coupling applied to the buried part of the walls.

Fig. 5.16 has been built in order to assess the influence of the wall and its burying in the soil over $\bar{A}_y$. For all cases, the depth to cross-section width ratio is $d/h = 20$, and the 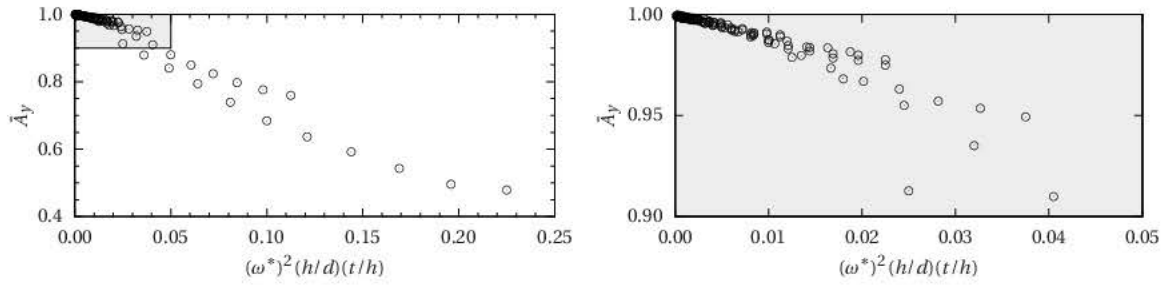cross-section width to wall thickness ratio is $h/t = 1$. The figure contains 3×3 graphs, where each column corresponds to a different porosity ϕ, and each row to a different depth to width d/w ratio. Each graph contains four curves corresponding to the open trench case and the open trench-wall case with three different wall burial depth to trench depth l/d ratios. For a given ϕ and d/w ratio, the differences between the open trench and the open trench-wall for $l/d = 0$ are small for $\omega^* > 1$, but for $\omega^* < 1$ the open trench-wall is slightly more efficient. For the other values of the l/d ratio, $\bar{A}_y$ gets worse, especially for $\omega^* < 1$. The smaller the porosity, the smaller $\bar{A}_y$ differences between the open trench and the open trench-wall for any l/d ratio. Likewise, the smaller the d/w ratio, the smaller the $\bar{A}_y$ differences between both kinds of wave barriers.

Fig. 5.17 contains graphs comparing the $\bar{A}_y$ response of configurations with different l/d ratios and different cross-sections. For all cases, the porosity is $\phi = 0.20$, and the depth to width ratio is $d/w = 2$. Each column corresponds to a different d/h ratio, and each row correspond to a different l/d ratio. Four curves are drawn on each graph, one corresponding with the open trench, and three corresponding with $h/t = \{1, 6, 20\}$. It is seen that the open trench-wall converges to the open trench as d/h and h/t increase, as it should be. The cross-sections corresponding with a plate with uniform thickness ($h/t = 1$) have a considerable impact on $\bar{A}_y$, increasing the effectiveness for $\omega^* < 1$ and $l/d = 0$, but decreasing it in the rest of the cases. The cross-sections associated with the sheet pile idealization have a small influence on the effectiveness when compared with the open trench.

Figure 5.16: $\bar{A}_y$ comparison between open trench and open trench-wall for different ϕ, d/w and l/d ratios ($b^* = 0.2$, $v_{\rm s} = 0.30$, $d/h = 20$, $h/t = 1$)

5.3.4 Concluding remarks

The open trench, simple wall and open trench-wall are studied varying their geometry, soil properties and frequency. The soil is assumed to be a sandstone following a linear relationship between porosity and solid dry bulk modulus. In the study, several values of porosity ϕ, Poisson's ratio $v_{\rm s}$ and dimensionless dissipation coefficient b^* are considered. From the point of view of isolation efficiency of all wave barriers, it is found that the porosity ϕ is relevant when is near the critical porosity $\phi_{\rm cr}$ and the dimensionless dissipation coefficient is $b^* < 5$. Also, results do not vary significantly beyond $b^* > 5$, and Poisson's ratio $v_{\rm s}$ becomes relevant only for dimensionless frequency $\omega^* < 0.8$. Qualitatively, the open trench and the simple wall (thin in-filled trench) behave similarly to those in elastic soils, except for high porosities and small dimensionless dissipation coefficients. For the evaluation of the isolation efficiency of an open trench-wall, it is found that the influence of the walls can be ignored if they are typical sheet piles, and if the dimensionless frequency ω^* lies between 0.5 and 1.5. This is not the case when walls with bigger cross-sections are used, leading in general to an efficiency loss. Wall burial depths $l/d > 0$ lead to efficiency losses, especially for high porosities and low dimensionless frequencies $\omega^* < 1$.
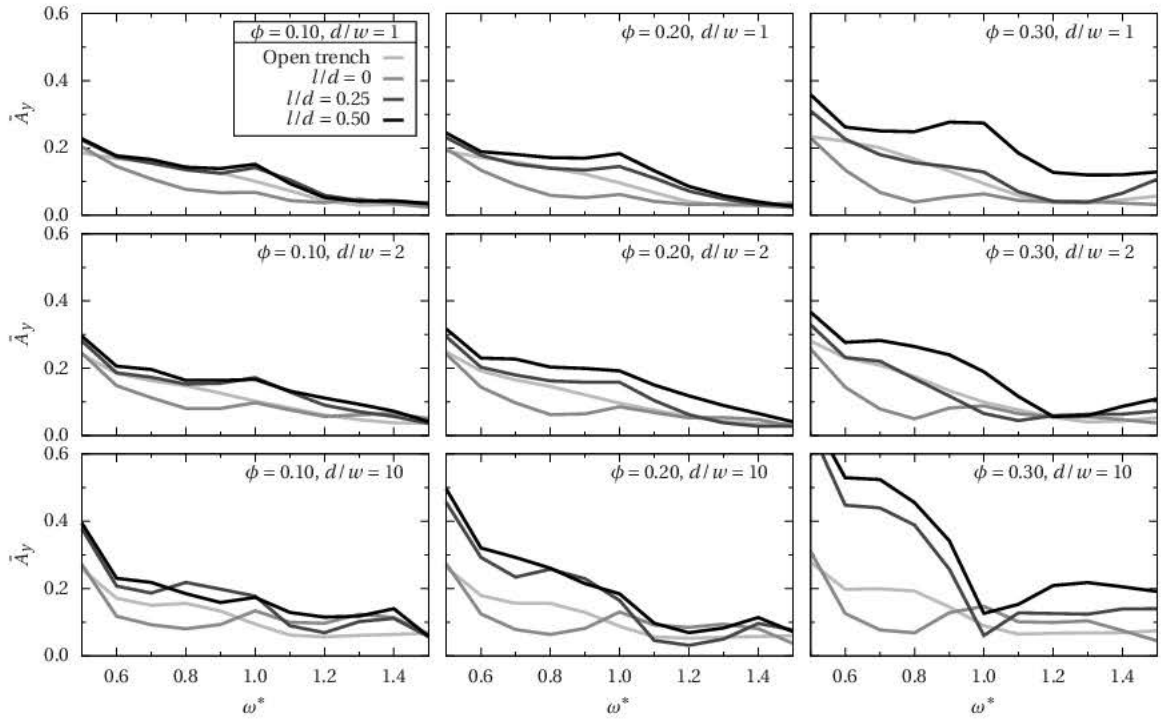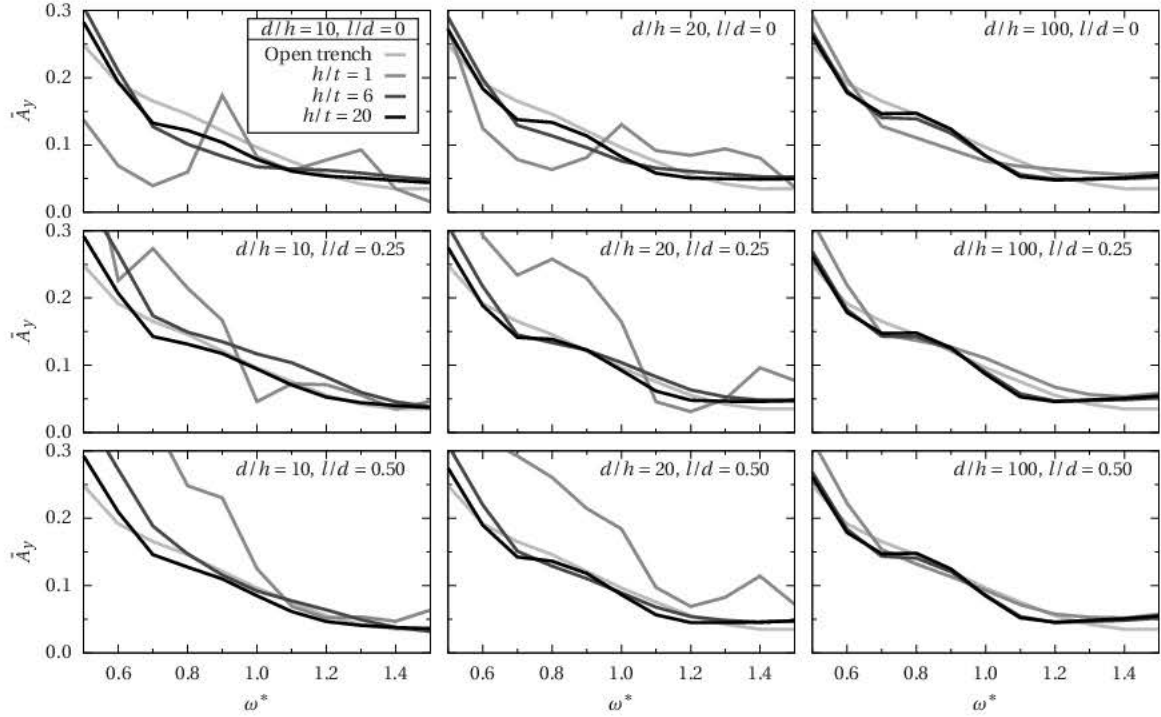
Figure 5.17: $\bar{A}_y$ comparison between open trench and open trench-wall for different d/h, l/d and h/t ratios ($\phi = 0.20$, $b^* = 0.2$, $\nu_s = 0.30$, $d/w = 2$)

5.4 Three-dimensional wave barrier

In this section, the three-dimensional DBEM–FEM dynamic model is used in a wave diffraction problem, and compared against a multi-region BEM model [14, 17]. A curved vibration isolation wall buried in a poroelastic half-space under a Rayleigh wave field is considered. The wall has a radius of 6 m, a depth of $H = 4$ m, covers an angle of $90°$, and different thicknesses $t = \{0.80, 0.40, 0.08, 0.04\}$ m are studied. Thus, slendernesses ranging from $H/t = 5$ to $H/t = 100$ are analysed. The wall is considered to be made of concrete with density $\rho = 2400$ kg/m^3, shear modulus $\mu = 6.5$ GPa, Poisson's ratio $\nu = 0.15$, and hysteretic damping ratio $\xi = 0.05$, where the complex shear modulus used is $\mu^* = (1 + i2\xi)\mu$. The poroelastic half-space has the following properties taken from Kassir et al. [196]: $\rho_f = 1000$ kg/m^3, $\rho_s = 1425$ kg/m^3, $\lambda = \mu = 32.18$ MPa, $\phi = 0.35$, $\rho_a = 0$ kg/m^3, $R = 248$ MPa, $Q = 461$ MPa, $b = 1.1986 \cdot 10^7$ N $\cdot$ s/m^4; and the free-surface is permeable, i.e. $\tau = t_k = 0$ at $z = 0$. As a source of vibrations, an incident Rayleigh wave field with unitary vertical displacements is impinging along the x-axis at $f = 50$ Hz, see Appendix E. Since the zx-plane is a symmetry plane, only one-half of the domain is discretised and appropriate symmetry conditions are thus enforced.

    Figure 5.18 shows an example of multi-region BEM and DBEM–FEM meshes, where it can be observed the simplicity of the latter. At the wall, there are two conforming meshes in the DBEM–FEM model: a BE mesh with crack boundary elements representing the soil-wall interface, and a FE mesh with shell finite elements representing the wall. For each

Soil - wall: coupled ordinary BE - BE

(a) Multi-region BEM example mesh

Soil - wall: coupled crack BE - shell FE

(b) DBEM-FEM example mesh

Figure 5.18: Curved wall barrier (models with one-half symmetry)

thickness, the multi-region BEM model requires a new discretisation, while the DBEM-FEM model only requires changing the shell thicknesses. The multi-region BEM model requires some control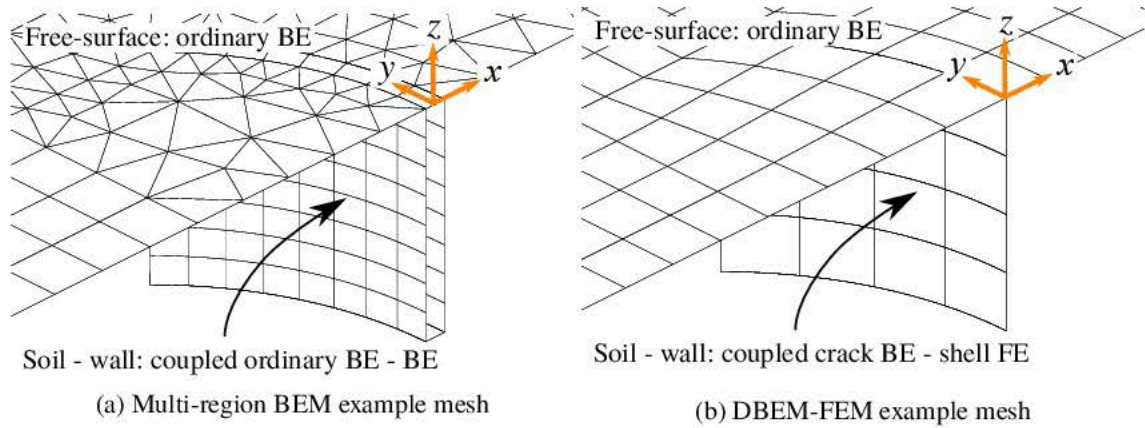 of the element size with respect to the thickness in order to avoid integration and conditioning problems. Also, due to the presence of the geometrical details of the wall, more degrees of freedom are required for the wall edges and the free-surface near the wall, especially for small thicknesses. Since the DBEM–FEM model does not require different meshes for different wall thicknesses, they can be changed without needing to build the whole linear system of equations for each case, but only the stiffness and mass matrices.

Figures 5.19 and 5.20 show respectively far-field and near-field results for all thicknesses, which are arranged in columns. Figure 5.19 shows Amplitude Reduction ratios in x and z directions ($AR_j = \text{abs}(u_j/u_j^{\text{incident}})$) along the x-axis for $y = z = 0$. Figure 5.20 shows displacements, fluid equivalent stress and tractions along the depth of the outer face of the wall, i.e. along the z-axis for $y = 0$ and $x = t/2$ (multi-region BEM) and $x = 0^+$ (DBEM–FEM).

Multi-region BEM meshes are similar to that shown in Figure 5.18, where a mesh of 11×11, 8×8, 8×8 and 8×8 nine-node quadrilateral boundary elements are used for the faces of the wall with respectively $t = 0.04, 0.08, 0.4$ and 0.8 m. The criteria to mesh the wall and its surroundings have been: a) at least six elements per wavelength, and b) elements of lengths up to ten times the wall thickness. Two DBEM–FEM meshes are considered: (1) soil and wall discretised with a mesh of 8×8 nine-node quadrilateral crack boundary elements and MITC9 shell finite elements, and (2) with a coarse mesh of only 4×4 elements.

Results show the convergence of the DBEM-FEM model when $H/t \to \infty$, having excellent agreement for slendernesses $H/t \geq 10$. Nevertheless, the DBEM–FEM model is able to roughly capture the response even for the case of slenderness $H/t = 5$. Results regarding Amplitude Reduction ratios clearly show that in the DBEM–FEM model interaction is happening on the wall mid-surface rather than on the real boundaries of the wall. It is able to reproduce the displacement field, although with a spatial shift that depends on the thickness of the shell structure. This approximation may or may not be acceptable depending on the application at hand. Results along the outer face of the wall demonstrate that even near-field results
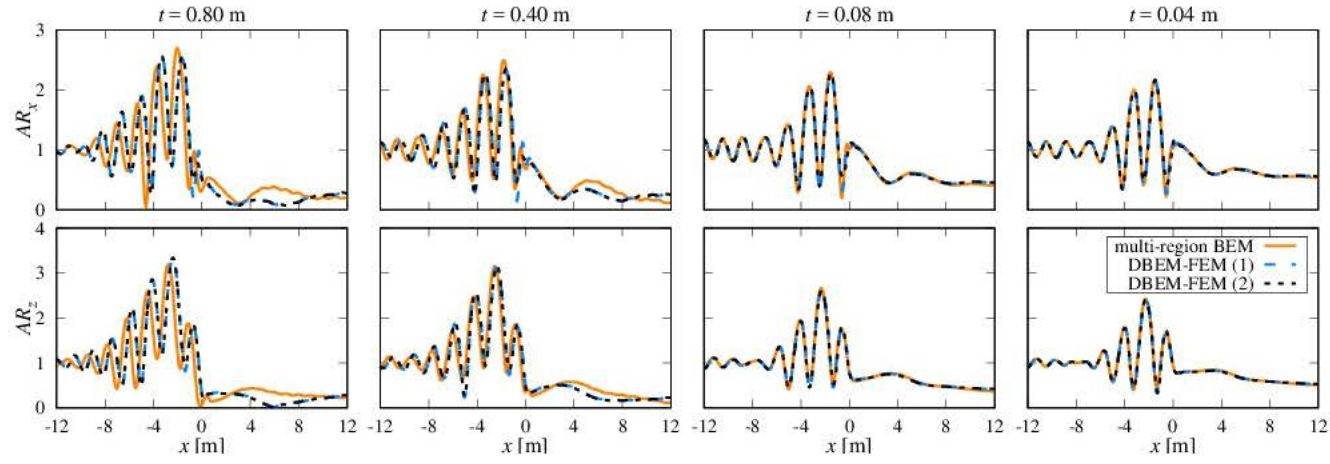
Figure 5.19: Amplitude Reduction of horizontal (AR_x) and vertical (AR_z) solid displacements along the free-surface at $y = z = 0$. Rayleigh incident wave with unitary vertical displacements at $f = 50$ Hz.
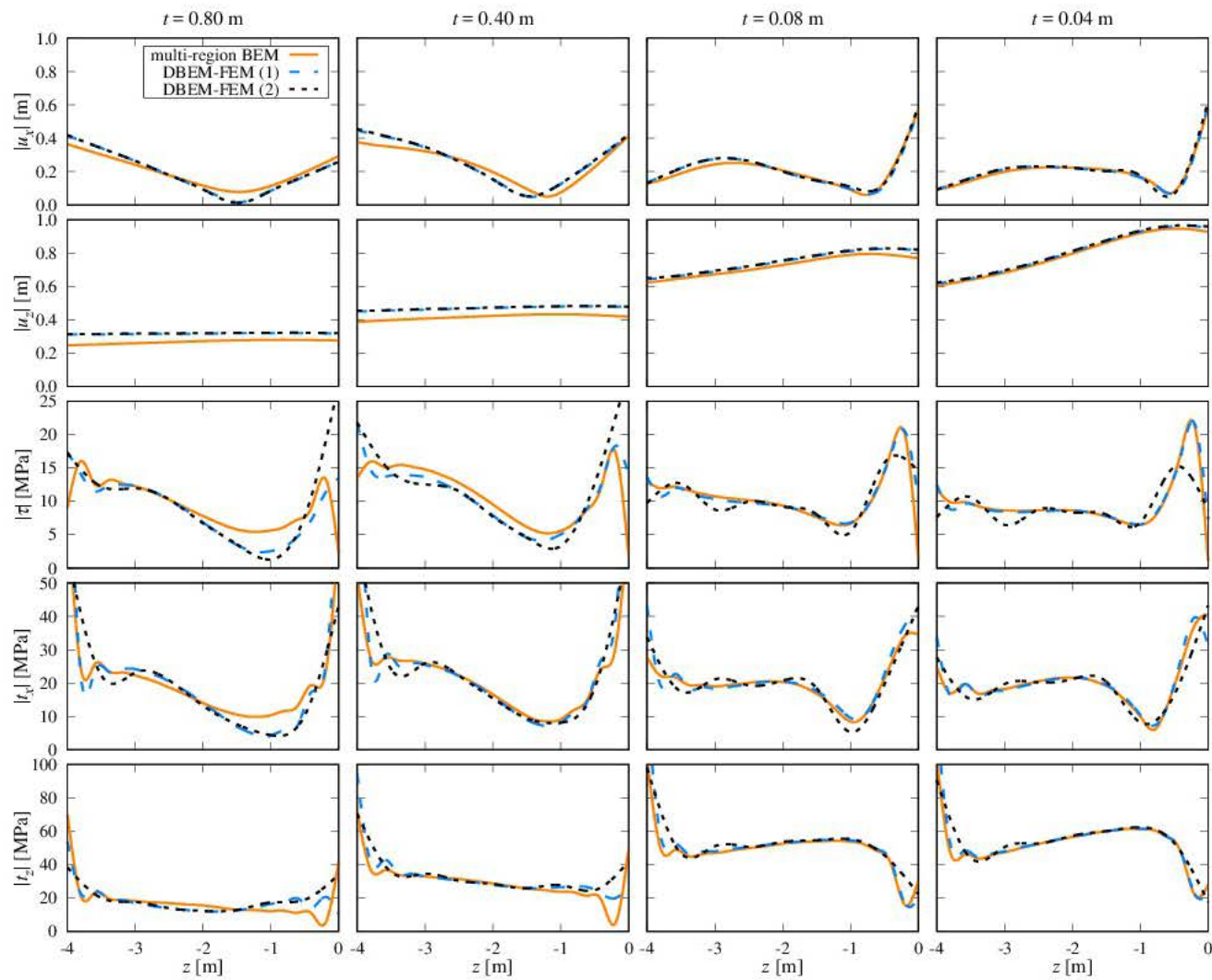
Figure 5.20: Displacements u_x and u_z, fluid equivalent stress τ, and solid tractions t_x and t_z along the outer face of the wall. Rayleigh incident wave with unitary vertical displacements at $f = 50$ Hz.

Mesh	N_{DOF}	t_{build} [s]	t_{solve} [s]	t_{total} [s]
BEM / $t = 0.04$ m	39851	207	175	382
BEM / $t = 0.08$ m	35729	175	128	303
BEM / $t = 0.40$ m	34177	158	113	271
BEM / $t = 0.80$ m	34161	158	112	270
DBEM–FEM (1)	32935	151	101	252
DBEM–FEM (2)	29623	125	75	200

Table 5.3: Computation times for solving the wave diffraction problem

are in good agreement with those of the multi-region BEM model. Differences are mainly found near the edges, although these become appreciable only for the smaller slendernesses. Coarse DBEM-FEM mesh (2) gives almost identical results than the fine DBEM-FEM mesh (1) regarding results along the free-surface. However, there are small differences on the fluid equivalent stress and solid tractions along the wall, being appreciable near the edges for the smaller slendernesses.

Table 5.3 shows computation times when solving the problem for each wall thickness and mesh using a 28×2.6 GHz workstation. Computation times for DBEM–FEM meshes correspond to the solution of the problem for one individual thickness. Despite the additional costs of evaluating the HBIE, the building time of DBEM–FEM models is only moderately affected when comparing multi-region BEM and DBEM–FEM meshes. More important is the fact that the DBEM–FEM intrinsically leads to a considerable reduction of the number of degrees of freedom, which is what greatly decrease the total computation time. This is clearly more advantageous as the wall thickness reduces, where the approximation introduced by the DBEM–FEM model is also less relevant.

5.5 Optimisation of two-dimensional wave barriers

In this section, the problem under consideration is the shape optimization of a wave barrier system located within a square design domain $[d_1^{min}, d_1^{max}] \times [d_2^{min}, d_2^{max}]$. The design domain is between a point source located at $\mathbf{x}^s$ and a point receiver located at $\mathbf{x}^r$, both of them at the half-plane free-surface, see Fig. 5.21. The half-plane (soil) and the barrier system are homogeneous, isotropic, linear elastic solids with bonded contact conditions. Time harmonic analyses are used to measure the performance of the wave barrier, which is given in terms of insertion losses at the receiver location:

$$IL(f, \mathbf{x}^r) = 20 \log_{10} \left(\frac{\sqrt{\left|u_1^{wob}(f, \mathbf{x}^r)\right|^2 + \left|u_2^{wob}(f, \mathbf{x}^r)\right|^2}}{\sqrt{\left|u_1^{wb}(f, \mathbf{x}^r)\right|^2 + \left|u_2^{wb}(f, \mathbf{x}^r)\right|^2}} \right) \tag{5.5}$$

where u_k denotes displacement components, superscript wob stands for "without barrier", superscript wb stands for "with barrier", and f is a frequency (in Hz).

The problem at hand is a non-convex non-linear constrained optimization which can be formulated as:

$$\min_{\mathbf{a}} \quad \chi \tag{5.6a}$$

$$\text{s.t.} \quad a_j^{\min} \leq a_j \leq a_j^{\max}, \, j = 1, \ldots, N_{\text{dv}} \qquad \text{(bounds)} \tag{5.6b}$$

$$d_k^{\min} \leq p_k^{(q)} \leq d_k^{\max}, \, k = 1, 2, \, q = 1, \ldots, N_{\text{gp}} \qquad \text{(design domain)} \tag{5.6c}$$

$$g_m \leq 0, \, m = 1, \ldots, N_{\text{c}} \qquad \text{(compatibility)} \tag{5.6d}$$

$$A \leq A^{\max} \qquad \text{(economic)} \tag{5.6e}$$

where three different types of objective functions are considered:

$$\chi = \chi^{\text{s}} = -IL\left(f^{\text{opt}}, \mathbf{x}^{\text{r}}\right) \tag{5.7}$$

$$\chi = \chi^{\text{avg}} = -\frac{1}{N_{\text{f}}} \sum_{i=1}^{N_{\text{f}}} IL\left(f_i^{\text{opt}}, \mathbf{x}^{\text{r}}\right) = -\overline{IL}\left([f_1^{\text{opt}}, f_{N_{\text{f}}}^{\text{opt}}], \mathbf{x}^{\text{r}}\right) \tag{5.8}$$

$$\chi = \chi^{\text{mm}} = \max_{i=1,\ldots,N_{\text{f}}} -IL\left(f_i^{\text{opt}}, \mathbf{x}^{\text{r}}\right) = -\check{IL}\left([f_1^{\text{opt}}, f_{N_{\text{f}}}^{\text{opt}}], \mathbf{x}^{\text{r}}\right) \tag{5.9}$$

Four types of constraints are defined: Eq. (5.6b) establishes the design variables bounds, Eq. (5.6c) limit the parametrized geometry points within the design domain, Eq. (5.6d) establishes the geometric compatibility constraints, and finally Eq. (5.6e) imposes an economic constraint by limiting the barrier area (amount of material). Regarding objective functions, the first type of objective function defined by Eq. (5.7) is the insertion loss at a receiver point $\mathbf{x}^{\text{r}}$ for a given frequency f^{opt}, where a change in sign is used in order to formulate a minimization problem. This objective function focuses on obtaining an optimized wave barrier for a very well defined single-frequency source. The second type of objective function defined by Eq. (5.8) is an average insertion loss for a given set of N_{f} frequencies, which aims obtaining an optimized wave barrier for a broadband source. The third type of objective function defined by Eq. (5.9) represents the worst insertion loss within a a given set of frequencies, whose aim is to obtaining a wave barrier appropriate for a harmonic source within a frequency range.

In order to solve the considered optimization problem, MATLAB© [197] is used. For objective functions of Eqs. (5.7) and (5.8), the function `fmincon` with the `sqp` algorithm is used, i.e. a Sequential Quadratic Programming method. For objective function indicated by Eq. (5.9), the function `fminimax` is used. The gradient of the objective function is supplied by using the the chain rule and the displacements sensitivities obtained from the Geometric Sensitivity BEM analyses.

In this problem many local minima may appear, and it is not possible to guarantee that the best local minima found is in fact the real global minima. To overcome this issue, a simple multi-start procedure [198] is used. To do so, randomly generated feasible starting points are studied until the difference between the number of expected local minima (Proposition 2 in [198]) and the number of different local minima found is below a tolerance (0.2 is chosen), or until the number of starting points studied is greater than an established maximum (50 is
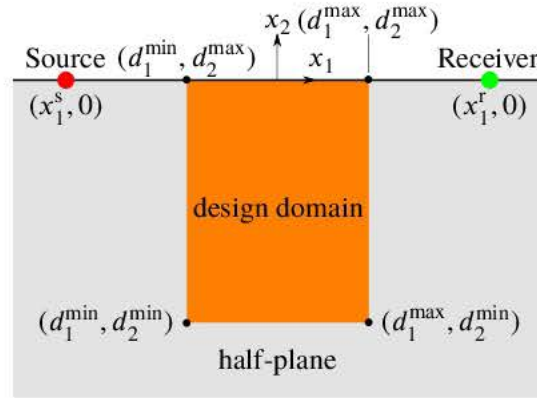
Figure 5.21: Problem layout

(a) Single wall barrier

(b) Double wall barrier
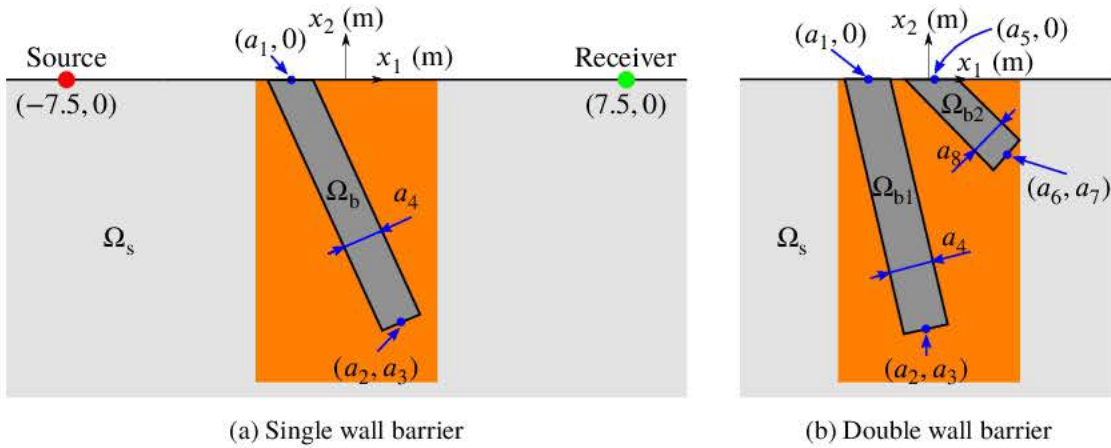
Figure 5.22: Studied wave barrier topologies located inside a design domain of 5 m × 8 m (in orange)

chosen). As Rinnooy Kan et al. [198] discussed, it is very interesting to note that, based on Bayesian analysis, the number of starting points to be studied depends on previously found local minima, and not on the dimension of the problem.

Two wave barrier topologies are studied: a single wall barrier, and a double wall barrier. Figure 5.22 shows the general setting and the wave barrier topologies together with the corresponding design variables.

Source and receiver are 15 meters apart ($\mathbf{x}^s = (-7.5, 0)$, $\mathbf{x}^r = (7.5, 0)$), and the design domain is 5 meters wide and 8 meters deep ($d_1^{min} = -2.5$, $d_1^{max} = 2.5$, $d_2^{min} = -8$, $d_2^{max} = 0$). The soil region Ω_s has a shear modulus $\mu_s = 80$ MPa, Poisson's ratio $\nu_s = 1/3$ and density $\rho_s = 2000$ kg · m^{-3}. Regions Ω_b, Ω_{b1} and Ω_{b2} represent elastic regions of the barrier with shear modulus $\mu_b = 605$ MPa, Poisson's ratio $\nu_b = 1/4$ and density $\rho_b = 2000$ kg · m^{-3}. A conventional hysteretic damping ratio of 5% is considered for all regions, i.e. $\xi_s = \xi_b = 0.05$. Any value between 0% and 7% has a limited influence in this type of problems [187]. The range of frequencies of interest is $f \in [20, 80]$ Hz, and a set of eleven frequencies $f^{opt} =$

$\{20, 26, 32, \dots, 80\}$ Hz are considered for objective functions.

The shear wave velocities are $c_{Ss} = 200$ m $\cdot$ s^{-1} and $c_{Sb} = 550$ m $\cdot$ s^{-1} for the soil and barrier regions, respectively. The ratio of $c_{Ss}/c_{Sb} = 2.75$ is greater than the minimal value of 2.5 suggested by Ahmad et al. [187]. The Rayleigh wave velocity in the soil is $c_{Rs} = 186.4$ m $\cdot$ s^{-1}. Since the range of frequencies of interest is $f \in [20, 80]$ Hz, Rayleigh wavelengths λ_{Rs} vary from 2.33 m to 9.32 m. Therefore, for the lowest frequencies, the design domain limits the barrier depth up to approximately one Rayleigh wavelength. In that situation, the optimization search for solutions that increases the insertion loss without going deeper. For higher frequencies, there is a compromise between depth and width. Ahmad et al. offer an explanation of the related physical phenomena for a vertical wall barrier. An optimal depth to width ratio is present in such wall barriers when the dimensionless area is $A/\lambda_{Rs}^2 > 0.2$, and varies between 1.2 and 2.8. These conclusions of Ahmad et al. give very useful design rules for single vertical wall barriers, and serve as a starting point for the more complex designs studied in the present work.

5.5.1 Optimal single wall barriers

The simplest wave barrier topology corresponds to a single wall barrier with wall top and bottom position, and thickness freedoms, see Figure 5.22a. It is defined by four design variables ($N_{dv} = 4$): a_1 is the horizontal coordinate of the wall top ($-2.5 \leq a_1 \leq 2.5$), a_2 and a_3 are respectively the horizontal and vertical coordinates of the wall bottom ($-2.5 \leq a_2 \leq 2.5$, $-8 \leq a_3 \leq -0.1$), and a_4 is the wall thickness ($0.1 \leq a_4 \leq 5$). There are four parametrized geometry points ($N_{gp} = 4$), which can be be obtained from:

$$
\begin{aligned}
\mathbf{p}^{(1)} &= \left(a_1 + (a_4/2)/\cos\theta, 0 \right), \quad \mathbf{p}^{(2)} = \left(a_2 + (a_4/2)\cos\theta, a_3 + (a_4/2)\sin\theta \right) \\
\mathbf{p}^{(3)} &= \left(a_2 - (a_4/2)\cos\theta, a_3 - (a_4/2)\sin\theta \right), \quad \mathbf{p}^{(4)} = \left(a_1 - (a_4/2)/\cos\theta, 0 \right)
\end{aligned}
\tag{5.10}
$$

where $\theta = \arctan\left((a_1 - a_2)/a_3 \right)$. These points correspond respectively to the top right, bottom right, bottom left and top left corner points of the wall. The bounds established previously for design variables are less strict than those of points $\mathbf{p}^{(q)}$ (Eq. 5.6c), in such a way that the design space allows any barrier within the design domain. This is also done for the rest of topologies.

5.5.1.1 Optimized base cases

The first optimization problem is a simplified one from the general case stated above by doing $a_1 = a_2 = 0$. The aim is to study to what extent the design rules of design of stiff vertical wall barriers are optimal. Also, since these are the simplest single wall barrier designs to install, it is appropriate to compare the performance of more involved designs with such simple ones. Because of that, these are referred as optimized base cases in the following. Optimization is performed for four different maximum area constraints $A_{max} = \{2, 4, 8, 12\}$ m^2, and thus the dimensionless area is within $0.025 < A_{max}/\lambda_R^2 < 2.22$.

For the objective function in Eq. (5.7) related to single-frequency sources, the obtained global minima are depicted in Fig. 5.23 together with their insertion loss spectra. Three

(a) $A_{max} = 2$ m^2

(b) $A_{max} = 4$ m^2

(c) $A_{max} = 8$ m^2

(d) $A_{max} = 12$ m^2
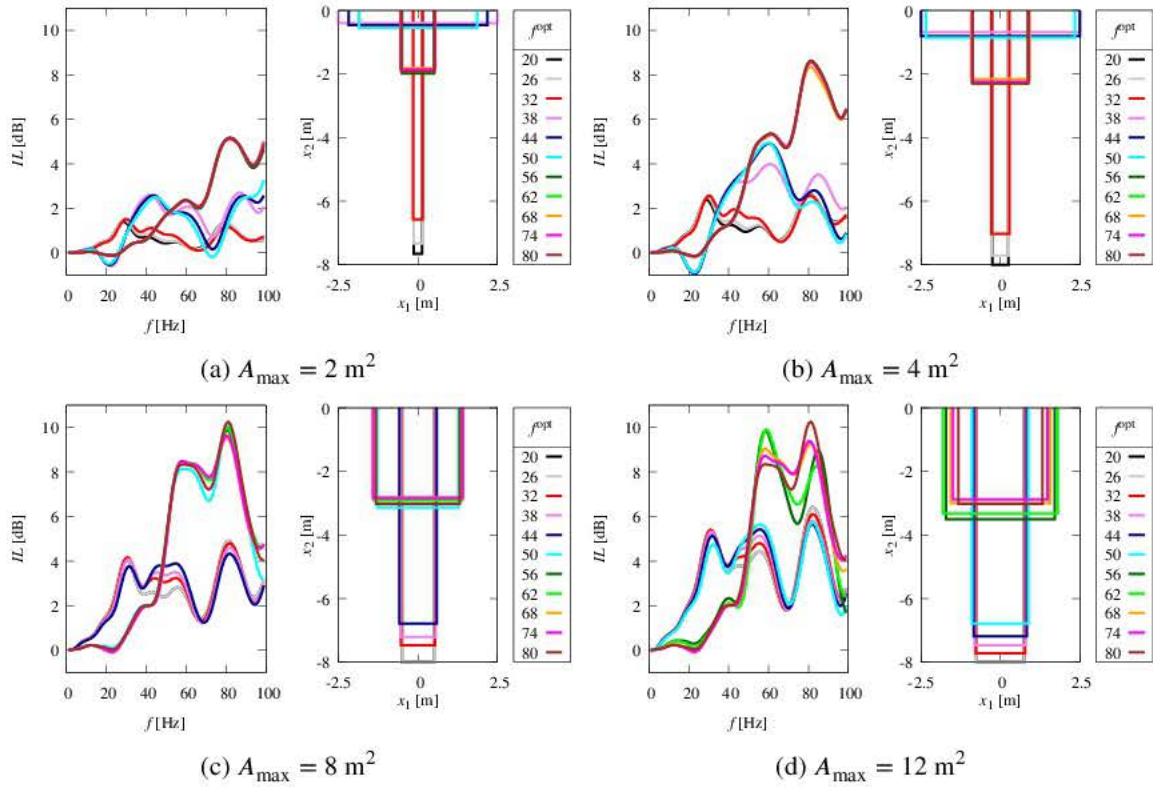
Figure 5.23: Optimal vertical and centered single wall barriers for single-frequency sources

types of optimal designs with different aspect ratios are found: deep walls (optimal for low frequencies), floors (optimal for mid frequencies in some cases), and thick walls (optimal for high-frequencies). Results show that there is no smooth transition between these types of optimal designs as the target frequency increases. In fact, these are more or less similar within a frequency interval, and only small changes take place in order to achieve optimal performance at each target frequency. The frequencies at which the type of optimal design shifts are different depending on the amount of material available (A_{max}). For $A_{max} = 8$ and $A_{max} = 12$ m^2, there is a sudden shift from deep walls to a thick walls at approximately 50 Hz ($\lambda_R = 3.728$ m). For $A_{max} = 2$ and $A_{max} = 4$ m^2, there is a shift from deep walls to floors at approximately 30 Hz, and then from floors to thick walls at approximately 50 Hz. Despite being very practical, it is clear that the rule of thumb of limiting the depth of the barrier at one Rayleigh wavelength is generally not optimal for a given amount of material.

In order to compare the differences between all three kinds of designs, Fig. 5.24 shows color maps of the magnitude of the real part of displacements and insertion losses within a domain of interest ($-20 \leq x_1 \leq 20 \times -20 \leq x_2 \leq 0$ m^2) for the three local minima of the case $f^{opt} = 50$ Hz, $A_{max} = 12$ m^2: floor-like design ($a_1 = a_2 = 0$ m, $a_3 = -1.05$ m, $a_4 = 5$ m, $IL = 4.7$ dB), thick wall design ($a_1 = a_2 = 0$ m, $a_3 = -3.288$ m, $a_4 = 2.642$ m, $IL = 5.1$ dB), and deep wall design ($a_1 = a_2 = 0$ m, $a_3 = -6.785$ m, $a_4 = 1.769$ m, $IL = 5.2$ dB). Fig. 5.25 shows the insertion loss spectrum for each local minima. This case is interesting because all three minima have insertion losses around 5 dB at the receiver

Figure 5.24: Comparison between three approximately similar local minima working with different isolation mechanisms ($f^{\text{opt}} = 50$ Hz, $A_{\text{max}} = 12$ m^2)

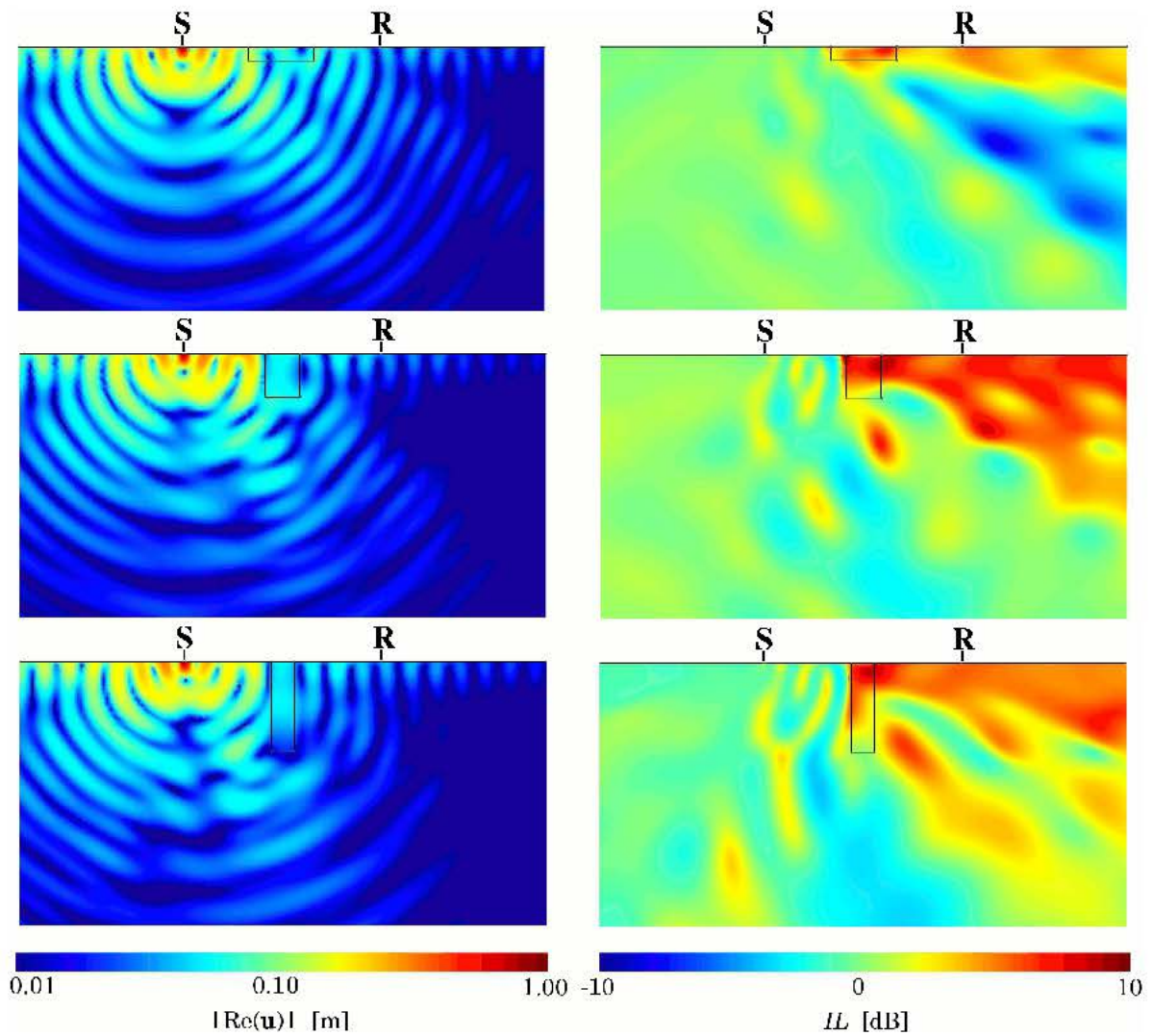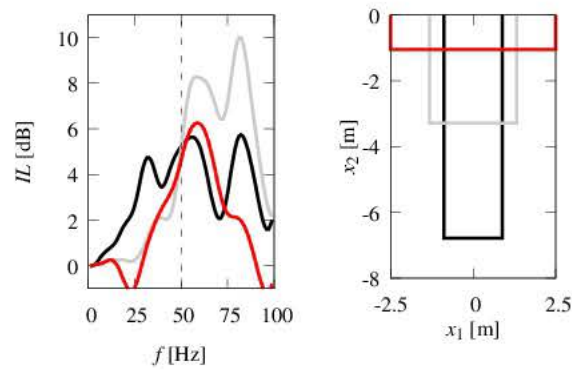Figure 5.25: Insertion loss spectra of three approximately similar local minima working with different isolation mechanisms ($f^{\text{opt}} = 50$ Hz, $A_{\text{max}} = 12$ m^2)
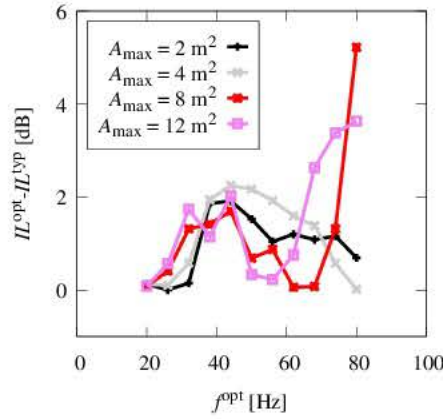
Figure 5.26: Insertion loss improvement of optimized design (see Fig. 5.23) with respect to typical designs ($a_3 = -\lambda_R(f^{\mathrm{opt}})$, $a_4 = A_{\mathrm{max}}/\lambda_R(f^{\mathrm{opt}})$) for each target frequency f^{opt}

location, as can be see in Fig. 5.25. In Fig. 5.24, it can be seen that the floor is a fast path for incoming waves, which produces inclined transmitted body waves. The overall effect is a significant insertion loss near the surface along the receiver side. The thick wall partially converts incoming Rayleigh waves into body waves by reflecting them on the wall and also sending body waves through the bottom of the wall into the half-space. The deep wall also makes both types of conversion, but reflection is predominant in this case. Despite having close insertion losses at the receiver point, the thick wall design have better insertion losses along all the receiver side whereas the floor-like design has a more localized effect. Fig. 5.25 also shows that floor-like design is effective only in a narrower range of frequencies than thick or deep walls.

Fig. 5.26 shows the difference between optimized designs and typical designs with a depth of one Rayleigh wavelength for a given target frequency. It shows that optimization is irregularly effective within the range of target frequencies studied. Improvements are small for low frequencies, and increase as frequencies get higher. This behavior is reasonable since the available dimensionless area increases with the frequency, and also the design domain is larger in dimensionless terms. Improvements between 1 and 2 dB are achievable, which are significant 11% to 21% better Amplitude Reduction ratios.

For the objective function in Eq. (5.8) related to optimization for broadband sources, the obtained global minima are depicted in Fig. 5.27 together with their insertion loss spectra. Since the objective function is an average of insertion losses within a given frequency range, optimization improves insertion losses where they can be easily increased, i.e. at high-frequencies. In fact, optimal designs for this objective function are very similar to those of high frequency sources. There is a clear improvement as the maximum area is increased, except for $A_{\mathrm{max}} = 12$ m^2. The optimal solution in this case does not make use of all the available area, which is something that also happened when dealing with some of the previous high frequency single-frequency sources. The reason behind this is that, compared to the optimal design, insertion losses in the high frequency range decrease considerably and in the low frequency range slightly increase when the depth of the barrier is increased to reach
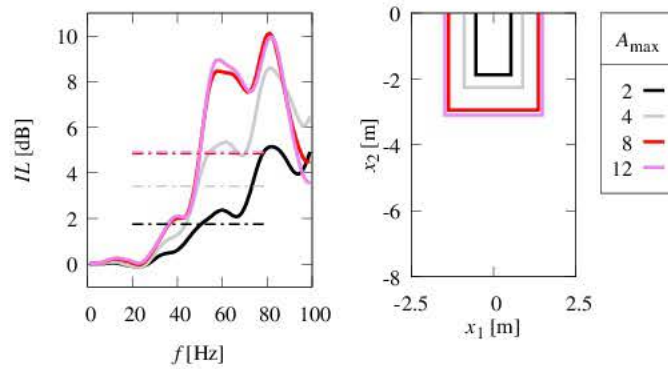
Figure 5.27: Optimal vertical and centered single wall barriers for broadband sources ($f^{\text{opt}} = [20, 80]$ Hz)
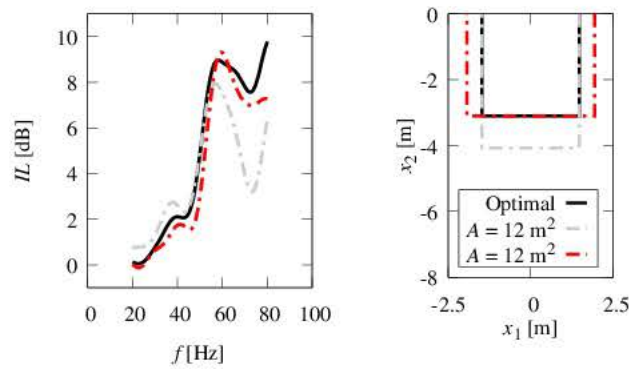
Figure 5.28: Effect of increasing width or depth for the optimal vertical and centered single wall barrier for broadband sources ($f^{\text{opt}} = [20, 80]$ Hz, $A_{\text{max}} = 12$ m^2)

$A = A_{\text{max}}$, see Fig. 5.28. Conversely, when the width of the barrier is increased to reach $A = A_{\text{max}}$, insertion losses in the high frequency range increase and in the low frequency range decrease.

For the objective function in Eq. (5.9) related to optimization for harmonic sources within a frequency range, the obtained global minima are depicted in Fig. 5.27 together with their insertion loss spectra. There are no practical design rules for this objective function, and thus optimization is quite necessary in this case. However, since lowest insertion losses are usually but not always located at the lowest frequency, good starting points are those barriers designed for single-frequency sources at the lowest frequency. Results show that optimal designs are indeed similar to those obtained for single-frequency sources at the lowest frequency. Nevertheless, another minimum insertion losses are located at approximately 70 Hz. Since the objective function is evenly sampled from 20 to 80 Hz in steps of 6 Hz, minimum insertion losses used during the optimization are only approximated ones, as can be seen in Fig. 5.27. As expected, it can be observed that optimal designs for each A_{max} achieve better minimal insertion losses as A_{max} increases.

Figure 5.29: Optimal vertical and centered single wall barriers for harmonic sources within a frequency range ($f^{\text{opt}} = [20, 80]$ Hz)
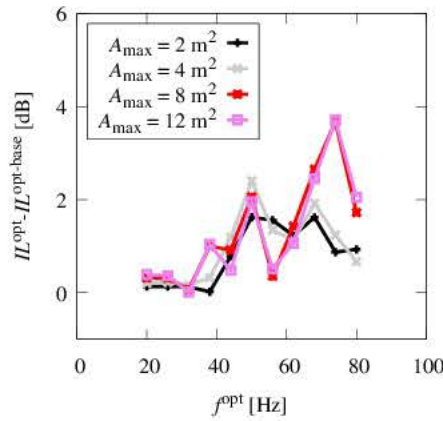
Figure 5.30: Insertion loss improvement of optimized single wall barriers with respect to optimized base cases for each target frequency f^{opt}

5.5.1.2 *Optimized single wall barriers*

In this section, single wall barriers with all four design variables are optimized. Compared to the previous case, the horizontal position of the top and bottom parts of the wall are now included in the optimization, which gives freedom to the horizontal position and angle of the wall.

For the objective function in Eq. (5.7) related to single-frequency sources, the improvement of the obtained global minima with respect to the optimized base cases is depicted in Fig. 5.30. It is observed that the improvement is negligible for low frequencies, and becomes significant as the frequency increases, although it is quite irregular. For frequencies higher than 40 Hz, an improvement roughly between 1 and 2 dB can be achieved.

The optimal designs for single-frequency sources of 20, 26, 44, 50, 74 and 80 Hz are shown in Fig. 5.31. As in the case of vertical and centered single wall barriers, there is no clear and smooth transition between maximum depth reached by optimal designs and wavelengths associated with the frequency of the source. For low frequency sources, optimal

(a) $f^{\text{opt}} = 20$ Hz

(b) $f^{\text{opt}} = 26$ Hz

(c) $f^{\text{opt}} = 44$ Hz

(d) $f^{\text{opt}} = 50$ Hz

(e) $f^{\text{opt}} = 74$ Hz

(f) $f^{\text{opt}} = 80$ Hz

Figure 5.31: Optimal single wall barriers for single-frequency sources

walls have a small inclination and reach the maximum depth. These changes, however, do not improve significantly the corresponding optimized base cases, as shown in Fig. 5.30. For mid frequency sources, optimal walls are highly inclined towards the receiver and cover the available width of the design domain. For sources of 38 and 44 Hz and the highest values of A_{max}, slightly inclined deep walls are obtained as optimal designs. Depths reached for the former cases are around 2 meters, which is much less that one wavelength. In this sense, these designs can be seen as an evolution of floor designs obtained in several optimized base cases. A more sophisticated version of this type of design was also obtained by Van hoorickx et al. [199] via topology optimization. For high frequency sources, optimal walls are highly inclined towards the source and cover almost all the available width of the design domain. In some cases, nearly squared blocks also appear as optimal designs. In the former cases, the depth reached by walls is approximately of 4 meters, more than one Rayleigh wavelength. This type of design also appears in a more complicated fashion in [199]. Most of the designs for the same frequency and different A_{max} have very similar inclination and position, showing that these are key factors for tuning the design for the single-frequency source. For mid and high frequency sources, insertion loss spectra show a clearly defined peak at the optimized frequency.

Fig. 5.32 shows the insertion loss color maps for optimized base cases and optimized single wall barriers for single-frequency sources of 50 and 74 Hz, with $A_{max} = 8$ m^2, and within a given domain of interest ($-20 \leq x_1 \leq 20 \times -20 \leq x_2 \leq 0$ m^2). For both single-frequency sources, the optimized single wall barriers relocate insertion loss maxima occurring along the receiver side such that one maximum is placed at the receiver point. Despite that optimization is performed for the receiver point, insertion losses are also significantly improved along all the receiver side. The optimized single wall barrier inclined towards the receiver side ($f^{opt} = 50$ Hz) reflects incoming waves and also acts as a waveguide redirecting waves away from the surface. The insertion loss map of the optimized single wall barrier inclined towards the source side ($f^{opt} = 74$ Hz) behaves essentially similar to a deep wall, see e.g. Fig. 5.24, but inclination improves insertion losses behind the wall.

For objective functions in Eqs. (5.8) and (5.9) related to optimization for broadband sources and for harmonic sources within a frequency range respectively, the obtained global minima are depicted in Figs. 5.33 and 5.34 together with their insertion loss spectra. Improvements with respect to the optimized base cases (Figs. 5.27 and 5.29) are less that 0.5 dB for both objective functions, which is a relatively small gain.

5.5.2 Optimal double wall barriers

The second barrier topology is a double wall barrier with position, orientation, length and thickness freedoms for both walls, see Figure 5.22b, and thus it has eight design variables ($N_{dv} = 8$). Design variables a_1 to a_4 are the same as those of the single wall barrier, and they are associated with the left wall (Ω_{b1}). Analogously, design variables a_5 to a_8 are related to the right wall (Ω_{b2}). There are eight parametrized geometry points ($N_{gp} = 8$), which can be
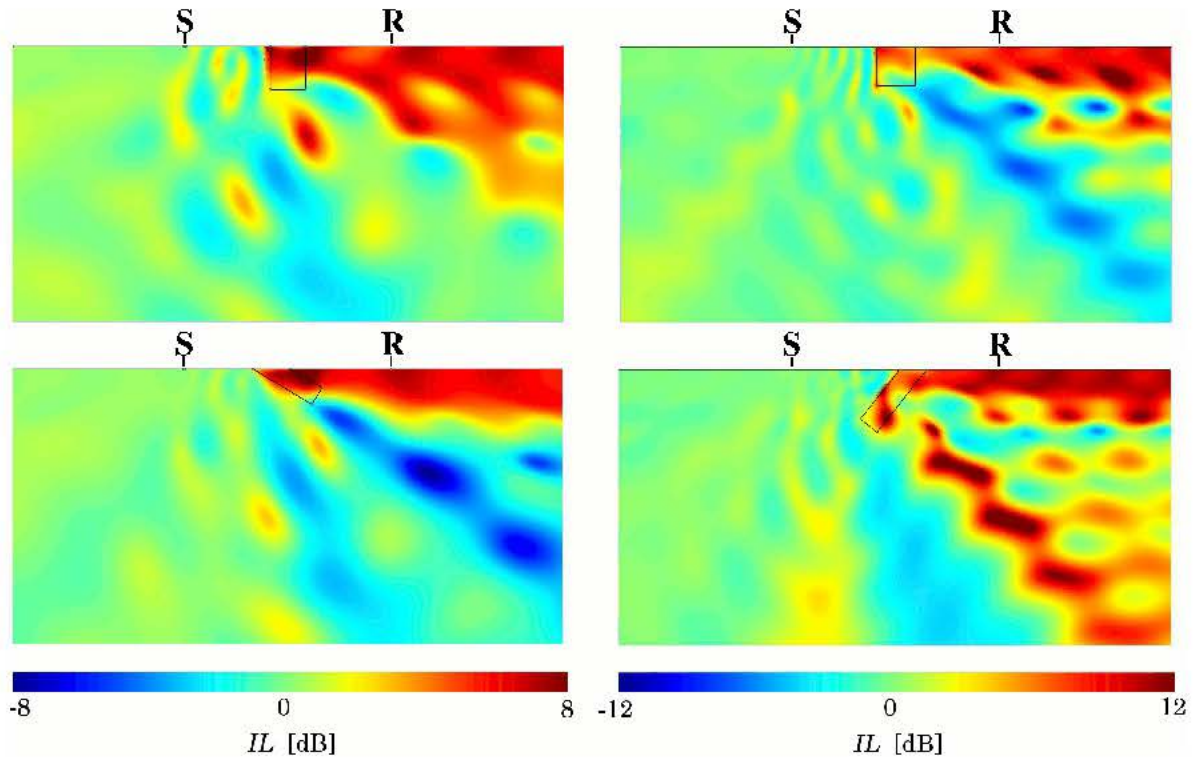
Figure 5.32: Comparison between IL color maps of optimized base cases (top) and optimized single wall barriers (bottom) for $f^{\text{opt}} = 50$ Hz (left) and $f^{\text{opt}} = 74$ Hz (right) when $A_{\max} = 8$ m^2
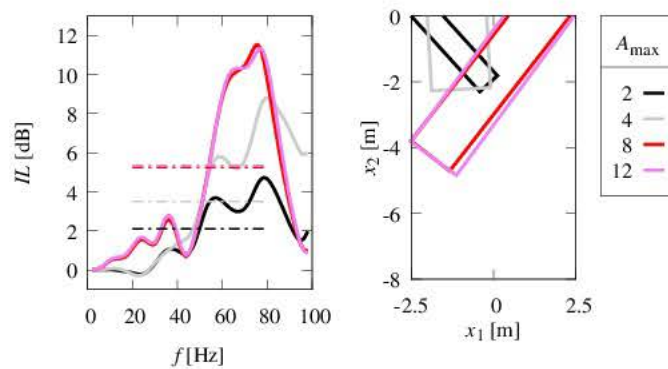
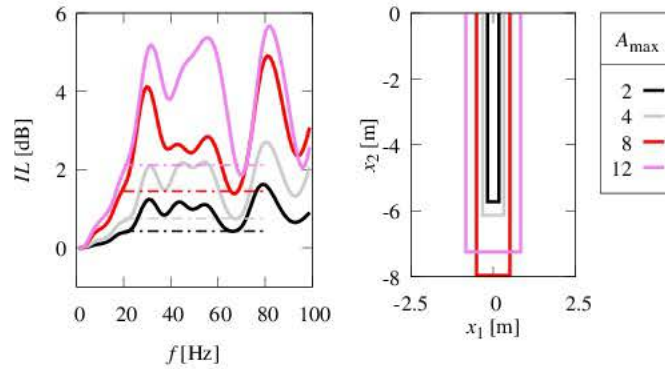Figure 5.33: Optimal single wall barriers for broadband sources ($f^{\text{opt}} = [20, 80]$ Hz)
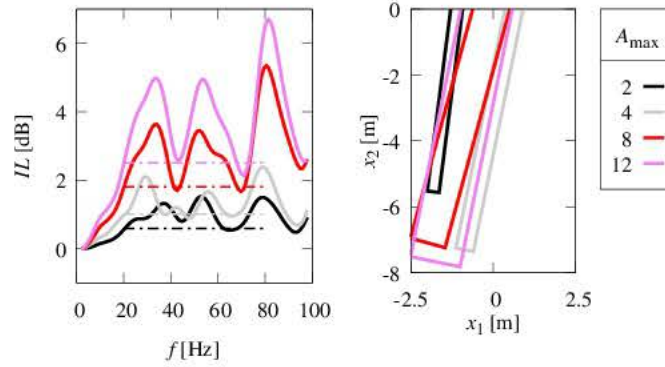
Figure 5.34: Optimal single wall barriers for harmonic sources within a frequency range ($f^{\mathrm{opt}} = [20, 80]$ Hz)
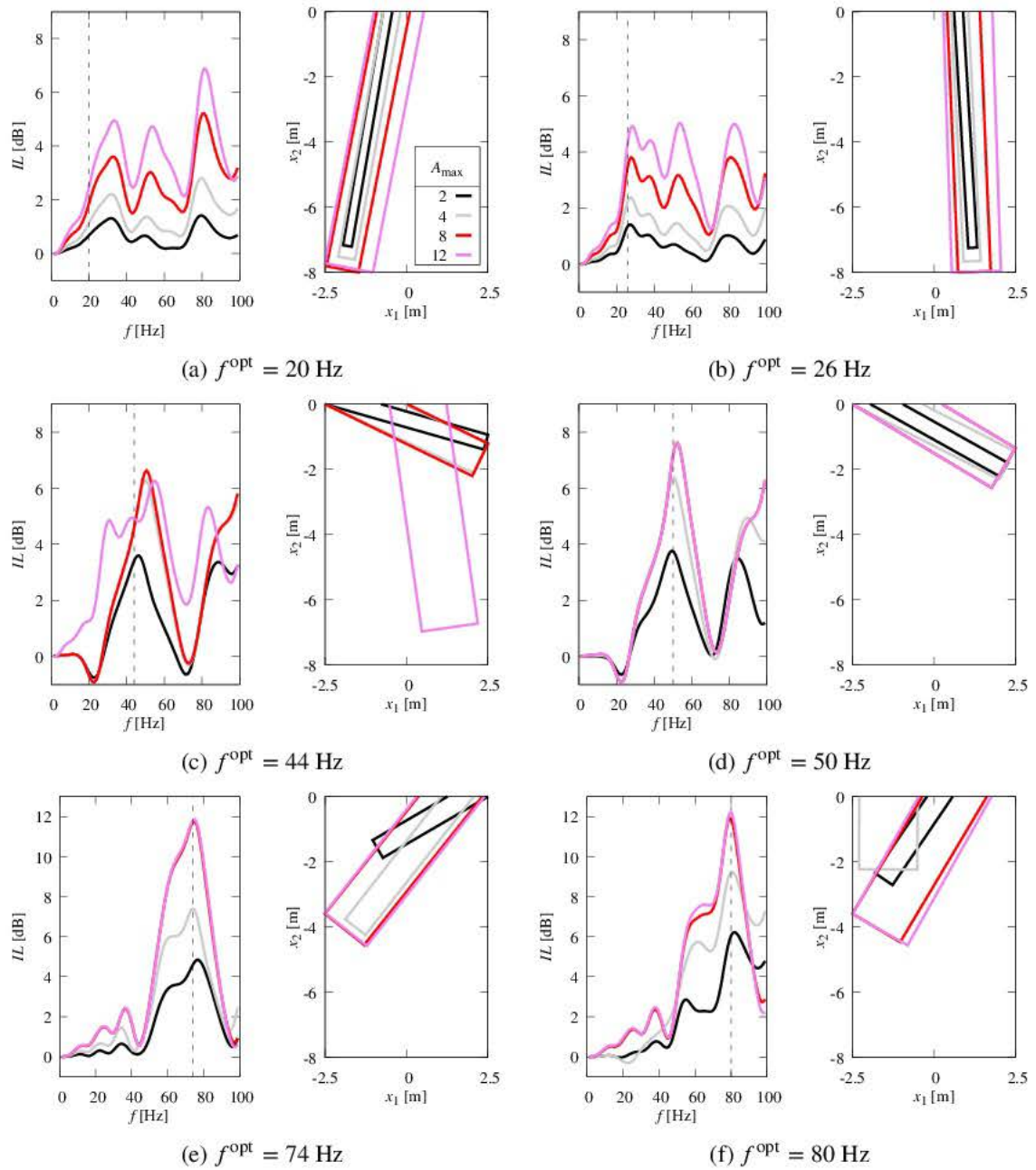
be obtained from:

$$
\begin{aligned}
\mathbf{p}^{(1)} &= \left(a_1 + (a_4/2)/\cos\theta_1, 0 \right), \quad \mathbf{p}^{(2)} = \left(a_2 + (a_4/2)\cos\theta_1, a_3 + (a_4/2)\sin\theta_1 \right) \\
\mathbf{p}^{(3)} &= \left(a_2 - (a_4/2)\cos\theta_1, a_3 - (a_4/2)\sin\theta_1 \right), \quad \mathbf{p}^{(4)} = \left(a_1 - (a_4/2)/\cos\theta_1, 0 \right) \\
\mathbf{p}^{(5)} &= \left(a_5 + (a_8/2)/\cos\theta_2, 0 \right), \quad \mathbf{p}^{(6)} = \left(a_6 + (a_8/2)\cos\theta_2, a_7 + (a_8/2)\sin\theta_2 \right) \\
\mathbf{p}^{(7)} &= \left(a_6 - (a_8/2)\cos\theta_2, a_7 - (a_8/2)\sin\theta_2 \right), \quad \mathbf{p}^{(8)} = \left(a_5 - (a_8/2)/\cos\theta_2, 0 \right)
\end{aligned}
\tag{5.11}
$$

where $\theta_1 = \arctan\left((a_1 - a_2)/a_3\right)$ and $\theta_2 = \arctan\left((a_5 - a_6)/a_7\right)$. In order to preserve the topology during the optimization, three additional constraints ($N_c = 3$) between points of both walls are imposed:

$$
p_1^{(1)} < p_1^{(8)} \Rightarrow g_1 = p_1^{(1)} - p_1^{(8)} + \epsilon \leq 0
\tag{5.12a}
$$

$$
A^{1,2,7} > 0 \Rightarrow g_2 = -A^{1,2,7} + \epsilon \leq 0
\tag{5.12b}
$$

$$
A^{8,2,7} > 0 \Rightarrow g_3 = -A^{8,2,7} + \epsilon \leq 0
\tag{5.12c}
$$

where $A^{i,j,k}$ denotes the signed area of the triangle formed by points $\mathbf{p}^{(i)}$, $\mathbf{p}^{(j)}$, and $\mathbf{p}^{(k)}$, and ϵ is a small constant that guarantees the original strict inequality. Constraints indicated by Eqs. (5.12a-5.12c) guarantees that the quadrilateral formed by points $\mathbf{p}^{(1)}$, $\mathbf{p}^{(2)}$, $\mathbf{p}^{(7)}$ and $\mathbf{p}^{(8)}$ is convex, thus collision between walls is completely avoided.

For the objective function associated to single-frequency sources, the improvement of the obtained global minima with respect to the optimized base cases is shown in Fig. 5.35. It is observed that the improvement is small (< 0.5 dB) for the lowest frequency (20 Hz), but it is roughly proportional to the frequency and the available area A_{max} and reaches remarkably high gains with respect to the optimized base cases. Unlike single wall barriers (see Fig. 5.30), which exhibit an irregular improvement within the considered range of single-frequency sources, one can always expect that optimization would achieve relevant improvement.

The optimal designs for single-frequency sources of 20, 26, 44, 50, 74 and 80 Hz are shown in Fig. 5.36. Most optimal designs for low and mid frequency sources, i.e. from $f^{\mathrm{opt}} = 20$ to $f^{\mathrm{opt}} = 50$ Hz, share several characteristics with the corresponding optimal
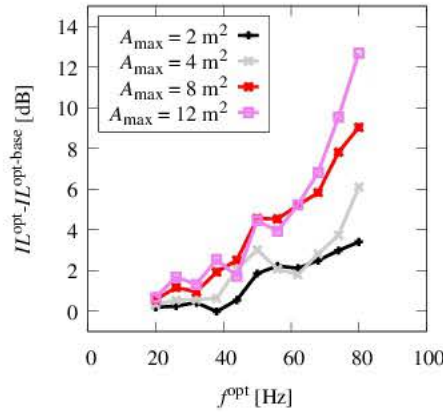
Figure 5.35: Insertion loss improvement of optimized double wall barriers with respect to optimized base cases for each target frequency f^{opt}

single wall barriers (see Fig. 5.31). For 20 and 26 Hz sources, walls on the left hand side have similar angle and position regardless of A_{max}, and the same happens with the walls on the right hand side for 44 and 50 Hz sources. The opposite walls are located at the boundary of the design domain, and are approximately 5 meters deep, i.e. $1.18\lambda_R$ for 44 Hz and $1.34\lambda_R$ for 50 Hz. Some cases seem not to completely follow this description, but this is simply because those designs are suboptimal solutions and are not shown. For high frequency sources, there are also some characteristics similar to the corresponding optimal single wall barriers. The depth reached by the walls on the left hand side are around 2 meters, i.e. $0.8\lambda_R$ for 74 Hz and $0.86\lambda_R$ for 80 Hz, and they are thin walls or very thick walls (nearly squared blocks). The depth reached by walls on the right hand side are around 2 meters or 4 meters, and they all are relatively thin walls.

Except for a 20 Hz harmonic source, optimized double wall barriers lead to significant improvements with respect to optimized single wall barriers. In the following paragraphs, we are going to discuss in more detail what is happening physically for optimized designs for low (26 Hz), medium (50 Hz) and high (74 Hz) frequency sources.

Fig. 5.37 shows a comparison between the optimized base case and optimized double wall barrier for a single-frequency source of $f^{\text{opt}} = 26$ Hz. A modest 1.2 dB improvement is achieved by the optimized double wall barrier ($IL = 4.4$ dB) with respect to the optimized base case ($IL = 3.2$ dB) at the receiver point. The comparison between diffracted displacement fields shows that optimized double wall barrier relies less on reflection, and instead transmitted waves carry most of the energy towards the inside of the half-space and away from the receiver. The overall effect is a better insertion loss along the receiver side, and incidentally less insertion gain along the source side.

Fig. 5.38 shows insertion loss maps for optimized double wall barriers for $f^{\text{opt}} = 50$ Hz and $f^{\text{opt}} = 74$ Hz when the available area is $A_{\text{max}} = 8$ m^2. It is shown individually the insertion loss maps for walls on the left and right hand side, and finally the complete double wall barrier. The idea is to observe the contribution of each wall, and their combined effect. For the case $f^{\text{opt}} = 50$ Hz, the wall on the left hand side acts as a deep wall (depth is $1.25\lambda_R$),

(a) $f^{\mathrm{opt}} = 20$ Hz   (b) $f^{\mathrm{opt}} = 26$ Hz

(c) $f^{\mathrm{opt}} = 44$ Hz   (d) $f^{\mathrm{opt}} = 50$ Hz

(e) $f^{\mathrm{opt}} = 74$ Hz   (f) $f^{\mathrm{opt}} = 80$ Hz
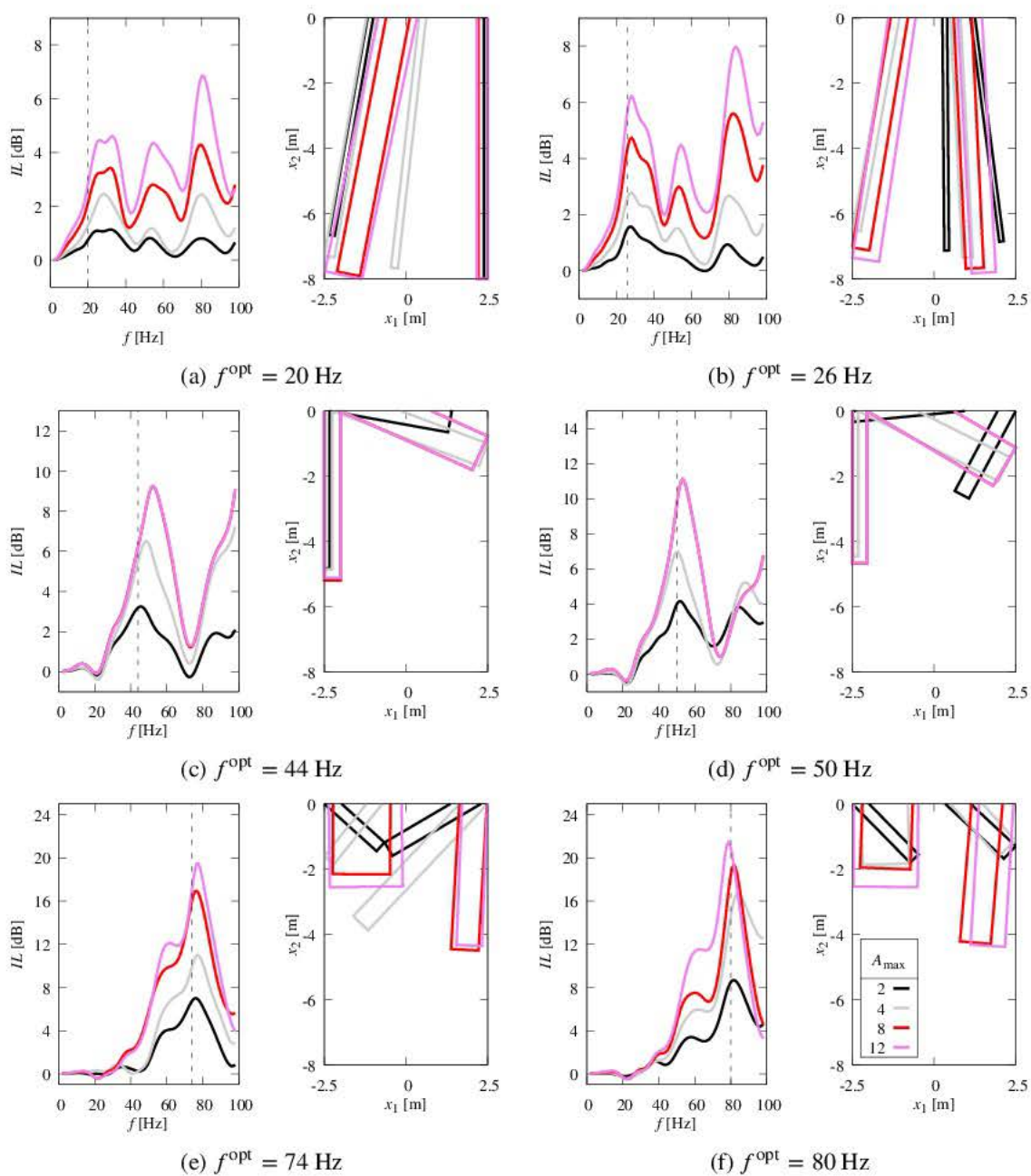
Figure 5.36: Optimal double wall barriers for single-frequency sources
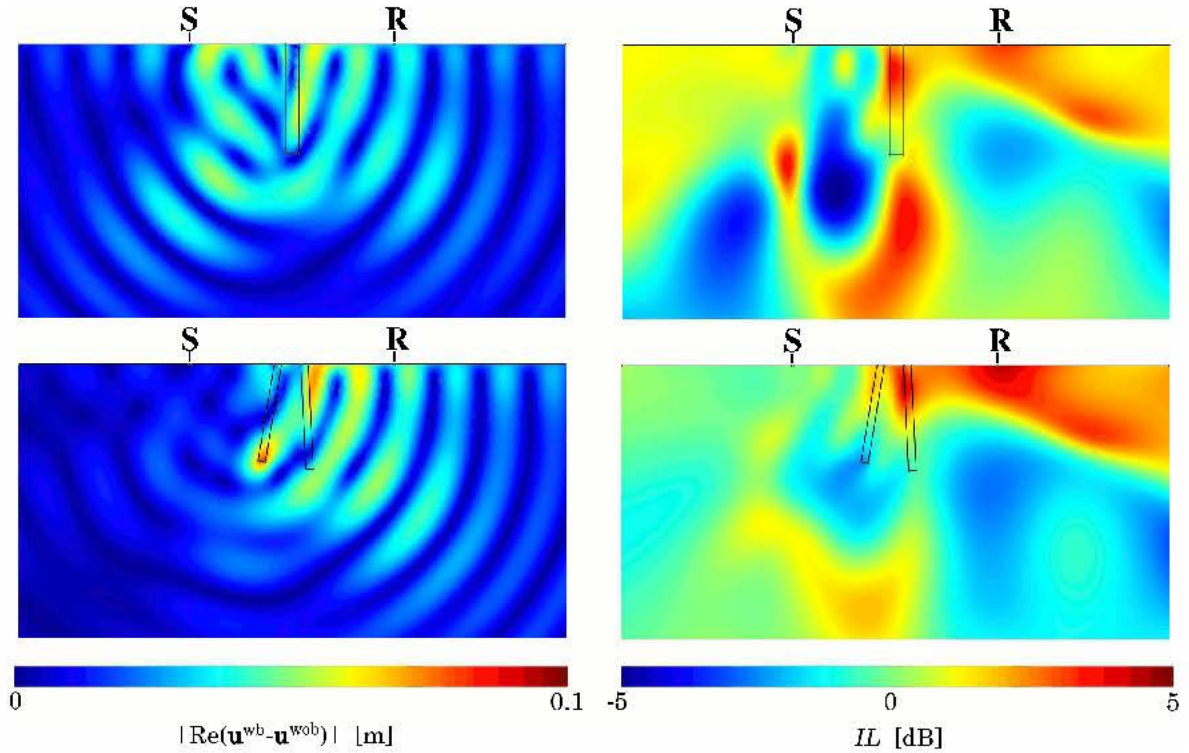
Figure 5.37: Comparison between diffracted displacement field and IL color maps of optimized base case (top) and optimized double wall barrier (bottom) for $f^{opt} = 26$ Hz and $A_{max} = 8$ m^2

and the individual insertion loss at the receiver point is 1.31 dB. The wall on the right hand side is a highly inclined thick wall that partly reflects incoming waves, but also acts as a waveguide taking transmitted waves towards the inside of the soil. The insertion loss of the latter wall alone is 6.15 dB at the receiver point. Since the insertion loss of the double wall barrier is 9.65 dB, they nicely work together in a synergic way. For the case $f^{opt} = 74$ Hz, the wall on the left hand side is a deep and thick wall (depth is $0.86\lambda_R$) which is partly reflecting incoming waves but also producing inclined transmitted waves away from the source. The insertion loss at the receiver point of this wall alone is 6.77 dB. The wall at the right hand side is a very deep wall (depth is $1.78\lambda_R$), and the individual insertion loss at the receiver point is only 2.7 dB. The complete double wall barrier works by partly reflecting incoming waves on the wall on the left hand side, which also produces inclined transmitted waves that are partly reflected on the wall on the right hand side. Both walls work in a very productive manner producing an insertion loss of 15.9 dB, which is much higher than individual contributions.

For objective functions related to optimization for broadband sources and for harmonic sources within a frequency range the obtained global minima are respectively depicted in Figs. 5.39 and 5.40 together with their insertion loss spectra. As in the case of single wall barriers, optimal designs for broadband sources are very similar to those for high frequency harmonic sources, and optimal barriers for harmonic sources within a frequency range are quite similar to those of low frequency harmonic sources. In the case of optimizing for broadband sources,
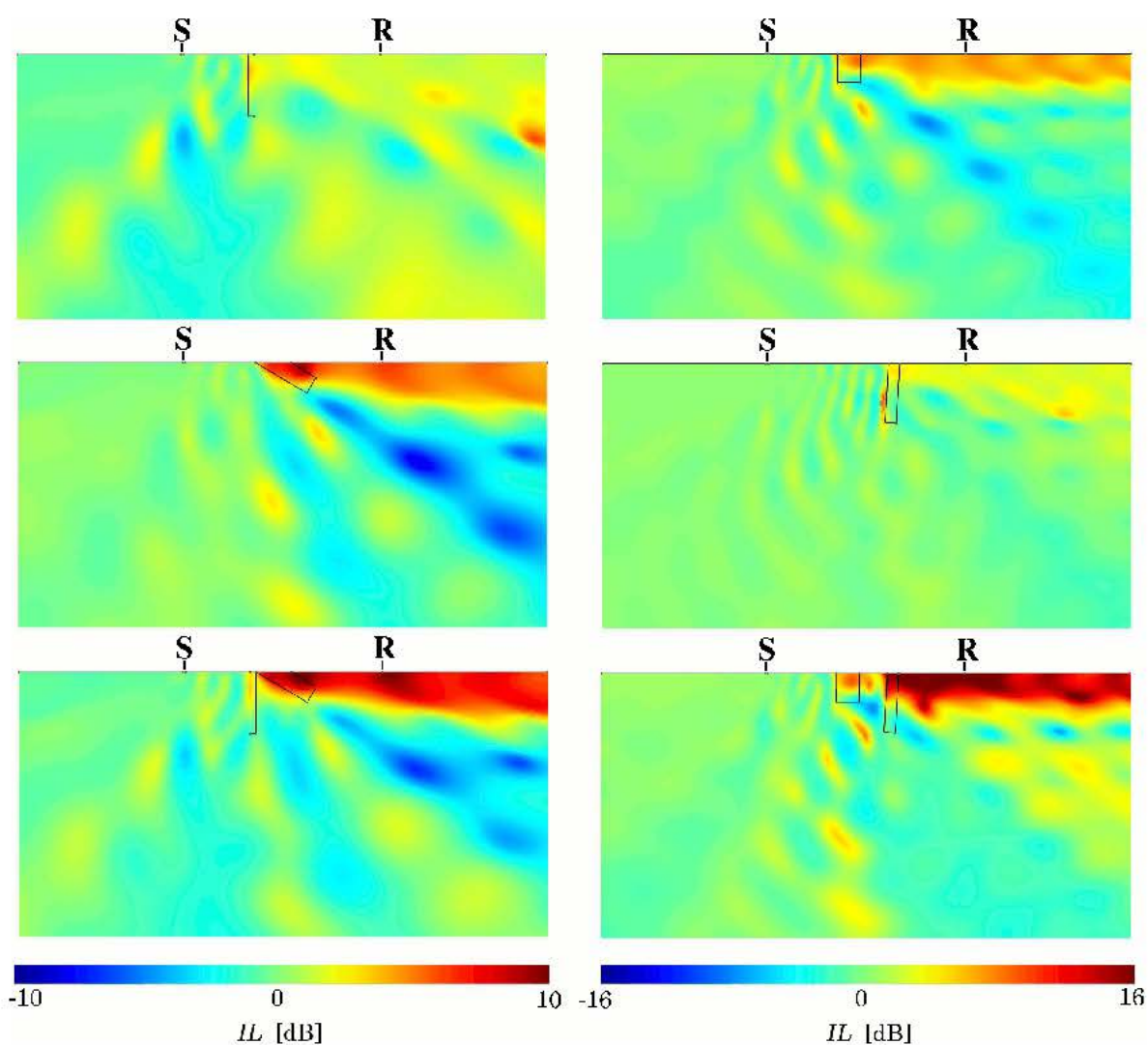
Figure 5.38: Comparison between IL color maps of optimized double wall barriers for $f^{\text{opt}} = 50$ Hz (left) and $f^{\text{opt}} = 74$ Hz (right) when $A_{\text{max}} = 8$ m^2. Top: wall on the left hand side. Middle: wall on the right hand side. Bottom: double wall barrier.
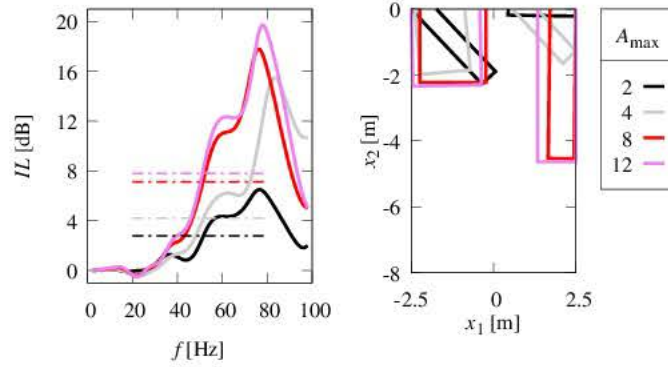
Figure 5.39: Optimal double wall barriers for broadband sources ($f^{\mathrm{opt}} = [20, 80]$ Hz)
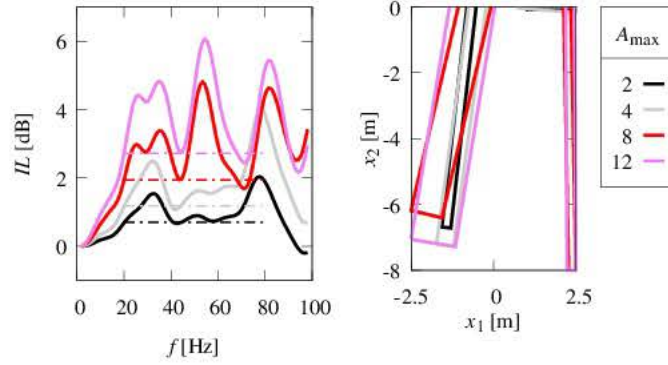
Figure 5.40: Optimal double wall barriers for harmonic sources within a frequency range ($f^{\mathrm{opt}} = [20, 80]$ Hz)

the improvements with respect to the optimized base cases shown in Figs. 5.27 and 5.29) are greater than 1 dB, and increase with the available area reaching up to 3 dB for $A_{\mathrm{max}} = 12 \; \mathrm{m}^2$. In the case of optimizing for harmonic sources within a frequency range, the improvements hardly reach 0.5 dB for all values of A_{max}.

5.5.3 Concluding remarks

In this section, we have examined the possibilities of shape optimization of two wave barrier topologies: a single wall barrier, and a double wall barrier. In the former case, we have also studied the vertical and centered particular case, which has been taken as the optimized base case. Despite the relative simplicity of these topologies, they offer room for improvement with respect to the conventional design rules.

When the depth of the design domain is limited up to approximately one Rayleigh wavelength, the optimization of the studied barrier topologies does not lead to significant improvements. Once the depth of the design domain is greater than $1.1\lambda_{\mathrm{R}}$ ($f > 26$ Hz in our case study), relevant room for optimization is observed, especially for double wall barriers.

For the simplest case of a vertical and centered single wall barrier, it is observed that the typical design rule of having a wall depth of λ_{R} and width $A_{\mathrm{max}}/\lambda_{\mathrm{R}}$ is far from optimal.

Optimized designs fall into one of three types of barriers: a) deep walls, b) floors, or c) thick wall of nearly unitary aspect ratio. Each one of these may become optimal depending on the frequency and the available material.

For general single wall barriers, it is found little room for optimization in the low frequency range ($f > 38$ Hz in our case study). For greater frequencies, improvements of 1 to 2 dB with respect to optimized base cases can be achieved. However, these seem to be irregular along the frequency range.

For double wall barriers, small improvements with respect to optimized base cases are found at low frequencies. However, they increases significantly with the frequency and the available area (A_{max}), reaching quite remarkable gains between 2 and 13 dB.

In the optimization for broadband sources, designs very similar to those of the highest frequency are consistently obtained. This conclusion is reasonable because the objective function is a simple average of insertion losses within the frequency range. Therefore, for this particular objective function, it is appropriate to start with a single-frequency optimization of the highest frequency, and then use the results as initial points.

In the optimization for harmonic sources within a frequency range, designs very similar to those of the lowest frequency are obtained. Analogously to the optimization for broadband sources, this conclusion should be used to establish better initial points.

6.1 Introduction

Bucket foundations (or suction caisson foundations) are used as anchors and foundations of offshore platforms, and more recently as foundations of offshore wind turbines when suitable water depths and soil conditions are encountered [200]. Foundations of offshore wind turbines experience important horizontal and moment loadings, which are larger for deeper waters. Single bucket or monopod foundations are used for wind turbines installed at moderate water depths. When monopod foundations are not enough to carry these loads, three or four small buckets can be combined to form what are known as tripod or tetrapod foundations. In general, wind turbines with bucket foundations are well suited for water depths between 20 to 50 meters [201].

Despite the experience gained from oil and gas industries, their application to wind turbines face several new challenges [200, 202]. They must be designed to withstand large horizontal forces and overturning moments, and in addition these are of dynamic nature. These loads mainly comes from steady-state operation of the machine (rotor rotation), wind field, water current field, water waves, tidal effects, and earthquakes. Furthermore, the installation process and the soil conditions of the seabed near the foundation introduce several uncertainties. These designs should be able to operate under such conditions for a number of years in order to be economically viable. Therefore, it is necessary to advance towards the development of rigorous models able to take into account realistic conditions.

Many aspects of the installation and design of bucket foundations have been studied, and the literature is large. A very complete review about bearing capacity and installation was published by Foglia and Ibsen [203]. In the context of dynamics, a recent work of Kourkoulis et al. [204] uses a non-linear FEM model to study the behaviour of bucket foundations of offshore wind turbines under lateral monotonic, cyclic, and earthquake loading. They give an interesting discussion about the interface conditions between soil and foundation. Liingaard et al. [41] studied the impedances of bucket foundations in elastic soils, including the variation of these under changes of geometry and soil properties. The aim of the present chapter is to perform a preliminary exploration into the influence of poroelastic soils on the impedances of bucket foundations.

The chapter is organised as follows. Section 6.2 briefly describes the problem and the main aspects of the model used to analyse it. In Section 6.3, a comparison between previous results and results obtained with the proposed model is made, where soils are considered elastic. In Section 6.4, impedances are studied for a range of poroelastic soils. Finally, Section 6.5 gives some final remarks and further research.

6.2 Impedances of bucket foundations

A bucket foundation has two main parts: the lid, which is a stiffened circular steel plate in contact with the mudline, and the skirt, which is a cylindrical steel shell buried into the seabed soil. Due to the stiffening, the lid can be considered rigid for the present analysis. Therefore, the geometry is defined by the bucket diameter D (or radius R), the skirt length L, and the skirt thickness t.

(a) Picture of a bucket foundation (monobucket).
Source: `all-at-sea.org`
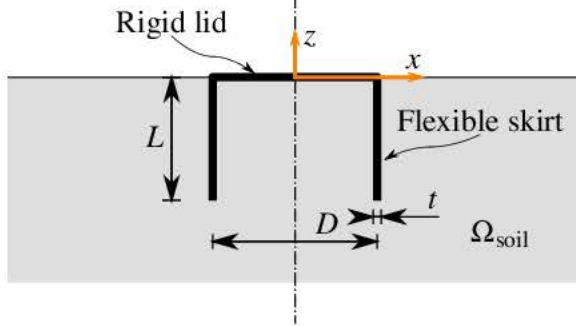
(b) Layout of the problem
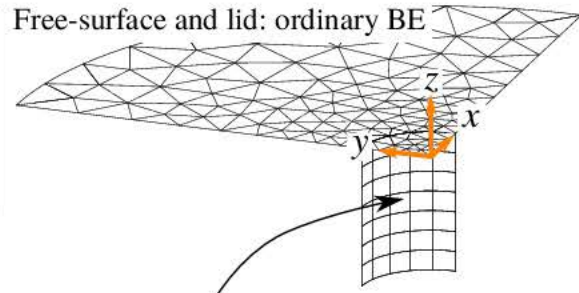
(c) DBEM–FEM example mesh

Figure 6.1: Bucket foundation

The impedances are calculated with respect to the displacements and rotations at the centre of the rigid lid. In order to obtain them, unitary displacement and rotations are given to the lid, and then resultant forces and moments are evaluated. Given that the foundation is axisymmetric, the 6 DOF impedance matrix $\mathbf{S}$ is composed of 5 different impedances: swaying S_{HH}, vertical S_{VV}, rocking S_{MM}, rocking - swaying coupling S_{MH}, and torsional S_{TT}; which can be arranged in a dimensionless fashion as follows:

$$
\begin{Bmatrix} F_1/\mu R^2 \\ F_2/\mu R^2 \\ F_3/\mu R^2 \\ M_1/\mu R^3 \\ M_2/\mu R^3 \\ M_3/\mu R^3 \end{Bmatrix} = \begin{bmatrix} S_{HH} & 0 & 0 & 0 & S_{MH} & 0 \\ 0 & S_{HH} & 0 & -S_{MH} & 0 & 0 \\ 0 & 0 & S_{VV} & 0 & 0 & 0 \\ 0 & -S_{MH} & 0 & S_{MM} & 0 & 0 \\ S_{MH} & 0 & 0 & 0 & S_{MM} & 0 \\ 0 & 0 & 0 & 0 & 0 & S_{TT} \end{bmatrix} \begin{Bmatrix} U_1/R \\ U_2/R \\ U_3/R \\ \theta_1 \\ \theta_2 \\ \theta_3 \end{Bmatrix}
\tag{6.1}
$$

In the following, the bucket foundation is considered massless ($\rho = 0$ kg/m^3), with a Young's modulus $E = 210$ GPa, Poisson's ratio $\nu = 1/4$ and hysteretic damping ratio $\xi = 0.01$ ($E^* = E(1 + i2\xi)$). The diameter is $D = 10$ m, and the thickness $t = 0.05$ m. Because of the nature of the DBEM–FEM model, the mass distribution through the soil-structure interface is continuous according to the density of the soil despite the structure is considered massless.

It is assumed that the bucket is installed in an elastic or poroelastic half-space, with perfectly bonded (non-relaxed) interface conditions. Figure 6.1 depicts the layout of the problem and an example mesh, including the considered coordinate reference system. Symmetry properties of the problem are exploited and only a quarter of the domain is discretised.

The soil region Ω_{soil} has three BE boundaries: the seabed free-surface $\Gamma_{\text{free-surface}}$, the soil-skirt interface $\Gamma_{\text{soil-skirt}}$ (a crack-like boundary), and the bucket lid Γ_{lid}. The skirt region Ω_{skirt} is a mesh of degenerated shell FE. The seabed free-surface $\Gamma_{\text{free-surface}}$ is a permeable traction-free boundary, i.e. $\tau = 0$ and $t_k = 0$. The bucket lid Γ_{lid} has prescribed fluid and solid displacements according to the impedance that is being being calculated. Shell FE nodes in ($x > 0$, $y > 0$, $z = 0$) and in zx and yz symmetry planes are 6 DOF shell nodes, while the rest are 5 DOF nodes. By doing so, it is easy to establish the prescribed displacements and rotations to the 6 DOF nodes according to the impedance that is being calculated and the symmetric/anti-symmetric conditions imposed by the displacement field. Both $\Gamma_{\text{soil-skirt}}$ and Ω_{skirt} are discretized with conforming meshes of 8-noded quadrilateral elements. Boundaries Γ_{lid} and $\Gamma_{\text{free-surface}}$ are discretized with 6-noded triangular elements. The size of the elements of the foundation and its surroundings is at least of 6 elements per wavelength, while at least 4 elements per wavelength is used beyond it.

6.3 Impedances of bucket foundations in elastic soils

In order to check the validity of the DBEM-FEM model, a comparison between several results of Liingaard et al. [41] and the present model is done. Figure 6.2 shows impedances (normalized magnitude and angle) for bucket foundations with several length to diameter ratios $L/D = \{1/4, 1, 2\}$. The given elastic soil properties are $\mu = 1$ MPa, $\nu = 1/3$ and $\xi = 0.025$. In the present model, it is used a poroelastic soil with the same properties for the solid phase, air properties for the fluid phase, and a small porosity $\phi \to 0$. Figure 6.2 demonstrates very good agreement between results. Although not shown here for the sake of conciseness, all other static and dynamic results presented in [41] also agree with results obtained by our model.

Liingaard et al. [41] give a detailed physical interpretation of the results. In particular, the location of anti-resonance and resonance peaks observed in the vertical impedances are related to those of an infinite long cylinder under axial excitation. Likewise, the location of anti-resonance and resonance peaks observed in the horizontal impedance are related to those of an infinite hollow cylinder.
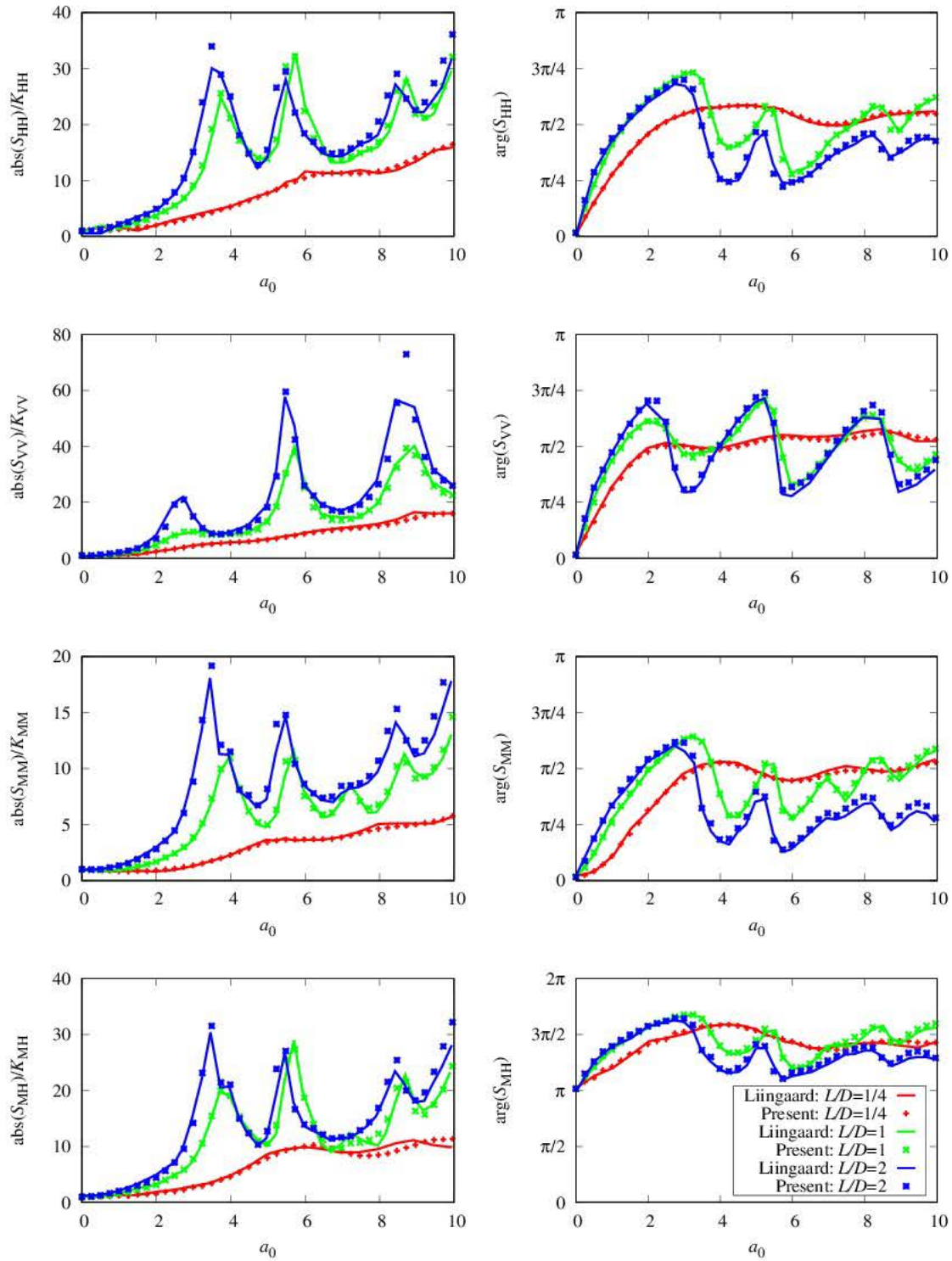
Figure 6.2: Comparison between Liingaard et al. [41] and the present approach. From top to bottom: normalized horizontal, vertical, rocking, and horizontal-rocking coupling impedances.

6.4 Impedances of bucket foundations in poroelastic soils

Elastic soils can be defined by a small set of properties, for example shear modulus μ, Poisson's ratio ν, density ρ and a hysteretic damping ratio ξ ($\mu^* = \mu(1 + i2\xi)$). Hence, fully dimensionless studies can be carried out by defining some shape factors of the structure, a dimensionless frequency a_0 with the help of a length of the structure and a wave velocity of the soil, and setting the Poisson's ratio and damping ratio of the soil. In the case of poroelastic soils, this task becomes impractical due to the number of properties involved, and the difficulties of knowing if a given set of values of the properties represents a realistic soil or not. For these reasons, we have decided to use realistic seabed soils taken from Buchanan and Gilbert [205], see Table 6.1. All results are shown using a dimensionless frequency $a_0 = \omega R/c_S^u$, where R is the radius of the bucket, and $c_S^u = \sqrt{\mu/(\phi\rho_f + (1 - \phi)\rho_s)}$ is the undrained S-wave velocity.

Seabed soils taken from Buchanan and Gilbert [205], see Table 6.1, cover a wide range of possible realistic soils, from gravels, sands, silts, to clays. These soils are denoted as "sb1" to "sb5" in the following tables and graphs. Three length to diameter ratios $L/D = \{1/4, 1, 2\}$ are studied. Table 6.2 shows the dimensionless quasi-static stiffnesses for all cases, where they are calculated for a small dimensionless frequency $a_0 = 10^{-6}$. Nondimensionalization of impedances is performed using the shear modulus μ of the soil and the radius R of the bucket. Figures 6.3 to 6.5 show the impedances for all cases, where in the low-frequency range ($a_0 = [10^{-6}, 1]$) only their magnitudes are analysed, and in a broader frequency range ($a_0 = [0, 6)$) also their angles are shown. Taking into account the definition of the dimensionless frequency a_0, the low-frequency range corresponds approximately to frequencies below $1 - 6$ Hz depending on the seabed soil. Also, the broader frequency range corresponds approximately to frequencies between $1 - 6$ Hz and 40 Hz depending on the seabed soil.

Dimensionless quasi-static stiffnesses are similar in magnitude to those obtained by Liingaard et al [41] for elastic soils, considering the seabed as a drained elastic soil. In fact, Table 6.2 includes the results using an elastic solid with the drained conditions of the porous medium, and the discrepancy is small. Differences are due to a not sufficiently small dimensionless frequency for the calculation of the quasi-static stiffness.

As can be seen in the left hand side graphs of Figures 6.3 to 6.5, impedance functions are almost constant and approximately equal to the quasi-static value in the low-frequency range. This is characteristic of any elastic soil, which is even more smooth. In the case of poroelastic soils, the smaller length to diameter ratio the less regular behaviour at low-frequencies. In the case of buckets with $L/D = 1/4$, it is very noticeable the variation of impedances when $a_0 \to 0$. The effect is due to the permeability of the porous medium, the smaller permeability the more pronounced variation. It is more relevant for buckets with smaller length to diameter ratios because of the relevance of the compressional interaction of the bucket lid with respect to the total impedance.

In Figure 6.4, results of the corresponding undrained elastic soils are included, and they are normalized with respect to the quasi-static stiffnesses of the correspoding porous media. Along the low-frequency range (except when $a_0 \to 0$), it is quite clear that neither the drained nor the undrained elastic soil is able to reproduce the real poroelastic behaviour.

The right hand side and central graphs of Figures 6.3 to 6.5 show impedance functions

Figure 6.3: Impedances of bucket foundations with $L/D = 1/4$ in poroelastic soils. From top to bottom: horizontal, vertical, rocking, and horizontal-rocking coupling impedances normalized with respect to the corresponding quasi-static stiffness.
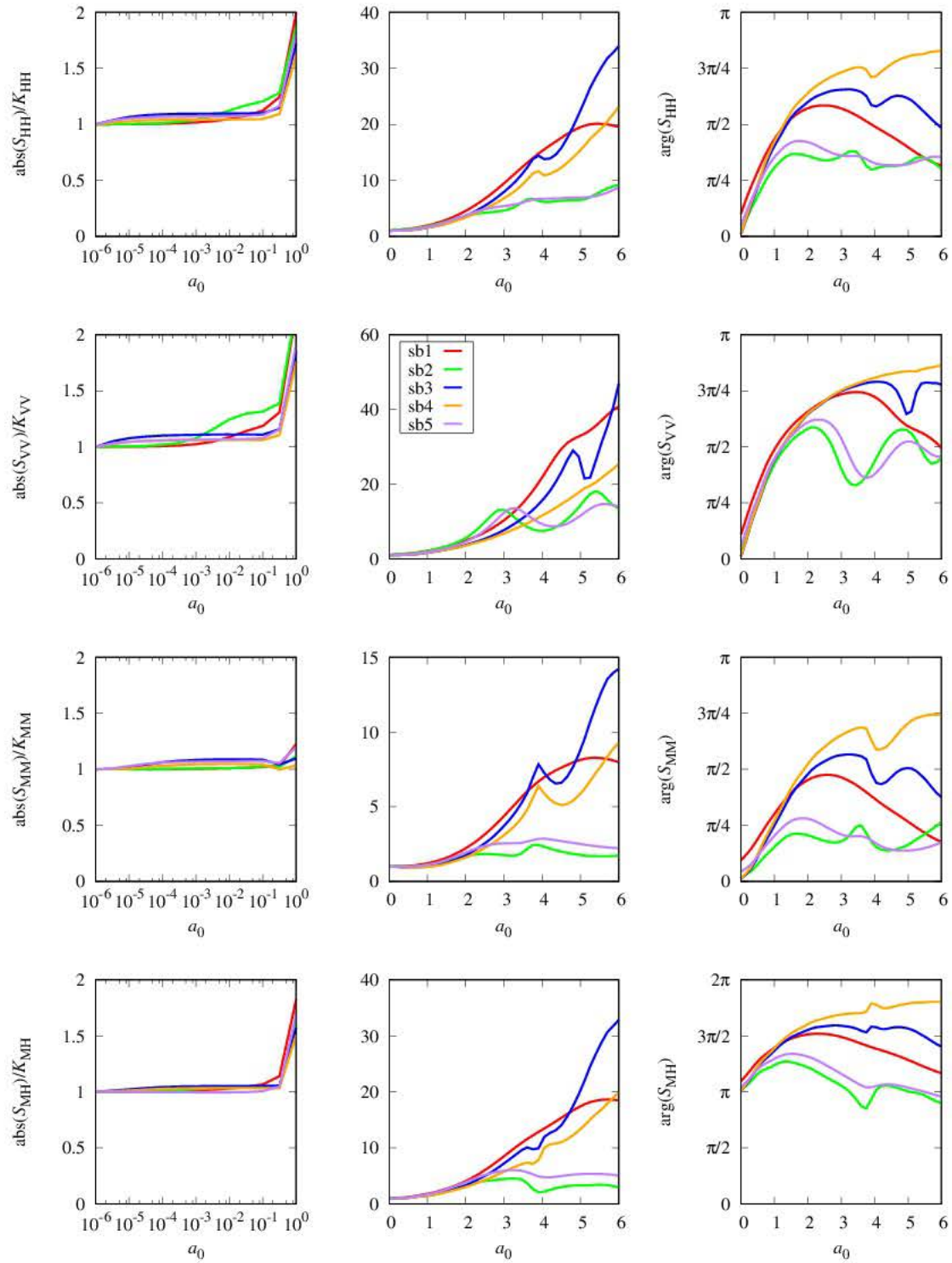
Figure 6.4: Impedances of bucket foundations with $L/D = 1$ in poroelastic soils and corresponding undrained elastic soils (dashed lines) . From top to bottom: horizontal, vertical, rocking, and horizontal-rocking coupling impedances normalized with respect to the corresponding quasi-static stiffness using the poroelastic soil.
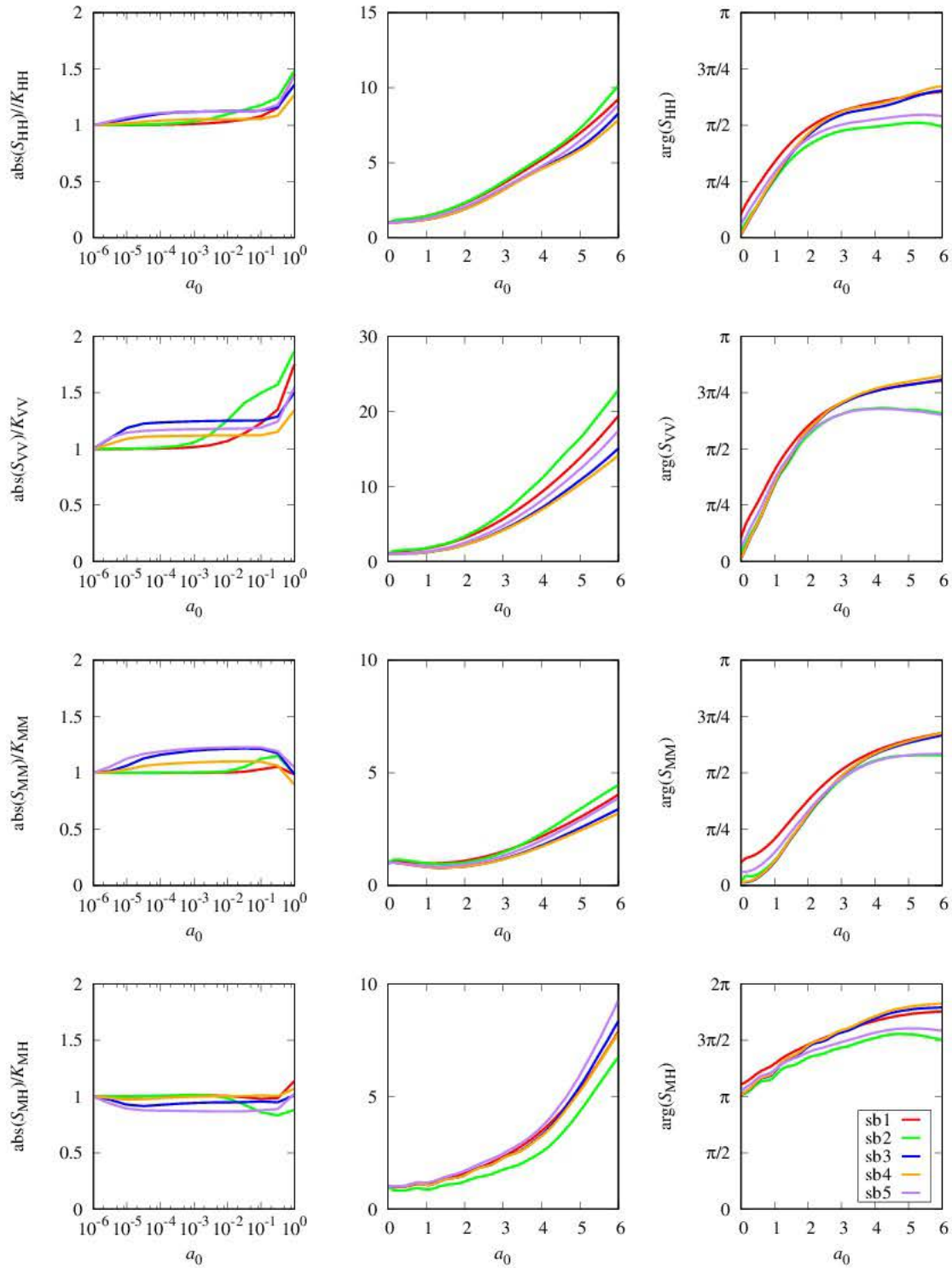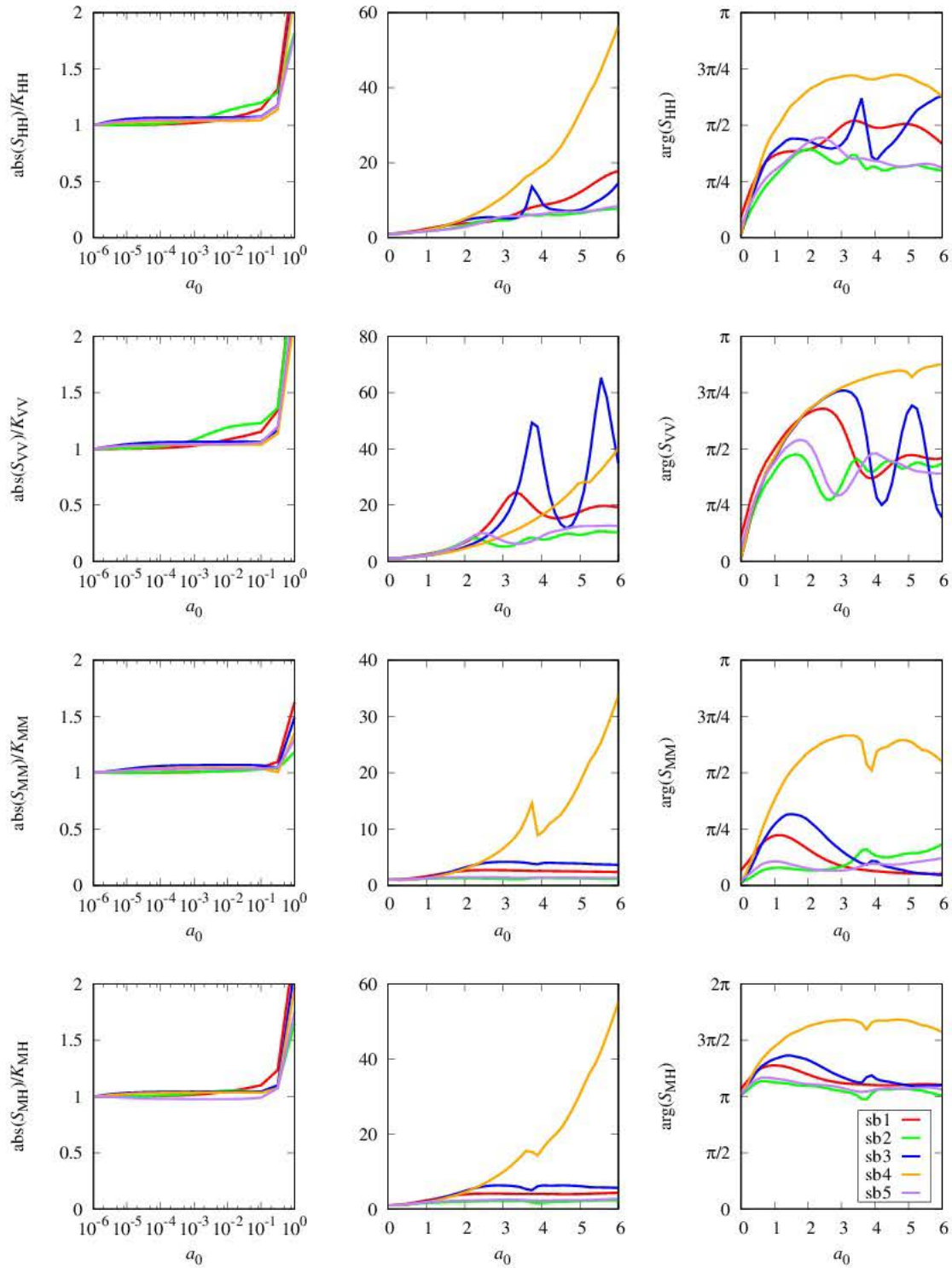
Figure 6.5: Impedances of bucket foundations with $L/D = 2$ in poroelastic soils. From top to bottom: horizontal, vertical, rocking, and horizontal-rocking coupling impedances normalized with respect to the corresponding quasi-static stiffness.

Property, symbol and units	Coarse sand and fine gravel (sb1)	Coarse sand (sb2)	Fine sand (sb3)	Silty clay (sb4)	Silty sand (sb5)
Frame shear modulus Re (μ^*) [MPa]	12.50	74.00	7.12	0.79	41.00
Frame shear modulus Im (μ^*) [MPa]	4.50	4.70	0.23	0.03	7.90
Frame bulk modulus Re (K^*) [MPa]	27.10	52.00	9.49	3.67	29.00
Frame bulk modulus Im (K^*) [MPa]	0.90	0.74	0.30	0.12	1.30
Poisson's ratio ν [–]	0.30	0.02	0.20	0.40	0.02
Porosity ϕ [–]	0.30	0.38	0.43	0.68	0.65
Fluid bulk modulus K_f [GPa]	2.38	2.40	2.39	2.38	2.40
Biot's coupling paramater Q [GPa]	1.666	1.488	1.362	0.762	0.840
Biot's coupling paramater R [GPa]	0.714	0.912	1.028	1.618	1.560
Fluid density ρ_f [kg/m^3]	1000	1000	1000	1000	1000
Solid density ρ_s [kg/m^3]	2680	2710	2670	2680	2670
Tortuosity α [–]	1.25	1.25	1.25	3.00	3.00
Additional apparent den. ρ_a [kg/m^3]	75	95	107.5	1360	1300
Fluid viscosity η [mPa $\cdot$ s]	1.01	1.01	1.01	1.01	1.01
Permeability κ [m^2]	$2.6 \cdot 10^{-10}$	$7.5 \cdot 10^{-11}$	$3.1 \cdot 10^{-14}$	$5.2 \cdot 10^{-14}$	$6.3 \cdot 10^{-15}$
Hydraulic conductivity k [m/s]	$2.5 \cdot 10^{-3}$	$7.3 \cdot 10^{-4}$	$3.0 \cdot 10^{-7}$	$5.1 \cdot 10^{-7}$	$6.2 \cdot 10^{-8}$
Disipation constant b [N $\cdot$ s/m^4]	$3.52 \cdot 10^5$	$1.95 \cdot 10^6$	$5.99 \cdot 10^9$	$8.98 \cdot 10^9$	$6.74 \cdot 10^{10}$
Undrained Poisson's ratio ν^u [–]	0.4992153	0.4942119	0.4993609	0.4998878	0.4945113
Bulk density ρ [kg/m^3]	2176	2060	1952	1538	1585
Undrained S-wave velocity c_S^u [m/s]	75.8	189.5	60.4	22.6	160.9

Table 6.1: Properties of seabed soils taken from Buchanan [205]. Top: poroelastic medium. Bottom: undrained solid.

for a broader frequency range ($a_0 = [0, 6]$). By comparing these graphs and those obtained by Liingaard et al. [41] for elastic soils, the same qualitative behaviour is observed. For small length to diameter ratios, results tend to the solution of a disc foundation, while for larger ratios results tend to the solution of an infinite hollow cylinder. As shown in Figure 6.4, the behaviour is not only qualitatively similar, but also numerically if the corresponding undrained elastic soil is used. The difference between the real poroelastic soil and the undrained elastic soil is very small.

Figure 6.6 shows the absolute values of impedances for bucket foundations of different L/D ratios buried in "fine sand" (sb3 in Table 6.1) with different hydraulic conductivities. The bucket has the same geometry and properties as previous results, except that the considered L/D ratios now range from 0 (bucket without skirt), 0.5, 1 and 2. According to Lin et al. [195], for a fine sand and within the area where Biot's theory is applicable, the hydraulic conductivity k can range between 10^{-2} and 10^{-6} m/s. Therefore, five different hydraulic conductivities ranging from drained, partially drained and undrained soils are considered: $k \to \infty$ (drained elastic soil), $k = 10^{-2}$, $k = 10^{-4}$, $k = 10^{-6}$, and $k \to 0$ (undrained elastic soil) m/s. The frequency range and scaling shown in Figure 6.6 has been chosen so that the transition from drained to undrained conditions can be clearly seen for each impedance and bucket geometry.

It is well known that for $a_0 \to 0$ the response using a poroelastic model with finite hy-
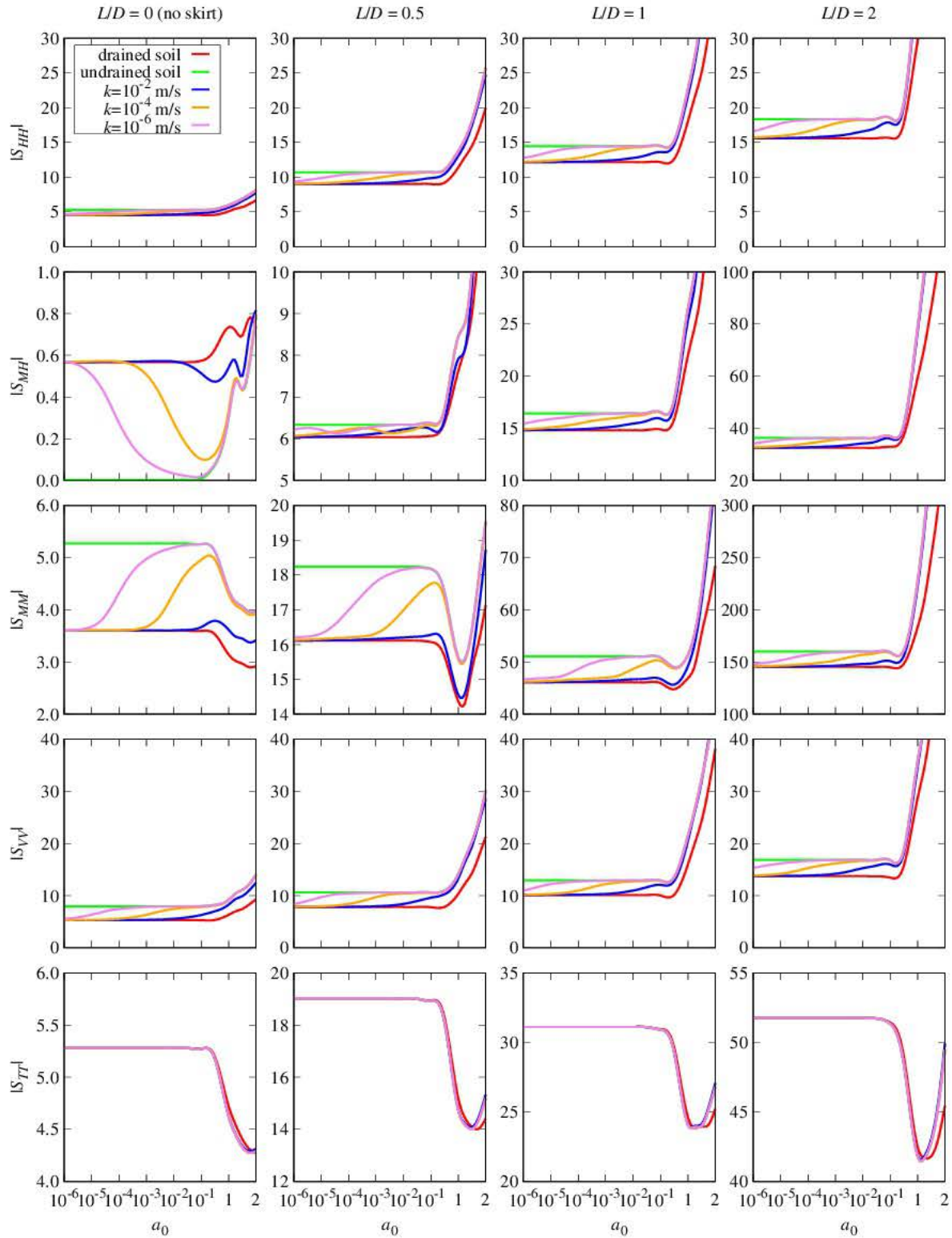
Figure 6.6: Impedances (absolute value) of bucket foundations of different L/D ratios installed in sandy soils

Quasi-static stiffness (porous: $a_0 = 10^{-6}$)	Seabed soil	$\frac{L}{D} = \frac{1}{4}$	$\frac{L}{D} = 1$		$\frac{L}{D} = 2$
		Porous	Porous	Drained	Porous
K_{HH}	sb1	7.774	13.073	13.116 (0.3%)	16.137
	sb2	6.186	8.900	8.892 (0.1%)	9.385
	sb3	7.445	13.198	12.175 (7.8%)	17.754
	sb4	8.065	14.516	14.069 (3.1%)	21.614
	sb5	7.216	11.525	9.956 (13.6%)	12.723
K_{VV}	sb1	7.557	11.288	11.336 (0.4%)	15.502
	sb2	5.822	8.954	8.946 (0.1%)	11.952
	sb3	7.483	11.662	10.124 (13.2%)	16.013
	sb4	8.403	12.321	11.58 (6.0%)	16.731
	sb5	7.904	11.849	9.283 (21.7%)	15.407
K_{MM}	sb1	8.739	47.368	47.48 (0.2%)	131.429
	sb2	7.066	28.100	28.096 (0.0%)	44.571
	sb3	8.003	46.973	46.246 (1.5%)	153.538
	sb4	8.993	53.106	52.728 (0.7%)	217.156
	sb5	7.581	35.139	34.53 (1.7%)	68.016
K_{MH}	sb1	-2.778	-15.539	-15.572 (0.2%)	-30.881
	sb2	-2.464	-8.816	-8.806 (0.1%)	-10.950
	sb3	-2.729	-16.036	-15.307 (4.5%)	-37.250
	sb4	-2.700	-17.923	-17.561 (2.0%)	-51.545
	sb5	-2.550	-11.751	-11.112 (5.4%)	-17.182

Table 6.2: Quasi-static stiffnesses of the studied bucket foundations and seabed soils

draulic conductivity k tends to a drained elastic soil, while for $a_0 \to \infty$ the response of a poroelastic model tends to the undrained elastic soil. However, the difference between impedances under drained and undrained conditions, and the location where the transition takes place in the frequency domain, depends on several factors.

The most important factor influencing the difference between impedances under drained and undrained conditions is the presence of P waves. Due to the bucket geometry and the absence of P waves in the torsional mode, the torsional impedance shown in Figure 6.6 does not depend on hydraulic conductivity, and any poroelastic soil behaves as the undrained elastic one. All other impedances imply P waves and hence are sensitive to hydraulic conductivity, although their origin and relevance are different. In the vertical mode, P waves are mostly originated from the lid, and thus, for a given diameter D, the difference between drained and undrained impedances does not depend on the length L nor L/D ratio. However, in relative terms, this difference is more important for small L/D ratios because the impedance values are smaller. In the swaying mode, P waves are mainly originated from the skirt, and then the difference between drained and undrained impedances does depend on both diameter D and length L. In relative terms, however, these differences are equally significant for different L/D ratios because they increase as the impedance values increase. The rocking mode produces P waves from the lid and the bucket, and hence both diameter D and length L influence the difference between drained and undrained impedances. The difference of impedances measured in relative terms is considerable for all L/D ratios studied, being more important

for smaller L/D ratios. Rocking-swaying impedances have significant differences between completely drained and undrained impedances. They are approximately constant in relative terms for all L/D ratios, except for the case $L/D = 0$ of a bucket without skirt (circular footing). The influence of this coupling impedance in the impedance matrix is negligible for very small L/D ratios because its magnitude is much smaller than swaying and rocking impedances, but as L/D increases the coupling impedance becomes appreciable.

For all impedances except the rocking impedance, soils are virtually behaving in undrained conditions for dimensionless frequencies $a_0 > 1$, i.e. $f > 2\,Hz$ for the considered soil. For the rocking impedance, soils start behaving in undrained conditions at higher frequencies, especially for small L/D ratios. As expected, the drained to undrained transition frequency decreases as the hydraulic conductivity decreases.

This type of foundations is now very important because of its potential as foundations of Offshore Wind Turbines. The range of frequencies of interest depends on the type of analysis, the site environmental conditions and the wind turbine [206]. For dynamic loading analysis, one could take a range from about 0.05 Hz to a few Hertz typically. This corresponds to dimensionless frequencies greater than $a_0 = 10^{-2}$ for the soil properties used in this example. It can be seen in Figure 6.6 that, for hydraulic conductivities greater than 10^{-4} m/s, the drained/undrained transition takes place within the range of frequencies of interest. The importance of this fact depends on multiple factors: soil properties, foundation design, wind turbine, etc.; but it should certainly be taken into account.

6.5 Final remarks and further research

In this chapter, a preliminary study on impedances of bucket foundations in poroelastic soils has been carried out. The main conclusion is finding that impedances of bucket foundations depends significantly on the hydraulic conductivity. The relevance of this dependence vary from impedance to impedance, and it also depends on the length to diameter ratio.

As a preliminary study, there are several aspects missing, and they are going to be considered in future research. The main aspects to be developed are:

- Perform a parametric study for a wider set of soil properties. One of the main challenges when considering such a study for poroelastic soils is choosing the sets of properties to be analysed. In this sense, three possibilities might be explored. The first one could be using an extensive set of realistic soils collected from the literature. The second possibility could be using an approximate model with a reduced set of properties, in the same spirit of the model for water-saturated sandstones used by Lin, Lee and Trifunac [195], which has actually been used in Chapter 5. The third choice could be using judiciosly selected sets of constant and variable properties.

- Study the influence of the water layer above the mudline and the interface condition between soil and water. Due to the nature of the resulting problem, an appropriate absorbing boundary condition must be included in the water layer.

- Study of the influence of the contact conditions between bucket and soil.

- Study of interaction factors for seismic SSI response.

- Study the relevance of the previous aspects on the response of Offshore Wind Turbines founded on bucket foundations (monobucket or multiple bucket foundations).

7.1 Summary and conclusions

This dissertation proposes a simplified fluid- and soil-structure dynamic model for the analysis of immersed or buried buried shell structures [28–30], which is tackled in Chapter 2. It makes use of the Dual Boundary Element Method (DBEM), which is more commonly used for crack analysis, in order to produce an approximate but natural and direct coupling between the shell structure and its surroundings.

The shell structure is modelled with shell finite elements based on the degeneration from the solid. The shear and membrane locking intrinsic of this type of elements is avoided by using the Mixed Interpolation of Tensorial Components (MITC) proposed by Bathe [93], which is also free from spurious modes.

The resulting DBEM–FEM model has been developed for two- and three-dimensional problems, where curved shell structures can be coupled to ideal fluid, elastic solid or Biot's poroelastic medium. It has been implemented in a code based on previous BEM–BEM multi-region codes of the Research Team, and hence it essentially enriches the previous capabilities.

The main difficulty of the model lies in the development of one of the ingredients of the Dual BEM, the Hypersingular Boundary Integral Equation. In order to do so, we have used the regularisation techniques proposed by Saéz, Gallego, Domínguez and Ariza [12, 60–62, 207], which had been used for potential and elastic problems. We have extended it to the Biot's poroelastic medium, for which Singular Boundary Integral Equations had been proposed by Domínguez, Maeso and Aznárez [14, 15, 70, 74].

We have also explored the extension of the model to gradient-based shape optimisation. Its completion is still underway, but the already explored branches are collected in Chapter 3. Its contents are limited to two-dimensional formulations, and structural finite elements have not been yet considered. The approach for the BEM for geometric sensitivity is based on previous works of Gallego, Suárez and Rus [103–107], and it is used in a BEM–BEM multi-region setting.

The implemented BEM formulations lead to the numerical evaluation of a greater number, more difficult and costlier integrals when compared to the conventional BEM. Therefore, Chapter 4 collects a recapitulation of the subject, and shows some advances regarding economical and robust numerical integration algorithms.

The proposed models have extended the range of problems that the Research Team is able to tackle. These have been applied to a number of problems in this thesis:

- *Two-dimensional flexible noise barriers.* Usually, noise barriers are considered as rigid obstacles. In this study, the effect of considering their flexibility is taken into account. The main conclusion is that insertion losses predicted by rigid models may be too optimistic, specially at low frequencies.

- *Two-dimensional wave barriers in poroelastic soils.* In this study, the amplitude reduction ratio (or insertion loss) of three different wave barriers buried in poroelastic soils is studied.

- *Three-dimensional curved wave barriers in poroelastic soils.* This problem is used to study the range of applicability of the DBEM–FEM model by observing near- and

far-field variables for a number of wave barriers of different thicknesses. The DBEM–FEM model is compared against a multi-region BEM model. The main conclusion is that the DBEM–FEM model have excellent agreement for slendernesses (length to thickness ratio) beyond 10, but it also shows acceptable results for slendernesses of 5 and coarse meshes.

- *Optimisation of two-dimensional wave barriers in elastic soils.* In this research, the optimisation of insertion losses of single and double wall barriers is performed. Three different objective functions corresponding to three different types of sources are considered: harmonic single frequency source, broadband source and harmonic sources within a frequency range. In this problem, we have found that the resulting optimal designs greatly improves conventional design rules, especially when the relevant part of the frequency spectrum is relatively high with respect to the depth of the design domain. In this sense, for the same amount of material, the double wall barrier outperform the single wall barrier.

- *Impedances of bucket foundations in poroelastic soils.* Since bucket foundations are installed on the seabed, we have considered the calculation of impedances using a more realistic Biot's soil than in previous works. In this sense, we have used a set of realistic seabeds taken from the literature, an for one of them we have varied the hydraulic conductivity. It has been found that impedances significantly depends on the hydraulic conductivity, except the torsional one.

For these problems, more specific conclusions are given in their corresponding chapters.

7.2 Future research directions

The proposed DBEM–FEM model has been developed for a wide range of situations: two- and three-dimensional problems, ideal fluid, elastic solid or Biot's poroelastic medium; and integrated in a code based on a previous multi-region BEM code of the Research Team. Likewise. the BEM for shape sensitivity analysis, only for two-dimensional problems, has also been integrated in that code. This means that the number of potential problems that may be considered from the present Ph. D. Thesis is large. At the same time, the experience gained from the developments done in this work put us in a better position to be able to propose new models and to face new problems. Some of the possible future research directions are:

- **Short-term**
  - *Bucket foundations.* The proposed DBEM–FEM model can directly be used to tackle a number of problems regarding bucket foundations and their application to offshore wind turbines:
    * *Impedances.* Since for an appropriate design of offshore turbines the first and second natural frequencies should avoid the most energetic part of wave and wind loading spectrum [206], it is very important to accurately estimate the foundation impedances. For elastic soils, there are several works proposing

formulas for their calculation [208,209]. Our results suggest that there may be relevant differences between impedances under drained and undrained conditions which might affect the first natural frequency. Therefore, it is important to study and predict this transition frequency, or at least to know in what conditions this is important.

* *Kinematic interaction factors.* Current recommendations suggest performing seismic analyses of the wind turbine. Therefore, it is of interest to study the kinematic interaction factors for a number of geometrical and material properties.

* *Group effect.* Foundations of offshore wind turbines come in two fashions: monobucket (a large bucket), or supporting a three or four legged jacket (three or four small buckets). For the latter, buckets operate with a push-pull mechanism, and thus mainly vertical impedances are relevant. In this situation, for design purposes it is relevant to know if fully coupled direct models are required, or if simplified sub-structuring procedures may be used.

* *Influence of water depth and contact conditions.* Incorporate absorbing boundary elements for a three-dimensional water layer, and study the influence of water depth and contact conditions between the seabed and water.

– *Inclined seismic waves in multi-layered poroelastic soils.* Formulation and implementation of more general incident field for the poroelastic half-space [195,210]. The aim is to further study the Kinematic Interaction Factors of buckets foundations and the insertion losses of wave barriers in multi-layered half-spaces.

– *Poroelastic cracks.* Given that in this work we have developed the Dual BEM for the Biot's poroelastic medium, we can use it for the study of Stress Intensity Factors (SIFs) of poroelastic cracks. In fact, after developing the two-dimensional version, we performed a comparison against already published analytical results [211, 212], with no success. We suspect that the relatively small but significant discrepancies are due to the SIF definition or the stress incident field used.

• **Medium-term**

– *Optimisation of wave barriers.* The optimisation of wave barriers performed in the present work is somewhat limited by the problem configuration considered. A further optimisation study should include a more general excitation, like a Rayleigh incident field, and also consider a more general receptor area. Also, soil stratification may play a relevant role and hence it should also be studied.

– *Pile-soil mixed dimensional model for porous medium.* Given that in the present work the HBIE has been studied, it may be used together in some combination with the SBIE in order to propose a BEM–FEM model like that of Padrón et al. [18] but for poroelastic soils.

– *Public software release.* We would like to make a public release of software developed in the course of this work. This could be in form of open source libraries or programs, or directly executables.

Let $\mathbf{x}$ and $\mathbf{n}$ be the position and unit normal vectors of the observation point, while $\mathbf{x}^i$ and $\mathbf{n}^i$ are those of the collocation point. The distance vector between both points is $\mathbf{r} = \mathbf{x} - \mathbf{x}^i$, its norm is $r = |\mathbf{r}|$, and the distance derivative is denoted as $r_{,j} = \partial r / \partial x_j$. The partial derivatives of the distance with respect to the unit normal vectors are $\partial r / \partial n = r_j n_j$ and $\partial r / \partial n^i = -r_j n_j^i$. For the sake of brevity, the wavenumbers are rewritten as $k_j = k_{Pj}$ and $k_3 = k_S$, and the following frequency-dependent parameters are defined:

$$J = \frac{1}{\hat{\rho}_{22}\omega^2}, \quad Z = \frac{\hat{\rho}_{12}}{\hat{\rho}_{22}}, \quad \alpha_j = k_j^2 - \frac{\mu}{\lambda + 2\mu}k_3^2, \quad \beta_j = \frac{\mu}{\lambda + 2\mu}k_j^2 - \frac{k_1^2 k_2^2}{k_3^2} \tag{A.1}$$

The matrices $\mathbf{I}_S^i$ and $\mathbf{I}_H^i$ appearing respectively in SBIE and HBIE are:

$$\mathbf{I}_S^i = \begin{bmatrix} J & 0 \\ 0 & \delta_{lk} \end{bmatrix}, \quad \mathbf{I}_H^i = \begin{bmatrix} 1 & 0 \\ 0 & \delta_{lk} \end{bmatrix} \tag{A.2}$$

A.1 Two-dimensional problem

The complex function $K_n(z)$ is the modified Bessel function of the second kind, order n and complex argument z.

A.1.1 Singular Boundary Integral Equation

The fundamental solution matrix $\mathbf{U}^*$ is:

$$\mathbf{U}^* = \begin{bmatrix} -\tau_{00}^* & u_{0k}^* \\ -\tau_{l0}^* & u_{lk}^* \end{bmatrix} \tag{A.3}$$

where:

$$\tau_{00}^* = \frac{1}{2\pi}\eta \tag{A.4}$$

$$\eta = \frac{1}{k_1^2 - k_2^2}\left[\alpha_1 K_0(ik_1 r) - \alpha_2 K_0(ik_2 r)\right] \tag{A.5}$$

$$u_{0k}^* = -\frac{1}{2\pi}\Theta r_{,k}, \quad \Theta = \left(\frac{Q}{R} - Z\right)\frac{1}{\lambda + 2\mu}\frac{1}{k_1^2 - k_2^2}\left[ik_1 K_1(ik_1 r) - ik_2 K_1(ik_2 r)\right] \tag{A.6}$$

$$\tau_{l0}^* = \frac{1}{2\pi J}\Theta r_{,l} \tag{A.7}$$

$$u_{lk}^* = \frac{1}{2\pi\mu}\left(\psi\delta_{lk} - \chi r_{,l}r_{,k}\right)$$

$$\psi = K_0(ik_3 r) + \frac{1}{ik_3 r}K_1(ik_3 r) - \frac{1}{k_1^2 - k_2^2}\left[\beta_1\frac{1}{ik_1 r}K_1(ik_1 r) - \beta_2\frac{1}{ik_2 r}K_1(ik_2 r)\right] \tag{A.8}$$

$$\chi = K_2(ik_3 r) - \frac{1}{k_1^2 - k_2^2}\left[\beta_1 K_2(ik_1 r) - \beta_2 K_2(ik_2 r)\right]$$

The fundamental solution matrix $\mathbf{T}^*$ is:

$$\mathbf{T}^* = \begin{bmatrix} -(U_{n00}^* + J X_j'^* n_j) & t_{0k}^* \\ -U_{nl0}^* & t_{lk}^* \end{bmatrix} \tag{A.9}$$

where:

$$U_{n00}^* + J X_j'^* n_j = \frac{1}{2\pi} W_0 \frac{\partial r}{\partial n} \tag{A.10}$$

$$W_0 = \left(Z\Theta - J\frac{\partial \eta}{\partial r} \right) \tag{A.11}$$

$$t_{0k}^* = \frac{1}{2\pi} \left[T_{01} r_{,k} \frac{\partial r}{\partial n} + T_{02} n_k \right] \tag{A.12}$$

$$T_{01} = -2\mu \left(\frac{\partial \Theta}{\partial r} - \frac{1}{r}\Theta \right) \tag{A.13}$$

$$T_{02} = -\lambda \left(\frac{\partial \Theta}{\partial r} + \frac{1}{r}\Theta \right) - 2\mu\frac{1}{r}\Theta + \frac{Q}{R}\eta \tag{A.14}$$

$$U_{nl0}^* = \frac{1}{2\pi\mu} \left[W_1 r_{,l} \frac{\partial r}{\partial n} + W_2 n_l \right] \tag{A.15}$$

$$W_1 = Z\chi - \mu \left(\frac{\partial \Theta}{\partial r} - \frac{1}{r}\Theta \right) \tag{A.16}$$

$$W_2 = -Z\psi - \mu\frac{1}{r}\Theta \tag{A.17}$$

$$t_{lk}^* = \frac{1}{2\pi} \left[T_1 r_{,l} r_{,k} \frac{\partial r}{\partial n} + T_2 \left(\frac{\partial r}{\partial n}\delta_{lk} + r_{,k} n_l \right) + T_3 r_{,l} n_k \right] \tag{A.18}$$

$$T_1 = -2 \left(\frac{\partial \chi}{\partial r} - \frac{2}{r}\chi \right) \tag{A.19}$$

$$T_2 = \frac{\partial \psi}{\partial r} - \frac{1}{r}\chi \tag{A.20}$$

$$T_3 = \frac{\lambda}{\mu} \left(\frac{\partial \psi}{\partial r} - \frac{\partial \chi}{\partial r} - \frac{1}{r}\chi \right) - \frac{2}{r}\chi + \frac{Q}{RJ}\Theta \tag{A.21}$$

A.1.2 Hypersingular Boundary Integral Equation

The fundamental solution matrix $\mathbf{D}^*$ is:

$$\mathbf{D}^* = \begin{bmatrix} -d_{00}^* & d_{0k}^* \\ -d_{l0}^* & d_{lk}^* \end{bmatrix} \tag{A.22}$$

where:

$$d_{00}^* = \frac{1}{2\pi J} W_0 \frac{\partial r}{\partial n^{\mathrm{i}}} \tag{A.23}$$

$$d_{0k}^* = \frac{1}{2\pi\mu} \left(-W_1 r_{,k} \frac{\partial r}{\partial n^{\mathrm{i}}} + W_2 n_k^{\mathrm{i}} \right) \tag{A.24}$$

$$d_{l0}^* = \frac{1}{2\pi J} \left(-T_{01} r_{,l} \frac{\partial r}{\partial n^{\mathrm{i}}} + T_{02} n_l^{\mathrm{i}} \right) \tag{A.25}$$

$$d_{lk}^* = \frac{1}{2\pi} \left[T_1 r_{,l} r_{,k} \frac{\partial r}{\partial n^{\mathrm{i}}} - T_2 \left(-\frac{\partial r}{\partial n^{\mathrm{i}}} \delta_{lk} + r_{,l} n_k^{\mathrm{i}} \right) - T_3 r_{,k} n_l^{\mathrm{i}} \right] \tag{A.26}$$

The fundamental solution matrix $\mathbf{S}^*$ is:

$$\mathbf{S}^* = \begin{bmatrix} -s_{00}^* & s_{0k}^* \\ -s_{l0}^* & s_{lk}^* \end{bmatrix} \tag{A.27}$$

where:

$$s_{00}^* = \frac{1}{2\pi} \left[Q_1 \frac{\partial r}{\partial n} \frac{\partial r}{\partial n^{\mathrm{i}}} + Q_2 n_j n_j^{\mathrm{i}} \right] \tag{A.28}$$

$$Q_1 = \frac{Z^2}{\mu} \chi - 2Z \left(\frac{\partial \Theta}{\partial r} - \frac{1}{r} \Theta \right) + J \left(\frac{\partial^2 \eta}{\partial r^2} - \frac{1}{r} \frac{\partial \eta}{\partial r} \right) \tag{A.29}$$

$$Q_2 = \frac{Z^2}{\mu} \psi + 2Z \frac{1}{r} \Theta - J \frac{1}{r} \frac{\partial \eta}{\partial r} \tag{A.30}$$

$$s_{0k}^* = \frac{1}{2\pi} \left\{ S_{01} r_{,k} \frac{\partial r}{\partial n} \frac{\partial r}{\partial n^{\mathrm{i}}} + S_{02} n_k \frac{\partial r}{\partial n^{\mathrm{i}}} + S_{03} \left[n_k^{\mathrm{i}} \frac{\partial r}{\partial n} + r_{,k} n_j n_j^{\mathrm{i}} \right] \right\} \tag{A.31}$$

$$S_{01} = -2Z \left(\frac{\partial \chi}{\partial r} - \frac{2}{r} \chi \right) - 2\mu \left[-\frac{\partial^2 \Theta}{\partial r^2} + \frac{3}{r} \left(\frac{\partial \Theta}{\partial r} - \frac{1}{r} \Theta \right) \right] \tag{A.32}$$

$$\begin{aligned} S_{02} = {} & Z \left[\frac{\lambda}{\mu} \left(\frac{\partial \psi}{\partial r} - \frac{\partial \chi}{\partial r} - \frac{1}{r} \chi \right) - \frac{2}{r} \chi \right] + \lambda \left[\frac{\partial^2 \Theta}{\partial r^2} + \frac{1}{r} \left(\frac{\partial \Theta}{\partial r} - \frac{1}{r} \Theta \right) \right] \\ & + 2\mu \frac{1}{r} \left(\frac{\partial \Theta}{\partial r} - \frac{1}{r} \Theta \right) + \frac{Q}{RJ} \left(Z\Theta - J \frac{\partial \eta}{\partial r} \right) \end{aligned} \tag{A.33}$$

$$S_{03} = -Z \left(\frac{\partial \psi}{\partial r} - \frac{1}{r} \chi \right) - 2\mu \frac{1}{r} \left(\frac{\partial \Theta}{\partial r} - \frac{1}{r} \Theta \right) \tag{A.34}$$

$$s_{l0}^* = \frac{1}{2\pi} \left\{ -S_{01} r_{,l} \frac{\partial r}{\partial n} \frac{\partial r}{\partial n^i} + S_{02} n_l^i \frac{\partial r}{\partial n} - S_{03} \left[-n_l \frac{\partial r}{\partial n^i} + r_{,l} n_j n_j^i \right] \right\} \tag{A.35}$$

$$s_{lk}^* = \frac{\mu}{2\pi} \left\{ S_1 \left[r_{,l} n_k^i \frac{\partial r}{\partial n} - r_{,k} n_l \frac{\partial r}{\partial n^i} - \frac{\partial r}{\partial n} \frac{\partial r}{\partial n^i} \delta_{lk} + r_{,k} r_{,l} n_j n_j^i \right] \right.$$
$$+ S_2 \left(r_{,k} n_l^i \frac{\partial r}{\partial n} - r_{,l} n_k \frac{\partial r}{\partial n^i} \right) + S_3 r_{,l} r_{,k} \frac{\partial r}{\partial n} \frac{\partial r}{\partial n^i} \tag{A.36}$$
$$\left. + S_4 \left[n_j n_j^i \delta_{lk} + n_l n_k^i \right] + S_5 n_k n_l^i \right\}$$

$$S_1 = -\frac{\partial^2 \psi}{\partial r^2} + \frac{1}{r} \left(\frac{\partial \psi}{\partial r} + 3 \frac{\partial \chi}{\partial r} - \frac{6}{r} \chi \right) \tag{A.37}$$

$$S_2 = 2 \frac{\lambda}{\mu} \left[-\frac{\partial^2 \psi}{\partial r^2} + \frac{\partial^2 \chi}{\partial r^2} + \frac{1}{r} \left(\frac{\partial \psi}{\partial r} - \frac{2}{r} \chi \right) \right] + \frac{4}{r} \left(\frac{\partial \chi}{\partial r} - \frac{2}{r} \chi \right) - \frac{2Q}{RJ} \left(\frac{\partial \Theta}{\partial r} - \frac{1}{r} \Theta \right) \tag{A.38}$$

$$S_3 = 4 \left[-\frac{\partial^2 \chi}{\partial r^2} + \frac{1}{r} \left(5 \frac{\partial \chi}{\partial r} - \frac{8}{r} \chi \right) \right] \tag{A.39}$$

$$S_4 = -\frac{2}{r} \left(\frac{\partial \psi}{\partial r} - \frac{1}{r} \chi \right) \tag{A.40}$$

$$S_5 = \frac{\lambda^2}{\mu^2} \left[-\frac{\partial^2 \psi}{\partial r^2} + \frac{\partial^2 \chi}{\partial r^2} + \frac{1}{r} \left(-\frac{\partial \psi}{\partial r} + 2 \frac{\partial \chi}{\partial r} \right) \right] - \frac{\lambda}{\mu} \frac{4}{r} \left(\frac{\partial \psi}{\partial r} - \frac{\partial \chi}{\partial r} - \frac{1}{r} \chi \right)$$
$$+ \frac{4}{r^2} \chi + \frac{Q}{R} \frac{1}{J} \left[-2 \frac{\lambda}{\mu} \left(\frac{\partial \Theta}{\partial r} + \frac{1}{r} \Theta \right) - \frac{4}{r} \Theta + \frac{Q}{R\mu} \eta \right] \tag{A.41}$$

A.2 Three-dimensional problem

A.2.1 Singular Boundary Integral Equation

The fundamental solution matrix $\mathbf{U}^*$ is:

$$\mathbf{U}^* = \begin{bmatrix} -\tau_{00}^* & u_{0k}^* \\ -\tau_{l0}^* & u_{lk}^* \end{bmatrix} \tag{A.42}$$

where:

$$\tau_{00}^* = \frac{1}{4\pi} \eta \tag{A.43}$$

$$\eta = \frac{1}{k_1^2 - k_2^2} \left[\frac{\alpha_1}{r} e^{-ik_1 r} - \frac{\alpha_2}{r} e^{-ik_2 r} \right] \tag{A.44}$$

$$u_{0k}^* = -\frac{1}{4\pi}\Theta r_{,k} \tag{A.45}$$

$$\Theta = \frac{Q/R - Z}{\lambda + 2\mu}\frac{1}{k_1^2 - k_2^2}\left[\left(\frac{1}{r^2} + \frac{ik_1}{r}\right)e^{-ik_1 r} - \left(\frac{1}{r^2} + \frac{ik_2}{r}\right)e^{-ik_2 r}\right] \tag{A.46}$$

$$\tau_{l0}^* = \frac{1}{4\pi J}\Theta r_{,l} \tag{A.47}$$

$$u_{lk}^* = \frac{1}{4\pi\mu}\left(\delta_{lk}\psi - \chi r_{,l}r_{,k}\right) \tag{A.48}$$

$$\psi = \frac{1}{r}e^{-ik_3 r} + \frac{1}{r}\left(\frac{1}{ik_3 r} + \frac{1}{(ik_3 r)^2}\right)e^{-ik_3 r} - \frac{1}{k_1^2 - k_2^2}\cdot$$
$$\left[\frac{\beta_1}{r}\left(\frac{1}{ik_1 r} + \frac{1}{(ik_1 r)^2}\right)e^{-ik_1 r} - \frac{\beta_2}{r}\left(\frac{1}{ik_2 r} + \frac{1}{(ik_2 r)^2}\right)e^{-ik_2 r}\right] \tag{A.49}$$

$$\chi = \frac{1}{r}\left(1 + \frac{3}{ik_3 r} + \frac{3}{(ik_3 r)^2}\right)e^{-ik_3 r} - \frac{1}{k_1^2 - k_2^2}\cdot$$
$$\left[\frac{\beta_1}{r}\left(1 + \frac{3}{ik_1 r} + \frac{3}{(ik_1 r)^2}\right)e^{-ik_1 r} - \frac{\beta_2}{r}\left(1 + \frac{3}{ik_2 r} + \frac{3}{(ik_2 r)^2}\right)e^{-ik_2 r}\right] \tag{A.50}$$

The fundamental solution matrix $\mathbf{T}^*$ is:

$$\mathbf{T}^* = \begin{bmatrix} -(U_{n00}^* + J X_j'^* n_j) & t_{0k}^* \\ -U_{nl0}^* & t_{lk}^* \end{bmatrix} \tag{A.51}$$

where:

$$U_{n00}^* + J X_j'^* n_j = \frac{1}{4\pi}W_0\frac{\partial r}{\partial n} \tag{A.52}$$

$$W_0 = Z\Theta - J\frac{\partial \eta}{\partial r} \tag{A.53}$$

$$t_{0k}^* = \frac{1}{4\pi}\left[T_{01}r_{,k}\frac{\partial r}{\partial n} + T_{02}n_k\right] \tag{A.54}$$

$$T_{01} = -2\mu\left(\frac{\partial\Theta}{\partial r} - \frac{1}{r}\Theta\right) \tag{A.55}$$

$$T_{02} = -\lambda\left(\frac{\partial\Theta}{\partial r} + \frac{2}{r}\Theta\right) - 2\mu\frac{1}{r}\Theta + \frac{Q}{R}\eta \tag{A.56}$$

$$U_{nl0}^* = \frac{1}{4\pi\mu}\left[W_1 r_{,l}\frac{\partial r}{\partial n} + W_2 n_l\right] \tag{A.57}$$

$$W_1 = Z\chi - \mu\left(\frac{\partial\Theta}{\partial r} - \frac{1}{r}\Theta\right) \tag{A.58}$$

$$W_2 = -Z\psi - \mu\frac{1}{r}\Theta \tag{A.59}$$

$$t_{lk}^* = \frac{1}{4\pi} \left[T_1 r_{,l} r_{,k} \frac{\partial r}{\partial n} + T_2 \left(\delta_{lk} \frac{\partial r}{\partial n} + r_{,k} n_l \right) + T_3 r_{,l} n_k \right] \tag{A.60}$$

$$T_1 = -2 \left(\frac{\partial \chi}{\partial r} - \frac{2}{r} \chi \right) \tag{A.61}$$

$$T_2 = \frac{\partial \psi}{\partial r} - \frac{1}{r} \chi \tag{A.62}$$

$$T_3 = -\frac{2}{r} \chi + \frac{\lambda}{\mu} \left(\frac{\partial \psi}{\partial r} - \frac{\partial \chi}{\partial r} - \frac{2}{r} \chi \right) + \frac{Q}{R} \frac{1}{J} \Theta \tag{A.63}$$

A.2.2 Hypersingular Boundary Integral Equation

The fundamental solution matrix $\mathbf{D}^*$ is:

$$\mathbf{D}^* = \begin{bmatrix} -d_{00}^* & d_{0k}^* \\ -d_{l0}^* & d_{lk}^* \end{bmatrix} \tag{A.64}$$

where:

$$d_{00}^* = \frac{1}{4\pi J} W_0 \frac{\partial r}{\partial n^i} \tag{A.65}$$

$$d_{0k}^* = \frac{1}{4\pi \mu} \left(-W_1 r_{,k} \frac{\partial r}{\partial n^i} + W_2 n_k^i \right) \tag{A.66}$$

$$d_{l0}^* = \frac{1}{4\pi J} \left(-T_{01} r_{,l} \frac{\partial r}{\partial n^i} + T_{02} n_l^i \right) \tag{A.67}$$

$$d_{lk}^* = \frac{1}{4\pi} \left[T_1 r_{,l} r_{,k} \frac{\partial r}{\partial n^i} - T_2 \left(-\delta_{lk} \frac{\partial r}{\partial n^i} + r_{,l} n_k^i \right) - T_3 r_{,k} n_l^i \right] \tag{A.68}$$

The fundamental solution matrix $\mathbf{S}^*$ is:

$$\mathbf{S}^* = \begin{bmatrix} -s_{00}^* & s_{0k}^* \\ -s_{l0}^* & s_{lk}^* \end{bmatrix} \tag{A.69}$$

where:

$$s_{00}^* = \frac{1}{4\pi} \left[Q_1 \frac{\partial r}{\partial n} \frac{\partial r}{\partial n^i} + Q_2 \left(\mathbf{n} \cdot \mathbf{n}^i \right) \right] \tag{A.70}$$

$$Q_1 = \frac{Z^2}{\mu} \chi - 2Z \left(\frac{\partial \Theta}{\partial r} - \frac{1}{r} \Theta \right) + J \left(\frac{\partial^2 \eta}{\partial r^2} - \frac{1}{r} \frac{\partial \eta}{\partial r} \right) \tag{A.71}$$

$$Q_2 = \frac{Z^2}{\mu} \psi + 2Z \frac{1}{r} \Theta - J \frac{1}{r} \frac{\partial \eta}{\partial r} \tag{A.72}$$

$$s_{0k}^* = \frac{1}{4\pi} \left\{ S_{01} r_{,k} \frac{\partial r}{\partial n} \frac{\partial r}{\partial n^i} + S_{02} n_k \frac{\partial r}{\partial n^i} + S_{03} \left[n_k^i \frac{\partial r}{\partial n} + r_{,k} \left(\mathbf{n} \cdot \mathbf{n}^i \right) \right] \right\} \tag{A.73}$$

$$S_{01} = -2Z \left(\frac{\partial \chi}{\partial r} - \frac{2}{r} \chi \right) - 2\mu \left[-\frac{\partial^2 \Theta}{\partial r^2} + \frac{3}{r} \left(\frac{\partial \Theta}{\partial r} - \frac{1}{r} \Theta \right) \right] \tag{A.74}$$

$$S_{02} = \frac{Q}{R}\left(\frac{Z}{J}\Theta - \frac{\partial\eta}{\partial r}\right) + Z\left[\frac{\lambda}{\mu}\left(\frac{\partial\psi}{\partial r} - \frac{\partial\chi}{\partial r} - \frac{2}{r}\chi\right) - \frac{2}{r}\chi\right] +$$
$$\lambda\left[\frac{\partial^2\Theta}{\partial r^2} + \frac{2}{r}\left(\frac{\partial\Theta}{\partial r} - \frac{1}{r}\Theta\right)\right] + 2\mu\frac{1}{r}\left(\frac{\partial\Theta}{\partial r} - \frac{1}{r}\Theta\right) \quad \text{(A.75)}$$

$$S_{03} = -Z\left(\frac{\partial\psi}{\partial r} - \frac{1}{r}\chi\right) - 2\mu\frac{1}{r}\left(\frac{\partial\Theta}{\partial r} - \frac{1}{r}\Theta\right) \quad \text{(A.76)}$$

$$s_{l0}^* = \frac{1}{4\pi}\left\{-S_{01}r_{,l}\frac{\partial r}{\partial n}\frac{\partial r}{\partial n^{\mathrm{i}}} + S_{02}n_l^{\mathrm{i}}\frac{\partial r}{\partial n} - S_{03}\left[-n_l\frac{\partial r}{\partial n^{\mathrm{i}}} + r_{,l}\left(\mathbf{n}\cdot\mathbf{n}^{\mathrm{i}}\right)\right]\right\} \quad \text{(A.77)}$$

$$s_{lk}^* = \frac{\mu}{4\pi}\left\{S_1\left[r_{,l}n_k^{\mathrm{i}}\frac{\partial r}{\partial n} - r_{,k}n_l\frac{\partial r}{\partial n^{\mathrm{i}}} - \delta_{lk}\frac{\partial r}{\partial n}\frac{\partial r}{\partial n^{\mathrm{i}}} + r_{,k}r_{,l}\left(\mathbf{n}\cdot\mathbf{n}^{\mathrm{i}}\right)\right] + \right.$$
$$S_2\left(r_{,k}n_l^{\mathrm{i}}\frac{\partial r}{\partial n} - r_{,l}n_k\frac{\partial r}{\partial n^{\mathrm{i}}}\right) + S_3 r_{,l}r_{,k}\frac{\partial r}{\partial n}\frac{\partial r}{\partial n^{\mathrm{i}}} +$$
$$\left. S_4\left[\delta_{lk}\left(\mathbf{n}\cdot\mathbf{n}^{\mathrm{i}}\right) + n_l n_k^{\mathrm{i}}\right] + S_5 n_k n_l^{\mathrm{i}}\right\} \quad \text{(A.78)}$$

$$S_1 = -\frac{\partial^2\psi}{\partial r^2} + \frac{1}{r}\left(\frac{\partial\psi}{\partial r} + 3\frac{\partial\chi}{\partial r} - \frac{6}{r}\chi\right) \quad \text{(A.79)}$$

$$S_2 = 2\frac{\lambda}{\mu}\left[-\frac{\partial^2\psi}{\partial r^2} + \frac{\partial^2\chi}{\partial r^2} + \frac{1}{r}\left(\frac{\partial\psi}{\partial r} + \frac{\partial\chi}{\partial r} - \frac{4}{r}\chi\right)\right] +$$
$$\frac{4}{r}\left(\frac{\partial\chi}{\partial r} - \frac{2}{r}\chi\right) - 2\frac{Q}{R}\frac{1}{J}\left(\frac{\partial\Theta}{\partial r} - \frac{1}{r}\Theta\right) \quad \text{(A.80)}$$

$$S_3 = 4\left[-\frac{\partial^2\chi}{\partial r^2} + \frac{1}{r}\left(5\frac{\partial\chi}{\partial r} - \frac{8}{r}\chi\right)\right] \quad \text{(A.81)}$$

$$S_4 = \frac{2}{r}\left(-\frac{\partial\psi}{\partial r} + \frac{1}{r}\chi\right) \quad \text{(A.82)}$$

$$S_5 = \frac{4}{r^2}\chi + \frac{\lambda}{\mu}\frac{4}{r}\left(-\frac{\partial\psi}{\partial r} + \frac{\partial\chi}{\partial r} + \frac{2}{r}\chi\right) +$$
$$\frac{\lambda^2}{\mu^2}\left[-\frac{\partial^2\psi}{\partial r^2} + \frac{\partial^2\chi}{\partial r^2} + \frac{2}{r}\left(-\frac{\partial\psi}{\partial r} + 2\frac{\partial\chi}{\partial r} + \frac{1}{r}\chi\right)\right] +$$
$$\frac{Q}{R}\frac{1}{J}\left[-2\frac{\lambda}{\mu}\left(\frac{\partial\Theta}{\partial r} + \frac{2}{r}\Theta\right) - \frac{4}{r}\Theta + \frac{Q}{R\mu}\eta\right] \quad \text{(A.83)}$$

B.1 Modified Bessel functions of the second kind

Modified Bessel functions of the second kind K_0, K_1 y K_2 appear in two-dimensional fundamental solutions, and they can be decomposed by using the limiting form for small arguments $z \to 0$ [213] as:

$$K_0(z) = -\ln\frac{z}{2} - \gamma + K_0^R(z)$$

$$K_1(z) = \frac{1}{z} + \frac{z}{2}\left(\ln\frac{z}{2} + \gamma - \frac{1}{2}\right) + K_1^R(z)$$

$$K_2(z) = \frac{2}{z^2} - \frac{1}{2} - \frac{z^2}{8}\left(\ln\frac{z}{2} + \gamma - \frac{3}{4}\right) + K_2^R(z)$$

(B.1)

where $K_n^R(z) = \mathcal{O}\left(z^{n+2}\ln z\right)$. Argument z has the general form of $z_m = ik_m r$, and thus, when substituting decomposed K_n in the fundamental solution components, it is possible to decomposed these in terms of order $\mathcal{O}[r^p(\ln r)^q]$ with $p \geq -2$ and $q = 0,1$. Note that this decomposition differs from that proposed in Domínguez [6] for $K_2(z)$, in order to handle more appropriately two-dimensional hypersingular formulations.

B.2 Exponential function

Three-dimensional fundamental solutions are composed by a linear combination of terms of the type:

$$f_{mn}(r) = \frac{1}{r^n}e^{-ik_m r}$$

(B.2)

where k_m is the wavenumber m, in general a complex number, $n \in \mathbb{N}$, and $r = |\mathbf{x} - \mathbf{x}^i|$ is the distance between observation and collocation points. Each wavenumber and coefficient of the linear combination is constant for a given frequency and properties. Therefore, for a given problem and frequency of analysis, these terms only depends on the distance r. When $r \to 0^+$, then $e^{-ik_m r} \to 1$, $r^{-n} \to +\infty$, and $f_{mn}(r) \to +\infty$. When $r \to +\infty$ and $\text{Im}(k_m) \leq 0$, then $e^{-ik_m r}$ is oscillating but evanescence, $r^{-n} \to 0^+$, and $f_{mn}(r) \to 0$. For small $k_m r$, it is necessary to segregate the different parts of the exponential function. This admits the following power series expansion:

$$e^z = \sum_{k=0}^{k=\infty}\frac{z^k}{k!}$$

(B.3)

where if we define the residue of order l as:

$$E_l(z) = \sum_{k=l}^{k=\infty}\frac{z^k}{k!}$$

(B.4)

the l first terms of the expansion can be segregated:

$$e^z = 1 + z + \frac{z^2}{2} + \ldots + E_l(z)$$

(B.5)

Then, each term $f_{mn}(r)$ can be segregated in several terms of different degrees of singularity $\mathcal{O}(r^j)$ with respect to r:

$$
\begin{aligned}
f_{mn}(r) &= \frac{1}{r^n} - ik_m \frac{1}{r^{n-1}} + \ldots + \frac{(-ik_m)^{n-1}}{(n-1)!} \frac{1}{r} + \frac{(-ik_m)^n}{n!} + \frac{1}{r^n} E_{n+1}(z) \\
&= \mathcal{O}(r^{-n}) + \ldots + \mathcal{O}(r^0) + \mathcal{O}(r^1) \quad \text{(B.6)}
\end{aligned}
$$

The idea of regularising singular integrals in the context of the Boundary Element Method by using a form of the Stokes' theorem can be traced back to the seminal work of Cruse [214, Appendix 2] almost 50 years ago. In fact, the identity shown by Equation (C.1) is already present in that paper. In all these years, many authors have been using the idea in one way or another. Although a little bit old, a review of the subject was presented by Tanaka, Sladek and Sladek [63] back in 1994.

We base our work for three-dimensional formulations in the developments done by Domínguez, Ariza and Gallego [61], who presented an elegant and explicit regularisation process. They clearly demonstrate the cancellation of all unbounded terms at the Boundary Integral Equation level. One of the difficulties is finding the appropriate identities that allow using the Stokes' theorem to turn strongly singular and hypersingular surface integrals into weakly singular surface integrals and nearly singular line integrals. The identities used in the present work are:

$$\frac{r_{,l}n_k - r_{,k}n_l}{r^2} = \epsilon_{lkj}\left(\boldsymbol{\nabla} \times \frac{\mathbf{e}_j}{r}\right)\cdot\mathbf{n} \tag{C.1}$$

$$\frac{\mathbf{n}\cdot\mathbf{n}^i}{r^3} = -\frac{3}{r^3}\frac{\partial r}{\partial n}\frac{\partial r}{\partial n^i} + \left(\boldsymbol{\nabla} \times \frac{\mathbf{r}\times\mathbf{n}^i}{r^3}\right)\cdot\mathbf{n} \tag{C.2}$$

$$\frac{r_{,k}\left(\mathbf{n}\cdot\mathbf{n}^i\right)}{r^2} = -\frac{n_k}{r^2}\frac{\partial r}{\partial n^i} + \left(\boldsymbol{\nabla} \times \frac{\mathbf{e}_k\times\mathbf{n}^i}{r}\right)\cdot\mathbf{n} \tag{C.3}$$

$$\frac{r_{,l}r_{,k}\left(\mathbf{n}\cdot\mathbf{n}^i\right)}{r^3} = -\frac{5r_{,l}r_{,k}}{r^3}\frac{\partial r}{\partial n}\frac{\partial r}{\partial n^i} - \frac{r_{,l}n_k^i + r_{,k}n_l^i}{r^3}\frac{\partial r}{\partial n} + \left[\boldsymbol{\nabla} \times \left(r_{,l}r_{,k}\frac{\mathbf{r}\times\mathbf{n}^i}{r^3}\right)\right]\cdot\mathbf{n} \tag{C.4}$$

$$\frac{n_k}{r^3} = \frac{3r_{,k}}{r^3}\frac{\partial r}{\partial n} + \left(\boldsymbol{\nabla} \times \frac{\mathbf{r}\times\mathbf{e}_k}{r^3}\right)\cdot\mathbf{n} \tag{C.5}$$

$$\frac{r_{,l}r_{,k}r_{,j}\left(\mathbf{n}\cdot\mathbf{n}^i\right)}{r^2} = -\frac{1}{3}\frac{r_{,j}n_kn_l^i}{r^2} - \frac{1}{3}\frac{r_{,l}n_kn_j^i}{r^2} + \delta_{lk}\frac{1}{3}\frac{r_{,j}\left(\mathbf{n}\cdot\mathbf{n}^i\right)}{r^2} + \delta_{jk}\frac{1}{3}\frac{r_{,l}\left(\mathbf{n}\cdot\mathbf{n}^i\right)}{r^2} - \frac{r_{,l}r_{,j}n_k}{r^2}\frac{\partial r}{\partial n^i} + \frac{1}{3}\left[\boldsymbol{\nabla} \times \left(r_{,l}r_{,j}\frac{\mathbf{e}_k\times\mathbf{n}^i}{r}\right)\right]\cdot\mathbf{n} \tag{C.6}$$

where $\mathbf{r} = \mathbf{x} - \mathbf{x}^i$ is the distance vector between observation and collocation point, $r = |\mathbf{r}|$, $r_{,k} = \partial r/\partial x_k$, $\mathbf{n}$ is the unit normal at the observation point, $\mathbf{n}^i$ is the unit normal at the collocation point, $\mathbf{e}_j$ is the unit vector of the Cartesian axis j, δ_{lk} is the Kronecker delta and ϵ_{lkj} is the Levi-Civita symbol. Equations (C.1–C.4) are equal to those shown in [61, 62]. However, Equations (C.5) and (C.6) differ from respectively Equations (B17) and (B20) because it seems that they contain some errata. In the former case, it seems that some indices are misplaced. In the latter case, it lacks two terms. In the following, we demonstrate these identities.

Proof of Equation (C.5)   Using tensor notation, the vector field in the rotational term is:

$$\frac{\mathbf{r} \times \mathbf{e}_k}{r^3} = \epsilon_{nlm} \frac{r_l}{r^3} \delta_{mk} \tag{C.7}$$

Applying the rotational:

$$\nabla \times \frac{\mathbf{r} \times \mathbf{e}_k}{r^3} = \epsilon_{ijn} \frac{\partial}{\partial x_j} \epsilon_{nlm} \frac{r_l}{r^3} \delta_{mk} = \epsilon_{ijn} \epsilon_{nlm} \left(\frac{r_l}{r^3} \right)_{,j} \delta_{mk} \tag{C.8}$$

where the derivative is:

$$\left(\frac{r_l}{r^3} \right)_{,j} = \frac{\delta_{lk} - 3 r_{,l} r_{,j}}{r^3} \tag{C.9}$$

which results in:

$$\nabla \times \frac{\mathbf{r} \times \mathbf{e}_k}{r^3} = \epsilon_{ijn} \epsilon_{nlm} \delta_{mk} \frac{\delta_{lk} - 3 r_{,l} r_{,j}}{r^3} = \frac{\delta_{ik}}{r^3} - \frac{3 r_{,i} r_{,k}}{r^3} \tag{C.10}$$

after applying some properties of the Levi-Civita symbol and the Kronecker delta. Finally, doing the dot product by the unit normal, $\mathbf{n}$ on the left and n_i on the right:

$$\left(\nabla \times \frac{\mathbf{r} \times \mathbf{e}_k}{r^3} \right) \cdot \mathbf{n} = \frac{\delta_{ik} n_i}{r^3} - \frac{3 r_{,k} r_{,i} n_i}{r^3} = \frac{n_k}{r^3} - \frac{3 r_{,k}}{r^3} \frac{\partial r}{\partial n} \tag{C.11}$$

which demonstrates the identity shown in Equation (C.5).

Proof of Equation (C.6)   Using tensor notation, the vector field is:

$$r_{,l} r_{,j} \frac{\mathbf{e}_k \times \mathbf{n}^i}{r} = r_{,l} r_{,j} \frac{\epsilon_{imn} \delta_{mk} n_n^i}{r} = \epsilon_{imn} \delta_{mk} n_n^i \frac{r_{,l} r_{,j}}{r} \tag{C.12}$$

The rotational of this vector field is:

$$\nabla \times \left(r_{,l} r_{,j} \frac{\mathbf{e}_k \times \mathbf{n}^i}{r} \right) = \epsilon_{pqi} \frac{\partial}{\partial x_q} \epsilon_{imn} \delta_{mk} n_n^i \frac{r_{,l} r_{,j}}{r} = \epsilon_{pqi} \epsilon_{imn} \delta_{mk} n_n^i \left(\frac{r_{,l} r_{,j}}{r} \right)_{,q} \tag{C.13}$$

where the derivative is:

$$\left(\frac{r_{,l} r_{,j}}{r} \right)_{,q} = \frac{\delta_{lq} r_{,j}}{r^2} + \frac{\delta_{jq} r_{,l}}{r^2} - \frac{3 r_{,l} r_{,j} r_{,q}}{r^2} \tag{C.14}$$

which results in:

$$\nabla \times \left(r_{,l} r_{,j} \frac{\mathbf{e}_k \times \mathbf{n}^i}{r} \right) = \left(\delta_{pk} n_q^i - \delta_{qk} n_p^i \right) \left(\frac{\delta_{lq} r_{,j}}{r^2} + \frac{\delta_{jq} r_{,l}}{r^2} - \frac{3 r_{,l} r_{,j} r_{,q}}{r^2} \right) \tag{C.15}$$

after applying some properties of the Levi-Civita symbol and the Kronecker delta. Lastly, doing the dot product by the unit normal, $\mathbf{n}$ on the left and n_p on the right:

$$\left[\nabla \times \left(r_{,l} r_{,j} \frac{\mathbf{e}_k \times \mathbf{n}^i}{r} \right) \right] \cdot \mathbf{n} = \left(n_k n_q^i - \delta_{qk} (\mathbf{n} \cdot \mathbf{n}^i) \right) \left(\frac{\delta_{lq} r_{,j}}{r^2} + \frac{\delta_{jq} r_{,l}}{r^2} - \frac{3 r_{,l} r_{,j} r_{,q}}{r^2} \right) \tag{C.16}$$

which results in Equation (C.6) once the right hand side is expanded.

D.1 Fundamental solution

The elastodynamic fundamental solution and its derivatives were presented in Equations (3.204-3.208). In the present appendix, their main terms U_i, V_i, T_i and R_i are decomposed by using the decomposition of Bessel functions shown in Equation (B.1). Note that terms V_3, R_1, R_4 and R_6 have been omitted for brevity, see Equations (3.205) and (3.208).

$$U_1 = -\frac{1}{2}\left(\frac{k_1^2}{k_2^2}+1\right)\ln r - \frac{1}{2}\left[\gamma + \ln\frac{ik_2}{2} + \frac{1}{2} + \frac{k_1^2}{k_2^2}\left(\gamma + \ln\frac{ik_1}{2} - \frac{1}{2}\right)\right] + \mathrm{K}_0^\mathrm{R}\left(ik_2 r\right)$$
$$- \frac{k_1^2}{k_2^2}\frac{1}{ik_1 r}\mathrm{K}_1^\mathrm{R}\left(ik_1 r\right) + \frac{1}{ik_2 r}\mathrm{K}_1^\mathrm{R}\left(ik_2 r\right) \tag{D.1}$$

$$U_2 = \frac{1}{2}\left(\frac{k_1^2}{k_2^2}-1\right) + \frac{1}{8}\left(k_2^2 - \frac{k_1^4}{k_2^2}\right)r^2\ln r$$
$$+ \frac{1}{8}\left[k_2^2\left(\gamma + \ln\frac{ik_2}{2} - \frac{3}{4}\right) - \frac{k_1^4}{k_2^2}\left(\gamma + \ln\frac{ik_1}{2} - \frac{3}{4}\right)\right]r^2 - \frac{k_1^2}{k_2^2}\mathrm{K}_2^\mathrm{R}\left(ik_1 r\right) + \mathrm{K}_2^\mathrm{R}\left(ik_2 r\right) \tag{D.2}$$

$$V_1 = -\frac{1}{2}\left(\frac{k_1^2}{k_2^2}+1\right)\frac{1}{r} + \frac{1}{8}\left(\frac{k_1^4}{k_2^2}+3k_2^2\right)r\ln r$$
$$+ \frac{1}{2}\left\{\frac{1}{4}\left[\frac{k_1^4}{k_2^2}\left(\gamma + \ln\frac{ik_1}{2} - \frac{3}{4}\right) - k_2^2\left(\gamma + \ln\frac{ik_2}{2} - \frac{3}{4}\right)\right] + k_2^2\left(\gamma + \ln\frac{ik_2}{2} - \frac{1}{2}\right)\right\}r \tag{D.3}$$
$$- ik_2\mathrm{K}_1^\mathrm{R}\left(ik_2 r\right) + \frac{k_1^2}{k_2^2}\frac{1}{r}\mathrm{K}_2^\mathrm{R}\left(ik_1 r\right) - \frac{1}{r}\mathrm{K}_2^\mathrm{R}\left(ik_2 r\right)$$

$$V_2 = \left(\frac{k_1^2}{k_2^2}-1\right)\frac{1}{r} + \frac{1}{8}\left(\frac{k_1^4}{k_2^2}-k_2^2\right)r - ik_1\frac{k_1^2}{k_2^2}\mathrm{K}_1^\mathrm{R}\left(ik_1 r\right) + ik_2\mathrm{K}_1^\mathrm{R}\left(ik_2 r\right)$$
$$- \frac{k_1^2}{k_2^2}\frac{4}{r}\mathrm{K}_2^\mathrm{R}\left(ik_1 r\right) + 4\mathrm{K}_2^\mathrm{R}\left(ik_2 r\right) \tag{D.4}$$

$$T_1 = 2\left(\frac{k_1^2}{k_2^2}-1\right)\frac{1}{r} + \frac{1}{4}\left(\frac{k_1^4}{k_2^2}-k_2^2\right)r - 2ik_1\frac{k_1^2}{k_2^2}\mathrm{K}_1^\mathrm{R}\left(ik_1 r\right) + 2ik_2\mathrm{K}_1^\mathrm{R}\left(ik_2 r\right)$$
$$- \frac{k_1^2}{k_2^2}\frac{8}{r}\mathrm{K}_2^\mathrm{R}\left(ik_1 r\right) + \frac{8}{r}\mathrm{K}_2^\mathrm{R}\left(ik_2 r\right) \tag{D.5}$$

$$T_2 = -\frac{k_1^2}{k_2^2}\frac{1}{r} + \frac{1}{4}\left(\frac{k_1^4}{k_2^2}+k_2^2\right)r\ln r + \frac{1}{4}\left[\frac{k_1^4}{k_2^2}\left(\gamma + \ln\frac{ik_1}{2} - \frac{3}{4}\right) + k_2^2\left(\gamma + \ln\frac{ik_2}{2} - \frac{1}{4}\right)\right]r$$
$$- ik_2\mathrm{K}_1^\mathrm{R}\left(ik_2 r\right) + \frac{k_1^2}{k_2^2}\frac{2}{r}\mathrm{K}_2^\mathrm{R}\left(ik_1 r\right) - \frac{2}{r}\mathrm{K}_2^\mathrm{R}\left(ik_2 r\right) \tag{D.6}$$

$$T_3 = \frac{k_1^2}{k_2^2}\frac{1}{r} + \frac{1}{4}\left(2k_1^2 - k_2^2 - 3\frac{k_1^4}{k_2^2}\right) r\ln r$$

$$+ \frac{1}{4}\left[2k_1^2\left(\gamma + \ln\frac{ik_1}{2} - \frac{1}{2}\right) - k_2^2\left(\gamma + \ln\frac{ik_2}{2} - \frac{3}{4}\right) - 3\frac{k_1^4}{k_2^2}\left(\gamma + \ln\frac{ik_1}{2} - \frac{5}{12}\right)\right] r \quad \text{(D.7)}$$

$$+ ik_1\left(2\frac{k_1^2}{k_2^2} - 1\right) \mathrm{K}_1^{\mathrm{R}}(ik_1r) + \frac{k_1^2}{k_2^2}\frac{2}{r}\mathrm{K}_2^{\mathrm{R}}(ik_1r) - \frac{2}{r}\mathrm{K}_2^{\mathrm{R}}(ik_2r)$$

$$R_2 = 2\frac{k_1^2}{k_2^2}\frac{1}{r^2} + \frac{1}{4}\left(\frac{k_1^4}{k_2^2} + k_2^2\right) - k_2^2\mathrm{K}_0^{\mathrm{R}}(ik_2r) - 2ik_1\frac{k_1^2}{k_2^2}\frac{1}{r}\mathrm{K}_1^{\mathrm{R}}(ik_1r) + 4ik_2\frac{1}{r}\mathrm{K}_1^{\mathrm{R}}(ik_2r)$$

$$- 8\frac{k_1^2}{k_2^2}\frac{1}{r^2}\mathrm{K}_2^{\mathrm{R}}(ik_1r) + 8\frac{1}{r^2}\mathrm{K}_2^{\mathrm{R}}(ik_2r) \quad \text{(D.8)}$$

$$R_3 = 8\left(1 - \frac{k_1^2}{k_2^2}\right)\frac{1}{r^2} + \frac{1}{2}\left(k_2^2 - \frac{k_1^4}{k_2^2}\right) - 2\frac{k_1^4}{k_2^2}\mathrm{K}_0^{\mathrm{R}}(ik_1r) + 2k_2^2\mathrm{K}_0^{\mathrm{R}}(ik_2r)$$

$$+ 16ik_1\frac{k_1^2}{k_2^2}\frac{1}{r}\mathrm{K}_1^{\mathrm{R}}(ik_1r) - 16ik_2\frac{1}{r}\mathrm{K}_1^{\mathrm{R}}(ik_2r) + 48\frac{k_1^2}{k_2^2}\frac{1}{r^2}\mathrm{K}_2^{\mathrm{R}}(ik_1r) - 48\frac{1}{r^2}\mathrm{K}_2^{\mathrm{R}}(ik_2r) \quad \text{(D.9)}$$

$$R_5 = -2\frac{k_1^2}{k_2^2}\frac{1}{r^2} + \frac{1}{4}\left(-3\frac{k_1^4}{k_2^2} + 2k_1^2 - k_2^2\right) + \left(2\frac{k_1^4}{k_2^2} - k_1^2\right)\mathrm{K}_0^{\mathrm{R}}(ik_1r)$$

$$+ 2ik_1\left(1 - 3\frac{k_1^2}{k_2^2}\right)\frac{1}{r}\mathrm{K}_1^{\mathrm{R}}(ik_1r) + 2ik_2\frac{1}{r}\mathrm{K}_1^{\mathrm{R}}(ik_2r) - 8\frac{k_1^2}{k_2^2}\frac{1}{r^2}\mathrm{K}_2^{\mathrm{R}}(ik_1r) + 8\frac{1}{r^2}\mathrm{K}_2^{\mathrm{R}}(ik_2r) \quad \text{(D.10)}$$

D.2 Free-term b_{lkjm}^{i}

The values of the free-term b_{lkjm}^{i} existing in the elastostatic (and elastodynamic) δSBIE for boundary collocation points are presented, see Equation (3.153).

$$B = -\frac{1}{4\pi(1-\nu)} \quad \text{(D.11)}$$

$$b_{1111}^{\mathrm{i}} = \frac{B}{2}\sin(\theta_1 - \theta_2)\left[-4(\nu - 1)\cos(\theta_1 + \theta_2) + \cos(3\theta_1 + \theta_2) + \cos(\theta_1 + 3\theta_2)\right] \quad \text{(D.12)}$$

$$b_{1112}^{\mathrm{i}} = -\frac{B}{2}\left[\cos(2\theta_1) - \cos(2\theta_2)\right]\left[\cos(2\theta_1) + \cos(2\theta_2) - 2\nu + 1\right] \quad \text{(D.13)}$$

$$b_{1121}^{\mathrm{i}} = -\frac{B}{2}\left[\cos(2\theta_1) - \cos(2\theta_2)\right]\left[\cos(2\theta_1) + \cos(2\theta_2) - 2\nu + 3\right] \quad \text{(D.14)}$$

$$b_{1122}^{\mathrm{i}} = -\frac{B}{2}\sin(\theta_1 - \theta_2)\left[-4(\nu - 1)\cos(\theta_1 + \theta_2) + \cos(3\theta_1 + \theta_2) + \cos(\theta_1 + 3\theta_2)\right] \quad \text{(D.15)}$$

$$b^i_{1211} = -\frac{B}{2}\Big[\cos(2\theta_1) - \cos(2\theta_2)\Big]\Big[\cos(2\theta_1) + \cos(2\theta_2) - 2\nu + 1\Big] \tag{D.16}$$

$$b^i_{1212} = \frac{B}{4}\Big[4\nu\sin(2\theta_1) - \sin(4\theta_1) - 4\nu\sin(2\theta_2) + \sin(4\theta_2)\Big] \tag{D.17}$$

$$b^i_{1221} = -\frac{B}{2}\sin(\theta_1 - \theta_2)\Big[-4(\nu - 1)\cos(\theta_1 + \theta_2) + \cos(3\theta_1 + \theta_2) + \cos(\theta_1 + 3\theta_2)\Big] \tag{D.18}$$

$$b^i_{1222} = \frac{B}{2}\Big[\cos(2\theta_1) - \cos(2\theta_2)\Big]\Big[\cos(2\theta_1) + \cos(2\theta_2) - 2\nu + 1\Big] \tag{D.19}$$

$$b^i_{2111} = -\frac{B}{2}\Big[\cos(2\theta_1) - \cos(2\theta_2)\Big]\Big[\cos(2\theta_1) + \cos(2\theta_2) + 2\nu - 1\Big] \tag{D.20}$$

$$b^i_{2112} = -\frac{B}{2}\sin(\theta_1 - \theta_2)\Big[4(\nu - 1)\cos(\theta_1 + \theta_2) + \cos(3\theta_1 + \theta_2) + \cos(\theta_1 + 3\theta_2)\Big] \tag{D.21}$$

$$b^i_{2121} = \frac{B}{4}\Big[-4\nu\sin(2\theta_1) - \sin(4\theta_1) + 4\nu\sin(2\theta_2) + \sin(4\theta_2)\Big] \tag{D.22}$$

$$b^i_{2122} = \frac{B}{2}\Big[\cos(2\theta_1) - \cos(2\theta_2)\Big]\Big[\cos(2\theta_1) + \cos(2\theta_2) + 2\nu - 1\Big] \tag{D.23}$$

$$b^i_{2211} = -\frac{B}{2}\sin(\theta_1 - \theta_2)\Big[4(\nu - 1)\cos(\theta_1 + \theta_2) + \cos(3\theta_1 + \theta_2) + \cos(\theta_1 + 3\theta_2)\Big] \tag{D.24}$$

$$b^i_{2212} = \frac{B}{2}\Big[\cos(2\theta_1) - \cos(2\theta_2)\Big]\Big[\cos(2\theta_1) + \cos(2\theta_2) + 2\nu - 3\Big] \tag{D.25}$$

$$b^i_{2221} = \frac{B}{2}\Big[\cos(2\theta_1) - \cos(2\theta_2)\Big]\Big[\cos(2\theta_1) + \cos(2\theta_2) + 2\nu - 1\Big] \tag{D.26}$$

$$b^i_{2222} = \frac{B}{2}\sin(\theta_1 - \theta_2)\Big[4(\nu - 1)\cos(\theta_1 + \theta_2) + \cos(3\theta_1 + \theta_2) + \cos(\theta_1 + 3\theta_2)\Big] \tag{D.27}$$

The Rayleigh waves are surface waves that exist when a half-space is in contact with the vacuum through its free-surface. For a half-space $y \leq 0$, three different cases can be considered at the free-surface $y = 0$: permeable ($\tau_{ij} n_j = 0$, $\tau = 0$), impermeable ($(\tau_{ij} + \tau \delta_{ij}) n_j = 0$, $(U_j - u_j) n_j = 0$) or partially permeable. In this work, only the permeable case is considered.

The potentials for the surface mode are composed by unknown functions $R_i = R_i(y)$ and a wave propagating in the positive x direction:

$$\varphi_i = R_i^{(P)} e^{-ik_R x}, \quad \psi_i = R_i^{(S)} e^{-ik_R x} \tag{E.1}$$

Once substituted into the governing equations, a set of four ordinary differential equations are obtained. It can be converted into a fourth order equation in terms of $R_1^{(P)}$, and a second order equation in terms of $R_1^{(S)}$. The solution of the fourth order equation leads to:

$$R_1^{(P)} = P_{11} e^{k_{RP1} y} + P_{12} e^{k_{RP2} y} \tag{E.2}$$

$$R_2^{(P)} = P_{21} e^{k_{RP1} y} + P_{22} e^{k_{RP2} y} = D_1 P_{11} e^{k_{RP1} y} + D_2 P_{12} e^{k_{RP2} y}$$

$$D_j = \frac{(\lambda + 2\mu) k_{Pj}^2 - \omega^2 \left(\hat{\rho}_{11} - Q/R \hat{\rho}_{12} \right)}{\omega^2 \left(\hat{\rho}_{12} - Q/R \hat{\rho}_{22} \right)} \tag{E.3}$$

where the wavenumbers k_{RPj} are obtained from:

$$k_{RPj} = \pm \sqrt{k_R^2 - k_{Pj}^2} \tag{E.4}$$

being physically meaningful only those with $\text{Re}(k_{RPj}) > 0$, i.e. those producing evanescent displacements when $y \to -\infty$. The solution of the second order equation leads to:

$$R_1^{(S)} = S_1 e^{k_{RS} y} \tag{E.5}$$

$$R_2^{(S)} = S_2 e^{k_{RS} y} = -\hat{\rho}_{12}/\hat{\rho}_{22} e^{k_{RS} y} \tag{E.6}$$

where the wavenumber k_S is:

$$k_{RS} = \pm \sqrt{k_R^2 - k_S^2} \tag{E.7}$$

being meaningful only that with $\text{Re}(k_{RS}) > 0$. Therefore, the potentials are:

$$\varphi_i = \left(P_{i1} e^{k_{RP1} y} + P_{i2} e^{k_{RP2} y} \right) e^{-ik_R x}, \quad \psi_i = S_i e^{k_{RS} y} e^{-ik_R x} \tag{E.8}$$

At this point, displacements and stresses can be written as functions of three amplitudes (P_{11}, P_{12} and S_1) and the Rayleigh wavenumber k_R. Applying the permeable boundary conditions $\tau_{xy} = 0$, $\tau_{yy} = 0$ and $\tau = 0$ to the free-surface at $y = 0$, one obtains the following set of three equations:

$$\left[-2\mu i k_R k_{RP1} \right] P_{11} + \left[-2\mu i k_R k_{RP2} \right] P_{12} + \left[\mu \left(2k_R^2 - k_S^2 \right) \right] S_1 = 0$$

$$\left[2\mu k_R^2 - (N + Q D_1) k_{P1}^2 \right] P_{11} + \left[2\mu k_R^2 - (N + Q D_2) k_{P2}^2 \right] P_{12} + \left[2\mu i k_R k_{RS} \right] S_1 = 0 \tag{E.9}$$

$$\left[-(Q + R D_1) k_{P1}^2 \right] P_{11} + \left[-(Q + R D_2) k_{P2}^2 \right] P_{12} = 0$$

where $N = \lambda + 2\mu + Q^2/R$. After some algebraic manipulations using the relationships between wavenumbers given by Eqs. (2.21), (2.23), (E.4) and (E.7), the characteristic equation associated with this homogeneous set of equations can be written in a similar fashion than that of the elastic case [47, Eq. (5.95)]:

$$\left(2 - r^2\right)^2 - 4\sqrt{1 - r^2}\left(H_2\sqrt{1 - G_1 r^2} - H_1\sqrt{1 - G_2 r^2}\right) = 0 \qquad (E.10)$$

where:

$$r = \frac{k_S}{k_R}, \quad H_j = \frac{[\mu/(\lambda + 2\mu)]\, k_S^2 - k_{Pj}^2}{k_{P1}^2 - k_{P2}^2}, \quad G_j = \frac{k_{Pj}^2}{k_S^2} \qquad (E.11)$$

Eq. (E.10) is arranged in a new way which is more tractable than others previously obtained, e.g. [215, 216]. In fact, all terms are dimensionless, well behaved, and depend only on the bulk wavenumbers and Lamé's parameters. It is direct to verify that this equation collapse into the elastic equation; if $\phi \to 0$, then $k_{P1} \to 0$, $k_{P2} \to k_P^{\text{elastic}}$, $k_S \to k_S^{\text{elastic}}$ and $(\lambda + 2\mu)/\mu \to (k_S^{\text{elastic}}/k_P^{\text{elastic}})^2$.

Título de la Tesis Doctoral: Modelo acoplado de elementos finitos y elementos de contorno para el análisis dinámico de estructuras laminares enterradas[1]

F.1 Objetivos

El objetivo principal de la Tesis es la formulación e implementación de un modelo acoplado de Elementos Finitos (EF) y Elementos de Contorno (EC) para el análisis dinámico de problemas de interacción suelo-estructura que implica a estructuras donde las hipótesis laminares son válidas.

Para llevar a cabo dicha tarea, se requieren dos desarrollos paralelos: a) el Método Dual de los Elementos de Contorno, b) elemento finito tipo lámina curva adecuada para los objetivos del modelo. El modelo resultante debe ser capaz de llevar a cabo el análisis the problemas de propagación de ondas de carácter sísmico en estructuras enterradas de tipo laminar, la respuesta dinámica de muros y estructuras de retención, y la caracterización dinámica (impedancias y factores de interacción cinemática) de cimentaciones basadas en estructuras laminares. La metodología simplificada podría facilitar la etapa de pre-proceso dado que la geometría detallada de la estructura laminar no se require. Asimismo, ello podría conllevar la reducción del número de grados de libertad y, por consiguiente, de los recurso de computación.

En el camino para alcanzar dichos objetivos principales, existe una serie de objetivos parciales a considerar:

- Estudio de las bases teóricas necesarias: elastodinámica y poroelastodinámica lineal, elementos de contorno y elementos finitos en problemas dinámicos, así como los modelos y programas desarrollados por el Grupo que servirán de base para la consecución del objetivo propuesto.

- Formulación e implementación de un modelo acoplado EF-EC bidimensional para el análisis de estructuras laminares. Se pretende con ello ajustar las posibilidades de la estrategia que se propone sobre un problema más sencillo dimensionalmente.

- Extensión del modelo a problemas tridimensionales. En primera fase, estudio del elemento finito lámina más adecuado a los propósitos del modelo.

- Desarrollo e implementación de un código de elementos de contorno basado en la Formulación Dual del Método. Formulación e implementación del modelo acoplado EF-EC para problemas tridimensionales de propagación de ondas en medios fluidos y viscoelásticos. Aplicación del modelo desarrollado sobre problemas patrón y validación de los resultados con los obtenidos de la aplicación del modelo acoplado de

---

[1]En este apéndice se presenta un breve resumen en castellano de la Tesis Doctoral de entre 5 y 20 páginas, de acuerdo con la Resolución del Vicerrector de Coordinación y Proyectos Institucionales de la Universidad de Las Palmas de Gran Canaria de fecha 10 de febrero de 2017, relativa a los plazos de registro, depósito y defensa de las Tesis Doctorales desarrolladas en los Programas de Doctorado a extinguir, regulados por el Real Decreto 1393/2007 de 29 de octubre.

elementos de contorno preexistente ya mencionado. Esta fase permitirá calibrar el programa, estudiar su sensibilidad a los parámetros del problema (geometría, frecuencia, discretización, etc.) y establecer sus límites de aplicación.

- Extensión del modelo a la interacción entre láminas y medios de naturaleza poroelástica (modelo de Biot, [39]). Implementación y validación con el software disponible

- Aplicación del modelo desarrollado al estudio de problemas de interacción dinámica de interés: difracción de ondas sísmicas por estructuras laminares enterradas (ello implica la obtención de la respuesta de la estructura: desplazamientos, esfuerzos y la influencia sobre éstos de las características del suelo o la presencia de estructuras cercanas), el cálculo de impedancias de cimentaciones resueltas a base de vasos de succión (muy habituales estructuras off-shore), la respuesta sísmica de estructuras/muros de contención, silos, etcétera, y, muy relacionado con el problema de difracción mencionado al principio, la evaluación de la eficacia en el aislamiento de vibraciones (de cualquier origen) en determinado emplazamiento, provocado por el enterramiento en cercanías de estructuras de estas características.

- Difusión de los resultados obtenidos en artículos y ponencias en congresos internacionales de primer nivel.

F.2 Modelo DBEM–FEM

En este trabajo se propone un modelo dinámico simplificado fluido- y suelo-estructura para el análisis de estructuras laminares enterradas o sumergidas [28–30]. Éste hace uso del Método Dual de los Elementos de Contorno, o Dual Boundary Element Method (DBEM) en inglés, que es más comúnmente usado para el análisis de grietas, pero que este modelo permite obtener un acoplamiento aproximado pero natural y directo de la estructura laminar y del medio circundante. Véase Figura F.1.

La estructura laminar se modela con elementos finitos tipo lámina basados en la degeneración del sólido tridimensional. El bloqueo de cortante y membrana intrínsecos en este tipo de elementos se evita usando la Interpolación Mixta de Componentes Tensoriales, o Mixed Interpolation of Tensorial Components (MITC) en inglés, propuesta por Bathe [93], que a su vez también carece de modos espúreos.

El modelo resultante se ha denominado modelo DBEM–FEM, y ha sido desarrollado para problemas bidimensional así como tridimensionales, donde estructuras laminares, en general curvas, pueden acoplarse con medios fluidos (fluido ideal), elásticos o poroelásticos basados en la teoría de Biot. Ello ha sido implementado sobre un código basado en un código BEM multidominio desarrollado previamente por el grupo. Por tanto, este nuevo método enriquece las habilidades ya existentes en el código.

La principal dificultad del modelo se sitúa en el desarrollo de uno de los integredientes del DBEM, esto es la Ecuación Integral Hipersingular en el Contorno, o Hypersingular Boundary Integral Equation (HBIE) en inglés. Para enfrentarnos a dicha ecuación, hemos hecho uso de las técnicas de regularización propuestas por Saéz, Gallego, Domínguez y Ariza [12, 60–

$$U_n^+, u_k^+, \tau^+, t_k^+ \qquad u_k^s, \rho_r^s, t_k^s \qquad U_n^-, u_k^-, \tau^-, t_k^-$$

$\mathbf{n}^+$ $\mathbf{n}^-$

EC grieta (cara $+$)   EC grieta (cara $-$)
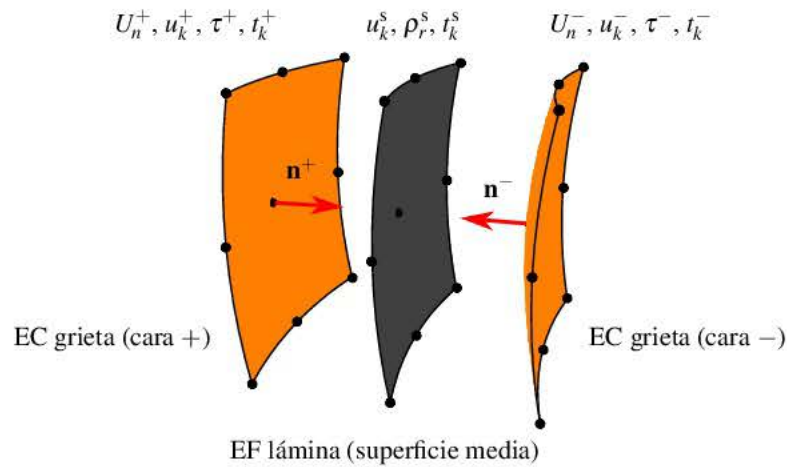
EF lámina (superficie media)

Figura F.1: Vista explosionada del acoplamiento de un elemento de contorno tipo grieta con un elemento finito tipo lámina

62, 207], los cuales la aplicaron a problemas de potencial y elásticos. Nosotros la hemos extendido para tratar también medios porosos de Biot, cuya formulación singular había sido propuesta previamente por Domínguez, Maeso y Aznárez [14, 15, 70, 74].

F.3 Sensibilidad geométrica usando el MEC

Se ha explorado también la extensión del modelo para optimización de forma (geométrica) basada en métodos de gradiente. El alcance de dicha investigación se limita a modelos bidimensionales, en donde sólo elementos continuos (no estructurales) han sido tratados. El enfoque para el análisis de sensibilidad haciendo uso del BEM se basa en trabajos previos de Gallego, Suárez y Rus [103–107], y son utilizados para la solución de problemas multidominio, como se verá en los siguientes apartados.

F.4 Problemas bidimensionales estudiados

F.4.1 Pantallas acústicas flexibles bidimensionales

Normalmente las pantallas acústicas se consideran rígidas. En este problem se estudia la cuál es la relevancia de considerar la verdadera flexibilidad haciendo uso del modelo DBEM–FEM propuesto. Para ello, se consideran cinco tipos de barrera, todos con la misma altura efectiva, pero con diferentes configuraciones en la cabeza de la barrera: barrera simple, barrera doble, barrera en Y, barrera en U, y barrera en E. Asimismo, se consideran tres tipos de materiales con propiedades típicas. La Figura F.2 muestra resultados de pérdida por inserción para las configuraciones estudiadas.
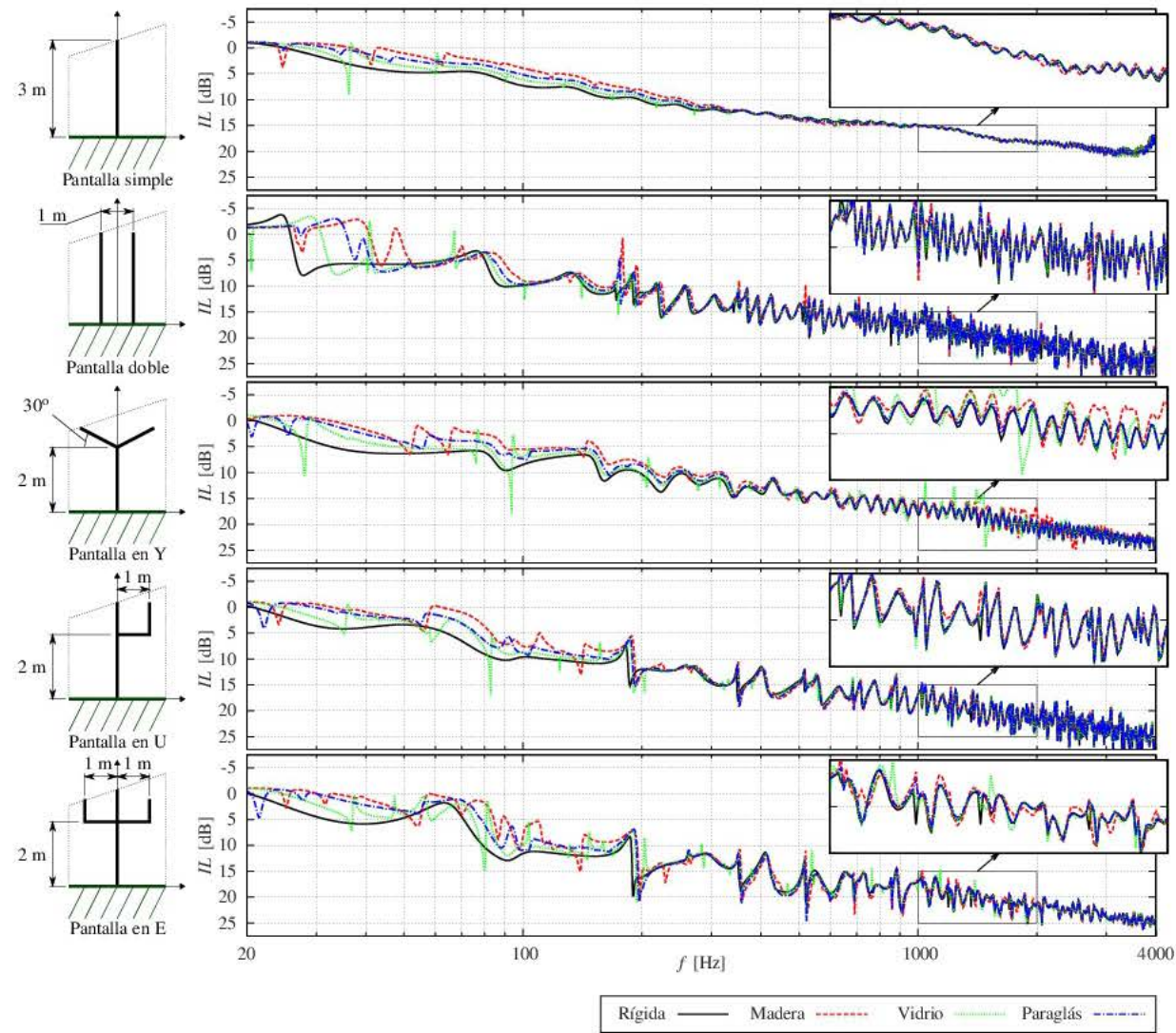
Figura F.2: IL (pérdida por inserción) para diferentes tipos de barreras y materiales
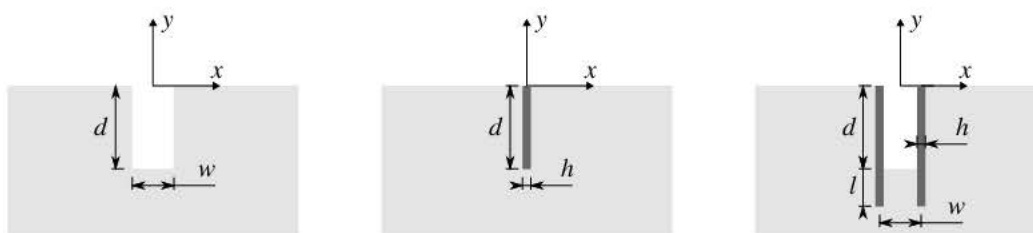
Figura F.3: Topologías de pantallas consideradas: zanja abierta (izquierda), pantalla o pared enterrada (centro), y zanja entibada (derecha).
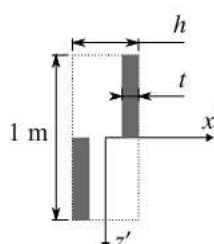

Figura F.4: Sección de pared equivalente a una tablestaca

F.4.2 Pantallas de aislamiento de vibraciones bidimensionales en suelos porosos

En este problema se estudian distintos tipos de pantallas o barreras de aislamiento de vibraciones en suelos porosos: zanja abierta, pantalla o pared enterrada, y zanja entibada a base de tablestacas; véase Figura F.3. Las secciones de las paredes se consideran en equivalencia a tablestacas, véase Figura F.4.

F.4.3 Optimización geométrica de pantallas de aislamiento de vibraciones

Se estudia la optimización geométrica de pantallas de aislamiento de vibraciones en suelos elásticos homogéneos. Se consideran hasta tres tipos de funciones objetivo dependiendo del tipo de fuente: fuente a frecuencia fija, fuente con espectro relevante en un cierto rango de frecuencias y fuente armónica cuya frecuencia puede estar entre ciertos valores mínimos y máximos de frecuencia. Se considera asimismo una restricción de carácter económico al imponer un área (sección) máxima de pantallas.

La Figura F.5 muestra los dos tipos de pantallas consideradas: pantalla simple, y pantalla doble; así como la configuración de fuente y receptor. La Figura F.6 muestra los diseños óptimos de barreras dobles para fuentes pulsantes a una única frecuencia f^{opt}, y también muestra el espectro de pérdidas por inserción en un rango de frecuencias dado. Se observa cómo la optimización produce diseños que maximizan la pérdida por inserción a la frecuencia de la fuente.

(a) Pantalla simple   (b) Pantalla doble
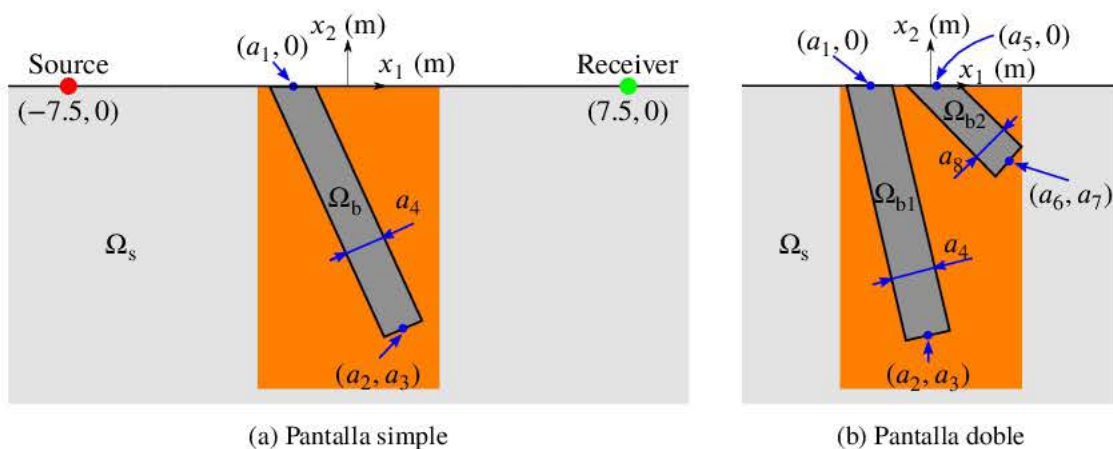
Figura F.5: Pantallas de aislamiento de vibraciones consideradas en un dominio de diseño de 5 m $\times$ 8 m (en color naranja)

(a) $f^{\text{opt}} = 20$ Hz   (b) $f^{\text{opt}} = 26$ Hz

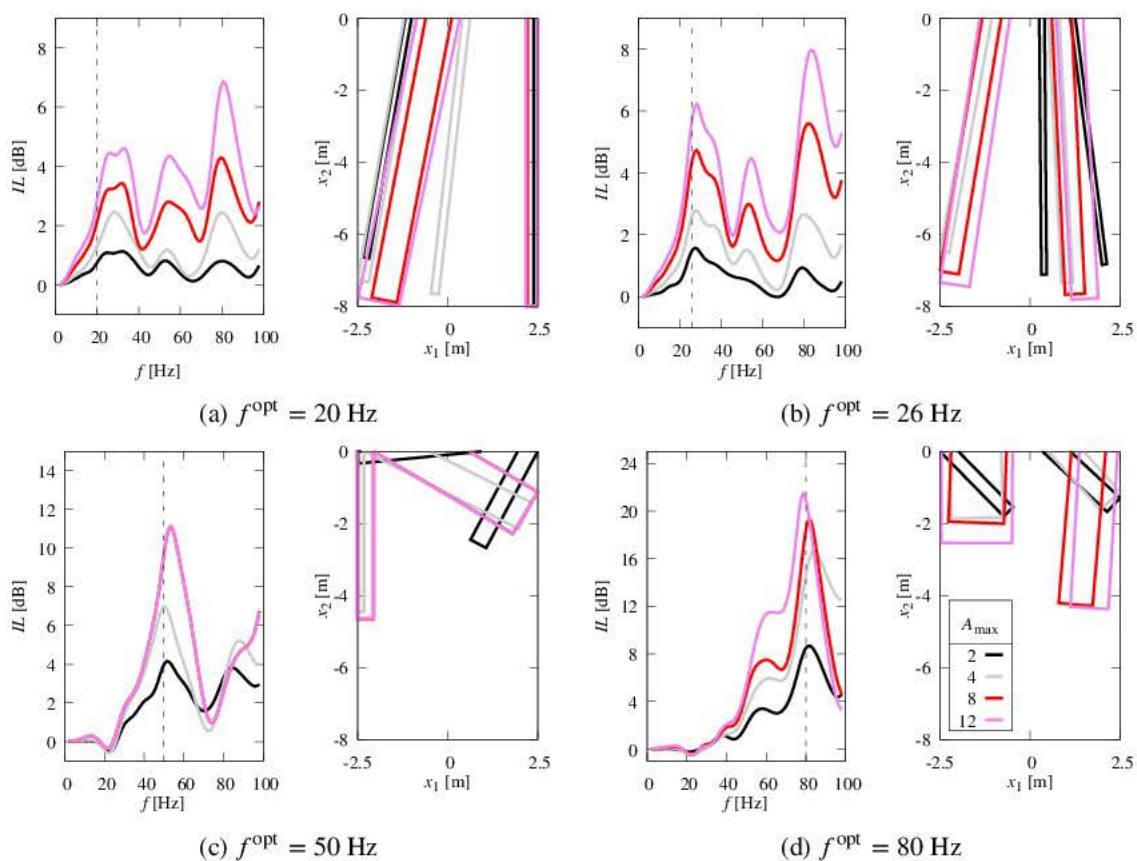(c) $f^{\text{opt}} = 50$ Hz   (d) $f^{\text{opt}} = 80$ Hz

Figura F.6: Diseños óptimos de pantallas dobles ante fuentes pulsantes a una frecuencia dada f^{opt} para distintas áreas máximas $A_{\max}$

F.5 Problemas tridimensionales estudiados

F.5.1 Pantalla de aislamiento de vibraciones en suelos porosos

Este problema consiste en una pantalla de aislamiento de vibraciones curva y tridimensional enterrada en un suelo poroso. La excitación es una onda de Rayleigh, que incide en la parte cóncava de la pantalla. El objetivo de este problema es la verificación y estudio del rango de aplicabilidad del modelo DBEM–FEM tridimensional. Para ello los resultados the campo cercano y lejano obtenidos con dicho modelo se comparan con resultados de un modelo BEM multi-región. Se comparan varios espesores de la pantalla, así como varias discretizaciones de la misma.

La Figura F.7 muestra un ejemplo comparando las mallas requeridas para el modelo multi-región BEM y para el modelo DBEM–FEM. A pesar de la aproximación geométrica y física que este modelo produce, los resultados muestran que es posible utilizarlo en programas de difracción para estructuras de esbeltez (longitud máxima / espesor) 5, e incluso utilizando mallas gruesas.

F.5.2 Impedancias de vasos de succión en suelos porosos

Se estudian las impedancias de vasos de succión de diferentes relaciones de longitud y diámetro, así como distintas propiedades del suelo poroso saturado. Mientras que para los suelos elásticos el número de propiedades es reducido, para los suelos poroelásticos modelados con la teoría de Biot es necesario definir multitud de propiedades. Por ello, se decidió tomar propiedades de lecho marino realistas disponibles en la literatura [205]. Asimismo, se tomó uno de éstos suelos y se estudió la influencia de la conductividad hidráulica en particular.

La Figura F.8 muestra una de las mallas usadas para los cálculos, en donde se pueden observar las distintas partes del modelo DBEM–FEM contemplado. En la figura, el dominio

(a) Ejemplo de malla BEM multi-región
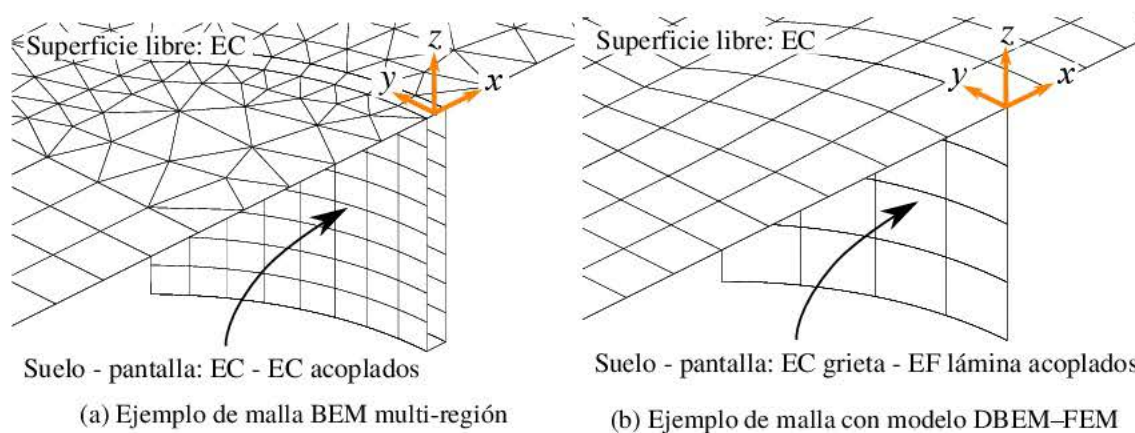
(b) Ejemplo de malla con modelo DBEM–FEM

Figura F.7: Pantalla tridimensional curva (las mallas incorporan simetría un medio con respecto al plano xz)
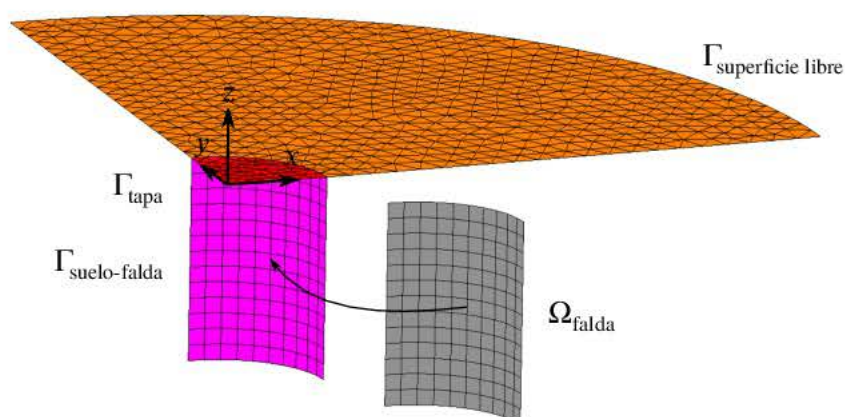
Figura F.8: Descripción de la malla del vaso de succión instalado ($L/D = 1$)

Ω_{falda} correspondiente a la estructura laminar se ha desplazado de su localización real, que es coincidente geométricamente con el contorno tipo grieta $\Gamma_{\text{suelo-falda}}$, para visualizar la idea principal del modelo DBEM–FEM. En cuanto a resultados, la conclusión principal de este estudio ha sido que la conductividad hidráulica influye de manera significativa en las distintas impedancias, excepto en la impedancia de torsión.

F.6 Conclusiones y desarrollos futuros

En esta Tesis se ha desarrollado un modelo numérico simplificado pero riguroso y ventajoso desde el punto de vista metodológico y computacional para el análisis dinámico de estructuras laminares enterradas. Dicho modelo hace uso del Método Dual de Elementos de Contorno, lo cual permite un acoplamiento natural y directo entre el suelo y el elemento finito tipo lámina. De no utilizar la metodología propuesta, sería necesario crear interfases artificiales [41]. El modelo ha sido usado en problemas de aislamiento de vibraciones así como en el cálculo de impedancias de vasos de succión.

En la misma línea, se ha comenzado ha desarrollar dicho modelo para aplicarlo a problemas de optimización basados en información de tipo gradiente. Para ello se hace uso del Método de Elementos de Contorno para análisis de sensibilidad geométrica. El resultado obtenido en esta línea es un modelo BEM multi-región para su uso en análisis de sensibilidad geométrica o de forma. Este modelo ha sido usado para la optimización de pantallas de aislamiento de vibraciones con éxito, resultando en mejoras significativas de las pérdidas por inserción con respecto a las reglas de diseño más habituales.

Dado que el modelo DBEM–FEM ha sido desarrollado para problemas bi- y tridimensionales, para medios tipo fluido ideal, sólido elástico y medio poroelástico de Biot, y además ha sido integrado en el código BEM multi-region existente en el grupo, el número de problemas abordables por el grupo ha incrementado significativamente. Algunas de las líneas de trabajo futuro que se plantean son:

- **Corto plazo**

– *Vasos de succión.* El modelo DBEM–FEM puede directamente abordar diversos problemas relacionados con vasos de succión y su aplicación a aerogeneradores marinos:

* Impedancias. Dado que para el apropiado diseño de los aerogeneradores marinos es necesario que los primeros modos estén localizados lejos de las principales frecuencias de las excitaciones asociadas al oleaje y al viento [206], es importante determinar correctamente las impedancias de la cimentación. Dado que los aerogeneradores marinos descansan fundamentalmente en un medio poroelástico por naturaleza, excepto si se trata quizás de un lecho rocoso, es necesario determinar ante qué condiciones es necesario utilizar propiedades drenadas o no drenadas, en caso de utilizar un modelo elástico, o si resulta ser importante usar un modelo poroelástico como el de Biot.

* Factores de interacción cinemática. Las recomendaciones y normativas actuales sugieren el análisis sísmico de los aerogenerados. Por lo tanto, es de interés la determinación de los factores de interacción cinemática para diversas configuraciones y propiedades.

* Efecto de grupo. Los vasos de succión utilizado en el contexto de aerogeneradores marinos han sido utilizados de dos maneras: utilizando un vaso de succión de gran tamaño, o bien utilizando típicamente tres o cuadro vasos más pequeños conectados a un jacket.

– *Campo incidente con ángulo de incidencia variable en medio poroelástico estratificado.* Se propone la formulación e implementación de un campo incidente de ángulo de incidencia variable en medio poroelástico estratificado basado en trabajo previos como los de Lin et al. [195] y Feng et al. [210]. Ello permitiría analizar, por ejemplo, el efecto que tiene el nivel freático sobre la respuesta dinámica de las cimentaciones y por ende de las superestruturas.

– *Grietas en medio poroso.* Dado que para el desarrollo del modelo DBEM–FEM se ha tenido que desarrollar el Método Dual de Elementos de Contorno para los medios poroelásticos, resulta claro que se tiene una buena oportunidad para avanzar en el análisis de grietas en este tipo de medios. En particular, la variable de interés es el Factor de Intensidad de Tensiones. Hay muy pocos trabajos en este campo, en donde cabe destacar los trabajos de Phurkhao [211, 212]. En el momento en el que se desarrolló la formulación dual, se trató de reproducir los resultados de Phurkhao sin éxito. Sospechamos que la causa puede estar en la definición del problema, ya sea en la definición del factor the intensidad de tensiones, o bien en el campo incidente utilizado.

• **Medio plazo**

– *Optimización de pantallas de aislamiento de vibraciones* Se propone incluir una excitación de carácter más general, como puede ser un campo incidente de ondas de Rayleigh. Asimismo, estudiar las consecuencias en el proceso de optimización cuando se varía el número y posición de los receptores. Por último, se propone estudiar el efecto de la estratigrafía.

– *Modelo BEM–FEM para pilotes en medio poroso* En la misma línea del trabajo de Padrón [18], la disponibilidad ahora de la formulación hipersingular para medios poroelásticos puede permitir la confección de un modelo pilote-suelo poroso.

– *Publicación de software en abierto.* Se contempla la posibilidad de la publicación en abierto de software derivado del presente trabajo, ya sea en forma de librerías y código fuente, o en forma de ejecutables.

[1]   O. C. Zienkiewicz. The birth of the finite element method and of computational mechanics. *International Journal for Numerical Methods in Engineering*, 2004.

[2]   T. A. Cruse. Boundary Integral Equation – A Personal View. *Electronic Journal of Boundary Elements*, 1(1):19–25, 2003.

[3]   A. H. D. Cheng and D. T. Cheng. Heritage and early history of the boundary element method. *Engineering Analysis with Boundary Elements*, 29:268–302, 2005.

[4]   C. A. Brebbia. The birth of the boundary element method from conception to application. *Engineering Analysis with Boundary Elements*, 77:iii–x, 2017.

[5]   O. C. Zienkiewicz and R. L. Taylor. *The Finite Element Method*. Butterworth-Heinemann, 6 edition, 2005.

[6]   J. Domínguez. *Boundary Elements in Dynamics*. International Series on Computational Engineering. Computational Mechanics Publications / Elsevier Applied Science, 1993.

[7]   L. C. Wrobel and M. H. Aliabadi. *The Boundary Element Method*. Wiley, 2002.

[8]   A. Sommerfeld. Die greensche funktion der schwingungsgleichung. *Jahresbericht der Deutschen Mathematiker-Vereinigung*, 21:309–353, 1912.

[9]   O. C. Zienkiewicz, D. W. Kelly, and P. Bettess. The coupling of the finiete element method and boundary solution procedures. *International Journal for Numerical Methods in Engineering*, 11:355–375, 1977.

[10]   F. Chirino and J. Domínguez. Dynamic analysis of cracks using boundary element method. *Engineering Fracture Mechanics*, 34(5/6):1051–1061, 1989.

[11]   J. M. Emperador and J. Domínguez. Dynamic response of axisymmetric embedded foundations. *Earthquake Engineering and Structural Dynamics*, 18(8):1105–1117, 1989.

[12]   A. Sáez, R. Gallego, and J. Domínguez. Hypersingular quarter-point boundary elements for crack problems. *International Journal for Numerical Methods in Engineering*, 38:1681–1701, 1995.

[13]   F. Chirino and R. Abascal. Dynamic and static analysis of cracks using the hypersingular formulation of the boundary element method. *International Journal for Numerical Methods in Engineering*, 43:365–388, 1998.

[14]   O. Maeso, J. J. Aznárez, and J. Domínguez. Three-dimensional models of reservoir sediment and effects on the seismic response of arch dams. *Earthquake Engineering and Structural Dynamics*, 33(10):1103–1123, 2004.

[15] J. J. Aznárez, O. Maeso, and J. Domínguez. BE analysis of bottom sediments in dynamic fluid-structure interaction problems. *Engineering Analysis with Boundary Elements*, 30:124–136, 2006.

[16] F. Medina, J. Domínguez, and J. Tassoulas. Response of dams to earthquakes including effects of sediments. *Journal of Structural Engineering*, 116(11):3108–3121, 1990.

[17] O. Maeso, J. J. Aznárez, and F. García. Dynamic impedances of piles and groups of piles in saturated soils. *Computers and Structures*, 83:769–782, 2005.

[18] L. A. Padrón, J. J. Aznárez, and O. Maeso. BEM-FEM coupling model for the dynamic analysis of piles and pile groups. *Engineering Analysis with Boundary Elements*, 31:473–484, 2007.

[19] L.A. Padrón, J.J. Aznárez, and O. Maeso. Dynamic analysis of piled foundations in stratified soils by a BEM-FEM model. *Soil Dynamics and Earthquake Engineering*, 28:333–346, 2008.

[20] L. A. Padrón. *Numerical model for the dynamic analysis of pile foundations*. PhD thesis, Instituto Universitario de Sistemas Inteligentes y Aplicaciones Numéricas en Ingeniería, June 2009.

[21] L.A. Padrón, J.J. Aznárez, O. Maeso, and A. Santana. Dynamic stiffness of deep foundations with inclined piles. *Earthquake Engineering and Structural Dynamics*, 39:1343–1367, 2010.

[22] C. Medina, L. A. Padrón, J. J. Aznárez, A. Santana, and O. Maeso. Kinematic interaction factors of deep foundations with inclined piles. *Earthquake Engineering and Structural Dynamics*, 43:2035–2050, 2014.

[23] G. M. Álamo, A. E. Marínez-Castro, L. A. Padrón, J. J. Azn'arez, R. Gallego, and O. Maeso. Efficient numerical model for the computation of impedance functions of inclined pile groups in layered soils. *Engineering Structures*, 126:379–390, 2016.

[24] R. Toledo, J. J. Aznárez, O. Maeso, and D. Greiner. Optimization of thin noise barrier design using Evolutionary Algorithms and a Dual BEM formulation. *Journal of Sound and Vibration*, 334:219–238, 2015.

[25] R. Toledo, J. J. Aznárez, D. Greiner, and O. Maeso. Shape design optimization of road acoustic barriers featuring top-edge devices by using genetic algorithms and boundary elements. *Engineering Analysis with Boundary Elements*, 63:49–60, 2016.

[26] S. Bhattacharya. Challenges in design of foundations for offshore wind turbines. *The Institution of Engineering and Technology*, pages 1–9, 2014.

[27] B. W. Byrne and G. T. Houlsby. Foundations for offshore wind turbines. *Philosophical Transactions of the Royal Society of London A*, 361:2909–2930, 2003.

[28] J. D. R. Bordón, J. J. Aznárez, and O. Maeso. A 2D BEM-FEM approach for time harmonic fluid-structure interaction analysis of thin elastic bodies. *Engineering Analysis with Boundary Elements*, 43:19–29, 2014.

[29] J. D. R. Bordón, J. J. Aznárez, and O. Maeso. Two-dimensional numerical approach for the vibration isolation analysis of thin walled wave barriers in poroelastic soils. *Computers and Geotechnics*, 71:168–179, 2016.

[30] J. D. R. Bordón, J. J. Aznárez, and O. Maeso. Dynamic model of open shell structures buried in poroelastic soils. *Computational Mechanics*, (accepted), available online on April 2017.

[31] G. M. Álamo, J. D. R. Bordón, J. J. Aznárez, and O. Maeso. Relevance of soil-pile tangential tractions for the estimation of kinematic seismic forces: a Winkler approach. *Bulletin of Earthquake Engineering*, (under review), submitted on January 2017.

[32] J. D .R. Bordón, J. J. Aznárez, and O. Maeso. A 2D BEM-FEM model of thin structures for time harmonic fluid-soil-structure interaction analysis including poroelastic media. In V. Mallardo and M. H. Aliabadi, editors, *Advances in Boundary Element and Meshless Techniques XV*, pages 375–382, Florence, Italy, 15–17 July 2014.

[33] J. D. R. Bordón, J. J. Aznárez, and O. Maeso. Three-dimensional BE–FE model of bucket foundations in poroelastic soils. In M. Papadrakakis, V. Papadopoulos, G. Stefanou, and V. Plevris, editors, *VII European Congress on Computational Methods in Applied Sciences and Engineering*, Crete Island, Greece, 5–10 June 2016. ECCOMAS.

[34] G. M. Álamo, J. D. R. Bordón, F. García, J. J. Aznárez, L. A. Padrón, F. Chirino, and O. Maeso. Revisión de modelos numéricos para el estudio del comportamiento dinámico de cimentaciones profundas para el diseño y proyecto de aerogeneradores. In *Proceedings of 20th International Congress on Project Management and Engineering*, Cartagena, Spain, 13–15 July 2016.

[35] U. Basu and A. K. Chopra. Perfectly matched layers for time-harmonic elastodynamics of unbounded domains: theory and finite-element implementation. *Computer Methods in Applied Mechanics and Engineering*, 192:1337–1375, 2003.

[36] H. Rokhlin. Rapid solution of integral equations of classical potential theory. *Journal of Computational Physics*, 60(2):187–207, 1985.

[37] W. Hackbusch and Z. P. Nowak. On the fast matrix multiplication in the boundary element method by panel clustering. *Numerische Mathematik*, 73:207–243, 1989.

[38] W. Hackbusch. A sparse matrix arithmetic based on H-matrices. Part i: introduction to H-matrices. *Computing*, 62:89–108, 1999.

[39] M. A. Biot. Theory of propagation of elastic waves in a fluid-saturated porous solid. I. Low-frequency range. *Journal of Acoustical Society of America*, 28(2):168–178, 1956.

[40] O. von Estorff. *Boundary Elements in Acoustics*. WIT Press, 2000.

[41] M. Liingaard, L. Andersen, and L.B. Ibsen. Impedance of flexible suction caissons. *Earthquake Engineering and Structural Dynamics*, 36:2249–2271, 2007.

[42] H.-K Hong and J.T. Chen. Derivations of integral equations of elasticity. *Journal of Engineering Mechanics*, 114(6):1028–1044, 1988.

[43] Y. Mi and M. H. Aliabadi. Dual boundary element method for three-dimensional fracture mechanics analysis. *Engineering Analysis with Boundary Elements*, 10:161–171, 1992.

[44] A. Portela, M. H. Aliabadi, and D. P. Rooke. The dual boundary element method: effective implementation for crack problems. *International Journal for Numerical Methods in Engineering*, 33:1269–1287, 1992.

[45] P. M. Morse. *Vibration and Sound*. The American Institute of Physics, 1983.

[46] O. Maeso and J.J. Aznárez. *Estrategias para la reducción del impacto acústico en el entorno de carreteras. Una aplicación del método de los elementos de contorno.* Universidad de Las Palmas de Gran Canaria, 2005. in Spanish.

[47] J. D. Achenbach. *Wave propagation in elastic solids*, volume 16 of *Applied mathematics and mechanics*. North-Holland, 1973.

[48] A. C. Eringen and E. S. Suhubi. *Elastodynamics.*, volume II. Linear Theory. Academic Press, 1975.

[49] V. D. Kupradze. *Three-dimensional problems of the mathematical theory of elasticity and thermoelasticity*, volume 25 of *Applied mathematics and mechanics*. North-Holland, 1979.

[50] S. Bougacha and J. L. Tassoulas. Seismic analysis of gravity dams I: modeling of sediments. *Journal of Engineering Mechanics*, 117(8):1826–1837, 1991.

[51] T. J. Plona. Observation of a second bulk compressional wave in a porous medium at ultrasonic frequencies. *Applied Physics Letters*, 36(4):259–261, 1980.

[52] J. G. Berryman. Confirmation of Biot's theory. *Applied Physics Letters*, 37(4):382–384, 1980.

[53] M. A. Biot. Mechanics of deformation and acoustic propagation in porous media. *Journal of Applied Physics*, 33(4):1482–1498, 1962.

[54] H. Deresiewicz and R. Skalak. On uniqueness in dynamic poroelasticity. *Bulletin of the Seismological Society of America*, 53(4):783–788, 1963.

[55] V. de la Cruz and T. J. T. Spanos. Seismic boundary conditions for porous media. *Journal of Geophysical Research*, 94(B3):3025–3029, 1989.

[56] B. Gurevich and M. Schoenberg. Interface conditions for Biot's equations of poroelasticity. *Journal of Acoustical Society of America*, 105(5):2585–2589, 1999.

[57] C. A. Brebbia and J. Domínguez. *Boundary Elements: An Introductory Course*. WIT Press, 1992.

[58] P. W. Partridge, C. A. Brebbia, and L. C. Wrobel. *The Dual Reciprocity Boundary Element Method*. Computational Mechanics Publications / Elsevier Applied Science, 1992.

[59] J. J. Aznárez. *Efectos de los fenómenos de interacción incluyendo los factores espaciales y sedimentos de fondo en la respuesta sísmica de presas bóveda*. PhD thesis, Universidad de Las Palmas de Gran Canaria – Departamento de Ingeniería Civil, Septiembre 2002.

[60] R. Gallego and J. Domínguez. Hypersingular BEM for transient elastodynamics. *International Journal for Numerical Methods in Engineering*, 39:1681–1705, 1996.

[61] J. Domínguez, M. P. Ariza, and R. Gallego. Flux and traction boundary elements without hypersingular or strongly singular integrals. *International Journal for Numerical Methods in Engineering*, 48:111–135, 2000.

[62] P. Ariza and J. Domínguez. General BE approach for three-dimensional dynamic fracture analysis. *Engineering Analysis with Boundary Elements*, 26:639–651, 2002.

[63] M. Tanaka, V. Sladek, and J. Sladek. Regularization techniques applied toboundary element methods. *Applied Mechanics Reviews*, 47:457–499, 1994.

[64] M. Guiggiani. Hypersingular formulation for boundary stress evaluation. *Engineering Analysis with Boundary Elements*, 14:169–180, 1994.

[65] M. Bonnet and M. Guiggiani. Tangential derivative of singular boundary integrals with respect to the position of collocation points. *International Journal for Numerical Methods in Engineering*, 41:1255–1275, 1998.

[66] R. Gallego and A. E. Marínez-Castro. Boundary integral equation for tangential derivative of flux in laplace and helmholtz equations. *International Journal for Numerical Methods in Engineering*, 66:334–363, 2006.

[67] A. J. Burton and G. F. Miller. The application of integral equation methods to the numerical solution of some exterior boundary-value problems. *Proceedings of the Royal Society of London*, 323:201–210, 1971.

[68] G. Bonnet. Basic singular solutions for a poroelastic medium in the dynamic range. *Journal of Acoustical Society of America*, 82(5):1758–1762, 1987.

[69] A. H.-D. Cheng, T. Badmus, and D. E. Beskos. Integral equation for dynamic poroelasticity in frequency domain with BEM solution. *Journal of Engineering Mechanics*, 117(5):1136–1157, 1991.

[70] J. Domínguez. An integral formulation for dynamic poroelasticity. *Journal of Applied Mechanics*, 58:588–591, 1991.

[71] G. D. Manolis and D. E. Beskos. Integral formulation and fundamental solutions of dynamic poroelasticity and thermoelasticity. *Acta Mechanica*, 76(1-2):89–104, 1989.

[72] M. Messner and M. Schanz. A regularized collocation boundary element method for linear poroelasticity. *Computational Mechanics*, 47:669–680, 2011.

[73] M. Messner and M. Schanz. A symmetric Galerkin boundary element method for 3d linear poroelasticity. *Acta Mechanica*, 223:1751–1768, 2012.

[74] J. Domínguez. Boundary element approach for dynamic poroelastic problems. *International Journal for Numerical Methods in Engineering*, 35:307–324, 1992.

[75] M. Guiggiani and A. Gigante. A general algorithm for muldimensional cauchy principal value integrals in the boundary element method. *Transactions of the ASME*, 57:906–915, 1990.

[76] M. Guiggiani, G. Krishnasamy, T.J. Rudolphi, and F.J. Rizzo. A general algorithm for the numerical solution of hypersingular boundary integral equations. *Journal of Applied Mechanics*, 59:604–614, 1992.

[77] P. A. Martin, F. J. Rizzo, and T. A. Cruse. Smoothness-relaxation strategies for singular and hypersingular integral equations. *International Journal for Numerical Methods in Engineering*, 42:885–906, 1998.

[78] P. C. Ricardella. An implementation of the boundary integral technique for planar problems in elasticity and elastoplasticity. Technical Report SM-73-10, Department of Mechanical. Engineering, Carnegie Mellon University, 1973.

[79] V. Mantič and F. París. Existence and evaluation of the two free terms in the hypersingular boundary integral equation of potential theory. *Engineering Analysis with Boundary Elements*, 16:253–260, 1995.

[80] V. Mantič. A new formula for the C-matrix in the Somigliana identity. *Journal of Elasticity*, 33:191–201, 1993.

[81] J. M. Xu and C. A. Brebbia. Optimum positions for the nodes in discontinuous boundary elements. In M. Tanaka and C. A. Brebbia, editors, *Boundary Elements VIII*, pages 751–767. Springer-Verlag, 1986.

[82] S. Marburg. *Computational Acoustics of Noise Propagation in Fluids - Finite and Boundary Element Methods*, chapter 11. Discretization Requirements: How many Elements per Wavelength are Necessary?, pages 309–332. Springer, 2008.

[83] V. Sladek and J. Sladek. Why use double nodes in BEM? *Engineering Analysis with Boundary Elements*, 8(2):109–112, 1991.

[84] S.R. Subia, M.S. Ingber, and A.K. Mitra. A comparison of the semidiscontinuous element and multiple node with auxiliary boundary collocation approaches for the boundary element method. *Engineering Analysis with Boundary Elements*, 15(1):19 – 27, 1995.

[85] M. Costabel and E. P. Stephan. On the convergence of collocation methods for boundary integral equations on polygons. *Mathematics of Computation*, 49(180):461–478, 1987.

[86] S. Amini and S. M. Kirkup. Solution of helmholtz equation in the exterior domain by eleelement boundary integral methods. *Journal of Computational Physics*, 118:208–221, 1995.

[87] S. Ahmad, B. M. Irons, and O. C. Zienkiewicz. Analysis of thick and thin shell structures by curved finite elements. *International Journal for Numerical Methods in Engineering*, 2(3):419–451, 1970.

[88] K. J. Bathe. *Finite Element Procedures*. Prentice Hall, 1996.

[89] H. Parish. A critical survey of the 9-node degenerated shell element with special emphasis on thin shell application and reduced integration. *Computer Methods in Applied Mechanics and Engineering*, 20:323–350, 1979.

[90] H. Stolarski and T. Belytschko. Membrane locking and reduced integration for curved elements. *Journal of Applied Mechanics*, 49:172–176, 1982.

[91] E. Oñate. *Structural Analysis with the Finite Element Method. Linear Statics*, volume 2: Beams, Plates and Shells. CIMNE - Springer, 2013.

[92] H. T. Y. Yang, S. Saigal, A. Masud, and R. K. Kapania. A survey of recent shell finite elements. *International Journal for Numerical Methods in Engineering*, 47:101–127, 2000.

[93] K. J. Bathe and E. N. Dvorkin. A formulation of general shell elements – the use of mixed interpolation of tensorial components. *International Journal for Numerical Methods in Engineering*, 22:697–722, 1986.

[94] M. L. Bucalem and K. J. Bathe. Higher-order MITC general shell elements. *International Journal for Numerical Methods in Engineering*, 36:3729–3754, 1993.

[95] E. N. Dvorkin and K. J. Bathe. A continuum mechanics based four-node shell element for general non-linear analysis. *Engineering Computations*, 1:77–88, 1984.

[96] P. S. Lee and K. J. Bathe. Development of MITC isotropic triangular shell finite elements. *Computers and Structures*, 82:945–962, 2004.

[97] A. M. Kaynia and E. Kausel. Dynamic stiffness and seismic response of pile groups. Research Report R83-03, Massachusetts Institute of Technology, Cambridge, MA, 1982.

[98] C. A. Brebbia, J. C. F. Telles, and L. C. Wrobel. *Boundary Element Techniques*. Springer-Verlag, 1984.

[99] T. A. Cruse and J. R. Osias. Issues in merging the finite element and boundary integral equation methods. *Mathematical and Computer Modelling*, 15(3–5):103–118, 1991.

[100] T. Belytschko, H. S. Chang, and Y. Y. Lu. A variationally coupled finite element - boundary element method. *Computers & Structures*, 33:17–20, 1989.

[101] Y. Y. Lu, T. Belytschko, and W. K. Liu. A variationally coupled FE-BE method for elasticity and fracture mechanics. *Computer Methods in Applied Mechanics and Engineering*, 85:21–37, 1991.

[102] T. Belytschko and Y. Y. Lu. Singular integration in variationally coupled FE-BE method. *Journal of Engineering Mechanics*, 117:820–835, 1991.

[103] R. Gallego and J. Suárez. Solution of inverse problems by boundary integral equations without residual minimization. *International Journal of Solids and Structures*, 37:5629–5652, 2000.

[104] R. Gallego and J. Suárez. Numerical solution of the variation boundary integral equation for inverse problems. *International Journal for Numerical Methods in Engineering*, 49:501–518, 2000.

[105] G. Rus. *Numerical methods for nondestructive identification of defects*. PhD thesis, University of Granada, 2001.

[106] G. Rus and R. Gallego. Boundary integral equation for inclusion and cavity shape sensitivity in harmonic elastodynamics. *Engineering Analysis with Boundary Elements*, 29:77–91, 2005.

[107] G. Rus and R. Gallego. Hypersingular shape sensitivity boundary integral equation for crack identification under harmonic elastodynamic excitation. *Computational Methods in Applied Mechanics and Engineering*, 196:2596–2618, 2007.

[108] J. Nocedal and S. J. Wright. *Numerical optimization*. Springer Series in Operations Research. Springer, 1999.

[109] D. E. Goldberg. *Genetic Algorithms in Search, Optimization and Machine Learning*. Addison-Wesley Longman Publishing Co., Inc., Boston, MA, USA, 1st edition, 1989.

[110] K. Deb. *Multi-Objective Optimization using Evolutionary Algorithms*. John Wiley & Sons, 2001.

[111] S. Arnout. *Optimization of shell and truss structures based on size and shape parameterization*. PhD thesis, Katholieke Universiteit Leuven – Faculty of Engineering Science, 2012.

[112] K. K. Choi and N. H. Kim. *Structural Sensitivity Analysis and Optimization 1: Linear Systems*. Mechanical Engineering Series. Springer, 2005.

[113] F. van Keulen, R. T. Haftka, and N. H. Kim. Review of options for structural design sensitivity analysis. Part 1: Linear systems. *Computational Methods in Applied Mechanics and Engineering*, 194:3213–3243, 2005.

[114] J. S. Arora. An exposition of the material derivative approach for structural shape sensitivity analysis. *Computer Methods in Applied Mechanics and Engineering*, 105(1):41–62, 1993.

[115] J. C. Townsend, J. A. Samareh, R. P. Weston, and W. E. Zorumski. Integration of a CAD system into an MDO framework. TM-1998-207672, NASA, 1998.

[116] J. A. Samareh. A survey of shape parameterization techniques. CP-1999-209136, NASA, 1999.

[117] K. K. Choi and N. H. Kim. *Structural Sensitivity Analysis and Optimization 2: Nonlinear Systems and Applications*. Mechanical Engineering Series. Springer, 2005.

[118] M. R. Barone and D. A. Caulk. Optimal arrangement of holes in a two-dimensional heat conductor by a special boundary integral method. *International Journal for Numerical Methods in Engineering*, 18:675–685, 1982.

[119] R. A. Meric. Boundary integral equation and conjugate gradient methods for optimal boundary heating of solids. *International Journal of Heat and Mass Transfer*, 26:261–268, 1983.

[120] R. A. Meric. Boundary element methods for optimization of distributed parameter systems. *International Journal for Numerical Methods in Engineering*, 20:1291–1306, 1984.

[121] R. A. Meric. Optimal loading of solids by the boundary element method. *International Journal of Engineering Science*, 23:1101–1111, 1985.

[122] C.A. Mota Soares, H. C. Rodrigues, and K. K. Choi. Shape optimal structural design using boundary elements and minimum compliance techniques. *Journal of Mechanisms, Transmissions, and Automation in Design*, 106:518–523, 1984.

[123] J. H. Kane and S. Saigal. Design-sensitivity analysis of solids using bem. *Journal of Engineering Mechanics*, 114:1703–1722, 1988.

[124] M. R. Barone and R. J. Yang. Boundary integral equations for recovery of design sensitivities in shape optimization. *AIAA Journal*, 26:589–594, 1988.

[125] M. R. Barone and R. J. Yang. A boundary element approach for recovery of shape sensitivities in three-dimensional elastic solids. *Computer Methods in Applied Mechanics and Engineering*, 74:69–82, 1989.

[126] R. Aithal and S. Saigal. Adjoint structure approach for shape-sensitivity analysis using bem. *Journal of Engineering Mechanics*, 116:2663–2680, 1990.

[127] R. Aithal and S. Saigal. Shape sensitivity analysis in thermal problems using bem. *Engineering Analysis with Boundary Elements*, 15:115–120, 1995.

[128] S. C. Mellings and M. H. Aliabadi. Dual boundary element formulation for inverse potential problems in crack identification. *Engineering Analysis with Boundary Elements*, 12:275–281, 1993.

[129] S. C. Mellings and M. H. Aliabadi. Flaw identification using the boundary element method. *International Journal for Numerical Methods in Engineering*, 38:399–419, 1995.

[130] N. Nishimura and S. Kobayashi. Determination of cracks having arbitrary shapes with the boundary integral equation method. *Engineering Analysis with Boundary Elements*, 15:189–195, 1994.

[131] M. Bonnet. BIE and material differentiation applied to the formulation of obstacle inverse problems. *Engineering Analysis with Boundary Elements*, 15:121–136, 1995.

[132] M. Bonnet. Regularized BIE formulations for first- and second-order shape sensitivity of elastic fields. *Computers & Structures*, 56:799–811, 1995.

[133] M. Bonnet. Boundary element based formulations for crack shape sensitivity analysis. *Engineering Analysis with Boundary Elements*, 25:347–362, 2001.

[134] M. Bonnet, T. Burczynski, and M. Nowakowski. Sensitivity analysis for shape perturbation of cavity or internal crack using BIE and adjoint variable approach. *International Journal of Solids and Structures*, 39:2365–2385, 2002.

[135] M. Bonnet. Differentiability of strongly singular and hypersingular boundary integral formulations with respect to boundary perturbations. *Computational Mechanics*, 19:240–246, 1997.

[136] M. Bonnet. *Boundary Integral Equation Methods for Solids and Fluids*. Wiley, 1999.

[137] C. A. Brebbia and J. Domínguez. *Boundary Elements - An Introductory Course*. WIT Press - Computational Mechanics Publications, 1989.

[138] M. A. Khayat and D. R. Wilton. An improved transformation and optimized sampling scheme for the numerical evaluation of singular and near-singular potentials. *IEEE Antennas and Wireless Propagation Letters*, 7:377–380, 2008.

[139] J. Rong, L. Wen, and J. Xiao. Efficiency improvement of the polar coordinate transformation for evaluating bem singular integrals on curved elements. *Engineering Analysis with Boundary Elements*, 38:83–93, 2014.

[140] A. Tadeu, J. António, L. Godinho, and P. Amado. Simulation of sound absorption in 2d thin elements using a coupled BEM/TBEM. *Journal of Sound and Vibration*, 331:2386–2403, 2012.

[141] S. G. Mogilevskaya and D. V. Nikolskiy. The use of complex integral representations for analytical evaluation of three-dimensional BEM integrals – potential and elasticity problems. *Quarterly Journal of Mechanics and Applied Mathematics*, 67(3):505–523, 2014.

[142] F. Pourahmadian and S. G. Mogilevskaya. Complex variables-based approach for analytical evaluation of boundary integral representations of three-dimensional acoustic scattering. *Engineering Analysis with Boundary Elements*, 53:9–17, 2015.

[143] P. J. Davis and P. Rabinowitz. *Methods of Numerical Integration*. Academic Press, 1984.

[144] A. Stroud and D. Secrest. *Gaussian Quadrature Formulas*. Prentice Hall, 1966.

[145] P. Sylvester. Symmetric quadrature formulae for simplexes. *Mathematics of Computation*, 24:95–100, 1969.

[146] G. R. Cowper. Gaussian quadrature formulas for triangles. *International Journal for Numerical Methods in Engineering*, 7:405–408, 1973.

[147] J. N. Lyness and D. Jespersen. Moderate degree symmetric quadrature rules for the triangle. *Journal of the Institute of Mathematics and its Applications*, 15:19–32, 1975.

[148] D. A. Dunavant. High degree efficient symmetrical gaussian quadrature rules for the triangle. *International Journal for Numerical Methods in Engineering*, 21:1129–1148, 1985.

[149] S. Wandzura. Symmetric quadrature rules on a triangle. *Computer and Mathematics with Applications*, 45:1829–1840, 2003.

[150] J.C. Lachat and J.O. Watson. Effective numerical treatment of boundary integral equations: a formulation for three-dimensional elastostatics. *International Journal for Numerical Methods in Engineering*, 10:991–1005, 1976.

[151] L. Jun, G. Beer, and J.L. Meek. Efficient evaluation of integrals of order $1/r$, $1/r^2$ and $1/r^3$ using Gauss quadrature. *Engineering Analysis*, 2(3):118–123, 1985.

[152] D. Elliot and P. R. Johnston. Error analysis for a sinh transformation used in evaluating nearly singular boundary element integrals. *Journal of Computational and Applied Mathematics*, 203:103–124, 2007.

[153] G. Karami and D. Derakhshan. An efficient method to evaluate hypersingular and supersingular integrals in boundary integral equations analysis. *Engineering Analysis with Boundary Elements*, 23:317–326, 1999.

[154] S. Mukherjee. CPV and HFP integrals and their applications in the boundary element method. *International Journal of Solids and Structures*, 37:6623–6634, 2000.

[155] Xiao-Wei Gao. An effective method for numerical evaluation of general 2D and 3D high order singular boundary integrals. *Computer Methods in Applied Mechanics and Engineering*, 199:2856–2864, 2010.

[156] J.C.F. Telles. A self-adaptive co-ordinate transformation for efficient numerical evaluation of general boundary element integrals. *International Journal for Numerical Methods in Engineering*, 24:959–973, 1987.

[157] P. R. Johnston. Application of sigmoidal transformations to weakly singular and near-singular boundary element integrals. *International Journal for Numerical Methods in Engineering*, 45:1333–1348, 1999.

[158] P. R. Johnston and D. Elliot. Transformations for evaluating singular boundary element integrals. *Journal of Computational and Applied Mathematics*, 146:231–251, 2002.

[159] J. J. Granados and R. Gallego. Regularization of nearly hypersingular integrals in the boundary element method. *Engineering Analysis with Boundary Elements*, 25:165–184, 2001.

[160] S. Marburg. Six boundary elements per wavelewave: is that enough? *Journal of Computational Acoustics*, 10(1):25–51, 2002.

[161] J.C.F. Telles and R.F. Oliveira. Third degree polynomial transformation for boundary element integrals: further improvements. *Engineering Analysis with Boundary Elements*, 13:135–141, 1994.

[162] H. Ma and N. Kamiya. Distance transformation for the numerical evaluation of near singular boundary integrals with various kernels in boundary element method. *Engineering Analysis with Boundary Elements*, 26:329–339, 2002.

[163] R. S. Barsoum. Application of quadratic isoparametric finite elements in linear fracture mechanics. *International Journal of Fracture*, 10(4):603–605, 1974.

[164] M. G. Duffy. Quadrature over a pyramid or cube of integrands with a singularity at a vertex. *SIAM Journal on Numerical Analysis*, 19(6):1260–1262, 1982.

[165] H. B. Li, G. M. Han, and H. A. Mang. A new method for evaluating singular integrals in stress analysis of ssolid by the boundary element method. *International Journal for Numerical Methods in Engineering*, 33:2071–2098, 1985.

[166] D. G. Anderson. Gaussian quadrature fformula for $\int_0^1 -\ln(x)f(x)\,\mathrm{d}x$. *Mathematics of Computation*, 19(91):477–481, 1965.

[167] J. A. Crow. Quadrature of integrands with a logarithmic singularity. *Mathematics of Computation*, 60(201):297–301, 1993.

[168] R. N. L. Smith. Direct gauss formulae for logarithmic singularities on isoparametric elements. *Engineering Analysis with Boundary Elements*, 24:161–167, 2000.

[169] M. Cristescu and G. Laubignac. Gaussian quadrature formulas for functions with singularities in 1/r over triangles and quadrangles. In *Recent Advances in Boundary Element Methods*, 1978.

[170] C. Schwab and W. L. Wendland. On numerical cubatures of singular surface integrals in boundary element methods. *Numerische Mathematik*, 62:343–369, 1992.

[171] R. N. L. Smith. A boundary element method for curved crack problems in two dimensions. In C. A. Brebbia, editor, *Proceedings of the 4th International Conference on Boundary Elements*, pages 472–484. Springer, 1982.

[172] W. Gautschi. OPQ: A MATLAB suite of programs for generating orthogonal polynomials and related quadrature rules. `https://www.cs.purdue.edu/archives/2002/wxg/codes/OPQ.html`, 2002.

[173] W. Gautschi. *Orthogonal Polynomials: Computation and Approximation*. Clarendon Press, Oxford, 2004.

[174] P. Partheymüler, R. A. Bialecki, and G. Kuhn. Self-adapting algorithm for evaluation of weakly singular integrals arising in the boundary element method. *Engineering Analysis with Boundary Elements*, 14:285–292, 1994.

[175] K. Hayami. *A Projection Transformation Method for Nearly Singular Surface Boundary Element Integrals*, volume 73. Springer-Verlag, 1992.

[176] H. Fletcher and W. A. Munson. Loudness, its definition, measurement and calculation. *Journal of the Acoustical Society of America*, 5:82–108, 1933.

[177] ISO 2631-1:1997: Mechanical vibration and shock – evaluation of human exposure to whole-body vibration.

[178] D. Hothersall, S. Chandler-Wilde, and M. Hajmirzae. Efficiency of single noise barriers. *Journal of Sound and Vibration*, 146(2):303–322, 1991.

[179] D. Hothersall, D.H. Crombie, and S.N. Chandler-Wilde. The performance of t-profile and associated noise barriers. *Applied Acoustics*, 32:269–287, 1991.

[180] D. Crombie, D. Hothersall, and S. Chandler-Wilde. Multiple-edge noise barriers. *Applied Acoustics*, 44(4):353–367, 1995.

[181] G. Watts and P. Morgan. Acoustic performance of an interference-type noise barrier profile. *Applied Acoustics*, 49:1–16, 1996.

[182] T. Okubo and K. Fujiwara. Efficiency of a noise barrier on the ground with an acouacoustic soft cylindrical edge. *Journal of Sound and Vibration*, 216:771–790, 1998.

[183] M. Monazzam and Y. Lam. Performance of profiled single noise barriers covered with quadratic residue diffusers. *Applied Acoustics*, 66:709–730, 2005.

[184] R.D. Woods. Screening of surface waves in soils. *Journal of the Soil Mechanics and Foundation Division, Proceedings of the ASCE*, 94(SM4):951–979, 1968.

[185] P. H. Tsai and T. S. Chang. Effects of open trench siding on vibration-screening effectiveness using the two-dimensional boundary element method. *Soil Dynamics and Earthquake Engineering*, 29:865–873, 2009.

[186] D. E. Beskos, B. Dasgupta, and I. G. Vardoulakis. Vibration isolation using open or filled trenches. Part 1: 2-D homogeneous soil. *Computational Mechanics*, 1:43–63, 1986.

[187] S. Ahmad and T. M. Al-Hussaini. Simplified design for vibration screening by open and in-filled trenches. *Journal of Geotechnical Engineering*, 117:67–88, 1991.

[188] A. Saikia. Numerical study on screening of surface waves using a pair of softer backfilled trenches. *Soil Dynamics and Earthquake Engineering*, 65:206–213, 2014.

[189] A. Dijckmans, A. Ekblad, A. Smekal, G. Degrande, and G. Lombaert. A sheet piling wall as a wave barrier for train induced vibrations. In M. Papadrakakis, V. Papadopoulos, and V. Plevris, editors, *4 th ECCOMAS Thematic Conference on Computational Methods in Structural Dynamics and Earthquake Engineering*, Kos Island, Greece, 12–14 June 2013, 2013.

[190] J. Avilés and F. J. Sánchez-Sesma. Foundation isolation from vibrations using piles as barriers. *Journal of Engineering Mechanics*, 114:1854–1870, 1988.

[191] S. E. Kattis, D. Polyzos, and D. E. Beskos. Vibration isolation by a row of piles using a 3-D frequency domain BEM. *International Journal for Numerical Methods in Engineering*, 46:713–728, 1999.

[192] P. Jean. The effect of structural elasticity on the efficiency of noise barriers. *Journal of Sound and Vibration*, 237(1):1–21, 2000.

[193] R.W. Clough and J. Penzien. *Dynamics of Structures*. Computers and Structures, Incorporated, 2003.

[194] R. Seznec. Diffraction of sound around a barrier: use of the boundary elements technique. *Journal of Sound and Vibration*, 73:195–209, 1980.

[195] C. H. Lin, V. W. Lee, and M. D. Trifunac. The reflection of plane waves in a poroelastic half-space saturated with inviscid fluid. *Soil Dynamics and Earthquake Engineering*, 25:205–223, 2005.

[196] M. K. Kassir and J. Xu. Interaction functions of a rigid strip bonded to saturated elastic half-space. *International Journal of Solids and Structures*, 24(9):915–936, 1988.

[197] MATLAB. *version 8.3.0 (R2014a)*. The MathWorks Inc., Natick, Massachusetts, 2014.

[198] A. H. G. Rinnooy Kan and G. T. Timmer. Stochastic global optimization methods. Part I: clustering methods. *Mathematical Programming*, 39:27–56, 1987.

[199] C. Van hoorickx, O. Sigmund, M. Schevenels, B. S. Lazarov, and G. Lombaert. Topology optimization of two-dimensional elastic wave barriers. *Journal of Sound and Vibration*, 376:95–111, 2016.

[200] G.T. Houlsby and B.W. Byrne. Suction caisson foundations for offshore wind turbines and anemometer masts. *Wind Engineering*, 24:249–255, 2000.

[201] Design of offshore wind turbine structures.

[202] G.T. Houlsby, L.B. Ibsen, and B.W. Byrne. Suction caissons for wind turbines. In S. Gourvenec and M. Cassidy, editors, *Frontiers in Offshore Geotechnics: IS-FOG2005*, Perth, September 19-21 2005.

[203] A. Foglia and L.B. Ibsen. Bucket foundations: a literature review. DCE Technical Reports 176, Department of Civil Engineering, Aalborg University, 2014.

[204] R.S. Kourkoulis, P.C. Lekkakis, F.M. Gelagotia, and A.M. Kaynia. Suction caisson foundations for offshore wind turbines subjected to wave and earthquake loading: effect of soil–foundation interface. *Géotechnique*, 64:171–185, 2014.

[205] J. L. Buchanan and R. P. Gilbert. Transmission loss in the far field over a one-layer seabed assuming the biot sediment model. *Journal of Applied Mathematics & Mechanics*, 2:121–135, 1997.

[206] L. Arany, S. Bhattacharya, J. Macdonald, and S. J. Hogan. Simplified critical mudline bending moment spectra of offshore wind turbine support structures. *Wind Energy*, 18:2171–2197, 2015.

[207] P. Ariza. *Modelo numérico con representación integral de tensiones en el contorno, para prproblem de mecánica de la fractura*. PhD thesis, Universidad de Sevilla – Departamento de Mecánica de Medios Continuos, Teoría de Estructuras e Ingeniería del Terreno, Enero 2002.

[208] J. P. Doherty and A. J. Deeks. Elastic response of circular footings embedded in a non-homogeneous half-space. *Géotechnique*, 53:1–11, 2003.

[209] J. P. Doherty, G. T. Houlsby, and A. J. Deeks. Stiffness of flexible caisson foundations embedded in nonhomogeneous elastic soil. *Journal of Geotechnical and Geoenvironmental Engineering*, 131(12):1498–1508, 2005.

[210] S. J. Feng, Z. L. Chen, and H. X. Chen. Effects of multilayered porous sediment on earthquake-induced hydrodynamic response in reservoir. *Soil Dynamics and Earthquake Engineering*, 94:47–59, 2017.

[211] P. Phurkhao. Wave diffraction by a line of finite crack in a saturated two-phase medium. *International Journal of Solids and Structures*, 50:1044–1054, 2013.

[212] P. Phurkhao. Compressional waves in fluid-saturated porous solid containing a penny-shaped crack. *International Journal of Solids and Structures*, 50:4292–4304, 2013.

[213] M. Abramowitz and I.A. Stegun. *Handbook of Mathematical Functions: with Formulas, Graphs,and Mathematical Tables.* Number 55 in Applied Mathematics. New York, Dover Publications, 1964.

[214] T. A. Cruse. Numerical solutions in three dimensional elastostatics. *International Journal of Solids and Structures*, 5:1259–1274, 1969.

[215] H. Deresiewicz. The effect of boundaries on wave propagation in a liquid-filled porous solid: IV. Surface waves in a half-space. *Bulletin of the Seismological Society of America*, 52(3):627–638, 1962.

[216] J. Yang. A note on Rayleigh wave velocity in saturated soils with compressible constituents. *Canadian Geotechnical Journal*, 38(6):1360–1365, 2001.